frontiers | Research Topics

Advanced cooperative control and optimization strategies for integrated energy systems

Edited by
Rui Wang, Dehao Qin, Wei Hu, Franklin Chang and Jiawei Wang

Published in
Frontiers in Energy Research

ISSN 1664-8714
ISBN 978-2-83251-522-8
DOI 10.3389/978-2-83251-522-8

About Frontiers

Frontiers is more than just an open access publisher of scholarly articles: it is a pioneering approach to the world of academia, radically improving the way scholarly research is managed. The grand vision of Frontiers is a world where all people have an equal opportunity to seek, share and generate knowledge. Frontiers provides immediate and permanent online open access to all its publications, but this alone is not enough to realize our grand goals.

Frontiers journal series

The Frontiers journal series is a multi-tier and interdisciplinary set of open-access, online journals, promising a paradigm shift from the current review, selection and dissemination processes in academic publishing. All Frontiers journals are driven by researchers for researchers; therefore, they constitute a service to the scholarly community. At the same time, the *Frontiers journal series* operates on a revolutionary invention, the tiered publishing system, initially addressing specific communities of scholars, and gradually climbing up to broader public understanding, thus serving the interests of the lay society, too.

Dedication to quality

Each Frontiers article is a landmark of the highest quality, thanks to genuinely collaborative interactions between authors and review editors, who include some of the world's best academicians. Research must be certified by peers before entering a stream of knowledge that may eventually reach the public - and shape society; therefore, Frontiers only applies the most rigorous and unbiased reviews. Frontiers revolutionizes research publishing by freely delivering the most outstanding research, evaluated with no bias from both the academic and social point of view. By applying the most advanced information technologies, Frontiers is catapulting scholarly publishing into a new generation.

What are Frontiers Research Topics?

Frontiers Research Topics are very popular trademarks of the *Frontiers journals series*: they are collections of at least ten articles, all centered on a particular subject. With their unique mix of varied contributions from Original Research to Review Articles, Frontiers Research Topics unify the most influential researchers, the latest key findings and historical advances in a hot research area.

Find out more on how to host your own Frontiers Research Topic or contribute to one as an author by contacting the Frontiers editorial office: frontiersin.org/about/contact

Advanced cooperative control and optimization strategies for integrated energy systems

Topic editors
Rui Wang — Northeastern University, China
Dehao Qin — Clemson University, United States
Wei Hu — Zhejiang University, China
Franklin Chang — Nanyang Technological University, Singapore
Jiawei Wang — Technical University of Denmark, Denmark

Citation
Wang, R., Qin, D., Hu, W., Chang, F., Wang, J., eds. (2023). *Advanced cooperative control and optimization strategies for integrated energy systems*.
Lausanne: Frontiers Media SA. doi: 10.3389/978-2-83251-522-8

Table of contents

frontiers | Frontiers in Energy Research

TYPE Editorial
PUBLISHED 18 January 2023
DOI 10.3389/fenrg.2022.1055142

Editorial: Advanced cooperative control and optimization strategies for integrated energy systems

Hu Liu[1], Rui Wang[1]* and Wei Hu[2]

[1]College of Information Science and Engineering, Northeastern University, Shenyang, China, [2]College of Mechanical and Vehicle Engineering, Hunan University, Changsha, China

KEYWORDS

integrated energy systems, distributed energy, planning and control, nonlinear control, 5G technologies

OPEN ACCESS

EDITED AND REVIEWED BY
ZhaoYang Dong,
Nanyang Technological University,
Singapore

*CORRESPONDENCE
Rui Wang,
1610232@stu.neu.edu.cn

SPECIALTY SECTION
This article was submitted to Smart Grids, a section of the journal Frontiers in Energy Research

RECEIVED 27 September 2022
ACCEPTED 27 October 2022
PUBLISHED 18 January 2023

CITATION
Liu H, Wang R and Hu W (2023), Editorial: Advanced cooperative control and optimization strategies for integrated energy systems.
Front. Energy Res. 10:1055142.
doi: 10.3389/fenrg.2022.1055142

Editorial on the Research Topic
Advanced cooperative control and optimization strategies for integrated energy systems

With the increasingly serious problems of energy consumption and environmental pollution, the research and development of advanced energy infrastructures such as smart grids, smart transportation networks, and smart natural gas networks is extremely urgent. To this end, an integrated energy system (IES) that integrates multiple energy sources in a region and realizes coordinated planning, optimal operation, collaborative management, and complementation of multiple systems could improve resource utilization and reduce system operating costs and CO_2 emissions. Furthermore, IESs are regarded as a popular form of elastic energy utilization for future development. However, the current coordinated control and optimal strategies of integrated energy systems still have much room for improvement. Therefore, we must develop and optimize the control strategies of existing IESs to alleviate problems such as energy consumption and environmental pollution.

This Research Topic aims to explore the latest developments in this field, focusing on: 1) the distributed energy management structures and frameworks of IESs, 2) coupled mechanism modeling of IESs, 3) spatiotemporal data analysis and the cooperative control development of IESs, 4) optimal planning, operation, and control of IESs, 5) standard modeling of IESs, 6) nonlinear control and optimization of IESs, 7) the impact of cyber and physical security on the controller and optimizer of IESs, 8) the application of AI and 5G technologies on the controller and optimizer of IESs, and 9) distributed cooperative control and optimization strategies for IESs.

In recent years, with the growing popularity of electric vehicles, additional uncertainties have been added to the virtual power plant (VPP). To this end, Wensi et al. proposed a VPP economic dispatching model that considers the uncertainty factors of distributed power generation based on the classical scenario set. In this paper, Latin hypercube sampling combined with K-means clustering was used to generate the classical scene set; the model was solved using an improved particle swarm algorithm (PSO) that incorporated a genetic mechanism. A comparison of the classical scenario set and the general scenario set verified that the former was the optimal configuration of the VPP, significantly improving the net return of the VPP.

Considering the significant amount of data in a distributed power network and the low efficiency of communication between distributed units, Wang et al. proposed a consensus dispatch model based on multi-access edge computing (MEC) and a multi-agent system (MAS). The model solved the optimal dispatching scheme of the distributed power system by dividing the consistent variables of each unit. The established MEC-MAS–based power network communication model could provide a stable operating framework for distributed systems. This study constructed a hierarchical scheduling model consisting of edge nodes and cloud centers. The authors then divided and solved the consensus variables using the objective function of the hierarchical scheduling model; the distributed unit could optimize the unified objective under the constraints, obtaining an improved distributed grid scheduling scheme.

The broad development of integrated heat and electricity systems (IHES) has improved the energy utilization efficiency; however, it has also increased the risk of cascaded accidents and the difficulty of operation. To this end, Wang et al. proposed a method for constructing an IHES safe region considering thermodynamics based on the equivalent thermal model. In order to formulate an accurate security region (SR), a method of IHES SR construction that considers thermal dynamics was proposed. Based on the hyperplane method, an SR boundary formula was proposed. From the simulation, it was observed that this method was effective for heating system analysis. Due to the additional restrictions of the heating system, combined operation of the power system and the HS reduced the size of the SR.

The uncertainty and volatility of renewable energy generation leads to large amounts of abandoned electricity. An electricity-hydrogen coupling microgrid (EHCM) consists of a proton-exchange-membrane electrolytic cell, a liquid organic hydrogen carrier, hydrogen storage, and a proton-exchange-membrane fuel cell. This structure increases the utilization of wind and photovoltaic power. The scheduling of an EHCM is very challenging. To this end, Liu et al. proposed the optimal operation of microgrids considering the uncertainties of wind speed, light, electricity, and hydrogen coupling. An electricity-hydrogen coupling model and a hydrogen market model were constructed. The microgrid provided ancillary services to the grid while meeting hydrogen demand. The above model was solved using a two-stage optimization method involving day-ahead and intra-day time scales. The electricity-hydrogen coupling microgrid not only met the demands for hydrogen and electricity production, but also considered the application of liquid organic hydrogen carrier technology as well as the sale of oxygen, thereby improving safety and economy.

Large-scale, new energy sources such as photovoltaic power generation can reduce the original damping and inertia of a power system, resulting in oscillation of the system. Self-adaptive virtual synchronous generator (SDVSG)–controlled, grid-connected inverters can provide virtual damping and inertia to support the frequency and voltage of the grid. To combine SDVSG control with stand-alone PV systems, a mainstream solution to configure energy storage systems is required. To this end, Zhu et al. proposed a coordinated controlled, SDVSG, grid-connected photovoltaic energy storage system. An adaptive, variable-step conductance increment method was adopted to realize maximum power point tracking of the photovoltaic array, avoiding oscillation and untimely tracking near the maximum power point. A variable-domain, fuzzy logic, DC/DC control converter was designed for the grid connection of photovoltaic systems to overcome large overshoot and to rapidly obtain the required reference voltage. An adaptive virtual synchronous generator control strategy was also developed for the photovoltaic energy storage system's power supply to provide variable damping and inertia and to improve the stability of the power supply. The coordinated control strategy was proposed to realize the grid-connected power balance function, improving the generation efficiency and stabilizing the DC bus voltage.

Author contributions

All authors listed have made a substantial, direct, and intellectual contribution to the work and approved it for publication.

Conflict of interest

The authors declare that the research was conducted in the absence of any commercial or financial relationships that could be construed as a potential conflict of interest.

Publisher's note

frontiers
in Energy Research

ORIGINAL RESEARCH
published: 25 February 2022
doi: 10.3389/fenrg.2022.855649

UKF-Based Parameter Estimation and Identification for Permanent Magnet Synchronous Motor

***Zhiwei Wang*[1]*, Xin Liu*[1]*, Wenzhuo Wang*[1]*, Yunling Lv*[2]**, Bo Yuan*[1]*, Wujing Li*[1]*, Qiufang Li*[1]*, Shijie Wang*[1]*, Qianchang Chen*[1] *and Yi Zhang*[3]**

[1]Northwest Branch of State Grid Corporation of China, Xi'an, China, [2]The School of Electrical Engineering, Xi'an University of Technology, Xi'an, China, [3]The Nari Technology Co., Ltd., Nanjing, China

The accuracy of rotor position estimation determines the performance of the sensorless control system of a permanent magnet synchronous motor. In order to realize the accurate control of rotor position and speed, it is necessary to identify the motor parameters. Modeling and simulation of the state estimation are investigated for a permanent magnet synchronous motor with parameter identification based on the unscented Kalman filter (UKF) in this article. Based on the mathematical model of the motor, the unscented Kalman filter is used to identify the rotor flux and quadrature axis inductance simultaneously, and the identified parameters are used to update the motor model in the sensorless vector control algorithm. The simulation results show that the unscented Kalman filter can converge to the real value in a short time with small errors. It can follow the changes of motor parameters well and achieve high-precision speed and position estimation.

Keywords: permanent magnet synchronous motor (PMSM), unscented Kalman filter (UKF), speed estimation, parameter estimate, parameter identification

Edited by:
Rui Wang,
Northeastern University, China

Reviewed by:
Songsong Cheng,
Anhui University, China
Chenghao Sun,
Northeastern University, China

Correspondence:
Yunling Lv
lvyunling@stu.xaut.edu.cn

Specialty section:
This article was submitted to
Smart Grids,
a section of the journal
Frontiers in Energy Research

Received: *15 January 2022*
Accepted: *25 January 2022*
Published: *25 February 2022*

Citation:
Wang Z, Liu X, Wang W, Lv Y, Yuan B, Li W, Li Q, Wang S, Chen Q and Zhang Y (2022) UKF-Based Parameter Estimation and Identification for Permanent Magnet Synchronous Motor.
Front. Energy Res. 10:855649.
doi: 10.3389/fenrg.2022.855649

INTRODUCTION

Permanent magnet synchronous motor (PMSM) has been widely used in the fields of new energy vehicles, power generation, and servo drive due to its advantages of large starting torque, high operation efficiency, high power density, and low failure rate (Chen et al., 2014; Chen et al., 2019; Cui et al., 2020; Wang et al., 2021). In the traditional vector control system, sensors are usually used to obtain rotor speed and position information; but in practical application, the existence of sensors increases the motor volume and system cost, and it is difficult to install and maintain in some harsh environments, which reduces the reliability of the system (Pan and Gao, 2018). Therefore, the research of new control strategy to improve the performance of the PMSM control system and ensure the reliable and safe operation of PMSM has become a research hotspot in the field of motor control (Zhu et al., 2014; Cheng et al., 2015; Deng et al., 2019; He and Wu, 2019). With the development of sensorless drive technology of permanent magnet synchronous motor, many methods have been proposed to estimate the speed and position of the rotor, such as the model reference adaptive control method (Zhong and Lin, 2017; Zhong et al., 2018; Wang et al., 2020a), sliding mode observer method (Liu et al., 2016; Liang et al., 2017; Lu et al., 2021), Kalman filter algorithm (Moon and Kwon, 2016; Yang et al., 2016; Luo et al., 2019), and artificial intelligence algorithm (Fadil et al., 2015). It is worth mentioning that the UKF can be applied to a nonlinear model and has been widely used in the estimation of the rotor position and speed of the PMSM drive system (An and Hameyer, 2014; Zhou et al., 2018; Tao and Guo, 2019; Yin et al., 2019).

The accuracy of rotor position estimation determines the performance of the PMSM sensorless control system. Accurate position estimation relies on accurate motor parameters. In some cases, the parameters displayed on the motor nameplate and data manual may change due to high temperature, demagnetization, and other operating conditions in long-term operation, which will affect the control precision (Nahid-Mobarakeh et al., 2004; Wang et al., 2019; Wang et al., 2020b). Therefore, accurate parameter identification is of great significance for motor control. In the vector control system, good operation of the system depends on whether the controller design of the speed ring and current ring is reasonable (He et al., 2019), while the parameter setting of the controller of the speed ring needs to obtain the value of the permanent magnet flux chain (Cao et al., 2015), and the current loop needs to call the stator resistance and inductance value. In order to ensure the control effect as much as possible, in recent years, the parameter identification method combined with the control of sensorless has been widely concerned and studied.

At present, PMSM parameter identification technology can be divided into three categories: 1) frequency-domain identification; 2) time-domain identification, such as the recursive least square method (RLS), unscented Kalman filter (UKF), and model reference adaptive method; and 3) artificial intelligence methods, such as neural network identification and genetic algorithm,. Comparing the abovementioned methods, it is found that although the frequency-domain identification is relatively mature, it requires strict input signal and cannot reflect the nonlinearity in the dynamic process. The recursive least square method needs to use the derivative of the objective function to the motor parameters in the optimization process, which is sensitive to the measurement noise and speed fluctuation. The model reference adaptive method can effectively estimate the rotor position, but the premise is to establish an accurate mathematical model (Kyoon, 2017). The research on the identification method based on artificial neural network is not mature in theory and needs the support of special hardware. Therefore, it is difficult to achieve satisfactory results in the actual system with these methods.

The UKF is one of the effective methods to estimate the parameters of PMSM, which is widely used in sensorless PMSM systems. The UKF is based on unscented transformation (UT). For the nonlinear model, the conventional processing method is EKF, and many scholars have used EKF to estimate the motor state. EKF is the Taylor expansion of the model function of a highly complex nonlinear system and the first-order linear truncation of the expansion. In this way, the model can be transformed into a linear problem processed by using a computer and then the Kalman filter. Compared with the approximation of nonlinear function, the approximation of Gaussian distribution is much simpler. The UKF carries out UT transformation near the estimation point, so that the mean and covariance of the obtained sampling point set match the original statistical characteristics (Moon and Kwon, 2016). Then, the nonlinear mapping of these sampling point sets is directly carried out to eliminate the error caused by the linearization of extended Kalman filter (EKF) algorithm, which not only realizes the accurate estimation of rotor speed and position but also accurately estimates the parameters of the motor. It has the characteristics of simple method and good system stability and can effectively improve the control accuracy of the motor. The UKF overcomes the noise sensitivity of the least square method to some extent, which can jointly estimate the states and parameters of PMSM.

In this article, considering the influence of motor parameters on the rotor position, a parameter identification method of permanent magnet synchronous motor is proposed based on the UKF. The main contributions of this article can be outlined as follows.

(1) Based on the analysis of the mathematical model of PMSM in a static coordinate system, this article investigates a state observer with the unscented Kalman filter in the sensorless control of PMSM. It not only estimates the speed and position of the motor but also realizes the identification of motor inductance L_d and L_q and flux linkage ψ_f.
(2) The resistance R_s changes under the influence of temperature, which will affect the identification results. In this article, we treat the influence of temperature and other factors as the state noise of the motor. The inductance and flux linkage are identified to ensure that the steady-state error is smaller than that obtained in the study of Moon and Kwon, 2016, and Zhou et al., 2018.
(3) The parameter identification results can be used for parameter configuration of the PMSM control system. This article provides a solution to improve the performance of the PMSM control system via the UKF and verifies the superiority of this method in state estimation.

The rest of this article is organized as follows. In *Mathematical Model of PMSM*, we present the mathematical model of PMSM. In *Main Results*, we analyze the principle of the UKF control scheme and present the main results. A simulation result is used to verify the proposed method in *The Simulation Case*. Finally, *Conclusion* concludes this article.

MATHEMATICAL MODEL OF PMSM

PMSM is a nonlinear and strong coupled complex system. It is very difficult to study and control the motor by using the mathematical model in a three-phase coordinate system. However, if we use the mathematical model of a two-phase coordinate system to study it, it will be much simpler. The stator current of the motor can be divided into two components in the two-phase coordinate system. The control of the two components can achieve the effect of controlling the motor. During the research and analysis of the PMSM control system, the first step is to build the mathematical model of the system. In different coordinate systems, there are different mathematical models. It is very important to select the appropriate model for different operating environments.

PMSM has the characteristics of being multivariable, strong coupling, and nonlinearity. In order to achieve good speed regulation performance, it is necessary to realize the approximate decoupling of the control object. Therefore, the mathematical model is established in the $\alpha\beta$-axis rotating coordinate system to analyze the performance of PMSM. The voltage equation of PMSM in the $\alpha\beta$-axis rotating coordinate system is as follows:

$$\begin{cases} u_\alpha = R_s i_\alpha + \dfrac{d\psi_\alpha}{dt}; \\ u_\beta = R_s i_\beta + \dfrac{d\psi_\beta}{dt}. \end{cases} \tag{1}$$

The flux linkage equation is

$$\begin{cases} \psi_\alpha = Li_\alpha + \psi_f \cos\theta; \\ \psi_\beta = Li_\beta + \psi_f \sin\theta. \end{cases} \tag{2}$$

The electromagnetic torque equation is

$$T_e = p_n [\psi_\alpha i_\beta - \psi_\beta i_\alpha]. \tag{3}$$

The mechanical motion equation is

$$\frac{d\omega_e}{dt} = \frac{p_n}{J}(T_e - T_l - B\omega_e). \tag{4}$$

Here, u_α and u_β are the voltage of α and β axes, respectively, i_α and i_β are the current of α and β axes, respectively, ψ_α and ψ_β are the flux of α and β axes, respectively, L_α and L_β are the inductance of α and β axes respectively, R_s is the stator resistance, ω_e is the rotor angular speed, ψ_f is the rotor flux, p_n is the pole number of the motor, T_e is the electromagnetic torque, T_l is the load torque, J is the moment of inertia, and B is the friction coefficient. According to **Eqs. 1–4**, the state equation of PMSM can be written as

$$\begin{cases} \dfrac{di_\alpha}{dt} = -\dfrac{R_s}{L} i_\alpha + \omega_e \dfrac{\psi_f}{L}\sin\theta + \dfrac{u_\alpha}{L}; \\ \dfrac{di_\beta}{dt} = -\dfrac{R_s}{L} i_\beta - \omega_e \dfrac{\psi_f}{L}\cos\theta + \dfrac{u_\beta}{L}; \\ \dfrac{d\omega_e}{dt} = \dfrac{p_n^2}{J}\psi_f (i_\beta \cos\theta - i_\alpha \sin\theta) - \dfrac{B}{J}\omega_e - p_n \dfrac{T_l}{J}; \\ \dfrac{d\theta}{dt} = \omega_e. \end{cases} \tag{5}$$

From the model, permanent magnet motor is a 4-order, nonlinear, and coupling model, and we set the stator current i_α and i_β, rotor angular speed ω_e, and rotor position angle θ as state variables and stator voltage u_α and u_β as control variables.

We define state vector $x = [\, i_\alpha \;\; i_\beta \;\; \omega_e \;\; \theta \,]^{\mathrm{T}}$ and input vector $u = [\, u_\alpha \;\; u_\beta \,]^{\mathrm{T}}$. Rotor angular speed and rotor position angle state components are estimators, and only current state components are measurable, which is detected by the system current sensor.

The nonlinear model of permanent magnet linear synchronous motor given by **Eq. 5** is deterministic. Due to non-ideal factors such as asymmetry of motor parameters and current detection error, the stochastic state space model may be more accurate. Therefore, we consider the state equation as follows:

$$\dot{x} = f(x, u) + w. \tag{6}$$

In **Eq. 5**, speed and position state components are estimators, and only current state components are measurable. The phase current of PMSM is detected by the system current sensor, and the output phase current of the two-phase motor is obtained through the Clarke transformation from *abc* three-phase to $\alpha\beta$ static two-phase. Therefore, the measurement equation of the sensorless driving system is linear, and it can be written as

$$z = hx + v, \tag{7}$$

where $h = \begin{bmatrix} 1 & 0 & 0 & 0 \\ 0 & 1 & 0 & 0 \end{bmatrix}$.

In **Eqs. 6**, **7**, the system produces process noise w and observation noise v due to non-ideal factors such as asymmetry of motor parameters and current detection error. The process noise w is assumed to be a Gaussian white noise with zero mean and covariance Q and is independent of state variables x. The observation noise v is a Gaussian white noise with zero mean and covariance R, which is independent of w and v.

Therefore, we consider the state space model as follows:

$$\begin{cases} \dot{x} = f(x, u) + w; \\ z = hx + v. \end{cases} \tag{8}$$

where x, u, and z are the state variables, control variables, and measurement variables, respectively. $f(\cdot)$ is the nonlinear function of the motor, and $h(\cdot)$ is the measurement matrix.

MAIN RESULTS

We divide this section into two parts. First, we introduce the principle of UKF and estimate the rotor speed and position. Second, the parameter identification algorithm based on the UKF is given.

Brief Introduction of the UKF and State Estimation of PMSM Based on the UKF

Unscented Kalman filter (UKF) algorithm is another extended algorithm of Kalman filter algorithm. It carries out parameter identification by estimating the state matrix at each time. By giving an initial state quantity and then performing traceless transformation on the mean and covariance, the state quantity at the next time interval is obtained. When the parameter in the state matrix is stable, it is the identification value of the parameter.

The state space expression of the sensorless system of permanent magnet synchronous motor is

$$\begin{cases} x_{k+1} = f(x_k, u_k) + w_k; \\ z_k = h(x_k) + v_k. \end{cases} \tag{9}$$

where x_{k+1} and x_k are the system state vectors of the current time and the previous time, respectively; u_k is the system input vector; w_k is the system process noise vector; v_k is the measurement noise vector of the system; and z_k is the output vector of the system. In the recursive calculation of UKF, the noise vectors w_k and v_k are not used directly, but the covariance matrix Q of w_k and the covariance matrix R of v_k are used.

The state vector estimation process of the nonlinear system shown in **Eq. 9** based on UKF algorithm is divided into four stages: state vector initialization, sigma point calculation, time update, and measurement update.

Step 1: initialization.

$$\begin{cases} \hat{x}_0 = \mathbb{E}\{x_0\} \\ P_0 = \mathbb{E}\left\{(x_0 - \hat{x}_0)(x_0 - \hat{x}_0)^{\mathrm{T}}\right\} \end{cases} \tag{10}$$

Step 2: we select proportional symmetric sampling to determine the sigma point set and introduce UT transform to approximate the nonlinearity, and $2n + 1$ sigma points can be obtained.

UT transformation uses a fixed number of parameters to approximate a Gaussian distribution. Its implementation principle is some points in the original distribution are selected according to a certain rule; the mean and covariance of the state distribution of these points are equal to the mean and covariance of the original state distribution. These points are substituted into the nonlinear function to obtain the set of nonlinear function value points. Through these point sets, the transformed mean and covariance can be obtained. For any nonlinear system, a posterior mean and covariance accurate to the third moment can be obtained by using this set of sampling points.

$$\begin{cases} \chi_{i,k|k} = \hat{x}_{k|k},\ i = 0 \\ \chi_{i,k|k} = \hat{x}_{k|k} + \left(\sqrt{(n+\lambda)P_{k|k}}\right)_i,\ i = 1, 2, \ldots, n \\ \chi_{i,k|k} = \hat{x}_{k|k} - \left(\sqrt{(n+\lambda)P_{k|k}}\right)_i,\ i = n+1, \ldots, 2n \end{cases} \tag{11}$$

$$\begin{cases} \omega_i^{(m)} = \dfrac{\lambda}{n+\lambda},\ i = 0 \\ \omega_i^{(c)} = \dfrac{\lambda}{n+\lambda} + (1 - \alpha^2 + \beta),\ i = 0 \\ \omega_i^{(m)} = \omega_i^{(c)} = \dfrac{1}{2(n+\lambda)},\ i = 1, 2, \ldots, 2n \end{cases} \tag{12}$$

where $\lambda = \alpha^2 (n + k) - n$, $\alpha \in [0.000\,1, 1]$ is the proportion factor, and the distribution distance of particles can be adjusted by changing the value of α to reduce the error. k is the redundancy, which is generally 0 and is optimal at $\beta = 2$. $\left(\sqrt{(n+\lambda)P_{k|k}}\right)_i$ is the i-th column of the square root of the matrix, $\omega_i^{(m)}$ is the weighted mean, and $\omega_i^{(c)}$ is the weighted covariance.

Step 3: time update: the sigma point transfer is realized according to the discrete system state, **Eq. 9**:

$$\chi_{i,k+1|k} = f\left(\chi_{i,k|k}\right). \tag{13}$$

The predicted mean and covariance of the state vector are obtained according to the transmission results.

$$\hat{x}_{k+1|k} = \sum_{i=0}^{2n} \omega_i^{(m)} \chi_{i,k+1|k} \tag{14}$$

$$P_{k+1|k} = \sum_{i=0}^{2n} \omega_i^{(c)} \left[\chi_{i,k+1|k} - \hat{x}_{k+1|k}\right]\left[\chi_{i,k+1|k} - \hat{x}_{k+1|k}\right]^{\mathrm{T}} + Q. \tag{15}$$

Step 4: measurement update.

The sampling point prediction equation of observation is given as follows:

$$z_{i,k|k-1} = h(x_{k|k-1}). \tag{16}$$

The transformation value $z_{i,k|k-1}$ obtained by **Eq. 10** is weighted and summed to obtain the measurement prediction value $\hat{z}_{k|k-1}$ of the system and the variance $P_{z,k|k-1}$ and cross covariance $P_{xz,k|k-1}$ of the system measurement variables.

$$\hat{z}_{k|k-1} = \sum_{i=0}^{2n} \omega_i^{(m)} z_{i,k|k-1}. \tag{17}$$

The time update equation is established as follows:

$$\hat{x}_{k+1} = \hat{x}_{k+1|k} + K_{k+1}\left(z_{k+1} - h(\hat{x}_{k+1|k})\right), \tag{18}$$

where $\hat{x}_{k+1}$ is the posterior estimation of the state vector at time $k + 1$ and $\hat{x}_{k+1|k}$ is the prior estimation of the state vector at time $k + 1$. The difference $z_{k+1} - h(\hat{x}_{k+1|k})$ between the measured variable and its prediction is called the innovation or residue of the measurement process, which reflects the inconsistency between the predicted value and the real value. The matrix K_{k+1} is called the residual gain.

The posteriori error is

$$e_{k+1} = x_{k+1} - \hat{x}_{k+1} = x_{k+1} - \hat{x}_{k+1|k} - K_{k+1}\left(z_{k+1} - \hat{z}_{k+1}\right). \tag{19}$$

The posteriori error covariance is

$$P_{k+1} = \mathbb{E}\left(e_{k+1} e_{k+1}^{\mathrm{T}}\right). \tag{20}$$

Let$\frac{\partial P_{k+1}}{\partial K_{k+1}} = 0$, and the Kalman gain is found.

$$K_{k+1} = P_{xz,k+1|k} P_{z,k+1|k}^{-1}. \tag{21}$$

Then,

$$\begin{aligned} P_{z,k+1|k} &= \sum_{i=0}^{2n} \omega_i^{(c)} \left[z_{i,k+1|k} - \hat{z}_{k+1|k}\right]\left[z_{i,k+1|k} - \hat{z}_{k+1|k}\right]^{\mathrm{T}} + R \\ P_{xz,k+1|k} &= \sum_{i=0}^{2n} \omega_i^{(m)} \left[\chi_{i,k+1|k} - \hat{x}_{k+1|k}\right]\left[z_{i,k+1|k} - \hat{z}_{k+1|k}\right]^{\mathrm{T}}. \end{aligned} \tag{22}$$

From **Eq. 9**, we can use Eqs. 11–21 to carry out the iterative operation of the unscented Kalman filter. Thus, the rotor speed and position of the permanent magnet synchronous motor are estimated.

Parameter Identification of PMSM Based on the UKF

Considering the short control period of the discrete-time system, it can be considered that the rotor flux linkage ψ_f and the quadrature axis inductance L do not change in each control cycle. The motor parameters are regarded as a state of slow change concering time, so as to form an extended nonlinear system with the current equation according to the voltage equation of **Eq. 1** and the flux linkage **Eq. 2**.

$$\begin{cases} \dfrac{di_\alpha}{dt} = -\dfrac{R_s}{L}i_\alpha + \omega_e\dfrac{\psi_f}{L}\sin\theta + \dfrac{u_\alpha}{L}; \\ \dfrac{di_\beta}{dt} = -\dfrac{R_s}{L}i_\beta - \omega_e\dfrac{\psi_f}{L}\cos\theta + \dfrac{u_\beta}{L}; \\ \dfrac{d}{dt}\psi_f = 0; \\ \dfrac{d}{dt}L = 0. \end{cases} \tag{23}$$

It can be seen from **Eq. 24** that the rank of the identification equation is 2 and can only realize the full rank identification of two parameters. Therefore, we regard R_s as a constant and only apply it to synchronous identification of two parameters of rotor flux ψ_f and inductor L.

We define state vector $x = [\,i_\alpha \;\; i_\beta \;\; \psi_f \;\; L\,]^{\mathrm{T}}$, input vector $u = [\,u_\alpha \;\; u_\beta\,]^{\mathrm{T}}$, and output vector $z = [\,i_\alpha \;\; i_\beta\,]^{\mathrm{T}}$. The system and output measurements are

$$\frac{d}{dt}\begin{bmatrix} i_\alpha \\ i_\beta \\ \psi_f \\ L \end{bmatrix} = \begin{bmatrix} -\dfrac{R_s}{L}i_\alpha + \hat{\omega}_e\dfrac{\psi_f}{L}\sin\hat{\theta} \\ -\dfrac{R_s}{L}i_\beta - \hat{\omega}_e\dfrac{\psi_f}{L}\cos\hat{\theta} \\ 0 \\ 0 \end{bmatrix} + \begin{bmatrix} \dfrac{1}{L} & 0 \\ 0 & \dfrac{1}{L} \\ 0 & 0 \\ 0 & 0 \end{bmatrix}\begin{bmatrix} u_\alpha \\ u_\beta \end{bmatrix}. \tag{24}$$

$$z = \begin{bmatrix} 1 & 0 & 0 & 0 \\ 0 & 1 & 0 & 0 \end{bmatrix}x. \tag{25}$$

The results show that the rotor flux observer is a 4-order nonlinear system. After calculating the Jacobian matrix of the nonlinear equation, the linear system is obtained as follows:

$$\dot{x} = \begin{bmatrix} -\dfrac{R_s}{L} & 0 & \hat{\omega}_e\dfrac{1}{L}\sin\hat{\theta} & -\hat{\omega}_e\psi_f\dfrac{1}{L^2}\sin\hat{\theta} \\ 0 & -\dfrac{R_s}{L} & -\hat{\omega}_e\dfrac{1}{L}\cos\hat{\theta} & \hat{\omega}_e\psi_f\dfrac{1}{L^2}\cos\hat{\theta} \\ 0 & 0 & 0 & 0 \\ 0 & 0 & 0 & 0 \end{bmatrix}x + \begin{bmatrix} 1 & 0 \\ 0 & 1 \\ 0 & 0 \\ 0 & 0 \end{bmatrix}u. \tag{26}$$

Discretizing **Eqs. 25**, **26**, we can get

$$\begin{cases} x_{k+1} = F_k x + M_k u + w_k; \\ z_k = C_k x + v_k. \end{cases}, \tag{27}$$

where

$$F_k = \begin{bmatrix} 1 - \dfrac{R_s}{L}T_s & 0 & \hat{\omega}_e\dfrac{1}{L}\sin\hat{\theta}T_s & -\hat{\omega}_e\psi_f\dfrac{1}{L^2}\sin\hat{\theta}T_s \\ 0 & 1 - \dfrac{R_s}{L}T_s & -\hat{\omega}_e\dfrac{1}{L}\cos\hat{\theta}T_s & \hat{\omega}_e\psi_f\dfrac{1}{L^2}\cos\hat{\theta}T_s \\ 0 & 0 & 1 & 0 \\ 0 & 0 & 0 & 1 \end{bmatrix},$$

$$M_k = \begin{bmatrix} \dfrac{1}{L}T_s & 0 \\ 0 & \dfrac{1}{L}T_s \\ 0 & 0 \\ 0 & 0 \end{bmatrix}, C_k = \begin{bmatrix} 1 & 0 & 0 & 0 \\ 0 & 1 & 0 & 0 \end{bmatrix}, \tag{28}$$

where T_s represents the time interval from time k to time $k + 1$.

After the system equation is obtained, the parameter identification algorithm is obtained by step 2 to step 4 for iteration.

THE SIMULATION CASE

In order to verify the correctness of speed and motor parameter identification based on UKF algorithm, it is applied to the PMSM vector control system, and the system simulation model based on **Figure 1** structure is established in the Matlab/Simulink environment.

The control strategy of the motor and the structure block diagram of the control system are shown in **Figure 1**. Three-phase current i_a, i_b, i_c is transformed into two-phase current i_α, i_β after Clark transformation; after Park transformation, the AC flow is equivalent to two DC components d and q for operation, and through the calculation of i_d and i_q, the given voltage value u_d^* and u_q^* is obtained. They are converted into a PWM pulse to drive the high-power IGBT through the voltage space vector generation module, which generates the rotating voltage vector and makes the motor run. Clark and Park transformation need position information of motor rotor, and position angle θ is still used here.

The control system adopts the speed and current double closed-loop control strategy. The sampling value of stator current is obtained by a sampling circuit, and then, the current is decomposed into mutually perpendicular current components i_d and i_q by coordinate transformation. The voltage of the motor cannot be measured, so the given value of the voltage is used instead of the actual value. In the sensorless part, UKF algorithm is used to estimate the motor speed. According to the abovementioned analysis, the accuracy of identification is easily affected by the changes of motor parameters, so this article estimates the speed and identifies the motor parameters and uses the identified parameters to update the reference model. Since the parameters to be identified include motor speed ω, position θ, inductance L, and flux ψ_f, this article adopts a step-by-step identification algorithm. First, we fix inductance L and flux ψ_f and use UKF algorithm to identify speed ω and position θ on line. Then, we fix speed ω and position θ and use UKF algorithm to identify inductance L and flux ψ_f on line.

In order to verify the effectiveness of the parameter identification scheme of PMSM under sensorless control, the UKF estimation module uses Matlab/Simulink for simulation. The parameters of the simulation motor are shown in **Table 1**.

In general, the random interference in the system and part of the measurement noise are unknown. Therefore, the covariance

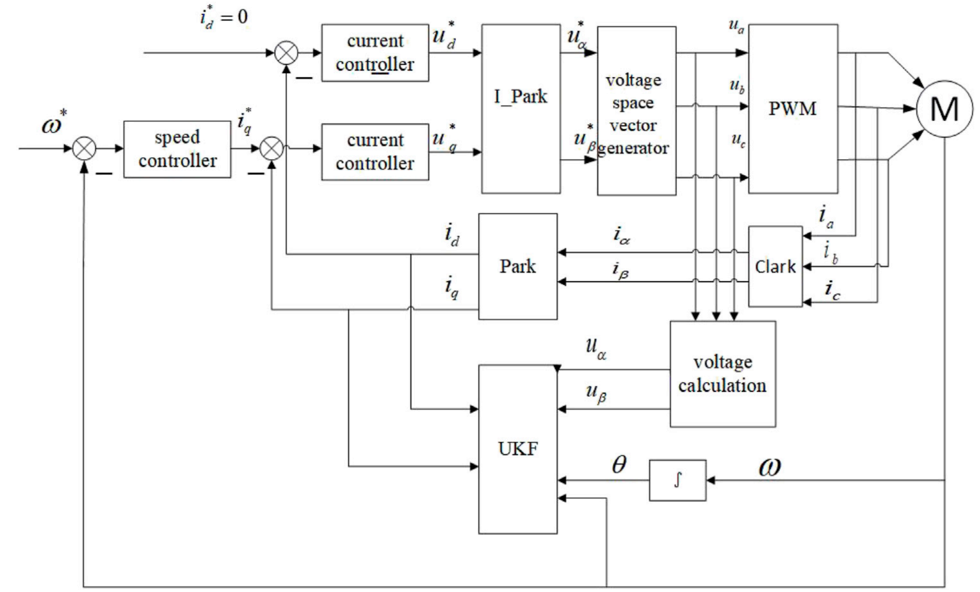

FIGURE 1 | Block diagram of the vector control scheme for PMSM without a position sensor with parameter identification.

TABLE 1 | Parameters of PMSM.

Motor parameters	Symbol	Parameter value
Voltage of the *d*-axis	u_d	220 v
Voltage of the *q*-axis	u_q	220 v
Rotor flux	ψ_f	0.12 Wb
Inductance of *d* and *q* axes	L	8.5 mH
Stator resistance	R_s	2.875 Ω
Rotor angular speed	ω	500 rad/min
Pole number of the motor	p_n	4
Electromagnetic torque	T_e	6 N · m
Load torque	T_l	5 N · m
Moment of inertia	J	0.008 kg · m^2
Sampling time	T_s	1 e^{-6}

matrix of system noise and measurement noise will be determined by experience and simulation. Appropriate initial value selection can make the algorithm have high-precision prediction results under the premise of convergence. In this article, the following covariance matrix and initial value are used on the premise of a large number of research and experiments.

$$Q = \begin{bmatrix} 0.1 & 0 & 0 & 0 \\ 0 & 0.1 & 0 & 0 \\ 0 & 0 & 1 & 0 \\ 0 & 0 & 0 & 0.01 \end{bmatrix}, R = \begin{bmatrix} 0.2 & 0 \\ 0 & 0.2 \end{bmatrix}.$$

The simulation results are shown in **Figures 2–5**. First, the control system with a position sensor is simulated, and the motor voltage, current, speed, and position signals are recorded. The UKF is used to estimate the speed and position of the PMSM and compare with the simulated speed and position signals. **Figure 2** and **Figure 3** are the speed and position diagrams of PMSM estimated by the UKF, respectively, and **Figure 4** and **Figure 5** are the estimation errors of speed and position, respectively. It can be seen from the simulation results that the estimated value obtained by UKF algorithm can better track the actual value.

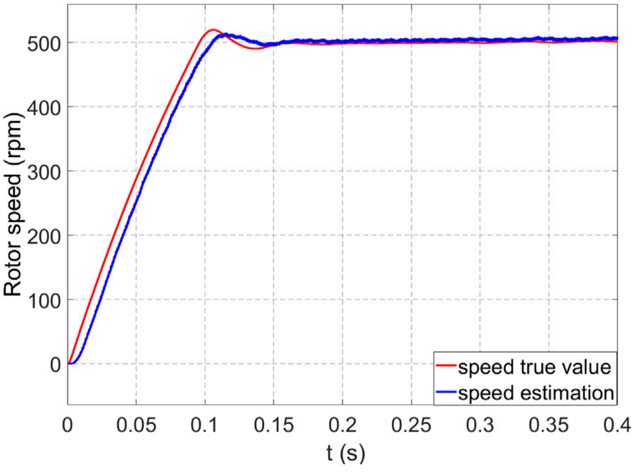

FIGURE 2 | Rotor speed.

Figure 4 and **Figure 5** show that there is a deviation between the estimation value and the actual value, but after iterative correction for 0.15 s, the speed regulation is stable.

Motor parameters play an important role in the mathematical model of motor. It has an impact on the state equation of motor and the stability, accuracy, and rapidity of the whole system. In the motor mathematical model and equation discussed above, there are mainly the following parameters: resistance R_s, inductance L, and flux ψ_f. Through the simulation, it is found

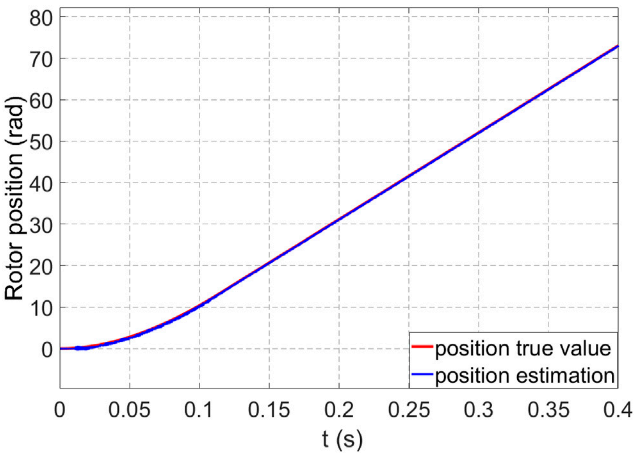

FIGURE 3 | Rotor position.

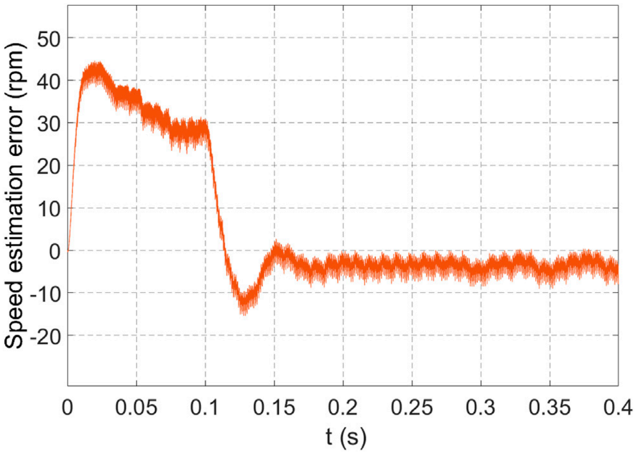

FIGURE 4 | Speed estimation error.

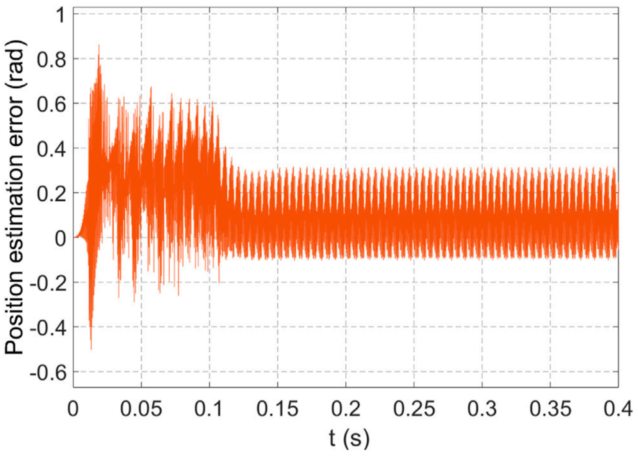

FIGURE 5 | Position estimation error.

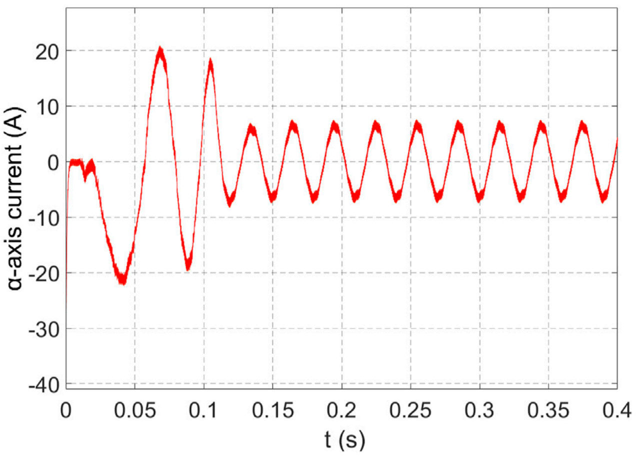

FIGURE 6 | Identification value of α-axis current.

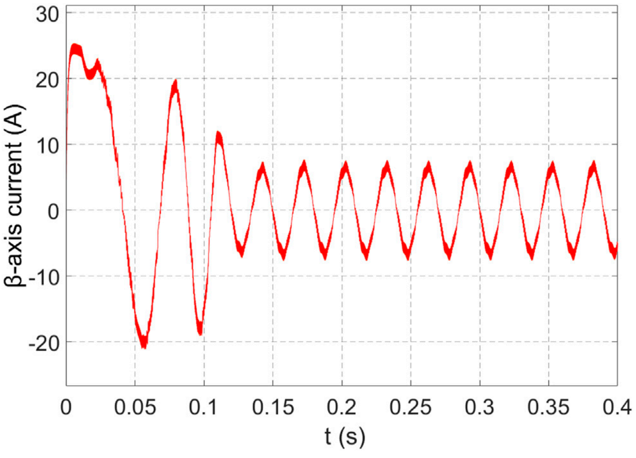

FIGURE 7 | Identification value of β-axis current.

that the motor resistance has little influence on the speed and position estimation results, while the rotor flux and inductance deviation have great influence on the estimation results.

After UKF algorithm, the estimated values of each state variable are obtained, as shown in **Figures 6–11**. It can be seen from **Figures 6**, **7** that the UKF can not only accurately identify the stator flux but also accurately identify the stator current.

Figures 6, **7** of $\alpha\beta$-axis currents tend to be stable after 0.15 s. This is consistent with the change of speed in **Figure 2**. The speed is controlled by the current loop. After one and a half cycles, currents reach the rated current value of 5A. After coordinate transformation, the $\alpha\beta$ two-phase current has a phase difference of 90 under the shaft system.

This reflects the effectiveness of the observer. **Figure 8** is the result of motor flux identification. The identified flux is 0.12 wb, which has good stability and is close to the actual value of 0.12 wb, and the error is close to zero, which verifies the effectiveness of the

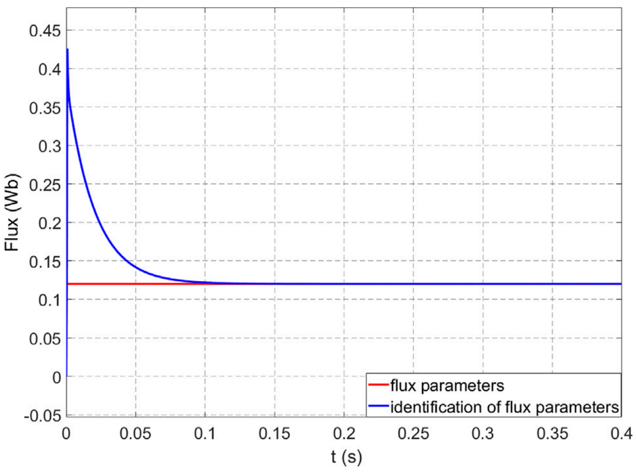

FIGURE 8 | Flux identification value.

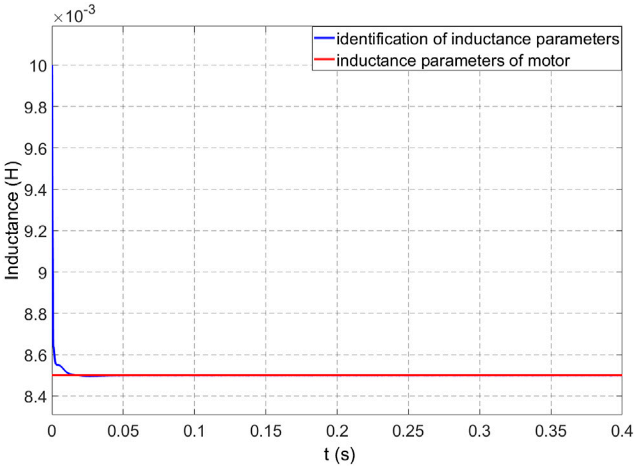

FIGURE 9 | Inductance identification value.

identification method. **Figure 9** is the result of inductance identification, and the identification value tends to 8.5 mH quickly, which is basically the same as the actual value. Both the inductance L and the flux linkage ψ_f can converge to the true value, and the error is almost zero.

The flux linkage parameters and inductance parameters identified by the UKF are applied to the UKF system in real time to estimate the motor speed and position, and good control effect is obtained, as shown in **Figures 10, 11**.

The identified parameters are fed back to the system, and the UKF can update the motor parameters in the mathematical model in time, which greatly reduces the estimation error. After the identified parameters are fed back to the sensorless vector control scheme, the control performance and parameter identification results of the whole scheme remain stable in dynamic and steady state.

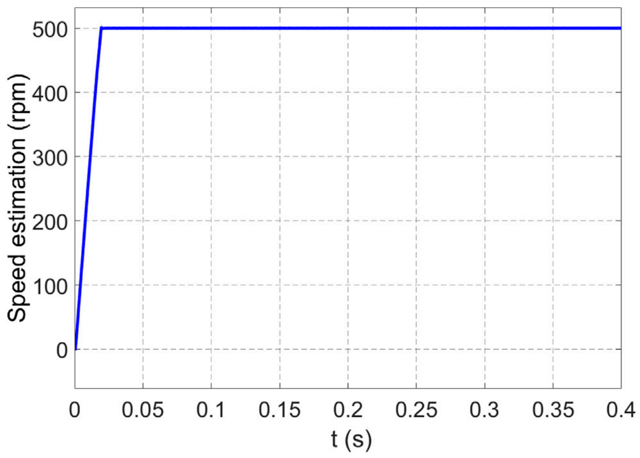

FIGURE 10 | Speed estimation with parameter identification.

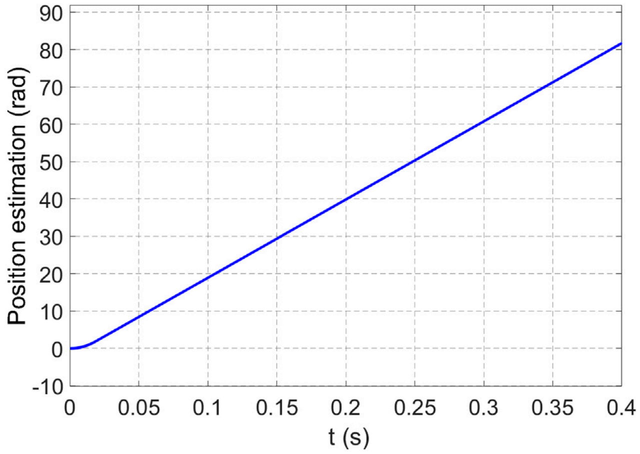

FIGURE 11 | Position estimation with parameter identification.

CONCLUSION

In this article, UKF-based parameter identification was considered for permanent magnet synchronous motor. The rotor flux and inductance parameters based on the UKF model have been modified in real time, and the estimation effect of the UKF has been compensated effectively. UKF algorithm requires less computation, but the accuracy of identification results is high. It is a very advantageous online motor parameter identification method, which is suitable for state estimation and model identification of nonlinear systems. The performance of a PMSM sensorless control system can be guaranteed even if the motor parameters have some errors. The simulation results have shown that the parameter identification algorithm can effectively identify the rotor flux linkage and inductance in real time and can effectively estimate the speed and position with high estimation accuracy, which can meet the real-time requirements of motor control.

DATA AVAILABILITY STATEMENT

The original contributions presented in the study are included in the article/Supplementary Materials, and further inquiries can be directed to the corresponding author.

REFERENCES

An, L., and Hameyer, K. (2014). Rotor Position and Speed Estimation of Interior Permanent Magnet Synchronous Motor Using Unscented Kalman Filter. In 17th International Conference on Electrical Machines and Systems (ICEMS). Hangzhou, 727–732. doi:10.1109/icems.2014.7013577

Cao, R., Cheng, M., and Zhang, B. (2015). Speed Control of Complementary and Modular Linear Flux-Switching Permanent-Magnet Motor. *IEEE Trans. Ind. Electron.* 62 (7), 4056–4064. doi:10.1109/tie.2015.2390194

Chen, L., Sun, X., Jiang, H., and Xu, X. (2014). High Performance Control of a Permanent Magnet Synchronous Motor for Electric Vehicle Applications. *Jnl Comp. Theo Nano.* 11 (3), 706–710. doi:10.1166/jctn.2014.3415

Chen, Z., Zhang, H., Tu, W., Luo, G., Manoharan, D., and Kennel, R. (2019). Sensorless Control for Permanent Magnet Synchronous Motor in Rail Transit Application Using Segmented Synchronous Modulation. *IEEE Access.* 7, 76669–76679. doi:10.1109/access.2019.2921916

Cheng, S., Luo, D., Huang, S., Chen, Z., and Huang, K. (2015). Control Strategy for Permanent Magnet Synchronous Motor with Contra-rotating Rotors under Unbalanced Loads Condition. *IET Electric Power Appl.* 9 (1), 71–79. doi:10.1049/iet-epa.2014.0130

Cui, F., Sun, Z., Xu, W., Zhou, W., and Liu, Y. (2020). Comparative Analysis of Bilateral Permanent Magnet Linear Synchronous Motors with Different Structures. *Trans. Electr. Mach. Syst.* 4 (2), 142–150. doi:10.30941/cestems.2020.00019

Deng, T., Su, Z., Li, J., Tang, P., Chen, X., and Liu, P. (2019). Advanced Angle Field Weakening Control Strategy of Permanent Magnet Synchronous Motor. *IEEE Trans. Veh. Technol.* 68 (4), 3424–3435. doi:10.1109/tvt.2019.2901275

Fadil, H., Driss, Y., and Aite, Y. (2015). Sliding-mode Speed Control of PMSM With Fuzzy-Logic Chattering Minimization-Design and Implementation. *Information.* 6 (3), 432–442. doi:10.3390/info6030432

He, B., Deng, Y., He, D., Tian, H., and Liu, Y. (2019). Vector Control Strategy of Permanent Magnet Synchronous Motor with Motor Driven Actuator. *Micromotors.* 52 (3), 62–68.

He, C., and Wu, T. (2019). Analysis and Design of Surface Permanent Magnet Synchronous Motor and Generator. *Trans. Electr. Mach. Syst.* 3 (1), 94–100. doi:10.30941/cestems.2019.00013

Kyoon, K. (2017). Robust Adaptive Speed Regulator With Self-Tuning Law for Surfaced-Mounted Permanent Magnet Synchronous Motor. *Control. Eng. Pract.* 11, 55–71. doi:10.1016/j.conengprac.2017.01.014

Liang, D., Li, J., and Qu, R. (2017). Sensorless Control of Permanent Magnet Synchronous Machine Based on Second-Order Sliding-Mode Observer with Online Resistance Estimation. *IEEE Trans. Ind. Applicat.* 53 (4), 3672–3682. doi:10.1109/tia.2017.2690218

Liu, X., Yu, X., Ma, G., and Xi, H. (2016). On Sliding Mode Control for Networked Control Systems with Semi-Markovian Switching and Random Sensor Delays. *Inf. Sci.* 337-338, 44–58. doi:10.1016/j.ins.2015.12.023

Lu, W., Tang, B., Ji, K., Lu, K., Wang, D., and Yu, Z. (2021). A New Load Adaptive Identification Method Based on an Improved Sliding Mode Observer for PMSM Position Servo System. *IEEE Trans. Power Electron.* 36 (3), 3211–3223. doi:10.1109/tpel.2020.3016713

Luo, S., Chen, X., Song, Y., Guo, C., and Shu, H. (2019). Design of Model Predictive Controllers for PMSM Drive System Based on the Extended Kalman Filter Observer. *Ijehv.* 11 (4), 378–394. doi:10.1504/ijehv.2019.10024319

Moon, C., and Kwon, Y. A. (2016). Sensorless Speed Control of Permanent Magnet Synchronous Motor by Unscented Kalman Filter Using Various Scaling Parameters. *J. Electr. Eng. Technology.* 11 (2), 347–352. doi:10.5370/jeet.2016.11.2.347

Nahid-Mobarakeh, B., Meibody-Tabar, F., and Sargos, F.-M. (2004). Mechanical Sensorless Control of PMSM with Online Estimation of Stator Resistance. *IEEE Trans. Ind. Applicat.* 40 (2), 457–471. doi:10.1109/tia.2004.824490

Pan, S., and Gao, J. (2018). Summarization of Sensorless Control Technology for Permanent Magnet Synchronous Motor. *Micromotors.* 51 (3), 62–69.

Tao, C., and Guo, Z. (2019). The Identification for Rotor Flux Linkage of Permanent Magnet Synchronous Motor Base on Dual Unscented Kalman Filter Algorithm. *Sci. Technology Eng.* 19 (6), 122–128.

Wang, R., Sun, Q., Hu, W., Li, Y., Ma, D., and Wang, P. (2021). SoC-Based Droop Coefficients Stability Region Analysis of the Battery for Stand-Alone Supply Systems With Constant Power Loads. *IEEE Trans. Power Electron.* 36 (7), 7866–7879. doi:10.1109/tpel.2021.3049241

Wang, R., Sun, Q., Ma, D., and Liu, Z. (2019). The Small-Signal Stability Analysis of the Droop-Controlled Converter in Electromagnetic Timescale. *IEEE Trans. Sustain. Energ.* 10 (3), 1459–1469. doi:10.1109/tste.2019.2894633

Wang, R., Sun, Q., Ma, D., and Hu, X. (2020a). Line Impedance Cooperative Stability Region Identification Method for Grid-Tied Inverters Under Weak Grids. *IEEE Trans. Smart Grid.* 11 (4), 2856–2866. doi:10.1109/TSG.2020.2970174

Wang, R., Sun, Q., Zhang, P., Gui, Y., Qin, D., and Wang, P. (2020b). Reduced-Order Transfer Function Model of the Droop-Controlled Inverter via Jordan Continued-Fraction Expansion. *IEEE Trans. Energ. Convers.* 35 (3), 1585–1595. doi:10.1109/TEC.2020.2980033

Yang, S., Wang, J., Zhang, G., Yang, X., and Wang, S. (2016). A Review on Induction Motor Control Based on the Kalman Filter. *Control Eng. China.* 23 (1), 30–37.

Yin, Z., Tang, R., Du, C., and Wang, Y. (2019). Moment of Inertia Identification Based on Unscented Kalman Filter for Permanent Magnet Synchronous Motors. In 14th IEEE Conference on Industrial Electronics and Applications (ICIEA), 1141–1145. doi:10.1109/iciea.2019.8834168

Zhong, C., and Lin, Y. (2017). Model Reference Adaptive Control (MRAC)-based Parameter Identification Applied to Surface-Mounted Permanent Magnet Synchronous Motor. *Int. J. Electronics.* 104 (11), 1854–1873. doi:10.1080/00207217.2017.1329946

Zhong, Z., Jin, M., and Shen, J. (2018). Full Speed Range Sensorless Control of Permanent Magnet Synchronous Motor with Phased PI Regulator-Based Model Reference Adaptive System. *Proc. CSEE* 38 (4), 1203–1211. doi:10.13334/j.0258-8013.pcsee.162121

Zhou, H., Liu, Z., and Yang, X. (2018). Motor Torque Fault Diagnosis for Four Wheel Independent Motor-Drive Vehicle Based on Unscented Kalman Filter. *IEEE Trans. Veh. Technol.* 67 (3), 1969–1976. doi:10.1109/tvt.2017.2751750

Zhu, Q., Zhang, Z., Yang, H., and Zhu, Y. (2014). Research on Sensorless PMSM Current Control Strategies. *Control. Eng. China* 21 (4), 547–553.

AUTHOR CONTRIBUTIONS

All authors listed have made a substantial, direct, and intellectual contribution to the work and approved it for publication.

Conflict of Interest: ZW, XL, WW, BY, WL, QL, SW, and QC were employed by the Northwest Branch of State Grid Corporation of China. YZ was employed by the Nari Technology Co., Ltd.

The remaining authors declare that the research was conducted in the absence of any commercial or financial relationships that could be construed as a potential conflict of interest.

frontiers
in Energy Research

ORIGINAL RESEARCH
published: 16 March 2022
doi: 10.3389/fenrg.2022.848805

Research on Optimal Scheduling of VPP Based on Latin Hypercube Sampling and K-Means Clustering

Cao Wensi[1], *Wang Shuo*[1]*, *Min Chao*[1] *and Xu Mingming*[2]

[1]*School of Electric Power, North China University of Water Resources and Electric Power, Zhengzhou, China,* [2]*State Grid Henan Electric Power Research Institute, Zhengzhou, China*

Based on the classical scenario set, the VPP economic dispatch model is proposed taking into account the uncertainty factors of distributed power sources. The basic model of the VPP is first analyzed, followed by the proposed operation strategy of the VPP based on the basic model, while considering the impact of the time-of-use electricity price on the economics of the VPP. Latin hypercube sampling combined with K-means clustering is used to generate the classical scene set; at the same time, the model is solved using an algorithm that incorporates a genetic mechanism in an improved particle swarm algorithm (PSO). Finally, according to the established model, a calculation example is used to verify. The design is based on two scenarios of the classic scene set and general scene. The optimization configuration results are compared and analyzed. It is confirmed that the VPP optimization configuration under the classic scene set can improve the net income of the VPP.

Keywords: VPP (virtual power plant), Latin hypercube sampling, K-means clustering, economic analysis, improved particle swarm optimization

Edited by:
Rui Wang,
Northeastern University, China

Reviewed by:
Xuguang Hu,
Northeastern University, China
Tianyang Zhao,
Jinan University, China

Correspondence:
Wang Shuo
2043676307@qq.com

Specialty section:
This article was submitted to
Smart Grids,
a section of the journal
Frontiers in Energy Research

Received: *05 January 2022*
Accepted: *23 February 2022*
Published: *16 March 2022*

Citation:
Wensi C, Shuo W, Chao M and Mingming X (2022) Research on Optimal Scheduling of VPP Based on Latin Hypercube Sampling and K-Means Clustering.
Front. Energy Res. 10:848805.
doi: 10.3389/fenrg.2022.848805

INTRODUCTION

The rapid development of technologies that rely on natural energy sources has led to massive consumption of fossil energy. In this regard, many solutions have been proposed to mitigate phenomena such as air pollution and global warming. The concept of the VPP (virtual power plant) was developed. The VPP can provide an effective means of managing distributed generation (DG) at a time when distributed energy is growing rapidly. At present, there is no authoritative definition of the VPP, and most people accept the concept that it uses advanced control, communication, and computing technologies in a distributed network where different types of distributed energy sources can be aggregated and further distribute energy so that these DGs can operate as a whole, while also effectively mitigating the instability of distributed energy sources.

The VPP has been studied in great depth in many literatures. The concept of the responsive VPP was first introduced in the literature (Department Of Energy (, 2006)) during the theoretical exploration and proof stage; relying on the different ways of achieving the response, two working models of the VPP were proposed: incentive-based power plant models and lump sum–based power plant models, and these were verified through calculation examples. A comprehensive account of the VPP is presented in the literature (Xia and Liu, 2016; Lin, 2017; Gong, 2018; Li et al., 2021). Hong et al., 2017; Wang, 2017; Yuan, 2017; Wen and Guoen, 2019; Liu et al., 2020; Yang et al., 2020 investigate the problem regarding the management of renewable energy sources in the grid, which considers the VPP to be able to integrate distributed energy sources optimally. In the literature (Pudjianto et al., 2007; Zhou and Lin, 2019), distributed energy sources, such as CHP units, are aggregated to form a VPP to participate in market trading and realize a VPP model for distributed energy sources, such as energy storage and demand response. You et al., (2009) consider the uncertainty of power market prices and new energy generation, such as wind and PV consider both controllable and uncontrollable distributed power sources; and propose a day-ahead bidding strategy for the VPP with the goal of maximizing economic efficiency. Yuan et al., (2016) investigate the economic efficiency of the VPP based on particle swarm optimization (PSO) algorithms, taking into account time-of-use electricity prices. The strategies proposed in the literature (Soltani et al., 2012) consider the effect of reliability and determine the optimal hourly operating strategy for DERs by Monte Carlo simulation methods. However, these scheduling strategies are proposed based on deterministic market prices.

As the role played by the VPP in the power system increases in proportion, the issue of operating and scheduling the VPP is a problem we must face. The abovementioned literatures summarize the VPP and even propose a day-ahead bidding strategy for the VPP, but the VPP contains a large number of distributed power sources, which have uncertainty in their power output, and currently in the power system, to offset the uncertainty in the system, the method of the reserved rotating reserve is usually used as carried out by Yi and Li, (2018); the so-called reserved rotating reserve method is applied to reduce the error by compensating the prediction error at a certain confidence level by a certain rotating reserve capacity. Robust optimization methods are generally used to deal with uncertainty in the model; however, although robust optimization methods are good, but the results are often conservative and extreme. Stochastic optimization methods based on scenario sets are generally used to deal with uncertainty in models by discretizing a continuous problem into a finite number of scenarios with certain probabilities and then finding the optimal expectation, often including the generation of multiple scenarios and decimation of scenarios to derive classical scenario sets such as those obtained by Zhinong et al., (2018). In the literature (Liu, 2018), a Markov chain-based PV ultrashort-term prediction model was constructed for historical PV data; the relationship between PV curve description quantity characteristics and collection granularity was investigated; the main evaluation indexes reflecting the continuous fluctuation characteristics of PV power were extracted according to the PV power change state, and a multiobjective optimization–based PV power collection granularity calibration model was established. In the literature (Liu et al., 2021), a two-level collaborative optimal scheduling model for the VPP considering carbon neutral benefits was proposed to further enhance the adaptability and accuracy of the model under a carbon neutral layout by considering carbon emissions and carbon neutrality in a multitime-scale optimal scheduling model for the VPP to fill the gap of VPP optimal scheduling in the field of carbon emissions. In the literature (Wei et al., 2015; Zhao and Fan, 2019a; Gao, 2019), a double-layer optimal dispatching model of the VPP based on time-of-use electricity prices was proposed, and the study showed that the VPP based on time-of-use electricity prices can maximize the revenue to enhance the level of new energy consumption and ensure the balance of supply and demand in the region. Lin et al., (2021) used the stochastic optimization and adaptive robust optimization methods to model the uncertainty of electricity price, wind power output, and demand response and then linearized the model formulation based on the engineering game idea to establish a two-stage, three-level day-ahead dispatch model. The optimal solution is obtained by the PSO algorithm, and it is verified that this model can effectively improve the economy and safety of VPP operation.

The VPP is proposed to integrate various distributed power sources, controllable loads, and energy storage devices, etc., and gather various distributed power sources together to form a whole through advanced communication technology to participate in the operation and dispatch of the grid in a unified manner. The control of the VPP is divided into two types: decentralized control and centralized control. However, a new distributed coordination controller proposed in the literature (Sun et al., 2015), combined with a multi–intelligence-based consensus algorithm, is applied to the distributed generators of the energy Internet, which can maintain the consistency of electrical angles and amplitudes between the energy Internet and MG. In the second part of the article, a control architecture based on a multi-intelligence system is proposed to describe the information exchange between different parts.

Translated with www.DeepL.com/Translator (free version). In the previous studies of optimal scheduling of the VPP, they all gave priority to the use of traditional power generation methods with lower generation costs in order to maximize benefits, while ignoring the consumption of new energy sources, such as wind power and photovoltaics, resulting in the waste of new energy generation costs, which actually undermines the ultimate benefits of the VPP. The study establishes an optimal configuration model of the VPP. First, the basic mathematical model of the VPP is analyzed, followed by the uncertainty factors in the VPP using Latin hypercube sampling and K-means clustering to form a classical scenario set. Then, the objective function is to maximize the net revenue of the VPP, and the constraints are considered to establish the optimal configuration model of the VPP consisting of wind power, photovoltaic power generation, energy storage system, and gas turbine, and finally, the algorithm of adding genetic mechanism to the improved PSO algorithm is used to solve the model. In addition, a VPP operation strategy is proposed, which takes into account the economy of the VPP according to the time-of-use electricity price. The rationality and effectiveness of this strategy are verified by examples.

GENERATION OF CLASSIC SCENE SETS

Latin Hypercube Sampling to Form Multiple Scenes

Latin hypercube sampling is a method proposed by M. D. McKay, R. J. Beckman, and W. J. Conover in 1979, which can effectively use the distribution of sample response random variables (McKay et al., 2012). Latin hypercube sampling is a typical stratified sampling, and for all sampling areas, this sampling method can be used to cover a smaller and unduplicated sample. The sampling is performed by the following steps:

1) Dividing the sample into equal intervals on the cumulative probability scale 0 to 1.

Let the random variable A be the object of our study and its probability distribution function be

$$Y = F(\mathrm{A}). \tag{1}$$

Let B be the number of samples, and then the vertical axis of $Y = F(A)$ is divided into B equal intervals; each interval is independent of each other without repetition, and the width of the interval is 1/B.

2) Generate random numbers in each interval.

$$\left(\frac{i-1}{B}, \frac{i}{B}\right), 1 \le i \le B. \tag{2}$$

A random number u is generated in the interval shown in **Equation 2** and u is a random variable adhering to uniform distribution on the interval (0, 1); then, a random number d_i can be generated for the ith interval and can be expressed as

$$d_i = \frac{u}{B} + \frac{i-1}{B}. \tag{3}$$

3) Inverted conversion generates the sampled values.

The sampled values are calculated by the inverse function as follows:

$$A_i = F^{-1}(d_i). \tag{4}$$

The specified B sample values can be obtained by the abovementioned steps.

Yang et al., (2013) studied the distributed wind power output using a two-parameter Will distribution, and Zhou et al., (2016) studied the distributed PV using a β distribution.

K-Means Clustering Reduction Scenario

K-means clustering minimizes the sum of squares of the Euclidean distance between each sampled point and its nearest clustering center. K-means first selects the initial cluster centers randomly or manually and then divides the data set into several clusters (a data point belongs to the cluster whose cluster center is closest to the data point) and calculates the mean of the clusters as the cluster centers. K-means repeatedly updates the clustering centers and clusters until convergence. The main distance metrics are Manhattan distance, Euclidean distance, Marxian distance, Chebyshev distance, and other methods.

The set of samples $X = (x_1, x_2, x_3, ..., x_n)$ is known, the number of categories is k, and the sum of point-to-center distances is chosen as the objective function:

$$E = \sum_{i=1}^{k}\sum_{j=1}^{n} d_{ij}\left\|x_j - w_i\right\|^2. \tag{5}$$

In **Eq. 5**, $d_{ij} = \begin{cases} 1, x_j \in U_i \\ 0, x_j \notin U_i \end{cases}$; w_i represents the cluster center of the ith class and U_i represents the set of samples of the ith class after clustering.

VIRTUAL POWER PLANT ECONOMIC MODEL

Objective Function

The objective function is to maximize the net income of the VPP, in which the income first mainly includes the income of wind power generation and photovoltaic power generation, which are distributed power sources to supply the load, followed by the income of the difference between charging and discharging of energy storage batteries, while considering the income generated by gas turbine auxiliary power generation, and the income of the difference between the income earned by the VPP from the sale of electricity to the grid and the cost of electricity purchased by the VPP from the grid; the three main sources of costs are operation and management costs, energy consumption costs, and penalty costs.

$$F = \max \sum_{s=1}^{N} \alpha(s)\left(P^s - C^s\right). \tag{6}$$

In **Eq. 6**, F represents the net income of the VPP, N represents the number of classic scene sets, $\alpha(s)$ represents the probability of scene occurrence, P^s represents the income of the VPP under scenario s, and C^s represents the cost of the VPP under scenario s.

P^s can, in turn, be expressed as follows:

$$P^s = \sum_{t=1}^{24} A_{1,t}\left(P^s_{PW,t} + P^s_{PV,t} + P^s_{GT,t} + P^s_{Discharge,t} + P^s_{Sell,t} - P^s_{Charge,t} - P^s_{Buy,t}\right). \tag{7}$$

In **Eq. 7**,t represents time series, $A_{1,t}$ represents the price of electricity sold during t, $P^s_{PW,t}$, $P^s_{PV,t}$, $P^s_{GT,t}$, $P^s_{Discharge,t}$, $P^s_{Charge,t}$, $P^s_{Sell,t}$, $P^s_{Buy,t}$ represent the power of wind power generation, photovoltaic power generation, gas turbine, energy storage, etc. in the time period t under the scenario s.

$$C^s = C^s_{om,t} + C^s_{es,t} + C^s_{pu,t}. \tag{8}$$

$$C^s_{om,t} = \sum_{t=1}^{24}\Big[E_{om,PW}P^s_{PW,t} + E_{om,PV}P^s_{PV,t} + E_{om,GT}P^s_{GT,t} + E_{om,Batttry}\left(P^s_{Discharge,t} + P^s_{Charge,t}\right)\Big]. \tag{9}$$

$$C^s_{ec,t} = \sum_{t=1}^{24} P_{GT}P^s_{GT,t}. \tag{10}$$

$$C^s_{pu,t} = \sum_{n=1}^{24} A_{2,t}\left|D_n - P^s_{PW,t} - P^s_{PV,t} - P^s_{GT,t} - P^s_{Discharge,t}\right|. \tag{11}$$

In the formula, $C^s_{om,t}$, $C^s_{ec,t}$, and $C^s_{pu,t}$, respectively, represent operation management cost, energy consumption cost, and penalty cost; $E_{om,PW}$, $E_{om,PV}$, $E_{om,GT}$, and $E_{om,Batttry}$ means cost factor; $A_{2,t}$ represents the electricity purchase price in t period; and P_{GT} represents the fuel cost of gas turbine unit power generation and the unit power generation cost of the gas turbine (Cui et al., 2010):

$$P_{GT} = \frac{P_{NG}}{\eta L_{NG}}. \tag{12}$$

In **Eq. 12**, P_{GT} represents the price of natural gas, η represents power generation efficiency, and L_{NG} represents the low calorific value of natural gas.

The VPP declares its planned contribution to the grid:

$$D = \begin{cases} D_{PW} + D_{PV} + \eta P_{GT,t\max}; A_{2,t} > P_{GT,t} \\ D_{PW} + D_{PV}; A_{2,t} < P_{GT,t} \end{cases}. \tag{13}$$

In **Eq. 13**, D_{PW} and D_{PV} represent the planned output of wind power generation and photovoltaic power generation in time t, respectively, and $P_{GT,t\max}$ represents the maximum output of the gas turbine.

Constraints

1) Power balance constraint

$$D_t + P^s_{Charge,t} = P^s_{PW,t} + P^s_{PV,t} + P^s_{GT,t} + P^s_{Discharge,t}. \tag{14}$$

In **Eq. 14**, D_t represents the interactive power between the VPP and power grid during t period.

2) Gas turbine constraints

$$P_{GT,\min} \le P^s_{GT,t} \le P_{GT,\max}. \tag{15}$$

In **Eq. 15**, $P_{GT,\max}$ and $P_{GT,\min}$, respectively, represent the upper and lower limits of the gas turbine during normal operation.

3) Gas turbine climb rate constraint

$$-R^A_g \Delta t \le P^s_{GT,t} - P^s_{GT,t-1} \le R^B_g \Delta t. \tag{16}$$

In **Eq. 16**, R^A_g and R^B_g represent the upward and downward climbing rate of the gas turbine, respectively.

4) Battery capacity constraints of energy storage systems

The energy storage system must comply with the law of conservation of energy in the process of dispatching, that is, the electrical energy stored now is equal to the sum of the electrical energy stored in the previous moment and the charging and discharging energy in the process of two moments, which is as follows:

$$S^s_{ca,t} = S^s_{ca,t-1} + \frac{\Delta t\left(\eta_1 P^s_{Charge,t} - P^s_{Discharge,t}/\eta_2\right)}{E_{bat}}. \tag{17}$$

At the same time, **Eq. 18** must be satisfied:

$$S_{ca,\min} \le S^s_{ca,t} \le S_{ca,\max}. \tag{18}$$

In **Eq. 18**, $S^s_{ca,t}$ and $S^s_{ca,t-1}$ represent the capacity of the energy storage battery in t period and t-1 period, respectively; Δt represents the time interval; η_1 and η_2 represent charging efficiency and discharging efficiency, respectively; E_{bat} represents the installed capacity of the energy storage system; and $S_{ca,\max}$ and $S_{ca,\min}$, respectively, represent the upper and lower limits of the energy storage capacity.

5) Charging and discharging constraints of energy storage batteries

$$P_{Charge,\min} \le P^s_{Charge,t} \le P_{Charge,\max}. \tag{19}$$

$$P_{Discharge,\min} \le P^s_{Discharge,t} \le P_{Discharge,\max}. \tag{20}$$

$$M^s_{Charge,t} + M^s_{Discharge,t} \le 1. \tag{21}$$

$$P^s_{c,t} = M^s_{Charge,t} P^s_{Charge,t} + M^s_{Discharge,t} P^s_{Discharge,t}. \tag{22}$$

In the abovementioned formula, $P_{Charge,\max}$ and $P_{Charge,\min}$, respectively, represent the extreme value of the upper and lower limit of the charging power of the energy storage system; $P_{Discharge,\max}$ and $P_{Discharge,\min}$, respectively, represent the extreme value of the upper and lower limits of the discharge power of the energy storage system; $P^s_{c,t}$ denotes the power (charging or discharging) of the energy storage system in time period t under the scenario s; $M^s_{Charge,t}$ and $M^s_{Discharge,t}$, respectively, represent the state variable of the charging and discharging of the energy storage system in the time period t under the scenario s; and the value is 0 or 1.

Virtual Power Plant Operation Strategy Based on Time-Of-Use Electricity Price

1) The form of interaction between the VPP and grid

Based on the existence of time-of-use electricity price, there are three main aspects of the interaction between the VPP and grid:

1) If the price of electricity is at peak hours at this time, the energy storage and gas turbines in the VPP will sell all the excess power to the grid to earn benefits under the condition that the load demand is met;
2) If the price of electricity is in the usual period, the distributed power source will be powered first, followed by the energy storage system, and the gas turbine will decide whether to power up by comparing the cost of power generation with the grid price;
3) If the price of electricity is in the valley, the cost of gas turbine power generation is lower than the price of grid electricity, and the gas turbine does not produce power, the VPP to purchase electricity from the grid, part of the load, another part of the power stored in the storage system, to be sold at the right time to earn the difference in price.

2) VPP operation strategy

The operation strategy of the VPP mainly considers the power output of distributed power sources, such as wind power and photovoltaic power, the power output of energy storage systems, and the power output of gas turbines.

Distributed power output: wind power and photovoltaic power generation as new energy; the VPP within its capacity to achieve priority utilization. When the output of the distributed power is greater than the load demand, all the load demand will come from the distributed power, and the remaining power will be stored in the energy storage system or sold to the grid according to the time-sharing tariff; when the output of distributed power is less than the load demand, all the output of distributed power will be used for the load demand.

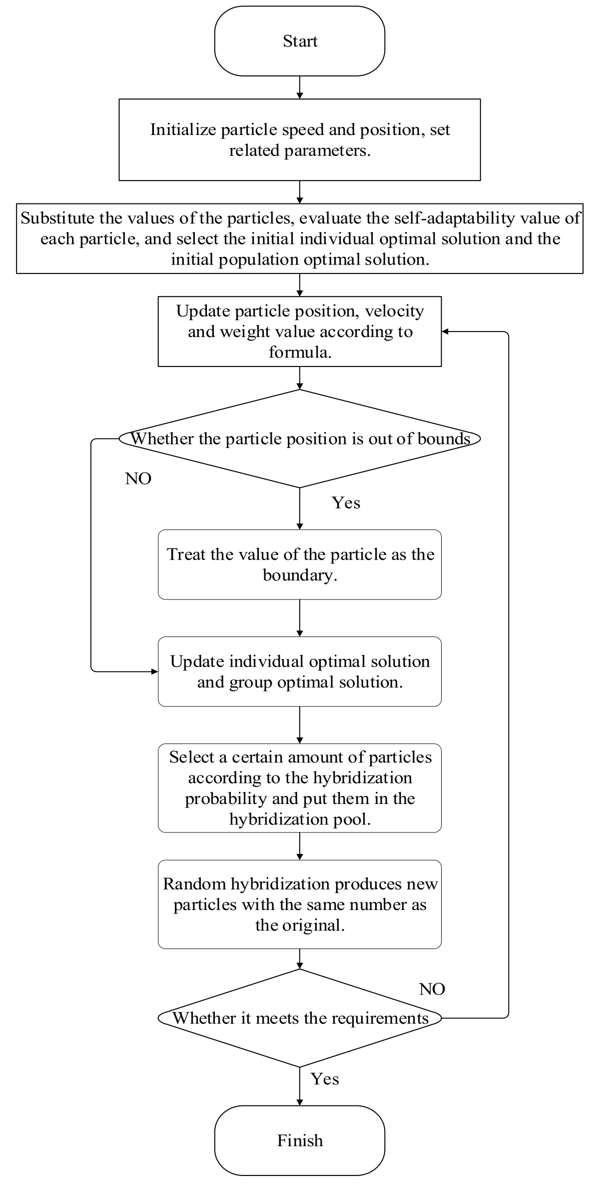

FIGURE 1 | Basic flow chart of the improved PSO algorithm.

TABLE 1 | Basic parameters of the fan.

Parameter	Numerical value
Rated power (kW)	1,000
Wind operation and management cost coefficient/ $CNY \cdot (kWh)^{-1}$	0.0306

TABLE 2 | Basic parameters of photovoltaics.

Parameter	Numerical value
Rated power (kW)	1,000
Photovoltaic operation management cost coefficient/ $CNY \cdot (kWh)^{-1}$	0.0098

TABLE 3 | Specific parameters of the gas turbine.

Parameter	Numerical value
Output range/kW	(0, 400)
Power generation efficiency	0.92
Natural gas price/ $CNY \cdot m^{-3}$	2.05
Natural gas status calorific value/ $MJ \cdot m^{-3}$	40
Uphill rate/(MW/h)	0.1
Downhill rate/(MW/h)	0.2
Cost coefficient of gas turbine operation management/ $CNY \cdot (kWh)^{-1}$	0.12

TABLE 4 | Partly parameters of the energy storage system.

Parameter	Numerical value
Charge and discharge power (kW)	400
Charge and discharge efficiency	0.87
$SOC_{\max}$ /%	0.9
$SOC_{\min}$/%	0.1
Energy storage operation management cost coefficient/ $CNY \cdot (kWh)^{-1}$	0.083

The output of the energy storage system: The VPP gives priority to the power output from distributed power sources. If the distributed power sources cannot meet the load demand, the energy storage system will be discharged, and if there is a supply of distributed power sources that exceeds the demand, the energy storage system will be charged and discharged at the right time.

Gas turbine output: The gas turbine plays an auxiliary role in the VPP as a controllable load, ensuring that it functions when distributed power sources, energy storage, etc. are not available to generate power to supply the load, storage, and the grid. Whether or not the gas turbine is powered depends on the demand of the load and its cost of power generation compared to the grid tariff, and then the decision is made whether or not to power it.

MODEL SOLVING ALGORITHM

In view of the shortcomings, such as the basic particle swarm being prone to fall into local optimum, a new improved PSO algorithm is proposed based on the basic PSO algorithm. The following improvements are made relative to the basic PSO algorithm:

The adaptive weight calculation formula is set as follows:

$$\omega = \begin{cases} \omega_{\min} - \dfrac{(\omega_{\max} - \omega_{\min}) \times (f - f_{\min})}{f_{avg} - f_{\min}}, f \le f_{avg} \\ \omega_{\max}, f > f_{avg} \end{cases}. \quad (23)$$

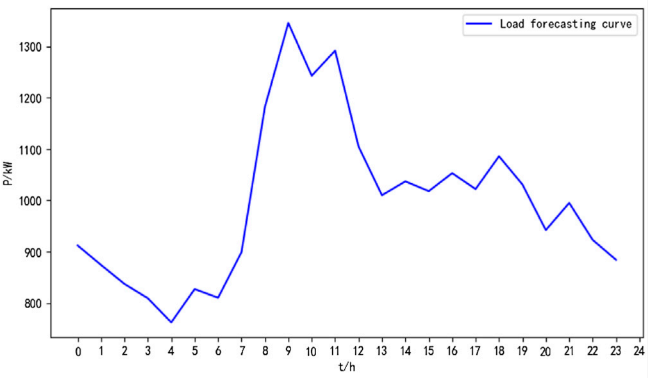

FIGURE 2 | Typical daily load forecast curve.

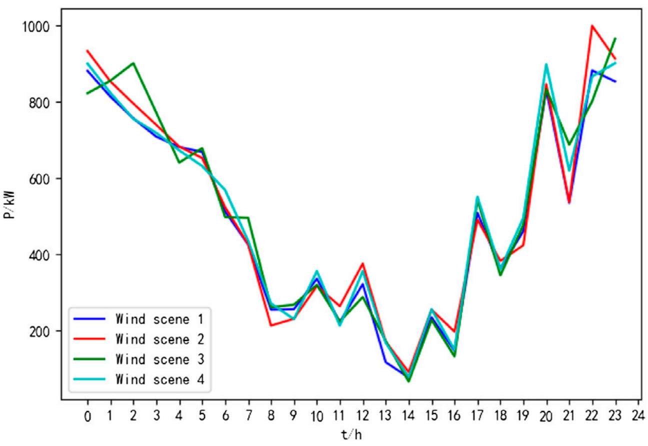

FIGURE 3 | Wind classic scene set.

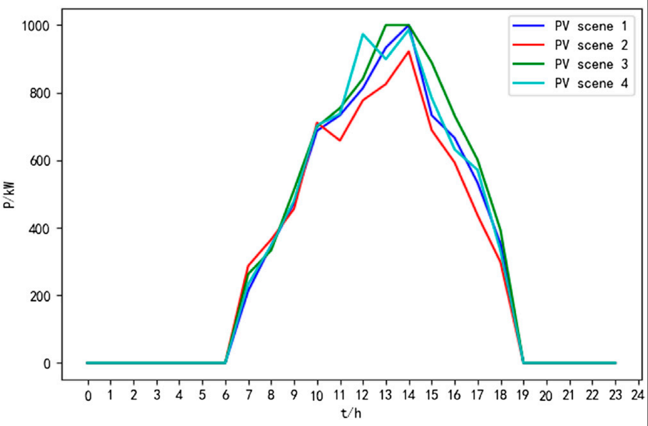

FIGURE 4 | Photovoltaic classic scene set.

In **Eq. 22**:

$$f_{avg} = \frac{1}{n}\sum_{i=1}^{n} f_i. \tag{24}$$

TABLE 5 | Wind scenario probability.

Scenes	1	2	3	4
Probability	0.18	0.17	0.45	0.2

TABLE 6 | Probability of the PV scenario.

Scenes	1	2	3	4
Probability	0.36	0.20	0.23	0.21

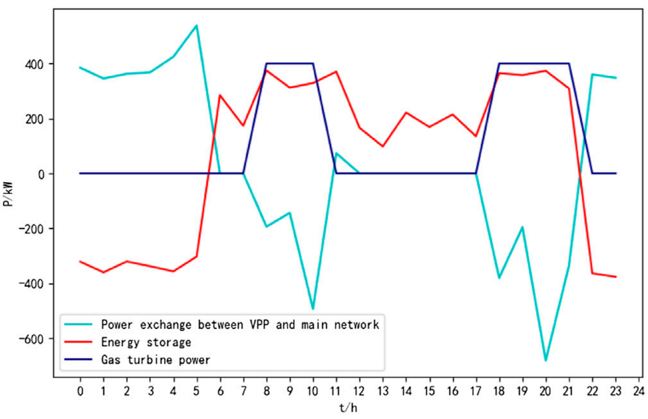

FIGURE 5 | Output curve of each part.

In the formula, n is the current iteration number; f is the real-time objective function of the particle,; $\omega_{\max}$ and $\omega_{\min}$ represent the maximum and minimum values of inertia weight, respectively; and $f_{\min}$ and f_{avg}, respectively, represent the minimum target value and average value of all current particles.

To enhance the global search capability of the algorithm, the concept of hybridization in genetic algorithms is added to the PSO algorithm (Lu et al., 2020). Suppose there is an existing hybridization pool, a certain number of particles is added in this pool, and then the particles in the pool are allowed to hybridize, which will generate a certain number of particles; let that number be the same as the original particles, and at the same time, the original particles are replaced with the newly generated particles so that the global search ability of the algorithm can be enhanced.

The positions and velocities of the new particles are obtained by crossing the positions of the original particles:

$$nx = i * mx(1) + (1 - i) * mx(2). \tag{25}$$

$$nv = \frac{mv(1) + mv(2)}{|mv(1) + mv(2)|}|mv|. \tag{26}$$

In the abovementioned formula, nx indicates the position of the new particle, mx indicates the position of the original particle;

TABLE 7 | Economic comparison in two scenarios.

Scenes	Configuration	Net income (RMB)
Scene 1	Classic scene set	14,495.27
Scene 2	Typical situation	13,282.77

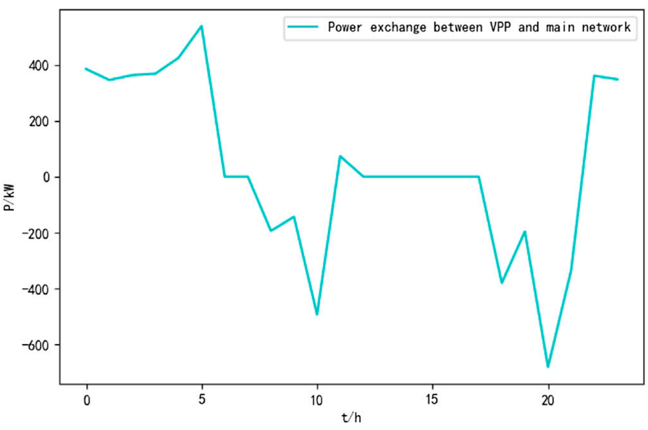

FIGURE 6 | Power interaction curve between the VPP and grid.

i is a uniform random number between 0 and 1, nv represents the velocity of the new particle, and mv represents the velocity of the original particle.

The flow chart of the improved PSO is shown in **Figure 1**.

SIMULATION EXAMPLE

Calculation Example Settings

In order to verify the feasibility of the abovementioned VPP energy storage system optimization configuration and algorithm, a VPP containing 1000 kW of wind power, 1000 kW of photovoltaic power, and 400 kW of gas turbine and an energy storage system with a rated capacity of 1600 kWh were selected. All the data in this study and the final results are derived on the Matlab simulation platform. Specific parameter information is shown in **Tables 1**, **2**, **3**, **4**.

The time-sharing electricity price is selected as the reference (Zhao and Fan, 2019b) for each distributed energy operation and management cost factor for non-summer industrial, commercial, and other electricity consumption in Shanghai. In this study, a typical daily load curve of a location is selected as the load forecast, and the results are shown in **Figure 2**.

Based on the historical data, the abovementioned Latin hypercube sampling is used to generate scenes and K-means clustering is used to reduce the scenes. In this study, the number of classical scenes of wind power output and PV power output is predetermined to be four each, so there are 4 × 4 scenes in the classical scene set. The results are shown in **Figure 3** and **Figure 4**. The probability of each scene is shown in **Table 5** and **Table 6**.

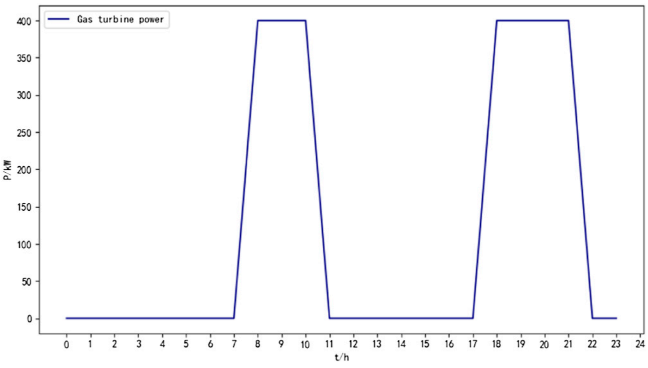

FIGURE 7 | Gas turbine output curve.

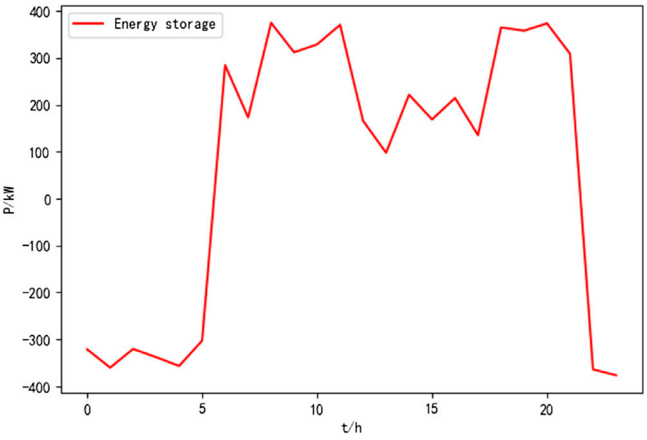

FIGURE 8 | Energy storage system output curve.

Simulation Results and Analysis

Running the developed model and solving it by an improved PSO algorithm, the net benefits of the VPP under different scenarios are shown in **Table 7**.

Running the developed model, the net revenue and the output of each component of the virtual power plant under the influence of the time-sharing tariff for Scenario 1 can be obtained, as shown in **Figure 5**.

It can be seen from **Figure 6** that during the time period 22:00–6:00 of the following day, the VPP has maintained the purchase of electricity from the grid mainly due to the fact that the price of electricity at this time is in the valley hours; during the time period 6:00–7:00, the electricity price is in the usual period, and the VPP does not interact with the grid for power; during the time period 8:00–11:00, when electricity prices are at their peak and trough, the VPP makes a profit by selling electricity to the grid while ensuring the demand of the load; during the period 11:00–18:00, the electricity is in the usual period, and the VPP does not interact with the grid for power; in the time period 18:00–22:00, when the electricity price is in the peak and valley hours, the VPP sells electricity to the grid to earn the difference but purchases electricity from the grid around 20:

00, which is due to the fact that PV power generation almost stops at this time, and the distributed power and gas turbine output still cannot guarantee the demand of the load, so the power needs to be purchased from the grid; then 22:00 enters the valley hours and the VPP purchases electricity from the grid.

From **Figure 7**, we can see that when the grid electricity price is at 22:00–6:00 the next day, the gas turbine does not generate electricity because the electricity price of the VPP from the grid is lower than the generation cost of the gas turbine; while the electricity price is at peak hours, the grid electricity price is higher than the generation cost of the gas turbine and the gas turbine generates electricity at almost full capacity and sells the electricity to the grid after satisfying the load demand, thus gaining benefits, when at the time 11:00–18:00. Although the electricity price is at normal hours, the distributed power supply and energy storage system can meet the load demand, and the gas turbine does not generate electricity at this time.

From **Figure 8** we can see that when the electricity price is at 22:00–6:00 the next day, the energy storage system is in the charging state, and when the time period reaches 8:00–11:00, the energy storage system is in the discharging state, which is due to the fact that the energy storage system sells the electricity stored in the valley hours to the grid under the premise of ensuring normal operation of the load, and thus earning the difference in price in the time period of 12:00–22:00. In the time period of 12:00–22:00, the electricity price is in the normal or peak period, and under the premise of satisfying the load demand, the energy storage will sell the excess power to the grid to earn the price difference, and then when entering the valley hours, the VPP purchases power from the grid and stores it in the energy storage system.

CONCLUSION

A VPP optimization model based on the classical scenario set is simulated and analyzed for specific arithmetic cases. Two different scenarios are set up for the optimal configuration, and the net benefits and output of each component are obtained for different cases. The effectiveness of the improved PSO algorithm is verified by solving the developed model with the improved PSO algorithm incorporating genetic mechanism. Finally, by comparing the net returns under different scenarios, it is verified that the optimal configuration of the VPP under the classical scenario set can significantly improve the net returns of the VPP.

Outlook: In recent years, with the popularity of electric vehicles, more uncertainties have been added to the VPP. Electric vehicles can be seen as a mobile power source, and their charging and discharging are highly random and have a greater relationship with human factors. At present, countries around the world are reducing carbon emissions, and in the future, considering electric vehicle access to the VPP, taking into account the economy and environmental protection (carbon emissions) of the VPP will be the focus of our research.

DATA AVAILABILITY STATEMENT

The raw data supporting the conclusion of this article will be made available by the authors, without undue reservation.

AUTHOR CONTRIBUTIONS

CW and WS completed the model building of the VPP and the simulation and reduction of wind power photovoltaic output scenarios. WS completed the debugging of the algorithm. MC completed the drawing of the graph. XM read the manuscript and corrected the grammatical errors.

FUNDING

This study was supported by the Key Scientific Research Projects Plan of Henan Higher Education Institutions under Grant Number 19A470006 and the cultivation plan of young backbone teachers in colleges and universities of Henan Province under Grant Number 2019GGJS104.

REFERENCES

Cui, H., Guo, Y., and Xia, C. (2010). Research on Optimal Configuration of Distributed Power Generation Considering Environmental Benefits[J]. *East China Electric Power* 38 (12), 1968–1971.

Gao, Z. (2019). *Research on Bidding Strategy and Coordinated Dispatching of VPP with Multiple Distributed Energy sources[D]*. Shanghai: Shanghai Jiaotong University.

Gong, C. (2018). *Research on Optimal Scheduling of VPP Group Considering Uncertainty Factors and Complementarity of Deviation Electricity[D]*. Changsha: Changsha University of Science and Technology.

Hong, B., Li, Q., and He, Y. (2017). Etc. Application and prospect of VPP in Distributed Photovoltaic Power Generation Application Demonstration Area[J]. *Electric Power Construction* 38 (09), 32–37.

Li, Z., Liu, X., Ni, C., Ge, X., and Wu, H. (2021). Study on Optimal Configuration of Energy Storage System in VPP Based on Scenario Set[J]. *Electr. Drive* 51 (16), 65–71.

Lin, W. (2017). *Research on Coordinated Control Strategy of Multiple Distributed Energy Sources under VPP[D]*. Huaqiao: Huaqiao University.

Lin, Y., Miao, S., Yang, W., Yin, B., Tu, Q., and Chang, Y. (2021). A Day-Ahead Optimal Scheduling Strategy for VPP Facing Multiple Uncertain Environments [J/OL]. *Power Automation Equipment*, 1–8.

Liu, C., Pang, P., Shi, W., Shen, J., Sun, Y., and Bao, H. (2021). Double-layer Collaborative Optimal Scheduling of VPP in Consideration of Carbon Neutralization Benefits and Clean Energy Consumption[J]. *Power Supply* 38 (09), 19–27.

Liu, D. (2018). *Economical Optimal Dispatch of VPP Considering Distributed Photovoltaic Power generation[D]*. Beijing): North China Electric Power University.

Liu, D., Fan, Q., You, H., Dai, X., Huang, Y., and Shao, Z. (2020). Research Status and Prospects of VPP under Ubiquitous Power Internet of Things[J]. *Eng. Sci. Tech.* 52 (04), 3–12.

Lu, G., Ou, Y., and Du, S. (2020). Research on the Internal Reactive Power Optimization of Wind Farms Based on Improved HPSO Algorithm[J]. *Electr. Meas. Instrumentation* 57 (10), 36–42.

McKay, M. D., Beckman, R. J., and Conover, W. J. (2012). in A comparison of Three Methods for Selecting Values of Input Variables in the Analysis of Output from a Computer Code: proceedings of the 37 th conference on winter simulation[J] (Alexandria, VA: American Statistical Association), 42202–42208.1.

Pudjianto, D., Ramsay, C., and Strbac, G. (2007). Virtual Power Plant and System Integration of Distributed Energy Resources. *IET Renew. Power Gener.* 1 (1), 10–16. doi:10.1049/iet-rpg:20060023

Soltani, M., Raoofat, N., and Rostami, M. A. (2012). "Optima L Reliable Strategy of Virt Tual Power Plant in Energy and Frequen Cy Control Markets[C]," in Electrical Power Distri bution Networks,2012 Proceedings of 17th Conference on.IE] EE, 1–6.

Sun, Q., Han, R., Zhang, H., Zhou, J., and Guerrero, J. M. (2015). A Multiagent-Based Consensus Algorithm for Distributed Coordinated Control of Distributed Generators in the Energy Internet. *IEEE Trans. Smart Grid* 6 (6), 3006–3019. Nov. 2015. doi:10.1109/TSG.2015.2412779

US Department Of Energy (2006). *Benefits of Demand Response in Electricity Markets and Recommendations for Achieving them[R]*. Washington DC, USA: US Department of Energy.

Wang, Yao. (2017). Research on VPP in Distributed Power Dispatching Management Mode[J]. *Shandong Ind. Tech.* (11), 208.

Wei, L., Bo, Z., and Hongbin, W. U. (2015). Optimal allocatic on model of energy storag e system in VPP envi ironment with a high pen etration of distributed pl hotovoltaic Generation[J]. *Automatio n of Electric Power Systen* 1s (23), 66–74.

Wen, X., and Guoen, W. (2019). Etc. Research on the Application of VPP in Distributed Photovoltaic Power Generation[J]. *Electr. Tech. Econ.* (04), 62–64.

Xia, Y., and Liu, J. (2016). Summary of Research on VPP Based on Distributed Generation[J]. *Electric Power Automation Equipment* 36 (4), 100–106.

Yang, N., Wang, B., Liu, D., Zhao, J., and Wang, H. (2013). An Integrated Supply-Demand Stochastic Optimization Method Considering Large-Scale Wind Power and Flexible Load [J]. *Proc. CSEE* 33 (26), 63–69. (in Chinese).

Yang, X., Tao, X., and Han, Li. (2020). The Status Quo and Prospects of VPP Technology[J]. *Huadian Tech.* 42 (05), 73–78.

Yi, Z., and Li, Z. (2018). Hot Spot Joint Dispatch Strategy Taking into Account the thermal Inertia of Heat Storage and Heating Area in Heating Network[J]. *Power Syst. Tech.* 42 (5), 1378–1384.

You, S., Traeholt, C., and Poulsen, B. (2009). in A market-based VPP[C]// International Conference on Clean Electrical Power (IEEE), 460–465.

Yuan, G., Chen, S., Liu, Y., and Fang, F. (2016). The Economical Optimal Dispatch of VPP Based on Time-Of-Use Electricity Prices[J]. *Power Syst. Tech.* 40 (03), 826–832.

Yuan, Y. (2017). The Application of VPP in Distributed Energy[J]. *Sci. Fortune* (24), 128.

Zhao, F., and Fan, Y. (2019). Double-level Optimal Dispatch of Multi-Energy VPP under the Influence of Time-Of-Use Electricity Prices[J]. *Power Syst. Prot. Control* 47 (20), 33–40.

Zhao, F., and Fan, Y. (2019). Dual-level Optimal Dispatch of Multi-Energy VPP under the Influence of Time-Of-Use Electricity Prices[J]. *Power Syst. Prot. Control* 47 (20), 62–73.

Zhinong, W., Chen, Y., Huang, W., Zheng, X., and Sun, G. (2018). Etc. VPP Multi-Power Capacity Optimization Configuration Model Considering Conditional value-at-Risk[J]. *Automation Electric Power Syst.* 42 (04), 39–46.

Zhou, B., and Lin, L. (2019). Research on VPP Trading Strategy Considering Combined Heat and Power Dispatch[J]. *Electr. Meas. Instrumentation* 59 (10), 75–81.

Zhou, N., Liu, N., and Zhang, J. (2016). PV-based Microgrid Operation Contrastive Research Considering On-Grid Power Tariff Regulation. *J]Electric Power Construction* 37 (3), 82–89. (in Chinese).

Conflict of Interest: The authors declare that the research was conducted in the absence of any commercial or financial relationships that could be construed as a potential conflict of interest.

frontiers
in Energy Research

METHODS
published: 24 March 2022
doi: 10.3389/fenrg.2022.874533

Improved Sliding-Mode Vector Control Strategy Combined With Extended Reactive Power for MMC Under Unbalanced Grid Condition

Tianyi Guan[1,2]*, *Xin Zhao*[1], *Wenjing Zheng*[3], *Hu Liu*[1], *Yao Liu*[4] and *Qiuye Sun*[1]

[1]College of Information Science and Engineering, Northeastern University, Shenyang, China, [2]Stare Grid Shenyang Electric Power Supply Company, Shenyang, China, [3]State Grid Liaoning Marketing Service Center, Shenyang, China, [4]Computer Science and Engineering, University of New South Wales, Sydney, NSW, Australia

Proportional–integral vector control (PIVC) has been proposed as an effective control strategy for modular multi-level converter (MMC) under balanced grid conditions. However, the PIVC using traditional power theory has unsatisfactory performances under unbalanced grid conditions, which cannot maintain the AC current sinusoidal while eliminating the twice grid-frequency ripples in active and reactive power. Therefore, an improved sliding-mode vector control (ISMVC) strategy combined with the extended reactive power (ERP) for MMC-based DC power system is proposed in this paper, which can cope with the problems above and work effectively under both balanced and unbalanced grid conditions. Furthermore, the proposed ISMVC shows better dynamic response and robustness than PI and conventional sliding-mode control (SMC) due to the novel design of sliding surface and reaching law. Comparative simulation experiments of the ISMVC and PIVC using the traditional and extended reactive power for MMC are conducted to verify the validity and superiority of the proposed control strategy under different grid conditions.

Keywords: modular multi-level converter (MMC), extended reactive power (ERP), sliding-mode control (SMC), vector control (VC), unbalanced grid condition

Edited by:
Wei Hu,
Zhejiang University, China

Reviewed by:
Xiangke Li,
Hong Kong Polytechnic University,
Hong Kong SAR, China
Tianyang Zhao,
Jinan University, China

***Correspondence:**
Tianyi Guan
931163745@qq.com

Specialty section:
This article was submitted to Smart Grids, a section of the journal Frontiers in Energy Research

Received: *12 February 2022*
Accepted: *01 March 2022*
Published: *24 March 2022*

Citation:
Guan T, Zhao X, Zheng W, Liu H, Liu Y and Sun Q (2022) Improved Sliding-Mode Vector Control Strategy Combined With Extended Reactive Power for MMC Under Unbalanced Grid Condition.
Front. Energy Res. 10:874533.
doi: 10.3389/fenrg.2022.874533

1 INTRODUCTION

Due to the attractive features of high waveform quality, low loss and well expansibility compared with traditional voltage sourced converter (VSC) which only has two or three levels, the modular multi-level converter (MMC) is increasingly used in modern high voltage direct current (HVDC) power systems (Zou et al., 2018; Liu et al., 2021; Wang et al., 2021). Therefore, more rigorous requirements are posed on MMC, especially when the grid conditions are unbalanced, which is very common in actual MMC-HVDC power system (Guo et al., 2019).

Currently, the vector control (VC) has been widely used in MMC-based DC power system (Nami et al., 2015; Wang et al., 2015; Xia et al., 2021), which is a direct current control strategy characterized by fast current feedback. The specific forms of VC is double closed-loop control using PI control strategy (PIVC), which can obtain the high quality current response. Based on VC, MMC-HVDC can achieve great steady-state performance. However, PI controller cannot ensure a satisfying dynamic response and robustness due to the lag characteristic of integrator under complex work conditions, e.g., parameter perturbation.

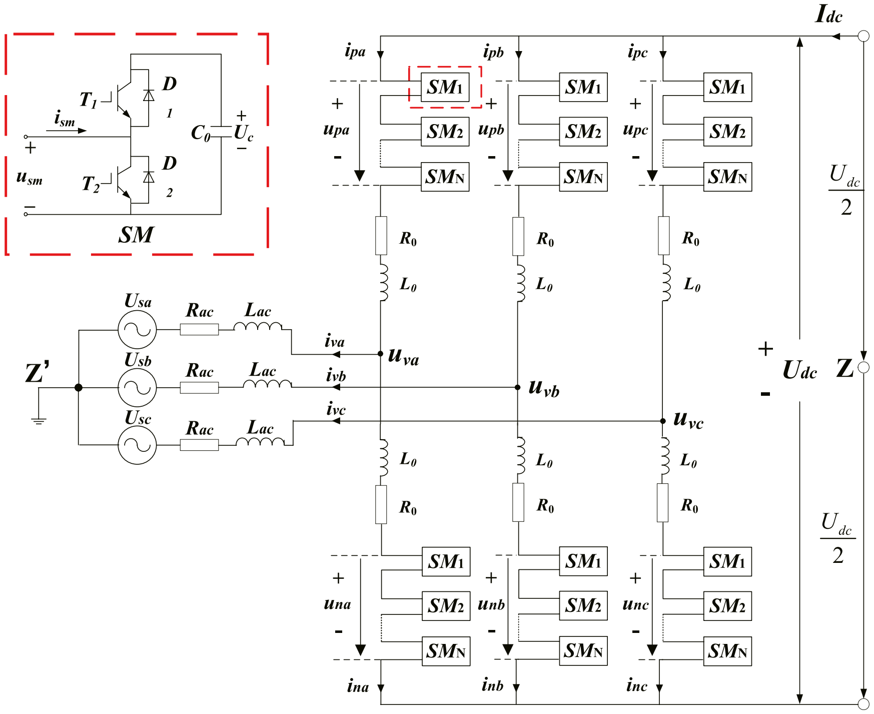

FIGURE 1 | MMC equivalent circuit.

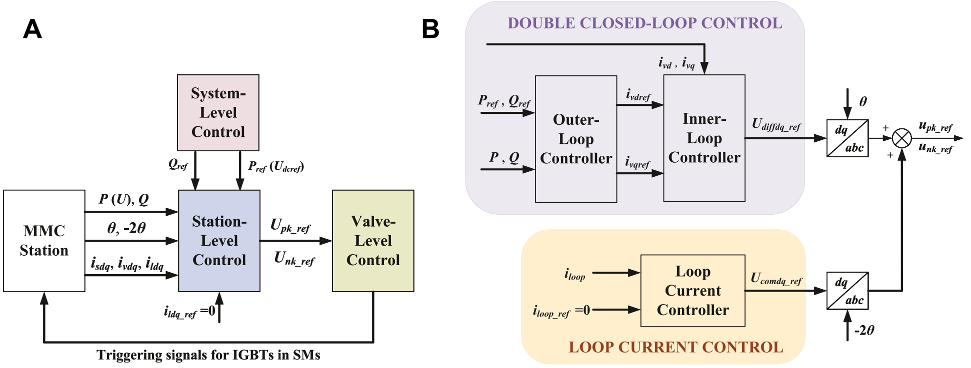

FIGURE 2 | Block diagram of overall control architecture, **(A)** block diagram of three control levels of MMC, **(B)** detailed station-level control of MMC.

Sliding-mode control (SMC), which is an effective nonlinear control method (Hu et al., 2010; Song et al., 2021), is extensively applied in doubly fed induction generator (DFIG), pulse width modulation-based rectifiers, AC/DC converters (Hemdani et al., 2015; Dan et al., 2018; Long et al., 2021) thanks to the well-known advantages of satisfactory steady-state precision, excellent dynamic control performance and disturbance rejection. Further researches apply SMC strategy in the VC system, and an improved SMC strategy is presented for MMC in Li et al. (2020), which has better dynamic response, great disturbance rejection and less chattering. However, the control strategies discussed earlier assume that the grid condition is balanced. In fact, the grid condition always becomes unbalanced in actual engineering due to grid harmonics, imbalance fault, etc. (Hao et al., 2020; Wang S. et al., 2020; Freytes et al., 2021), resulting in negative sequence components in the grid voltage and current, which seriously affects the operating performance of MMC-HVDC. Consequently, in order to improve the transient control performance of AC/DC converters under unbalanced grid conditions, a great deal of researches have been widely studied with two basic transient control objectives which are restraining negative-sequence current and eliminating the oscillating components at twice the fundamental grid frequency (2ω oscillations) in active power and reactive power simultaneously under unbalanced grid conditions (Kong et al., 2013).

Further studies are presented for the transient control of VSC/MMC under unbalanced grid condition. Classic VC strategy with two sets of PI controllers (PIVC) under unbalanced grid conditions is proposed in Chen and Xu (2007), the outer-loop controller calculates the positive- and negative-sequence reference current in *dq* reference frame while the inner-loop controller achieves current-tracking by PI control strategy. However, the active and reactive power fluctuations cannot be eliminated simultaneously and the robustness of PI control is deficient. Furthermore, proportional-resonant (PR) control and proportional-integral-resonant (PIR) control are also combined with VC strategy for grid-connected converters in Zhou et al. (2013) and Yang and Nian (2015), respectively, which are similar to PIVC.

As an alternative solution, resonant compensation control is widely studied for unbalanced conditions which adds compensations to corresponding control reference values to realize different transient objectives (Wei et al., 2011; Nian and Cheng, 2013). A resonant compensation control strategy is proposed in Wei et al. (2011), which combines the dual $\alpha\beta$-PR method with the power pulsation compensation to suppress the 2ω oscillations in active and reactive power to a small range. However, the control system cannot eliminate power oscillations completely. An improved direct power control strategy combining with a resonant regulator is presented in Nian and Cheng (2013), which can suppress the 2ω oscillations in active and reactive power at the same time by constructing a resonant closed-loop. However, the AC current would have non-sine aberration when the active and reactive power keep constant.

Conventionally, these control strategies above are all using the traditional instantaneous power definition (Akagi et al., 2008), which cannot ensure that the AC-side current remains sinusoidal while eliminating both active and reactive power fluctuations under unbalanced grid conditions. To cope with the problem, an extended reactive power (ERP) is proposed in Sun and Lipo (2006), which only modifies the definition of traditional instantaneous reactive power to be more suitable for AC/DC converters under unbalanced grid conditions. In Zhang and Qu (2015), Liang (2017), the ERP is used in different control systems such as predictive control and reduced-order vector resonance control for AC/DC converter, which shows a better performance when grid conditions are unbalanced. However, the ERP has not been combined with SMC for MMC to obtain a satisfactory control performance under unbalanced grid conditions.

The main contribution of this paper is to propose an improved sliding-mode vector control (ISMVC) strategy combined with ERP for MMC, which can eliminate the 2ω oscillations in the active power and ERP simultaneously under unbalanced grid conditions while obtaining sinusoidal AC-side currents. Compared with the PIVC, the proposed ISMVC has obvious control advantages in dynamic response and robustness. The rest of this paper is organized as follows. In **Section 2**, the mathematical of MMC and overall control scheme are simply presented. In **Section 3**, contrastive theoretical analysis of traditional reactive power (TRP) and ERP are conducted under unbalanced grid conditions while the formulas of the ERP-based outer-loop controllers are deduced. In addition, the ISMVC is proposed and applied to the positive- and negative-sequence inner-loop controllers with discussions on its stability. In **Section 4**, comparative simulations in PSCAD/EMTDC of the ISMVC and PIVC using different reactive power definition are carried out to validate the feasibility and superiority of the proposed methods under different grid conditions. In the end, conclusions are drawn in **Section 5**.

2 MATHEMATICAL MODEL AND OVERALL CONTROL ARCHITECTURE

Figure 1 shows a lumped schematic of the MMC. Among this figure, Z and Z' represent the neutral points ($U_{zz'} = 0$). R_{ac}, L_{ac}, and R_0, L_0 indicate the equivalent resistance and inductance of AC grid and per bridge arm, respectively; u_{pk}, u_{nk}, and i_{pk}, i_{nk} ($k = a$, b, c), respectively, represent the SM voltages and bridge arm current in the high-side and low-side bridge arms; the AC and DC grid voltages are expressed as U_{sk} and U_{dc}, respectively; u_{vk} and i_{vk} are AC voltage and current output by MMC.z

By using Kirchhoff's laws, the mathematical model for AC circuit and DC circuit of MMC in **Figure 1** can be derived separately as

$$\begin{cases} L\dot{i}_{vk} + Ri_{vk} = U_{diffk} - U_{sk} \\ L_0\dot{i}_{lk} + R_0 i_{lk} = \dfrac{U_{dc}}{2} - U_{comk} \end{cases} \tag{1}$$

where $U_{diffk} = (U_{nk} - U_{pk})/2$ and $U_{comk} = (U_{nk} + U_{pk})/2$ denote the differential-mode voltage (DMV) and common-mode voltage (CMV) in phase k, respectively; $i_{lk} = (i_{pk} + i_{nk})/2$ denotes the loop current of phase k, which consists of DC component and second harmonic components (Li et al., 2020); $R = R_{ac} + R_0/2$; $L = L_{ac} + L_0/2$.

Conducting Park Transformation on **Eq. 1** for better control effect, **Eq. 1** in *dq* reference frame can be transformed as

$$\begin{cases} L\begin{bmatrix} \dot{i}_{vd} \\ \dot{i}_{vq} \end{bmatrix} = \begin{bmatrix} -R & \omega L \\ -\omega L & -R \end{bmatrix}\begin{bmatrix} i_{vd} \\ i_{vq} \end{bmatrix} + \begin{bmatrix} U_{diffd} \\ U_{diffq} \end{bmatrix} - \begin{bmatrix} U_{sd} \\ U_{sq} \end{bmatrix} \\ L_0\begin{bmatrix} \dot{i}_{ld} \\ \dot{i}_{lq} \end{bmatrix} = \begin{bmatrix} -R_0 & -2\omega L_0 \\ 2\omega L_0 & -R_0 \end{bmatrix}\begin{bmatrix} i_{ld} \\ i_{lq} \end{bmatrix} - \begin{bmatrix} U_{comd} \\ U_{comq} \end{bmatrix} \end{cases} \tag{2}$$

where ω is the fundamental grid angular frequency; U_{sd} ,i_{vd}, U_{diffd}, U_{comd}, i_{lq} and U_{sq}, i_{vq}, U_{diffq}, U_{comd}, i_{lq} are d-axis and q-axis component of corresponding electrical variables in **Eq. 1**, respectively.

Figure 2 shows the common hierarchical control structure of the MMC-HVDC control system, consisting of three control levels which ensure the proper operation of MMC from different dimensions. Among them, the station-level control provides the DMV and CMV in **Eq. 1** by controlling the inner-loop current i_{vk} precisely according to the reference value of DC voltage, active power and reactive power, which decides the control effects of MMC directly.

When the AC grid condition in **Figure 1** become unbalanced, the grid voltage and current may contain the positive-sequence, negative-sequence and zero-sequence components, respectively. Since the transformer on the AC side often adopts the Y-Δ connection method in actual projects, the zero-sequence component of valve-side current is eliminated. Thus, the MMC controller is designed without considering the zero-sequence component in this paper. Due to the structure of the three-phase circuit on the AC side of MMC is approximately symmetrical in **Figure 1**, the mathematical model for AC circuit of MMC under unbalanced grid conditions can be rewritten from **Eq. 2** as

$$\begin{cases} L\begin{bmatrix} \dot{i}^+_{vd} \\ \dot{i}^+_{vq} \end{bmatrix} = \begin{bmatrix} -R & \omega L \\ -\omega L & -R \end{bmatrix}\begin{bmatrix} i^+_{vd} \\ i^+_{vq} \end{bmatrix} + \begin{bmatrix} U^+_{diffd} \\ U^+_{diffq} \end{bmatrix} - \begin{bmatrix} U^+_{sd} \\ U^+_{sq} \end{bmatrix} \\ L\begin{bmatrix} \dot{i}^-_{vd} \\ \dot{i}^-_{vq} \end{bmatrix} = \begin{bmatrix} -R & \omega L \\ -\omega L & -R \end{bmatrix}\begin{bmatrix} i^-_{vd} \\ i^-_{vq} \end{bmatrix} + \begin{bmatrix} U^-_{diffd} \\ U^-_{diffq} \end{bmatrix} - \begin{bmatrix} U^-_{sd} \\ U^-_{sq} \end{bmatrix} \end{cases} \tag{3}$$

where U^+_{sd}, U^+_{sq}, U^+_{diffd}, U^+_{diffq}, i^+_{vd}, i^+_{vq}, and U^-_{sd}, U^-_{sq}, U^-_{diffd}, U^-_{diffq}, i^-_{vd}, i^-_{vq} are positive-sequence components and negative-sequence components of corresponding electrical variables in **Eq. 2**, respectively.

According to **Eq. 3**, the inner-loop controller in **Figure 2B** can be further decomposed into two parts, namely, positive- and negative-sequence inner-loop controllers, which collaborate to achieve different control objectives by controlling the positive current i^+_{vdq} and negative current i^+_{vdq} in dqreference frame track their reference values accurately, respectively.

It should be noted that the reference value of loop current in the DC circuit of MMC is always set to zero during the whole control process in **Figure 2**, which means the loop current controller is independent of the unbalanced grid conditions. Therefore, this paper is focused on the improved double closed-loop control of MMC in **Figure 2B** which aims to obtain constant active and reactive power as well as distortionless grid current at any time especially when the grid condition is unbalanced.

3 IMPROVED SLIDING-MODE VECTOR CONTROL FOR MODULAR MULTI-LEVEL CONVERTER USING EXTENDED REACTIVE POWER

The traditional AC-side complex power S can be expressed as

$$S = 1.5U_{\alpha\beta}i^*_{\alpha\beta} \tag{4}$$

where "*" denotes the conjugate of a complex vector; U_α, i_α and U_β, i_β are the α-axis and β-axis components of the voltage and current on the AC side, respectively.

Thus, the traditional power can be expressed as

$$\begin{cases} P = \frac{3}{2}Re\left(U_{\alpha\beta}i^*_{\alpha\beta}\right) \\ Q = \frac{3}{2}Im\left(U_{\alpha\beta}i^*_{\alpha\beta}\right) \end{cases} \tag{5}$$

When the traditional active and reactive power are chosen as the controlled variables of outer-loop controller in **Figure 2** under unbalanced grid conditions, the active and reactive power will contain 2ω oscillations otherwise the grid current will have non-sine aberration, which is pernicious to the grid operation and the MMC itself. Consequently, the control method of MMC needs further improvement to be more applicable under unbalanced grid conditions.

In this paper, an ERP is introduced to improve the control performance of MMC under unbalanced grid conditions (Sun and Lipo, 2006), which can be expressed as

$$Q^{new} = \frac{3}{2}Re\left(U^{lag}_{\alpha\beta}i^*_{\alpha\beta}\right) \tag{6}$$

where, $U^{lag}_{\alpha\beta} = U_{\alpha\beta}(t - T/4)$ lags $U_{\alpha\beta}$ by a quarter of electrical period.

When the grid condition becomes unbalanced, the grid voltage and current can be calculated as

$$\begin{cases} U_{\alpha\beta} = U^+_{\alpha\beta} + U^-_{\alpha\beta} = U^+_{dq}e^{j\omega t} + U^-_{dq}e^{-j\omega t} \\ i_{\alpha\beta} = i^+_{\alpha\beta} + i^-_{\alpha\beta} = i^+_{dq}e^{j\omega t} + i^-_{dq}e^{-j\omega t} \end{cases} \tag{7}$$

where $U^+_{\alpha\beta}$, $i^+_{\alpha\beta}$, and $U^-_{\alpha\beta}$, $i^-_{\alpha\beta}$, represent the positive- and negative-sequence grid voltage and current vectors in the stationary reference frame respectively, which rotate counterclockwise at ω and $-\omega$ respectively; U^+_{dq}, i^+_{dq}, and U^-_{dq}, i^-_{dq} are positive- and negative-sequence grid voltage and current vectors in the forward and backward dq reference frame respectively, which rotate counterclockwise at ω and $-\omega$ respectively.

According to the rotating direction of forward and backward dq reference frame, the delayed grid voltage vector under unbalanced grid condition can be expressed as

$$U^{lag}_{\alpha\beta} = U^+_{dq}e^{j\left(\omega t - \frac{\pi}{2}\right)} + U^-_{dq}e^{-j\left(\omega t - \frac{\pi}{2}\right)} = -jU^+_{dq}e^{j\omega t} + jU^-_{dq}e^{-j\omega t} \tag{8}$$

Substituting **Eqs 7**, **8** into **Eqs 5**, **6**, the active power, TRP and ERP under unbalanced grid condition can be expressed as

$$\begin{cases} P = P_0 + P_{2c}\cos(2wt) + P_{2s}\sin(2wt) \\ Q = Q_0 + Q_{2c}\cos(2wt) + Q_{2s}\sin(2wt) \\ Q^{new} = Q^{new}_0 + Q^{new}_{2c}\cos(2wt) + Q^{new}_{2s}\sin(2wt) \end{cases} \tag{9}$$

where, P_0, Q_0, and Q^{new}_0 denote the DC components of the active power, TRP, and ERP, respectively, which should be the reference value of the outer-loop controller; P_{2c}, Q_{2c} and Q^{new}_{2c} denote the coefficients of 2ω cosine oscillating component of the active power, TRP, and ERP, respectively; P_{2s}, Q_{2s}, and Q^{new}_{2s} denote the coefficients of 2ω sinusoidal oscillating components of the active power, TRP, and ERP, respectively.

For better illustration, the coefficients of 2ω cosine and sinusoidal components of the active power, TRP, and ERP can be expressed in the matrix form as

$$\begin{bmatrix} P_0 \\ P_{2c} \\ P_{2s} \\ Q_0 \\ Q_{2c} \\ Q_{2s} \\ Q^{new}_0 \\ Q^{new}_{2c} \\ Q^{new}_{2s} \end{bmatrix} = \frac{3}{2}\begin{bmatrix} U^+_d & U^+_q & U^-_d & U^-_q \\ U^-_d & U^-_q & U^+_d & U^+_q \\ U^-_q & -U^-_d & -U^+_q & U^+_d \\ U^+_q & -U^+_d & U^-_q & -U^-_d \\ U^-_q & -U^-_d & U^+_q & -U^+_d \\ -U^-_d & -U^-_q & U^+_d & U^+_q \\ U^+_q & -U^+_d & -U^-_q & U^-_d \\ -U^-_q & U^-_d & U^+_q & -U^+_d \\ U^-_d & U^-_q & U^+_d & U^+_q \end{bmatrix}\begin{bmatrix} i^+_d \\ i^+_q \\ i^-_d \\ i^-_q \end{bmatrix} \tag{10}$$

According to **Eq. 10**, the outer-loop controller in **Figure 2** which select active power and reactive power as controlled variables (P/Q control) to obtain constant output power can be designed.

For the PIVC using TRP, the positive and negative current reference value in their corresponding synchronous frame which are the reference inputs of the positive- and negative-sequence inner-loop controllers can be derived as

$$\begin{bmatrix} i^{+}_{vdref} \\ i^{+}_{vqref} \\ i^{-}_{vdref} \\ i^{-}_{vqref} \end{bmatrix} = \frac{2}{3}\begin{bmatrix} U^{+}_{sd} & U^{+}_{sq} & U^{-}_{sd} & U^{-}_{sq} \\ U^{-}_{sd} & U^{-}_{sq} & U^{+}_{sd} & U^{+}_{sq} \\ U^{-}_{sq} & -U^{-}_{sd} & -U^{+}_{sq} & U^{+}_{sd} \\ U^{+}_{sq} & -U^{+}_{sd} & U^{-}_{sq} & -U^{-}_{sd} \end{bmatrix}^{-1}\begin{bmatrix} P_{0ref} \\ P_{2c} \\ P_{2s} \\ Q_{0ref} \\ Q_{2c} \\ Q_{2s} \end{bmatrix} \tag{11}$$

Since the reference values of active and reactive power (P_{0ref}, Q_{0ref}) are default setting received from system-level control in **Figure 2**, there are only two available controlled variables left (choose two controlled variables from P_{2c}, Q_{2c}, P_{2s}, Q_{2s}), which should eliminate the 2ω oscillations in active power and reactive power simultaneously.

It can be concluded from **Eq. 10** that

$$\begin{cases} P_{2c} = 0 \rightarrow U^{-}_{d} i^{+}_{d} + U^{-}_{q} i^{+}_{q} = -U^{+}_{d} i^{-}_{d} - U^{+}_{q} i^{-}_{q} \\ P_{2s} = 0 \rightarrow U^{-}_{q} i^{+}_{d} - U^{-}_{d} i^{+}_{q} = U^{+}_{q} i^{-}_{d} - U^{+}_{d} i^{-}_{q} \end{cases} \tag{12}$$

$$\begin{cases} Q_{2c} = 0 \rightarrow U^{-}_{q} i^{+}_{d} - U^{-}_{d} i^{+}_{q} = U^{+}_{d} i^{-}_{q} - U^{+}_{q} i^{-}_{d} \\ Q_{2s} = 0 \rightarrow U^{-}_{d} i^{+}_{d} + U^{-}_{q} i^{+}_{q} = U^{+}_{d} i^{-}_{d} + U^{+}_{q} i^{-}_{q} \end{cases} \tag{13}$$

Obviously, **Eqs 12**, **13** cannot hold at the same time which means the 2ω oscillations in TRP still exist when the 2ω oscillating component coefficients of active power in **Eq. 11** are set to zero ($P_{2cref} = P_{2sref} = 0$) under unbalanced grid conditions. Consequently, they cannot be eliminated concurrently by adopting TRP under unbalanced grid conditions, otherwise, it will only lead to distortion of the AC current with high harmonics.

Similarly, for the ERP, it can be seen from **Eq. 10** that

$$\begin{cases} P_{2c} = Q^{new}_{2s} \\ P_{2s} = -Q^{new}_{2c} \end{cases} \tag{14}$$

which means the 2ω oscillations in ERP will be eliminated completely with grid current keeping sinusoidal when choose P_{2c} and P_{2s} as controlled variables and set them to zero under unbalanced grid conditions, which is why the ERP is more suitable than TRP under unbalanced conditions as well as reducing the control complexity to improve the control performance.

Therefore, choosing active power and the ERP as controlled variables under unbalanced conditions with $P_{2c} = P_{2s} = 0$ in **Eq. 10**, the positive- and negative-sequence current reference value in their corresponding synchronous frame can be derived as

$$\begin{aligned} \begin{bmatrix} i^{+}_{vdref} \\ i^{+}_{vqref} \\ i^{-}_{vdref} \\ i^{-}_{vqref} \end{bmatrix} &= \frac{2}{3}\begin{bmatrix} U^{+}_{sd} & U^{+}_{sq} & U^{-}_{sd} & U^{-}_{sq} \\ U^{-}_{sd} & U^{-}_{sq} & U^{+}_{sd} & U^{+}_{sq} \\ U^{-}_{sq} & -U^{-}_{sd} & -U^{+}_{sq} & U^{+}_{sd} \\ U^{+}_{sq} & -U^{+}_{sd} & -U^{-}_{sq} & U^{-}_{sd} \end{bmatrix}^{-1}\begin{bmatrix} P_{0ref} \\ 0 \\ 0 \\ Q^{new}_{0ref} \end{bmatrix} \\ &= \frac{2P_{0ref}}{3A}\begin{bmatrix} U^{+}_{sd} \\ U^{+}_{sq} \\ -U^{-}_{sd} \\ -U^{-}_{sq} \end{bmatrix} + \frac{2Q^{new}_{0ref}}{3A}\begin{bmatrix} U^{+}_{sq} \\ -U^{+}_{sd} \\ U^{-}_{sq} \\ -U^{-}_{sd} \end{bmatrix} \end{aligned} \tag{15}$$

where $A = [(U^{+}_{sd})^2 + (U^{+}_{sq})^2] - [(U^{-}_{sd})^2 + (U^{-}_{sq})^2] \neq 0$; P_{0ref} and Q^{new}_{0ref} are the reference values of active power and ERP respectively.

Moreover, when grid condition keeps balanced, it can be seen from **Eqs 5**, **6** that

$$\begin{cases} Q = 1.5Im\left(U_{\alpha\beta} i^{\star}_{\alpha\beta}\right) = U_{\beta} i_{\alpha} - U_{\alpha} i_{\beta} \\ Q^{new} = 1.5Re\left(U^{lag}_{\alpha\beta} i^{\star}_{\alpha\beta}\right) = U_{\beta} i_{\alpha} - U_{\alpha} i_{\beta} \end{cases} \tag{16}$$

It can be seen from **Eq. 16** that the ERP can still remain effective under balanced grid condition which increases the applicability of the proposed control strategy.

After obtaining the reference values of positive- and negative-sequence dq form grid current in **Eq. 15**, the next-step work is to design a better inner-loop controller to track these reference value accurately. Thus, an ISMVC strategy is proposed in this paper to enhance the control performance of the inner-loop controller in response speed and robustness compared with the traditional PI control strategy. Since the control structure of the positive- and negative-sequence inner-loop controllers are identical, the rest of this section will focus on the positive-sequence inner-loop controller as an example.

The first stage in the design of SMC is to select an effective sliding surface. Due to the minimal steady-state error and great chattering rejection (Jiang and Gao, 2021), the integral sliding surface is adopted in this paper to improve the steady-state control performance, which can be designed as

$$S = [\,S_1 \;\; S_2\,]^T \tag{17}$$

$$\begin{cases} S_1 = e^{+}_{p} + k^{+}_{p}\displaystyle\int_0^t e^{+}_{p}(\tau)d\tau \\ S_2 = e^{+}_{q} + k^{+}_{q}\displaystyle\int_0^t e^{+}_{q}(\tau)d\tau \end{cases} \tag{18}$$

where k^{+}_{p} and k^{+}_{q} denote the integral coefficients of the positive-sequence d-axis and q-axis grid current, respectively; e^{+}_{p}, e^{+}_{q} are the tracking errors of the positive-sequence d-axis and q-axis grid current, respectively, i.e.

$$\begin{cases} e^{+}_{p} = i^{+}_{vdref} - i^{+}_{vd} \\ e^{+}_{q} = i^{+}_{vqref} - i^{+}_{vq} \end{cases} \tag{19}$$

To guarantee that the reaching and sliding conditions of SMC which enables uncertain chaotic systems to reach sliding-mode surface within finite time are satisfied, a Lyapunov function (Wang et al., 2019; Wang R. et al., 2020) is defined as

$$V = KS^T S = K\left(S_1^2 + S_2^2\right) \geq 0 \tag{20}$$

where, K is a positive constant.

The derivative of V can be calculated as

$$\frac{dV}{dt} = S_1\frac{dS_1}{dt} + S_2\frac{dS_2}{dt} = S^T\frac{dS}{dt} \tag{21}$$

From **Eqs 18**, **19**, the derivative of S can be calculated as

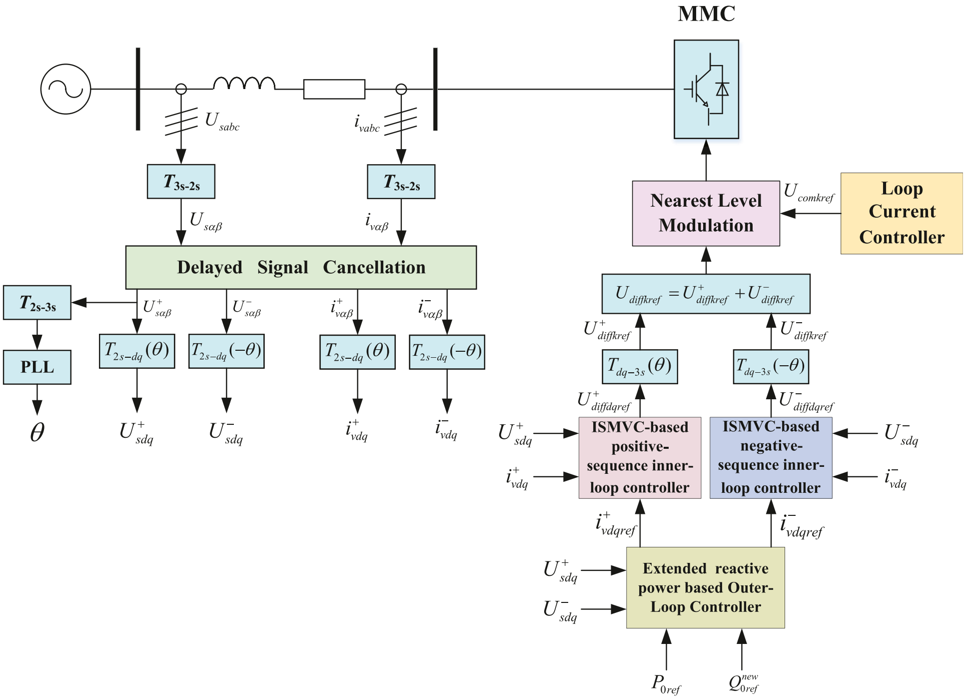

FIGURE 3 | Control diagram of the proposed ISMVC for MMC.

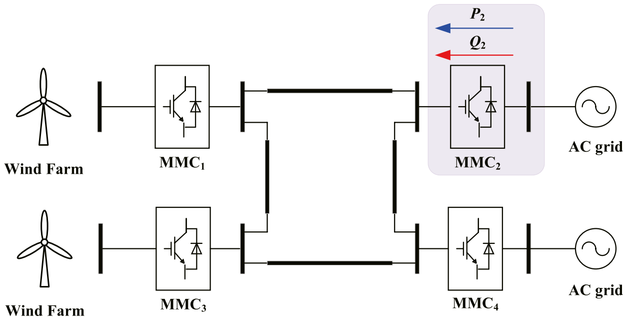

FIGURE 4 | Four-terminal MMC-based DC power system.

TABLE 1 | Table I parameters of MMC$_2$.

System parameters	Values
DC-bus reference voltage	±200 kV
AC line-to-line voltage	220 kV
SM capacitance	9,750 μF
Inductance of each bridge arm	36.7 mH
SM numbers in per bridge arm	100

$$\frac{dS}{dt}=\frac{d}{dt}\begin{bmatrix}S_1\\S_2\end{bmatrix}=\frac{d}{dt}\begin{bmatrix}i^+_{vdref}-i^+_{vd}\\i^+_{vqref}-i^+_{vq}\end{bmatrix}+\begin{bmatrix}k^+_pe^+_p\\k^+_qe^+_q\end{bmatrix}\tag{22}$$

Taking **Eq. 3** into **Eq. 22**, the derivative of S can be rewritten as

$$\frac{dS}{dt}=J+DU\tag{23}$$

where

$$J=\frac{1}{L}\left\{\begin{bmatrix}R&-\omega L\\\omega L&R\end{bmatrix}\begin{bmatrix}i^+_{vd}\\i^+_{vq}\end{bmatrix}+\begin{bmatrix}U^+_{sd}\\U^+_{sq}\end{bmatrix}+\begin{bmatrix}k^+_pe^+_p\\k^+_qe^+_q\end{bmatrix}+\frac{d}{dt}\begin{bmatrix}i^+_{vdref}\\i^+_{vqref}\end{bmatrix}\right\}$$

$$D=-\frac{1}{L}\,U=\begin{bmatrix}U^+_{diffd}\\U^+_{diffq}\end{bmatrix}.$$

For the purpose of better dynamic performance and robustness with less chattering phenomena compared with the conventional exponential trending law (Mozayan et al., 2016), an improved exponential trending law is proposed as follows:

$$\frac{d}{dt}\begin{bmatrix}S_1\\S_2\end{bmatrix}=-\begin{bmatrix}\varepsilon_1|e^+_p|^g sat(S_1)\\\varepsilon_2|e^+_q|^h sat(S_2)\end{bmatrix}-\begin{bmatrix}k_1S_1\\k_2S_2\end{bmatrix}\tag{24}$$

where, ε_1, ε_2, k_1, k_2 are positive control parameters; g and h are positive power parameters; $sat\,(S_i)$ denote the saturation function which can be expressed as

$$sat\,(S_i)=\begin{cases}1 & S_i>\beta_i\\\dfrac{S_i}{\beta_i} & |S_i|\le\beta_i\\-1 & S_i<-\beta_i\end{cases}\tag{25}$$

where, β_i represents the range of the boundary layer; i = 1, 2.

In **Eq. 24**, the saturation function is adopted to design a boundary layer on both sides of the sliding surface which can reduce the high-frequency chattering phenomena introduced by

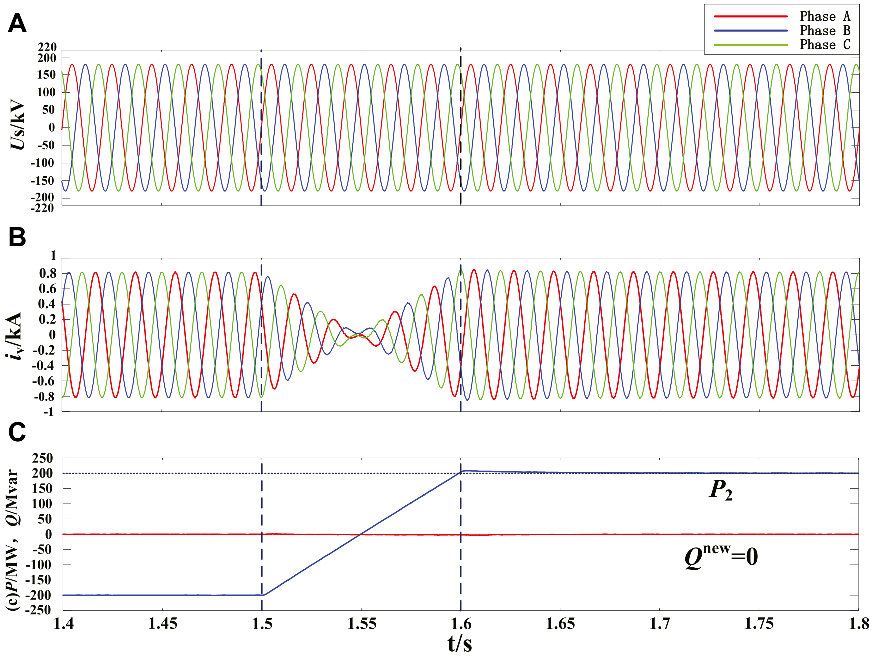

FIGURE 5 | Simulation results under balanced grid condition, **(A)** AC grid voltage at MMC$_2$ side, **(B)** AC grid current output by MMC$_2$, **(C)** active power and ERP output by MMC$_2$ using the novel ISMVC.

traditional sign-function sgn (S_i). $-\varepsilon_i|e|^h sat\,(S_i)$ and $-k_iS_i$ are variable and constant velocity term, respectively, which work together to propel the state trajectory towards the sliding surface with adaptive speed. Thus, good dynamic performance and less chattering phenomena can be balanced effectively.

Substituting **Eq. 24** into **Eq. 21**, the derivative of function V can be rewritten as

$$\frac{dV}{dt} = -2K\left[\,S_1 \quad S_2\,\right]\left\{\begin{bmatrix}\varepsilon_1|e_p^+|^h sat\,(S_1)\\ \varepsilon_2|e_q^+|^j sat\,(S_2)\end{bmatrix} + \begin{bmatrix}k_1S_1\\ k_2S_2\end{bmatrix}\right\} \le 0 \qquad (26)$$

Obviously, it can be seen from **Eq. 20** to **Eq. 26** that function V and its derivative are positive-definite and negative-definite, respectively, which means that the proposed ISMVC strategy is proved to be asymptotically stable according to the Lyapunov theory.

Combining **Eqs 23**, **24**, the actual control variables of positive-sequence inner-loop controller $U^+_{diffdref}$ and $U^+_{diffqref}$ can be expressed as

$$\begin{bmatrix}U^+_{diffdref}\\ U^+_{diffqref}\end{bmatrix} = \begin{bmatrix}L\left(\varepsilon_1|e_p^+|^g sat\,(S_1) + k_1S_1 + k_p^+e_p^+\right)\\ L\left(\varepsilon_2|e_q^+|^h sat\,(S_2) + k_2S_2 + k_q^+e_q^+\right)\end{bmatrix} + \begin{bmatrix}R & -\omega L\\ \omega L & R\end{bmatrix}\begin{bmatrix}i^+_{vd}\\ i^+_{vq}\end{bmatrix} + \begin{bmatrix}U^+_{sd}\\ U^+_{sq}\end{bmatrix} + L\frac{d}{dt}\begin{bmatrix}i^+_{vdref}\\ i^+_{vqref}\end{bmatrix} \qquad (27)$$

Similarly, the actual control variables of the negative-sequence inner-loop controller $U^-_{diffdref}$ and $U^-_{diffqref}$ can be obtained from **Eq. 3** to **Eq. 27** as

$$\begin{bmatrix}U^-_{diffdref}\\ U^-_{diffqref}\end{bmatrix} = \begin{bmatrix}L\left(\varepsilon_3|e_p^-|^m sat\,(S_3) + k_3S_3 + k_p^-e_p^-\right)\\ L\left(\varepsilon_4|e_q^-|^n sat\,(S_4) + k_4S_4 + k_q^-e_q^-\right)\end{bmatrix} + \begin{bmatrix}R & \omega L\\ -\omega L & R\end{bmatrix}\begin{bmatrix}i^-_{vd}\\ i^-_{vq}\end{bmatrix} + \begin{bmatrix}U^-_{sd}\\ U^-_{sq}\end{bmatrix} + L\frac{d}{dt}\begin{bmatrix}i^-_{vdref}\\ i^-_{vqref}\end{bmatrix} \qquad (28)$$

where e_p^- and e_q^- are the tracking errors of the negative-sequence d-axis and q-axis grid current, respectively; ε_3, ε_4, k_3, k_4 are positive control parameters; m and n are positive power parameters; k_p^- and k_q^- are the integral coefficients.

Figure 3 shows the control diagram of the proposed ISMVC for MMC. First, the ERP is adopted in the design of the outer-loop controller to obtain the reference value of the positive- and negative-sequence grid current in dq reference frame which are regarded as the input reference of the ISMVC-based positive- and negative-sequence inner-loop controllers. Then, the reference value of DMV can be deduced while the CMV reference can be easily obtained from loop current controller. Finally, the triggering signals for IGBT in SMs can be calculated by the nearest level modulation (NLM) method (Chen et al., 2020). In addition, it should be noted that the positive- and negative-sequence components of the grid voltage and current are extracted by delayed signal cancellation (DSC) strategy (Timbus et al., 2007).

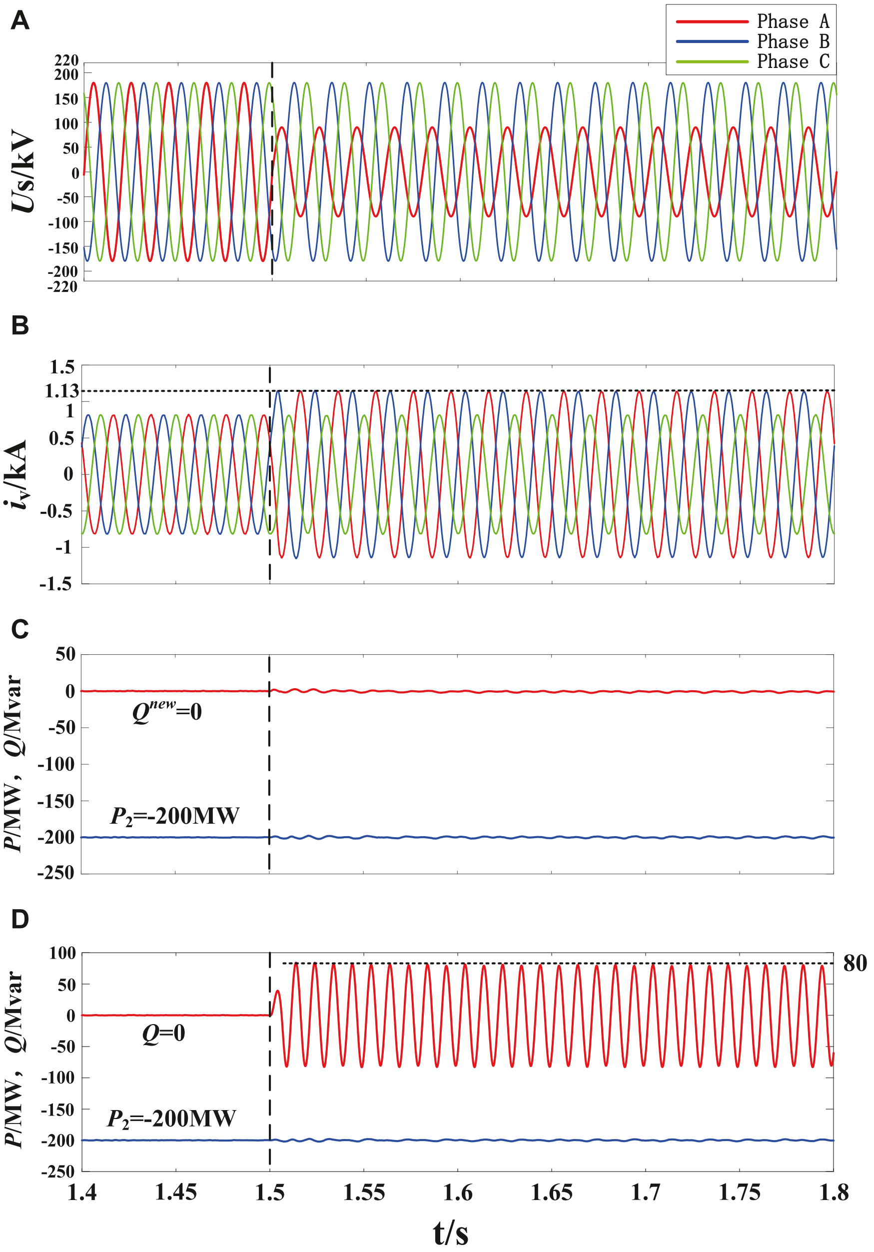

FIGURE 6 | Control performance of the traditional ISMVC and novel ISMVC under unbalanced grid condition, **(A)** AC grid voltage at MMC_2 side, **(B)** AC grid current output by MMC_2, **(C)** active power and ERP output by MMC_2 using the novel ISMVC, **(D)** active power and reactive power output by MMC_2 using the traditional ISMVC.

4 SIMULATIONS

4.1 Simulation Model

To validate the effectiveness of the proposed ISMVC strategy combined with ERP for MMC, a four-terminal MMC-based DC power system simulation shown in **Figure 4** is carried out in PSCAD/EMTDC whose sampling frequency set as 50 kHz to consistent with practical projects. The DC-bus voltage stability and the power balance of the DC system are controlled by other MMCs, since we choose MMC_2 as an example to adopt the proposed ISMVC strategy with ERP to achieve constant power control under different grid conditions. The simulation parameters are illustrated in **Table 1**.

Contrastive simulation experiments are carried out for the MMC_2 with different control strategies and reactive power definitions under both balanced and imbalanced grid conditions, which are illustrated in **Figures 5–8**. To simplify the analysis, novel ISMVC and novel PIVC are used to designate the ISMVC and PIVC using the ERP, respectively, while traditional ISMVC denotes the ISMVC using TRP in this section.

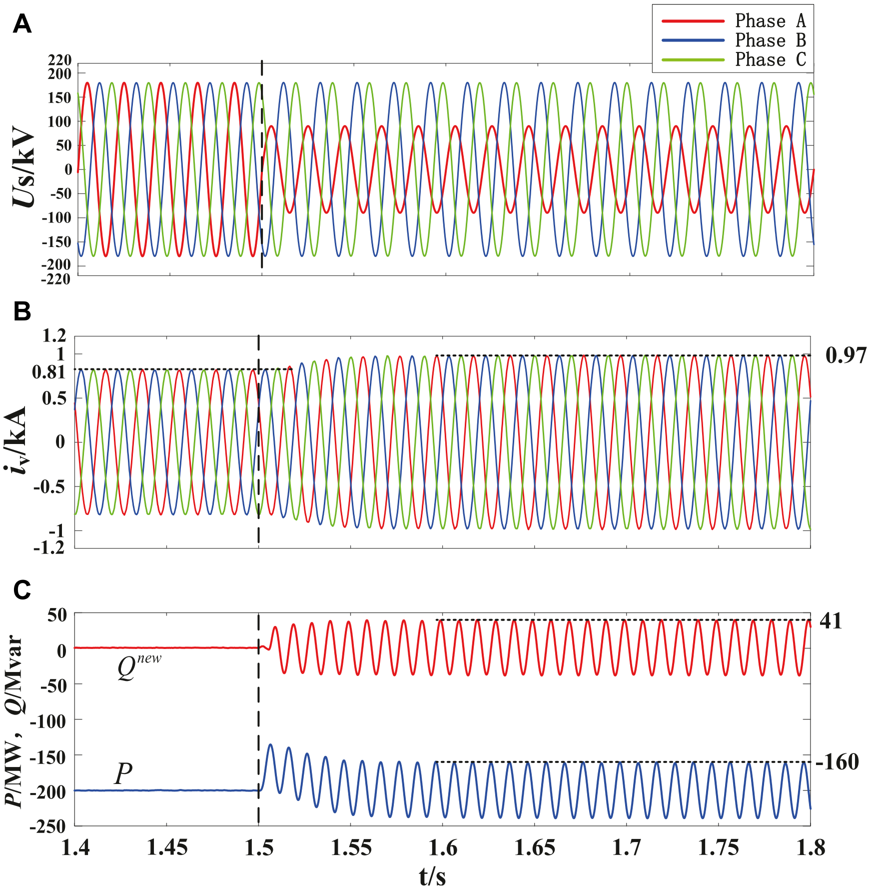

FIGURE 7 | Control performances of restraining negative sequence current of MMC$_2$ under unbalanced grid condition, **(A)** AC grid voltage at MMC$_2$ side, **(B)** AC grid current output by MMC$_2$, **(C)** active power and ERP output by MMC$_2$ using the novel ISMVC.

4.2 Case Study Under Balanced Grid Condition

The control performance of MMC$_2$ under balanced grid condition is analyzed in this part to show the effectiveness of the proposed novel ISMVC strategy. The initial reference value of active and reactive power are set to be −200 MW and 0 MVar, respectively. Load flow reversal are setup during 1.5–1.6 s while the reference value of active power change linearly from −200 to 200 MW within 0.1 s. It can be seen from **Figure 5** that the novel ISMVC can achieve accurate tracking of active and reactive power references, validating that the ERP can work effectively under balanced grid condition. At t = 1.5 s, as the load flow begins to reverse, the active power output by MMC$_2$ can accurately track the real-time change of reference values with low overshoot, while the valve-side current always follows the trend of active power smoothly. Therefore, the novel ISMVC is feasible for MMC under balanced grid condition.

4.3 Case Studies Under Unbalanced Conditions

Figure 6 compares the control performances of the traditional ISMVC and novel ISMVC strategy when the control objective is to suppress the 2ω oscillations in active power output by MMC$_2$ under unbalanced grid condition. The initial power reference is the same as **Figure 5**. At t = 1.5 s, as a 50% voltage dip in the phase A (a phase A high-impedance-grounded fault is set in the simulation), the three-phase grid voltages become unbalanced. Although the traditional ISMVC keeps the active power constant under unbalanced condition, the 2ω oscillations with an amplitude of 80 MW in reactive power still exists, which means that the traditional ISMVC cannot eliminate the 2ω oscillations in active power and reactive power simultaneously under imbalanced grid voltages. On the contrary, the active power and the ERP output by MMC$_2$ can accurately track their constant reference values while obtaining sinusoidal valve-side grid current which means that the 2ω oscillations in the active power and ERP can be eliminated at the same time by using the novel ISMVC. According to the figure, it can be seen that the ERP is more appropriate to be a controlled variable in constant power control of MMC than the TRP.

Figure 7 shows the control performances of restraining negative-sequence current of MMC$_2$ under unbalanced grid condition by using the novel ISMVC. The initial power reference and the voltage dip time of phase A are the same

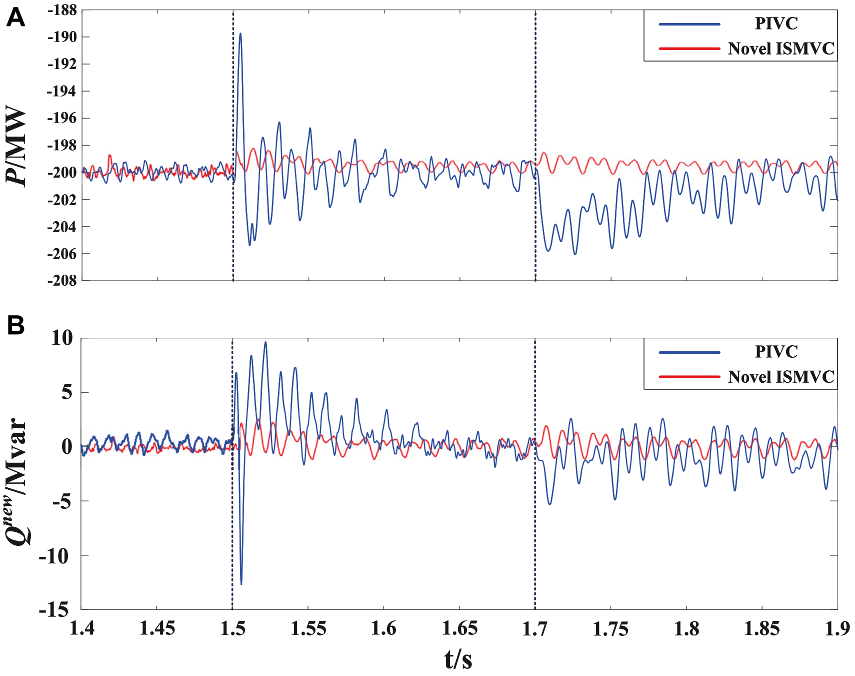

FIGURE 8 | Simulation results of dynamic power responses and robustness using the PIVC and novel ISMVC, **(A)** active power output by MMC_2 using the PIVC and novel ISMVC, **(B)** ERP output by MMC_2 using the PIVC and novel ISMVC.

as **Figure 6**. It can be seen that the valve-side grid current remain three phase symmetry all the time and their amplitude only increases by 19.75% compared with that before the voltage dip, which means suppressing the negative-sequence current can effectively restrain the increase level of the fault current and facilitate the safe and economic operation of MMC under unbalanced grid condition. However, since the negative-sequence voltage has not been eliminated, there is still a certain amount of 2ω oscillations in active power and ERP output by MMC_2. Besides, it should be noted that as the negative-sequence current has been eliminated completely, the amplitude of the 2ω oscillations in active power and ERP is only about 40MW, which is lower than that in **Figure 6**.

Figure 8 contrasts the novel ISMVC with the novel PIVC in terms of the dynamic control responses and robustness under unbalanced grid condition, where the initial power reference and voltage dip time of phase A are the same as **Figure 6**. It can be seen from **Figure 8** that the response speed of active power and ERP controlled by ISMVC strategy is better than that controlled by PIVC strategy which has smaller overshoot and faster response when the grid voltage dip occurs. At $t = 1.7s$, the bridge arm inductance changes from 36.7 to 45 mH which simulates the random parameter perturbations during the actual operation of MMC. It can be seen clearly that when the PIVC strategy applied to MMC_2, the active power and ERP are significantly affected during parameter perturbations. On the contrary, the variation of parameters only has slight influence which can be negligible on the active power and ERP controlled by the proposed ISMVC strategy which can still accurately track their reference values. Moreover, the chattering phenomenon has been suppressed to a small range thanks to the improved SMC strategy. According to the simulation results, it can be seen that the proposed ISMVC has a greater advantage over the PIVC in terms of dynamic response and robustness, which proves that the ISMVC can fully exploit the superiority of the ERP under unbalanced grid condition.

5 CONCLUSION

This paper proposes an ISMVC strategy combined with ERP for MMC under balanced and unbalanced grid conditions. The proposed method guarantees the valve-side grid current sinusoidal when eliminating the 2ω oscillations in active power and ERP simultaneously under unbalanced grid conditions. Faster dynamic response, better robustness and less chattering phenomena are provided by the improved SMC adopted in the positive- and negative-sequence inner-loop controllers of MMC due to the novel design of the sliding surface and reaching law, which can fully exerts the advantages of the ERP. Contrastive simulations of a four-terminal MMC-based DC power system based on the ISMVC and PIVC combined with the TRP and ERP are carried out to confirm the effectiveness and superiority of the proposed method under both balanced and unbalanced grid conditions. Therefore, the proposed method can work effectively under any grid conditions with fast dynamic response and good robustness.

DATA AVAILABILITY STATEMENT

The original contributions presented in the study are included in the article/Supplementary Material, further inquiries can be directed to the corresponding author.

REFERENCES

Akagi, H., Kanazawa, Y., and Nabae, A. (2008). Instantaneous Reactive Power Compensators Comprising Switching Devices without Energy Storage Components. *IEEE Trans. Industry Appl.* IA-20, 625–630.

Chen, H., and Xu, Z. (2007). Transient Model and Controller Design for Vsc-Hvdc Based on Synchronous Reference Frame. *Trans. China Electrotechnical Soc.* 22, 121–126.

Chen, X., Liu, J., Song, S., and Ouyang, S. (2020). Circulating Harmonic Currents Suppression of Level-Increased Nlm Based Modular Multilevel Converter with Deadbeat Control. *IEEE Trans. Power Electron.* 35, 1. doi:10.1109/tpel.2020.2982781

Dan, S., Wang, X., Nian, H., and Zhu, Z. Q. (2018). A Sliding-Mode Direct Power Control Strategy for Dfig under Both Balanced and Unbalanced Grid Conditions Using Extended Active Power. *IEEE Trans. Power Electron.* 33, 1.

Freytes, J., Li, J., De-Preville, G., and Thouvenin, M. (2021). Grid-Forming Control with Current Limitation for Mmc under Unbalanced Fault Ride-Through. *IEEE Trans. Power Deliv.* 36, 1. doi:10.1109/tpwrd.2021.3053148

Guo, C., Yang, J., and Zhao, C. (2019). Investigation of Small-Signal Dynamics of Modular Multilevel Converter under Unbalanced Grid Conditions. *IEEE Trans. Ind. Electron.* 66. doi:10.1109/tie.2018.2831193

Hao, Q., Li, Z., Yue, C., Gao, F., and Wang, S. (2020). Small-Signal Model and Dynamics of Mmc- Hvdc Grid under Unbalanced Grid Conditions. *IEEE Trans. Power Deliv.* 36, 1.

Hemdani, A., Dagbagi, M., Naouar, W. M., Idkhajine, L., Slama Belkhodja, I., and Monmasson, E. (2015). Indirect Sliding Mode Power Control for Three Phase Grid Connected Power Converter. *IET Power Electron.* 8, 977–985. doi:10.1049/iet-pel.2013.0945

Hu, J., Shang, L., He, Y., and Zhu, Z. Q. (2010). Direct Active and Reactive Power Regulation of Grid-Connected Dc/ac Converters Using Sliding Mode Control Approach. *IEEE Trans. Power Electron.* 26, 210–222.

Jiang, B., and Gao, C. (2021). Decentralized Adaptive Sliding Mode Control of Large-Scale Semi-markovian Jump Interconnected Systems with Dead-Zone Input. *IEEE Trans. Automatic Control.* 67, 1.

Kong, M., Tang, G., Zhiyuan, H. E., and Yang, J. (2013). A Control Strategy for Modular Multilevel Converter Based Hvdc of Unbalanced Ac Systems. *Proc. Csee* 33, 41–49.

Li, B., Xie, Y., Wen, W., and Guan, T. (2020). Improved Sliding-Mode Control for Mmc in Dc Power System. *IET Renew. Power Generation* 14. doi:10.1049/iet-rpg.2020.0493

Liang, Y. (2017). "Direct Power Control Strategy Based on Reduced Order Vector Resonant Controller for Mmc-Hvdc under Unbalanced Grid Voltages," in Proceedings of the CSEE.

Liu, Y., Huang, M., Chi, K. T., Iu, H. C., and Zha, X. (2021). Stability and Multiconstraint Operating Region of Grid-Connected Modular Multilevel Converter under Grid Phase Disturbance. *IEEE Trans. Power Electron.* 36, 1. doi:10.1109/tpel.2021.3078465

Long, B., Cao, T., Shen, D., Rodriguez, J., Guerrero, J. M., and Chong, K. T. (2021). Sequential Model Predictive Fault-Tolerance Control for T-Type Three-Level Grid-Connected Converters with LCL Filter. *IEEE Trans. Ind. Electron.* 69, 1. doi:10.1109/tie.2021.3114711

Mozayan, S. M., Saad, M., Vahedi, H., Fortin-Blanchette, H., and Soltani, M. (2016). Sliding Mode Control of Pmsg Wind Turbine Based on Enhanced Exponential Reaching Law. *IEEE Trans. Ind. Electron.* 63, 6148–6159. doi:10.1109/tie.2016.2570718

Nami, A., Liang, J., Dijkhuizen, F., and Demetriades, G. D. (2015). Modular Multilevel Converters for Hvdc Applications: Review on Converter Cells and Functionalities. *IEEE Trans. Power Electron.* 30, 18–36. doi:10.1109/tpel.2014.2327641

Nian, H., and Cheng, P. (2013). Resonant Based Direct Power Control Strategy for Pwm Rectifier under Unbalanced Grid Voltage Condition. *Trans. China Electrotechnical Soc.*

Song, J., Zheng, W. X., and Niu, Y. (2021). Self-Triggered Sliding Mode Control for Networked Pmsm Speed Regulation System: A Pso-Optimized Super-Twisting Algorithm. *IEEE Trans. Ind. Electron.* 69, 1.

Sun, Y., and Lipo, T. A. (2006). Modeling and Analysis of Instantaneous Active and Reactive Power for Pwm Ac/dc Converter under Generalized Unbalanced Network. *IEEE Trans. Power Deliv.* 21, 1530–1540.

Timbus, A. V., Rodriguez, P., Teodorescu, R., Liserre, M., and Blaabjerg, F. (2007). "Control Strategies for Distributed Power Generation Systems Operating on Faulty Grid," in IEEE International Symposium on Industrial Electronics.

Wang, G., Sun, C., Liu, R., Wang, F., and Feng, L. I. (2015). Modular Multilevel Converter Control Strategy Based on Arm Current Control. *Proc. Chin. Soc. Electr. Eng.* 35, 458–464.

Wang, R., Sun, Q., Ma, D., and Hu, X. (2020). Line Impedance Cooperative Stability Region Identification Method for Grid-Tied Inverters under Weak Grids. *IEEE Trans. Smart Grid* 11, 2856–2866.

Wang, R., Sun, Q., Ma, D., and Liu, Z. (2019). The Small-Signal Stability Analysis of the Droop-Controlled Converter in Electromagnetic Timescale. *IEEE Trans. Sustain. Energ.* 10, 1. doi:10.1109/tste.2019.2894633

Wang, R., Sun, Q., Tu, P., Xiao, J., and Wang, P. (2021). Reduced-order Aggregate Model for Large-Scale Converters with Inhomogeneous Initial Conditions in Dc Microgrids. *IEEE Trans. Energ. Convers.* 36. doi:10.1109/tec.2021.3050434

Wang, S., Dragicevic, T., Gao, Y., Chaudhary, S. K., and Teodorescu, R. (2020). Machine Learning Based Operating Region Extension of Modular Multilevel Converters under Unbalanced Grid Faults. *IEEE Trans. Ind. Electron.* 68, 1.

Wei, X., Sun, H., Wei, X., Qian, M. A., and Fengge, X. U. (2011). Control Strategy about Power Quality Improvement for Vsc-Hvdc under Unbalanced Ac Grid Conditions. *Proc. Csee* 31, 8–14.

Xia, X., Xu, L., Zhao, X., Zeng, X., and Yi, H. (2021). Modular Multilevel Converter Predictive Control Strategy Based on Energy Balance. *J. Power Electron.* 21. doi:10.1007/s43236-021-00225-9

Yang, H., and Nian, H. (2015). "Stability Analysis of Grid-Connected Converter Based on Interconnected System Impedance Modeling under Unbalanced Grid Conditions," in International Conference on Electrical Machines & Systems.

Zhang, Y., and Qu, C. (2015). Model Predictive Direct Power Control of Pwm Rectifiers under Unbalanced Network Conditions. *IEEE Trans. Ind. Electron.* 62, 1. doi:10.1109/tie.2014.2387796

Zhou, Y., Jiang, D., Guo, J., Hu, P., and Liang, Y. (2013). Analysis and Control of Modular Multilevel Converters under Unbalanced Conditions. *IEEE Trans. Power Deliv.* 28, 1986–1995. doi:10.1109/tpwrd.2013.2268981

Zou, C., Hong, R. G., Xu, S., Yan, L., and Bo, L. (2018). Analysis of Resonance Between a Vsc-Hvdc Converter and the Ac Grid. *IEEE Trans. Power Electron.* 33, 1. doi:10.1109/tpel.2018.2809705

AUTHOR CONTRIBUTIONS

TG: Conceptualization, writing-original draft. XZ: Editing. WZ:Editing. HL: Software. YL: Writing-review. QS: Data curation.

Conflict of Interest: Author TG was employed by Stare Grid Shenyang Electric Power Supply Company.

The remaining authors declare that the research was conducted in the absence of any commercial or financial relationships that could be construed as a potential conflict of interest.

frontiers in Energy Research

METHODS
published: 25 March 2022
doi: 10.3389/fenrg.2022.856304

Two-Stage Optimal Operation Management of a Microgrid Considering Electricity-Hydrogen Coupling Dynamic Characteristics

Xinrui Liu*, Weiyang Zhong, Min Hou and Yuqing Luo

College of Information Science and Engineering, Northeastern University, Shenyang, China

The uncertainty and volatility of renewable energy generation lead to large amounts of abandoned electricity. The electricity-hydrogen coupling microgrid (EHCM) consists of the proton exchange membrane electrolytic cell (PEMEC), liquid organic hydrogen carrier (LOHC) hydrogen storage, proton exchange membrane fuel cell (PEMFC). The structure helps to increase the utilization of wind and photovoltaic power. The scheduling of an EHCM is very challenging. This paper proposes the optimal operation of a microgrid considering the uncertainty of wind speed, light, and the coupling of electricity and hydrogen. The electricity-hydrogen coupling model and hydrogen market model are constructed. The microgrid provides ancillary services to the grid while meeting hydrogen demand. The above model is solved using a two-stage optimization method with time scales of day-ahead and intra-day. Finally, taking the IEEE 33-node microgrid as an example, the effectiveness of the proposed model is verified. The results of the case show that the proposed method can obtain more benefits and reduce carbon emissions.

Keywords: hydrogen generation, fuel cell, liquid organic hydrogen carrier, microgrid, renewable energy, grid auxiliary service

Edited by:
Wei Hu,
Zhejiang University, China

Reviewed by:
Xiangke Li,
Hong Kong Polytechnic University,
Hong Kong SAR, China
Lili Cui,
Shenyang Normal University, China

****Correspondence:***
Xinrui Liu
liuxinrui@ise.neu.edu.cn

Specialty section:
This article was submitted to
Smart Grids,
a section of the journal
Frontiers in Energy Research

Received: *17 January 2022*
Accepted: *25 January 2022*
Published: *25 March 2022*

Citation:
Liu X, Zhong W, Hou M and Luo Y (2022) Two-Stage Optimal Operation Management of a Microgrid Considering Electricity-Hydrogen Coupling Dynamic Characteristics. Front. Energy Res. 10:856304. doi: 10.3389/fenrg.2022.856304

INTRODUCTION

The 2015 Paris Climate Conference proposed limiting climate change to “well below 2°C”, which led to research on replacing traditional fossil energy with renewable energy. President Xi Jinping announced in 2020 that China will peak carbon dioxide emissions before 2030 and carbon neutrality before 2060. In this context, finding out green energy to replace fossil fuels to reduce carbon emissions is a very hot issue (Muyeen et al., 2011). Among various energy types, hydrogen is considered as a clean energy source. The reaction of the hydrogen fuel cell and the combustion of hydrogen are zero carbon emissions. Hydrogen can be used in heating systems, power generation systems (Chapman et al., 2019; Berger et al., 2020), industrial processes, and hydrogen fuel cell vehicles (Ramachandran and Menon, 1998; Marini et al., 2012; Zuo et al., 2021). It can be applied in many ways in the future (Jin et al., 2021; Liu et al., 2021; Zhang et al., 2021). The research about the production, transportation, and application of hydrogen is worthy of study.

It is very important to study the relationship between power systems and the application of hydrogen. Hydrogen production by electrolysis is considered to be one of the most efficient forms of hydrogen supply. In recent years, there has been a great deal of research into the use of renewable energy sources to produce hydrogen from abandoned electricity. China has the largest installed capacity of photovoltaic and wind power, and the renewable energy supply and demand show an inverse distribution trend. The installed wind power capacity in the "Three North" region accounts for 80%. The demand of electricity is concentrated in the central and eastern parts of China, which leads to an imbalance between electricity production and consumption (Liu et al., 2020; Qiu et al., 2022). The high penetration of renewable energy may cause intermittency and reliability problems for the grid. Microgrids provide efficient energy management for the integrated use of various distributed power sources, such as wind turbines and photovoltaics (Wang et al., 2013). Distributed generations are connected to the microgrid as a power bi-directional controllable aggregator. The distribution network does not have to directly face different types and nature of generating units (Zhang et al., 2017). The reliability and economy of distributed generations are enhanced. By using multi-energy complementarities and energy laddering (Wu et al., 2017), the energy utilization efficiency of the entire distribution network is eventually improved, and pollution emissions are significantly reduced (Jia et al., 2015; Li et al., 2015; Zhou et al., 2018).

The microgrid with the coupling of electricity and hydrogen can provide power to the grid, auxiliary services to the power market, and hydrogen to the hydrogen market.

A microgrid containing electrolytic cells and hydrogen fuel cells is established (Li et al., 2021), and a power capacity allocation with hydrogen as a flexible resource is proposed. A multi-objective optimization model with the lowest annual operating cost and the highest flexibility is established. The capacity allocation method of hybrid energy storage microgrid with the coupling of electricity and hydrogen is proposed in (Kong et al., 2021). The capacity allocation result with optimal integrated economy and power supply reliability is solved by particle swarm algorithm. In (García et al., 2013), an energy management model is proposed for microgrids containing renewable energy sources, batteries, and hydrogen storage devices to optimize the operating costs of individual microgrids. Similarly, a microgrid energy management system is proposed in (García et al., 2016). It takes into account the lifetime of the hydrogen system and battery storage to reduce operating costs. A hydrogen-based system for rural communities is built in (Mendis et al., 2015), where hydrogen is used to optimize renewable energy utilization and perform active/reactive power management.

In some remote areas where renewable energy is abundant, it is difficult to build large hydrogen transmission pipelines. Hydrogen is transported by liquefaction (Reuß et al., 2017). A promising method for storing and transporting hydrogen is hydrogen carriers, which keep hydrogen in some other chemical state (Fikrt et al., 2017). The concept of liquid organic hydrogen carriers (LOHCs) was introduced in the 1970s and 1980s (Taube et al., 1983). The process is to store hydrogen in the hydrogenation product through the reaction between unsaturated organic matter and hydrogen. The dehydrogenation process is to release hydrogen gas through a dehydrogenation reaction. The advantages are safety in transportation, storage, etc. Hydrogen can be transported and stored by appropriate adaptation of the existing infrastructure (Song et al., 2021). Hydrogenious Technologies (Hydrogenious LOHC Technologies, 2022) and H2-Industries (H2 Industries, 2022) of Germany used isomers of dibenzyltoluene as the main storage and transportation material for LOHCs. Wang et al. (Wang et al., 2017) compared N-ethylcarbazole hydrogen storage and high-pressure hydrogen storage. The efficiency of both can be equal without considering heat loss. Yang et al. (Yang et al., 2017) account that the hydrogen utilization using 70 and 35 MPa gas tanks and N-ethylcarbazole carriers are about 86, 88.3, and 88.7%. Niermann et al. (Niermann et al., 2019) studied a hydrogen storage process framework to compare the effect of different LOHCs materials and high-pressure hydrogen storage on the efficiency. Finally, considering the waste heat utilization of fuel cells, the overall chain efficiency of LOHCs exceeds that of high-pressure hydrogen storage. Therefore, LOHCs are recommended as a safer and more efficient way to store and transport hydrogen.

Hydrogen storage has been less studied in microgrids. A control scheme is proposed in (Recalde Melo and Chang-Chien, 2014) to coordinate offshore wind farms and hydrogen management systems to reduce the impact of wind power intermittency. Cost minimization and equivalent hydrogen consumption calculation methods are used in (Pu et al., 2019). Hydrogen storage is used for the consumption of excess electricity, which can achieve the minimum cost and energy storage state balance. An energy management method is proposed in (Li et al., 2020) to meet the demand of the microgrid, and to convert the excess electricity into hydrogen. The fuel cell is discharged when there is a power shortage. The energy management is achieved through coordinated control of various devices. The above work does not take into account the technical challenges of storage and transportation, while the ancillary services market is considered in the optimal scheduling model proposed in (El-Taweel et al., 2019). However, the model only considers demand response programs and ignores the possibility of using fuel cell units. The model in (El-Taweel et al., 2020) does not consider fuel cells, which limit the ability of the hydrogen production and storage system to provide multiple grid services. In summary, although previous work has included many aspects, a reasonable integrated model of microgrid coupled with electricity and hydrogen has not been studied. To solve the above problems, a coupling of electricity and hydrogen microgrid model based on LOHC for hydrogen storage and transportation is developed in this paper.

The contributions of this paper are as follows: *1*) The microgrid model considers the constraints of grid and electricity-hydrogen coupling units, the operational characteristics of power to hydrogen and hydrogen storage. It reduces errors arising from the fixed efficiency of the traditional model, and improves the utilization of renewable energy generation. *2*) The PEMFC power generation system consists of PEMFCs and batteries. And the characteristics of the PEMFC are considered to make it a guaranteed power generation unit. The microgrid can participate in grid auxiliary services to maximize microgrid revenue. *3*) Day-ahead and intra-day multi-timescale scheduling is adopted to deal with the uncertainty of renewable energy. The day-ahead objective is to maximize the daily income of the microgrid, which is dispatched

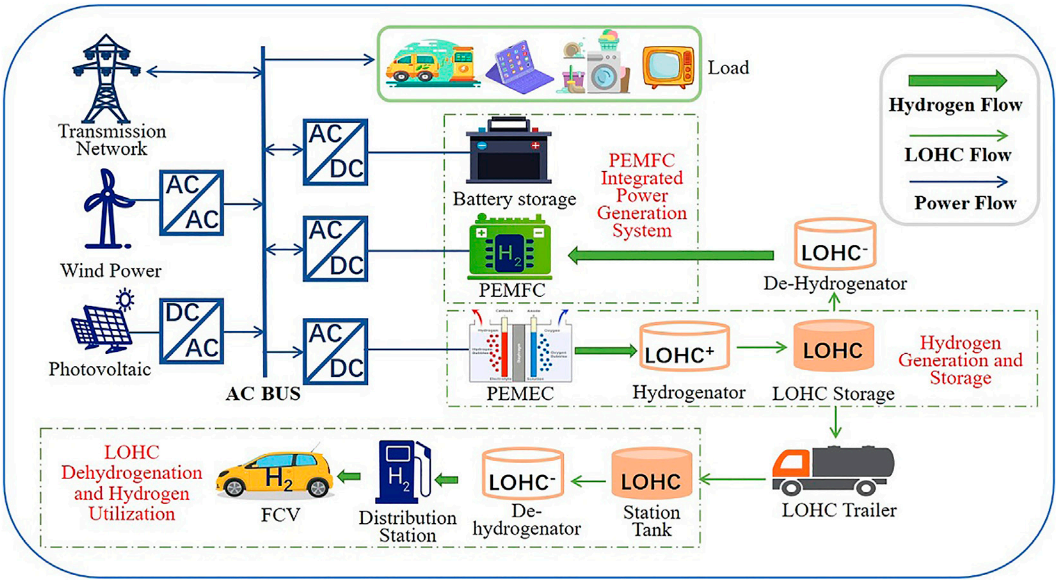

FIGURE 1 | The structure of EHCM.

using mixed integer linear programming (MILP). In intra-day scheduling, model predictive control (MPC) is embedded in mixed integer quadratic programming (MIQP) to reduce prediction errors and achieve real-time control. *4*) The EHCM meets hydrogen demand and power demand. The application of LOHC technology and the sale of oxygen is considered, which can improve safety and economy. The EHCM forms a zero-carbon energy system, which is significant for the future development and application of hydrogen.

THE EHCM MODEL

The Structure of an EHCM

The structure of the EHCM based on LOHC is shown in **Figure 1**. The EHCM mainly consists of wind turbines, PV panels, PEMEC, PEMFC, storage batteries, electrical loads, etc. It constitutes a closed-loop energy system of "electricity - hydrogen - electricity," and it can meet the hydrogen demand of the hydrogen market.

As can be seen from **Figure 1**, the LOHC-based hydrogen supply chain consists of an AC-DC converter, a PEMEC, a hydrogenator, and a LOHC storage tank. The PEMEC uses excess power to produce hydrogen, and hydrogen is passed through a hydrogenator to combine it with organic solvents to form LOHC. When the PEMFC receives the power generation signal, the hydrogen production and storage system based on LOHC uses the dehydrogenation reaction to meet the demand of the microgrid and grid auxiliary services. LOHC can also transport hydrogen to specific locations *via* tanker trucks, dehydrogenated and supplied to hydrogen refueling stations or industrial use, etc. To meet the demand for hydrogen and the high-power fluctuations of renewable energy, the PEMEC has a higher rated power.

The more commonly used alkaline electrolytic cells have disadvantages, such as low hydrogen production efficiency, insufficient dynamic response, etc. The membrane electrode of the PEMEC has many advantages over the alkaline electrolyte and asbestos diaphragm. It has good proton conduction characteristics, differential pressure resistance characteristics, high operating drop flow density, a wide range of adjustable power, and fast start-stop adjustment speed. Therefore, the EHCM uses PEMEC and PEMFC to realize the transfer of electricity and hydrogen.

Mathematical Model of Microgrid

Wind Power and Photovoltaic Models and Uncertainty Expression

The power model of wind turbines is shown as follows.

$$\begin{cases} P_{\mathrm{w},t} = 0\ , & V_{\mathrm{w},t} < V_{\mathrm{in}} \\ P_{\mathrm{w},t} = N \times P_N \times \dfrac{V_{\mathrm{w},t}^3 - V_{\mathrm{in}}^3}{V_{\mathrm{rated}}^3 - V_{\mathrm{in}}^3}\ , & V_{\mathrm{in}} \le V_{\mathrm{w},t} < V_{\mathrm{rated}} \\ P_{\mathrm{w},t} = N \times P_N, & V_{\mathrm{rated}} \le V_{\mathrm{w},t} < V_{\mathrm{out}} \\ P_{\mathrm{w},t} = 0\ , & V_{\mathrm{out}} \le V_{\mathrm{w},t} \end{cases} \tag{1}$$

Where $P_{\mathrm{w},t}$ is the output power of a wind turbine, N is the total number of wind turbines, P_N is the rated power, $V_{\mathrm{w},t}$ is the wind speed, V_{rated} is the rated output wind speed, V_{in} and V_{out} are the cut-in wind speed and cut-out wind speed of wind turbine.

To improve the accuracy of the PV model, the actual output power needs to take into account the light intensity and temperature, so the PV power is shown as follows.

$$P_{\mathrm{pv},t} = P_{\mathrm{pv}} f_{\mathrm{pv}} \frac{S_t}{S_{st}} \left[1 + \alpha (T_t - T_{\mathrm{st}})\right] \tag{2}$$

Where P_{pv} is the rated power of PV, f_{pv} is the efficiency of PV, S_t, S_{st} are the irradiation intensity and the standard light irradiation intensity, α is the temperature coefficient, $\alpha = 0.00485/°C$. T_t is the operating temperature, and it can be estimated from the light intensity and ambient temperature, T_{st} is the standard temperature of PV operation.

The wind speed and solar radiation follow a probability distribution function (PDF) based on the corresponding historical data (Farsangi et al., 2018) and do not affect the proposed model. To describe the uncertainty of wind power, the Weibull distribution function is used to describe the probability density function of wind power.

$$PDF(V) = \frac{k}{c}\left(\frac{V}{c}\right)^{k-1} \exp\left(-\left(\frac{V}{c}\right)^{k}\right) \tag{3}$$

Where c and k are the scale and shape parameters, c has the same dimension as the velocity, and k is dimensionless, V is the wind speed value.

The mean and maximum wind speed values are used to estimate the parameters of the Weibull function. The mean wind speed $\bar{V}$ is obtained from the meteorological data and the 10-min mean maximum wind speed $V_{\max}$ observed at time T, c and k are calculated by using **Eq. 4**.

$$\begin{cases} k = \ln(\ln T) \Big/ \ln\left(0.9V_{\max} \Big/ \bar{V}\right) \\ c = \bar{V} \Big/ \Gamma\left(1 + \frac{1}{k}\right) \end{cases} \tag{4}$$

The predicted wind speed value is $V_{w,t}^{pre}$. The processed wind speed is shown as follows.

$$V_{w,t} = PDF(V) \times V_{w,t}^{pre} \tag{5}$$

The uncertainty of the PV is coped with using the Beta distribution function, which is shown as follows.

$$PDF(S) = \frac{\Gamma(a+b)}{\Gamma(a)\Gamma(b)} \times S^{a-1} \times (1-S)^{b-1} \tag{6}$$

Where a and b are calculated using the mean μ and standard deviation σ.

$$\begin{cases} b = (1-\mu) \times \left(\frac{\mu \times (1-\mu)}{\sigma^2} - 1\right) \\ a = \frac{\mu \times b}{1-\mu} \end{cases} \tag{7}$$

According to the Beta probability distribution function, the radiation absorbed by the solar panel is shown as follows.

$$S_t = PDF(S) \times S_{ex,t} \tag{8}$$

Where $S_{ex,t}$ is the calculated astronomical radiation value.

Battery Model

The charging model of battery is shown as follows.

$$E_{bat,t} = E_{bat,t-1}(1-\delta) + P_{bat\_ch,t-1}\eta_{ch}\Delta t \tag{9}$$

The discharging model of battery is shown as follows.

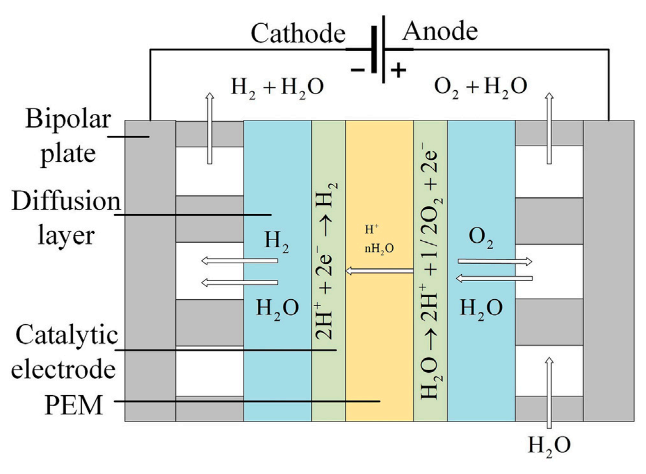

FIGURE 2 | Schematic diagram of PEMEC's single electrolytic chamber reaction principle.

$$E_{bat,t} = E_{bat,t-1}(1-\delta) - \frac{P_{bat\_dh,t-1}}{\eta_{dh}}\Delta t \tag{10}$$

Where $E_{bat,t}$ is the battery capacity, δ is the self-discharge rate, P_{bat_ch} and P_{bat_dh} are the charging and discharging power, η_{ch} and η_{dh} are the charging and discharging efficiency.

$$\begin{cases} P_{bat\_dh,t} = P_{bat,t} & P_{bat,t} > 0 \\ P_{bat\_ch,t} = P_{bat,t} & P_{bat,t} < 0 \end{cases} \tag{11}$$

Where $P_{bat,t}$ is the battery power.

Operating Characteristics Model of the PEMEC

Hydrogen production utilizes multiple parallel electrolytic cells which are composed of electrolytic chambers in series. By controlling the current of a single electrolytic cell, and discrete start-stop control of multiple electrolytic cells, the excess power can be used to produce hydrogen. The reaction principle of the PEMEC single electrolytic chamber is shown in **Figure 2**.

The voltage and current relationship for a single electrolytic chamber is shown as follows.

$$\begin{aligned} V_{cell,t} = V_{rev} + \frac{RTemp}{2F}\ln\left(\frac{p_{H_2}p_{O_2}^{\frac{1}{2}}}{a_{H_2O}}\right) + R_{cell}i_{cell,t} \\ + \frac{RTemp}{\alpha_{an}F}\text{arsinh}\left(\frac{i_{cell,t}}{2i_{an}}\right) + \frac{RTemp}{\alpha_{cat}F}\text{arsinh}\left(\frac{i_{cell,t}}{2i_{cat}}\right) \end{aligned} \tag{12}$$

Where $V_{cell,t}$ and $i_{cell,t}$ are the operating voltage and current density, V_{rev} is the reversible voltage, $Temp$ is the operating temperature, $t = 1, 2, \cdots, T_d$, T_d is the total number of scheduling periods, p_{H_2} and p_{O_2} are the partial pressure of hydrogen and oxygen, a_{H_2O} is the activity of water, R_{cell} is the total internal equivalent ohmic resistance, i_{an} and i_{cat} are the exchange current density of the anode and cathode, α_{an} and α_{cat} are the charge transfer coefficient of the anode and cathode, R and F are the ideal gas constant and Faraday's constant.

The hydrogen production efficiency of PEMEC decreases as the power consumption increases. The models with constant efficiency of electrolytic cells have some deviations. The power consumption $P_{\mathrm{el,t}}$ of the PEMEC and hydrogen flow rate $m_{\mathrm{H_2,t}}$ are shown in **Eqs 13, 14**. The non-linear relationship is shown in **Eq. 15**. The efficiency of the PEMEC is shown in **Eq. 16**, which is inversely proportional to the voltage and decreases with increasing current density.

$$P_{\mathrm{el,t}} = k_1 \sum_{i=1}^{N_{\mathrm{stack}}} u_{t,i} N_{\mathrm{cell}} V_{\mathrm{cell},t} I_{\mathrm{cell},t} \tag{13}$$

$$m_{\mathrm{H_2,t}} = k_2 \sum_{i=1}^{N_{\mathrm{stack}}} u_{t,i} \eta_{\mathrm{f}} N_{\mathrm{cell}} \frac{I_{\mathrm{cell,t}}}{2F} \tag{14}$$

$$m_{\mathrm{H_2},t} = \frac{k_2 \eta_{\mathrm{f}}}{2F k_1 V_{\mathrm{cell},t}} P_{\mathrm{el,t}} \tag{15}$$

$$\eta_{\mathrm{H_2},t} = \frac{m_{\mathrm{HHV,H_2}} m_{H_2,t}}{k_3 P_{\mathrm{el,t}}} = \frac{m_{\mathrm{HHV,H_2}} k_2^{'} \eta_{\mathrm{f}}}{2F k_1 V_{\mathrm{cell},t}} \tag{16}$$

Where $u_{t,i}^{e}$ is the 0–1 variable of the operating state of the i-th electrolytic cell, $I_{\mathrm{cell},t}$ is the operating current, N_{cell} and N_{stack} are the number of series and parallel electrolytic cells, η_{f} is the Faraday efficiency, $m_{\mathrm{HHV,H_2}}$ is the high heating value of H_2 under standard conditions, $k_1 = 0.001\,(\mathrm{W} \rightarrow \mathrm{kW})$, $k_3 = 3600\,(\mathrm{kW} \rightarrow \mathrm{kJ/h})$, $k_2 = 3600k_2^{'}$ $(\mathrm{mol/s} \rightarrow \mathrm{Nm^3/h})$ are the unit conversion factor, $k_2^{'} = RT_0/P_0$, T_0 and P_0 are the standard temperature and pressure.

The Model of PEMFC

The voltage equation of PEMFC is shown as follows.

$$\begin{cases} V_{\mathrm{fc},t} = V_{\mathrm{Nernst},t} - V_{\mathrm{act},t} - V_{\mathrm{ohm},t} - V_{\mathrm{conc},t} \\ V_{\mathrm{stack},t} = N_{\mathrm{fc}} \times V_{\mathrm{fc},t} \end{cases} \tag{17}$$

Where $V_{\mathrm{fc},t}$ is the cell voltage of single fuel cell, $V_{\mathrm{Nernst},t}$ is the thermodynamic electric potential, $V_{\mathrm{act},t}$ is the activation overvoltage, $V_{\mathrm{ohm},t}$ is the ohmic overvoltage, $V_{\mathrm{conc},t}$ is the concentration overvoltage, $V_{\mathrm{stack},t}$ is the voltage of PEMFC stack, N_{fc} is the number of single fuel cells in series.

The PEMFC power and hydrogen consumption rate are shown as follows.

$$P_{\mathrm{fcstack},t} = \sum_{j=1}^{N_{\mathrm{fcstack}}} v_{t,j} V_{\mathrm{stack},t} I_{\mathrm{fc},t} \tag{18}$$

$$Q_{\mathrm{H_2fcstack},t} = \sum_{j=1}^{N_{\mathrm{fcstack}}} v_{t,j} \frac{N_{\mathrm{fc}} I_{\mathrm{fc},t}}{2\eta_{\mathrm{fuel}} F} \tag{19}$$

Where $Q_{\mathrm{H_2fcstack},t}$ is the hydrogen consumption rate, N_{fcstack} is the number of PEMFC connected in parallel, $v_{t,j}$ is the 0–1 variable of PEMFC operating state, $I_{\mathrm{fc},t}$ is the current density, η_{fuel} is the fuel utilization rate.

Gas Storage Model

LOHC is used to store hydrogen. The storage of hydrogen is an exothermic hydrogenation reaction, while the release of hydrogen is a heat-absorbing dehydrogenation reaction. LOHCs can store hydrogen at chemically high densities under ordinary environmental conditions to improve the safety and flexibility of the system. The mathematical models of hydrogen storage and oxygen storage are shown as follows.

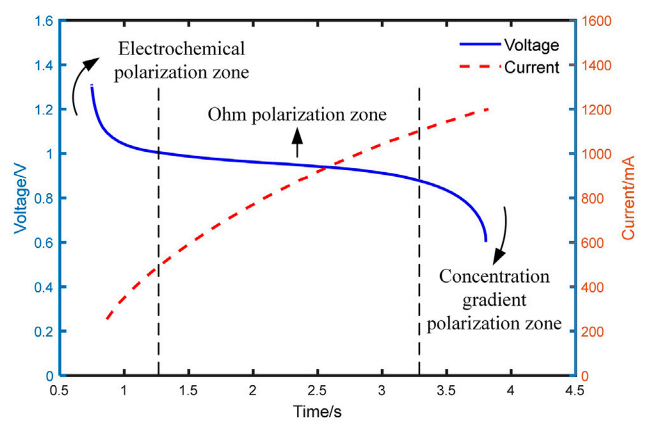

FIGURE 3 | Polarization curve of PEMFC power variation.

$$E_{\mathrm{H_2\,tan\,k},t} = E_{\mathrm{H_2\,tan\,k},t-1} + \left(P_{\mathrm{el},t-1} \eta_{\mathrm{H_2},t-1} \eta_{\mathrm{H^+}} - \frac{Q_{\mathrm{H_2fcstack},t}}{\eta_{\mathrm{H^-}}} - \sum_{h=0}^{H} Q_{\mathrm{H_2de},h,t} \right) \Delta t \tag{20}$$

$$E_{\mathrm{O_2\,tan\,k},t} = E_{\mathrm{O_2\,tan\,k},t-1} + \left(\frac{1}{2} P_{el,t-1} \eta_{\mathrm{H_2},t} \eta_{\mathrm{O_2tank}} - \sum_{l=0}^{L} Q_{\mathrm{O_2de},l,t} \right) \Delta t \tag{21}$$

Where $E_{\mathrm{H_2\,tan\,k},t}$, $E_{\mathrm{O_2\,tan\,k},t}$ are the hydrogen and oxygen stock, $\eta_{\mathrm{H^+}}$, $\eta_{\mathrm{H^-}}$ are the hydrogenation reaction and dehydrogenation reaction efficiency of LOHC, $\eta_{\mathrm{O_2tank}}$ is the efficiency of the oxygen storage tank.

ENERGY MANAGEMENT STRATEGIES OF THE PEMFC GENERATION SYSTEM

In the PEMFC generation system, the PEMFC is the primary power source to follow the load demand and provide energy support for grid auxiliary services. Considering the compensation of the soft characteristics of PEMFC, the battery is added to the EHCM. The battery stores energy when the system is overpowered and supplies power during cold start and power switching so that the PEMFC power quickly follows the load changes.

Characterization of PEMFC

The PEMFC has soft characteristics when in cold start and load change states. When the PEMFC is used alone, the power output response is not fast enough. There is not enough current output for the changing demands of the load, and there is a voltage dip inside the cell.

As shown in **Figure 3**, when the demand power increases, the output current increases while its voltage keeps dropping. When

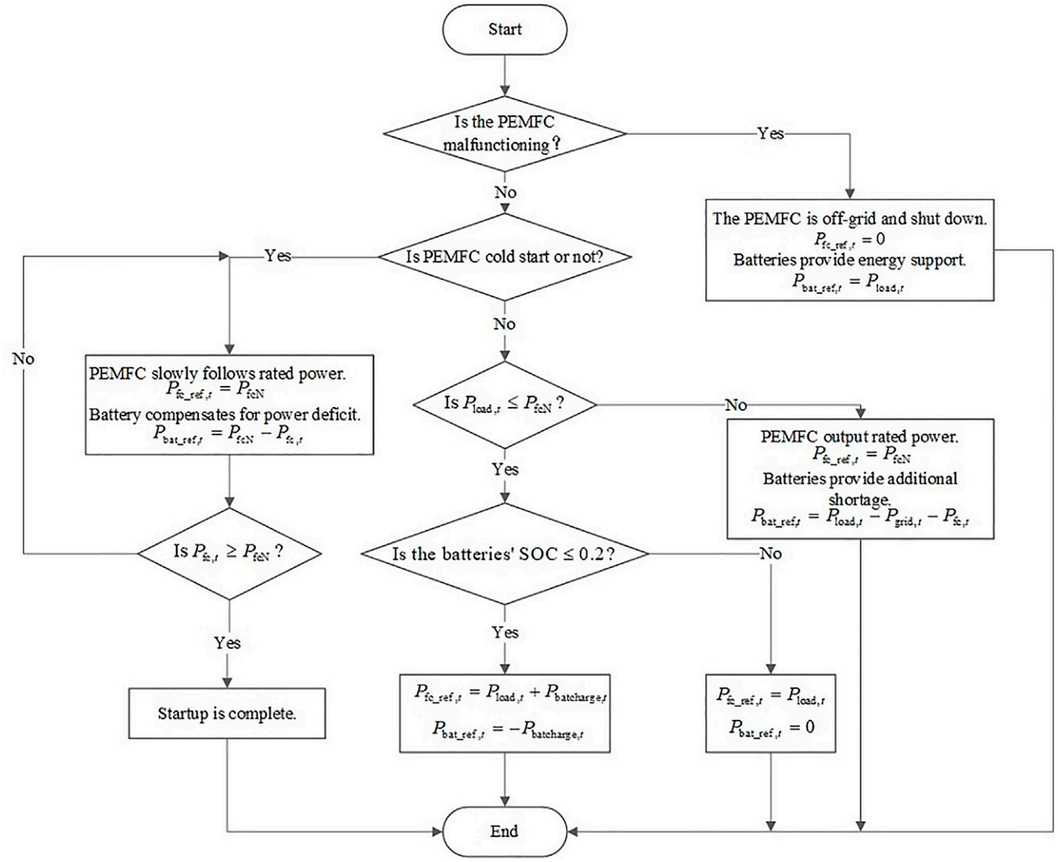

FIGURE 4 | Energy management flow chart.

the voltage drops to the lowest value, the PEMFC stack will shut down due to high internal temperature.

There is a gas delay in the chemical reaction process of the PEMFC. When the load increases, the current increases and the voltage drops accordingly. In contrast to the change in electrical power, the gas is supplied more slowly, and there is a transient drop in voltage. As the supply of sufficient gas gradually reaches a new balance in PEMFC, the time scale difference between the power and the gas reaction causes a delay in power output. The following equation will ensure the operation of the PEMFC.

$$V_{\text{fc},t} > V_{\text{lim}} \tag{22}$$

Where $V_{\text{fc},t}$ and V_{lim} are the operating voltage and the voltage protection threshold of PEMFC.

Considering the voltage protection threshold of the PEMFC stack, the output current shows a rise while the voltage drops and rises back when the current enters a plateau. The process keeps repeating inside the PEMFC. The response of the PEMFC is too slow to respond to rapid changes in load alone.

Work Modal Management

The PEMFC does not meet power supply standards in cold start and load switching states. It is used in combination with the battery to form a power supply system. To achieve power supply reliability of the PEMFC system, the energy management modes can be divided into four operating modes. The switching judgment and power command assignment between different operating modes are shown in **Figure 4**. The load of the microgrid is $P_{\text{load},t}$. The actual output power, power command, and rated output power of the PEMFC are $P_{\text{fc},t}$, $P_{\text{fc\_ref},t}$, P_{fcN}. The output power, power command and charging power of the battery are $P_{\text{bat},t}$, $P_{\text{bat\_ref},t}$, $P_{\text{batcharge},t}$. The power from the grid is $P_{\text{grid},t}$, and the current of the load is $i_{\text{load},t}$. The actual output current, current command and rated output current of the PEMFC and the battery are $i_{\text{fc},t}$, $i_{\text{fc\_ref},t}$, i_{fcN} and $i_{\text{bat},t}$, $i_{\text{bat\_ref},t}$, $i_{\text{batcharge},t}$.The output voltage, charge cutoff voltage and discharge cutoff voltage of the battery are $U_{\text{bat},t}$, U_{batCE}, U_{batDEC}.

Mode I (PEMFC Cold Start)

When the PEMFC cold started or power switched, the power output is slow and the battery is rapidly discharged to provide power for the microgrid bus. The energy flow diagram is shown in **Figure 5A**.

The power and the current output balance of the system are shown as follows.

$$\begin{cases} P_{\text{fc},t} + P_{\text{bat},t} = P_{\text{load},t} \\ i_{\text{fc\_ref},t} = i_{\text{fcN}} \\ i_{\text{bat\_ref},t} = i_{\text{load},t} - i_{\text{fc},t} \end{cases} \tag{23}$$

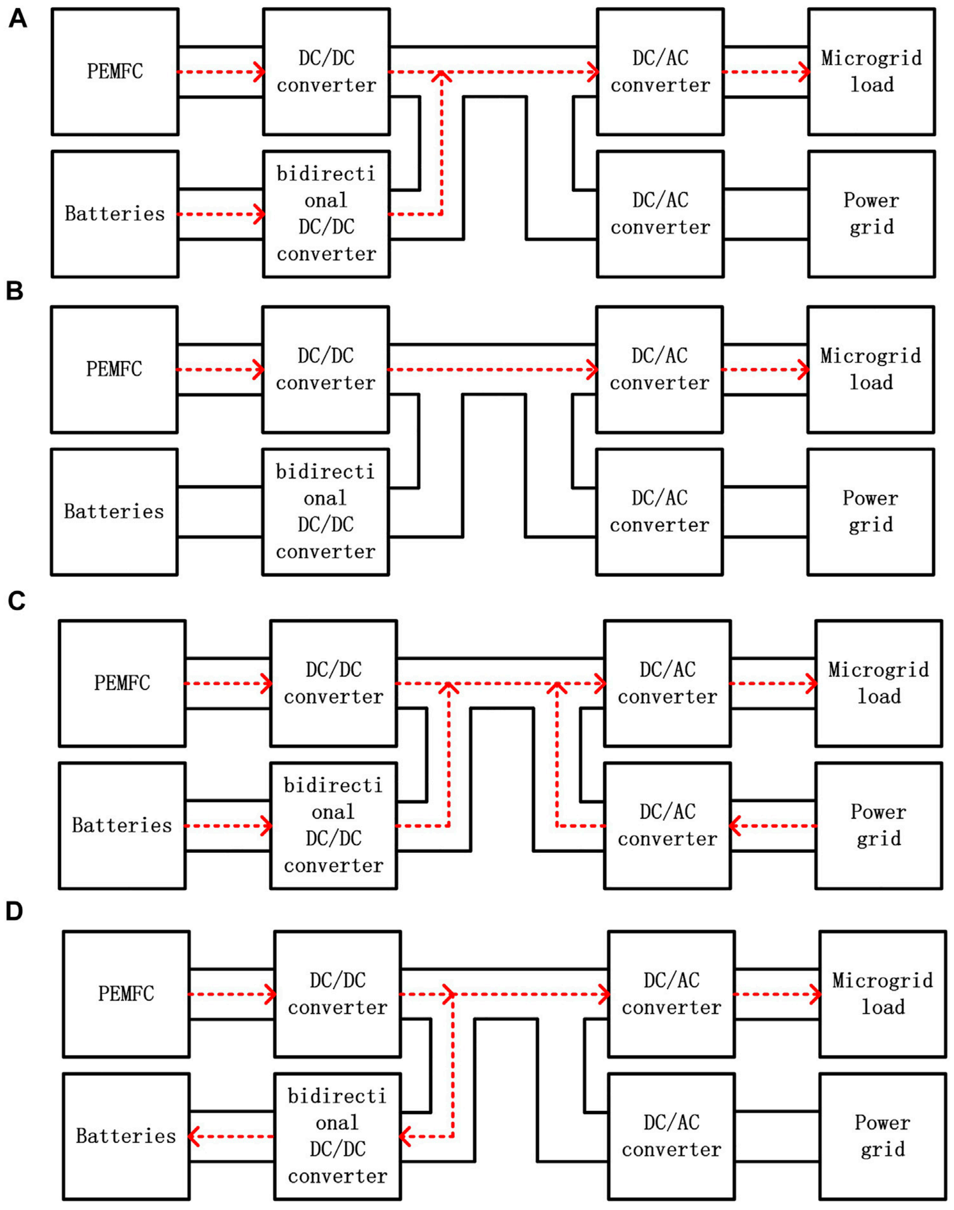

FIGURE 5 | (A) Energy flow diagram of mode I, **(B)** Energy flow diagram of mode II, **(C)** Energy flow diagram of mode III, **(D)** Energy flow diagram of mode IV.

Mode II (Rated Power Operating Mode)

When the output power of the system is rated, the PEMFC can follow the load. The battery is in standby mode and its SOC is in the normal range. Its energy flow diagram is shown in **Figure 5B**.

The power and the current output balance of the system are shown as follows.

$$\begin{cases} P_{\mathrm{fc},t} = P_{\mathrm{load},t} \\ i_{\mathrm{fc\_ref},t} = i_{\mathrm{load},t} \end{cases} \tag{24}$$

Mode III (Overload Operation Mode)

When the microgrid load is greater than the rated output power of the power supply system, the system is in an overload state. The battery provides power at its normal SOC. The load receives the remaining power from the grid. The energy flow diagram is shown in **Figure 5C**.

The power and the current output balance of the system are shown as follows.

$$\begin{cases} P_{\mathrm{fc},t} + P_{\mathrm{bat},t} + P_{\mathrm{grid},t} = P_{\mathrm{load},t} \\ i_{\mathrm{fc\_ref},t} = i_{\mathrm{fcN}} \\ i_{\mathrm{bat\_ref},t} = i_{\mathrm{load},t} - i_{\mathrm{fc},t} - i_{\mathrm{grid},t} \end{cases} \tag{25}$$

Mode IV (Reduced Load Operation Modes)

When the load is less than the rated output power of the PEMFC and the battery SOC is in the state of power deficit, the PEMFC generates more power to charge the battery to ensure the battery works in a healthy state to ensure its life. The energy flow diagram is shown in **Figure 5D**.

The power and the current output balance of the system are shown as follows.

$$\begin{cases} P_{\mathrm{fc},t} = P_{\mathrm{load},t} + P_{\mathrm{bat},t} \\ i_{\mathrm{fc\_ref},t} = i_{\mathrm{load},t} + i_{\mathrm{batcharge},t} \\ i_{\mathrm{bat\_ref},t} = -i_{\mathrm{batcharge},t} \end{cases} \tag{26}$$

MODEL SOLVING OF AN EHCM BASED ON LOHC

The electricity-hydrogen coupling model consists of PEMEC, LOHC hydrogen storage devices and PEMFC to realize the functions of hydrogen production, hydrogen storage and hydrogen power generation to meet hydrogen demand and load demand. We propose an EHCM scheduling model that considers the dynamic characteristics of PEMEC and PEMFC. Two-stage optimal scheduling with day-ahead global and intra-day real-time scheduling is adopted.

Day-Ahead Scheduling

Objective Function

The optimization goal of the day-ahead scheduling is to maximize the revenue of the microgrid. By optimizing the scheduling of generation, energy storage and electricity market auxiliary services, the operating costs of the microgrid can be reduced. It can also improve hydrogen production and grid auxiliary service revenue. The objective function is shown as follows.

$$F = \max\sum_{t=0}^{T}\left(REV_t - R_{\mathrm{OM},t}\right) \tag{27}$$

Where T is the scheduling period, REV_t is the revenue of EHCM, $R_{OM,t}$ is the operation and maintenance cost of the microgrid.

1. Revenue of the microgrid

$$REV_t = R_{\mathrm{H_2},t} + R_{\mathrm{O_2},t} + R_{\mathrm{DR},t} + R_{\mathrm{OR},t} + R_{\mathrm{TRN},t} \tag{28}$$

Where $R_{\mathrm{H_2},t}$, $R_{\mathrm{O_2},t}$, $R_{\mathrm{DR},t}$, $R_{\mathrm{OR},t}$, $R_{\mathrm{TRN},t}$ are hydrogen, oxygen, demand response services, operating reserve services and environmental revenues.

Revenues from sales of hydrogen and oxygen are shown as follows.

$$\begin{cases} R_{\mathrm{H_2},t} = \sum\limits_{h=0}^{H}\left(Q_{\mathrm{H_2de},h,t}\cdot S_{\mathrm{H_2},h,t} - D_h\cdot S_{\mathrm{tr},h,t}\right) \\ R_{\mathrm{O_2},t} = \sum\limits_{l=0}^{L}\left(Q_{\mathrm{O_2de},l,t}\cdot S_{\mathrm{O_2},l,t} - D_l\cdot S_{\mathrm{tr},l,t}\right) \end{cases} \tag{29}$$

Where h and l are the number of hydrogen and oxygen stations, H and L are the amount of hydrogen and oxygen stations, $S_{\mathrm{H_2},h,t}$ and $S_{\mathrm{O_2},l,t}$ are the market price of hydrogen and oxygen, $Q_{\mathrm{H_2de},h,t}$ and $Q_{\mathrm{O_2de},l,t}$ are the demand for hydrogen and oxygen, D_h and D_l are the distance of the hydrogen and oxygen stations, $S_{\mathrm{tr},h,t}$ and $S_{\mathrm{tr},l,t}$ are the hydrogen and oxygen transportation cost.

The electricity market auxiliary demand response revenue is shown as follows.

$$R_{\mathrm{DR},t} = S_{\mathrm{DRin},t}\cdot P_{\mathrm{DRin},t} + S_{\mathrm{DRout},t}\cdot P_{\mathrm{DRout},t} \tag{30}$$

Where $R_{\mathrm{DR},t}$ is the demand response revenue of auxiliary services, $S_{\mathrm{DRin},t}$ and $S_{\mathrm{DRout},t}$ are the price of auxiliary services, $P_{\mathrm{DRin},t}$ and $P_{\mathrm{DRout},t}$ are the demand response power.

The environmental revenue of reduced greenhouse gas emissions from hydrogen fuel cell vehicles compared to regular fuel vehicles is shown as follows.

$$R_{\mathrm{TRN},t} = \frac{E_{\mathrm{TRN}}}{\eta_{\mathrm{H_2FC}}}\cdot Q_{\mathrm{H_2de},t}\cdot\left(\lambda_{\mathrm{CO_2}} + \mu_{\mathrm{CO_2}}\right) \tag{31}$$

Where E_{TRN} is the amount of greenhouse gases emitted per kilometer by fuel cars, $\eta_{\mathrm{H_2FC}}$ is the amount of hydrogen consumed per kilometer by fuel cell cars, $\lambda_{\mathrm{CO_2}}$ and $\mu_{\mathrm{CO_2}}$ are the environmental revenue and penalty order of magnitude of CO_2.

2. Microgrid operation and maintenance costs

$$\begin{aligned} R_{\mathrm{OM},t} = {} & \Gamma_{\mathrm{w}}P_{\mathrm{w},t} + \Gamma_{\mathrm{pv}}P_{\mathrm{pv},t} + \Gamma_{\mathrm{bat}}P_{\mathrm{bat},t} + \Gamma_{\mathrm{el}}P_{\mathrm{el},t} + \Gamma_{\mathrm{fcstack}}P_{\mathrm{fcstack},t} \\ & + \Gamma_{\mathrm{grid}}P_{\mathrm{grid},t} + \Gamma_{\mathrm{H_2\,tan\,k}}E_{\mathrm{H_2\,tan\,k},t} + \Gamma_{\mathrm{O_2\,tan\,k}}E_{\mathrm{O_2\,tan\,k},t} \end{aligned} \tag{32}$$

Where Γ_{w}, Γ_{pv}, Γ_{bat}, Γ_{el}, $\mathit{\Gamma}_{\mathrm{fcstack}}$, $\Gamma_{\mathrm{H_2\,tan\,k}}$, $\Gamma_{\mathrm{O_2\,tan\,k}}$ are the unit operation and maintenance cost of wind turbine, PV, battery, PEMEC, PEMFC stack, hydrogen storage system and oxygen storage system, Γ_{grid} and $P_{\mathrm{grid},t}$ are the price and power provided by power grid.

Constraints

1. Power balance constraints

$$\begin{cases} P_{\mathrm{w},t} + P_{\mathrm{pv},t} = P_{\mathrm{load},t} + P_{\mathrm{bat\_ch},t} + P_{\mathrm{el,t}} + P_{\mathrm{grid},t} & \mathrm{d}P > 0 \\ P_{\mathrm{load}} = P_{\mathrm{w},t} + P_{\mathrm{pv},t} + P_{\mathrm{bat\_dh},t} + P_{\mathrm{fcstack},t} + P_{\mathrm{grid},t} & \mathrm{d}P < 0 \end{cases} \tag{33}$$

2. Battery charging and discharging constraints

$$P_{\mathrm{ch\,max\,,t}} = \max\{0, \mathrm{SOC_{max}}C_{\mathrm{bat}} - E_{\mathrm{bat,t}}\}\eta_{\mathrm{ch}} \tag{34}$$

$$P_{\mathrm{dh\,max\,,t}} = \frac{\max\{0, E_{\mathrm{bat,t}} - \mathrm{SOC_{min}}C_{\mathrm{bat}}\}}{\eta_{\mathrm{dh}}} \tag{35}$$

Where $\mathrm{SOC_{max}}$ and $\mathrm{SOC_{min}}$ are the upper and lower limits of the battery, C_{bat} is the capacity of the battery.

To protect the service life of the battery, the depth of charge and discharge is shown as follows.

$$0.2 < \mathrm{SOC}_t < 0.9 \tag{36}$$

3. PEMEC operating constraints

The operating constraints of the PEMEC include the nonlinear relationship between hydrogen production flow and power consumption, the range of current density regulation.

$$\begin{cases} u_t^e i_{\text{cell,min}} \le i_{\text{cell},t} \le u_t^e i_{\text{cell,max}} \\ u_t^e = \begin{cases} 0 & \sum_{i=1}^{N_{\text{stack}}} u_{t,i}^e = 0 \\ 1 & \sum_{i=1}^{N_{\text{stack}}} u_{t,i}^e \ne 0 \end{cases} \end{cases} \tag{37}$$

Where $i_{\text{cell,min}}$ and $i_{\text{cell,max}}$ are the lower and upper limits of current density, u_t^e is the 0–1 variable characterizing whether the PEMEC is operating or not.

4. PEMFC operating constraints

$$\begin{cases} v_t^e P_{\text{fcstack, min}} \le P_{\text{fcstack,t}} \le v_t^e P_{\text{fcstack, max}} \\ v_t^e = \begin{cases} 0 & \sum_{j=1}^{N_{\text{fcstack}}} v_{t,j}^e = 0 \\ 1 & \sum_{j=1}^{N_{\text{fcstack}}} v_{t,j}^e \ne 0 \end{cases} \end{cases} \tag{38}$$

Where $P_{\text{fcstack, min}}$ and $P_{\text{fcstack, max}}$ are the upper and lower limits of the output power of the PEMFC stack, v_t^e is the 0–1 variable that characterizes whether the PEMFC stack is operating or not.

To ensure the backup capacity to meet the grid auxiliary services, the upper and lower limits are constrained as follows.

$$0.5 < S_{\text{ohc},t} < 0.9 \tag{39}$$

5. Gas storage capacity constraints

The constraints of LOHC hydrogen and oxygen storage capacity are shown as follows.

$$\begin{cases} E_{\text{H}_2\,\text{tan kmin}} \le E_{\text{H}_2\,\text{tan k},t} \le E_{\text{H}_2\,\text{tan kmax}} \\ E_{\text{O}_2\,\text{tan kmin}} \le E_{\text{O}_2\,\text{tan k},t} \le E_{\text{O}_2\,\text{tan kmax}} \end{cases} \tag{40}$$

6. Grid power constraints

The grid power is affected by the feeder capacity and follows the following constraints.

$$-P_{\text{rated}} \le P_{\text{grid},t} \le P_{\text{rated}} \tag{41}$$

Intra-Day Scheduling

The prediction bias in the day-ahead scheduling leads to power fluctuations and scheduling errors. To make the intra-day scheduling close to the day-ahead scheduling and reduce the economic loss caused by uncertainty and the security of microgrid, intra-day scheduling is scheduled once every 15 min. The objective function is as follows.

$$\begin{gathered} F = \min \sum_{k}^{k+3} \left(\sum_{r=1}^{R} \left(\lambda_r \left(H_{r,k} - H_{r\_ref,k} \right)^2 \right) \right) R = 10 \\ H_{r,k} \in \left[P_{\text{w},k}, P_{\text{pv},k}, P_{\text{bat},k}, P_{\text{el},k}, P_{\text{fcstack},k}, P_{\text{grid},k}, \right. \\ \left. E_{\text{H}_2\,\text{tan k},k}, E_{\text{O}_2\,\text{tan k},k}, \text{SOC}_k, \text{S}_{\text{ohc},k} \right] H_{r\_ref,k} \in \\ \left[P_{\text{w}\_ref,k}, P_{\text{pv}\_ref,k}, P_{\text{bat}\_ref,k}, P_{\text{el}\_ref,k}, P_{\text{fcstack}\_ref,k}, P_{\text{grid}\_ref,k}, \right. \\ \left. E_{\text{H}_2\,\text{tan k}\_ref,k}, E_{\text{O}_2\,\text{tan k}\_ref,k}, \text{SOC}_{ref,k}, \text{S}_{\text{ohc}\_ref,k} \right] \end{gathered} \tag{42}$$

Where λ_r is the weight factor, $H_{r,k}$ is the real-time data at the time k, $H_{r\_ref,k}$ is the reference value for the day-ahead scheduling.

Solving Process

The optimal scheduling method proposed is day-ahead long-timescales scheduling and intra-day real-time scheduling. The specific solving optimization process is shown in **Figure 6**.

The day-ahead scheduling period is 24 h, and the step size is 1 h. Considering the uncertainty of wind power and PV, the optimization objective is to maximize the daily micro-grid revenue. The model is a mixed integer linear programming model, which is solved by Yalmip and Cplex to obtain global optimization results. However, the day-ahead optimal scheduling step is in hours. There is a prediction error, and the electricity-hydrogen microgrid cannot respond to the power fluctuation in time. The microgrid provides a demand response service and accepts signals from the power grid, which requires more accurate optimal scheduling. Based on the short-term prediction results, MPC model prediction control is used, and the optimization is rolled over every 15 min. The intra-day optimization is based on the day-ahead optimization results. The controllable unit of the EHCM corrects the day-ahead optimization results to reduce the prediction errors and improve the stability and economy of the microgrid.

CASE ANALYSIS

Basic Data

To verify the effectiveness of the proposed scheduling method, this section uses wind speed and light generation data from a microgrid in remote areas of western China, and the microgrid distribution structure diagram is shown in **Figure 7**. There is a surplus of wind and solar power, but it is expensive to build high power transmission lines and hydrogen pipelines. Hydrogen can be transported by ordinary tanker truck using LOHC hydrogen storage, and the transport distance is set at 100 km. The EHCM consists of four wind farms, three photovoltaic power plants, 48 MW PEMEC system, 10 MW PEMFC and 2 MWh battery power generation system. Typical daily scenarios in summer and winter are set up to solve the optimal scheduling results of this EHCM. The system economic parameters and specific equipment parameters are shown in **Tables 1**, **2**.

Scenarios Setting

To study the effects of electricity-hydrogen coupling, hydrogen demand and grid auxiliary services on the scheduling results, the following four scenarios are set up for comparison.

S1: A scheduling method considering the dynamic characteristics of electricity-hydrogen coupling and auxiliary services of power grid.

S2: A Scheduling method that ignores the dynamic characteristics of electricity-hydrogen coupling.

S3: Ignore the scheduling mode of grid auxiliary services.

S4: A scheduling method that ignores the electricity-hydrogen coupling and the dynamic characteristics of auxiliary services of power grid.

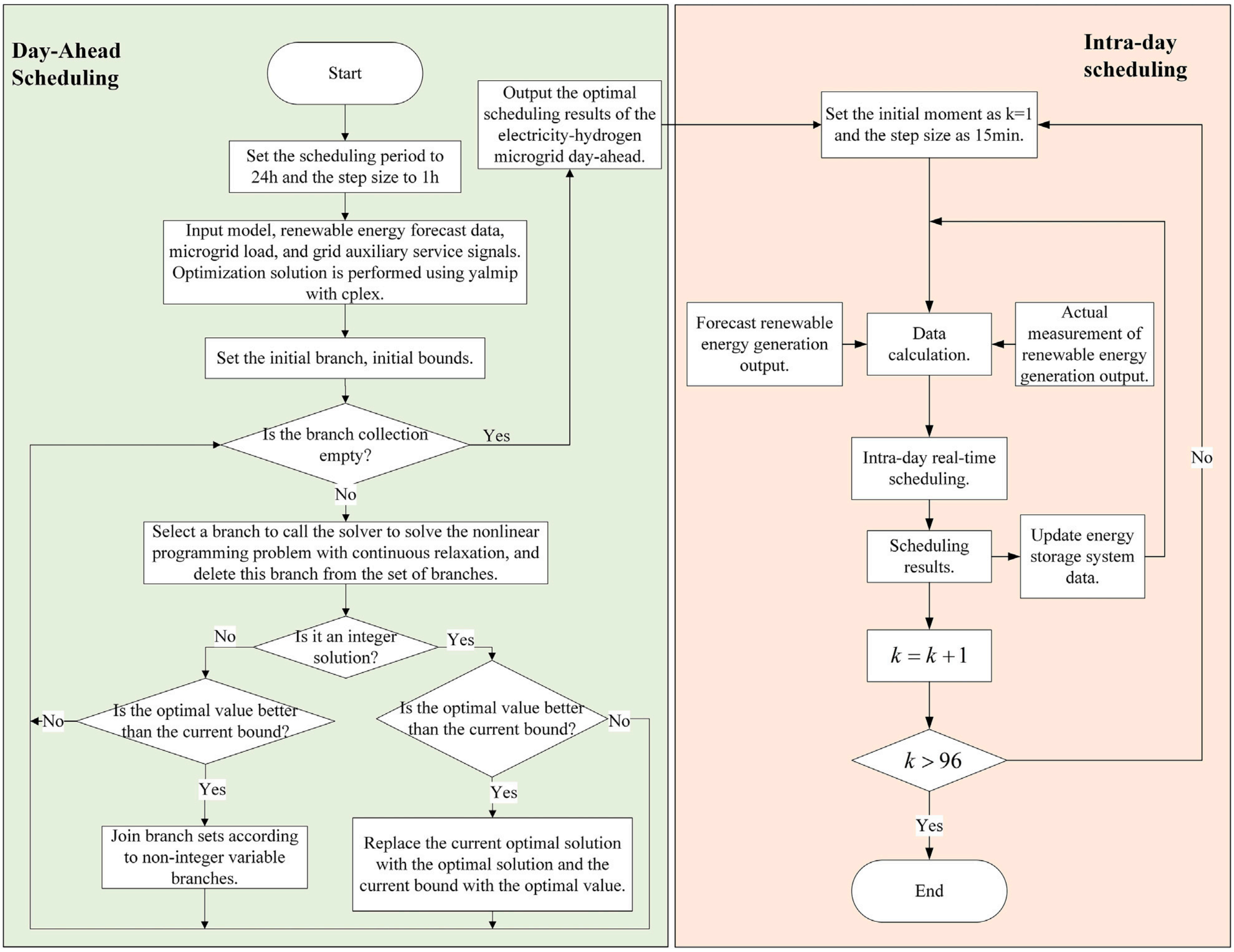

FIGURE 6 | Two-stage solution process for day-ahead and intra-day.

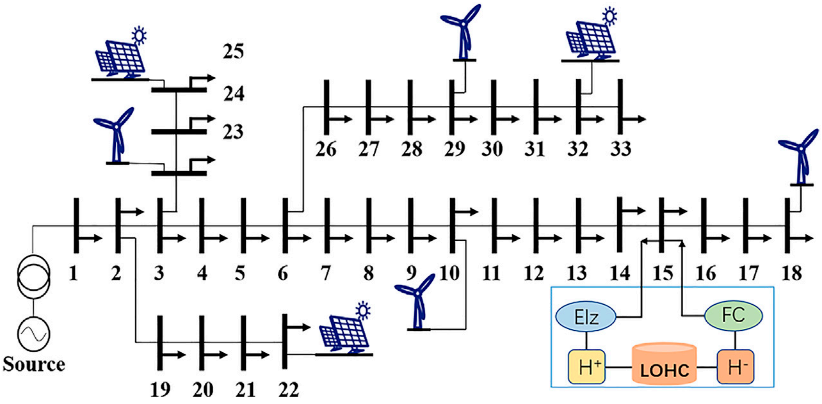

FIGURE 7 | IEEE 33-node EHCM distribution structure.

TABLE 1 | Parameters of the simulation example.

Types	Parameters			
PEMEC	$T = 335.15K$ $\alpha_{H_2O} = 1$ $V_{rev} = 1.23V$ $N_{cell} = 400$	$p_{H_2} = 29.80bar$ $\alpha_{an} = 2$ $R_{cell} = 0.12R \cdot cm^2$ $N_{stack} = 6$	$p_{O_2} = 2.80bar$ $i_{an} = 1e - 6A/cm^2$ $A_{cell} = 1100cm^2$ $i_{cell,min} = 0.15A/cm^2$	$\alpha_{cat} = 0.5$ $i_{cat} = 1e - 3A/cm^2$ $\eta_f = 99\%$ $i_{cell,max} = 3A/cm^2$
PEMFC	$0.6V \leq V_{fc,t} \leq 1.2V$ Pressure: 1~2bar	$0.4V \leq I_{fc,t} \leq 1.2V$ temperature: 30–100°C	η_{fuel}: 40 ~ 60% $N_{fcstack} = 20$	$N_{fc} = 6000$
LOHC	$\eta_{H^+} = 97\%$ $D_h = 100km$	$\eta_{H^-} = 99\%$ $D_l = 100km$	$\eta_{H_2tank} = 99\%$	$E_{H_2\,tank,t} = 50000Nm^3$
Batteries	$\delta = 0.46\%$ $P_{bat\_chN} = 1MW$	$\eta_{ch} = 90\%$ $P_{bat\_dhN} = 0.5MW$	$\eta_{dh} = 90\%$	$C_{bat} = 2MWh$
Others	$R = 8.314J/mol \cdot K$ $E_{TRN} = 0.14kg/km$ $S_{DRin,t} = 2¥/kWh$	$F = 9.64853399 \times 10^4 C/mol$ $\eta_{H_2FC} = 0.00776kg/km$ $S_{DRout,t} = 4¥/kWh$	$S_{H_2} = 2.67¥/Nm^3$ $\lambda_{CO_2} = 0.02275¥/kg$	$S_{O_2} = 0.09¥/Nm^3$ $\mu_{CO_2} = 0.01768¥/kg$

TABLE 2 | Related parameters of electricity-hydrogen coupling equipment.

Types	Parameters	Data
PEMEC	Construction costs/(¥/MW)	1×10^6
	O&M cost ratio	4%
	Life expectancy/year	20
PEMFC	Construction costs/(¥/MW)	4×10^6
	O&M cost ratio	4%
	Life expectancy/year	10
LOHC storage tank	Construction costs/(¥/MW)	5×10^3
	O&M cost ratio	1%
	Life expectancy/year	20
Oxygen tank	Construction costs/(¥/MW)	9×10^3
	O&M cost ratio	1%
	Life expectancy/year	20
Battery	Construction costs/(¥/MW)	3×10^6
	O&M cost ratio	1%
	Life expectancy/year	5

Analysis of Results

Day-Ahead Optimized Scheduling Results

Figures 8, **9** show the day-ahead optimal scheduling results for a typical day in summer and winter. **Figures 8A**, **9A** show the renewable energy generation forecast and microgrid load forecast for typical days in summer and winter. **Figures 8B**, **9B** show the output of each unit for typical days in summer and winter. **Figures 8C**, **9C** show the comparison of hydrogen production and hydrogen demand for typical days in summer and winter.

Summer light is strong in the northwest and wind speed is relatively low compared to other seasons. Photovoltaic and wind power systems are simultaneously used as the primary energy source for the EHCM. When the microgrid operates in island mode, renewable energy generation cannot meet the electric load demand. When there is power abandonment, PEMEC consumes excess electricity from renewable sources to produce hydrogen. It can realize the conversion of energy forms, and improve the utilization rate of renewable energy generation. When there is a shortage of electrical energy supply, the energy gap within the capacity can be supported by PEMFC with batteries to provide power for the load. The stored hydrogen is consumed and the microgrid forms a closed energy loop. The EHCM participates in the grid demand response service. Within the capacity of the microgrid, when the grid requires power during power consumption peaks, it is powered first by renewable energy generation and second by the PEMFC power systems. The PEMEC of the EHCM can provide a wide range of power consumption for the grid in a low consumption period.

In winter, the light intensity is weaker than in other seasons and the light hours become shorter, while the wind power generation is in the peak range for a long time. As shown in **Figure 9A**, wind power can meet the winter load of the microgrid. Hydrogen is produced in large quantities during the winter months, which can be highly profitable. In **Figure 9B**, the battery power and PEMFC power are 0 on a typical winter day. While the power of the PEMEC is high, the hydrogen production per unit time is at a high level. Using this energy can reduce renewable energy abandonment and reduce carbon emissions.

As can be seen in **Figures 8**, **9**, the primary power source of the EHCM in the proposed day-ahead optimization strategy comes from renewable energy generation and the PEMFC power generation system. The PEMFC is required for part of a typical day in summer, while wind power is more abundant in winter and the main load is the PEMEC. Hydrogen production is at a higher position in winter. In S1, the dynamic characteristics of the electricity-hydrogen coupling system are considered, which is neglected in S2. In the simulation results of **Figures 8C**, **9C**, that the hydrogen production shows a more significant deviation. Therefore, the dynamic characteristics of electricity-hydrogen coupling have a great influence on hydrogen production. If it is neglected, the control of hydrogen production will be very inaccurate and affect the accuracy and economy of the system.

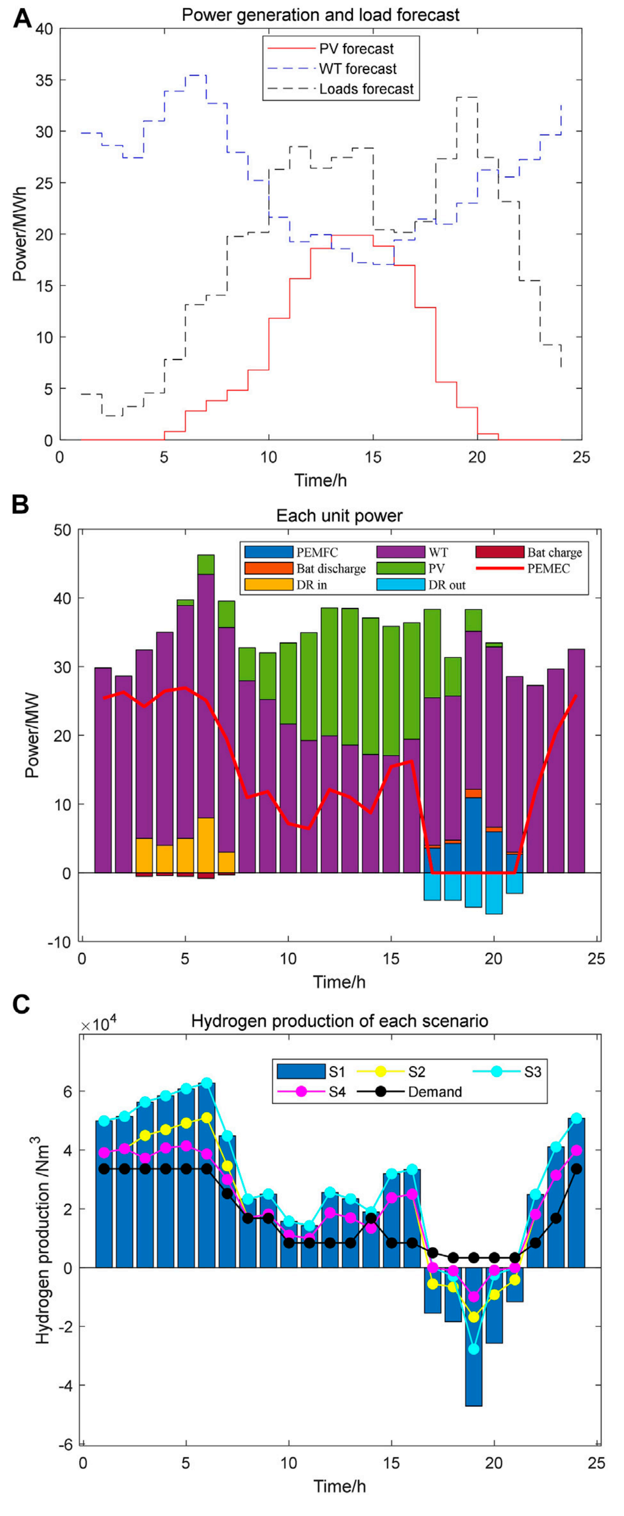

FIGURE 8 | (A) Day-ahead forecast results of a typical summer day, **(B)** each unit power of a typical summer day, **(C)** hydrogen production and hydrogen demand of a typical summer day.

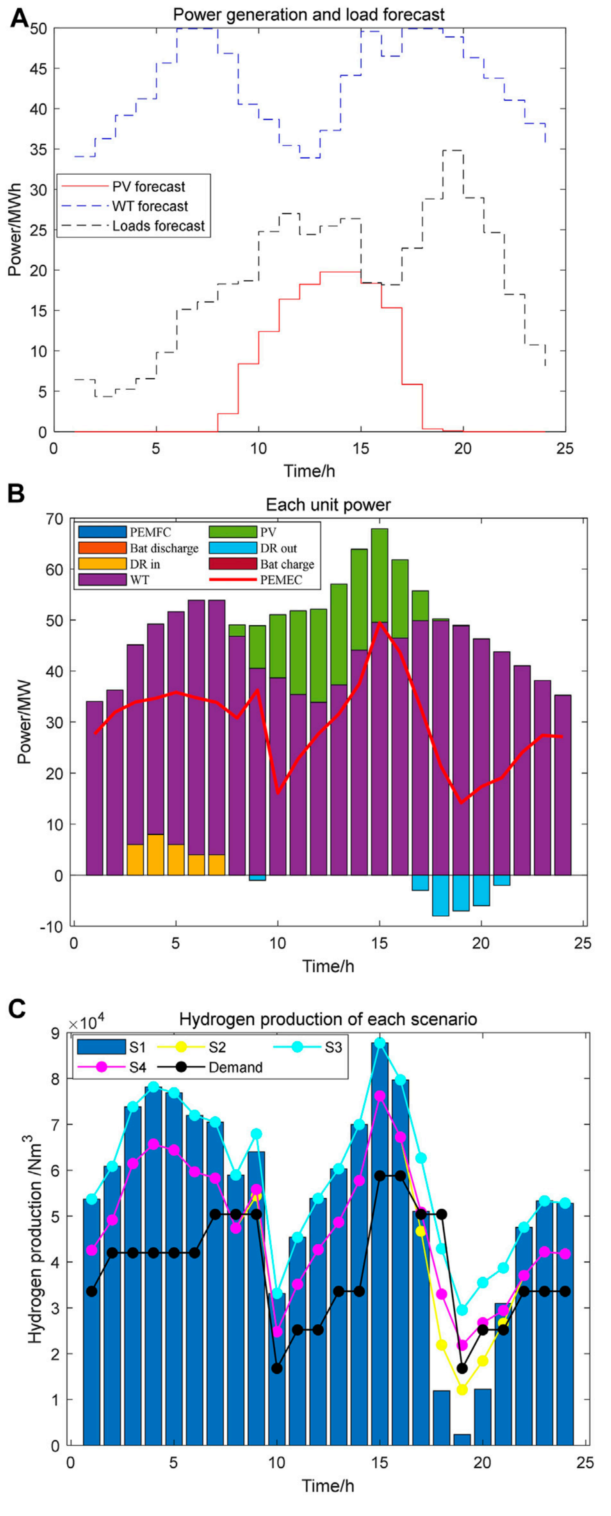

FIGURE 9 | (A) Day-ahead forecast results of a typical winter day, **(B)** each unit power of a typical winter day, **(C)** hydrogen production and hydrogen demand of a typical winter day.

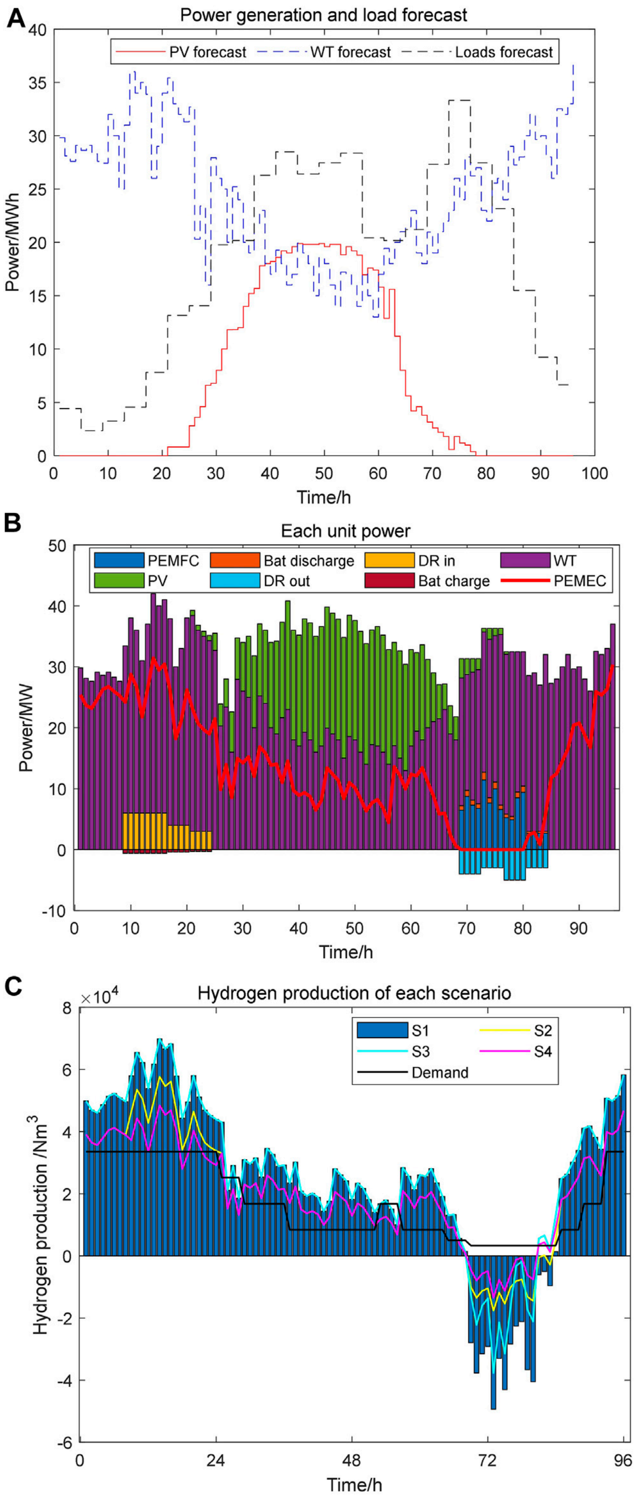

FIGURE 10 | (A) Intra-day forecast results of a typical summer day, **(B)** each unit power of a typical summer day, **(C)** hydrogen production and hydrogen demand of a typical summer day.

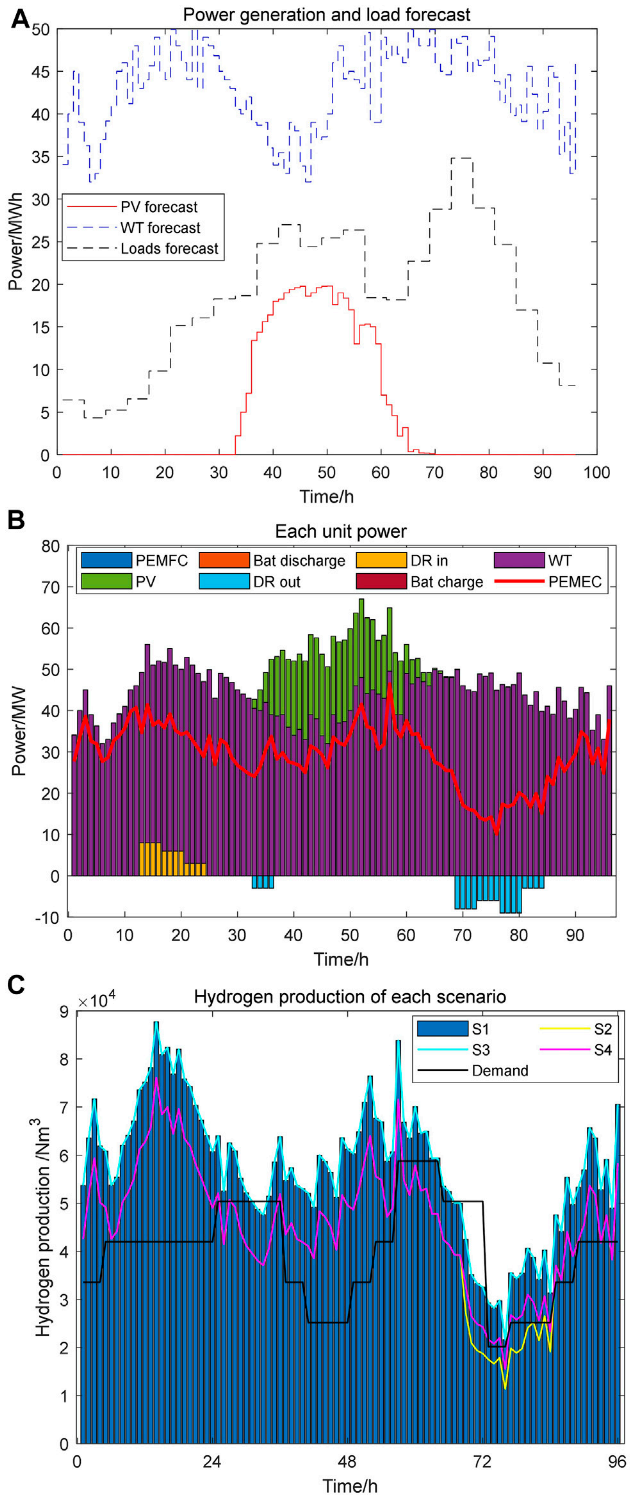

FIGURE 11 | (A) Intra-day forecast results of a typical winter day, **(B)** each unit power of a typical winter day, **(C)** hydrogen production and hydrogen demand of a typical winter day.

TABLE 3 | Microgrid revenue of typical day in summer/winter.

Scenarios			Total revenue/¥	Hydrogen sales revenue/¥	Oxygen sales revenue/¥	Demand response revenue/¥	Environmental revenue/¥	O&M costs/¥
Summer scenario	Day-ahead optimized scheduling results	S1	2068075	2503744	113807	138000	1883	689358
		S2	1576931	1877808	85355	138000	1412	525644
		S3	1956429	2493363	113335	0	1874	652143
		S4	1465285	1867427	84883	0	1403	488428
	Intra-day optimized scheduling results	S1	4253834	5264526	239297	164000	3956	1417945
		S2	3221125	3948394	179472	164000	2967	1073708
		S3	3968429	5057550	229889	0	3800	1322810
		S4	2976322	3793162	172416	0	2850	992107
Winter scenario	Day-ahead optimized scheduling results	S1	2259369	2741600	123935	144900	2058	753123
		S2	1721696	2056200	92952	144900	1543	573899
		S3	2141776	2730233	123421	0	2048	713925
		S4	1604103	2044833	92438	0	1534	534701
	Intra-day optimized scheduling results	S1	4654100	5775185	258680	167444	4158	1551367
		S2	3521970	4331389	194010	167444	3118	1173990
		S3	4350477	5548132	248510	0	3994	1450159
		S4	3262858	4161099	186382	0	2996	1087619

Intra-day Optimal Scheduling Results

Figures 10, **11** show the results of intra-day real-time optimal scheduling after model predictive control. The day-ahead optimal scheduling is in hours. The forecast results for wind and PV are relatively rough, and the microgrid scheduling cannot respond to load fluctuations in time. The real-time scheduling of intra-day is based on 15 min. Comparing the optimized scheduling results in **Figure 10** with those in **Figures 8**, **11** with those in **Figure 9**, the model prediction control can predict the real-time wind power and PV output more accurately than the day-ahead optimization results. The actual power consumed by PEMEC is more accurate and renewable power is fully consumed. When the real-time scheduling and the day-ahead scheduling results are close, the microgrid controllable units correct the individual scheduling results based on the day-ahead scheduling to reduce the error. When the intra-day scheduling differs significantly from the day-ahead scheduling results, the microgrid controllable units can be optimally scheduled in real time based on the actual renewable energy forecast values.

Considering the dynamic characteristics of electricity-hydrogen coupling, the intra-day scheduling results of the PEMEC and PEMFC generation systems are more accurate. The efficiency of the power to hydrogen is related to the absorbed power of the PEMEC, which allows the maximum approximation of actual hydrogen production. It can get a better overview of hydrogen production and the state of hydrogen storage. The power response of the PEMFC system can follow the load change, which can reduce the hydrogen consumption and guarantee the quality of the system power supply.

Economic Analysis of Day-Ahead and Intra-day Scheduling Results

Table 3 shows the optimization costs for day-ahead and intra-day scheduling of the EHCM for different scenarios. The time scale of the day-ahead optimal scheduling is broad. Uncertainty in renewable energy forecasts makes it difficult to accurately reflect actual power generation, leading to power shortages and abandonment. The intra-day optimal scheduling is based on the day-ahead optimal scheduling for error reduction. Therefore, it has a good impact on the microgrid economy. Intra-day scheduling improves microgrid economics by making corrections to optimization results in a short period. From **Table 3**, hydrogen sales revenue, oxygen sales revenue, demand response revenue, and reduced carbon emissions revenue in the typical summer day in S1 are improved by 9.5, 8.9, 5, and 9.3%, which in the typical winter day are improved by 9.7, 8.1, 2.1, and 5.1%. The microgrid day-ahead and intra-day optimal scheduling for S1 consider the dynamic characteristics of electricity-hydrogen coupling and demand response services. In terms of overall economics, the total revenues of day-ahead and intra-day scheduling for a typical day scenario in summer and winter are improved by 9.25 and 9.41%. The intra-day optimization revenue of each typical day is higher than that of the day-ahead scheduling results. It shows that intra-day scheduling can reduce the errors generated by day-ahead scheduling. The optimization method proposed in this paper has the effect of improving the economy.

Analysis of Optimized Scheduling Results for Different Scenarios

A comparison of typical daily scenarios in summer and winter shows that hydrogen production in the winter scenario is more than twice as high as in summer, due to the high wind speed and the larger capacity of the wind farm. S1 considers the dynamic characteristics of electricity-hydrogen coupling with participation in grid demand response services. S2 and S3 ignore electricity-hydrogen coupling dynamic characteristics and grid demand response services, while S4 ignores the above two. Analysis of the day-ahead optimal scheduling results for a typical summer day shows that the total revenue of the microgrid is the highest in S1. After ignoring the electricity-hydrogen coupling

TABLE 4 | Optimal revenue of different weight coefficients.

Scenarios	Typical summer day			Typical winter day		
	1	2	3	1	2	3
λ_1	0.2	0.3	0.5	0.2	0.3	0.5
λ_2	0.4	0.5	0.3	0.4	0.5	0.3
λ_3	0.3	0.2	0.4	0.3	0.2	0.4
λ_4	0.3	0.5	0.2	0.3	0.5	0.2
λ_5	0.2	0.3	0.5	0.2	0.3	0.5
λ_6	0.1	0.2	0.4	0.1	0.2	0.4
λ_7	0.2	0.3	0.1	0.2	0.3	0.1
λ_8	0.3	0.2	0.2	0.3	0.2	0.2
λ_9	0.2	0.1	0.4	0.2	0.1	0.4
λ_{10}	0.3	0.1	0.2	0.3	0.1	0.2
Total revenue × 10^4/¥	431.79	392.99	291.48	854.89	832.15	656.59
Hydrogen sales revenue × 10^4/¥	526.2	496.1	394.1	1078.3	1035.25	807.7
Oxygen sales revenue × 10^4/¥	17.1	23.2	22.9	47.15	45.1	34.85
Demand response revenue × 10^4/¥	14.9	13.2	16.1	17.7	21.6	32.8
Environmental revenue × 10^4/¥	0.29	0.39	0.38	0.79	0.8	0.59
O&M costs × 10^4/¥	127.3	140.1	142	289.05	270.6	219.35

characteristics, the revenue from hydrogen sales in the S2 scenario is decreased by 23.7%. This has a significant impact on the control of hydrogen production as the efficiency variation of the PEMEC is ignored. S3 only ignores the demand response service, and there is only a tiny change in hydrogen production revenue. For the microgrid with high-capacity PEMEC devices, precise control can be made for wide power fluctuations. The impact on hydrogen production and power fluctuations in the microgrid is minimal due to the low power of demand response. As a result, microgrids can provide additional ancillary services to increase revenue. S4 is the least profitable scenario because it ignores the electricity-hydrogen coupling characteristics and the grid auxiliary services.

In summary, an EHCM can improve the economy. Because PEMEC can cope with the wide range of power fluctuations caused by the uncertainty of renewable energy. Hydrogen and oxygen have a wide range of uses, and the revenue from the sale of gas from the microgrid is significant. The EHCM, which contains a PEMEC and a PEMFC power generation system, can absorb a large amount of abandoned electricity from renewable energy for hydrogen production. Hydrogen can also be used to supply loads by generating electricity through reactions of the PEMFC. Thus, the EHCM can provide the corresponding grid auxiliary services. As clean energy, when used as the energy for hydrogen fuel cell vehicles, the reaction products of hydrogen are only water. Therefore, from the environmental point of view, it can reduce carbon emissions to achieve economic benefits. But most importantly, it brings environmental benefits and enhances the overall environmental friendliness.

Analysis of Different Weighting Coefficients

Different weighting factors are used for intra-day real-time scheduling, and the optimized scheduling results are shown in **Table 4**. It presents the results of three sets of weighting coefficients for summer and winter typical days. The weighting factors λ_1, λ_2, λ_3, λ_4, λ_5 can show the amount of hydrogen produced in the EHCM, which can improve the revenue of gas sales and reduce carbon emissions of the microgrid. λ_6 has a significant impact on the income of grid auxiliary services. λ_7, λ_8, λ_9, λ_{10} can affect the hydrogen storage, oxygen storage, battery SOC and hydrogen storage status of the microgrid. They are used to limit the degree of deviation of the microgrid capacity reserve from the day-ahead scheduling results. In this paper, a weighting factor numbered 1 is used and the result obtained is the maximum intra-day total revenue, but not all gains are always top. It is verified that the weight coefficients selected in this paper can guarantee the correct intra-day optimization results.

CONCLUSION

In this paper, an EHCM model consisting of renewable energy generation, hydrogen production, hydrogen storage and PEMFC is built. A two-stage optimal scheduling model that considers the uncertainty of renewable energy generation is proposed. The two-stage scheduling scheme includes day-ahead optimized and MPC-based real-time optimized scheduling. The microgrid is required to meet hydrogen and electricity loads, while providing demand response ancillary services to the grid. Different scenarios are studied using examples to verify the effectiveness of the proposed method. The conclusions are as follows.

1) The EHCM model constructed in this paper provides electricity and hydrogen. The proposed two-stage optimization method can effectively improve the economic efficiency of the microgrid. Renewable energy generation increases and carbon emissions decrease. A win-win situation for both environmental protection and economic gain.
2) The microgrid model considers the nonlinear relationship between the hydrogen production flow of PEMEC and its power consumption, the dynamic characteristics of the

PEMFC stack power generation, and the modal management method of PEMFC stack. It can effectively improve the hydrogen production capacity of EHCMs and significantly enhance the economic benefits.

3) The EHCM can provide demand response auxiliary services to the grid by using its energy storage and generation functions. It improves the economy of microgrids while providing stable support for the grid.

DATA AVAILABILITY STATEMENT

The original contributions presented in the study are included in the article/Supplementary Material, further inquiries can be directed to the corresponding author.

AUTHOR CONTRIBUTIONS

XL, WZ, and MH contributed to conception and design of the study. XL organized the database. YL performed the statistical analysis. WZ wrote the first draft of the manuscript. MH and YL wrote sections of the manuscript. All authors contributed to manuscript revision, read, and approved the submitted version.

FUNDING

This work was supported by the National Key R&D Program of China under grant (2018YFA0702200), the National Natural Science Foundation of China (62173074), the Key Project of National Natural Science Foundation of China (U20A2019).

REFERENCES

Berger, M., Radu, D., Fonteneau, R., Deschuyteneer, T., Detienne, G., and Ernst, D. (2020). The Role of Power-To-Gas and Carbon Capture Technologies in Cross-Sector Decarbonisation Strategies. *Electric Power Syst. Res.* 180, 106039. doi:10.1016/j.epsr.2019.106039

Chapman, A., Itaoka, K., Hirose, K., Davidson, F. T., Nagasawa, K., Lloyd, A. C., et al. (2019). A Review of Four Case Studies Assessing the Potential for Hydrogen Penetration of the Future Energy System. *Int. J. Hydrogen Energ.* 44 (13), 6371–6382. doi:10.1016/j.ijhydene.2019.01.168

El-Taweel, N. A., Khani, H., and Farag, H. E. Z. (2019). Hydrogen Storage Optimal Scheduling for Fuel Supply and Capacity-Based Demand Response Program Under Dynamic Hydrogen Pricing. *IEEE Trans. Smart Grid* 10 (4), 4531–4542. doi:10.1109/TSG.2018.2863247

El-Taweel, N. A., Khani, H., and Farag, H. E. Z. (2020). Optimal Sizing and Scheduling of Lohc-Based Generation and Storage Plants for Concurrent Services to Transportation Sector and Ancillary Services Market. *IEEE Trans. Sustain. Energ.* 11, 1381–1393. doi:10.1109/TSTE.2019.2926456

Farsangi, A. S. N., Hadayeghparast, S., Mehdinejad, M., and Shayanfar, H. (2018). A Novel Stochastic Energy Management of a Microgrid with Various Types of Distributed Energy Resources in Presence of Demand Response Programs. *Energy* 160, 257–274. doi:10.1016/j.energy.2018.06.136

Fikrt, A., Brehmer, R., Milella, V.-O., Müller, K., Bösmann, A., Preuster, P., et al. (2017). Dynamic Power Supply by Hydrogen Bound to a Liquid Organic Hydrogen Carrier. *Appl. Energ.* 194 (MAY15), 1–8. doi:10.1016/j.apenergy.2017.02.070

García, P., Torreglosa, J. P., Fernández, L. M., Jurado, F., Langella, R., and Testa, A. (2016). Energy Management System Based on Techno-Economic Optimization for Microgrids. *Electric Power Syst. Res.* 131 (FEB.), 49–59. doi:10.1016/j.epsr.2015.09.017

García, P., Torreglosa, J. P., Fernández, L. M., and Jurado, F. (2013). Optimal Energy Management System for Stand-Alone Wind Turbine/photovoltaic/hydrogen/battery Hybrid System with Supervisory Control Based on Fuzzy Logic. *Int. J. Hydrogen Energ.* 38 (33), 14146–14158. doi:10.1016/j.ijhydene.2013.08.106

H2 Industries (2022). LOHC Technology Turns Hydrogen into a Safe Power Storage Technology. Available at: https:||h2-industries.com/zh-hans/technology/https://www.Hydrogenious.net/index.php/en/products (Accessed January 11, 2022).

Hydrogenious LOHC Technologies (2022). Products. Available at: https://www.Hydrogenious.net/index.php/en/products (Accessed January 11, 2022).

Jia, H., Wang, D., Xu, X., and Yu, X. (2015). Research on Some Key Problems Related to Integrated Energy Systems. *Automation Electric Power Syst.* 39 (07), 198–207. doi:10.7500/AEPS20141009011

Jin, C., Ren, D., Xiao, J., Hou, J., Du, E., and Zhou, Y. (2021). Optimization Planning on Power System Supply-Grid-Storage Flexibility Resource for Supporting the "carbon Neutrality" Target of China. *Electric Power* 54 (08), 164–174. doi:10.11930/j.issn.1004-9649.202012126

Kong, L., Yu, J., Cai, G., Wang, S., and Liu, C. (2021). Power Regulation of Off-Grid Electro-Hydrogen Coupled System Based on Model Predictive Control. *Proc. CSEE* 41 (09), 3139–3149. doi:10.13334/j.0258-8013.pcsee.200874

Li, Q., Pu, Y., Han, Y., and Chen, W. (2020). Hierarchical Energy Management for Electric-Hydrogen Island Direct Current Micro-grid. *J. Southwest Jiaotong Univ.* 55 (05), 912–919.

Li, Q., Zhao, S., Pu, Y., Chen, W., and Yu, J. (2021). Capacity Optimization of Hybrid Energy Storage Microgrid Considering Electricity-Hydrogen Coupling. *Trans. China Electrotechnical Soc.* 36 (03), 486–495. doi:10.19595/j.cnki.1000-6753.tces.200754

Li, Z., Zhang, F., Liang, J., Yun, Z., and Zhang, J. (2015). Optimization on Microgrid with Combined Heat and Power System. *Proc. CSEE* 35 (14), 3569–3576. doi:10.13334/j.0258-8013.pcsee.2015.14.011

Liu, M., Liang, X., Lin, Q., and Wang, L. (2021). Key Issues and Countermeasures of CCUS Projects Linking Carbon Emission Trading Market under the Target of Carbon Neutrality. *Proc. CSEE* 41 (14), 4731–4739. doi:10.13334/j.0258-8013.pcsee.210544

Liu, Z., Yu, S., and Liang, N. (2020). The Optimal Scheduling with Hydrogen Storage Participation for Interconnected Power System. *Electric Power Sci. Eng.* 36 (03), 45–51. doi:10.3969/j.ISSN.1672-0792.2020.03.007

Marini, S., Salvi, P., Nelli, P., Pesenti, R., Villa, M., Berrettoni, M., et al. (2012). Advanced Alkaline Water Electrolysis. *Electrochimica Acta* 82 (none), 384–391. doi:10.1016/j.electacta.2012.05.011

Mendis, N., Muttaqi, K. M., Perera, S., and Kamalasadan, S. (2015). An Effective Power Management Strategy for a Wind-Diesel-Hydrogen-Based Remote Area Power Supply System to Meet Fluctuating Demands Under Generation Uncertainty. *IEEE Trans. Ind. Applicat.* 51 (2), 1228–1238. doi:10.1109/TIA.2014.2356013

Muyeen, S. M., Takahashi, R., and Tamura, J. (2011). Electrolyzer Switching Strategy for Hydrogen Generation from Variable Speed Wind Generator. *Electric Power Syst. Res.* 81 (5), 1171–1179. doi:10.1016/j.epsr.2011.01.005

Niermann, M., Drünert, S., Kaltschmitt, M., and Bonhoff, K. (2019). Liquid Organic Hydrogen Carriers (LOHCs) - Techno-Economic Analysis of LOHCs in a Defined Process Chain. *Energy Environ. Sci.* 12 (1), 290–307. doi:10.1039/c8ee02700e

Pu, Y., Li, Q., Chen, W., Huang, W., Hu, B., Han, Y., et al. (2019). Energy Management for Islanded Dc Microgrid with Hybrid Electric-Hydrogen Storage System Based on Minimum Utilization Cost and Energy Storage State Balance. *Power Syst. Techn.* 43 (03), 918–927. doi:10.13335/j.1000-3673.pst.2018.1528

Qiu, Y., Zhou, S., Gu, W., Pan, G., and Chen, X. (2022). Proceedings of the CSEE (2022). Application Prospect Analysis of Hydrogen Enriched Compressed Natural Gas Technologies under the Target of Carbon Emission Peak and Carbon Neutrality. Available at: http://kns.cnki.net/kcms/detail/11.2107.TM.20211102.1629.005.html (Accessed February 7, 2022).

Ramachandran, R., and Menon, R. K. (1998). An Overview of Industrial Uses of Hydrogen. *Int. J. Hydrogen Energ.* 23 (7), 593–598. doi:10.1016/S0360-3199(97)00112-2

Recalde Melo, D. F., and Chang-Chien, L.-R. (2014). Synergistic Control Between Hydrogen Storage System and Offshore Wind Farm for Grid Operation. *IEEE Trans. Sustain. Energ.* 5 (1), 18–27. doi:10.1109/TSTE.2013.2272332

Reuß, M., Grube, T., Robinius, M., Preuster, P., Wasserscheid, P., and Stolten, D. (2017). Seasonal Storage and Alternative Carriers: A Flexible Hydrogen Supply Chain Model. *Appl. Energ.* 200, 290–302. doi:10.1016/j.apenergy.2017.05.050

Song, P., Hou, J., Mu, X., and Wang, X. (2021). Screening and Application Scenarios of Liquid Organic Hydrogen Carrier Systems. *Nat. Gas Chem. Industry (C1 Chem. Chem. Engineering)* 46 (01), 1–5+33.

Taube, M., Rippin, D., Cresswell, D., and Knecht, W. (1983). A System of Hydrogen-Powered Vehicles with Liquid Organic Hydrides. *Int. J. Hydrogen Energ.* 8 (3), 213–225. doi:10.1016/0360-3199(83)90067-8

Wang, C., Hong, B., Guo, L., Zhang, D., and Liu, W. (2013). A General Modeling Method for Optimal Dispatch of Combined Cooling, Heating and Power Microgrid. *Proc. CSEE* 33 (31), 26–33+3. doi:10.13334/j.0258-8013.pcsee.2013.31.006

Wang, H., Zhou, X., and Ouyang, M. (2017). Corrigendum to "Efficiency Analysis of Novel Liquid Organic Hydrogen Carrier Technology and Comparison with High Pressure Storage Pathway" [Int J Hydrogen Energy 41 (2016) 18062-18071]. *Int. J. Hydrogen Energ.* 42 (36), 23242. doi:10.1016/j.ijhydene.2017.06.189

Wu, M., Luo, Z., Ji, Y., Li, Y., and Kou, L. (2017). Optimal Dynamic Dispatch for Combined Cooling Heating and Power Microgrid Based on Model Predictive Control. *Proc. CSEE* 37 (24), 7174–7184+7431. doi:10.13334/j.0258-8013.pcsee.170576

Yang, M., Sun, Y., and Cheng, H. (2017). Comments on "Efficiency Analysis of Novel Liquid Organic Hydrogen Carrier Technology and Comparison with High Pressure Storage Pathway" [Int. J. Hydrogen Energy 41 (2016) 18062-18071]. *Int. J. Hydrogen Energ.* 42, S0360319917336625. doi:10.1016/j.ijhydene.2017.09.034

Zhang, X., Niu, H., and Zhao, J. (2017). Optimal Dispatch Method of Distribution Network with Microgrid. *Trans. China Electrotechnical Soc.* 32 (07), 165–173. doi:10.19595/j.cnki.1000-6753.tces.2017.07.019

Zhang, Y., Zhang, N., Dai, H., Zhang, S., Wu, X., and Xue, M. (2021). Model Construction and Pathways of Low-Carbon Transition of China's Power System. *Electric Power* 54 (03), 1–11. doi:10.11930/j.issn.1004-9649.202101058

Zhou, C., Zheng, J., Jing, Z., Wu, Q., and Zhou, X. (2018). Multi-objective Optimal Design of Integrated Energy System for Park-Level Microgrid. *Power Syst. Techn.* 42 (06), 1687–1697. doi:10.13335/j.1000-3673.pst.2018.0280

Zuo, Y., Dai, C., Guo, A., and Chen, W. (2021). Air Supply System of Proton Exchange Membrane Fuel Cell Based on Improved EKF Algorithm and Stack Power Demand Regulation. *Proc. CSEE* 41 (19), 6550–6560. doi:10.13334/j.0258-8013.pcsee.202328

Conflict of Interest: The authors declare that the research was conducted in the absence of any commercial or financial relationships that could be construed as a potential conflict of interest.

Publisher's Note: All claims expressed in this article are solely those of the authors and do not necessarily represent those of their affiliated organizations, or those of the publisher, the editors and the reviewers. Any product that may be evaluated in this article, or claim that may be made by its manufacturer, is not guaranteed or endorsed by the publisher.

frontiers | Frontiers in Energy Research

ORIGINAL RESEARCH
published: 05 May 2022
doi: 10.3389/fenrg.2022.901354

Advanced Control for Grid-Connected System With Coordinated Photovoltaic and Energy Storage

Yujie Zhu and Guanhua Chen *

College of Computer and Information Technology, China Three Gorges University, Yichang, China

The large-scale new energy sources such as photovoltaic power generation reduces the original damping and inertia of the power system, resulting in the oscillation of the system. Self-adaptive virtual synchronous generator (SDVSG) controlled grid-connected inverters can provide virtual damping and inertia to support the frequency and voltage of the grid. Combining SDVSG control with stand-alone PV systems, a mainstream solution is to configure energy storage systems for them. In this paper, a grid-connected PV storage system with SDVSG is proposed with coordination control; an adaptive variable-step conductivity increment method is adopted to achieve the maximum power point tracking (MPPT) for PV array, and variable domain fuzzy logic control methods of DC-DC converter are implemented as well. Finally, the simulation results prove the system has strong robustness and could handle the perturbations.

Keywords: new energy grid connection, photovoltaic, maximum power point tracking, energy storage, coordinated control, virtual synchronous generators, adaptive variable-step conductivity increment method

Edited by:
Rui Wang,
Northeastern University, China

Reviewed by:
Xuguang Hu,
Northeastern University, China
Yushuai Li,
University of Oslo, Norway

Correspondence:
Guanhua Chen
2019137131@ctgu.edu.cn

Specialty section:
This article was submitted to
Smart Grids,
a section of the journal
Frontiers in Energy Research

Received: *21 March 2022*
Accepted: *11 April 2022*
Published: *05 May 2022*

Citation:
Zhu Y and Chen G (2022) Advanced Control for Grid-Connected System With Coordinated Photovoltaic and Energy Storage.
Front. Energy Res. 10:901354.
doi: 10.3389/fenrg.2022.901354

1 INTRODUCTION

With the rapid development of renewable energy technologies such as photovoltaic and wind energy, increasing distributed generator (DG) systems are connected to the conventional power system. Compared with the centralized power generation system based on the synchronous generator, the inverter-based DG system has flexible control and fast response but reduces the original inertia and damping characteristics of the power system (Alipoor et al., 2014; Pattabiraman et al., 2018). The rotational inertia and damping characteristics of synchronous generators play an important role in maintaining the frequency stability of power systems. However, the increasing penetration of DG has led to a decreasing proportion of installed synchronous generator capacity in power systems. The inertia and damping of the system are relatively weakened and the rotating reserve is relatively reduced, which poses a serious challenge to the stable operation of the power system (Alipoor et al., 2015; Bri -Mathias et al., 2020).

To improve the inertia and damping of power systems containing high permeability, DGs enhance their ability to suppress frequency fluctuations and improve the compatibility between inverters and the grid. The virtual synchronous generator (VSG) and its working principle were invented to improve the damping and inertia of the system (Zhong and Weiss, 2011; Zhong et al., 2014). The main idea of VSG technology is to make the inverter simulate the external characteristics of a synchronous machine, especially the frequency characteristics, using control algorithms. To equip the inverter with the frequency characteristics of a synchronous generator, the control algorithm is required not only to simulate the inertia of the rotor of the synchronous generator but also to connect the inverter with an energy storage device to consume the power required to simulate the kinetic energy change of the rotor of the synchronous generator. The current research on VSG is mostly based on the premise that the DC side of the inverter can provide a stable voltage source (European FP6 project workshop, 2011; Zhong and Weiss, 2011; Chen et al., 2011; D'Arco et al., 2013; Hua et al., 2017), which is not satisfied by the inverter powered by PV only. As the capacity and number of grid-connected PV systems increase, it is important to equip them with the characteristics of synchronous generators for the stable operation of the grid. The reduced-order small-signal closed-loop transfer function model is proposed and impedance analysis is developed to verify the stability of DC Microgrids (Rui et al., 2020; Wang et al., 2021). This reduced-order model is a novel preprocessing approach for the real-time simulation of large-scale converters which could be provided for DC microgrid designers. The adaptive error correction method for voltage source inverters severally is embedded into both the outer and inner prediction loop (Ma et al., 2021). The impacts of different negative factors can be simultaneously processed and corrected through an adaptive error correction strategy.

There are two dominant functions of energy storage in renewable energy plants (Wei et al., 2019): one is to suppress the fluctuation of grid-connected power of renewable energy plants (Sun et al., 2019; Al- Shetwi et al., 2020; Kulyk and Zgurovets, 2020); the other is to control the operation of plants and energy storage systems to make their output meet the requirements of a given generation output curve, to achieve the purpose of economic dispatch of plants (Li et al., 2011; Ma et al., 2017). There is little research on how to utilize energy storage to make distributed generation systems with synchronous generator characteristics. In (Liu et al., 2017; Ma et al., 2017), it is pointed out that the utilize of energy storage simulates the kinetic energy change of the synchronous generator rotor, but the control method of energy storage and renewable energy is not fully researched. In (Velasco de la Fuente et al., 2013), energy storage is selected as a backup for photovoltaic power generation, so that the distributed generation system can operate in both grid-connected and off-grid modes, but the inverter still adopts PQ and droop control and does not have synchronous generator characteristics. In the literature (Liu et al., 2015; Zhao et al., 2017), a storage inverter based on VSG control is connected in parallel to the AC side of the PV inverter to increase the inertia of the system, but it does not make the grid-connected PV inverter itself have synchronous generator characteristics. The VSG control in photovoltaic storage power systems is analyzed in (Zhong et al., 2022), but still regard the PV array and energy storage as equivalent DC voltage sources. The control of energy storage charging and discharging is normally neglected, resulting in large fluctuations in the state of charge (SOC), which results over charging or discharging to shorten the battery life. The concept of virtual inertia for frequency control of MGs via an extended VSG is introduced in reference (Fathi et al., 2018) the proposed control inherits both properties of inertia response of real SGs and fast dynamics of power electronic interfaces. The decentralized deep policy gradient algorithm is developed and employed to find the optimal control policy for VSG (Li et al., 2021). The optimal policy in a model-free fashion is obtained and validated with this adaptive control. In (Zhang et al., 2020), a coordinate control for PV-storage grid-connected system was proposed, in which the energy storage unit implements the MPPT control and the photovoltaic inverter implements a VSG algorithm providing inertial and primary frequency support for the microgrid. Whereas the conventional MPPT and VSG can hardly handle the new energy systems with random perturbations and high permeability.

To mitigate the issues of the current research, the proposed topology and its advanced control in this paper have the following main characteristics.

- The Adaptive variable-step conductivity increment method is implemented to achieve MPPT for PV arrays to avoid oscillation and untimely tracking near the maximum power point.
- The variable domain fuzzy logic control for DC-DC converter is designed to overcome large overshoot while quickly obtaining the desired reference voltage
- An adaptive virtual synchronous generator control strategy is developed for the power supply of the PV energy storage system to provide variable damping and inertia, improving the stability of the power supply.
- A coordinated control strategy is proposed to achieve grid-connected power leveling function, improve power generation efficiency and ensure DC bus voltage stability.

The rest of this paper is organized as follows: In Section II, the configuration of the system is presented and introduced; In Section III, the advanced control of the DC-AC inverter, DC-DC converter, ADVSG, and coordinate strategy is introduced, respectively; In Section IV, the proposed design and its control method are verified by the simulation experiment in MATLAB/Simulink. In Section V, conclusions are summarized and potential research directions are mentioned as well.

2 COORDINATED PV AND BATTERY GRID-CONNECTED SYSTEMS

Conventional PV grid-connected systems are capable of maximum power tracking and grid-connected inverters. However, there are power leveling difficulties as well as low inertia and damping problems, which normally require external power sources for co-powering. In this section, the structure and characteristics of conventional PV grid-connected systems and energy storage-based PV grid-connected systems are introduced, respectively.

2.1 Conventional Grid-Connected PV Generator

The structure of two conventional PV grid-connected power generation systems is shown in **Figure 1**. In the direct PV system, the PV array is directly connected to the DC side of the inverter, as shown in **Figure 1A**. The power generated by the PV array is fed into the grid only through the DC/AC single-stage converter. The circuit of the two-stage grid-connected PV system is a two-stage power conversion circuit, as shown in **Figure 1B**. The front stage uses a boost converter to perform the step-up function of the output voltage of the PV array on the DC side and MPPT; the rear stage is a grid-

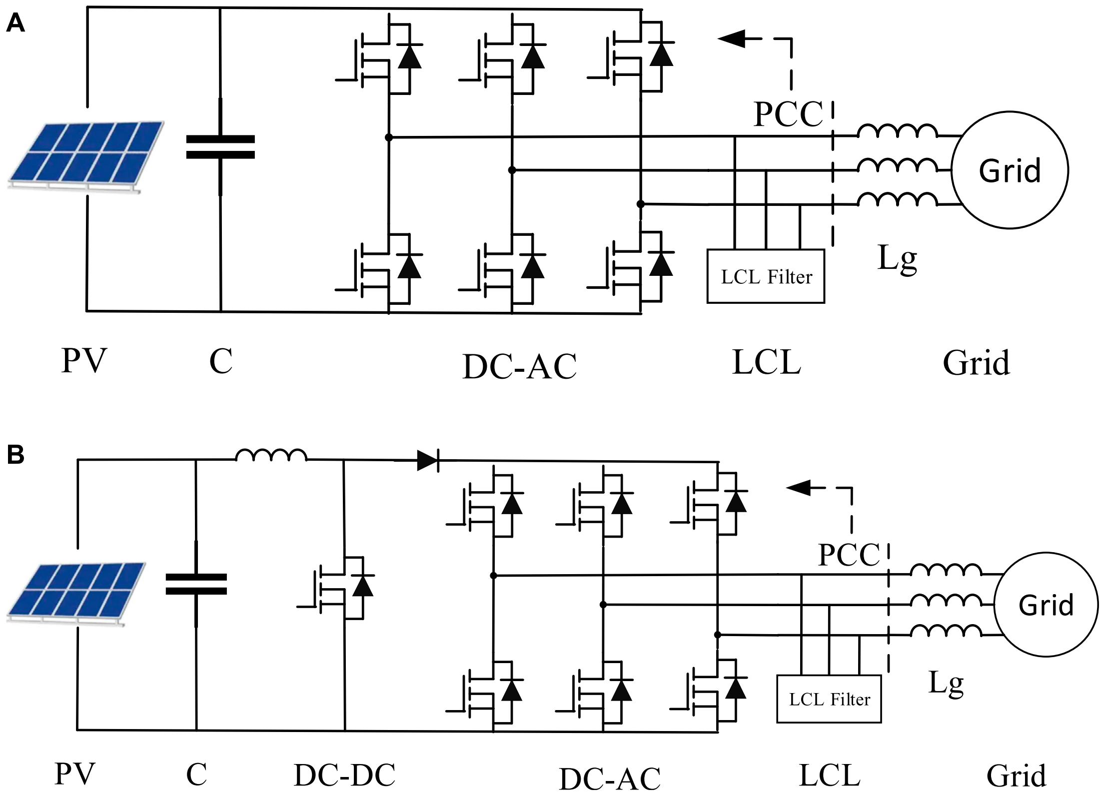

FIGURE 1 | Structure of conversational grid-connected PV system. **(A)** Direct photovoltaic power generation system **(B)** Photovoltaic power generation system with DC-DC converter.

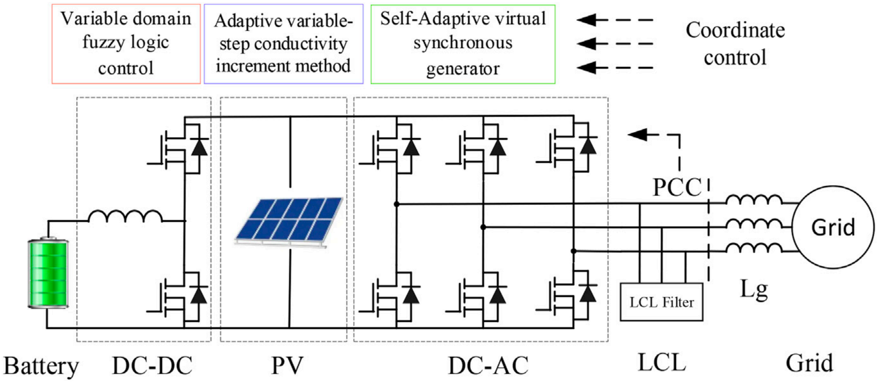

FIGURE 2 | Structure of grid-connected PV-energy storage system.

connected inverter to perform the power conversion and grid-connected function, and the control of the boost converter and the inverter are independent of each other.

The inverter control of a conventional grid-connected PV system generally consists of an outer loop of DC voltage and an inner loop of active and reactive currents, which are externally reflected as current source characteristics. Since there is no energy storage device, the system output active power can only follow the power generated by the PV array, which is intermittent and fluctuating. The inverter output frequency is the grid frequency obtained from the phase-locked loop, which does not have inertia and damping characteristics. Therefore, conventional PV systems, whether single-stage or two-stage, are unable to provide frequency support for the grid.

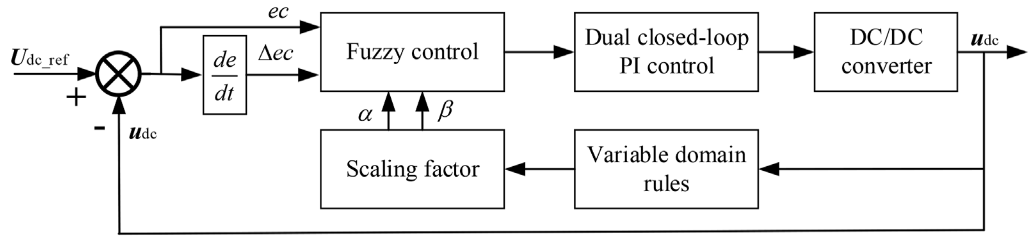

FIGURE 3 | Variable domain fuzzy-logic control for DC-DC converter.

2.2 Grid-Connected PV-Energy Storage System

The structure of the grid-connected energy storage PV system is shown in **Figure 2**. The system includes the PV array, the energy storage device, the bidirectional DC-DC converter, the inverter, and its filtering circuit. The PV array is directly connected to the DC bus of the inverter and connected in parallel with the energy storage device with a buck/boost converter, and the energy is fed into the grid by the inverter based on VSG control. The control system is divided into three main parts: the coordination control unit, the DC-DC control unit, and the VSG control unit. On the one hand, the coordination control unit is responsible for searching the maximum power point voltage UMPP of the PV array and transmitting it to the DC-DC control unit as the DC bus voltage command value U_{ref}, which controls the DC bus voltage according to the command, thus completing the MPPT of the PV array. On the other hand, the output power of VSG is adjusted according to the given rate command, while the reactive power command of VSG is given to control the charging and discharging power of energy storage, thus realizing the purpose of adjusting the SOC of energy storage. The VSG control unit implements the inverter to simulate the characteristics of the synchronous generator and to track the power command.

Compared with the traditional grid-connected PV power generation system, the energy storage PV grid-connected power generation system has the following features: 1) The energy storage device has an energy buffering effect so that the inverter output power does not have to be equal to the PV power, which not only reduces the fluctuation and intermittency of the grid-connected power but also meets the basic condition that the inverter simulates the rotor inertia of a synchronous generator. 2) The inverter in the grid-connected energy storage PV system is controlled by VSG, which simulates the characteristics of a synchronous generator and can realize the self-synchronous grid connection without the need for a phase-locking loop to detect the frequency and phase of the grid. 3) By simulating the synchronous generator characteristics, the energy storage PV grid-connected power generation system is externally characterized as a voltage source and has the ability of frequency inertia and damping frequency shift.

3 THE CONTROL OF GRID-CONNECTED PV ENERGY STORAGE SYSTEM

3.1 The Control for the DC-DC Converter

The DC-DC control strategy aims to control the DC bus voltage to track the commanded value of $U_{\mathrm{dc\_ref}}$ given by the coordinated control unit and to control the charging and discharging of the energy storage device by controlling the inductor current of the buck/boost converter during the system operation. Therefore, the DC-DC control strategy adopts an outer loop of DC bus voltage and an inner loop of inductor current to control the buck/boost converter, as shown in **Figure 3**, in which a proportional-integral (PI) regulator is used for the outer loop of voltage and a proportional regulator is used for the inner loop of current. When the dc bus voltage rises, the bidirectional converter operates in buck mode to store energy for charging; when the dc bus voltage decreases, the bidirectional converter operates in boost mode to store energy for discharging. It is worth noting that the energy storage device stabilizes the DC bus voltage.

It is worth noting that by stabilizing the DC bus voltage, the energy storage device not only achieves the MPPT function but more importantly, enables the VSG to simulate the rotor inertia of the synchronous generator. Assuming that the output power of the PV array is constant when the disturbance reduces the frequency of the VSG, the grid-connected inverter simulates the process of releasing energy from the rotor of the synchronous generator, increasing the active power; this causes the DC bus voltage to decrease, and the energy storage discharges to stabilize the DC bus voltage and vice versa. Meanwhile the energy change of the energy storage simulates the increase or decrease of the kinetic energy of the synchronous generator rotor.

To ensure the normal operation of the system, the energy storage always maintain the DC bus voltage at a level not lower than the minimum voltage for successful inverter operation. The scaling factor and variable domain for fuzzy control provide a fast response to track the reference values. On the one hand, the maximum discharge power of energy storage is required to be no less than the short-term maximum output power of the inverter based on VSG control; on the other hand, during the frequency shift and PV power fluctuation, when the energy generated by the PV array is less than the output energy

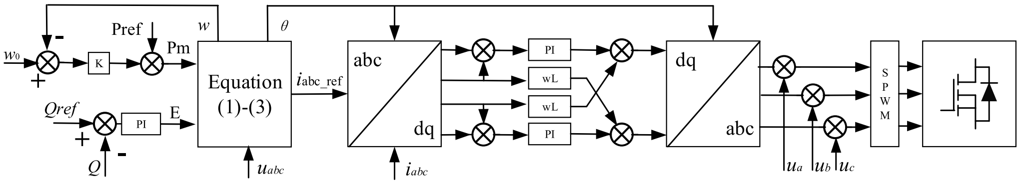

FIGURE 4 | Control of conventional VSG.

of the inverter, the output power of energy storage should be sufficient to make up the shortfall between them; and when the energy generated by the PV array is greater than the output energy of the inverter, which should have enough space to store the excess power.

3.2 DQ Decoupling for Photovoltaic Grid-Connected Inverters

This section will specifically introduce the principle of DQ-axis decoupling control of the inverter. The connection of the inverter to the grid can be approximated by the following equation.

$$U_{\text{abc}} = i_{abc}R + L\frac{di_{abc}}{dt} + e_{abc} \tag{1}$$

Where the subscript ***abc*** denotes the column vector composed of the quantities corresponding to the three phases of abc; $\boldsymbol{U}_{\text{abc}}$ denotes the voltage of the inverter; $\boldsymbol{i}_{\text{abc}}$ denotes the three-phase current, and $\boldsymbol{e}_{\text{abc}}$ denotes the three-phase voltage on the net side. A Park transformation of Eq/(1) yields the following equation.

$$\begin{cases} v_d = Ri_d + L\dfrac{di_d}{dt} - \omega Li_q + e_d \\ v_q = Ri_q + L\dfrac{di_q}{dt} + \omega Li_d + eq \end{cases} \tag{2}$$

Where $\boldsymbol{\omega}$ is the rotational angular velocity of the ***dq*** coordinate system in the Park variation. After the transformation, the active and reactive power output to the grid can be expressed as the following equation

$$\begin{cases} P = \dfrac{3}{2}\left(e_d i_d + e_q i_q\right) \\ Q = \dfrac{3}{2}\left(e_q i_d - e_d i_q\right) \end{cases} \tag{3}$$

Where ***P***, ***Q*** represents the active and reactive power output to the grid, respectively.

The active and reactive power can be controlled separately by controlling the DQ axis current. Assuming that the reference values of id and $\boldsymbol{i}_{\text{q}}$ ($\boldsymbol{i}$* d, $\boldsymbol{i}$* q) are known, then we can control the voltage output of the inverter so that $\boldsymbol{i}_{\text{d}} = \boldsymbol{i}$* d,$\boldsymbol{i}_{\text{q}} = \boldsymbol{i}$* q. First, the Laplace transform of **Eq. 2** is performed.

$$\begin{cases} i_d = \dfrac{V_d + \omega Li_q - e_d}{R + Ls} \\ i_q = \dfrac{V_q - \omega Li_d - e_q}{R + Ls} \end{cases} \tag{4}$$

Where ***s*** is the Laplace operator. $\boldsymbol{V}_{\text{d}}$ and $\boldsymbol{V}_{\text{q}}$ are the DQ voltages of the inverter, so these are the two quantities that we can control. These two control quantities are of the following form.

$$\begin{cases} V_d = e_d - \omega Li_q + \left(K_{pd} + K_{id}/s\right)\left(i_d^* - i_d\right) \\ V_q = e_q + \omega Li_q + \left(K_{pq} + K_{iq}/s\right)\left(i_q^* - i_q\right) \end{cases} \tag{5}$$

Taking 5) into (4), the controlled quantity is obtained as

$$\begin{cases} i_d = i_d^* \cdot \dfrac{K_{pd}s + K_{id}}{Ls^2 + \left(R + K_{pd}\right)s + K_{id}} \\ i_q = i_q^* \cdot \dfrac{K_{pq}s + K_{iq}}{Ls^2 + \left(R + K_{pq}\right)s + K_{iq}} \end{cases} \tag{6}$$

Eq. 6 shows that if the control variables could satisfy the relationship shown in **Eq. 5**, then the whole system can be represented as a second-order system shown in **Eq. 6**.

3.3 Self-Adaptive VSG Control

The control algorithm of VSG usually needs to calculate the output current or voltage of the synchronous generator in the current state based on a given mathematical model, and use it as a command to control the inverter to follow the command, to simulate the external characteristics of the synchronous generator. In this paper, the mathematical model of a synchronous generator is used as follows:

$$J\frac{dw}{dt} = T_m - T_e - D\left(w - w_g\right) \tag{7}$$

Where ***J*** is the rotor inertia of the synchronous generator, ***D*** is the damping factor, $\boldsymbol{T}_{\text{m}}$ and $\boldsymbol{T}_{\text{e}}$ are the mechanical torque and electromagnetic torque of the synchronous generator, respectively, $\boldsymbol{\omega}_{\text{g}}$ is the rated angular frequency of the grid, and ω is the measured angular frequency.

$$e_{abc} = E\begin{bmatrix} \sin\theta \\ \sin(\theta - 2\pi/3) \\ \sin(\theta + 2\pi/3) \end{bmatrix} \tag{8}$$

$$P_e = e_a i_a + e_b i_b + e_c i_c \tag{9}$$

The VSG control strategy is shown in **Figure 4**, where the filter capacitor voltage $\boldsymbol{u}_{\text{abc}}$ is considered as the terminal voltage, and the output current $\boldsymbol{i}_{\text{abc\_ref}}$ of the synchronous generator in this state is calculated according to **Eqs. 7–9** and used as the command value of the inverter output current $\boldsymbol{i}_{\text{abc}}$. To better simulate the synchronous generator characteristics, the inverter must track the commanded current $\boldsymbol{i}_{\text{abc}}$ ref without static difference and quickly. Therefore, in

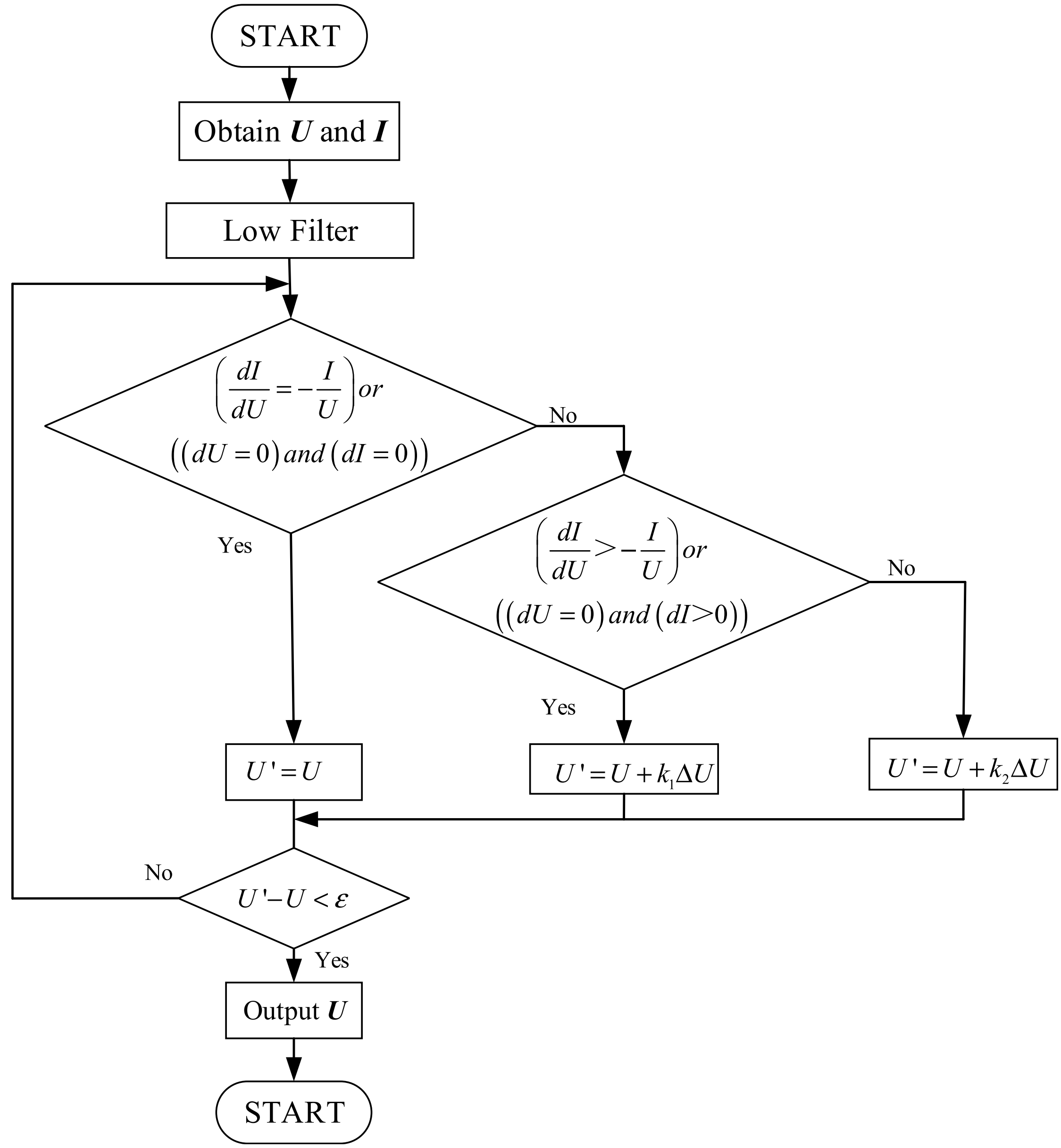

FIGURE 5 | Flowchart of Adaptive variable step conductance increment method.

this paper, the inverter is controlled in the synchronous coordinate system by using the angle $\boldsymbol{\theta}$ solved by the model; at the same time, the capacitor voltage $\boldsymbol{u}_{\mathrm{abc}}$ is used as a feedforward quantity to improve the accuracy and speed of the VSG control system.

It should be noted that since the frequency regulation factor $\boldsymbol{K}$ and the damping factor $\boldsymbol{D}$ in the governor are the same for frequency regulation, this paper ignores the governor, i.e., $\boldsymbol{P}_{\mathrm{ref}}$ is equal to $\boldsymbol{P}_{\mathrm{m}}$, and compensates for its role by adjusting $\boldsymbol{D}$.

The VSG connected in parallel with the grid must not only output active power to the grid but also can output a given amount of reactive power. In a conventional synchronous generator set, the reactive power can be regulated by adjusting the excitation current, i.e., the electric potential. Based on this principle, the variable $\boldsymbol{D}$ is adopted to obtain a better response of the characteristics of the excitation regulator. The difference between the commanded value of reactive power $\boldsymbol{Q}_{\mathrm{ref}}$ and the actual value $\boldsymbol{Q}$ of the VSG is utilized as the input of the PI regulator, and adjusts the electric potential $\boldsymbol{E}$ to realize the closed-loop control of reactive power in grid-connected operation without differences.

3.4 Adaptive Variable-Step Conductivity Increment Method

The mainstream MPPT algorithms are the perturbation observation method and the conductance increment method. For the poor dynamic performance of the conductance increment method in the range of low slope, this paper adopts the conductance

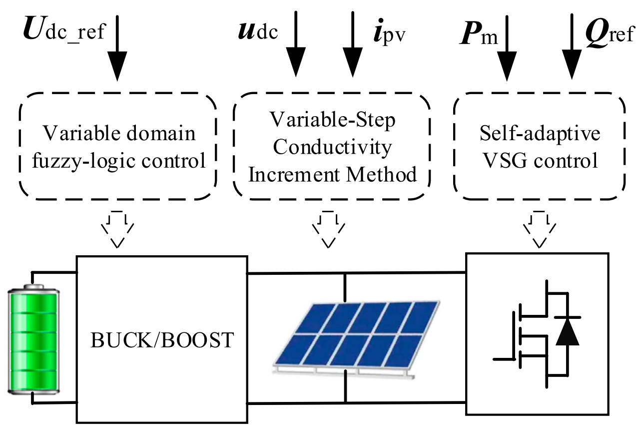

FIGURE 6 | Coordinated control for the system.

TABLE 1 | Key parameters in the simulation.

Items	Parameters	Values
System	Bus voltage	750 V
PV array	Parallel strings	46
	Series	12
	Module	A10 J-S72-175
Battery	Rated voltage	640 V
	Capacity	62.5AH
	Initial SOC	30%, 70%, 95%
Converter	Inductor	1000uH
	Capacitor	470uF

TABLE 2 | Control objects and methods.

Conditions	PV module	Battery	Inverter
Case 1	Constant power	Discharge	Control bus voltage
Case 2	MPPT	Power supply	Control bus voltage
Case 3	Constant power	Charge	Control bus voltage

increment method based on adaptive variable step size. First, when the light and temperature are constant, the PV output power P is considered as a function of the port voltage U. The output power shows a variation of increasing and then decreasing with the process of increasing voltage. The differentiation process is given as follows:

$$\frac{dP}{dU} = I + U\frac{dI}{dU} \tag{10}$$

Where I represents the current output from the PV. **Eq. 10** could be transferred into (11).

$$\frac{1}{U}\frac{dP}{dU} = \frac{I}{U} + \frac{dI}{dU} \tag{11}$$

To reduce the disturbance of the sampling process, the system noise can be reduced by the low-pass filtering method. The control period is T_s, and the sampling period is $T_s/10$, then the average value obtained from ten samples can be used to input the system for processing.

The adaptive variable step conductance increment method is when the operating point voltage is less than the maximum power point, and the operating voltage should be increased to approach the maximum power point. Besides, due to the low slope of the curve, the tracking of the maximum power point is accelerated by using a larger step size, i.e., k_1 takes a larger value. The voltage update process in the adaptive variable step size conductance increment method can be expressed as shown in **Eq. 12**

$$\begin{cases} U' = U, if\left(\frac{dI}{dU} = -\frac{I}{U}\right) or\,((dU = 0) and\,(dI = 0)) \\ U' = U + k_1 \Delta U, if\left(\frac{dI}{dU} > -\frac{I}{U}\right) or\,((dU = 0) and\,(dI > 0)) \\ U' = U + k_2 \Delta U, if\left(\frac{dI}{dU} < -\frac{I}{U}\right) or\,((dU = 0) and\,(dI < 0)) \end{cases} \tag{12}$$

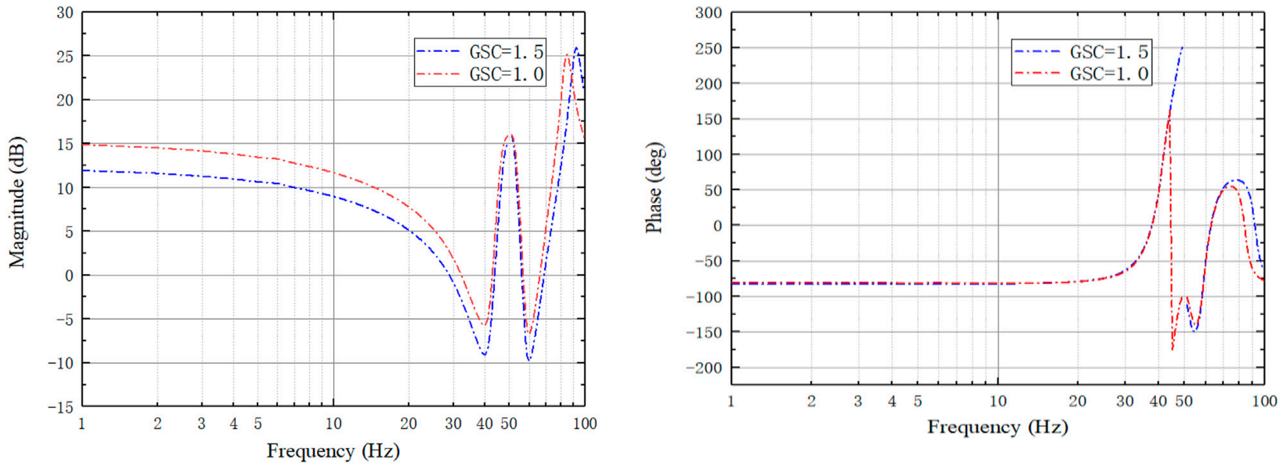

FIGURE 7 | Frequency response of the grid impedance.

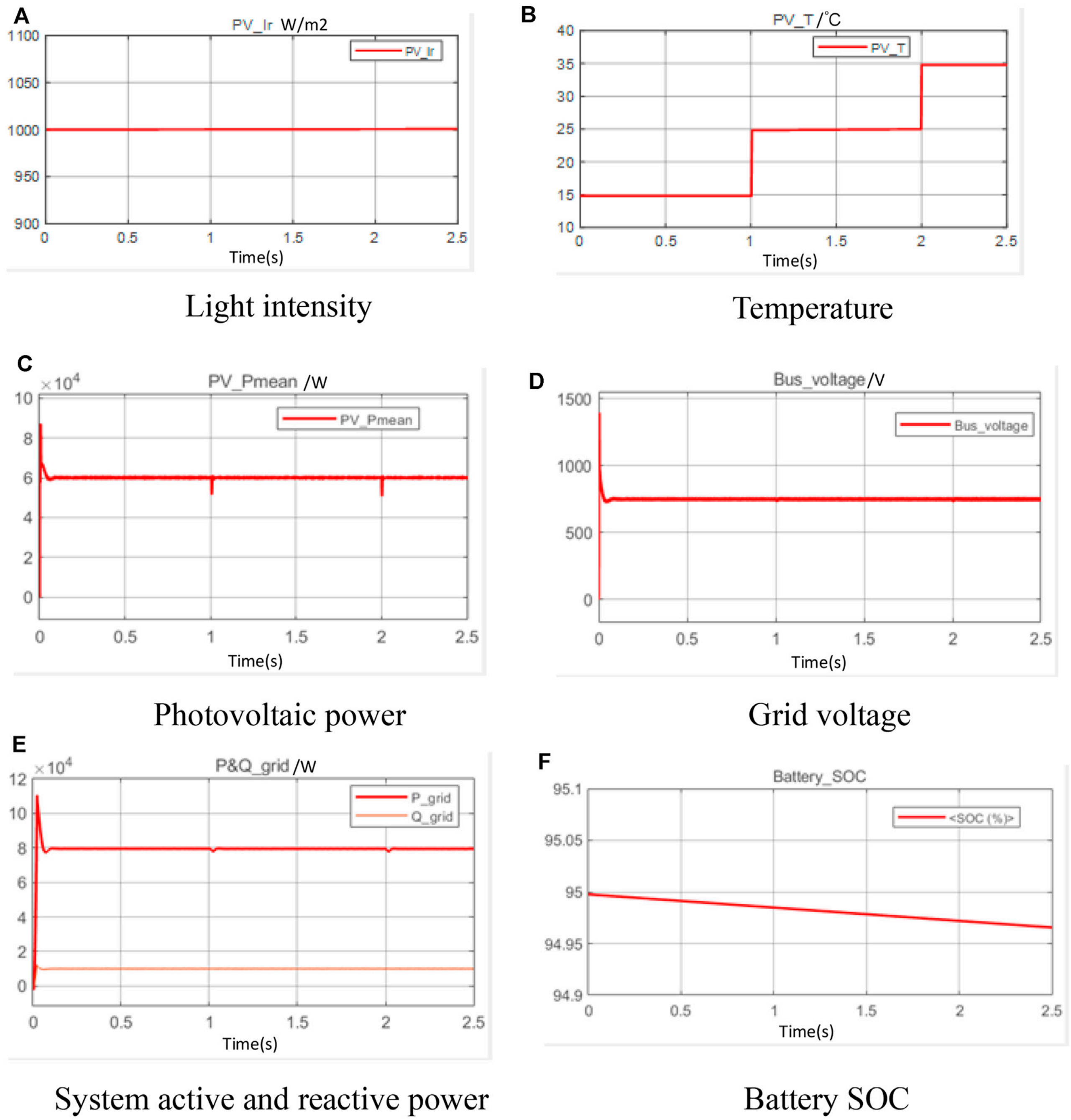

FIGURE 8 | Dynamic response in case 1. **(A)** Light intensity **(B)** Temperature **(C)** Photovoltaic power **(D)** Grid voltage **(E)** System active and reactive power **(F)** Battery SOC.

The flowchart of the proposed adaptive variable-step incremental method for MPPT is depicted in **Figure 5**.

3.5 The Optimized Coordinated Control

The task of the coordinated control unit is mainly two: first, to determine the maximum power point voltage U_{MPP} of the PV array; second, to control the charging and discharging power of the energy storage to adjust the SOC of the energy storage. The VSG reactive power command Q_{ref} is given directly and the active power command P_{ref} (i.e., P_{m}) is obtained by the coordinated control strategy. Based on the deviation of the charge/discharge power command value $P_{\mathrm{st\_ref}}$ ($P_{\mathrm{st\_ref}} > 0$ discharge, $P_{\mathrm{st\_ref}} < 0$ charges) from the actual value p_{st}, the PI regulator adjusts the mechanical

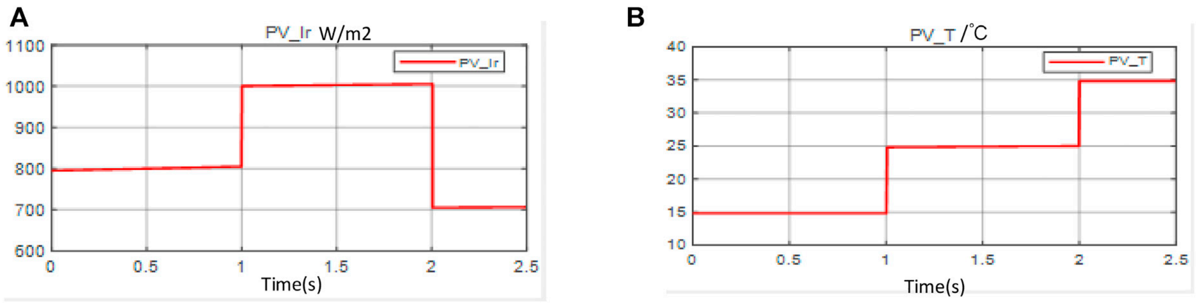

Light intensity

Temperature

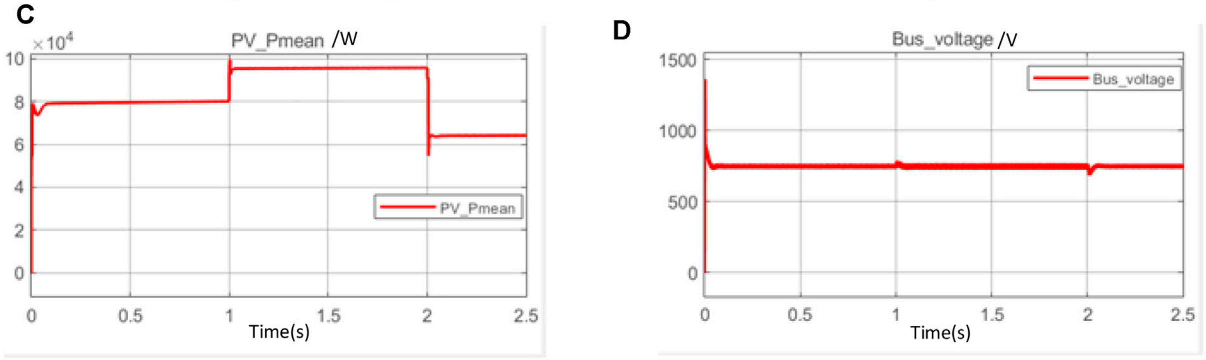

Photovoltaic power

Grid voltage

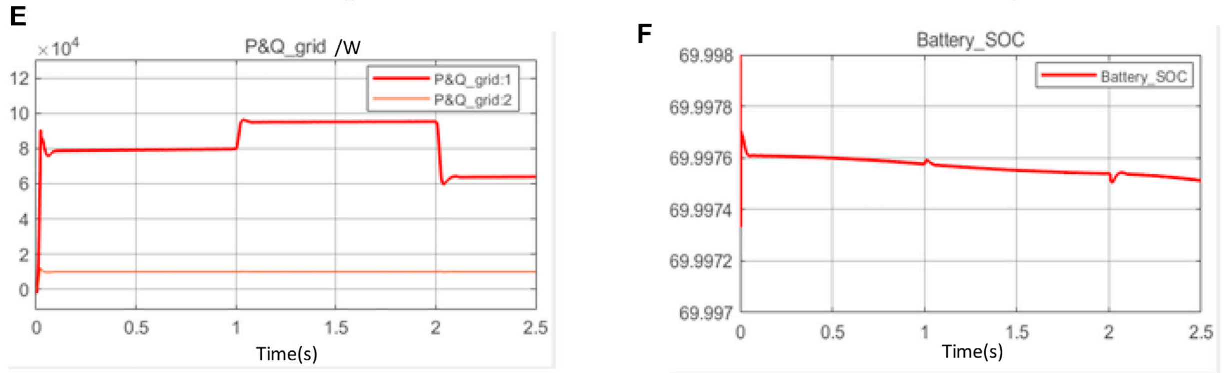

System active and reactive power

Battery SOC

FIGURE 9 | Dynamic response in case 2. **(A)** Light intensity **(B)** Temperature **(C)** Photovoltaic power **(D)** Grid voltage **(E)** System active and reactive power **(F)** Battery SOC.

power P_m of the VSG, and the grid-connected inverter changes its output power according to the characteristics of the synchronous generator, thus controlling p_{st} to track P_{st_ref}. For convenience, we assume that the SOC of energy storage is in the optimal range and set P_{st_ref} to 0. In this case, energy storage only compensates for the power imbalance between the PV array and VSG in the dynamic process, while maintaining a constant SOC in the steady-state. In practice, P_{st_ref} is adjusted by the energy management system according to the change of SOC. **Figure 6**.

The following is a detailed analysis of the process of controlling $p_{st.}$ The case of increasing light intensity is taken as an example: after the increase in light intensity, the PV power increases; at this time, the VSG output power remains unchanged, and the DC bus voltage increases; and the buck/boost converter will charge the battery to maintain a constant DC bus voltage, that is, $p_{st} < 0$; then, $P_{st\_ref} - p_{st} > 0$, which makes the PI regulator output P_m increase, and according to the principle of synchronous generator, the VSG output power gradually increases; after the PV power is stabilized, as the VSG output power increases, the charging power p_{st} will gradually decrease, until $p_{st} = P_{st\_ref} = 0$.

It can be seen that the coordinated control strategy can control p_{st} and thus adjust the SOC of energy storage, which

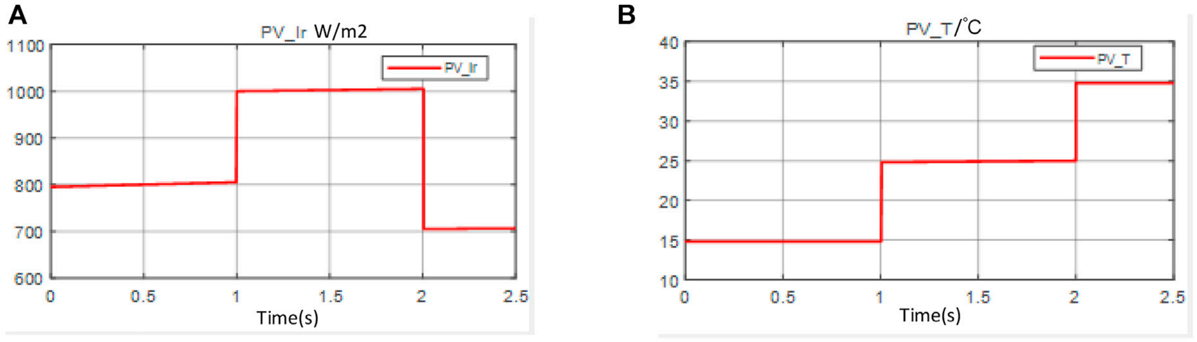

Light intensity

Temperature

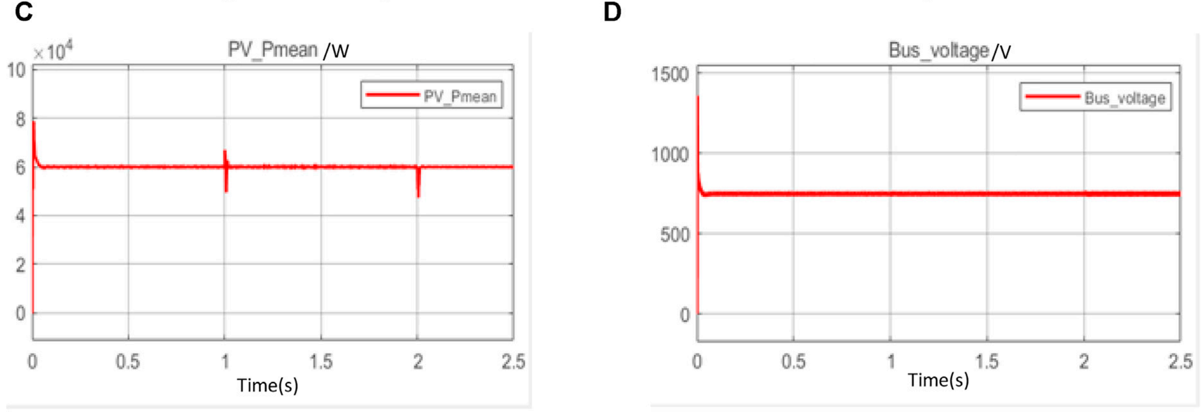

Photovoltaic power

Grid voltage

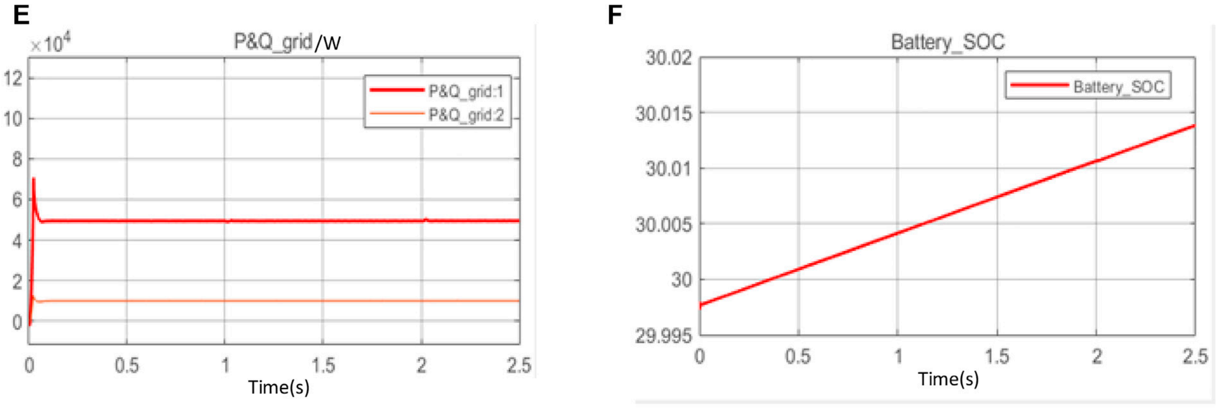

System active and reactive power

Battery SOC

FIGURE 10 | Dynamic response in case 3. **(A)** Light intensity **(B)** Temperature **(C)** Photovoltaic power **(D)** Grid voltage **(E)** System active and reactive power **(F)** Battery SOC.

can avoid deep charging and discharging to shorten the battery life. Hence, the dynamic and static performance of the system is closely related to the switching frequency, synchronous generator model parameters, and controller parameters.

4 SIMULATION AND VERIFICATION

To verify the feasibility of the above principle and the effectiveness of the system, the corresponding simulation model is built and experiments are conducted in MATLAB/Simulink environment.

Section 4.1 introduces and explains the relevant parameters in the experiments, and describes the experimental procedure, and section 4.2 compares and analyzes the simulation results.

4.1 Parameters for Simulation

In this section, the parameters are presented in **Table 1** as follows. the variation of the light intensity and the temperature is given in the following sections. Detailed descriptions of the dynamic response are provided as well.

In a steady-state, the larger the active damping coefficient and the greater the phase margin of the system is indicating the system stability is improved. And the variation of the inverter inductance has a smaller impact on the system stability. While the increase of the filter capacitance and grid inductance leads to the decrease of the phase margin and reduces the system stability. The disturbance amplitude was taken as 0.5% of the rated voltage, and the frequency response was recorded for the reference voltage of 1.0 *p. u.* and 1.5 *p. u.*, respectively, and the data were plotted as shown in **Figure 7**.

4.2 Results and Analysis

To further verify our design, three cases are set up to validate the proposed topology and its control. The descriptions of these three cases are given in **Table 2**.

4.2.1 Case 1

When the battery is overcharged (high SOC), the battery needs to be discharged with constant power, thus avoiding the battery from being damaged by overcharging. To obtain clear analysis results, constant light intensity was used in case1. three different temperatures were set in the PV module to verify the feasibility of constant power control. PV power, busbar voltage, and grid active and reactive power are recorded separately. The battery is in the discharge process and its output power and PV power together provide active power to the grid. The dynamic response of the above description is provided in **Figure 8**.

4.2.2 Case 2

In case2, both light intensity and temperature are changed, and the PV module can obtain the maximum power by MPPT control. Accordingly, the output power of the PV module will change abruptly, when the energy storage system can provide a certain buffer. Compared with the power conversion of PV modules, the power of the grid changes more smoothly with energy storage support. The role of the inverter is to maintain a stable grid voltage at all times. The output power of the battery changes in response to sudden changes in the power of the PV module, thus smoothing the actual power received by the grid. The dynamic response of the above description is provided in **Figure 9**.

4.2.3 Case 3

Case 3 uses the same light intensity variation and dimensional variation as case 2, and for a clear comparison between MPPT control and constant power control. Besides, the power control of the battery is protected in constant power charging mode. The dynamic response of the above description is provided in **Figure 10**.

The coordinate control proposed in this paper was validated through three test scenarios. Based on maintaining a constant grid voltage, the storage battery can smooth out the power variation of the PV; conversely, the PV system can also charge the energy storage system. Besides, the adaptive control adopted for MPPT and VSG significantly improved the stability of AC grid.

5 CONCLUSION AND FUTURE WORK

In this paper, an energy storage type grid-connected photovoltaic power generation system with synchronous generator characteristics is researched. The hardware structure, control strategy, and mathematical model of the system are established. The influence of the main parameters on the stability and dynamic performance of the system is analyzed in detail. The simulation results not only verify the correctness of the fundamental working principle, but also prove the proposed control strategy can simulate the characteristics of synchronous power generation and maximum power tracking, and control energy storage charging and discharging, and the following conclusions are obtained: 1) The self-adaptive VSG control enables the interface inverter of PV power generation system to simulate the characteristics of synchronous generator, which has the ability of variable frequency inertia and damping frequency shift and can effectively improve the performance of the grid-connected distributed PV power generation system. 2) The coordinate control can switch the charging and discharging power of energy storage, adjust the SOC of energy storage, and provide the power required for throughput simulation of synchronous generator rotor kinetic energy changes, and can effectively avoid the impact of deep charging and discharging on energy storage life; 3) The adaptive variable-step conductivity increment method for MPPT of the PV array to improve the power generation efficiency but also smooths out the fluctuation of the grid-connected power of the PV system.

Due to the constraints of the research platform and some other factors, some simplification is made in the simulation verification, which will not affect the experimental conclusions. Based on this, some potential future research directions are summarized: 1) The variations of each battery in the array to achieve the synergistic operation of internal energy balancing and smoothing system power; 2) adaptive VSG control have variable damping and inertia, which should be optimized in real-time, and the application of deep learning will be considered in the future.

DATA AVAILABILITY STATEMENT

The original contributions presented in the study are included in the article/Supplementary Material, further inquiries can be directed to the corresponding author.

AUTHOR CONTRIBUTIONS

GC contributed to the conception and design of the study. YZ performed the statistical analysis and wrote sections of the manuscript. All authors contributed to manuscript revision, read, and approved the submitted version.

REFERENCES

Al-Shetwi, A. Q., Hannan, M. A., Jern, K. P., Mansur, M., and Mahlia, T. M. I. (2020). Grid-Connected Renewable Energy Sources: Review of the Recent Integration Requirements and Control Methods. *J. Clean. Prod.* 253, 119831. doi:10.1016/j.jclepro.2019.119831

Alipoor, J., Miura, Y., and Ise, T. (2014). Power System Stabilization Using Virtual Synchronous Generator with Alternating Moment of Inertia. *IEEE J. Emerging Selected Top. Power Electron.* 3 (2), 451–458. doi:10.1109/JESTPE.2014.2362530

Alipoor, J., Miura, Y., and Ise, T. (2015). Power System Stabilization Using Virtual Synchronous Generator with Alternating Moment of Inertia. *IEEE J. Emerg. Sel. Top. Power Electron.* 3 (2), 451–458. doi:10.1109/jestpe.2014.2362530

Bri-Mathias, S. H., Himanshu, J., Carlo, B. M.-A., and Gab-Su, S. (2020). Addressing Technical Challenges in 100% Variable Inverter-Based Renewable Energy Power Systems. *Wiley Interdiscip. Rev. Energ. Environ.* 95, e376.

Chen, Y., Hesse, R., Turschner, D., and Hans-Peter, B. (2011). "Improving the Grid Power Quality Using Virtual Synchronous Machines," in 2011 International Conference on Power Engineering, Energy and Electrical Drives (POWERENG), Malaga, Spain (IEEE), 1–6. doi:10.1109/PowerEng.2011.6036498

D'Arco, S., Suul, J. A., and Fosso, O. B. (2013). "Control System Tuning and Stability Analysis of Virtual Synchronous Machines," in 2013 IEEE Energy Conversion Congress and Exposition (ECCE), Denver, USA (IEEE), 2664–2671. doi:10.1109/ECCE.2013.6647045

European FP6 project workshop (2011). *VSYNC Project Workshop [EB/O–L]*. Netherland: VSYNC Commission. Available at: http://www.vsync.eu/ (Accessed 15 3 2013).

Fathi, A., Shafiee, Q., and Bevrani, H. (2018). Robust Frequency Control of Microgrids Using an Extended Virtual Synchronous Generator. *IEEE Trans. Power Syst.* 33 (6), 6289–6297. doi:10.1109/TPWRS.2018.2850880

Hua, T., Yan, X., and Fan, W. (2017). "Research on Power Point Tracking Algorithm Considered Spinning Reserve Capacity in Gird-Connected Photovoltaic System Based on VSG Control Strategy," in 2017 IEEE 3rd International Future Energy Electronics Conference and ECCE Asia (IFEEC 2017-ECCE Asia) (IEEE). doi:10.1109/ifeec.2017.7992368

Kulyk, M., and Zgurovets, O. (2020). "Modeling of Power Systems with Wind, Solar Power Plants and Energy Storage," in *Systems, Decision and Control in Energy I* (Cham: Springer), 231–245. doi:10.1007/978-3-030-48583-2_15

Li, Q., Choi, S. S., Yuan, Y., and Yao, D. L. (2011). On the Determination of Battery Energy Storage Capacity and Short-Term Power Dispatch of a Wind Farm. *IEEE Trans. Sustain. Energ.* 2 (2), 148–158. doi:10.1109/tste.2010.2095434

Li, Y., Gao, W., Yan, W., Huang, S., Wang, R., Gevorgian, V., et al. (2021). Data-Driven Optimal Control Strategy for Virtual Synchronous Generator via Deep Reinforcement Learning Approach. *J. Mod. Power Syst. Clean Energ.* 9 (4), 919–929. doi:10.35833/MPCE.2020.000267

Liu, J., Miura, Y., and Ise, T. (2015). Comparison of Dynamic Characteristics Between Virtual Synchronous Generator and Droop Control in Inverter-Based Distributed Generators. *IEEE Trans. Power Electronics* 31 (5), 3600–3611.

Liu, J., Miura, Y., Bevrani, H., and Ise, T. (2017). Enhanced Virtual Synchronous Generator Control for Parallel Inverters in Microgrids. *IEEE Trans. Smart Grid* 8 (5), 2268–2277. doi:10.1109/tsg.2016.2521405

Ma, D., Cao, X., Sun, C., Wang, R., Sun, Q., Xie, X., et al. (2021). Dual-Predictive Control with Adaptive Error Correction Strategy for AC Microgrids. *IEEE Trans. Power Deliv.*, 1. doi:10.1109/TPWRD.2021.3101198

Ma, Y., Cao, W., Yang, L., Wang, F. F., and Tolbert, L. M. (2017). Virtual Synchronous Generator Control of Full Converter Wind Turbines with Short-Term Energy Storage. *IEEE Trans. Ind. Electron.* 64 (11), 8821–8831. doi:10.1109/tie.2017.2694347

Pattabiraman, D., Lasseter, R. H., and Jahns, T. M. (2018). "Comparison of Grid Following and Grid Forming Control for a High Inverter Penetration Power System," in 2018 IEEE Power & Energy Society General Meeting (PESGM), Portland, OR, USA, 5-10 Aug. 2018 (IEEE). doi:10.1109/PESGM.2018.8586162

Rui, W., Qiuye, S., Pinjia, Z., Yonghao, G., Dehao, Q., and Peng, W. (2020). Reduced-Order Transfer Function Model of the Droop-Controlled Inverter via Jordan Continued-Fraction Expansion. *IEEE Trans. Energ. Convers.* 35 (3), 1585–1595. doi:10.1109/TEC.2020.2980033

Sun, Y., Zhao, Z., Yang, M., Jia, D., Pei, W., and Xu, B. (2019). Overview of Energy Storage in Renewable Energy Power Fluctuation Mitigation. *CSEE J. Power Energ. Syst.* 6 (1), 160–173. doi:10.17775/CSEEJPES.2019.01950

Velasco de la Fuente, D., Rodríguez, C. L. T., Garcerá, G., Figueres, E., and Gonzalez, R. O. (2013). Photovoltaic Power System with Battery Backup with Grid-Connection and Islanded Operation Capabilities. *IEEE Trans. Ind. Electron.* 60 (4), 1571–1581. doi:10.1109/tie.2012.2196011

Wang, R., Sun, Q., Tu, P., Xiao, J., Gui, Y., and Wang, P. (2021). Reduced-Order Aggregate Model for Large-Scale Converters with Inhomogeneous Initial Conditions in DC Microgrids. *IEEE Trans. Energ. Convers.* 36 (3), 2473–2484. doi:10.1109/TEC.2021.3050434

Wei, Y., Dai, S., Yu, J., Wu, S., and Wang, J. (2019). "Research on Status and Prospects of Battery Energy Storage Stations on Energy Internet," in 2019 IEEE 3rd Information Technology, Networking, Electronic and Automation Control Conference (ITNEC), Chengdu, China, 15-17 March 2019 (IEEE), 964–969. doi:10.1109/ITNEC.2019.8729063

Zhang, X., Gao, Q., Guo, Z., Zhang, H., Li, M., and Li, F. (2020). Coordinated Control Strategy for a PV-Storage Grid-Connected System Based on a Virtual Synchronous Generator. *Glob. Energ. Interconnection* 3 (1), 51–59. doi:10.1016/j.gloei.2020.03.003

Zhao, H., Yang, Q., and Zeng, H. (2017). Multi-Loop Virtual Synchronous Generator Control of Inverter-Based DGs Under Microgrid Dynamics. *IET Generation, Transm. & Distribution Transmission Distribution* 11 (3), 795–803. doi:10.1049/iet-gtd.2016.0645

Zhong, C., Li, H., Zhou, Y., Lv, Y., Chen, J., and Li, Y. Virtual Synchronous Generator of PV Generation without Energy Storage for Frequency Support in Autonomous Microgrid. *Int. J. Electr. Power Energ. Syst.* 134 (2022), 107343.

Zhong, Q.-C., Nguyen, P.-L., Ma, Z., and Sheng, W. (2014). Self-Synchronized Synchronverters: Inverters without a Dedicated Synchronization Unit. *IEEE Trans. Power Electron.* 29 (2), 617–630. doi:10.1109/TPEL.2013.2258684

Zhong, Q.-C., and Weiss, G. (2011). Synchronverters: Inverters that Mimic Synchronous Generators. *IEEE Trans. Ind. Electron.* 58 (4), 1259–1267. doi:10.1109/TIE.2010.2048839

Conflict of Interest: The authors declare that the research was conducted in the absence of any commercial or financial relationships that could be construed as a potential conflict of interest.

frontiers | Frontiers in Energy Research

ORIGINAL RESEARCH
published: 26 May 2022
doi: 10.3389/fenrg.2022.898620

Distributionally Robust Optimal Bidding of Energy Hubs in the Joint Electricity and Carbon Market

Lifei Ma[1], *Shengwei Liu*[2]* and *Jizhen Liu*[1,2]

[1]*School of Control and Computer Engineering, North China Electric Power University, Beijing, China,* [2]*Energy and Electricity Research Center, Jinan University, Guangzhou, China*

To realize the lower carbon and more efficient operation of energy hubs in the joint electricity and carbon market, a day-ahead bidding strategy is proposed for the energy hub operator (EHO). Considering the uncertainties of prices, demands, and renewable energy sources, this strategy is formulated as a novel two-stage distributionally robust joint chance-constrained optimization problem. A total distance-based ambiguity set is proposed to preserve the mean value of uncertain factors. By introducing this indicator function, this problem is further reformulated as a mixed-integer linear programming (MILP) problem. Simulations are performed based on the electricity and carbon prices in Europe, and the relation between the carbon emission and operational cost is further investigated in the case studies.

Keywords: **energy hubs, carbon, optimal bidding, uncertainties, distributionally robust**

Edited by:
Rui Wang,
Northeastern University, China

Reviewed by:
Xuewei Pan,
Harbin Institute of Technology, China
Yalong Li,
China University of Mining and Technology, China

Correspondence:
Shengwei Liu
15622767651@163.com

Specialty section:
This article was submitted to Smart Grids,
a section of the journal Frontiers in Energy Research

Received: *18 March 2022*
Accepted: *11 April 2022*
Published: *26 May 2022*

Citation:
Ma L, Liu S and Liu J (2022) Distributionally Robust Optimal Bidding of Energy Hubs in the Joint Electricity and Carbon Market.
Front. Energy Res. 10:898620.
doi: 10.3389/fenrg.2022.898620

1 INTRODUCTION

1.1 Motivation

Energy hubs (EHs) are recognized as a powerful platform to realize the efficient energy conversion and utilization for the future low carbon society, e.g., buildings and industry parks (Mohammadi et al., 2017). With the deregulation of the energy market and the emergence of the carbon market, the energy hub operator (EHO) can participate in both electricity and carbon markets (Ding et al., 2020). It brings significant flexibility to the EHO in reducing the carbon emission (Olsen et al., 2018), while introducing additional risks to the operational cost, e.g., uncertain carbon prices (Sun and Huang, 2020). These uncertainties should be properly modeled and incorporated into the risk management scheme of EHOs.

1.2 Literature Review

The bidding strategies of EHOs within the electricity market, including the day-ahead and real-time electricity market, can always be modeled as deterministic optimization problems to reduce the operational cost (Brahman et al., 2015), emissions (Brahman et al., 2015), and maximize the utility (Li et al., 2018). A time-series technique for predicting the power generation of the photovoltaic (PV) cell is applied in (Brahman et al., 2015), and it is assumed that there is no bias from the actual renewable output to the forecast value. A mathematical program with equilibrium constraints is proposed for studying the strategic behaviors of profit-driven EHs in both the electricity and thermal markets from a deregulated market point of view, and the uncertainties of electricity and heating demand are neglected in the bidding optimization process, considering the conciseness of the model. However, one significant feature of EHs is to cope with the fluctuation and intermittency of the distributed renewable generation with the flexibility provided by multicarrier energy systems (Jadidbonab et al., 2020).

Furthermore, according to the uncertainties of renewable energy sources, loads, prices, etc., the deterministic strategies can be further extended to stochastic optimization (Davatgaran et al., 2018; Zhao et al., 2020; Jadidbonab et al., 2020), robust optimization (Lu et al., 2020), distributionally robust optimization (Zhao et al., 2019), and hybridization (Liu et al., 2021). The hybrid alternating current/direct current (AC/DC) microgrid is embedded as an electrical hub for EHs to realize the high efficiency of energy conversion, and a two-stage stochastic programming problem is proposed, where uncertain day-ahead prices, loads, PV, and ambient temperatures are depicted by scenario trees. Making full use of the thermal demand flexibility, the quality of thermal service is modeled as a chance constraint (Zhao et al., 2020). In Oskouei et al. (2021), a large set of industrial EHs are integrated into virtual EHs to trade energy in various markets, and the robust approach is coordinated with a stochastic programming model to formulate a hybrid expression of uncertainties, considering the priority of day-ahead electricity prices. The ability of EHs to participate in the joint electricity and thermal markets in the form of virtual power plants (VPPs) is explored in Jadidbonab et al. (2020), and a self-scheduling program is proposed for virtual EHs to maximize the revenue.

When the carbon emission is considered, the bidding management should consider the carbon emissions as objective functions (Yang et al., 2019) or constraints (Cheng et al., 2018). For the given carbon permit prices, a price-taker bidding strategy is proposed for the VPP operator to bid in the energy, ancillary services, and carbon market in (Yang et al., 2019), where carbon emissions, greenhouse gases, and pollutants are effectively reduced by the carbon trading mechanism. In Cheng et al. (2018), an analytical model called carbon emission flow is proposed to quantify the allocation of carbon emission among different energy carriers in delivery and conversion processes including both primary and secondary energy. This work is further used to realize the coordination between transmission and distribution systems with locational marginal electricity and uniform carbon prices in Cheng et al. (2020). Though there have been few studies about carbon trading in the existing literature, the uncertainties of carbon prices have not been considered in existing works (Yang et al., 2019; Cheng et al., 2018, 2020). It introduces additional risks to EHOs involving carbon markets.

The prevalent works on the risk hedging strategies of EHOs in various markets are to manage specific uncertainties. These uncertainties are the aggregation of prices, renewable energy output, loads, etc. They can be further depicted by the stochastic model (Zhao et al., 2020), uncertain sets (Lu et al., 2020), and ambiguity sets (Zhao et al., 2019). The required scenarios for stochastic optimization rapidly increase with a growing number of uncertainties to sustain an acceptable confidence level, or uncertainties are assumed to obey exact probability distributions which are normally unrealistic. In robust optimization, uncertainties are always depicted as an uncertainty set, e.g., polyhedron, which ignores the distribution information, and the optimized result by considering the worst condition can be overconservative. To address these limitations, the ambiguity sets are proposed under different metrics, e.g., total distance (Liu et al., 2021) and moment-based distances (Zhao et al., 2019). However, when the carbon price uncertainties are considered, the ambiguity sets have not been modeled.

To address the uncertainties under joint electricity and carbon markets, the EHO should optimize the conversion, storage, and consumption processes within EHs. As the distributed energy resources are to be integrated into EHs, the conversion process, from renewable energy sources and gas to electricity and thermal energy, has been embedded into the bidding strategies of EHOs (Davatgaran et al., 2018; Dai et al., 2017). Using existing electrical and thermal energy storage systems (ESSs), the electricity and thermal energy can be charged and discharged efficiently. The demand response programs have been considered from the energy consumption perspective, and the quality of thermal services has been utilized to reduce the operational risk (Zhao et al., 2020). The flexibility of the thermal demand has not been explored to reduce the risks under joint electricity and carbon markets.

1.3 Contributions

To manage the uncertainties in joint electricity and carbon markets, a novel day-ahead bidding strategy is proposed for the EHO. This strategy is formulated as a two-stage distributionally robust chance-constrained programming problem, where the uncertainties of prices, loads, renewable energy sources, and ambient temperature are formulated as a novel ambiguity set. The quality of service for the thermal demand is relaxed and treated as a joint chance constraint. Based on duality, the problem is reformulated as a mixed-integer linear programming (MILP) problem. The main contribution of this article can be summarized as follows:

- A novel ambiguity set is proposed for electrical prices and carbon prices. The first-order information is preserved in this set.
- A novel two-stage distributionally robust joint chance-constrained programming problem is proposed to manage the uncertainties in the joint electricity and carbon markets.

The rest of this article is organized as follows. The day-ahead bidding scheme is proposed in **Section 2**. The two-stage distributionally robust joint chance-constrained programming problem is formulated in **Section 3**. The deterministic reformulation method is given in **Section 4**. Case studies are performed in **Section 5**. Conclusions are drawn in **Section 6**.

2 DAY-AHEAD BIDDING OF ENERGY HUBS IN THE JOINT ELECTRICITY AND CARBON MARKET

In this section, a typical EH model is introduced, together with its bidding scheme in the joint electricity and carbon market.

2.1 Energy Hub Models

An EH is typically treated as a multiple-input and multiple-output energy conversion system, including the functions of conversion, storage, and consumption (Zhao et al., 2020). Considering the electrification of buildings, transportation, and industries in the coming decades, there exist electrical and thermal hubs in the system (Oskouei et al., 2021). The input of the EH is the utility grid (UG), PV generation, and natural gas. The energy conversion is realized by the combined heat and power (CHP) unit and air-conditioning. The AC/DC conversion in the electrical hub is realized by the bi-directional AC/DC converters. The battery and thermal ESSs are used to store electricity and thermal.

2.2 Day-Ahead Bidding Progress of Energy Hubs

The EHO is to manage the conversion, storage, and utilization processes in the EHs while participating in both electricity and carbon markets. The EHO acts as the price taker in both markets. The bidding procedure for the EHO is shown in **Figure 1**.

As shown in **Figure 1**, the EHO can buy and sell electricity in the day-ahead and real-time markets. The carbon permit is purchased in the day-ahead and real-time carbon markets. In the day-ahead bidding, the electricity and carbon prices are given, while the real-time electricity and carbon prices, together with PV output, demand, and ambient temperature, are uncertain, which is depicted by a scenario tree with uncertain probability density functions (PDFs).

3 DISTRIBUTIONALLY ROBUST BIDDING PROBLEM FORMULATION

The optimal day-ahead bidding problem for EHs is formulated as a bi-objective two-stage distributionally robust optimization problem in this section, including the day-ahead operation and real-time operation recourse.

3.1 Two-Stage Distributionally Robust Chance-Constrained Programming Problem

A two-stage distributionally robust chance constrained optimization problem is shown as follows:

$$\min_{\mathbf{x}\in\mathbf{X}} f(\mathbf{x}) + \max_{\mathbb{P}\in\mathcal{P}} \left\{\rho\mathbb{E}_{\omega\sim\mathbb{P}}[\mathcal{Q}(\mathbf{x},\omega)] + (1-\rho)\,\mathrm{CVaR}_{\alpha}[\mathcal{Q}(\mathbf{x},\omega)]\right\}, \tag{1}$$

where $\mathbf{x}$ represents the day-ahead bidding strategy of EHO, including the electricity and carbon permit purchase plan, as shown in **Eq. 6**. $\mathbf{X}$ is the first-stage constraint set, including box constraints **Eqs 7**, **8**. ρ is the weight factor between the expected value and conditional value at risk (CVaR), which is employed as a measure of the tail risk with the given confidence level α. The choice of ρ depends on the risk preference of the EHO. For instance, if the EHO is only concerned about the expected cost minimization, ignoring the potential trading risk in extreme conditions, ρ is set to be 0. The calculation of CVaR is shown as follows:

$$\mathrm{CVaR}_{\alpha}\left[\mathcal{Q}(\mathbf{x},\omega)\right] = \min_{\eta}\Big\{\Big(\eta + \frac{1}{1-\alpha}\,\mathbb{E}\left[(\mathcal{Q}[(\mathbf{x},\omega)-\eta]^{+}\right]\Big\}, \tag{2}$$

where η is the value at risk (VaR). For more details on VaR refer to Rockafellar and Uryasev (2000).

$\mathbb{P}$ is the probability within the following ambiguity set:

$$\mathcal{P} := \left\{\mathbb{P}\in\mathcal{M}(\Xi,\mathcal{F})\;\middle|\;\begin{array}{c}\mathbb{P}(\xi\in\Omega)=1\\ \sum_{\omega\in\Omega}|\pi_{\omega}-\pi_{0,\omega}|\le\tau\\ \sum_{\omega\in\Omega}\pi_{\omega}\xi_{\omega}=\xi_{0}\end{array}\right\}, \tag{3}$$

where π_{ω} and $\pi_{0,\omega}$ are the real probability density and nominal probability density of scenario ω. As shown in **Eq. 3**, the ambiguity set only limits the density function on the given support set Ω. The mean value of prices and renewable energy outputs is preserved by the third line of **Eq. 3** (Liu et al., 2021). This ambiguity set is further represented by the compact format $\mathbf{G}\omega \le \mathbf{e}$. $\mathcal{Q}(\mathbf{x},\omega)$ is the following recourse problem to capture the optimal decision of EHOs in real-time operation, with the given day-ahead bidding plan and uncertainties.

$$\mathcal{Q}(\mathbf{x},\omega) := \min_{\mathbf{y}_{\omega}\in\mathbf{Y}(\mathbf{x},\omega)}\left\{\mathbf{q}^{T}\mathbf{y}_{\omega}|\mathbf{D}\mathbf{y}_{\omega}\ge\mathbf{h}_{\omega}-\mathbf{T}_{\omega}\mathbf{x}\right\}, \tag{4}$$

where $\mathbf{D}\mathbf{y}_{\omega}\ge\mathbf{h}_{\omega}-\mathbf{T}_{\omega}\mathbf{x}$ is the compact representation of **Eqs 10–12**, **14–33**.

The following distributionally robust chance constraint is introduced to balance the feasibility of the recourse problem and uncertainties:

$$\Pr_{\omega\sim\Omega}\left\{\mathbf{E}\mathbf{y}_{\omega}+\mathbf{F}\xi_{\omega}\le\mathbf{g}_{\omega}\right\}\ge 1-\beta, \tag{5}$$

where β is the confidential level of the feasibility of the constraint (**Eq. 13**). The detailed formulation on the first stage and second stage optimization problems are given in the following subsections.

3.2 Day-Ahead Bidding Optimization

The first stage optimization is to minimize the total cost in the day-ahead market, including the electricity and carbon cost, as follows:

$$f(\mathbf{x}) = \sum_{t\in\mathcal{T}}\left[\lambda_{\mathrm{DA}}(t)P_{\mathrm{DA}}(t)+\mu_{\mathrm{DA}}(t)\Phi_{\mathrm{DA}}(t)\right], \tag{6}$$

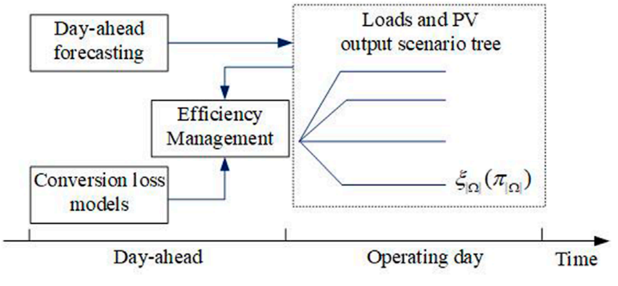

FIGURE 1 | Bidding process in the joint electricity and energy market.

where $\lambda_{\mathrm{DA}}(t)$ and $\mu_{\mathrm{DA}}(t)$ are the electricity and carbon prices in the day-ahead markets. The day-ahead bidding plan is limited by the following constraints:

$$P_{\mathrm{UG,min}} \le P_{\mathrm{DA}}(t) \le P_{\mathrm{UG,max}}, \forall t, \tag{7}$$

$$\Phi_{\mathrm{C,min}} \le \Phi_{\mathrm{DA}}(t) \le \Phi_{\mathrm{C,max}}, \forall t, \tag{8}$$

where $P_{\mathrm{UG,\,min}}$, $P_{\mathrm{UG,\,max}}$, $\Phi_{\mathrm{C,\,min}}$, and $\Phi_{\mathrm{C,\,max}}$ are the minimal and maximal electricity and carbon purchasing limits in the day-ahead and real-time markets.

3.3 Real-Time Operation Optimization

Real-time operation optimization is to minimize the real-time operational cost by optimal scheduling of the generation, conversion, and consumption processes within EHs. The objective function in the second stage optimization is depicted as follows:

$$\begin{aligned}\mathbf{q}^T\mathbf{y}_\omega = \sum_{t\in\mathcal{T}} \{ & c_{\mathrm{GAS}}\left[v_{\mathrm{CHP},\omega}(t) + v_{\mathrm{GAS},\omega}(t)\right] + c_{\mathrm{PV}}p_{\mathrm{PV},\omega}(t) \\ & + \lambda_{\mathrm{RT},\omega}p_{\mathrm{RT},\omega}(t) + c_{\mathrm{ES,CH}}p_{\mathrm{ES,CH},\omega}(t) \\ & + c_{\mathrm{ES,DC}}p_{\mathrm{ES,DC},\omega}(t) + \mu_{\mathrm{RT},\omega}(t)\,\phi_{\mathrm{RT},\omega}(t)\},\end{aligned} \tag{9}$$

where subscription ω represents for scenario ω. $\lambda_{\mathrm{RT},\omega}(t)$ and $\mu_{\mathrm{RT},\omega}(t)$ are the real-time electricity and carbon prices in the electricity and carbon markets. $p_{\mathrm{RT}}(t)$ and $\phi_{\mathrm{RT}}(t)$ are the real-time power between the EH and UG and carbon permit purchased, respectively. $c_{\mathrm{ES,CH}}$ and $c_{\mathrm{ES,DC}}$ are the charging and discharging cost of battery energy systems (BESs), respectively. $p_{\mathrm{ES,CH},\omega}(t)$ and $p_{\mathrm{ES,DC},\omega}(t)$ are the charging and discharging rates of the BES, respectively. c_{GAS} is the price of natural gas. $v_{\mathrm{CHP},\omega}(t)$ and $v_{\mathrm{GAS},\omega}(t)$ are the gas consumption of CHP and gas boiler, respectively.

The constraints for within the EHs include the thermal, electrical, conversion, storage, and carbon emission constraints, as shown in the following subsections.

3.3.1 Constraints for the Thermal Hub

The energy balance equations in the heating and cooling hubs of the EH are depicted as follows:

$$\begin{aligned}& q_{\mathrm{HVAC,TD},\omega}(t) + q_{\mathrm{TD},\omega}(t) + q_{\mathrm{AC},\omega}(t) + q_{\mathrm{HS,CH},\omega}(t) \\ & \quad = q_{\mathrm{GAS},\omega}(t) + q_{\mathrm{CHP},\omega}(t) + q_{\mathrm{HS,DC},\omega}(t), \forall t, \omega,\end{aligned} \tag{10}$$

$$\begin{aligned}& q_{\mathrm{HVAC,CD},\omega}(t) + q_{\mathrm{CD},\omega}(t) \\ & \quad = q_{\mathrm{CS,DC},\omega}(t) + q_{\mathrm{IAC},\omega}(t) + q_{\mathrm{CE},\omega}(t), \forall t, \omega,\end{aligned} \tag{11}$$

where $q_{\mathrm{HVAC,TD},\omega}(t)$ and $q_{\mathrm{HVAC,CD},\omega}(t)$ are the heating and cooling demand to control the indoor room temperature, respectively. $q_{\mathrm{TD},\omega}(t)$ and $q_{\mathrm{CD},\omega}(t)$ are the heating and cooling demand, respectively. $q_{\mathrm{AC},\omega}(t)$ and $q_{\mathrm{CE},\omega}(t)$ are the heating consumption and cooling output of the absorption chiller, respectively. $q_{\mathrm{CHP},\omega}(t)$ and $q_{\mathrm{GAS},\omega}(t)$ are the heating output of the CHP and gas boiler, respectively. $q_{\mathrm{HS,CH},\omega}$ and $q_{\mathrm{HS,DC},\omega}(t)$ are the charging and discharging rates of heating energy storage (HES), respectively. $q_{\mathrm{CS,CH},\omega}$ and $q_{\mathrm{CS,DC},\omega}(t)$ are the charging and discharging rates of cooling energy storage (CES), respectively. $q_{\mathrm{IAC},\omega}(t)$ is the cooling output of the inverter air-conditioning system.

Eqs 10, **11** depict the energy balance on the heating hub and cooling hub, respectively.

The indoor room temperature of a cluster of buildings is managed *via* the consumption of heating and cooling from the EH, as shown in **Figure 2**. Based on Fourier's law, the relationship between the heating/cooling loads and indoor room temperature can be approximated by the following linear equations (Zhang et al., 2018):

$$\begin{aligned}\frac{q_{\mathrm{HVAC,TD},\omega}(t) - q_{\mathrm{HVAC,CD},\omega}(t)}{\Delta t} = c_{\mathrm{air}} & \frac{\Theta_{\mathrm{in},\omega}(t) - \Theta_{\mathrm{in},\omega}(t-\Delta t)}{\Delta t} \\ & - \frac{\Theta_{\mathrm{am},\omega}(t) - \Theta_{\mathrm{in},\omega}(t)}{R_{\mathrm{T}}}, \forall t, \omega,\end{aligned} \tag{12}$$

where $\Theta_{\mathrm{in},\omega}(t)$ and $\Theta_{\mathrm{am},\omega}(t)$ are the indoor temperature and ambient temperature, respectively. c_{air} is the air heating capacity (kWh/°C), and R_{T} is the thermal resistance of the building envelope (°C/kW). To guarantee the thermal service quality, the indoor room temperature should be guaranteed within the given range as follows:

$$\Theta_{\mathrm{in,min}} \le \Theta_{\mathrm{in},p,k}(t) \le \Theta_{\mathrm{in,max}}, \forall t, \omega, \tag{13}$$

where $\Theta_{\mathrm{in,min}}$ and $\Theta_{\mathrm{in,max}}$ are the minimal and maximal limitations for the indoor room temperature, respectively.

3.3.2 Constraints of the Electrical Hub

In the electrical systems, the power balance equations on the AC bus and DC bus of the electrical hub can be depicted as follows:

$$\begin{aligned}& P_{\mathrm{DA}}(t) + p_{\mathrm{RT},\omega}(t) + p_{\mathrm{CHP},\omega}(t) + \eta_{\mathrm{BIC}}p_{\mathrm{DC2AC},\omega}(t) \\ & \quad = p_{\mathrm{AC},\omega}(t) + p_{\mathrm{AC2DC},\omega}(t), \forall t, \omega,\end{aligned} \tag{14}$$

$$\begin{aligned}& p_{\mathrm{ES,DC},\omega}(t) - p_{\mathrm{ES,CH},\omega}(t) + \eta_{\mathrm{BIC}}p_{\mathrm{AC2DC},\omega}(t) + p_{\mathrm{PV},\omega}(t) \\ & \quad = p_{\mathrm{DC},\omega}(t) + p_{\mathrm{DC2AC},\omega}(t) + p_{\mathrm{IAC},\omega}(t) + p_{\mathrm{CS},\omega}, \forall t, \omega,\end{aligned} \tag{15}$$

where $p_{\mathrm{CHP},\omega}(t)$ is the electric output of CHP, $p_{\mathrm{AC2DC},\omega}(t)$ and $p_{\mathrm{DC2AC},\omega}(t)$ are the power transferred from the AC bus to DC bus and DC bus to AC bus, respectively. $p_{\mathrm{AC},\omega}(t)$ and $p_{\mathrm{DC},\omega}(t)$ are the AC load and DC load, respectively. $p_{\mathrm{IAC},\omega}(t)$ is the electricity consumption of the inverter air-conditioning system. η_{BIC} is the efficiency of the bidirectional converter (BIC). **Eqs 14**, **15** depict the power balance on the AC bus and DC bus of the electrical hub, respectively.

The limitations for power exchange between the UG and EH and power transferring on the BIC are shown as follows:

$$P_{\mathrm{UG,min}} \le p_{\mathrm{RT},\omega}(t) \le P_{\mathrm{UG,max}}, \forall t, \omega, \tag{16}$$

$$P_{\mathrm{UG,min}} \le p_{\mathrm{RT},\omega}(t) + P_{\mathrm{DA}}(t) \le P_{\mathrm{UG,max}}, \forall t, \omega, \tag{17}$$

$$0 \le P_{\mathrm{DC2AC},\omega}(t) \le I_{\mathrm{DC2AC},\omega}(t)\,P_{\mathrm{BIC,max}}, \forall t, \omega, \tag{18}$$

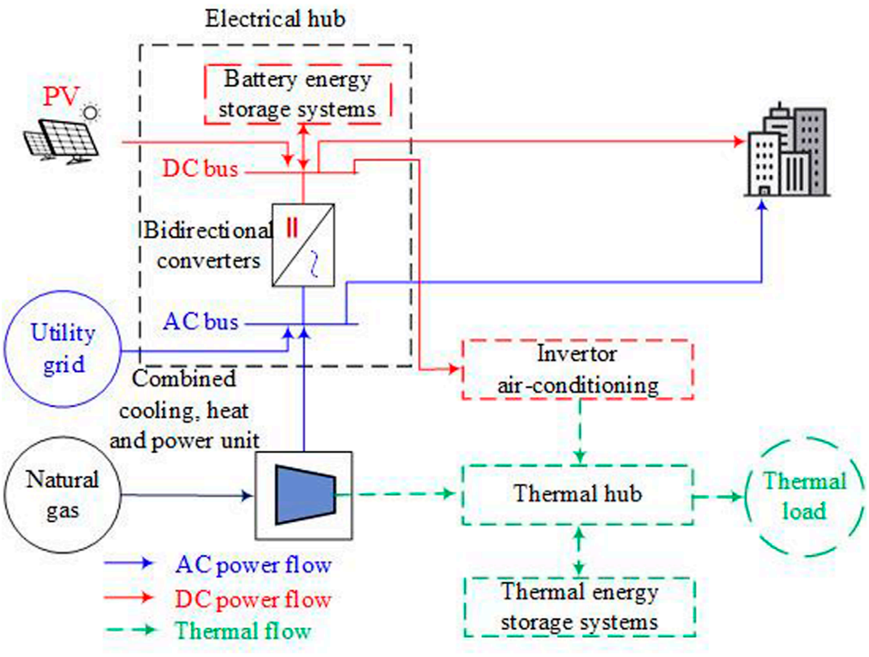

FIGURE 2 | Illustrative figure for the energy hub.

$$0 \le P_{\text{AC2DC},\omega}(t) \le \left(1 - I_{\text{DC2AC}\omega}(t)\right) P_{\text{BIC,max}}, \forall t, \omega, \tag{19}$$

where $P_{\text{BIC,max}}$ is the capacity of the BIC. $I_{\text{DC2AC},\omega}(t)$ is a binary variable, indicating the operating status of BICs, i.e., 1 if BIC is on the inverter mode and 0 on the rectifier mode.

Eqs 16, **17** represent the power range limitation on the day-ahead and real-time power exchange between the EH and utility grid. **Eqs 18**, **19** are the constraints for power conversion from the DC bus to AC bus and AC bus to DC bus, respectively. I_{DC2AC} forces the unidirection of power conversion on the BIC.

3.3.3 Constraints of Energy Conversion

The energy conversion constraints are to depict the relationship among energy carriers within the EH, which can be depicted as the following linear functions (Zhao et al., 2020):

$$v_{\text{CHP},\omega}(t)\,\eta_{\text{CHPe}} = p_{\text{CHP},\omega}(t), \forall t, \omega, \tag{20}$$

$$v_{\text{CHP},\omega}(t)\,\eta_{\text{CHPh}} = q_{\text{CHP},\omega}(t), \forall t, \omega, \tag{21}$$

$$v_{\text{GAS},\omega}(t)\,\eta_{\text{GAS}} = q_{\text{GAS},\omega}(t), \forall t, \omega, \tag{22}$$

$$p_{\text{IAC},\omega}(t)\,\eta_{\text{IAC}} = q_{\text{IAC},\omega}(t), \forall t, \omega, \tag{23}$$

$$p_{\text{CS},\omega}(t)\,\eta_{\text{PCS}} = q_{\text{CS,CH},\omega}(t), \forall t, \omega, \tag{24}$$

$$q_{\text{AC},\omega}(t)\,\eta_{\text{AC}} = q_{\text{CE},\omega}(t), \forall t, \omega, \tag{25}$$

where η_{CHPe} and η_{CHPh} are the electricity and heat conversion efficiency of CHP, respectively. η_{GAS}, η_{IAC}, η_{AC}, and η_{PCS} are the conversion efficiencies of the gas boiler, absorption chiller, air conditioner, and ice storage air conditioner, respectively.

Eq. 20 shows the energy conversion from gas to electricity. The conversion from gas to heating is depicted by **Eqs 21**, **22**, using the CHP and gas boiler, respectively. The conversion from electricity to cooling is depicted by **Eqs 23**, **24**, using the air conditioner and ice storage air conditioner, respectively. The conversion from heating to cooling is shown in **Eq. 25**. It should be noted that these linear functions might be oversimplified, especially for the CHP. If heat recovery and other processes are considered, their equations can be replaced by more accurate convex or non-convex models, balancing the optimality and feasibility (Dai et al., 2017).

3.3.4 Constraints of Energy Storage Systems

Considering the self-discharge, charge, and discharge of processes, the constraints for the ESSs, including BES, CES, and HES, are represented as follows (Zhao et al., 2018):

$$0 \le y_{\text{DC},\omega}(t) \le y_{\text{DC,max}}, \forall t, \omega, \tag{26}$$

$$0 \le y_{\text{CH},\omega}(t) \le y_{\text{CH,max}}, \forall t, \omega, \tag{27}$$

$$y_{\text{ES,min}} \le y_{\text{ES},\omega}(t) \le y_{\text{ES,max}}, \forall t \in \mathcal{T}, \tag{28}$$

$$y_{\text{ES},\omega}(t) = \eta_y y_{\text{ES},\omega}(t - \Delta t) + y_{\text{CH},\omega}(t)\,\eta_{y,\text{CH}}\Delta t - \frac{y_{\text{DC},\omega}(t)\,\Delta t}{\eta_{y,\text{DC}}}, \forall t, \omega, \tag{29}$$

$$y_{\mathrm{CH},\omega} \le I_{\mathrm{CH},\omega}(t)\, y_{\mathrm{CH,max}} \forall t, \omega, \tag{30}$$

$$y_{\mathrm{DC},\omega} \le \left(1 - I_{\mathrm{CH},\omega}(t)\right) y_{\mathrm{DC,max}} \forall t, \omega, \tag{31}$$

$$y_{\mathrm{ES},\omega}(T) = y_{\mathrm{ES}}(0), \forall \omega, \tag{32}$$

where $y_{\mathrm{DC}}(t)$, $y_{\mathrm{CH}}(t)$, and $y_{\mathrm{ES}}(t)$ represent the discharging, charging, and energy status of BES, HES, and CES, respectively. $I_{\mathrm{CH},k}(t)$ is a binary variable, indicating the charging and discharging status, respectively. $\eta_{y,\mathrm{CH}}$, $\eta_{y,\mathrm{DC}}$, and η_y represent the charging, discharging, and self-discharging efficiency of ESSs, respectively. $y_{\mathrm{DC,max}}$, $y_{\mathrm{CH,max}}$, $y_{\mathrm{ES,min}}$, and $y_{\mathrm{ES,max}}$ are the limitations for the discharging, charging, and energy status, respectively.

Eqs 26–28 are the limitations on the discharging, charging, and energy status of ESSs, respectively. The energy status dynamic is shown in **Eq. 29**. **Eqs 30–32** enforce that the ESS can only be either charging or discharging within each period. After the operation, the energy status should be the same as the initial status, as depicted by **Eq. 32**.

3.3.5 Constraints of Carbon Emission

The carbon emissions are generated by the utilized electricity and gas, which should be less than the purchased carbon permit in the day-ahead market and real-time market, as follows:

$$\begin{aligned}\sum_{t\in\mathcal{T}} \left[P_{\mathrm{DA}}(t) + p_{\mathrm{RT}}(t)\right] v_{\mathrm{ele}} + \left[v_{\mathrm{CHP},\omega}(t) + v_{\mathrm{GAS},\omega}(t)\right] v_{\mathrm{gas}} \\ \le \sum_{t\in\mathcal{T}} \left[\Phi_{\mathrm{DA}}(t) + \phi_{\mathrm{RT},\omega}(t)\right],\end{aligned} \tag{33}$$

where v_{ele} and v_{gas} are the carbon emission co-efficients of electricity and natural gas, respectively.

4 DETERMINISTIC REFORMULATION

As shown in **Eqs 1–5**, the formulated problem is a two-stage distributionally robust jointed chance-constrained programming problem. This problem cannot be solved directly as the density function is uncertain. It is further reformulated as its deterministic counterpart, which is a mixed-integer linear programming problem.

4.1 Deterministic Reformulation of Jointed Chance Constraints

To reformulate the joint chance constraints (**Eq. 5**) as a deterministic constraint, an indicator function is introduced as follows, to show whether **y** is feasible or not under scenario ω :

$$I_\omega = \begin{cases} 0, \mathbf{E}\mathbf{y}_\omega + \mathbf{F}\xi_\omega \le \mathbf{g}_\omega, \\ 1, \mathbf{E}\mathbf{y}_\omega + \mathbf{F}\xi_\omega > \mathbf{g}_\omega \end{cases} \tag{34}$$

Using the indicator function (**Eq. 34**), the joint chance constraint (**Eq. 5**) can be reformulated as the following constraints:

$$\sum_{\omega\in\Omega} I_\omega \pi_\omega \le \beta, \tag{35}$$

$$\mathbf{E}\mathbf{y}_\omega + \mathbf{F}\xi_\omega \le \mathbf{g}_\omega + I_\omega M, \tag{36}$$

where M is a scalar big enough to guarantee the feasibility of problem (**Eq. 4**), when I_ω is activated to 1. Based on the ambiguity set (3), constraint (**Eq. 35**) can be further reformulated as the following constraint:

$$\begin{aligned} &\mathbf{e}^{\mathrm{T}}\gamma \le \beta \\ &\mathbf{G}^{\mathrm{T}}\gamma \ge \mathbf{b}(I_\omega), \\ &\gamma \ge 0 \end{aligned} \tag{37}$$

where γ is the Lagrange multiplier of $\mathbf{G}\omega \le \mathbf{e}$, that is, the ambiguity set (**Eq. 3**), and $\mathbf{b}(I_\omega)$ is the vector to represent the $\Sigma_{\omega\in\Omega} I_\omega \pi_\omega$.

It can be seen that after the reformulation (**Eq. 37**), the jointed chance constraint can be solved by its deterministic counterpart.

4.2 Deterministic Reformulation of Second-Stage Optimization Problems

The expected CVaR value in **Eq. 1**, that is, $\max_{\mathbb{P}\in\mathcal{P}}\{\rho\mathbb{E}_{\omega\sim\mathbb{P}}[\mathcal{Q}(\mathbf{x},\omega)] + (1-\rho)\mathrm{CVaR}_\alpha[\mathcal{Q}(\mathbf{x},\omega)]\}$, can be reformulated based on Lagrange duality, as the following problem:

$$\begin{aligned} \min_{z,\nu,\eta,z_\omega^+,z_\omega^-,\kappa} \quad & \tau z + (1-\rho)\eta + \xi_0^{\mathrm{T}}\kappa + \sum_\omega \pi_{0,\omega}\left(z_\omega^+ - z_\omega^-\right) + \nu \\ \text{s.t.} \quad & \mathbf{q}^{\mathrm{T}}\mathbf{y}_\omega + \frac{1-\rho}{1-\beta}\nu_\omega \le z_\omega^+ - z_\omega^- + \nu + \xi_\omega^{\mathrm{T}}\kappa, \forall\omega \\ & z_\omega^+ - z_\omega^- \le z, \forall\omega \\ & \mathbf{q}^{\mathrm{T}}\mathbf{y}_\omega - \eta \le \nu_\omega, \forall, \omega \\ & z_\omega^+, z_\omega^-, \nu_\omega \ge 0, \forall\omega \end{aligned} \tag{38}$$

where $z, \nu, \eta, z_\omega^+, z_\omega^-, and\kappa$ are the auxiliary variables.

After the deterministic reformulation of the jointed chance constraints and the second-stage optimization problem, problems **(1)**–**(5)** can be treated as the following mixed-integer linear programming problem:

$$\begin{aligned} \min_{\mathbf{x},\mathbf{y}_\omega,I_\omega,z,\nu,\eta,z_\omega^+,z_\omega^-,\kappa,\gamma} \quad & \tau z + (1-\rho)\eta + \xi_0^{\mathrm{T}}\kappa \\ & + \sum_\omega \pi_{0,\omega}\left(z_\omega^+ - z_\omega^-\right) + \nu \\ \text{s.t.} \quad & \mathbf{D}\mathbf{y}_\omega \ge \mathbf{h}_\omega - \mathbf{T}_\omega\mathbf{x}, \forall\omega \\ & \mathbf{E}\mathbf{y}_\omega + \mathbf{F}\xi_\omega \le \mathbf{g}_\omega + I_\omega M, \forall\omega \\ & \mathbf{q}^{\mathrm{T}}\mathbf{y}_\omega + \frac{1-\rho}{1-\beta}\nu_\omega \le z_\omega^+ - z_\omega^- + \nu + \xi_\omega^{\mathrm{T}}\kappa, \forall\omega \\ & z_\omega^+ - z_\omega^- \le z, \forall\omega \\ & \mathbf{q}^{\mathrm{T}}\mathbf{y}_\omega - \eta \le \nu_\omega, \forall\omega \\ & z_\omega^+, z_\omega^-, \nu_\omega \ge 0, \forall\omega \\ & \mathbf{e}^{\mathrm{T}}\gamma \le \beta \\ & \mathbf{G}^{\mathrm{T}}\gamma \ge \mathbf{b}(I_\omega) \\ & \gamma \ge 0 \end{aligned} \tag{39}$$

Problem **(39)** can be solved by offshore commercial solvers, e.g., Gurobi and Cplex.

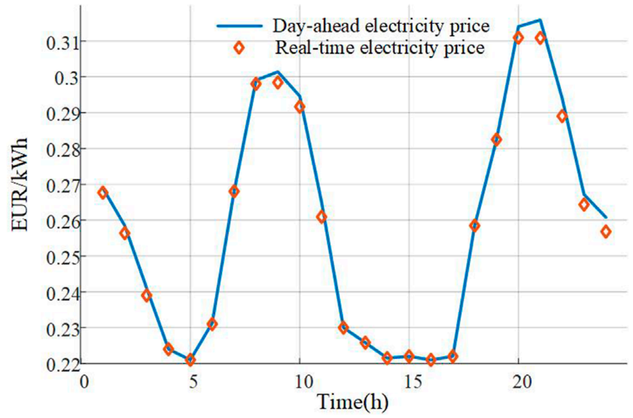

FIGURE 3 | Prices in the day-ahead and forecast prices in the real-time electricity markets.

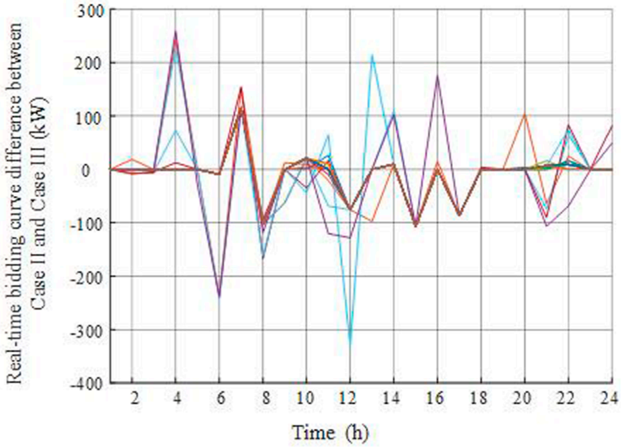

FIGURE 5 | Real-time bidding curve differences in different scenarios between case II and case III.

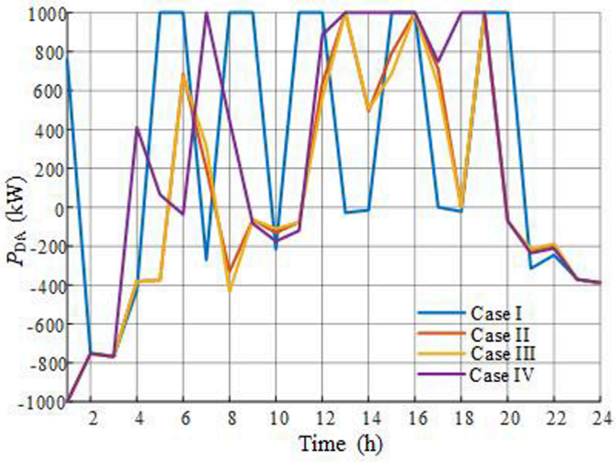

FIGURE 4 | Day-ahead bidding curves under different cases.

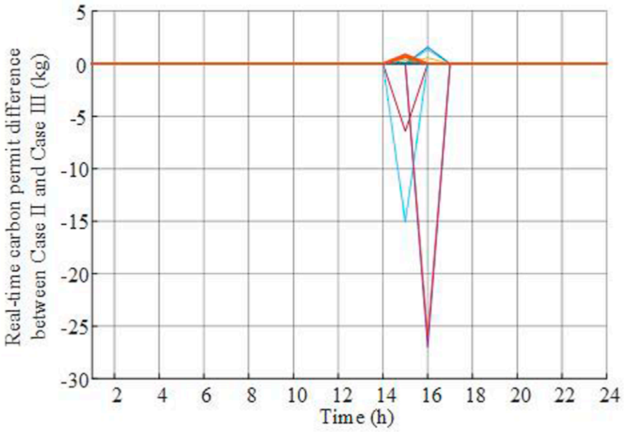

FIGURE 6 | Real-time bidding curve differences in different scenarios between case II and case III.

5 CASE STUDY

5.1 Case Description

To verify the effectiveness of the proposed bidding strategy, an EH test system is proposed, as shown in **Figure 2**. The bidirectional AC/DC converter is used to realize the AC/DC conversion in the electrical hub. The electrical load, heat load, and cooling load profiles are obtained from Sadeghian et al. (2017). The day-ahead electricity price and expected real-time electricity price profiles are obtained from energy market prices in Omie (2022), as shown in **Figure 3**, and carbon prices are extracted from EU Carbon Permits (Tradingeconomics, 2022a). For the second stage optimization, 100 scenarios are generated, including the electrical prices, loads, PV output, and ambient temperature. α is

TABLE 1 | Simulation results under different cases.

Case	I	II	III	IV	V
$f(\mathbf{x})$($)	5027.94	5136.68	5141.38	5128.93	5103.22
$\sum_t P_{\mathrm{DA}}(t)$(kWh)	6943.29	1385.68	1166.83	5346.13	2471.69
$\mathbb{E}_{\mathbb{P}_0}(\sum_t p_{\mathrm{RT}}(t))$(kWh)	9874.70	15421.00	15641.00	11264.33	14335.97
$\sum_t \Phi_{\mathrm{DA}}(t)+\mathbb{E}_{\mathbb{P}_0}(\sum_t \phi_{\mathrm{RT}}(t))$(kg)	5419.84	5420.35	5421.04	5365.70	5421.71

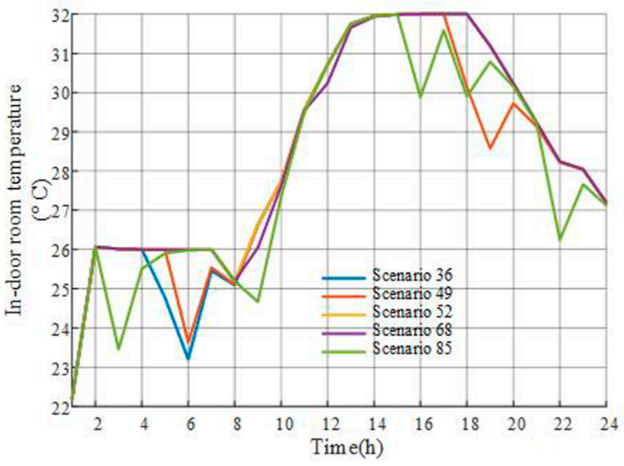

FIGURE 7 | Indoor room temperature in selected scenarios.

set to 0.95. Other parameter settings are obtained from Zhao et al. (2020).

Numerical simulations were carried out on a desktop with an Intel Xeon Gold 6226R CPU and 128 GB of RAM. The MILP problem in **Eq. 39** is solved by the commercial solver Gurobi with branch-and-cut and simplex methods.

To show the effectiveness of the proposed method, four different cases are performed as follows:

- Case I: The uncertainties have not been considered.
- Case II: $\tau = 0$, $\beta = 0$, and $\rho = 0.5$.
- Case III: $\tau = 0.1$, $\beta = 0$, and $\rho = 0.5$.
- Case IV: $\tau = 0.1$, $\beta = 0.1$, and $\rho = 0.5$.
- Case V: $\tau = 0$, $\beta = 0$, and $\rho = 1$.

5.2 Result Analysis

The simulation results under different cases are shown in **Table 1**, and the day-ahead bidding curves of the EHO in the day-ahead market are shown in **Figure 4**.

5.2.1 Impacts of Uncertainties

As shown in **Table 1**, an increase in the operational cost from 5027.94 $ to 5136.68 $ can be induced including uncertainties of PV output, demand, and ambient temperature. The day-ahead bidding curves of case I and case II vary, as shown in **Figure 4**, especially during the (0:00, 1:00). In case 1, the uncertainties have not been considered, which means forecast prices in the real-time market are accurate without bias, so it is specific for the EHO whether there is a need for arbitrage or not. In other words, the EHO tends to purchase as much electricity as possible, in the day-ahead market during time slots when the electricity price in the day-ahead market is lower than in the real-time market, e.g., (5:00, 6:00) and (8:00, 9:00). The purchased electricity during these time slots has reached the given upper limit, that is, 1000 kW.

To explore the effectiveness of the risk-averse, the risk factor ρ is set to be 1 in case V. In comparison with case II, the potential trading risk, which can be incurred in the extreme condition, is neglected by the EHO to search for a lower expected cost.

5.2.2 Impacts of Distributionally Robust Uncertainties

The real-time bidding and carbon permit trading difference curves between case II and case III are shown in **Figures 5**, **6**. The uncertainties of the probability distribution are considered, and the worst condition is found by the optimization process. The variance from the nominal distribution of case II increases the operational cost, which seems slight due to limited differences among scenarios. The expected electricity purchased under nominal PDF in the real-time market increased by 220 kWh in case III. An interesting observation is that even if the electricity is increased, the carbon emission almost remains the same. It indicates that the proposed bidding strategy can always reduce carbon emissions, while the electricity bidding can be adjusted accordingly.

5.2.3 Impacts of Joint Chance Constrain Relaxation

The indoor room temperature curve under scenarios 36, 49, 52, 68, and 85 are shown in **Figure 7**. In these five scenarios, the indoor room temperature has been relaxed as the highest temperature is more than 24°C, that is, the threshold temperature value. These relaxed scenarios can help reduce the carbon emission and operational cost. Furthermore, due to $\tau = 0.1$, the number of total relaxed scenarios is 5, while it should be 10 when $\tau = 0.0$, that is, the PDF is accurate.

6 CONCLUSION

In this study, a day-ahead bidding strategy is proposed for the EHO to manage its technical and economic behavior in the joint electricity and carbon market. To manage the ambiguity uncertainties of prices, loads, renewable energy output, and ambient temperature, this strategy is formulated as a two-stage distributionally robust joint chance-constrained programming problem and further been reformulated as a mixed-integer linear programming problem.

Simulations are performed on a test EH system, where the indoor room temperature can be relaxed in some scenarios. Results indicate that the proposed strategy can manage the uncertainties in the joint electricity and carbon market and reduce the operational cost and carbon emission by exploring the flexibility of the thermal demand.

DATA AVAILABILITY STATEMENT

The original contributions presented in the study are included in the article/Supplementary Material, further inquiries can be directed to the corresponding author.

AUTHOR CONTRIBUTIONS

JL completed the technical writing, idea consultation, and supervision of this work, and other authors listed also made a direct contribution to the work.

REFERENCES

Brahman, F., Honarmand, M., and Jadid, S. (2015). Optimal Electrical and thermal Energy Management of a Residential Energy Hub, Integrating Demand Response and Energy Storage System. *Energy and Buildings* 90, 65–75. doi:10.1016/j.enbuild.2014.12.039

Cheng, Y., Zhang, N., Wang, Y., Yang, J., Kang, C., and Xia, Q. (2018). Modeling Carbon Emission Flow in Multiple Energy Systems. *IEEE Trans. Smart Grid* 10, 3562–3574.

Cheng, Y., Zhang, N., Zhang, B., Kang, C., Xi, W., and Feng, M. (2020). Low-carbon Operation of Multiple Energy Systems Based on Energy-Carbon Integrated Prices. *IEEE Trans. Smart Grid* 11, 1307–1318. doi:10.1109/tsg.2019.2935736

Dai, Y., Chen, L., Min, Y., Chen, Q., Hu, K., Hao, J., et al. (2017). Dispatch Model of Combined Heat and Power Plant Considering Heat Transfer Process. *IEEE Trans. Sustain. Energ.* 8, 1225–1236. doi:10.1109/tste.2017.2671744

Davatgaran, V., Saniei, M., and Mortazavi, S. S. (2018). Optimal Bidding Strategy for an Energy Hub in Energy Market. *Energy* 148, 482–493. doi:10.1016/j.energy.2018.01.174

Ding, T., Lu, R., Xu, Y., Yang, Q., Zhou, Y., Zhang, Y., et al. (2020). Joint Electricity and Carbon Market for Northeast Asia Energy Interconnection. *Glob. Energ. Interconnection* 3, 99–110. doi:10.1016/j.gloei.2020.05.002

Jadidbonab, M., Mohammadi-Ivatloo, B., Marzband, M., and Siano, P. (2020). Short-term Self-Scheduling of Virtual Energy Hub Plant within thermal Energy Market. *IEEE Trans. Ind. Electron.* 68, 3124–3136.

Li, R., Wei, W., Mei, S., Hu, Q., and Wu, Q. (2018). Participation of an Energy Hub in Electricity and Heat Distribution Markets: An Mpec Approach. *IEEE Trans. Smart Grid* 10, 3641–3653.

Liu, S., Zhao, T., and Wang, P. (2021). "Strategic Bidding for Energy Hubs Based on Hybrid Stochastic/distributionally Robust Optimization," in 2021 IEEE Power & Energy Society General Meeting (PESGM) (IEEE), 1–5. doi:10.1109/pesgm46819.2021.9637912

Lu, X., Liu, Z., Ma, L., Wang, L., Zhou, K., and Feng, N. (2020). A Robust Optimization Approach for Optimal Load Dispatch of Community Energy Hub. *Appl. Energ.* 259, 114195. doi:10.1016/j.apenergy.2019.114195

Mohammadi, M., Noorollahi, Y., Mohammadi-Ivatloo, B., and Yousefi, H. (2017). Energy Hub: From a Model to a Concept - A Review. *Renew. Sustainable Energ. Rev.* 80, 1512–1527. doi:10.1016/j.rser.2017.07.030

Olsen, D. J., Zhang, N., Kang, C., Ortega-Vazquez, M. A., and Kirschen, D. S. (2018). Planning Low-Carbon Campus Energy Hubs. *IEEE Trans. Power Syst.* 34, 1895–1907.

Omie, (2022). Day-ahead Electricity price. Available at: https://www.omie.es/en/market-results/daily/daily-market/daily-hourly-price?scope=daily&date=2022-03-01.

Oskouei, M. Z., Mohammadi-Ivatloo, B., Abapour, M., Shafiee, M., and Anvari-Moghaddam, A. (2021). Strategic Operation of a Virtual Energy Hub with the Provision of Advanced Ancillary Services in Industrial parks. *IEEE Trans. Sustain. Energ.* 12, 2062–2073. doi:10.1109/tste.2021.3079256

Rockafellar, R. T., and Uryasev, S. (2000). Optimization of Conditional Value-At-Risk. *Jor* 2, 21–41. doi:10.21314/jor.2000.038

Sadeghian, H., Athari, M. H., and Wang, Z. (2017). "Optimized Solar Photovoltaic Generation in a Real Local Distribution Network," in Power & Energy Society Innovative Smart Grid Technologies Conference (ISGT), 2017 IEEE (IEEE), 1–5. doi:10.1109/isgt.2017.8086067

Sun, W., and Huang, C. (2020). A Carbon price Prediction Model Based on Secondary Decomposition Algorithm and Optimized Back Propagation Neural Network. *J. Clean. Prod.* 243, 118671. doi:10.1016/j.jclepro.2019.118671

Tradingeconomics (2022). Carbonprice. Available at: https://tradingeconomics.com/commodity/carbon.

Yang, D., He, S., Chen, Q., Li, D., and Pandžić, H. (2019). Bidding Strategy of a Virtual Power Plant Considering Carbon-Electricity Trading. *CSEE J. Power Energ. Syst.* 5, 306–314.

Zhang, C., Xu, Y., Li, Z., and Dong, Z. Y. (2018). Robustly Coordinated Operation of a Multi-Energy Microgrid with Flexible Electric and thermal Loads. *IEEE Trans. Smart Grid* 10, 2765–2775.

Zhao, P., Gu, C., Huo, D., Shen, Y., and Hernando-Gil, I. (2019). Two-stage Distributionally Robust Optimization for Energy Hub Systems. *IEEE Trans. Ind. Inform.* 16, 3460–3469.

Zhao, T., Pan, X., Yao, S., Ju, C., and Li, L. (2020). Strategic Bidding of Hybrid Ac/dc Microgrid Embedded Energy Hubs: A Two-Stage Chance Constrained Stochastic Programming Approach. *IEEE Trans. Sustain. Energ.* 11, 116–125. doi:10.1109/tste.2018.2884997

Zhao, T., Xiao, J., Koh, L. H., Wang, P., and Ding, Z. (2018). "Strategic Day-Ahead Bidding for Energy Hubs with Electric Vehicles," in 2018 2nd IEEE Conference on Energy Internet and Energy System Integration (EI2) (IEEE), 1–6. doi:10.1109/ei2.2018.8581935

FUNDING

The work was supported in part by the consulting research project of the Chinese Academy of Engineering (2021NXZD2) and in part by the National Natural Science Foundation of China (52061635102).

Conflict of Interest: The authors declare that the research was conducted in the absence of any commercial or financial relationships that could be construed as a potential conflict of interest.

frontiers | Frontiers in Energy Research

ORIGINAL RESEARCH
published: 30 May 2022
doi: 10.3389/fenrg.2022.901529

Multi-Objective Optimal Source–Load Interaction Scheduling of Combined Heat and Power Microgrid Considering Stable Supply and Demand

Jiaqi Chang, Xinglin Yang*, Zongnan Zhang, Shouqing Zheng and Bowei Cui

School of Energy and Power, Jiangsu University of Science and Technology, Zhenjiang, China

With the development of smart grids, it has become possible to take demand-side resource utilization into account to improve the comprehensive benefits of combined heat and power microgrids (CHP-MGs). In order to improve the benign interaction between the source and the load of the system, the source side decouples the thermoelectric linkage through energy storage devices and improves the system multi-energy supply capacity by introducing various energy flow forms of energy devices. On the demand side, considering the elasticity of electric heating load and the diversity of heating mode, an integrated demand response (IDR) model is established, and a flexible IDR price compensation mechanism is introduced. On this basis, aiming at the optimal stability of supply and demand and the minimum operating cost of the system, a multi-objective optimal operation model of combined heat and power source–load interaction is constructed, taking into account the user satisfaction with energy consumption and the internal equipment load constraints of the system. Finally, an improved multi-objective optimization algorithm is used to solve the model. The analysis of the algorithm shows that the source–load interaction multi-objective optimal scheduling of the cogeneration microgrid considering the stability of supply and demand can effectively improve the stability of supply and demand and the economy of the system.

Keywords: combined heat and power microgrid, integrated demand response, user satisfaction, pluripotent complementarity, thermocouple

Edited by:
Rui Wang,
Northeastern University, China

Reviewed by:
Yushuai Li,
University of Oslo, Norway
Xuguang Hu,
Northeastern University, China

****Correspondence:***
Xinglin Yang
YXL202101@163.com

Specialty section:
This article was submitted to
Smart Grids,
a section of the journal
Frontiers in Energy Research

Received: *22 March 2022*
Accepted: *11 April 2022*
Published: *30 May 2022*

Citation:
Chang J, Yang X, Zhang Z, Zheng S and Cui B (2022) Multi-Objective Optimal Source–Load Interaction Scheduling of Combined Heat and Power Microgrid Considering Stable Supply and Demand.
Front. Energy Res. 10:901529.
doi: 10.3389/fenrg.2022.901529

1 INTRODUCTION

Combined heat and power microgrid (CHP-MG) based on the concept of multi-energy complementation, energy cascade utilization, and the coordination and optimization of multi-type heterogeneous energy subsystems breaks the mode of discrete planning and operation between energy systems and effectively improves the utilization rate of energy (Alomoush, 2019; Blair and Mabee, 2020; Nojavan et al., 2020; Hemmati et al., 2021a; Wang et al., 2021a). In recent years, many scholars have done many pioneering research studies on the modeling and optimal scheduling of the source and load sides of the CHP-MG system (Freeman et al., 2017; Ippolito and Venturini, 2018; Zhao et al., 2019; Ronaszegi et al., 2020; Singh and Kumar, 2020; Jordehi, 2021).

On the source side, Pashaei-Didani et al. (2019) proposed a fuel cell system including a reformer, a hydrogen storage tank, and a fuel cell using natural gas as a raw material. At the same time, the heat production characteristics of hydrogen production from natural gas reforming and the thermoelectric hydrogen coupling characteristics of fuel cells were considered, which effectively reduced the microscopic grid emissions and costs. Hemmati et al. (2021b) improved system operation/recovery and reduced operation/energy costs by optimizing CHP size, location, and equipment operation. In the above research, the optimization target only considers the economic cost and environmental cost and lacks the consideration of the supply-side stability of the system. For example, frequent switching of the start-up state of the equipment or relatively large adjustment of the operating power not only affects the stability and service life of the equipment but also increases the complexity of the transportation, storage, and scheduling of natural gas and other fuels. For source-side optimization scheduling, Liu and Yang (2022) propose a primal–dual based dynamic weight distributed algorithm for multi-objective optimal scheduling of distributed integrated energy system, so as to reduce the operating cost and environmental cost of the system. It is proved that the algorithm has better flexibility, reliability, and adaptability and lower communication burden. Yi et al. (2020) proposed a distributed, neurodynamic-based approach for economic dispatch in an integrated energy system. Compared with other centralized and distributed optimization methods, it is shown that the proposed distributed optimization method has advantages in convergence speed and computational complexity. Anh and Cao (2020) proposed an optimal energy management (OEM) approach that uses smart optimization techniques to achieve optimal hybrid thermoelectric isolation microgrids. Naderipour et al. (2020) proposed the use of particle swarm optimization algorithm to optimize the configuration of the cogeneration system to reduce the operating cost on the basis of considering the maximum allowable capacity. It can be seen that the centralized algorithm is mostly used in a single energy system. For distributed large-scale energy systems, the distributed algorithm has better solving ability than the centralized algorithm.

For the load side, flexible electrical and thermal loads can also be used as potential targets for optimal scheduling of CHP-MG systems. How to quantify and guide the flexible load to participate in each link of the optimal operation of the system and promote the good interaction between source and load has gradually become a research hotspot (Liu et al., 2018; Mohseni et al., 2021; Zhou, 2019; Dranka et al., 2021; Hca et al., 2021; Jiang et al., 2021; Amir et al., 2019)

Integrated demand response should adopt price, policy, contract, and other methods to guide users to change their energy consumption habits and optimize the source–load matching relationship of the energy system, so we can obtain greater comprehensive benefits (Aghamohammadloo et al., 2021; Li et al., 2021a; Salehimaleh et al., 2022; Zhang et al., 2019). Lv et al. (2021) have built an IDR multi-time scale optimal scheduling model for power, gas, and heat loads. Zhang et al. (2015) proposed to use a piecewise linear function to characterize the cost of reducing the load and determine the IDR price according to the marginal cost corresponding to various energy consumption in a specific period. Munoz-Delgado et al. (2016) adopted the method of stochastic programming and generated a large number of discrete scenes based on the scene method to represent the uncertainty of DG output and load and convert the uncertainty problem into a deterministic problem. Shao et al. (2020) by incorporating the demand-side response of the energy hub into the integrated power and natural gas system solved the problem that the complex coupling relationship between power and natural gas may reduce the flexibility of system operation. Wc et al. (2021) proposed an optimization technique based on integrated demand response and tolerance of household energy management.

Most of the above studies focus on user load while ignoring the benign interaction between source and load. Load reduction and transfer will greatly affect user satisfaction with energy consumption. However, the conversion and substitution of heating forms (electric heating/gas heating) on the side of the load has little influence on the user's energy experience. And there are few studies to establish a comprehensive evaluation system that considers both the supply and the demand of users. In addition, most of them only focus on user load, ignoring the benign interaction between source and load. For example, renewable energy on the supply side has great volatility and randomness (Yang et al., 2018; Salama et al., 2021), and the negative impact of this factor can be alleviated through IDR. Li et al. (2019) introduced the interaction between energy supplier and customer into system model development. On this basis, considering the characteristics of different time scales of electricity and heat, an event-triggered distributed algorithm is used to optimize scheduling, smoothing real-time load changes and renewable resource fluctuations while maximizing day-ahead social welfare.

To sum up, this paper proposes a multi-objective coordinated optimal scheduling method for cogeneration microgrid source–load that considers the stability of supply and demand. Compared with the existing research, the difficulties and challenges as well as the innovations and contributions made in this paper are as follows:

1) The existing studies on the source side mostly consider economy and environmental protection but lack the consideration of supply stability. In this paper, the CHP-MG model makes use of energy storage equipment to decouple thermoelectric connection and expand the power supply capacity through multi-energy devices. Meanwhile, the supply stability is taken as one of the criteria to evaluate the operation.
2) For the demand response of the load side, most of them adopt the method of load reduction and transfer, which will greatly affect the user's energy satisfaction. Therefore, in addition to the construction of a comprehensive demand response model that includes the electrical load that can be time-shifted and interrupted, electrical loads that can be time-shifted and uninterrupted, the curtailable electrical load, the curtailable heat load, it also considers the integrated demand response

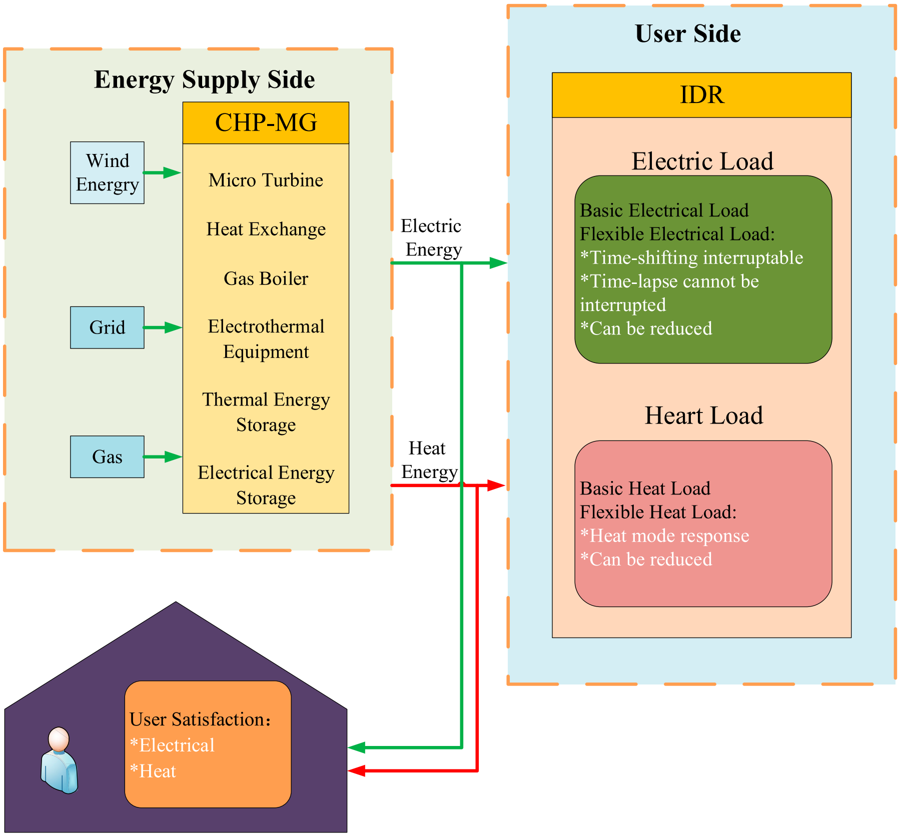

FIGURE 1 | System overall framework diagram.

model for heat supply mode conversion and introduces a flexible IDR price compensation mechanism. In addition, a comprehensive satisfaction evaluation system was established considering the demand-side user energy deviation degree, IDR compensation price, supply-side heating and power supply flexibility, and other factors.

3) For the problem that most IDR only focuses on user load but ignores the benign interaction between source and load, the fluctuation of renewable energy is smoothed by the IDR of load side.
4) The solution of CHP-MG model has the characteristics of high dimensionality and non-linearity, so an intelligent algorithm is needed to approximate the optimal solution. In addition, compared with the distributed large-scale energy system, the system is of single cogeneration type, and the amount of information and calculation is small, so the centralized optimization algorithm is adopted. In this paper, the improved multi-objective grey wolf optimizer (MOGWO) is used to carry out the source–charge interaction multi-objective optimal scheduling of microgrids, and through example analysis, it is verified that the algorithm can promote the benign interaction between source and load and ensure the stability of supply and demand (SDS) and economy of CHP-MG operation.

2 GENERAL FRAMEWORK OF THE SYSTEM

The system is roughly divided into two parts, the source side and the load side, and its framework is shown in **Figure 1**.

The source side contains wind energy and CHP-MG systems, which use wind energy, electric energy, and natural gas as sources to provide customers with both electric and thermal energy through the complementary use of multiple energy sources.

In the CHP-MG system, the gas boiler consumes natural gas to generate heat, and the gas turbine consumes natural gas to generate electricity and at the same time generates a large amount of high-temperature flue gas, which is recovered by the heat exchanger to supply heat energy to the load side, thereby realizing the cascade utilization of energy. When the thermal energy generated by a gas turbine and gas boiler is greater than the demand of heating load, the excess thermal energy is stored in the thermal storage equipment. When the thermal energy produced is less than the heating load demand, the thermal energy storage device releases thermal energy. Electricity storage devices are similar to thermal storage devices.

The load side takes the residential load as the core, and the load is divided into two categories: electrical load and thermal load. The electrical load is divided into uncontrollable load and controllable load. Controllable load is further divided into time-shifted and interrupted, time-shifted and uninterrupted. The

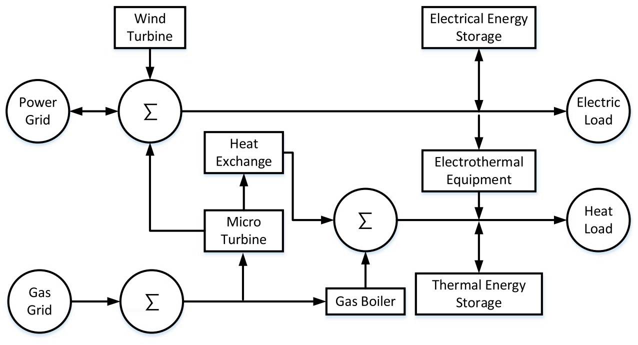

FIGURE 2 | CHP-MG source-side system structure diagram.

heat load is divided into the heat supply mode conversion load and the curtailable heat load. Among them, the heat load with convertible heating mode mainly considers the user's behavior of abandoning the heating mode of electric heating and turning to the gas-heat mode of central heating due to the influence of price. The curtailable heat load mainly considers the flexible hot water load.

In order to ensure user experience and prevent the loss of customer groups, this paper establishes a user satisfaction evaluation system. When user satisfaction is lower than the warning value, the scheme should be abandoned. Among them, user satisfaction includes electricity consumption satisfaction and heat consumption satisfaction.

3 SOURCE-SIDE MULTI-ENERGY COMPLEMENTARY MODEL

In this paper, the CHP-MG contains three energy forms: heat, electricity, and gas. The system energy equipment mainly includes a wind turbine (WT), micro-turbine (MT), and gas boiler (GB); energy storage equipment includes electric energy storage (EES) and thermal energy storage (TES); energy conversion equipment includes heat exchanger (HE) and electrothermal equipment (EE). Its structure is shown in **Figure 2**. This system has energy interaction with the external power grid (PG).

3.1 Wind Turbine

The research shows that the output power of wind turbine (P_w) depends on the wind speed and the rated output power of wind turbine (P_r). In addition, the wind speed obeys Weibull distribution. Therefore, the probability density function (PDF) of P_w can be expressed as

$$f_w(P_w) = \begin{cases} (khv_{in}/\varepsilon P_r) \times \\ [((1+hP_w/P_r)v_{in})/\varepsilon]^{k-1} \times \\ exp\{-[((1+hP_w/P_r)v_{in})/\varepsilon]^k\}, \\ P_w \in [0, P_r] \\ 0, \ otherwise \end{cases} \tag{1}$$

Here, ε is the scaling factor; k is the shape factor, reflecting the average wind speed or the average output power of the wind turbine in a certain period; and $h = (v_r/v_{in}) - 1$, in which v_{in} and v_r are the cut-in and rated wind speeds, respectively. More details of the probabilistic WT model can be found in the study of Yang et al. (2019).

In order to reduce the influence of uncertain wind power on system scheduling, this paper takes the mathematical expectation P_{WT}^t of P_w at each time period as the reference value (Li et al., 2021b).

3.2 Micro-Turbine

This paper focuses on the heat and power supply of MT, ignoring the effect of environmental changes on power generation and combustion efficiency. Its heat generation power Q_{MT}^t is

$$Q_{MT}^t = P_{MT}^t \frac{(1-\eta_{MT}-\eta_L)}{\eta_{MT}}. \tag{2}$$

Here, P_{MT}^t is the electric generation power of MT in period t and η_{MT}, η_L are the power generation efficiency and heat loss coefficient of MT.

Operating power constraints and climbing constraints are

$$\begin{cases} I_{MT}^t P_{MT,\min} \le P_{MT}^t \le I_{MT}^t P_{MT,\max}, \\ dP_{MT,\min} \le P_{MT}^t - P_{MT}^{t-1} \le dP_{MT,\max} \end{cases} \tag{3}$$

Here, $P_{MT,\max}/P_{MT,\min}$ and $dP_{MT,\max}/dP_{MT,\min}$ are the upper and lower limits of MT operating power and climbing rate and I_{MT}^t is the status flag bit of MT, which is 1 when running and 0 when stopped.

3.3 Heat Exchanger

The waste heat discharged from the MT is converted into usable heat energy by the HE:

$$Q_{HE}^t = Q_{MT}^t \eta_{MT} \tag{4}$$

Here, Q_{HE}^t is the heat production power of HE in period t and η_{MT} is the thermal efficiency of HE.

3.4 Gas Boiler

The GB generates heat energy by consuming natural gas to supplement the heat load when HE and TES are insufficient. The relationship between output power and input power is

$$\begin{cases} Q_{GB,\min} \le Q_{GB}^t \le Q_{GB,\max} \\ dQ_{GB,\min} \le Q_{GB}^t - Q_{GB}^{t-1} \le dQ_{GB,\max} \end{cases} \tag{5}$$

Here, $Q_{GB,\max}/Q_{GB,\min}$ and $dQ_{GB,\max}/dQ_{GB,\min}$ are the upper and lower limits of GB operating power and climbing rate.

3.5 Electrothermal Equipment

Electrothermal equipment consumes electric energy for heat production, such as air conditioners and electric boilers. The relationship that needs to be satisfied is

$$\begin{cases} Q_{EE}^t = Q_{EE}^t \eta_{EE} \\ Q_{EE,\min} \le Q_{EE}^t \le Q_{EE,\max} \end{cases} \tag{6}$$

Here, Q^t_{EE} is the heat generation power of EE in period t; η_{EE} is the thermal efficiency of EE; and $Q_{EE,\max}$, $Q_{EE,\min}$ are the upper and lower limits of EE heat generation power.

3.6 Energy Storage Equipment

In this paper, the energy storage device is mainly used to decouple the complex electrical and thermal connection, so that the CHP-MG system can get rid of the traditional mode of "determining electricity by heat" and "determining heat by electricity." On this basis, the system runs in the direction of supply and demand stability and optimal economy.

3.6.1 Electricity Storage Equipment

EES is often used in microgrids to achieve peak-shaving and valley-filling of electrical loads, smooth operation of generation equipment, and reduction of operating costs. The relationship between power and energy storage capacity during the operation of EES is shown below.

Energy storage constraint:

$$\begin{cases} E^t_{EES} = E^{t-1}_{EES} + \left(P^t_{EES,c}\eta_c - \dfrac{P^t_{EES,d}}{\eta_d} \right) \\ E_{EES,\min} \le E^t_{EES} \le E_{EES,\max}, \\ E^0_{EES} = E^{24}_{EES}. \end{cases} \tag{7}$$

Here, E^t_{EES} is the storage capacity of EES in period t; $P^{t-1}_{EES,c}$ is the charging power of EES in period t-1; $P^t_{EES,d}$ is the discharge power of EES in period t; η_c/η_d is the charge/discharge coefficient of EES; and $E_{EES,\max}/E_{EES,\min}$ is the maximum/minimum capacity of EES.

Power constraint:

$$\begin{cases} P_{EES,c,\min} I_{EES,c} \le P^t_{EES,c} \\ \qquad \le P_{EES,c,\max} I_{EES,c} \\ P_{EES,d,\min} I_{EES,d} \le P^t_{EES,d} \\ \qquad \le P_{EES,d,\max} I_{EES,d} \end{cases} \tag{8}$$

Here, $P_{EES,c,\max}/P_{EES,c,\min}$ is the maximum/minimum charging power of EES; $P_{EES,d,\max}/P_{EES,d,\min}$ is the maximum/minimum discharge power of EES; and $I_{EES,c}/I_{EES,d}$ is the charge/discharge status flag of EES, which is 0 when stopped and 1 when running. The mutual exclusion constraint needs to be satisfied, that is,

$$I_{EES,c} + I_{EES,d} \le 1 \tag{9}$$

$$\begin{cases} dP_{EES,c,\min} \le P^t_{EES,c} - P^{t-1}_{EES,c} \\ \qquad \le dP_{EES,c,\max} \\ dP_{EES,d,\min} \le P^t_{EES,d} - P^{t-1}_{EES,d} \\ \qquad \le dP_{EES,d,\max} \end{cases} \tag{10}$$

Here, $dP_{EES,c,\max}/dP_{EES,c,\min}$ is the maximum/minimum ramp rate for charging EES and $dP_{EES,d,\max}/dP_{EES,d,\min}$ is the maximum/minimum ramp rate of EES discharge.

3.6.2 Heat Storage Equipment

An energy storage device is a storage device for energy, not just for electrical energy. Generally, the peak of electricity consumption occurs during the day, and the peak of heat consumption occurs in the morning and evening, resulting in a mismatch between the electric heat output and the electricity load. Therefore, TES is used in this paper to realize the translation of heat time and solve the difference in the time of electric–thermal load. In order to simplify the model, without considering the influence of environmental factors on heat self-loss rate, the TES constraint relationship is similar to that of EES, as shown below.

Energy storage constraint:

$$\begin{cases} E^t_{TES} = (1-\delta)E^{t-1}_{TES} + \\ \left(Q^t_{TES,c}\delta_c - \dfrac{Q^t_{TES,d}}{\delta_d} \right) \\ E_{TES,\min} \le E^t_{TES} \le E_{TES,\max} \end{cases} \tag{11}$$

Here, E^t_{TES} is the heat storage of TES in period t; $Q^{t-1}_{TES,c}$ is the heat storage of EES in period t-1; $Q^t_{TES,d}$ is the exothermic power of TES in period t; δ_c/δ_d is the heat storage/release coefficient of TES; δ is the self-loss coefficient of TES; and $E_{TES,\max}/E_{TES,\min}$ is the maximum/minimum capacity of TES.

The power constraint and climbing constraint satisfied by TES are consistent with those of EES and will not be discussed in this paper.

4 COMPREHENSIVE DEMAND RESPONSE MODEL OF LOAD SIDE

The IDR behavior of users on the load side of the CHP-MG system is divided into the response of electric load demand and the response of thermal load demand. It is assumed that the user's IDR mode adopts the following strategies:

1) In the case of satisfying user satisfaction, the thermal load can be flexibly responded by adjusting the demand of electric/gas heat load and the reduction of heat load.
2) In the case of satisfying user satisfaction, the electrical load can be flexibly responded by shifting and interrupting and reducing the electrical load.

Among them, the flexible electrical loads, that is, electrical loads that participate in response, can be divided into the time-shiftable and interruptible electric load, the time-shiftable non-interruptible load, and the curtailable electric load. Flexible heat loads, that is, the heat loads that participate in response, are reducible heat loads. In addition, for flexible heat load, this paper considers the user's choice of heating mode.

4.1 Flexible Electrical Load

4.1.1 Time-Shiftable and Interruptible Load

Time-shiftable and interruptible load means that the load's power consumption time can be shifted and interrupted according to system requirements. The working duration and the number of interruptions of different electrical appliances are different. Assuming that the number of devices participating in demand response is $n_{b,int}$, the charging time of device n is $T_{b,n}$, the number of interrupts is $q_{b,n}$, and the transferable range is $[t_{b,n,s}, t_{b,n,e}]$, the following relationship must be satisfied:

$$\begin{cases} q_{b,n} \le q_{b,n,\max}, \\ U_b = \left[t_{b,n,s1}, t_{b,n,e1}\right] \cup \left[t_{b,n,s2}, t_{b,n,e2}\right] \\ \qquad \cdots \cup \left[t_{b,n,s\left(q_{b,n}+1\right)}, t_{b,n,e\left(q_{b,n}+1\right)}\right]. \end{cases} \tag{12}$$

Here, $q_{b,n,\max}$ is the maximum number of interruptions of device n; $t_{b,n,si}/t_{b,n,ei}$ is the actual time point of the ith start/end of device n; and U_b is the set of working time periods after the device n is shifted and interrupted.

The electric load L_{b0}^t/L_b^t expression before/after the translation and interruption is

$$\begin{cases} L_{b0}^t = \sum\limits_{n=1}^{n_{b,\text{int}}} L_{b0,n}^t \\ L_b^t = \sum\limits_{n=1}^{n_{b,\text{int}}} L_{b,n}^t \\ L_{b0,n}^t = \begin{cases} 0 & t \notin \left[t_{b,n,s0}, t_{b,n,e0}\right] \\ P_{b,n} & t \in \left[t_{b,n,s0}, t_{b,n,e0}\right] \end{cases} \\ L_{b,n}^t = \begin{cases} 0 & t \notin U_b \\ P_{b,n} & t \in U_b \end{cases} \end{cases} \tag{13}$$

Here, $P_{b,n}$ is the rated power of the device n; $L_{b0,n}^t$ is the ideal response of equipment n to the electrical load demand in time period t; and $L_{b,n}^t$ is the response electrical load demand of device n after time shift and interruption in time period t.

4.1.2 Time-Shiftable and Non-Interruptible Power Loads

Time-shiftable and non-interruptible power load means that the load's power consumption time can be shifted according to system requirements, and the working duration of different electrical appliances is different. The modeling process of the electrical loads L_{a0}^t, L_a^t, etc., before/after translation is only a case when the number of interruptions in 4.1.1 is 0, so this section will not repeat them.

4.1.3 Electric Load Can Be Reduced

In the case of satisfying user satisfaction, the electric load can be appropriately reduced, and the electric load curve of the system load side can be smoothed. The correlation is as follows:

$$\begin{cases} L_c^t = L_c^t - \Delta L_c^t, \\ \Delta L_c^t = I_{c,e} \varepsilon_{c,e}^t L_{c0}^t, \\ \varepsilon_{c,e,\min} \le \varepsilon_{c,e}^t \le \varepsilon_{c,e,\max}. \end{cases} \tag{14}$$

Here, ΔL_c^t is the electrical load difference before/after reduction in period t; L_c^t is the electrical load after reduction in time period t; L_{c0}^t is the electric load participating in the reduction in time period t; $\varepsilon_{c,e}^t$ is the electric load reduction coefficient after reduction in time period t; $\varepsilon_{c,e,\max}/\varepsilon_{c,e,\min}$ is the maximum/minimum load reduction factor; and $I_{c,e}$ is the sign indicating whether the electric load is reduced, which is 1 when it is reduced.

4.2 Flexible Heat Load

4.2.1 Response of Heating Mode

The peak period of electrical loads such as air conditioners and electric furnaces is roughly the same as the peak period of grid power supply. Under the stimulation of price, some users gave up the heating method of electric heating and switched to the gas heating method of central heating. The relevant relationship is as follows:

$$\begin{cases} \Delta H_a^t = I_{a,h} \varepsilon_{a,h}^t H_{a0}^t, \\ D_a^t = \Delta H_a^t, \\ H_a^t = H_{a0}^t - D_a^t, \\ \varepsilon_{a,h,\min} \le \varepsilon_{a,h}^t \le \varepsilon_{a,h,\max}. \end{cases} \tag{15}$$

Here, ΔH_a^t is the heat load difference before/after the response by the heating method in the period t; H_{a0}^t is the original gas heat load participating in the response of the heating mode in time period t; H_a^t/D_a^t is the gas/electric heating load demand after the response of the heating mode in the period t; $\varepsilon_{a,h}^t$ is the replacement coefficient in time period t; $\varepsilon_{a,h,\max}/\varepsilon_{a,h,\min}$ is the maximum/minimum replacement coefficient; and $I_{a,h}$ is the sign indicating whether the heating mode response occurs to the heat load, which is 1 when the response occurs.

4.2.2 Reduced Heat Load

The main consideration of the heat load that can be reduced is the hot water load. Under the lowest water temperature $T_{w,\min}$ acceptable by the user, appropriate reduction of the heat load can smooth the heat load curve on the load side of the system. The correlation is as follows:

$$\begin{cases} H_{b,\min}^t = C_w \rho_w v_w^t \left(T_{w,\min} - T_{w,ini}\right), \\ H_{b0}^t = C_w \rho_w v_w^t \left(T_w^t - T_{w,ini}\right), \\ H_b^t = H_{b0}^t - \Delta H_b^t, \\ \Delta H_b^t = I_{b,h} \varepsilon_{b,h}^t \left(H_{b0}^t - H_{b,\min}^t\right). \end{cases} \tag{16}$$

Here, C_w, ρ_w are the specific heat capacity and density of water; v_w^t is the user's hot water demand in time period t; T_{w0} is the initial water temperature (15°C); T_w^t is the ideal average temperature of hot water for the user in time period t; $H_{b,\min}^t$ is the minimum hot water power required by the user in time period t; ΔH_b^t is the hot water load difference before/after the reduction in period t; H_b^t is the hot water load reduced in time period t; H_{b0}^t is the hot water load participating in the reduction in time period t; $\varepsilon_{b,h}^t$ is the hot water load reduction coefficient in period t, whose value is between 0 and 1; and $I_{b,h}$ is a flag indicating whether the hot water load has been reduced, which is 1 when the reduction occurs.

4.3 IDR Price Compensation Mechanism

Price compensation encourages users to actively participate in demand response. Unlike the traditional fixed-ratio price compensation, this paper uses a flexible price compensation with the compensation cost f_c shown as follows:

$$f_c = \sum_{t=1}^{24} \begin{pmatrix} \lambda_{ab,e}^t c_{ab,e}^t \Delta L_a^t + \\ \lambda_{ab,e}^t c_{ab,e}^t \Delta L_b^t + \\ \lambda_{c,e}^t c_{c,e}^t \Delta L_c^t + \\ \lambda_{a,h}^t c_{a,h}^t \Delta H_a^t + \\ \lambda_{b,h}^t c_{b,h}^t \Delta H_b^t \end{pmatrix}. \tag{17}$$

Here, $c_{ab,e}^t$, $c_{c,e}^t$ are the unit compensation price for participating in time shift and interruption and reducing the response electric load in time period t; $c_{a,h}^t$, $c_{b,h}^t$ are the unit compensation price involved in adjusting the electric heating load and reducing the heat load response during period t; and $\lambda_{ab,e}^t$, $\lambda_{c,e}^t$, $\lambda_{a,h}^t$, and $\lambda_{b,h}^t$ are auxiliary variables with values between 0 and 1.

5 SOURCE–LOAD COORDINATION AND INTERACTIVE OPTIMIZATION SCHEDULING

The optimal operation model of CHP-MG with IDR, decoupling the thermoelectric connection through the energy storage device, considering the multi-energy complementary characteristics, jointly formulates the optimal output plan of each coupling device from both sides of the source and the load, so as to improve the economy and supply and demand of the microgrid stability.

5.1 Objectives

5.1.1 Economics

When considering CHP-MG economy F_1, both the supply side and the demand side need to be considered. The energy supply cost f_{CG} on the supply side includes the purchase cost of input energy and the aging cost of equipment, while the economy f_{CD} on the demand side is mainly reflected in the compensation cost of users participating in IDR:

$$\begin{cases} F_1 = \min\left(f_{CG} + f_{CD}\right), \\ f_{CG} = f_{grid} + f_{EES} + \\ f_{TES} + f_{MT} + f_{GB} + f_{H_a}, \\ f_{CD} = f_c. \end{cases} \tag{18}$$

1) Large grid electricity purchase cost f_{grid}:

$$f_{grid} = \sum_{t=1}^{24} P_{grid}^t c_{buy}^t \tag{19}$$

Here, P_{grid}^t and c_{buy}^t are the purchase power and unit price of electricity from the microgrid to the large grid in time period t, respectively.

2) EES charge and discharge aging cost f_{BT}:

$$f_{EES} = \sum_{t=1}^{24} E_{EES}^t c_{EES}^t \tag{20}$$

Here, c_{EES}^t is the unit aging price of EES in time period t.

3) TES charge and discharge aging cost f_{BT}:

$$f_{TES} = \sum_{t=1}^{24} E_{TES}^t c_{BT}^t \tag{21}$$

Here, c_{TES}^t is the unit aging price of TES in time period t.

4) MT natural gas cost f_{MT}:

$$f_{MT} = \sum_{t=1}^{24} c_{gas}^t \frac{P_{MT}^t}{\eta_{MT} LHV_{gas}}. \tag{22}$$

Here, c_{gas}^t is the price of natural gas in time period t and LHV_{gas} is the low calorific value of natural gas, which is 9.7 kWh/m^3.

5) GB natural gas cost f_{GB}:

$$f_{GB} = \sum_{t=1}^{24} c_{gas}^t \frac{Q_{GB}^t}{LHV_{gas}} \tag{23}$$

6) The cost of natural gas for electric heat to gas heat f_{H_a} is

$$f_{H_a} = \sum_{t=1}^{24} c_{gas}^t \frac{H_{H_a}^t \lambda_{H_a}}{LHV_{gas}} \tag{24}$$

Here, λ_{H_a} is the conversion factor of electricity–heat load.

5.1.2 Stability of Supply and Demand

While pursuing economy, CHP-MG system operators should also focus on providing a stable energy supply for users.

On the supply side, the stability of MT, GB, and external power grid is mainly considered. The stability of MT and GB output can reduce the frequent regulation of equipment, reduce the failure rate, and prolong the service life. In addition, as the main consumption equipment of natural gas, the MT and GB can also improve the input stability of natural gas and reduce the complexity of transportation and management. Keeping the power interaction with the external grid stable improves the stability and safety of the system while reducing the stress caused by the CHP-MG system to the outside.

On the demand side, it mainly measures the discrete degree of the difference between the user's electricity load and the wind power load (LW). Because wind power load is easily affected by environmental factors, its load curve is highly discrete, which increases the difficulty in hardware and software regulation of microgrid. The traditional load prediction curve is usually "peak-cutting and valley-filling" by an energy storage device, but the load prediction curve often represents a larger possible state of wind turbine output while ignoring other output possibilities. In this paper, the mathematical expectation P_{WT}^t of P_w in time period t is taken as the "equilibrium point" of output possibility of wind turbine in time period t, so that the optimized operation process of the system works near the "equilibrium point" of wind turbine. In addition, the CHP-MG system adjusts the electrical load curve through IDR and smoothes the difference curve between user power load and wind power load.

In this paper, the weighted value of the change rate of the output curve of each load or equipment is used to evaluate the supply and demand stability coefficient F_2, which is defined as

$$\begin{cases} F_2 = \min\left(f_2\right), \\ f_2 = a_1\sigma_{MT} + a_2\sigma_{GB} + a_3\sigma_{grid} + \\ \qquad a_4\sigma_{l-W} + a_5\sigma_{\sigma}, \\ \quad \sigma = \left[\sigma_{MT}, \sigma_{GB}, \sigma_{grid},\ \ \sigma_{l-W}\right]. \end{cases} \tag{25}$$

Here, σ_{MT}, σ_{GB}, σ_{grid}, and σ_{l-W} are the standard deviation of MT power generation, GB heat generation power, external grid output power, and LW; σ_{σ} is the penalty function of equilibrium within the stability of supply and demand, whose value is the standard deviation of matrix σ; and a_1, a_2 ... a_5 are coefficients greater than 0.

The relevant parameters must meet the following conditions:

$$\begin{cases} \sigma_{MT} \le \sigma_{MT,\max}, \\ \sigma_{GB} \le \sigma_{GB,\max}, \\ \sigma_{grid} \le \sigma_{grid,\max}, \\ \sigma_{l-W} \le \sigma_{l-W,\max}, \\ \sigma_{\sigma} \le \sigma_{\sigma,\max}, \\ a_1 + a_2 + a_3 + a_4 + a_5 = 5. \end{cases} \tag{26}$$

Here, $\sigma_{MT,\max}$, $\sigma_{GB,\max}$, $\sigma_{grid,\max}$, $\sigma_{l-W,\max}$ are upper bounds on σ_{MT}, σ_{GB}, σ_{grid}, σ_{l-W}.

5.2 Threshold

Whether the CHP-MG can provide a comfortable energy experience for customers is also an important measure indicating whether the microgrid is competitive in the energy market. To quantify this type of auxiliary service, user satisfaction is evaluated in terms of load deviation rate, IDR price compensation factor, and adjustable rate of electricity and heat production. In this paper, user satisfaction is divided into power supply satisfaction $f_{UC,e}$ and heating satisfaction $f_{UC,h}$, which need to meet

$$\begin{cases} f_{UC,e} \ge UC_{e,\min}, \\ f_{UC,h} \ge UC_{h,\min}. \end{cases} \tag{27}$$

Here, $UC_{e,\min}/UC_{h,\min}$ is the lower limit of power supply/thermal satisfaction.

5.2.1 Satisfaction of Power Supply

The CHP-MG system characterizes power supply satisfaction (ESS) by the electric load deviation rate, the power generation adjustable rate, and other indicators. Among them, price compensation for IDR can reduce the negative impact on user comfort caused by electrical load deviation. Its power supply satisfaction is defined as

$$f_{UC,e} = \theta_e\left(1 - d_e\right) \quad . \tag{28}$$

1) Adjustable rate of electricity production θ_e:

$$\begin{cases} \theta_e = c\theta_{e,do} + (1-c)\theta_{e,up}, \\ c \in (0,1). \end{cases} \tag{29}$$

Here, $\theta_{e,do}/\theta_{e,up}$ indicates the power generation can increase/cut the rate, respectively.

$\theta_{e,do}$ is given as

$$\theta_{e,do} = \frac{1}{24}\sum_{t=1}^{24}\theta_{e,do}^{t}. \tag{30}$$

Here, $\theta_{e,do}^{t}$ is the amount of power generation that can be reduced in time period t. The main consideration is the amount of electricity that can be reduced by MT and EES on the premise of meeting the upper and lower limit constraints and climbing constraints described above.

$\theta_{e,up}$ is the amount of electricity that can be added in the t period, similar to $\theta_{e,do}^{t}$. The main consideration is the amount of electricity that MT and EES can add on the premise of meeting the upper and lower limit constraints and climbing constraints described above.

2) The electrical load deviation rate d_e is related to $\kappa_{ab,e}^{t}$ (electric load deviation rate due to time shift and interruption), $\kappa_{c,e}^{t}$ (electric load deviation rate due to curtailment), $\lambda_{ab,e}^{t}$, $\lambda_{c,e}^{t}$. It is defined as

$$\begin{cases} d_e = \dfrac{b_1 e^{-b_1 d_{ab,e}} d_{ab,e} + b_2 e^{-b_2 d_{c,e}} d_{c,e}}{b_1 e^{-b_1 d_{ab,e}} + b_2 e^{-b_2 d_{c,e}}}, \\ d_{ab,e} = \dfrac{1}{24}\displaystyle\sum_{t=1}^{24}\left(\kappa_{ab,e}^{t} - \lambda_{ab,e}^{t}\right), \\ d_{c,e} = \dfrac{1}{24}\displaystyle\sum_{t=1}^{24}\left(\kappa_{c,e}^{t} - \lambda_{c,e}^{t}\right). \end{cases} \tag{31}$$

The influence of the deviation rate of power generation on user satisfaction is often dominated by the inferior party, so the exponential variable is introduced as the weight in the above formula. If $d_{ab,e}$ or $d_{c,e}$ is obviously too large, its weight will increase sharply.

5.2.2 Satisfaction With Heat Supply

In the CHP-MG system, heat supply satisfaction (HSS) is characterized by the heat load deviation rate and heat production adjustable rate. Among them, price compensation for IDR can reduce the negative impact on user comfort caused by thermal load deviation. Satisfaction with heat supply is defined as

$$f_{UC,h} = \theta_h\left(1 - d_h\right). \tag{32}$$

1) Heat production adjustable rate θ_h:

$$\begin{cases} \theta_h = g\theta_{h,do} + (1-g)\theta_{h,up}, \\ g \in (0,1). \end{cases} \tag{33}$$

Here, $\theta_{h,do}/\theta_{h,up}$ is the curtailment/increment of power generation in period t. The main consideration is the amount of power that can be cut/increased by GB and TES with the need to satisfy the upper and lower constraints and climbing constraints described above.

2) The heat generation deviation rate d_h is related to $d_{a,h}$ (the heat load deviation rate due to the selection of the heating method), $d_{a,h}$ (the heat load deviation rate due to the reduction), $\lambda_{a,h}^{t}$, and $\lambda_{b,h}^{t}$. Its definition is consistent with

the heat generation deviation rate and will not be repeated in this paper.

5.3 Constraints

The CHP-MG system constructed in this paper includes the demands of both thermal and electric loads and needs to satisfy the electric and thermal power balance and the large grid interaction power constraints in addition to the equipment operation constraints.

1) Electric power balance:

$$P_{WT}^{t} + P_{MT}^{t} + P_{grid}^{t} + P_{EES,d}^{t} = P_{EES,c}^{t} + P_{load} + L_{a}^{t} + L_{b}^{t} + L_{c}^{t} \quad (34)$$

Here, P_{WT}^{t} generates power of WT in time period t and P_{load} is the basic electrical load required by users on the load side in time period t.

2) Thermal power balance:

$$Q_{GB}^{t} + Q_{HE}^{t} + Q_{TES,d}^{t} = Q_{TES,c}^{t} + P_{phot} + H_{a}^{t} + H_{b}^{t} \quad (35)$$

Here, P_{phot} is the basic heat load required by users on the load side in time period T.

3) Large grid interactive power constraints:

$$\begin{cases} P_{grid,\min} \le P_{grid}^{t} \le P_{grid,\max}, \\ dP_{grid,\min} \le P_{grid}^{t} - P_{grid}^{t-1} \\ \qquad \le dP_{grid,\max}. \end{cases} \quad (36)$$

Here, $P_{grid,\max}/P_{grid,\min}$ and $dP_{grid,\max}/dP_{grid,\min}$ are the upper and lower limits of the power purchase and ramp rate of the large grid.

6 IMPROVED MULTI-OBJECTIVE GREY WOLF OPTIMIZER

6.1 Multi-Objective Grey Wolf Optimizer

The GWO (Mirjalili et al., 2014) is a new intelligent algorithm proposed by Mirialili et al., in 2014. In 2015, on this basis, an MOGWO (Mirjalili et al., 2016) was proposed.

The optimization process of MOGWO is divided into the following steps:

1) Social class stratification

In the MOGWO, the objective function value of grey wolf individuals in each iteration process is calculated, the non-dominated individuals are determined, and the excellent population Archive is updated. And the α, β, δ wolves are determined by the roulette method, and the rest are ω wolves, so as to realize the classification of the grey wolf population.

2) Surrounded

The position of the wolf represents a problem solved by the algorithm. The behavior of being surrounded by grey wolves during hunting is defined as

$$\begin{cases} D = \left|C \cdot X_p(t) - X(t)\right|, \\ X(t+1) = X_p(t) - A \cdot D. \end{cases} \quad (37)$$

Here, t is the current iteration number; D is the distance between the individual and the prey; A and C are synergy coefficient vectors; $X_p(t)$ represents the position vector of prey; and $X(t)$ represents the position vector of the current grey wolf. A and C are defined as follows:

$$\begin{cases} A = 2a \cdot r_1 - a, \\ C = 2 \cdot r_2. \end{cases} \quad (38)$$

Here, a is the convergence factor. For the specific definition, see **Eq. 41**. r_1 and r_2 are random variables between 0 and 1.

ω wolf surrounds its prey under the leadership of α, β, δ wolves, and its position update formula is as follows:

$$\begin{cases} D_\alpha = \left|C_1 \cdot X_\alpha(t) - X(t)\right|, \\ D_\beta = \left|C_2 \cdot X_\beta(t) - X(t)\right|, \\ D_\delta = \left|C_3 \cdot X_\delta(t) - X(t)\right|. \end{cases} \quad (39)$$

Here, D_α, D_β, D_δ are the distances between the α, β, δ wolves and the current individual grey wolf, respectively; $X_\alpha(t)$, $X_\beta(t)$, $X_\delta(t)$ are the current position vectors of α, β, δ wolves, respectively; and C_1, C_2, C_3 are random variables.

$$\begin{cases} X_1 = X_\alpha(t) - A_1 \cdot (D_\alpha), \\ X_2 = X_\beta(t) - A_2 \cdot \left(D_\beta\right), \\ X_3 = X_\delta(t) - A_3 \cdot (D_\delta), \\ X(t+1) = \dfrac{X_1 + X_2 + X_3}{3}. \end{cases} \quad (40)$$

Here, $X(t+1)$ is the updated position vector for ω wolf.

3) Attack prey

When the prey stops moving, the wolf attacks it to complete the hunt. The timing of the grey wolf attacking its prey is controlled by the value of a. As shown in **Eq. 41**, the size of a decreases linearly with the decrease of the number of iterations. When a drops to 0, that is, the maximum number of iterations, the encirclement is stopped and the prey is attacked, that is, the iteration is stopped, and the result is output:

$$a = 2 - 2 \cdot \frac{t}{t_{\max}} \quad (41)$$

Here, $t_{\max}$ is the maximum number of iterations.

6.2 Improved Multi-Objective Grey Wolf Optimizer

The optimization problems of CHP-MG systems are non-linear optimization problems with complex constraints and high solution dimensionality. When using the original MOGWO to solve such problems, it is easy to converge prematurely and fall into local optimum. To remedy such problems, Mirjalili et al. (2016) proposed a reduced-order aggregate model based on the balanced truncation approach and Wang et al. (2021b) proposed a reduced-order small-signal closed-loop transfer function model based on Jordan continued-fraction expansion. However, the dimensionality reduction method mentioned above is difficult to apply under the condition that the system input variables are closely related to the target value or threshold value. Therefore, the improvement of the multi-objective grey wolf optimization algorithm in this paper mainly focuses on the search process and form of wolves (Taha and Elattar, 2018; Rui et al., 2020a), as follows:

1) The MOGWO algorithm's insufficient exploration ability affects the global search ability and local convergence ability of the whole algorithm. The size of control parameter a in **Eq. 41a** affects the overall detection distance of the wolves. In this paper, the linearly reduced a is changed to the cosine function form of **Eq. 42**. In the early stage, the decline speed of a slowed down, which improved the global search ability of the algorithm. The local convergence of the algorithm can be ensured by slowing down the later descent speed:

$$a = 2 \cdot \cos\left(\frac{k}{2\pi k_{\max}}\right) \tag{42}$$

2) The original MOGWO, based on the crowding of the Archive population, uses a roulette wheel to pick wolves α, β, δ (the less crowded wolf is more likely to be chosen). However, when the three leading wolves are all local optimal solutions, the algorithm still has the risk of falling into local optimal solutions. In this paper, the wolves are divided into three groups by the FCM clustering algorithm, the non-dominant individuals in each group are determined, and Archive1~Archive3 are updated. The leader wolf from each group was selected as Wolf α,Wolf β, and Wolf δ by the above roulette method. This method increases the diversity of the population and avoids falling into local optimum.
3) The three groups of wolves (except the leader wolf) are randomly drawn with probability P to select the hunter, and its position is updated by **Eq. 37** (displacement update formula of grey wolf algorithm). The cooperative search ability of each group of pursuers is ensured. The other wolves (except the leader wolf) in the unselected groups were used as vigilant, and the target was the leader wolf in each group to ensure the search ability of the vigilant group within the group. The group update was carried out through **Eq. 43** (displacement updating formula of particle swarm optimizer) (Kennedy and Eberhart, 1995):

$$\begin{cases} \Delta w = \dfrac{(w_{\max} - w_{\min})\left[f\left(x_i^d\right) - f_{\min}^d\right]}{f_{average}^d - f_{\min}^d}, \\ w_i^d = \begin{cases} w_{\min} + \Delta w, f\left(x_i^d\right) \le f_{average}^d \\ w_{\max}, f\left(x_i^d\right) > f_{average}^d \end{cases} \\ V_i^{k+1} = w_i^d V_i^k + c_1 rand_1\left(P_{best} - X_i^k\right) + \\ \qquad c_2 rand_2\left(G_{best} - X_i^k\right), \\ X_i^{k+1} = X_i^k + V_i^{k+1}. \end{cases} \tag{43}$$

Here, w_i^d is the inertia weight; $w_{\max}/w_{\min}$ is the preset maximum/minimum inertia coefficient; $f_{average}^d$, $f_{\min}^d$ are the average fitness and minimum fitness of all particles in the dth iteration; V_i^k is the velocity of the kth iteration of the current particle; X_i^k is the position of the kth iteration of the current particle; P_{best} is the best solution for the individual; G_{best} is the best solution for the population; c_1 and c_2 are learning factors; and $rand_1$ and $rand_2$ are random numbers between 0 and 1.

The steps of applying the improved multi-objective grey wolf algorithm to CHP-MG system scheduling optimization are as follows:

Step 1: Set the parameters and data of the CHP-MG optimization model.
Step 2: Set parameters such as the number of grey wolves, the maximum number of iterations, and the excellent population Archive and initialize the grey wolf population.
Step 3: The grey wolf population (CHP-MG scheduling scheme) is grouped by the FCM clustering algorithm, and the α, β, and δ wolves are selected according to the improved method at (2), that is, the optimal scheme.
Step 4: The remaining wolves in each group except the leader wolf are randomly selected with probability P, that is, some schemes except the optimal scheme in each group of scheduling schemes are selected, and their positions are updated through the displacement update formula of the grey wolf algorithm.
Step 5: For each group of wolves that are not selected except the head wolf in step 4, take the head wolf of each group as the objective function (the optimal scheme of each group) and update their positions in groups through the displacement update formula of particle swarm optimization.
Step 6: Calculate the objective function value of the whole grey wolf population, filter the threshold, determine the non-dominated individuals, and update Archive.
Step 7: Judge whether the maximum number of iterations has been reached. If yes, output Archive. It is the Pareto solution set of the optimal scheduling scheme of CHP-MG system. On the contrary, skip to step 3 until the termination condition is met.

7 EXAMPLE ANALYSIS

7.1 Basic Data

In order to verify the effectiveness of the model and algorithm described in this paper, example simulation was carried out by referring to the system micro-source device parameters, energy storage device parameters, energy purchase and sale price, and load data in the examples in the literature (Li et al., 2021b; Yang et al., 2016; Wang et al., 2020; Li et al., 2021c; Li et al., 2021d; Lu et al., 2021; Zhang et al., 2021). The total scheduling time is 24 h, and the unit scheduling time is 1h.

TABLE 1 | Description of four scenarios.

Scene	Flexible electrical load	Flexible heat load
Case1	×	×
Case2	√	×
Case3	×	√
Case4	√	√

The prediction curves of basic heat load, hot water load, electric load, and response of heating mode are shown in **Supplementary Figure 1.** The wind turbine output prediction curve is shown in **Supplementary Figure 2.** The timeshare price of energy (power grid sales price and natural gas price) is shown in **Supplementary Figure 3.** Refer to **Supplementary Table 1** for the parameters of micro-source equipment. See **Supplementary Table 2** for the parameters of the energy storage device. Flexible time-shifting non-interruptible electrical load and time-shifting interruptible electrical load mainly consider the time-shifting characteristics and interruptible characteristics of washing machine (WM), dishwasher (DW), rice cooker (RC), dryer (DY), and sweeper (SE). A total of 500 households in this area are divided into five categories: A, B, C, D, and E, according to their energy consumption habits. The operating characteristics of various household appliances are shown in

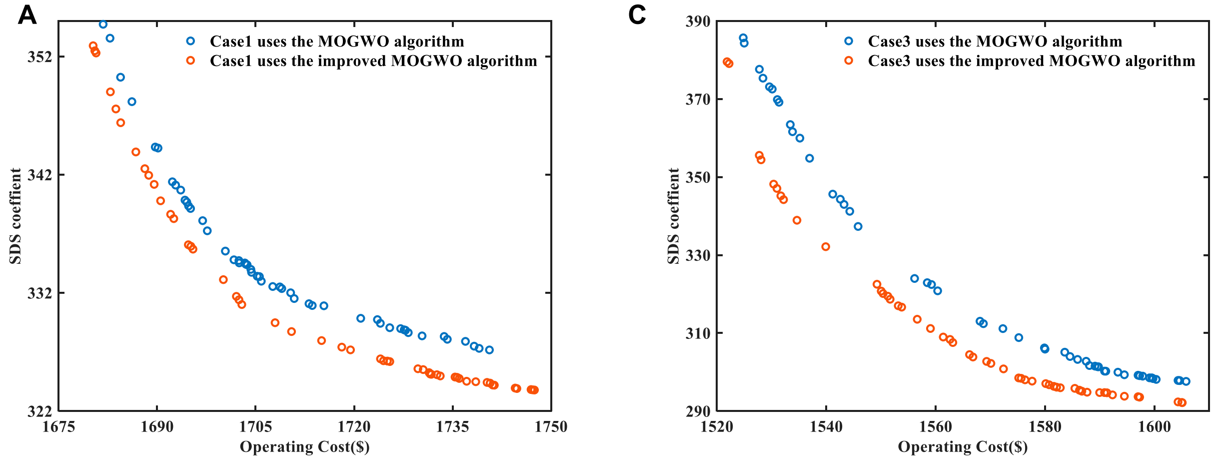

Case1 Pareto convergence curve of solution set

Case3 Pareto convergence curve of solution set

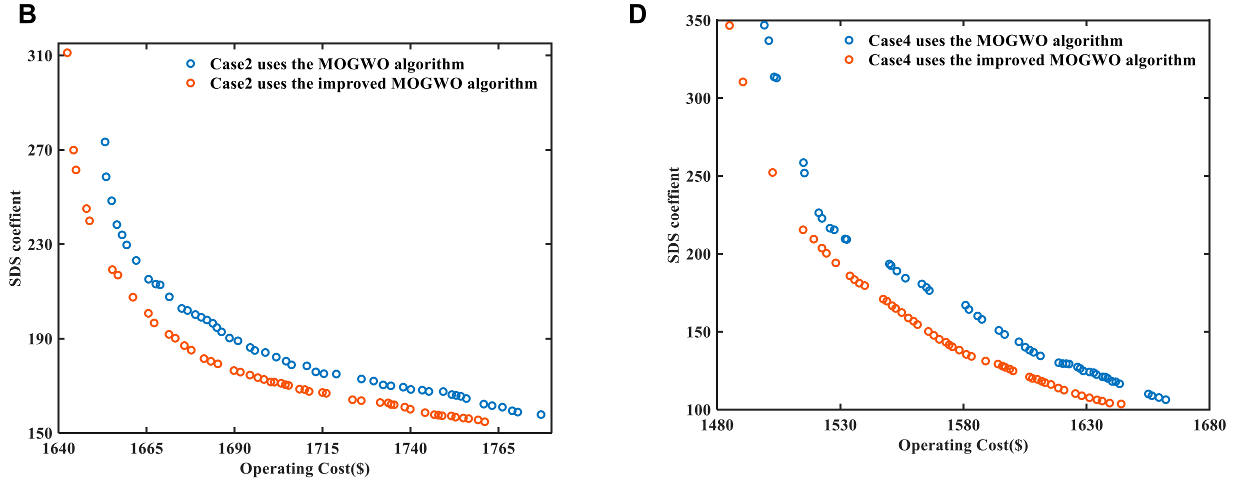

Case2 Pareto convergence curve of solution set

Case4 Pareto convergence curve of solution set

FIGURE 3 | Convergence curves of Pareto solution sets in four scenarios. **(A)** Case1 Pareto convergence curve of solution set. **(B)** Case2 Pareto convergence curve of solution set. **(C)** Case3 Pareto convergence curve of solution set. **(D)** Case4 Pareto convergence curve of solution set.

TABLE 2 | Numerical range of optimization results of four scenarios.

Scene	Total cost ($)	SDS coefficient
Case1	(1,680.25, 1747.47)	(323.78, 352.90)
Case2	(1,642.46, 1761.09)	(154.77, 311.16)
Case3	(1,521.87, 1605.07)	(292.16, 379.55)
Case4	(1,484.54, 1643.75)	(103.65, 346.61)

Supplementary Table 3. See **Supplementary Table 4** for energy use time for each type of household.

7.2 Analysis of Simulation Results

In order to further verify the validity of the model, four operating modes are selected for comparison, as shown in **Table 1**.

Using MATLAB software to calculate the above four scenarios, in the improved multi-objective grey wolf algorithm, the total population is 100. The Pareto solution set convergence curves of the four scenarios are shown in **Figure 3**, and the optimization results are shown in **Table 2**.

It can be seen from the analysis in **Figure 3** that the improved MOGWO has better convergence characteristics than the original MOGWO algorithm, and its search accuracy is also high. At the same time, due to the improvement of the update strategy of Pareto solution set, its diversity and distribution characteristics are better.

According to the analysis in **Table 2**, compared with traditional optimized operation (Case1), considering flexible electrical load and thermal load significantly improves the economy and stability of supply and demand of the system.

Considering the flexible electrical load (Case2), the total cost is only reduced by $37.79 compared to Case1, while the stability of supply and demand is improved by 52.20%. This is because the flexible electrical loads of Case2 can be time-shifted but not interrupted, and the time-shifted and interrupted electrical loads can improve the stability of supply and demand. However, the total load and energy supply form have not been greatly improved, so the cost cannot be effectively reduced. As for the curtailable electrical load, considering the user experience, the total amount of its participation in the demand response is small, and it can only slightly improve the system economy and the stability of supply and demand.

Considering the flexible heat load (Case3), the total cost is reduced by $158.38 compared to Case1, while the supply–demand stability factor is only increased by 9.77%. This is because the response of Case3’s flexible heat load heating mode turns electric heating to gas-heat central heating, which changes the energy supply form and reduces costs. For the curtailable electrical load, while adjusting the heat load curve to improving the stability of supply and demand, it avoids unnecessary waste of heat energy, thereby reducing costs. But similar to curtailable electrical loads, the effect is limited.

As for Case4, the advantages of Case2 and Case3 are taken into account because of both flexible electrical load and flexible thermal load, so that the economy and stability of supply and demand are optimal. The total cost was reduced by $195.71, and supply and demand stability improved by 67.99%.

7.2.1 Analysis of Electric Energy Operation Results

Select the scheme with the lowest total cost in Case1 ~ Case4 and analyze the power operation results through comparison.

The power operation results of Case1 are shown in **Figure 4A**. During 1–6 and 23–24 electricity price valley/gas price peak period, electricity load is mainly borne by wind energy, large grid, and electric energy stored in EES. During the electricity price peak/gas price valley period from 7 to 12 and 19 to 22, the electricity load is mainly borne by gas turbines, wind energy, and large power grids, and electricity storage equipment releases electricity. During the electricity price average/gas price peak period from 13 to 18, the electricity load is mainly borne by gas turbines, wind energy, and large power grids, and the electricity storage equipment stores excess electricity. The output of the gas turbine decreases relative to the peak period of electricity price/valley gas price.

The power operation results of Case2~Case4 are shown in **Figures 4B–D**. Compared with Case1, in the periods 7–24, the electrical load borne by the gas turbine gradually increases, and the electrical load borne by the large power grid gradually decreases. During the periods 1–6, the stored electric energy of the power storage equipment decreased significantly, and during the periods 21–24, the released electric energy increased significantly.

7.2.2 Analysis of Thermal Energy Operation Results

Select the scheme with the smallest total cost in Case1~Case4 and analyze the thermal energy operation results by comparison.

The power operation results of Case1 are shown in **Figure 5A**. During 1–6 and 23–24 electricity price valley/gas price peak period, the heat load is mainly borne by gas boilers and electric heating equipment. During the electricity price peak/gas price valley period from 7 to 12 and 19 to 22, the heat load is mainly borne by heat exchangers, gas boilers, and electric heating equipment. During the electricity price average/gas price peak period from 13 to 18, the heat load is mainly borne by heat exchangers, gas boilers, and electric heating equipment. Compared with the electricity price peak/gas price valley period, the output of the heat exchanger is reduced.

The thermal operation results of Case2~Case4 are shown in **Figures 5B–D**. Compared with Case1, in the period of 7–24, the heat load borne by the heat exchanger gradually increases. During the whole period, the heat load borne by the gas boiler increased significantly.

7.2.3 Economic Analysis

In order to further analyze the influence of the improvement mentioned above on system economy, this paper conducts economic analysis by comparing Case1 to Case4.

The scheme with the lowest total cost from Case1 to Case4 was selected for economic analysis by comparison. The optimization results are shown in **Table 3**.

Combining **Table 3** and **Figure 6**, the total cost of Case2 is reduced by $37.79 compared to that of Case1, of which the

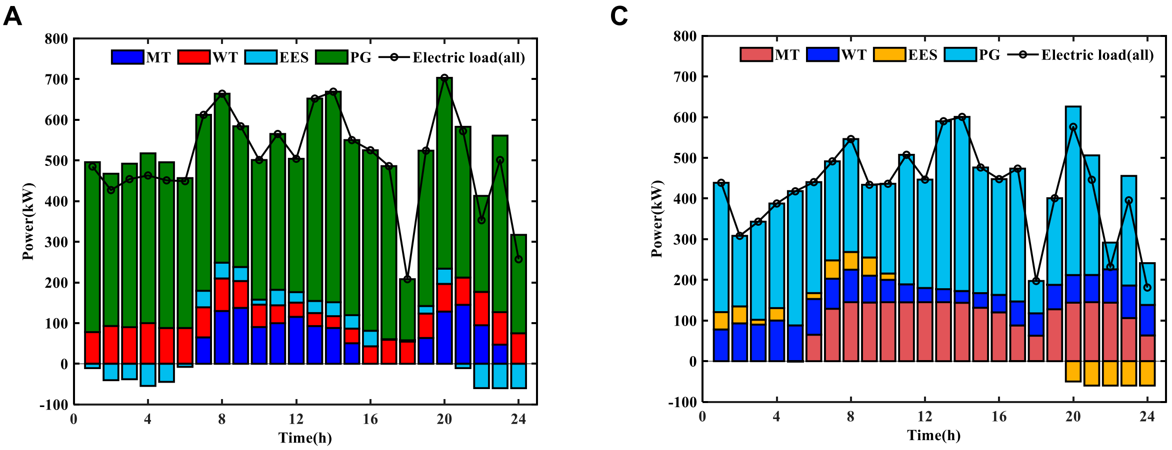

Case1 Electric energy operation results

Case3 Electric energy operation results

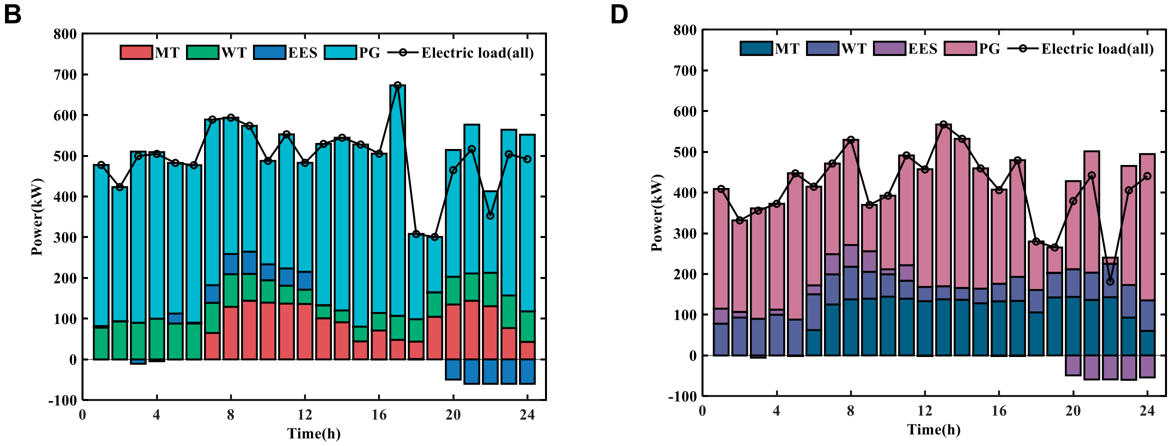

Case2 Electric energy operation results

Case4 Electric energy operation results

FIGURE 4 | Case1–4 electric energy operation results. **(A)** Case1 electric energy operation results. **(B)** Case2 electric energy operation results. **(C)** Case3 electric energy operation results. **(D)** Case4 electric energy operation results.

natural gas cost of the gas turbine is increased by $85.80 and that of the gas boiler is reduced by $6.57. The electricity purchase cost of the large grid decreased by $153.67; the aging costs of storage device were reduced by $0.03, which was negligible; an additional IDR compensation cost of $36.67 was incurred. This is because the load side of the Case2 system responds to demand by introducing flexible electrical loads to “cut peaks and fill valleys” for loads. It reduces the probability that the source-side gas turbine cannot supply energy in time due to factors such as ramp constraints, thereby increasing the natural gas cost of the gas turbine and indirectly reducing the power purchase cost of the large power grid.

Compared with that of Case1, the total cost of Case3 decreased by 158.36 dollars, of which the natural gas cost of gas turbine and gas boiler increased by 187.36 dollars and 33.42 dollars, respectively, and the power purchase cost of large power grid decreased by 406.64 dollars. This is because the response of the load-side heating mode of the system makes some users change from electric heating to more economical gas-heat central heating. Therefore, the output proportion of gas-fired boiler and heat exchanger of natural gas equipment on the source side increases, which directly or indirectly increases the natural gas cost consumed by a gas turbine and gas-fired boiler and reduces the power purchase cost of large power networks.

Compared with Case1~Case3, Case4 has the best economic indexes due to taking into account the above two advantages. The total cost decreased by $195.79. The cost of gas for the gas turbine and gas boiler increased by $195.71 and $34.18, respectively. The purchase of electricity by the large grid was reduced by $515.80. In addition, compared with Case1, Case4 increased the satisfaction of electricity consumption by 0.0715 and decreased the satisfaction degree of heat consumption by 0.2224. Among them, the improvement of power consumption satisfaction is because the load-side demand response makes users deviate from the power consumption time and the total

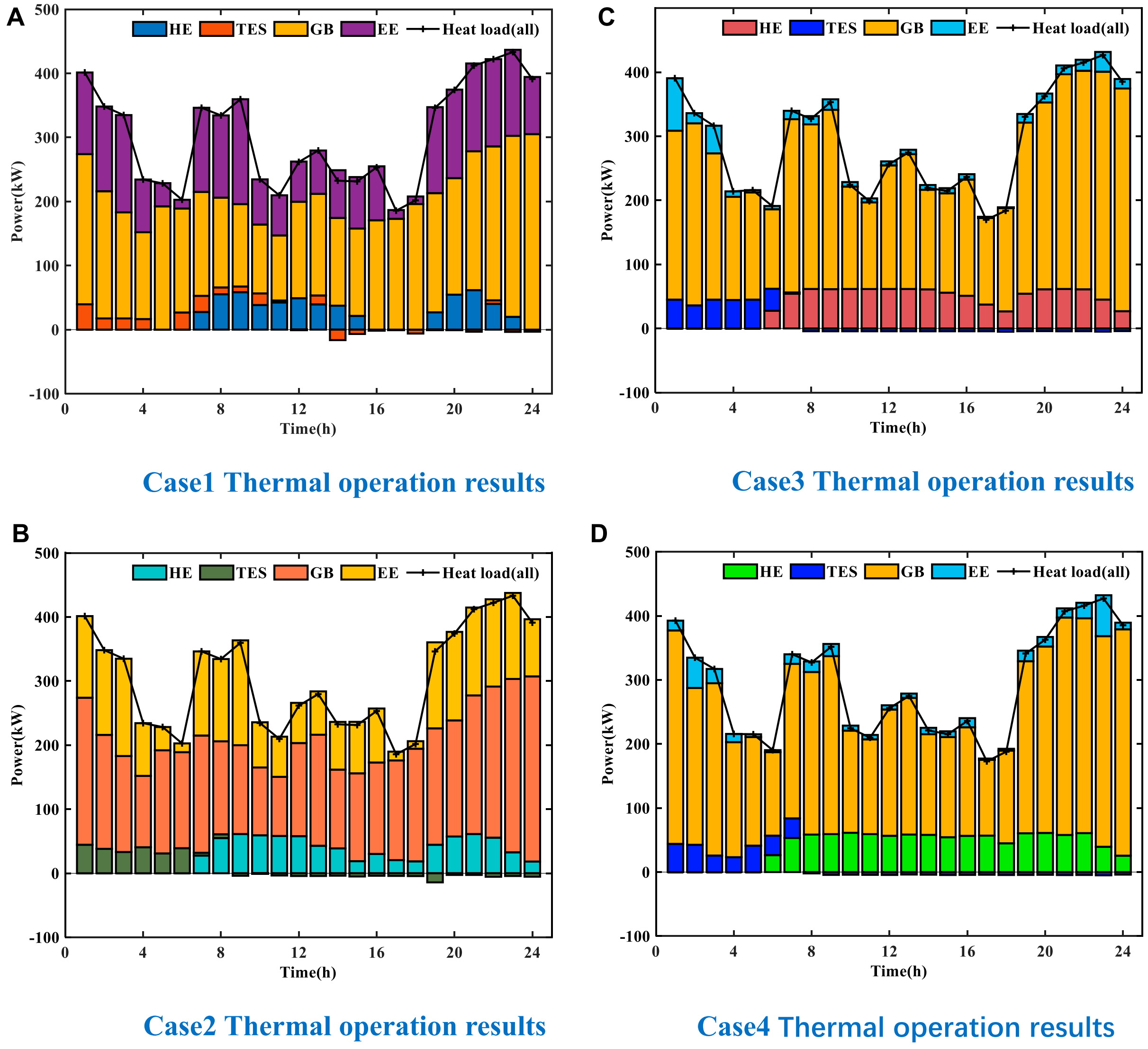

FIGURE 5 | Case1–4 thermal operation results. **(A)** Case1 thermal operation results. **(B)** Case2 thermal operation results. **(C)** Case3 thermal operation results. **(D)** Case4 thermal operation results.

TABLE 3 | Case1–4 economic-related indicators.

Scene	MT cost ($)	EES cost ($)	TES cost ($)	GB cost ($)	PG cost ($)	IDR compensation cost ($)	Total cost ($)	ESS	HSS
Case1	241.73	0.22	0.06	132.00	1,306.24	0	1,680.25	0.7794	0.9963
Case2	327.53	0.17	0.08	125.43	1,152.57	36.67	1,642.46	0.7943	0.9937
Case3	429.09	0.17	0.08	165.43	897.22	29.88	1,521.87	0.7332	0.8477
Case4	437.53	0.17	0.08	166.18	790.43	90.16	1,484.54	0.8509	0.7739

amount but also improves the power generation adjustable rate. The reduction in heat satisfaction is smaller, similar to electricity satisfaction.

7.2.4 Analysis of Supply and Demand Stability

In order to further analyze the impact of the above improvements on the stability of supply and demand of the system, this paper

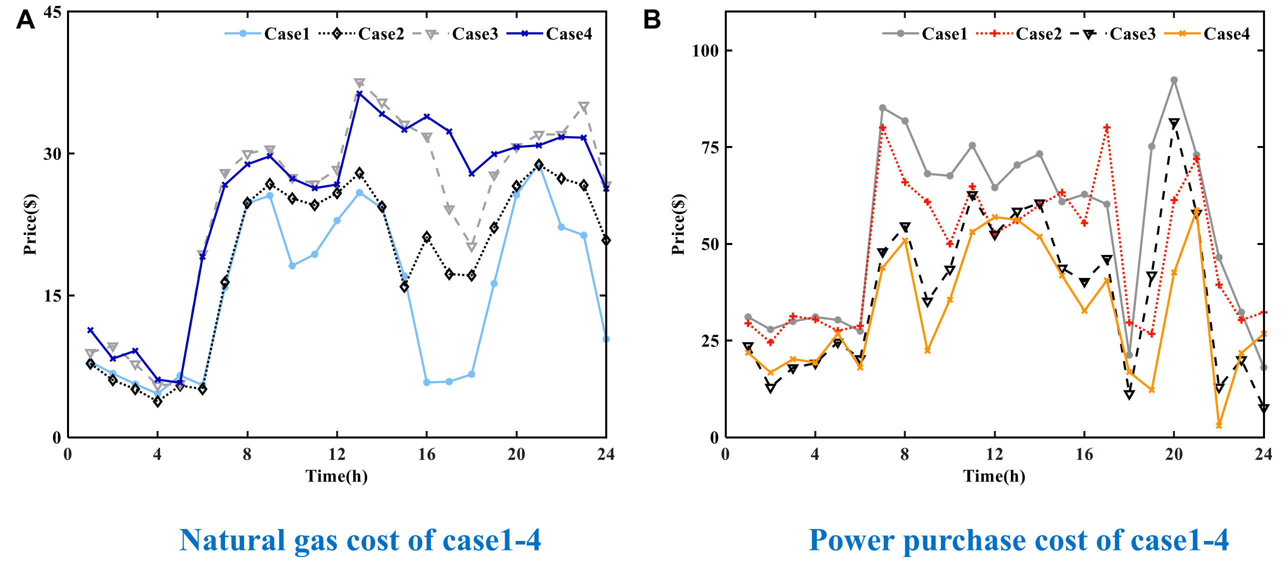

Natural gas cost of case1-4

Power purchase cost of case1-4

FIGURE 6 | Natural gas cost and power purchase cost of Case1–4. **(A)** Natural gas cost of Case1–4. **(B)** Power purchase cost of Case1–4.

TABLE 4 | Case1–4 indicators related to supply and demand stability.

Scene	LW dispersion	MT dispersion	GB dispersion	PG dispersion	SDS coefficient	ESS	HSS
Case1	128.63	28.66	47.33	76.61	323.78	0.8723	0.9859
Case2	49.32	24.46	46.88	18.52	154.77	0.7559	0.9836
Case3	99.65	43.02	58.19	67.37	292.16	0.8607	0.8221
Case4	28.16	19.56	35.78	8.37	103.65	0.7571	0.8359

conducts an analysis of the stability of supply and demand by comparing Case1~Case4.

The scheme with the smallest supply and demand stability coefficient of Case1~Case4 is selected, and the stability of supply and demand is analyzed by comparison. The optimization results are shown in **Table 4**.

As shown in **Table 4**, the overall supply and demand stability of Case2 is improved by 52.20% compared to that of Case1. The dispersion degree of LW, gas turbine, gas boiler, and large grid load curves decreased by 61.65%, 14.64%, 0.96%, and 75.51%, respectively. This is because the load side of the system reduces the dispersion degree of load curves of gas turbine, gas boiler, and large grid by introducing flexible electrical loads for demand response.

This is because the load side of the system performs demand response by introducing flexible electrical loads. While reducing the discrete degree of load curves of LW, gas boilers, and large power grids, more gas turbines are involved in power supply, which reduces the output stability of natural gas power generation equipment.

Compared with that of Case1, the overall supply and demand stability of Case3 is improved by 9.77%. The dispersion degree of LW and large grid load curves decreased by 22.53% and 10.90%, respectively, while the dispersion degree of gas turbine and gas boiler load curves increased by 50.13% and 22.94%, respectively. Obviously, the response of load side heating mode of the system not only reduces the dispersion of LW and large power grid load curve, but also makes natural gas heating equipment more involved in energy supply, thus improving the stability of its output.

Compared with that of Case1, the total stability of supply and demand of Case4 increased by 67.99%. The dispersion degree of LW, gas boilers, large power grids, and gas turbines decreases by 78.11%, 31.74%, 24.41%, and 88.92%, respectively. This is because the system load side avoids the adverse effects of Case1 and Case2 by introducing flexible electrical load and flexible thermal load to carry out demand response. Among them, the smoothness of LW curve was greatly improved, mainly reflected in the period from 7 to 24, as shown in **Figure 7A**. The smoothness of the gas turbine output curve has been greatly improved, mainly reflected in the periods 10–12, 15–19, and 1. The output curve is shown in **Figure 7B**. The smoothness of the output curve of the gas boiler has been improved to a certain extent as a whole, and its output curve is shown in **Figure 7C**. The smoothness of the output curve of the large power grid has been greatly improved as a whole, and the output curve is shown in **Figure 7D**.

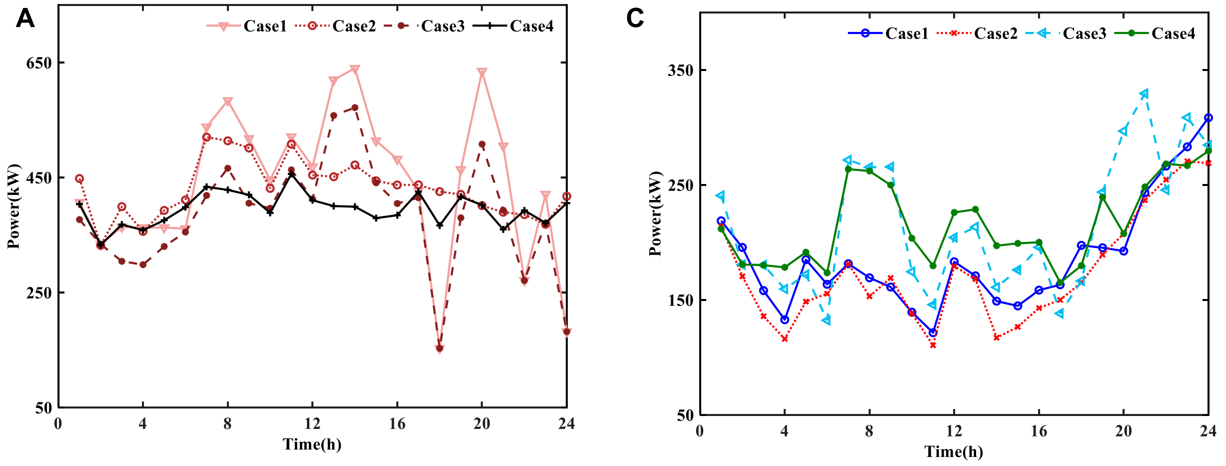

LW curve of Case1-4

Gas boiler output curve of Case1-4

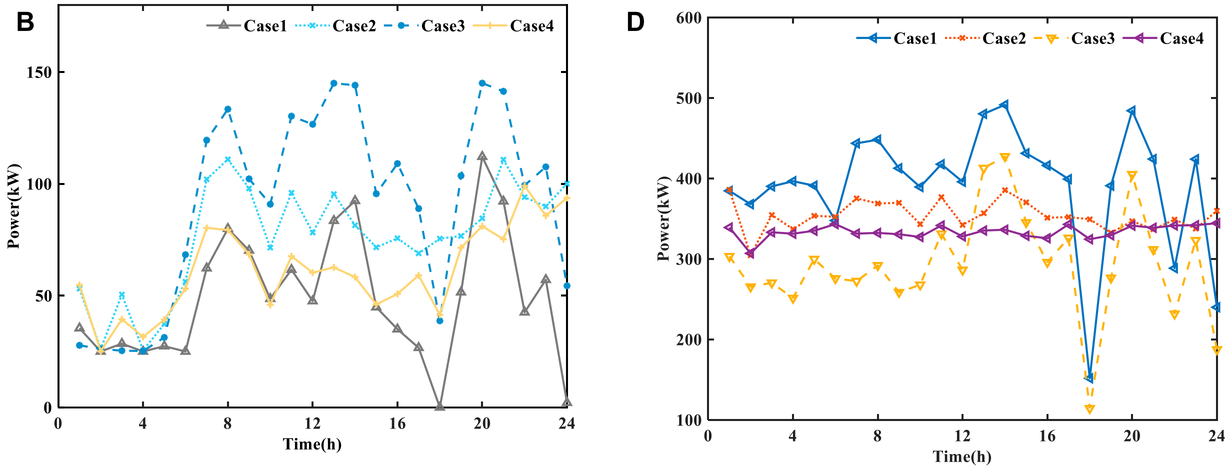

Gas turbine output curve under Case1-4

Large power grid output curve of Case1-4

FIGURE 7 | LW curve and output curve of large power grid, gas turbine, and gas boiler of Case1–4. **(A)** LW curve of Case1–4. **(B)** Gas turbine output curve of Case1–4. **(C)** Gas boiler output curve of Case1–4. **(D)** Large power grid output curve of Case1–4.

8 CONCLUSION

This paper proposes a multi-objective optimal source–load interaction scheduling of combined heat and power microgrid considering stable supply and demand. After comparing and analyzing the actual results, the conclusions are as follows:

1) The source side uses energy storage equipment to decouple the thermoelectric connection and introduces energy equipment to ensure the heating and power supply capacity of the system.
2) Flexible thermal and electrical loads are introduced on the load side for demand response, and an IDR compensation mechanism is established. It can effectively improve the economy of the system and the stability of supply and demand, in which the total cost is reduced by 11.65% and the stability of supply and demand is increased by 67.99%.
3) The comprehensive satisfaction evaluation system established by considering factors such as user energy deviation, IDR compensation price, supply-side heating, and power supply flexibility effectively guarantees the user's comfort when participating in demand response.
4) The improved multi-objective grey wolf optimization algorithm adopted realizes the multi-objective optimal scheduling of the source–load interaction, promotes the benign interaction between the system source and the load, and ensures the supply and demand stability and economy of the CHP-MG operation.

This paper discusses the benign interaction between the source and the load of microgrid system, which is suitable for the cooperative planning of energy equipment in the system. However, for other large-scale industrial systems, the fault diagnosis and monitoring of internal equipment (Rui et al., 2020b; Hu et al., 2021) has not been taken into consideration, and further research is needed in the future.

DATA AVAILABILITY STATEMENT

The original contributions presented in the study are included in the article/**Supplementary Material**, further inquiries can be directed to the corresponding author.

AUTHOR CONTRIBUTIONS

JC and XY conceived and designed the study. JC constructed and solved the model and wrote the first draft of the manuscript. ZZ and SZ translated the article and drew the tables. BC drew the schematic diagrams. All authors contributed to revision of the manuscript and read and approved the submitted version.

SUPPLEMENTARY MATERIAL

The Supplementary Material for this article can be found online at: https://www.frontiersin.org/articles/10.3389/fenrg.2022.901529/full#supplementary-material

REFERENCES

Aghamohammadloo, H., Talaeizadeh, V., Shahanaghi, K., Aghaei, J., Shayanfar, H., Shafie-khah, M., et al. (2021). Integrated Demand Response Programs and Energy Hubs Retail Energy Market Modelling. *J. Energy*, 234. doi:10.1016/j.energy.2021.121239

Alomoush, M. I. (2019). Microgrid Combined Power-Heat Economic-Emission Dispatch Considering Stochastic Renewable Energy Resources, Power Purchase and Emission Tax. *Energy Convers. Manag.* 200, 112090. doi:10.1016/j.enconman.2019.112090

Amir, V., Jadid, S., and Ehsan, M. (2019). *Operation of Networked Multi-Carrier Microgrid Considering Demand response[J]*. England: Compel Int J for Computation & Maths in Electrical & Electronic Eng.

Anh, H., and Cao, V. K. (2020). *Optimal Energy Management of Microgrid Using Advanced Multi-Objective Particle Swarm optimization[J]*. Wales: Engineering Computations.

Blair, M. J., and Mabee, W. E. (2020). Evaluation of Technology, Economics and Emissions Impacts of Community-Scale Bioenergy Systems for a Forest-Based Community in Ontario. *Renew. Energy* 151, 715–730. doi:10.1016/j.renene.2019.11.073

Dranka, G. G., Ferreira, P., and Vaz, A. (2021). *Integrating Supply and Demand-Side Management in Renewable-Based Energy systems[J]*. England: Energy, 120978.

Freeman, J., Hellgardt, K., and Markides, C. N. (2017). Working Fluid Selection and Electrical Performance Optimisation of a Domestic Solar-ORC Combined Heat and Power System for Year-Round Operation in the UK. *Appl. Energy* 186 (3), 291–303. doi:10.1016/j.apenergy.2016.04.041

Hca, B., Lin, G., and Zhong, Z. C. (2021). Multi-objective Optimal Scheduling of a Microgrid with Uncertainties of Renewable Power Generation Considering User Satisfaction[J]. *Int. J. Electr. Power & Energy Syst.* 131.

Hemmati, M., Mirzaei, M. A., Abapour, M., Zare, K., Mohammadi-ivatloo, B., Mehrjerdi, H., et al. (2021). Economic-environmental Analysis of Combined Heat and Power-Based Reconfigurable Microgrid Integrated with Multiple Energy Storage and Demand Response Program. *Sustain. Cities Soc.* 69, 102790. doi:10.1016/j.scs.2021.102790

Hemmati, R., Mehrjerdi, H., and Nosratabadi, S. M. (2021). Resilience-oriented Adaptable Microgrid Formation in Integrated Electricity-Gas System with Deployment of Multiple Energy Hubs. *Sustain. Cities Soc.* 71 (3), 102946. doi:10.1016/j.scs.2021.102946

Hu, X., Zhang, H., Ma, D., and Wang, R. (2021). Hierarchical Pressure Data Recovery for Pipeline Network via Generative Adversarial Networks. *IEEE Trans. Autom. Sci. Eng.* (99), 1–11. doi:10.1109/tase.2021.3069003

Ippolito, F., and Venturini, M. (2018). Development of a Simulation Model of Transient Operation of Micro-combined Heat and Power Systems in a Microgrid[J]. *J. Eng. Gas Turbines Power* 140 (3), 032001.1–032001.15. doi:10.1115/1.4037962

Jiang, Y., Mei, F., Lu, J., and Lu, J. (2021). Two-Stage Joint Optimal Scheduling of a Distribution Network with Integrated Energy Systems. *IEEE Access* 9, 12555–12566. doi:10.1109/access.2021.3051351

Jordehi, A. R . (2021). *Information Gap Decision Theory for Operation of Combined Cooling, Heat and Power Microgrids with Battery Charging stations[J]*. Netherlands: Sustainable Cities and Society.

Kennedy, J., and Eberhart, R. (1995). *Particle Swarm Optimization[C]//Icnn95-International Conference on Neural Networks*. IEEE.

Li, P., Wang, Z., Wang, J., Yang, W., Guo, T., and Yin, Y. (2021). Two-stage Optimal Operation of Integrated Energy System Considering Multiple Uncertainties and Integrated Demand Response. *Energy* 225 (4), 120256. doi:10.1016/j.energy.2021.120256

Li, Y., Han, M., and Yang, Z. (2021). *Coordinating Flexible Demand Response and Renewable Uncertainties for Scheduling of Community Integrated Energy Systems with an Electric Vehicle Charging Station: A Bi-level Approach[J]*.

Li, Y., Wang, B., and Yang, Z. (2021). *Optimal Scheduling of Integrated Demand Response-Enabled Community Integrated Energy Systems in Uncertain Environments[J]*.

Li, Y., Zhang, J., Ma, Z., Peng, Y., and Zhao, S. (2021). An Energy Management Optimization Method for Community Integrated Energy System Based on User Dominated Demand Side Response[J]. *Energies*, 14.

Li, Y., Zhang, H., Liang, X., and Huang, B. (2019). Event-Triggered-Based Distributed Cooperative Energy Management for Multienergy Systems. *IEEE Trans. Ind. Inf.* 15 (4), 2008–2022. doi:10.1109/TII.2018.2862436

Liu, L., and Yang, G.-H. (2022). Distributed Optimal Energy Management for Integrated Energy Systems. *IEEE Trans. Ind. Inf.*, 1. doi:10.1109/TII.2022.3146165

Liu, N., Wang, J., and Wang, L. (2018). Hybrid Energy Sharing for Multiple Microgrids in an Integrated Heat-Electricity Energy System[J]. *IEEE Trans. Sustain. Energy* 10 (3), 1139–1151.

Lu, J., Liu, T., and He, C.. Robust Day-Ahead Coordinated Scheduling of Multi-Energy Systems with Integrated Heat-Electricity Demand Response and High Penetration of Renewable Energy[J]. *Renew. Energy* 2021 (1).

Lv, H., Wang, Y., and Dong, X. (2021). *Optimization Scheduling of Integrated Energy System Considering Demand Response and Coupling Degree[C]//2021 IEEE/IAS 57th Industrial and Commercial Power Systems Technical Conference (I&CPS)*. IEEE.

Mirjalili, S., Saremi, S., Mirjalili, S. M., and Coelho, L. S. (2016). Multi-Objective Grey Wolf Optimizer: A Novel Algorithm for Multi-Criterion Optimization[J]. *Expert Syst. Appl.* 47, 106–119.

Mirjalili, S., Mirjalili, S. M., and Lewis, A. (2014). Grey Wolf Optimizer[J]. *Adv. Eng. Softw.*, 46–61.

Mohseni, S., Brent, A. C., and Kelly, S. (2021). *Strategic Design Optimisation of Multi-Energy-Storage-Technology Micro-grids Considering a Two-Stage Game-Theoretic Market for Demand Response aggregation[J]*. England: Applied Energy, 287.

Munoz-Delgado, G., Contreras, J., and Arroyo, J. M. (2016). Multistage Generation and Network Expansion Planning in Distribution Systems Considering

Uncertainty and Reliability. *IEEE Trans. Power Syst.* 31 (5), 3715–3728. doi:10.1109/tpwrs.2015.2503604

Naderipour, A., Abdul-Malek, Z., and Nowdeh, S. A. (2020). Optimal Allocation for Combined Heat and Power System with Respect to Maximum Allowable Capacity for Reduced Losses and Improved Voltage Profile and Reliability of Microgrids Considering Loading Condition[J]. *Energy* 196 (Apr.1), 117124.1–117124.13. doi:10.1016/j.energy.2020.117124

Nojavan, S., Akbari-Dibavar, A., Farahmand-Zahed, A., and Zare, K. (2020). Risk-constrained Scheduling of a CHP-Based Microgrid Including Hydrogen Energy Storage Using Robust Optimization Approach. *Int. J. Hydrogen Energy* 45 (56), 32269–32284. doi:10.1016/j.ijhydene.2020.08.227

Pashaei-Didani, H., Nojavan, S., Nourollahi, R., and Zare, K. (2019). Optimal Economic-Emission Performance of Fuel cell/CHP/storage Based Microgrid. *Int. J. hydrogen energy* 44 (13), 6896–6908. doi:10.1016/j.ijhydene.2019.01.201

Ronaszegi, K., Fraga, E. S., Darr, J., Shearing, P. R., and Brett, D. J. L. (2020). Application of Photo-Electrochemically Generated Hydrogen with Fuel Cell Based Micro-combined Heat and Power: A Dynamic System Modelling Study. *Molecules* 25 (1). doi:10.3390/molecules25010123

Rui, W., Qiuye, S., Pinjia, Z., Yonghao, G., Dehao, Q., and Peng, W. (2020). Reduced-Order Transfer Function Model of the Droop-Controlled Inverter via Jordan Continued-Fraction Expansion. *IEEE Trans. Energy Convers.* 35 (3), 1585–1595. doi:10.1109/TEC.2020.2980033

Rui, W., Qiuye, S., Pinjia, Z., Yonghao, G., Dehao, Q., and Peng, W. (2020). Reduced-Order Transfer Function Model of the Droop-Controlled Inverter via Jordan Continued-Fraction Expansion. *IEEE Trans. Energy Convers.* 35 (3), 1585–1595. doi:10.1109/TEC.2020.2980033

Salama, H. S., Said, S. M., and Aly, M. (2021). Studying Impacts of Electric Vehicle Functionalities in Wind Energy-Powered Utility Grids with Energy Storage Device[J]. *IEEE Access* (99), 1.

Salehimaleh, M., Akbarimajd, A., and Dejamkhooy, A. (2022). *A Shrinking-Horizon Optimization Framework for Energy Hub Scheduling in the Presence of Wind Turbine and Integrated Demand Response Program*.

Shao, C., Ding, Y., and Siano, P. (2020). Optimal Scheduling of the Integrated Electricity and Natural Gas Systems Considering the Integrated Demand Response of Energy Hubs[J]. *IEEE Syst. J.* (99), 1–9.

Singh, S., and Kumar, A. (2020). *Economic Dispatch for Multi Heat-Electric Energy Source Based microgrid[C]//2020 IEEE 9th Power India International Conference (PIICON)*. IEEE.

Taha, I., and Elattar, E. E. (2018). "Optimal Reactive Power Resources Sizing for Power System Operations Enhancement Based on Improved Grey Wolf Optimiser[J]," in *IET Generation* (England: Transmission & Distribution). doi:10.1049/iet-gtd.2018.0053

Wang, J., Liu, J., Li, C., Zhou, Y., and Wu, J. (2020). Optimal Scheduling of Gas and Electricity Consumption in a Smart Home with a Hybrid Gas Boiler and Electric Heating System. *Energy* 204, 117951. doi:10.1016/j.energy.2020.117951

Wang, R., Sun, Q., Hu, W., Li, Y., Ma, D., and Wang, P. (2021). SoC-Based Droop Coefficients Stability Region Analysis of the Battery for Stand-Alone Supply Systems with Constant Power Loads. *IEEE Trans. Power Electron.* 36 (7), 7866–7879. doi:10.1109/TPEL.2021.3049241

Wang, R., Sun, Q., Tu, P., Xiao, J., Gui, Y., and Wang, P. (2021). Reduced-Order Aggregate Model for Large-Scale Converters with Inhomogeneous Initial Conditions in DC Microgrids. *IEEE Trans. Energy Convers.* 36 (3), 2473–2484. doi:10.1109/TEC.2021.3050434

Wc, A., Xiao, P. B., and Bs, C. (2021). *Integrated Demand Response Based on Household and Photovoltaic Load and Oscillations Effects*.

Yang, B., Yu, T., Shu, H., Dong, J., and Jiang, L. (2018). Robust Sliding-Mode Control of Wind Energy Conversion Systems for Optimal Power Extraction via Nonlinear Perturbation Observers[J]. *Appl. Energy* 210, 711–723.

Yang, J., Huang, G., and Wei, C. (2016). Privacy-aware Electricity Scheduling for Home Energy Management System[J]. *Peer-to-Peer Netw. Appl.*.

Yang, L., Yang, Z., and Li, G. (2019). Optimal Scheduling of an Isolated Microgrid with Battery Storage Considering Load and Renewable Generation Uncertainties[J]. *IEEE Trans. Industrial Electron.* 66, 1565–1575.

Yi, Z., Xu, Y., Hu, J., Chow, M.-Y., and Sun, H. (2020). Distributed, Neurodynamic-Based Approach for Economic Dispatch in an Integrated Energy System. *IEEE Trans. Ind. Inf.* 16 (4), 2245–2257. doi:10.1109/TII.2019.2905156

Zhang, S., Rong, J., and Wang, B. (2021). An Optimal Scheduling Scheme for Smart Home Electricity Considering Demand Response and Privacy Protection. *Int. J. Electr. Power & Energy Syst.* 132 (4), 107159. doi:10.1016/j.ijepes.2021.107159

Zhang, X., Shahidehpour, M., and Alabdulwahab, A. (2015). Hourly Electricity Demand Response in the Stochastic Day-Ahead Scheduling of Coordinated Electricity and Natural Gas Networks[J]. *IEEE Trans. Power Syst.* 31 (1), 592–601.

Zhang, Y., Shen, H., and Wen, J. (2019). *Storage Control of Integrated Energy System for Integrated Demand Response[J]*. Beijing, China: Electric Power Construction.

Zhao, D., Xia, X., and Tao, R. (2019). *Optimal Configuration of Electric/Thermal Integrated Energy Storage for Combined Heat and Power Microgrid with Power to Gas[J]*. Nanjing, China: Automation of Electric Power Systems.

Zhou, C. (2019). Operation Optimization of Multi-District Integrated Energy System Considering Flexible Demand Response of Electric and Thermal Loads. *Energies* 12. doi:10.3390/en12203831

Conflict of Interest: The authors declare that the research was conducted in the absence of any commercial or financial relationships that could be construed as a potential conflict of interest.

NOMENCLATURE

CHP-MG Combined heat and power microgrid

SDS Supply and demand stability

ESS Power supply satisfaction

HSS Heat supply satisfaction

IDR Integrated demand response

LW Electrical load–wind energy

WT Wind turbine

MT Micro-turbine

GB Gas boiler

EES Electrical energy storage

TES Thermal energy storage

HE Heat exchanger

EE Electrothermal equipment

PG Power grid

P_{WT}^{t} Generated power of wind turbine in time period t

P_{MT}^{t} Electric generation power of micro-turbine in period t

Q_{HE}^{t} Heat production power of heat exchanger in period t

Q_{GB}^{t} Heat production power of gas boiler in period t

Q_{EE}^{t} Heat production power of electrothermal equipment in period t

E_{EES}^{t} Storage capacity of electrical energy storage in period t

E_{TES}^{t} Storage capacity of thermal energy storage in period t

frontiers | Frontiers in Energy Research

HYPOTHESIS AND THEORY
published: 01 June 2022
doi: 10.3389/fenrg.2022.915121

Multi-Energy Acquisition Modeling and Control Strategy of Underwater Vehicles

Shijun Shen[1], **Chaofan Wang**[1], **Zhiqiang Qiu**[2], **Zhiwu Ke**[2] **and Dawei Gong**[1]*

[1]*University of Electronic Science and Technology of China, Chengdu, China,* [2]*Key Laboratory of Thermal Power Technology, Wuhan Second Ship Design Institute, Wuhan, China*

An autonomous underwater vehicle (AUV) can only carry limited energy for improved flexibility, but this brings the problem of working endurance. The acquisition of environmental energy by an underwater robot is a positive way to supplement energy and increase endurance. However, the instability and difference in power output capacity of different environmental energies will lead to low utilization of environmental energy. In this study, a multi-energy acquisition model is established to manage the AUV's energy, which includes a heart rate sampling system, a mixed-energy circuit topology, and a maximum power output algorithm of environmental energy based on power trajectory tracking. The simulating results show that the power output control strategy can effectively improve the multi-energy acquisition and utilization efficiency of underwater vehicles, which has a positive significance and could improve endurance time.

Keywords: underwater robot, unstable multi-energy, integrated energy management, power trajectory tracking, maximum power output

Edited by:
Rui Wang,
Northeastern University, China

Reviewed by:
Shenquan Wang,
Changchun University of Technology, China
Lili Cui,
Shenyang Normal University, China
Shoulong Xu,
University of South China, China

***Correspondence:**
Dawei Gong
pzhzhx@126.com

Specialty section:
This article was submitted to Smart Grids, a section of the journal Frontiers in Energy Research

Received: *07 April 2022*
Accepted: *20 April 2022*
Published: *01 June 2022*

Citation:
Shen S, Wang C, Qiu Z, Ke Z and Gong D (2022) Multi-Energy Acquisition Modeling and Control Strategy of Underwater Vehicles . Front. Energy Res. 10:915121. doi: 10.3389/fenrg.2022.915121

INTRODUCTION

In modern society, the application of robots is becoming increasingly extensive, and they play more and more important roles in land, sky, sea, underground, and other occasions. Scholars from all over the world have conducted in-depth research on robot technology.

Underwater robots include manned submersible (HOV), autonomous underwater vehicles (AUV), remotely operated underwater vehicles (ROV), hybrid robots, etc. (Feng and Li, 2013), which are important tools for underwater resource exploration, underwater environment observation, and underwater scientific research. An autonomous underwater vehicle without cable (AUV) has better flexibility, a longer voyage, intelligent autonomous navigation, and other characteristics compared with a wired underwater remote robot, but the endurance time disadvantage is also obvious (Wynn et al., 2014). The endurance, load, voyage, and speed of the AUV are all affected by the energy supply (Feng et al., 2011). All behaviors of robots are based on power supply, but there are few research studies on this aspect (Sun, 2013; Yu, 2015). As the structure and function of AUVs have become increasingly complex, the problem of power matching and power driving has become an important bottleneck, restricting the development of robot technology.

The energy system of an AUV is presently being developed toward the goal of compact structure, small size, low weight, high energy density, and long endurance (Fang and Li, 2012). To date, AUV energy is roughly divided into traditional energy and new energy. Traditional energy is obtained from one of the various chemical batteries (lead-acid battery, lithium-ion battery, silver–zinc battery, lithium polymer battery, etc.) as the sole power of an AUV, but the non-renewable battery energy greatly limits the activity range of the AUV, and the operation to recycle the AUV to charge the

FIGURE 1 | Engineering prototype of the SAUV.

battery is certainly complex (Ren et al., 2017). Although conventional batteries still play a dominant role in AUV energy systems, environmental energy is being developed as a complementary energy source for AUVs.

In recent years, many scholars have begun to explore the possibility of application in the field of new energy and propose the scheme of environmental power generation on an AUV. Solar energy, thermoelectric energy, and wave energy are used as energy sources to support the long-term operation requirements of the AUV (Webb et al., 2001). Using renewable energy in an underwater environment such as the AUV's power can reduce or eliminate the cost of regular battery recharging, further freeing the AUV from the tether and allowing it to navigate autonomously.

For example, in January 1998, the Office of Naval Research of the United States produced the underwater solar robot engineering sample, the solar-powered autonomous underwater vehicle (SAUV) (**Figure 1**) and tested it in Vladivostok (Ageev et al., 2002). Eco Marine Power of Japan started the Aquarius USV study in 2011 and tested it in 2015. Aquarius USV is designed as a trimaran, with solar panels connected across each hull. The USV is 5 m long and 8 m wide and can reach a speed of 6 kn (Eco Marine Power, 2014).

The British company AutoNaut launched the wave-assisted surface unmanned boat AutoNaut USV in 2012 (Auto Naut, 2016). Solar panels in series on the surface of the robot can provide electricity of 125 W, and it can also be equipped with methanol fuel cells of 25 W to increase the endurance. The USV is propelled by thrusters with a speed of 1 kn ~ 2 kn and a maximum of 3 kn (National Oceanography Center, 2016). Researchers at the University of Pisa in Italy developed the wave energy recovery system module, shown in **Figure 2**. The module consists of two wings that can be mounted on an underwater glider. The wing ends are connected to the module by movable joints, and the internal joint mechanism of the module is connected to the generator. It was tested in the Tyrrhenian Sea in 2016, and it was found that the wave energy recovery system module can continuously generate power (Fenucci et al., 2016). Other applications, such as wind energy and thermoelectric energy, have also been extensively studied on underwater robots (Elkaim, 2006; Elkaim and Boyce Lee, 2007; Ma et al., 2016; Yang et al., 2016).

FIGURE 2 | Wave energy recovery system module.

In terms of energy management, most researchers are focusing on the energy distribution strategy of batteries (Bao and Zhang, 2016; Xie, 2018; Zhang and Li, 2018; Rui et al., 2020; Zhang et al., 2020). But, improving the mixed utilization efficiency of batteries and environmental energy will become the research and development focus of AUV technology in the future (Wynn et al., 2014). Wang et al. (2019); Rui et al. (2020); and Wang et al. (2021)studied SOC balancing speed and state of the battery based on improved droop control to solve the problem of battery state prediction under charge. Chen et al. (2021) adopted the load power following strategy in hybrid electric vehicles to achieve the goals of battery conservation and increased its working range. However, most of the research studies on energy management focus on battery charge and discharge management, and there are few research studies on how to improve the utilization efficiency of multi-environment mixed energy.

Taking the underwater robot as a platform and aiming at multi-environment energy acquisition and utilization, this study proposes an efficient energy acquisition circuit topology, an energy-saving and efficient heart rate sampling system, and a maximum power output control algorithm based on mixed-energy power trajectory tracking. The mathematical model is built and simulated by MATLAB. The simulation results show that the circuit topology combined with the algorithm can effectively improve the environmental hybrid energy utilization and underwater navigation time of the AUV.

MIXED-ENERGY ACQUISITION AND MANAGEMENT SCHEME FOR UNDERWATER ROBOTS

Considering the environment of the underwater robot, this study chose to collect mixed-energy sources, including wave energy, thermoelectric energy, and solar energy.

The battery is still the main energy source of the AUV. The charging and discharging state of the battery is switched according to the load power and the output power of the mixed energy of the AUV. It is assumed that the load power is P_L and the mixed energy output power is P_m. When $P_L > P_m$,

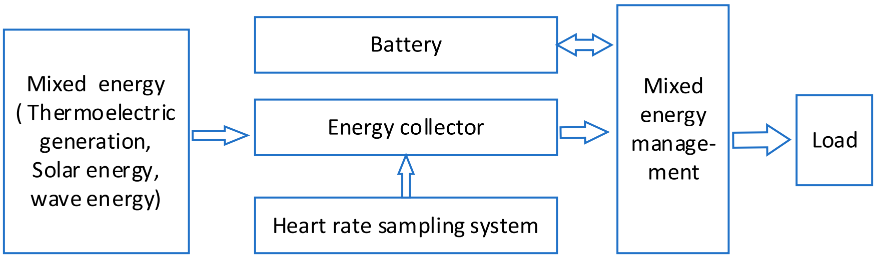

FIGURE 3 | Block diagram of hybrid energy acquisition and management of the AUV.

the battery discharges, and when $P_L < P_m$, the battery accepts the mixed energy for charging.

According to the design scheme in this study, the energy acquisition and management framework of the underwater robot is shown in **Figure 3**.

Among them, we will configure a supercapacitor for each energy module to store energy. The energy collector is a collection and execution module of mixed energy. The heart rate sampling system collects the output voltage and power of mixed energy and provides data support for the maximum power output algorithm based on power trajectory tracking. Mixed energy management is the core of system management, which internally stores the power curve data of mixed energy, controls the collection sequence of mixed energy, controls the output voltage of DC–DC, and controls the switch of battery charge and discharge.

To verify the effectiveness of the system, this study will establish all the mixed-energy models, establish the energy acquisition circuit topology, and use MATLAB to simulate and analyze.

A MULTI-ENERGY MODEL AND HEART RATE SAMPLING SYSTEM

Photovoltaic Cell Power Generation Model and Simulation

There is a transverse current in the electrode surface layer of the photovoltaic cell, so a resistor R_s needs to be connected in series in the equivalent circuit. The PN junction comprises the PN junction and series resistor R_s. The photovoltaic cell potential produces a photo-current I_{ph}, which depends on the irradiance, the area of the cell, and the temperature T, and I_{ph} is proportional to the irradiation intensity of the incident light. When the temperature rises, I_{sc} will rise slightly; R_{sh} is the shunt resistance used to replace the leakage current I_{sh} caused by the PN junction defect, and its direction is opposite; I_d is the forward current of the PN junction. The current on load R is represented by I, and the working current of load R is as follows:

$$I = I_{ph} - I_d - I_{sh} = I_{ph} - I_o\left\{\exp\left[\frac{q(U + IR_s)}{AKT}\right] - 1\right\} - \frac{U + IR_s}{R_{sh}}. \tag{1 – 1}$$

Here, I_{ph} is photo-generated current (A);

I_o is reverse saturation current of a photovoltaic cell in the absence of light (the order of the magnitude is $10^{-4}A$);

I_d is the forward current of PN junction (A); I_{sh} is the leakage current caused by the PN junction defect (A);

q is the electron charge constant ($1.6 \times 10^{-19}C$);

U is the load terminal voltage (V);

I is the working current of load (A);

R_s is the series resistor;

A is the constant factor of the diode (A = 1 when the positive bias voltage is large, A = 2 when the positive bias voltage is low);

K is the Boltzmann constant (1.38×10^{-23} J/K);

T is the degree K ; and

R_{sh} is the parallel resistance.

On the basis of **Equation 1-1**, the formula is simplified to obtain a practical engineering mathematical model (Dey and Qin, 2009). In photovoltaic cells, the resistance value of parallel resistance R_{sh} is generally large, whereas the resistance value of series resistance R_s is small. Because R_{sh} and R_s are, respectively, in parallel and in series in the circuit, the following approximation can be carried out in the following calculation. The resistance R_{sh} is very large so that $(U + I R_s)/R_{sh}$ is far less than the current of the photovoltaic cell, which usually can be ignored. Considering R_s is generally far less than the positive diode guide resistance, $I_{ph} = I_{sc}$is set and then

$$I = I_{sc} - I_o\left\{\exp\left[\frac{q(U + IR_s)}{AKT}\right] - 1\right\}, \tag{1 – 2}$$

where I_{sc} is the short-circuit current (A).

In addition, the relationship between current and voltage is also analyzed under the conditions of a maximum power point and open circuit:

(1) When the system is at the maximum power point, $U = U_m,\ I = I_m$, then

$$I_m = I_{sc} - I_o\left\{\exp\left[\frac{q(U_m + IR_s)}{AKT}\right] - 1\right\}. \tag{1 – 3}$$

(2) When the system is at an open circuit, $U = U_{oc},\ I = 0$, then

$$0 = I_{sc} - I_o\left\{\exp\left[\frac{q(U_{oc} + IR_s)}{AKT}\right] - 1\right\}, \tag{1 – 4}$$

where U_m—voltage at maximum power point (V);

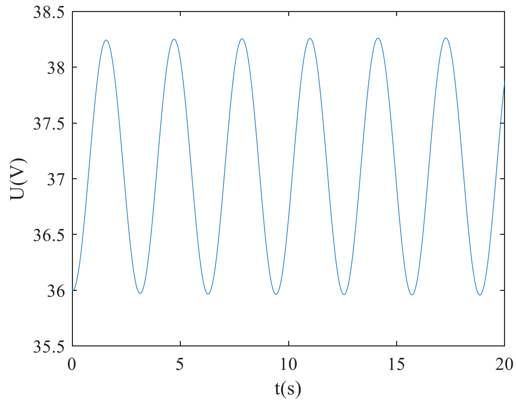

FIGURE 4 | U-t curve of the photovoltaic cell.

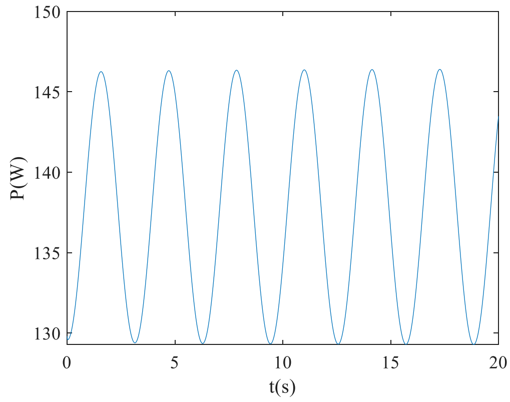

FIGURE 5 | P-t curve of the photovoltaic cell.

I_m—current at the maximum power point (A); and
U_{oc}—open-circuit voltage (V).

Based on the aforementioned analysis of the mathematical model of photovoltaic cells, **Equation (1-1)** can be simplified into **Equation (1-5)**.

$$I_L = I_{sc}\left\{1 - C_1\left[\exp\left(\frac{U}{C_{2U_{oc}}}\right) - 1\right]\right\}. \qquad (1-5)$$

Under normal temperature $\exp\left(\frac{U}{C_{2U_{oc}}}\right) >> 1$, then we can ignore the item "−1." After simplifying the aforementioned formula, we can get

$$C_1 = \left(1 - \frac{I_m}{I_{sc}}\right)\exp\left(\frac{-U_m}{C_{2U_{oc}}}\right), \qquad (1-6)$$

$$C_1 = \frac{U_m}{U_{oc}} - 1\left[\ln\left(1 - \frac{I_m}{I_{sc}}\right)\right]^{-1}. \qquad (1-7)$$

The I–V characteristic curve of photovoltaic cells is closely related to the irradiation intensity and external temperature. Formula (1-5) describes the characteristic curve under standard irradiation intensity $S_{ref} = 1000W/m^2$ and standard external temperature $T_{ref} = 25^oC$. When the external irradiation intensity and temperature change, it is necessary to consider the influence of external factors on the characteristics of photovoltaic cells, and it is necessary to modify the model of photovoltaic cells to describe its characteristic curve in the new environment.

According to the I_{sc}、I_m、U_m、U_{oc} under the reference of the photovoltaic cell temperature and radiation intensity to calculate the I_{sc1}、I_{m1}、U_{m1}、U_{oc1} under the new cell temperature and the new radiation intensity, **Equations (1-5)**, **Equations (1-6)**, and **Equations (1-7)** are substituted to obtain the characteristic curve under the new irradiation intensity and battery temperature.

$$I_{sc1} = I_{sc}S/S_{ref}(1 + a\Delta T), \qquad (1-8)$$

$$U_{oc1} = U_{oc}[(1 - c\Delta T)\ln(e + b\Delta S)], \qquad (1-9)$$

$$I_{m1} = I_m S/S_{ref}(1 + a\Delta T), \qquad (1-10)$$

$$U_{m1} = U_m[(1 - c\Delta T)\ln(e + b\Delta S)]. \qquad (1-11)$$

In the aforementioned equations, $a = 0.0025^o, b = 0.5, c = 0.00288^oC$, and e is the natural logarithm.

Based on the aforementioned analysis, this study established a solar power generation model in Simulink and the following conditions are set according to the actual situation.

(1) Select the Dx-60 (STP060-12/Sb) photovoltaic cells from Sun Tech-Power, whose main parameters are $I_m = 3.45$, $I_{sc} = 3.9$, $U_m = 17.4$, and $U_{oc} = 21.6$.

Here, I_m is the peak current, I_{sc} is the short-circuit current, U_m is the peak voltage, and U_{oc} is the open-circuit voltage.

(2) Set $T = 35^{\circ}$, $S_{ref} = 1000\,KW/m^2$, $T_{ref} = 25^oC$, and $R_L = 10\Omega$

Here, T is the ambient temperature, S_{ref} is the standard irradiation intensity, T_{ref} is the standard external temperature, and R_L is the load.

(3) To reflect the fluctuation of photovoltaic power generation, this study particularly sets the light intensity to change according to a sinusoidal curve. According to the actual situation, the light intensity of 0–3 m underwater is set as follows:

$$S = 1000 - \left(1.2t^{\frac{1}{8}} + 26\right)\cos(2t). \qquad (1-12)$$

The U-t curve and P-t curve are obtained after simulation, as shown in **Figure 4** and **Figure 5**.

Thermoelectric Generator Model

The thermoelectric effect is known as the Seebeck effect. A circuit comprising different materials X and Y will produce a current in the circuit when the temperature of the contact is varying, which is called the Seebeck effect (Chen et al., 2000; Xiao et al., 2011; Venkata Rao and Patel, 2013).

Suppose that joints A and B are maintained at different temperatures, there will be a potential difference between the

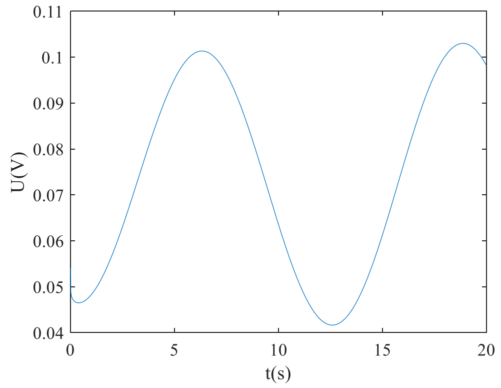

FIGURE 6 | U-t curve of the thermoelectric generator.

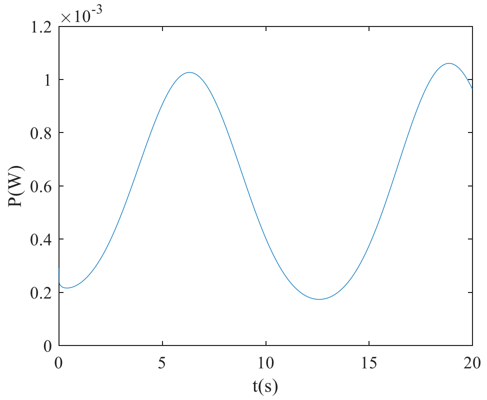

FIGURE 7 | P-t curve of the thermoelectric generator.

open position of conductor X, called the Seebeck voltage. Its value is

$$\Delta V_{12} = \alpha_{XY} \cdot (T_A - T_B), \qquad (2-1)$$

whereΔV_{12} is the electromotive force generated by the loop, whose unit is V;

α_{XY} is the relative Seebeck coefficient of the two conductor materials used, whose unit is $V \cdot K^{-1}$; and

T_A and T_B are, respectively, the temperature at nodes A and B, whose unit is K.

When the temperature difference $\Delta T = T_A - T_B$ between the two joints is not very large, the relationship is linear, that is, α_{XY} is a constant. This constant is defined as the relative Seebeck coefficient of two objects, which is as follows:

$$\alpha_{XY} = dV_{XY}/dT. \qquad (2-2)$$

The unit of the Seebeck coefficient is V/K. The positive or negative value of the Seebeck coefficient depends on the thermoelectric properties of the conductors X and Y and is independent of the magnitude and direction of the temperature gradient. However, the Seebeck coefficient of the same material is not a constant value but varies with temperature.

The thermoelectric generation module comprises semiconductor thermoelectric generation units in series and parallel. The main parameters describing the performance of a semiconductor thermoelectric generator include thermoelectric conversion efficiency, output power, and so on. Therefore, to study the performance parameters of the whole power generation module, we can start with the analysis of the temperature difference power generation unit. The following is a specific analysis of the temperature difference power generation unit from the perspective of energy balance. It is assumed that the sides of both n-type and P-type galvanic arms are adiabatic, that is, there is no heat exchange between these sides and the environment.

According to the Seebeck effect described previously, the Seebeck voltage generated in the circuit when the temperature difference exists at both ends of the semiconductor element is as follows:

$$V = \alpha (T_h - T_c). \qquad (2-3)$$

It can be seen that this voltage is applied to the internal resistance R of the thermogenerator and the load resistance R_L. Therefore, the voltage across the load resistance is the actual output voltage V_0 of the thermogenerator. It can be expressed as

$$V = \alpha (T_h - T_c) \frac{R_L}{R + R_L}. \qquad (2-4)$$

The current in the loop is expressed as

$$I = \frac{\alpha (T_h - T_c)}{R + R_L}. \qquad (2-5)$$

Therefore, the output power of the thermoelectric generator can be obtained as follows:

$$P = \frac{\alpha^2 (T_h - T_c) R_L}{(R + R_L)^2}. \qquad (2-6)$$

When the load resistance R_L and the temperature difference generator internal resistance R are matched, the temperature difference generator will have the maximum output power, which is

$$P_{max} = \frac{\alpha^2 (T_h - T_c)^2}{4R}. \qquad (2-7)$$

In this study, the AUV is assumed to be used in shallow water. The source of the temperature difference is the internal temperature and external water temperature of the AUV.

To reflect the fluctuation of the thermoelectric generator, the temperature of the hot side is kept unchanged, and the temperature of the cold side is especially set to change according to the sine curve. The input conditions of the thermoelectric module are set as

(1) $\alpha = 2^{e^{-4}}$, $T_h = 329K$, and $R_L = 10\Omega$,

where α is the Seebeck coefficient, T_h is the hot end temperature, and R_L is the load resistance.

(2) The temperature of the cold side is set according to the following formula:

$$T_c = \left(0.5t^{\frac{1}{8}} + 1\right) \cos(0.5t) + 325. \qquad (2-8)$$

Based on the aforementioned analysis of the mathematical model of the thermoelectric generator, the U-t and P-t curves of the thermoelectric generator are simulated in Simulink as shown in **Figure 6** and **Figure 7**.

Wave Energy Generation Model

Wave energy refers to the kinetic and potential energy of waves formed on the surface of the water. In practice, the energy can be obtained by using the oscillating and swaying motion generated by the robot under the action of waves (Luo et al., 2013; Sun, 2015).

Cylindrical floats absorb maximum wave energy, but there is a complex restriction relationship between the float and the parameters of a linear motor; therefore, the conversion efficiency of the system can be maximized only by optimizing the parameters of the whole device. The main advantage of the floating type is its convenience in construction. It has strong adaptability to the change in the tide level. Because of the superficiality of waves, to absorb wave energy, the device should be as close to the water as possible, while the floating type can meet this requirement well. Wave fluctuation is mainly manifested by longitudinal reciprocating motion. The longitudinal reciprocating movement of the water surface makes the buoy in the wave subject to longitudinal buoyancy that changes with the surface of the water so that the float vibrates up and down and drives the motor to generate electricity. At the same time, the motor also gives the buoy a force that hinders its movement. The amount of buoyancy on a float depends on its shape and size. Many factors affect the wave form, but so far, no mathematical model can accurately simulate the wave form. To facilitate calculation, this study uses sine waves to approximate the wave. When the linear motor is rated to work, the buoy vibrates up and down, so the resultant force on the buoy can be expressed as

$$\sum F = F_{\mathrm{f}} - G - F_{\mathrm{m}} = ma = m\ddot{S}(t), \qquad (3-1)$$

where F_f is the buoyancy of the buoy, G is the gravity of the device itself, F_m is the counter electromagnetic force received by the linear motor, m is the total mass of the buoy (including the float and the linear motor) and S (t) is the displacement of a particle on the wave surface.

The resultant force on the buoy has been obtained through the parameters of the motor and float. The steady-state operation analysis of the device can be obtained as follows:

$$S(t) = \frac{\rho g b A \lambda}{\pi\sqrt{2\left(4\rho g b^2 - \omega^2 m\right) + C_0^2\omega^2}} \sin\left(\frac{2\pi b}{\lambda}\right) \sin(\omega t - \alpha), \qquad (3-2)$$

where A is the wave height, ω is the angular velocity, and λ is the wave wavelength. It is supposed that the section of the cylinder is square, the side length is 2b, g is gravitational acceleration, and ρ is the seawater density.

It can be seen that the displacement of the buoy and the angular velocity of the wave have the same sine change, and the amplitude is calculated as follows:

$$A_0 = \frac{\rho g b A \lambda}{\pi\sqrt{2\left(4\rho g b^2 - \omega^2 m\right) + C_0^2\omega^2}} \sin\left(\frac{2\pi b}{\lambda}\right). \qquad (3-3)$$

In a steady-state operation, the velocity of the buoy is

$$V(t) = \ddot{S}(t) = A_0 \omega \cos(\omega t - \alpha). \qquad (3-4)$$

The linear speed of the buoy is directly proportional to the stator of the linear motor, and since there is no transmission device, it can be considered that the speed of the two is the same, so the electromagnetic power of the linear motor is

$$\begin{aligned} P_M(t) &= T\Omega = F_{\mathrm{m}} V(t) = C_0 V(t) * V(t) = C_0 * V(t)^2 \\ &= C_0 A_2{}^0 \omega^2 \cos^2(\omega t - \alpha), \end{aligned} \qquad (3-5)$$

where T is the electromagnetic torque of the motor and Ω is the angular velocity of the motor rotor.

Set the rated wave to be sinusoidal simple harmonic with constant wave length λ, wave height A, and angular velocity ω. For the generator buoy to operate stably, its amplitude must not be greater than that of the excitation wave. However, it can be seen from **Equation (3-2)** that the larger the buoy operation amplitude is, the larger the electromagnetic power of the generator will be. Therefore, to ensure the stable operation of the buoy and maximize the motor power, the maximum value of the buoy A can be equal to the half amplitude of the wave. When the resonance state is attained, C_0 is the largest, that is, b/λ = 0.323. At this time, the output power of the generator is as follows:

$$P(t) = \frac{0.145\rho g}{\pi} \lambda^2 A^2 \omega \cos^2(\omega t - \alpha). \qquad (3-6)$$

Depending on the possible reality of the environment in which the AUV is working, this study set the wave power generation input parameters as

(1)ρ = 1,025, $g = 9.8$, $\omega = 1$, and $R_L = 10\Omega$,

where ρ is the density of the water, g is the acceleration of gravity, ω is the angular frequency, and R_L is the load resistance.

(2) It is assumed that the wave is simple harmonic, and then Z is the harmonic equation of the displacement of a particle on the wave surface.

$$\mathrm{Z} = \frac{\mathrm{A}}{2} \sin\left(\omega t - \frac{2\pi x}{\lambda}\right), \qquad (3-7)$$

where wave amplitude A = 0.6, ω is the angular frequency, and wavelength $\lambda = 0.8$. Because of the structural particularity of the

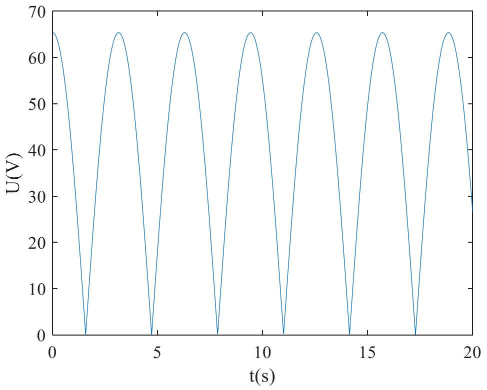

FIGURE 8 | U-t curve of wave energy generation.

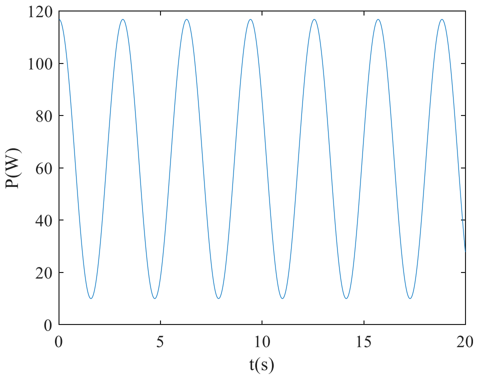

FIGURE 9 | P-t curve of wave energy generation.

wave energy acquisition module, its initial output voltage is AC, so we take the voltage after rectification as a reference. The wave energy rectification method is full-wave rectification.

Based on the aforementioned wave power generation model and setting conditions, the U-t and P-t curves are obtained by using Simulink as shown in **Figure 8** and **Figure 9**.

Heart Rate Sampling System

Environmental energy is characterized by instability and weakness. When an energy module is in an unfriendly environment, it is likely that the module will not be output. If the port voltage of each energy module is collected in real time without judgment, the additional system power consumption will be increased.

Therefore, according to the characteristics of environmental energy, this study designed a heart rate sampling system driven by an environmental energy module. The sampling sequence obtained by the system can be approximated to a nonuniform sampling sequence, which is analyzed by combining the theory of nonuniform sampling and restored by the nonuniform sampling reconstruction method.

To realize the signal sampling detection, the sampling frequency of uniform sampling is twice that of the sampled signal, that is, the low-frequency signal is sampled with high frequency. In real life, all kinds of signals include noise and high-frequency harmonic components. If only uniform sampling is used to sample such signals, a spectrum aliasing phenomenon is highly likely to occur.

Compared with uniform sampling, the most prominent advantage of nonuniform sampling is that the randomness of sampling points can realize the irregular arrangement of the aliasing signals to all frequency values so that the frequency values higher than half or even higher than the sampling frequency can be sampled, breaking the limit of the Shannon sampling theorem. Nonuniform sampling not only has the characteristics of random point sampling uniformity of anti-aliasing but also has the piecewise uniform quality.

The heart rate sampling system based on environmental energy collection is shown in **Figure 10**. As the controller of the system, the energy collector also needs to control the heart rate sampling system, while the sampling system is controlled by the output voltage of the environmental energy module.

A(t) is the sampled signal. The discontinuous energy generated by the environmental energy drives the sampling device to perform the sampling work; at the same time, the sampling sequence is thus obtained. The discontinuous energy replaces the continuous energy supply in the existing traditional sampling system to finish the original signal's sampling.

The RTC is used to record the time of the sampling site and its primary responsibility is to provide an accurate time baseline.

Because of the instability of environmental energy, the sampling system is prone to power failure. Therefore, a low-power power failure storage system "sample and hold" is designed in this study.

MIXED-ENERGY MANAGEMENT MODEL AND SIMULATION

Mixed-Energy Management Circuit Topology

Because of the instability and the functional difference of different environmental energies, after collecting the environmental energy, it needs to use a DC–DC boost (or step-down) and stabilize the voltage value at the value required by the load. There are basically two types of mixed-energy management circuit topologies, single-energy with single-voltage converter circuit topology (**Figure 11A**) and multi-energy with single-voltage converter circuit topology (**Figure 11B**).

As there are multiple DC–DC modules, there will be more voltage conversion losses and higher costs in the circuit topologies shown in **Figure 11A**. In **Figure 11B**, there is only one DC–DC, with relatively low cost and energy loss, but only one energy module is discharging at a time. That is to say, only the environmental energy module with the highest port voltage can output electric energy. This passive energy release prevents the lower-voltage energy module from discharging, which may result in environmental energy never being released, thus deteriorating the environmental energy that has been collected with great effort.

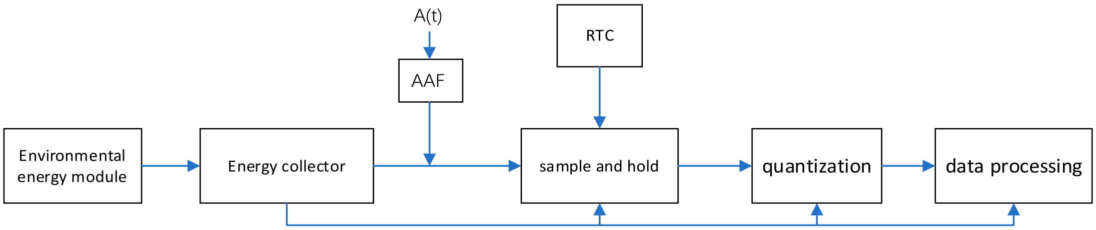

FIGURE 10 | Structural diagram of the heart rate sampling system.

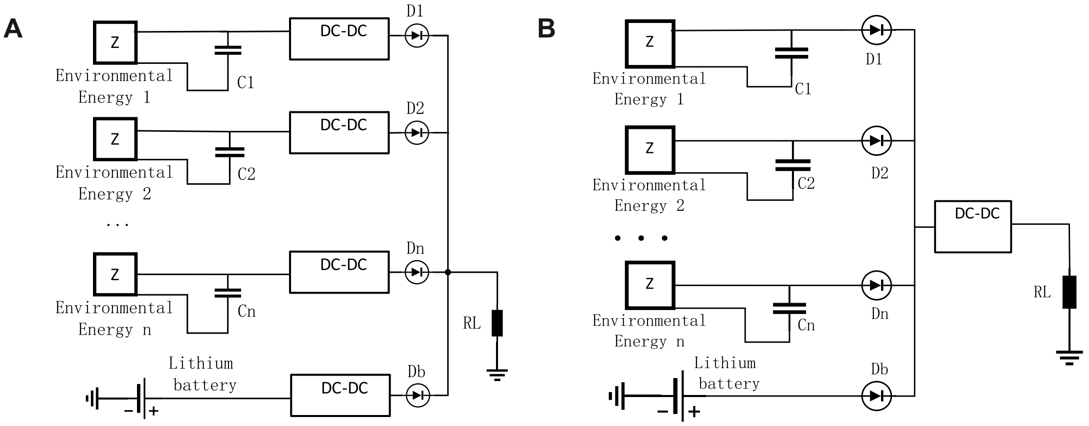

FIGURE 11 | Traditional multi-energy management circuit topology: **(A)** Single-module single DC–DC circuit topology and **(B)** Multi-module single DC–DC circuit topology.

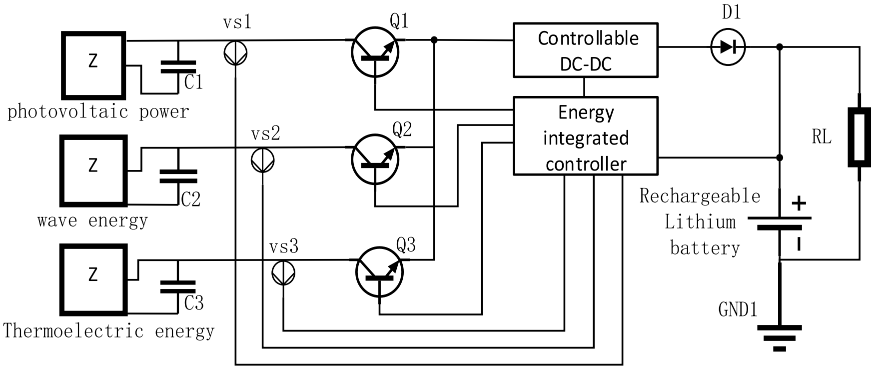

FIGURE 12 | Energy management circuit topology

It can be seen from the aforementioned analysis that the circuit topology shown in **Figure 11B** consumes less energy. Therefore, this study will optimize the circuit topology based on what is shown in **Figure 11B**. To make each channel of environmental energy be an active discharge, this study adds a controllable switch for each environmental energy module. To ensure that the power of the current discharging energy module is the maximum, this study designs the maximum output power algorithm based on power trajectory tracking. Combined with the heart rate sampling system, the improved circuit topology is shown in **Figure 12**.

C1, C2, and C3 are ultra-capacitors; VS.1, VS.2, and VS.3 are voltage sensors of the heart rate sampling system; Q1, Q2, and Q3 are three controllable triodes; and D1 is a single guided diode.

There is only one DC–DC module in this circuit topology, and all energy sources (except batteries) use the same DC–DC module, which can effectively reduce the loss of environmental energy in the conversion process. However, the problem caused by this topology is that energy sources with different port voltages cannot output their energy at the same time. Only one kind of energy can be output at a time, and other energies are temporarily stored by the ultra-capacitors.

There is one DC–DC module and three diodes in **Figure 11B**. One DC–DC module, one diode, and three controlled triodes are shown in **Figure 12**. Let us say that in two diagrams, we use the same type of DC–DC module and diode, so the second circuit has three more triodes and two fewer diodes than the first circuit.

It is supposed that the controlled triode we use is a kind of MOSFET whose internal resistance is 10 mΩ, and the diode is a common rectifying diode whose conduction voltage drop is 0.7 v. It is supposed that when the circuit current is 10 A, the power loss on the diode is 10*0.7 = 7 W, and the power loss of MOSFET is 10*10*0.01 = 1 W. The power loss of a total of three MOSFETs is 3 W, while the power loss of two diodes is 14 W. That means the power loss of the circuit in **Figure 12** is 11 W less than that of the circuit in **Figure 11** (b).

During the operation of this circuit, two (or more) energies may complete storing and need to be discharged to the load or the battery. According to previous studies, the order of energy release is generally determined according to the current voltage of the energy module, that is, the one with the highest voltage is the first to discharge. However, because of the randomness of environmental energy and the functional difference between different energy modules, the power released by the energy module with a high voltage value is not necessarily the maximum (the discharge current needs to be considered).

Different environmental conditions, different working principles, and different output power capacities will cause different energy acquisition modules to have different power output under the same (open road) output voltage. Therefore, when the environment energy is not connected to the load, we cannot determine its power output ability by the open-circuit voltage value.

It is assumed that the voltage and discharging power per unit time of two energy modules are V1 and V2 and P1 and P2, respectively. Even V1 > V2, but P2 > P1 may occur. In view of this situation, to effectively improve energy utilization, the maximum power control strategy based on power trajectory tracking is proposed in this study.

Maximum Power Control Strategy Based on Power Trajectory Tracking

The maximum power control strategy based on power trajectory tracking is to control the discharge sequence of the energy module in a sufficiently small period to ensure the environmental energy discharge with the maximum power output capacity at the moment. That means the strategy is used to ensure the maximum energy obtained by the load at the moment.

Based on this, the flow diagram of this energy management system is designed as shown in **Figure 13**.

To effectively improve the efficiency of the DC–DC module, this study sets a voltage threshold, and only the energy module that meets the threshold is allowed to output electric energy.

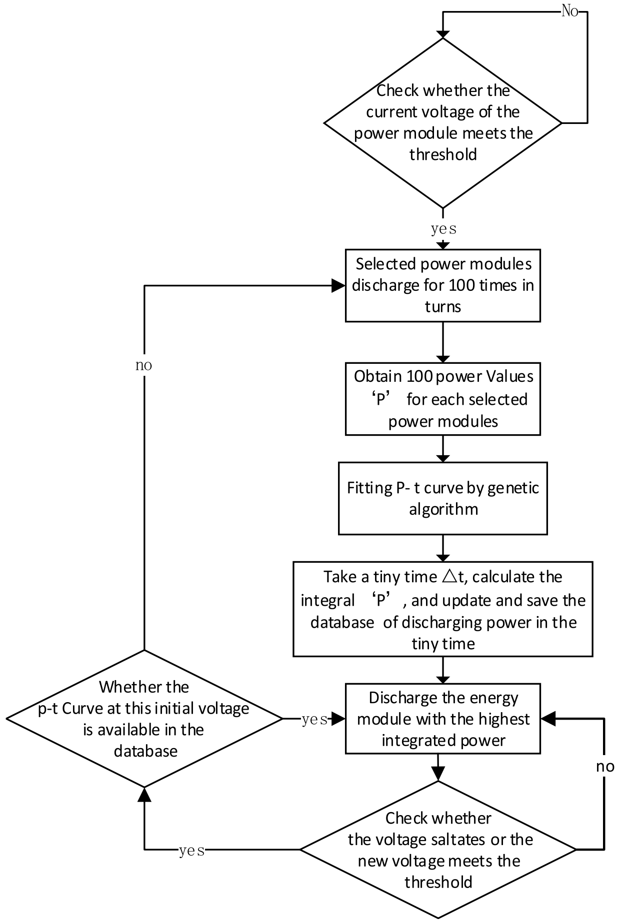

FIGURE 13 | Flow diagram of the maximum power control strategy based on power trajectory tracking.

In the process of simulation, it is found that solar energy and wave energy are basically at the same power level, while thermoelectric energy is far less than the other two kinds of energies. Thermoelectric energy will, therefore, be stored in an ultra-capacitor for a long time until its voltage reaches a threshold. The power-release time depends on whether the release power of the thermoelectric energy is the maximum during this period (compared with other environmental energy modules).

To ensure that the energy module with the highest power discharges at any time, we must know the discharge capacity of all energy modules. Therefore, we need to measure the discharge power of all energy modules in different environments, synthesize the power curve and save them, and form a large database of power curves at last.

In a real system, how to define different environments is an issue to consider. After studying enough environmental energy collection modules, it is found that the port voltage of the energy module has a certain proportional relationship with the external environment. Therefore, the control strategy in this study stipulates that those different environmental energies are determined by different energy module port voltages.

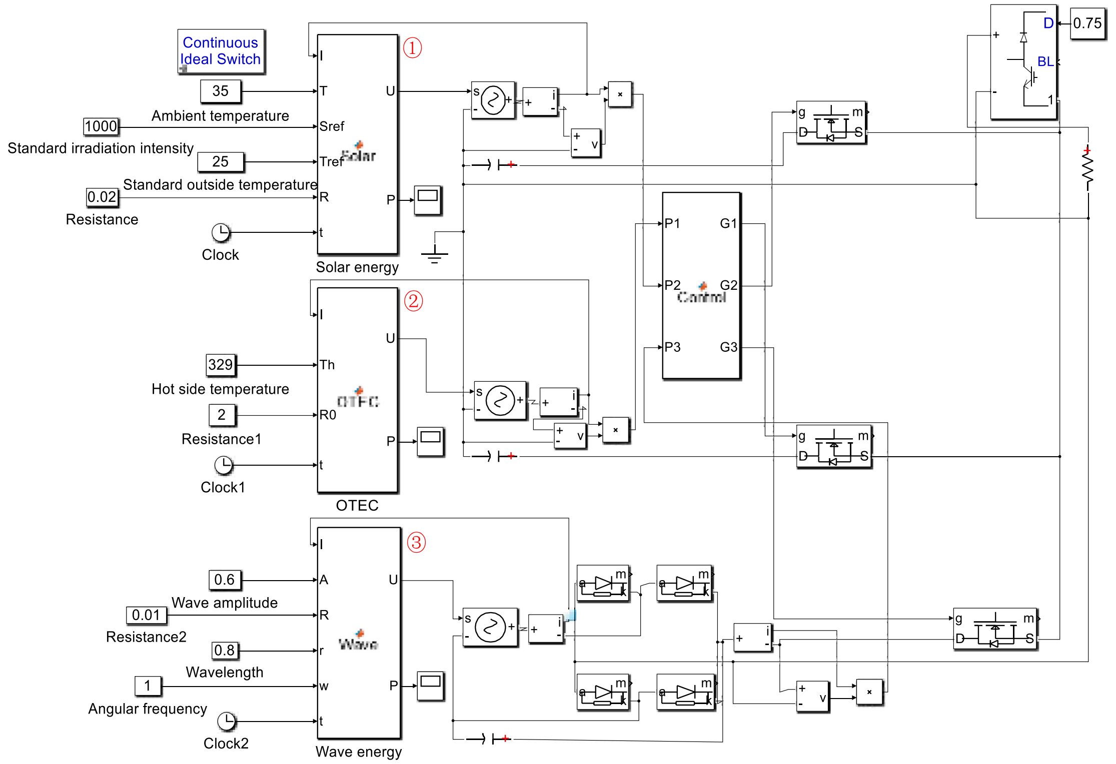

FIGURE 14 | Mixed environmental energy collection and the management system model.

Therefore, the aforementioned description can be summarized as follows: we need to measure the discharge power of all energy modules under different initial voltages, form and save power curves under different initial voltages, and form a large database of power curves under different initial port voltages.

The procedure of power tracking of all power modules that meet the voltage threshold is as follows.

1. The port voltage of all energy modules is measured by the heart rate sampling system, and the energy modules meeting the voltage threshold for a little period are opened in turn to obtain 100 power points of different energy modules.
2. The measured power points fit into P-t curves using the genetic algorithm.
3. A small unit time is selected and the power integral value in unit time is calculated according to this curve. This power integral value is saved, and a large database of power integral values in unit time is formed under different energy modules and different voltage values.

Next, the power module with the maximum power integral value at the current time to discharge to the load is chosen. During the discharge process, the voltage of each energy module has to be checked for a voltage mutation and whether the terminal voltage of the new energy module meets the voltage threshold. If not, the previous discharge sequence is performed. If yes, the power curve of the energy module is checked at the current voltage and stored in the power curve database. If not, it is necessary to collect the power values of 100 energy modules that meet the requirements again and fit them into P-t curves, integrate them again, and save and update the large database. However, if the data exist in the database, the energy module that is to be discharged at the next moment can be determined directly according to the integral value of the power per unit time saved in the big data.

To better explain the big data of the power curve of multi-energy modules, we assume that there are now two types of energy modules, E1 and E2. At the initial moment, the voltage of E1 is V1, and after discharging for a short period of time, different power values under different voltages are obtained, denoted as

$$\mathrm{E1}: \begin{bmatrix} \mathrm{V1}: & \mathrm{P11} & \mathrm{P12} & \ldots & \mathrm{P1100} \\ \mathrm{V2}: & \mathrm{P21} & \mathrm{P22} & \ldots & \mathrm{P2100} \\ \ldots & \ldots & \ldots & \ldots & \ldots \\ \mathrm{Vn}: & \mathrm{Pn1} & \mathrm{Pn1} & \ldots & \mathrm{Pn100} \end{bmatrix}. \tag{4 – 1}$$

Using the genetic algorithm to fit 100 power points which are under the voltage V1, V2 ... Vn into a power curve, denoted as

$$\mathrm{E1}: \begin{bmatrix} \mathrm{V1}: & \mathrm{P1}(t) \\ \mathrm{V2}: & \mathrm{P2}(t) \\ \ldots & \ldots \\ \mathrm{Vn}: & \mathrm{Pn}(t) \end{bmatrix}. \tag{4 – 2}$$

In total, 100 power points of E2 were obtained, fitted into the power curve, and saved in the same way.

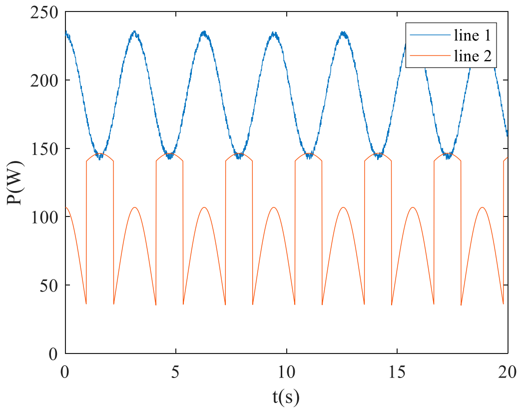

FIGURE 15 | Simulated cure of the maximum power control strategy based on power trajectory tracking.

The little period is taken Δt, the power integral of E1 and E2 under a certain initial voltage is calculated, the integral value of the two is compared, and then the energy model with the maximum integral value to discharge is selected.

The power integral large database saves the power integral values of different energy modules in a micro-period under certain environmental conditions. Any change in the output power of an energy module due to environmental changes is measured again and saved. That is, the database can self-update, self-preserve, and self-learn according to the measurement system and the learning results to determine the discharge sequence of energy modules. The aforementioned process shows that the longer the system runs, the larger its database will be, but the more efficient its execution will be.

The database does not use the original discharge power curve of the energy module (which can be obtained from the factory manual of the energy acquisition module) but uses the power curve synthesized by the real-time measuring system as a reference, which effectively avoids the error between the original power curve and the actual power curve caused by the decrease of the hardware working efficiency.

One of the biggest features of the maximum power output algorithm based on power trajectory tracking is adaptability. Combined with data acquisition and saving, the algorithm can adapt to different (environmental energy collection) hardware systems and automatically adjust the voltage threshold and the controlled triode through the output power of the system.

To sum up, the system can always maintain the maximum power output, effectively improve the utilization of environmental mixed energy, and improve the endurance of wearable devices.

To verify the effectiveness of the algorithm, a mixed environmental energy collection and management system model was established in Simulink, as shown in **Figure 14**.

Modules ①, ②, ③ are the solar power generation, wave power generation, and thermoelectric power generation, respectively.

To reflect the circuit topology of the energy acquisition and the energy efficiency of the maximum power algorithm, this study builds a model in Simulink according to the circuit topology in **Figure 11B** and adds exactly the same energy module as shown in **Figure 14** with the same input conditions.

After the two model simulations, the power curve of the system is shown in **Figure 15**.

Line 1 is the simulation result of the corresponding model shown in **Figure 14**, and line 2 is the simulation result of the corresponding model shown in **Figure 11B**. It can be seen from line 2 that the passive circuit topology only outputs the energy with the highest voltage value at the current time. Because the solar and wave energies set in the simulation model are relatively high, the ultra-capacitor with a certain capacity cannot store too much energy for a long time, resulting in a serious waste of energy with a low current voltage. It can be seen from line 1 that the active circuit topology combined with the maximum power algorithm can ensure the maximum power output at the current moment and the supercapacitor can repeatedly store and discharge energy in a short time to maximize the discharge of the collected environmental energy.

As we know, the smaller the time Δt in the system, the better the system control effect will be. However, calculating the integral under an extremely small Δt will occupy many computing resources and increase the energy consumption of the system. Therefore, $\Delta t = 0.1$ ms is adopted in this study.

CONCLUSION

This study designed an active and controllable environmental energy acquisition circuit topology that establishes a heart rate sampling system, and innovatively designs a maximum output power algorithm based on power trajectory tracking. According to the application environment of an AUV, solar energy, wave energy, and temperature difference energy were selected as the environmental energy sources of the AUV. The mathematical models of these three energies were analyzed, established, and simulated in MATLAB and Simulink. Finally, passive (**Figure 11** (b)) and active (**Figure 14**) circuit models were established in Simulink, and identical input configurations were set for the two circuit models. The simulation results show that compared with the passive environmental energy acquisition mode, the active and controllable environmental energy acquisition circuit combined with the maximum power algorithm can effectively avoid the waste of environmental energy, improve the utilization of environmental energy, and improve the endurance of the underwater robot.

DATA AVAILABILITY STATEMENT

The original contributions presented in the study are included in the article/Supplementary Material; further inquiries can be directed to the corresponding author.

AUTHOR CONTRIBUTIONS

SS completed the active and controllable circuit topology design, maximum power algorithm design, and wrote the manuscript.

CW completed the establishment and simulation of all the models. ZQ completed research on underwater robots that use environmental energy. ZK completed the mathematical analysis of environmental energy in the manuscript. DG completed the structure design, algorithm and circuit correctness analysis, and simulation data analysis of the whole manuscript.

FUNDING

This work was supported by the National Natural Science Foundation of China (Nos. 61803285 and 62001332) and the National Defense Pre-Research Foundation of China (No. H04W201018).

REFERENCES

Ageev, M. D., Blidberg, D. R., Jalbert, J., Melchin, C. J., and Troop, D. P. (2002). "Results of the Eval-Uation and Testing of the Solar Powered AUV and its Subsys-Tems," in Autonomous Underwater Vehicles, 2002. Proceedings of the 2002 Workshop on, February 2002 (Piscataway, USA: IEEE), 137–145. doi:10.1109/AUV.2002.1177216

Auto Naut (2016). Autonaut in Chichester Marina [EB/OL]. AvaliableAt: http://www.autonautusv.com/gallery/autonaut-chichester-marina.

Bao, Z. K., and Zhang, H. F. (2016). Optimal Local Control Strategy for Disease Transmission over Two-Dimensional Kleinberg Networks[J]. *J. Univ. Electron. Sci. Technol. China* 45 (3), 475–480. doi:10.3969/j.issn.1001-0548.2016.02.028

Chen, J., Lin, B., Wang, H., and Lin, G. (2000). Optimal Design of a Multi-Couple Thermoelectric Generator. *Semicond. Sci. Technol.* 15 (2), 184–188. doi:10.1088/0268-1242/15/2/318

Chen, W., Li, J., and Qi, L. (2021). Power Following Control Strategy for SOC Dynamic Adjustment of Fuel Cell Compact Vehicle [J]. *J. Southwest Jiaot. Univ.* 56 (1), 197–205. doi:10.3969/j.issn.0258-2724.20190552

Dey, B., and Qin, C. (2009). Mathematical Model and Simulation Analysis of Photovoltaic Module Electrical Characteristics. *Semicond. Optoelectron.* 30 (1), 47–50. doi:10.16818/j.issn1001-5868.2009.01.011

Eco Marine Power (2014). Aquarius Unmanned Surface Vessel [EB/OL]. AvaliableAt: http://www.ecomarinepower.com/en/aquarius-usv.

Elkaim, G. H., and Boyce Lee, C. O. (2007). "Experimental Validation of GPS-Based Control of an Unmanned Wing-Sailed Catamaran[C]," in ION GNSS 20th International Meeting of the Satellite Division, Fort Worth Convention Center, USA, September 25 - 28, 2007 (North MiamiBeach, USA: Curran Associates Inc.), 1950–1956.

Elkaim, G. H. (2006). The Atlantis Project: A GPS-Guided Wing-Sailed Autonomous Catamaran. *Navigation* 53 (4), 237–247. doi:10.1002/j.2161-4296.2006.tb00386.x

Fang, H., and Li, Z. (2012). Review of Energy System Technology for Autonomous Underwater Vehicle [J]. *J. Electr. Power Syst. Automation*. doi:10.19635/j.cnki.csu-epsa.000965

Feng, X. S., and Li, Y. P. (2013). Thirty Years Evolution of SIA's Unmanned Marine Vehicles[J]. *China Sci. Bull.* 58 (s2), 2–7. doi:10.1360/972013-1120

Feng, X., Li, Y., and Xu, H. (2011). The Next Generation of Unmanned Marine Vehicles Dedicated to the 50 Anniversary of the Human World Record Diving 10912 M. *Robot* 33 (1), 113–118. doi:10.3724/sp.j.1218.2011.00113

Fenucci, D., Caffaz, A., Costanzi, R., Fontanesi, E., Manzari, V., Sani, L., et al. (2016). "WAVE: A Wave En-Ergy Recovery Module for Long Endurance Gliders and AUVs[C]," in OCEANS 2016 MTS/IEEE Monterey, Monterey, CA, USA, 19-23 Sept. 2016 (Piscataway, USA: IEEE). doi:10.1109/OCEANS.2016.7761136

Luo, J., Yang, Y., and Dong, H. T. (2013). Energy and Harvesting Technology in Underwater Environment[J]. *Mine Warf. Ship Self Def.* 21 (2), 29–33. doi:10.1109/EIT.2012.6220721

Ma, Z., Wang, Y., Wang, S., and Yang, Y. (2016). Ocean Thermal Energy Harvesting with Phase Change Material for Underwater Glider. *Appl. Energy* 178, 557–566. doi:10.1016/j.apenergy.2016.06.078

National Oceanography Center (2016). Autonomous Surface Vehicles [EB/OL]. Avaliable at: http://noc.ac.uk/facilities/marine-autonomous-robotic-systems/asv.

Ren, L., Lin, S., Qing, Z., Fei, D., and Liu, X. J. (2017). Application Status and Development Trend of Power Battery for AUV[J]. *Chin. J. Power Sources* 41 (6), 952–955. doi:10.3969/j.issn.1002-087X.2017.06.040

Rui, W., Qiuye, S., Pinjia, Z., Yonghao, G., Dehao, Q., and Peng, W. (2020). Reduced-Order Transfer Function Model of the Droop-Controlled Inverter via Jordan Continued-Fraction Expansion. *IEEE Trans. Energy Convers.* 35 (3), 1585–1595. doi:10.1109/tec.2020.2980033

Sun, X. (2013). Discussion on Energy Storage of Long Endurance AUV[J]. *Electron. World* 20, 188–189.

Sun, Z. F. (2015). Development Status of Marine Energy Utilization Technology at Home and Abroad[J]. *Ship Build. China* 56 (S2), 519–526. doi:10.1155/2013/941781

Venkata Rao, R., and Patel, V. (2013). Multi-objective Optimization of Two Stage Thermoelectric Cooler Using a Modified Teaching-Learning-Based Optimization Algorithm. *Eng. Appl. Artif. Intell.* 26 (1), 430–445. doi:10.1016/j.engappai.2012.02.016

Wang, R., Sun, Q., Hu, W., Li, Y., Ma, D., and Wang, P. (2021). SoC-Based Droop Coefficients Stability Region Analysis of the Battery for Stand-Alone Supply Systems with Constant Power Loads. *IEEE Trans. Power Electron.* 36 (7), 7866–7879. doi:10.1109/tpel.2021.3049241

Wang, R., Sun, Q., Ma, D., and Liu, Z. (2019). The Small-Signal Stability Analysis of the Droop-Controlled Converter in Electromagnetic Timescale. *IEEE Trans. Sustain. Energy* 10 (3), 1459–1469. doi:10.1109/tste.2019.2894633

Webb, D. C., Simonetti, P. J., and Jones, C. P. (2001). SLOCUM: an Underwater Glider Propelled by Environmental Energy:an Underwater Glider Propelled by Environmental Energy[J]. *IEEE J. Ocean. Eng.* 26 (4), 447–452. doi:10.1109/48.972077

Wynn, R. B., Huvenne, V. A. I., Le Bas, T. P., Murton, B. J., Connelly, D. P., Brtt, B. J., et al. (2014). Autonomous Underwater Vehicles (AUVs): Their Past, Present and Future Contributions to the Advancement of Marine Geoscience[J]. *Mar. Geol.* 352, 451–468. doi:10.1016/j.margeo.2014.03.012

Xiao, X., Meng, X., Le, D. D., and Takarada, T. (2011). Two-stage Steam Gasification of Waste Biomass in Fluidized Bed at Low Temperature: Parametric Investigations and Performance Optimization. *Bioresour. Technol.* 102 (2), 1975–1981. doi:10.1016/j.biortech.2010.09.016

Xie, R. (2018). *Research on Rule-Based Control Strategy for Extended Range Electric Vehicle [D]*. Beijing: Beijing University of Technology.

Yang, Y., Wang, Y., Ma, Z., and Wang, S. (2016). A Thermal Engine for Underwater Glider Driven by Ocean Thermal Energy. *Appl. Therm. Eng.* 99, 455–464. doi:10.1016/j.applthermaleng.2016.01.038

Yu, T. (2015). *Research on Contactless Power Transmission of Autonomous Underwater Vehicle[D]*. Harbin: Harbin Engineering University.

Zhang, B. D., Guo, S., Zhang, X., Xue, C., and Teng, L. (2020). Adaptive Smoothing Power Following Control Strategy Based on an Optimal Efficiency Map for a Hybrid Electric Tracked Vehicle[J]. *Energies* 13 (8), 1–25. doi:10.3390/en13081893

Zhang, B., and Li, K. (2018). Research on Global Optimal Control Strategy for Plug-In Hybrid Electric Vehicle Based on Dynamic Programming[J]. *Automot. Technol.* 7, 16–21. doi:10.19620/j.cnki.1000-3703.20170789

Conflict of Interest: The authors declare that the research was conducted in the absence of any commercial or financial relationships that could be construed as a potential conflict of interest.

frontiers | Frontiers in Energy Research

ORIGINAL RESEARCH
published: 02 June 2022
doi: 10.3389/fenrg.2022.907359

Consensus Dispatch of Distributed Power Network Based on Multi-Access Edge Computing and Multi-Agent System

Liming Wang[1,2], **Yingming Liu**[1]*, **Xiaodong Wang**[1], **Hanbo Wang**[1] **and Guoxian Guo**[1]

[1]*School of Electrical Engineering, Shenyang University of Technology, Shenyang, China,* [2]*College of Information, Shenyang Institute of Engineering, Shenyang, China*

This paper presents a consensus dispatch model of the distributed power network based on multi-access edge computing (MEC) and multi-agent system (MAS).MEC decentralizes the processing and storage of data in the distributed power system to the edge node combined with MAS, which reduces the amount of calculation in the dispatch center. The model formulates different objective functions for the edge nodes and the cloud center nodes of the MEC to optimally allocate the output of each unit. Meanwhile, in order to meet the consensus dispatch of distributed units, the operational benefits of flexible load, the operating cost of thermal power units, the penalty cost of abandoning wind and solar power for new energy units, and the operation of energy storage devices are utilized as consensus variables. Based on these consensus variables, an optimal dispatch method of the distributed power network is established. Compared with the traditional dispatch model, this model integrates distributed units and autonomous sub-regions through MAS and MEC, which ensures the system performs consensus dispatch under the balance of supply and demand, and also improves the proportion of new energy consumption.

Keywords: distributed power system, edge computing, multi-agent system, consensus dispatch, optimal dispatch method

OPEN ACCESS

Edited by:
Rui Wang,
Northeastern University, China

Reviewed by:
Kun She,
University of Electronic Science and Technology of China, China
Xuguang Hu,
Northeastern University, China

***Correspondence:**
Yingming Liu
lym@sut.edu.cn

Specialty section:
This article was submitted to Smart Grids, a section of the journal Frontiers in Energy Research

Received: *29 March 2022*
Accepted: *25 April 2022*
Published: *02 June 2022*

Citation:
Wang L, Liu Y, Wang X, Wang H and Guo G (2022) Consensus Dispatch of Distributed Power Network Based on Multi-Access Edge Computing and Multi-Agent System.
Front. Energy Res. 10:907359.
doi: 10.3389/fenrg.2022.907359

1 INTRODUCTION

With the penetration of renewable energy, the structure of the power system is facing many changes. Through the continuous upgrading of communication network technology, the power system develops rapidly towards scale and intelligence. The Ubiquitous Electric Internet of Things (UEIOT), which is built on a distributed power system, emerges at this moment (Li et al., 2017).The structure of distributed power systems is more complex than the traditional power transmission network. For example, the reduced-order aggregate model for large-scale converters with inhomogeneous initial conditions in DC microgrids, and reduced-order transfer function model of the droop-controlled inverter via Jordan continued-fraction expansion proposed in certain studies both involve large-scale power systems (Wang et al., 2020; Wang et al., 2021). With the development of large-scale power systems, the proportion of internal distributed power sources has gradually increased. The amount of data inside the UEIOT is also substantial based on distributed power systems, which brings tremendous pressure to the transmission and processing of power data.

In the context of continuous development of intelligent technology and large-scale growth of power data, many smart terminal devices have been deployed on the power distribution side. The basic configuration of UEIOT gradually takes shape, and the research on flexible dispatch of distributed power systems has attracted the attention of many scholars. In the existing research, edge computing (EC) technology is integrated into the power system. It calculates the data of power grid perception layer at the edge side, which saves time and cost of network transmission (Sun et al., 2019; Li et al., 2020). The role of EC is analyzed from the perspective of the practical application of the smart grid, which shows that the cloud-side collaboration mechanism of EC can better coordinate the information communication and flexible dispatch of distributed units (Li et al., 2018).Multi-access edge computing (MEC) derived from EC realizes high-speed access and read of terminal software using wireless network information. Multi-agent system (MAS) has good concentration and dispersion characteristics and is widely used in distributed power systems. For example, Kumar Nunna and Doolla (2013) utilizes a multi-agent system to control the power balance. MAS takes multiple microgrids as a whole to participate in the operation of the upper-layer network, which provides an idea for multi-unit control in distributed unit hierarchical dispatch.

The distributed control technology of MAS and the unique edge-side processing mechanism of EC can provide a novel operation framework for the multi-node and multi-stage optimization dispatch of the power system (He et al., 2019).However, due to the uncertain output of new energy sources, the high penetration of flexible loads, and the demand for “plug and play” of some power components, the topology of power network will change. Meanwhile, the centralized optimal dispatch for distributed units has higher requirements for the stability of the communication network between units, which may lead to unreasonable dispatch results (Gong et al., 2018).

Based on the technology of MEC-MAS, this paper establishes a hierarchical dispatch model with the maximum proportion of new energy consumption and the minimum cost of system operation. The model solves the optimal dispatch plan of distributed power systems by dividing consistent variables of each unit, and improves the proportion of new energy consumption and the system stability.

The main contributions of this paper are listed below:

1) The established power network communication model based on MEC-MAS can provide a stable operating framework for distributed systems;
2) The constructed hierarchical dispatching model composed of edge nodes and cloud centers is constructed. Compared with the traditional centralized processing mode, the edge processing of data can effectively improve the dispatching efficiency;
3) By dividing and solving the consensus variables through the objective function of the hierarchical dispatching model, the distributed units can optimize the unified objective under the constraints, and a better distributed power grid dispatching scheme can be obtained.

The remainder of this paper is organized as follows. **Section 2** presents an EC model of the power system based on MAS. **Section 3** establishes the distributed multi-agent consensus dispatch model. **Section 4** shows the results of the case study. **Section 5** illustrates the conclusion.

2 EC MODEL OF THE POWER SYSTEM BASED ON MAS

2.1 Integration of EC and Power System

With the large amount of new energy connected to the grid, the power supply mode is gradually transformed from the centralized to the distributed. Therefore, a distributed network topology is formulated among distributed power sources, energy storage systems and loads. For this topology, traditional power dispatch strategies are inefficient and unreasonable. MEC is a new computing model that performs computing at the edge of the network. MEC can be installed on the edge of the power distribution network, and the edge data can be processed nearby. MEC can also selectively upload data to the cloud computing center to reduce system network transmission costs and improve data transmission efficiency.

2.2 Topology Structure of Power System Network Based on MEC-MAS

As shown in **Figure 1**, the model of MEC is introduced into the distributed network topology of the power system. The system is divided into autonomous sub-regions of edge nodes according to the geographic location of distributed power sources and loads, and the capacity of energy storage systems. Each autonomous sub-region model includes conventional units, wind turbines, photovoltaic devices, energy storage systems, loads, and corresponding data processing devices.

The hierarchical optimal dispatch model consisting of edge nodes and cloud center nodes is established. MAS is introduced into edge nodes, which can further integrate the data perception layer, network layer, edge layer, and application function layer of the autonomous sub-region in the edge node (Guan et al., 2020).The data perception layer corresponds to the bottom layer of MAS, and is used for data collection. The data perception receives upper-layer data and starts actions based on data collection and upload. The network layer corresponds to the middle layer of MAS, and does not participate in data processing and dispatching. The network layer is only utilized for uploading and delivering dispatch information. The edge layer includes edge terminals with high-density computing and reliable storage capabilities. The application function layer can realize the collection and real-time processing of data on the power generation and distribution sides. The edge layer and the application function layer correspond to the top layer of MAS. The top layer of MAS uses the upper-level dispatch goal of the edge node as its operation goal for data calculation and power dispatch (Xing et al., 2018).

After the edge node performs power dispatch according to the dispatch goal (the largest proportion of new energy consumption), the cloud center node dispatches through the data processed by the edge node (Feng et al., 2019).The cloud center node makes the entire system operate economically by optimally allocating the power output and power exchange of each autonomous sub-region.

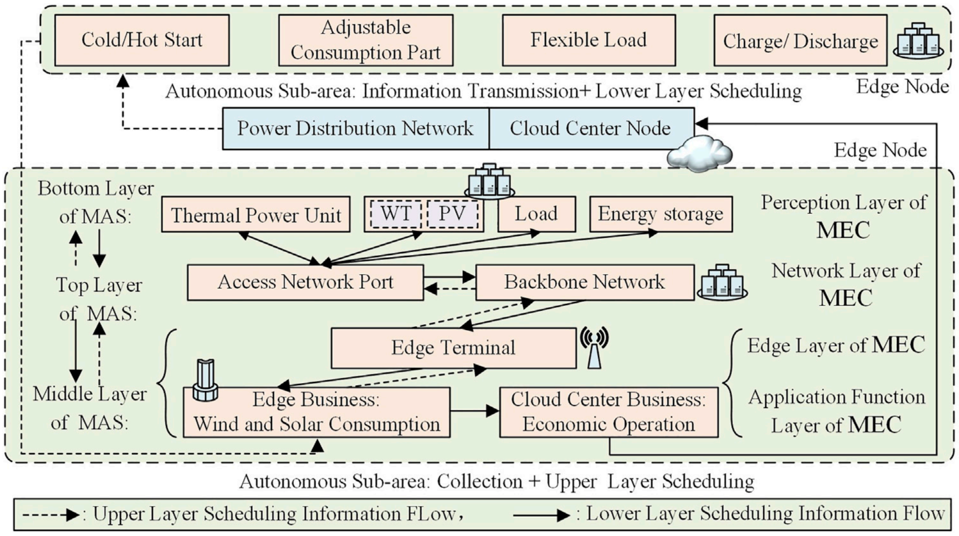

FIGURE 1 | Structure of the distributed power network based on MEC-MAS.

2.3 Hierarchical Optimal Dispatch Model of MEC-MAS

To improve new energy consumption, this paper divides new energy output power into the adjustable and fixed consumption parts (Zhang et al., 2019).The fixed consumption part is the new energy output power which must be consumed. The adjustable consumption part is the new energy output power which can be abandoned, but requires certain penalty costs. The penalty cost function of new energy output power abandonment can be written as

$$A_k\left(P_{nk}\right) = \eta_k\left(P_{nk,max} + P_{nk}\right)^2, \quad k \in S_n, \tag{1}$$

where $A_k(P_{nk})$ is the penalty cost function of new energy output power abandonment for the unit k; P_{nk} is the adjustable consumption part of new energy output power for the unit k; $P_{nk,max}$ is the maximum power of the adjustable consumption part; η_k is the constant coefficient of new energy output power abandonment; S_n is the total number of new energy power generation units.

In the MEC-MAS model, the top layer of MAS in the edge node issues commands, and the edge node uses the bottom layer function to obtain the information of each sub-area. The edge node returns units' and loads' data in the autonomous sub-area to the top layer through the middle layer. The edge layer and application function layer perform optimal dispatch of units with the goal of the largest proportion of new energy consumption. The objective function can be expressed as

$$\max F_1 = \max\begin{cases} 1, \quad P_{nk} = 0, \\ \sum\limits_{f\in S_n} P_{nf} \Big/ \left(\sum\limits_{f\in S_n} P_{nf} + \sum\limits_{k\in S_n} P_{nk}\right), \quad P_{nk} \neq 0, \end{cases} \tag{2}$$

$$0 \le P_{nk} \le P_{nk,\max}, \tag{3}$$

where F_1 is the proportion of new energy consumption; P_{nf} is the fixed consumption part of new energy output power for the unit f.

After each autonomous sub-area is dispatched by the edge node at the upper level, the edge node uploads new energy power generation results to the cloud center node (the power distribution station).After receiving the information, the cloud center node formulates dispatch strategies for various units in each autonomous sub-region with the operation goal. The cloud center node feeds back the dispatch strategy to each edge node for the associated power supply, flexible loads and energy storage units (Sun et al., 2012).The objective function of the cloud center node is designed by

$$\min F_2 = \min\left(\sum_{m\in S_s} E_m\left(P_{sm}\right) + \sum_{i\in S_G} C_i\left(P_{Gi}\right) + \sum_{k\in S_n} A_k\left(P_{nk}\right) - \sum_{j\in S_L} D_j\left(P_{Lj}\right)\right), \tag{4}$$

where F_2 is the operation cost of the system; $E_m(P_{sm})$ is the operation cost function of the energy storage device m; P_{sm} is the electrical energy delivered by the energy storage device m to the power system (in the charging state, P_{sm} is negative); S_s is the total number of energy storage devices; $C_i(P_{Gi})$ is the power generation cost of the thermal power unit i; P_{Gi} is the output power of the thermal power unit i; S_G is the total number of thermal power units; $D_j(P_{Lj})$ is the operation benefit of the flexible load j; P_{Lj} is the demand power of the flexible load j; S_L is the total number of flexible loads.

The constraints of the system operation are expressed as

$$\sum_{j\in S_L} P_{Lj} - \sum_{m\in S_s} P_{sm} - \sum_{f\in S_n} P_{nf} - \sum_{k\in S_n} P_{nk} - \sum_{i\in S_G} P_{Gi} = 0, \tag{5}$$

$$P_{Gi,\min} \le P_{Gi} \le P_{Gi,\max}, \tag{6}$$

$$P_{Lj,\min} \leq P_{Lj} \leq P_{Lj,\max}, \tag{7}$$

$$P_{sm,\min} \leq P_{sm} \leq P_{sm,\max}, \tag{8}$$

where $P_{Gi,\min}$ and $P_{Gi,\max}$ are the lower and upper limits of the output of thermal power units; $P_{Lj,\min}$ and $P_{Lj,\max}$ are the lower and upper limits of the demand power of flexible loads; $P_{sm,\min}$ and $P_{sm,\max}$ are the lower and upper limits of the electrical energy delivered.

The existing research results mostly use centralized optimization technology to solve the distributed economic dispatch problem. When the centralized optimization method is employed, the dispatch center needs to issue commands to dispatch all power supplies, loads, and other devices in the system. The dispatch center needs to make dispatch arrangements for each dispatch object. If the communication connection fails, it may cause problems such as unstable system operation and unreasonable power distribution. Therefore, a reliable communication mechanism based dispatch strategy can play a good role in coordinating and managing distributed power sources and adjustable loads.

3 MAS CONSENSUS DISPATCH MODEL

In the distributed optimization algorithm, in order to meet the comprehensive optimization of the system, the dispatch goals of all nodes need to be unified as a whole. Then, multi-agents can reach consensus under the MEC-MAS system (Xu et al., 2019).This paper uses MEC-MAS as the dispatching framework, and adds the stage of distributed unit consensus dispatching on the basis of traditional power system dispatching. Each distributed unit determines its own independent goals according to its own operating cost/benefit, and each type of unit pursues the maximization of its own interests. At the same time, since all types of units belong to the same system, their operation needs to be constrained by the overall power balance of the system. Therefore, while all kinds of generating units are pursuing the maximization of their own interests in a distributed manner, they also achieve the overall dispatching objective of the traditional dispatching meaning—maximizing the economy of system operation.

3.1 Operation Model of Distributed Multi-Agent

In the MEC-MAS system, there are many flexible loads, which can be switched and transferred according to demand during the dispatch and operation. As a result, flexible loads can reduce the pressure on the power grid during peak and valley periods (Yang et al., 2013).The operation benefit of the flexible load is expressed as

$$D_j\left(P_{Lj}\right) = a_j P_{Lj}^2 + b_j P_{Lj} + c_j, \quad j \in S_L\,, \tag{9}$$

where a_j, b_j and c_j are the function coefficients.

The power generation cost of the thermal power unit can be determined by

$$C_i\left(P_{Gi}\right) = \alpha_i P_{Gi}^2 + \beta_i P_{Gi} + \gamma_i, \quad i \in S_G\,, \tag{10}$$

where α_i, β_i and γ_i are the function coefficients.

When we only consider the discharge of energy storage devices, the cost curve of energy storage devices approaches a binary function with a minimum point at the origin (Wang et al., 2021).It can be computed by

$$E_m\left(P_{sm}\right) = \zeta_m P_{sm}^2, \quad m \in S_s\,, \tag{11}$$

where ζ_m is the coefficient of energy storage cost function.

3.2 Consensus Algorithm for Distributed Variables

Within the framework of MEC-MAS, this paper defines the power generation cost of thermal power units, the benefits of the flexible load operation, the penalty cost of adjustable consumption part of new energy units, and the operation cost of energy storage devices (only the discharge conditions are considered) as distributed multi-agent consensus variables IG, IL, IA, and IE (Zhang and Chow, 2012). Then, calculate the optimal solution of the distributed optimization problem through the consensus algorithm.

Through the transformation of **Equations 1**, **4**, we use the Lagrangian multiplier method to process the distributed coordination optimization model according to the principle of extraction of consensus variables. The processed model is formulated by

$$\begin{aligned} Q &= F_2 + \lambda\left(\sum_{j\in S_L} P_{Lj} - \sum_{m\in S_s} P_{sm} - \sum_{f\in S_n} P_{nf} - \sum_{k\in S_n} P_{nk} - \sum_{i\in S_G} P_{Gi}\right) \\ &= \sum_{m\in S_s} E_m\left(P_{sm}\right) + \sum_{i\in S_G} C_i\left(P_{Gi}\right) + \sum_{k\in S_n} A_k\left(P_{nk}\right) - \sum_{j\in S_L} D_j\left(P_{Lj}\right) \\ &\quad + \lambda\left(\sum_{j\in S_L} P_{Lj} - \sum_{m\in S_s} P_{sm} - \sum_{f\in S_n} P_{nf} - \sum_{k\in S_n} P_{nk} - \sum_{i\in S_G} P_{Gi}\right), \end{aligned} \tag{12}$$

where λ is the constant coefficient of the Lagrangian multiplier method.

Applying the classical Lagrangian multiplier method to the partial derivatives of each variable of **Equation 12**, the conditional equations of the distributed optimal solution can be given by

$$\frac{\partial Q}{\partial P_{Gi}} = \frac{\partial C_i}{\partial P_{Gi}} - \lambda = 0, \tag{13}$$

$$\frac{\partial Q}{\partial P_{Lj}} = -\frac{\partial D_j}{\partial P_{Lj}} + \lambda = 0, \tag{14}$$

$$\frac{\partial Q}{\partial P_{nk}} = \frac{\partial A_k}{\partial P_{nk}} - \lambda = 0, \tag{15}$$

$$\frac{\partial Q}{\partial P_{sm}} = \frac{\partial E_m}{\partial P_{sm}} - \lambda = 0, \tag{16}$$

$$\sum_{j\in S_L} P_{Lj} - \sum_{m\in S_s} P_{sm} - \sum_{f\in S_n} P_{nf} - \sum_{k\in S_n} P_{nk} - \sum_{i\in S_G} P_{Gi} = 0. \tag{17}$$

Organizing **Equations 13–17** yields

$$\frac{\partial C_i}{\partial P_{Gi}} = \frac{\partial D_j}{\partial P_{Lj}} = \frac{\partial A_k}{\partial P_{nk}} = \frac{\partial E_m}{\partial P_{sm}} = \lambda. \tag{18}$$

The distributed consensus variables IG, IL, IA and IE are written as

$$\mathrm{IG} = \lambda_{Gi} = \beta_i + 2\alpha_i P_{Gi}, \tag{19}$$

$$\mathrm{IL} = \lambda_{Lj} = b_j + 2a_j P_{Lj}, \tag{20}$$

$$\mathrm{IA} = \lambda_{nk} = 2\eta_k P_{nk} - 2\eta_k P_{nk,\max}, \tag{21}$$

$$\mathrm{IE} = \lambda_{sm} = 2\zeta_m P_{sm}. \tag{22}$$

The system formed by MEC-MAS is a distributed network structure. Therefore, in topological graph theory, we assume that there is information interaction between devices (D'Andrea and Dullerud, 2003).The state characteristics of each power component are expressed as

$$x_i(k+1) = x_i(k) + \sum_{j=1}^{n} a_{ij}\big(x_j(k) - x_i(k)\big), \tag{23}$$

where a_{ij} if the node x_i is connected with the node x_j; otherwise, $a_{ij} = 0$.

In the iterative process of the aforementioned formula, the corresponding consensus variables update their variables according to the adjacent variables. Choose a set of variables IG, IL, IA, and IE to ensure convergence accuracy considering 'law of equal consumption micro-increasing'. We regard them as standard consensus variables and introduce correction values to them (Zhu et al., 2015).At the same time, in order to meet the constraints of system operation, we take the difference between system operation benefits and costs as a correction (Olfati-Saber et al., 2007).The correction is defined as

$$\Delta P = \sum_{j\in S_L} P_{Lj} - \sum_{m\in S_s} P_{sm} - \sum_{f\in S_n} P_{nf} - \sum_{k\in S_n} P_{nk} - \sum_{i\in S_G} P_{Gi}. \tag{24}$$

The update formulas of the consensus variable corresponding to each equipment are formulated as follows:

$$\lambda_{Gi}(t+1) = \lambda_{Gi}(t) + \sum_{z=1}^{n} a_{iz}\left(\lambda_{Gz}(t) - \lambda_{Gi}(t)\right) + \delta\Delta P, \quad i \in S_G, \tag{25}$$

$$\lambda_{Lj}(t+1) = \lambda_{Lj}(t) + \sum_{z=1}^{n} a_{jz}\big(\lambda_{Lz}(t) - \lambda_{Lj}(t)\big) + \delta\Delta P, \quad j \in S_L, \tag{26}$$

$$\lambda_{sm}(t+1) = \lambda_{sm}(t) + \sum_{z=1}^{n} a_{sz}\left(\lambda_{sz}(t) - \lambda_{sm}(t)\right) + \delta\Delta P, \quad m \in S_s, \tag{27}$$

$$\lambda_{nk}(t+1) = \lambda_{nk}(t) + \sum_{z=1}^{n} a_{kz}\left(\lambda_{nz}(t) - \lambda_{nk}(t)\right) + \delta\Delta P, \quad k \in S_n, \tag{28}$$

where δ is the convergence coefficient.

The constraints of the system operation are given by

$$P_{Gi}(t) = \begin{cases} P_{Gi,\min}, & P_{Gi,\min} \le \dfrac{\lambda_{Gi} - \beta_i}{2\alpha_i} \le P_{Gi,\max}, \\ \dfrac{\lambda_{Gi} - \beta_i}{2\alpha_i}, & \dfrac{\lambda_{Gi} - \beta_i}{2\alpha_i} \le P_{Gi,\min}, \\ P_{Gi,\max}, & \dfrac{\lambda_{Gi} - \beta_i}{2\alpha_i} \ge P_{Gi,\max}, \end{cases} \tag{29}$$

$$P_{Dj}(t) = \begin{cases} P_{Dj,\min}, & P_{Dj,\min} \le \dfrac{\lambda_{Dj} - b_j}{2a_j} \le P_{Dj,\max}, \\ \dfrac{\lambda_{Dj} - b_j}{2a_j}, & \dfrac{\lambda_{Dj} - b_j}{2a_j} \le P_{Dj,\min}, \\ P_{Dj,\max}, & \dfrac{\lambda_{Dj} - b_j}{2a_j} \ge P_{Dj,\max}, \end{cases} \tag{30}$$

$$P_{nk}(t) = \begin{cases} P_{nk,\min}, & P_{nk,\min} \le \dfrac{\lambda_{nk} + 2\eta_k P_{nk,\max}}{2\eta_k} \le P_{nk,\max}, \\ \dfrac{\lambda_{nk} + 2\eta_k P_{nk,\max}}{2\eta_k}, & \dfrac{\lambda_{nk} + 2\eta_k P_{nk,\max}}{2\eta_k} \le P_{nk,\min}, \\ P_{nk,\max}, & \dfrac{\lambda_{nk} + 2\eta_k P_{nk,\max}}{2\eta_k} \ge P_{nk,\max}, \end{cases} \tag{31}$$

$$P_{sm}(t) = \begin{cases} P_{sm,\min}, & P_{sm,\min} \le \dfrac{\lambda_{sm}}{2\zeta_m} \le P_{sm,\max}, \\ \dfrac{\lambda_{sm}}{2\zeta_m}, & \dfrac{\lambda_{sm}}{2\zeta_m} \le P_{sm,\min}, \\ P_{sm,\max}, & \dfrac{\lambda_{sm}}{2\zeta_m} \ge P_{sm,\max}. \end{cases} \tag{32}$$

4 CASE STUDY

To verify the efficiency of this model, the IEEE30 node system is improved. **Figure 2** is the improved system structure diagram. **Figure 2** shows that the improved system contains six thermal power units, five new energy units (three wind turbines and two photovoltaic devices), three energy storage devices, and 16 load nodes. The dotted line in the figure represents the structure of the communication system. Communication points 1-6 correspond to thermal power units, communication points 7-11 correspond to new energy generating units, communication points 12–14 correspond to energy storage devices, and communication points 15–30 correspond to loads. This paper takes a certain regional power grid as an example to process the actual load data, wind power data, and photovoltaic power data.

4.1 Analysis of Economic Dispatch Results

According to the MEC-MAS hierarchical dispatching model, the edge node extracts the power generation and load data of each sub-area to form the individual information through the integration ability of MAS to distributed nodes (Pu et al., 2016). Then, the edge node performs upper-layer dispatching of various units in the sub-area to form individual dispatching information. After the cloud center node of MEC receives the individual dispatching information of the sub-area, the cloud

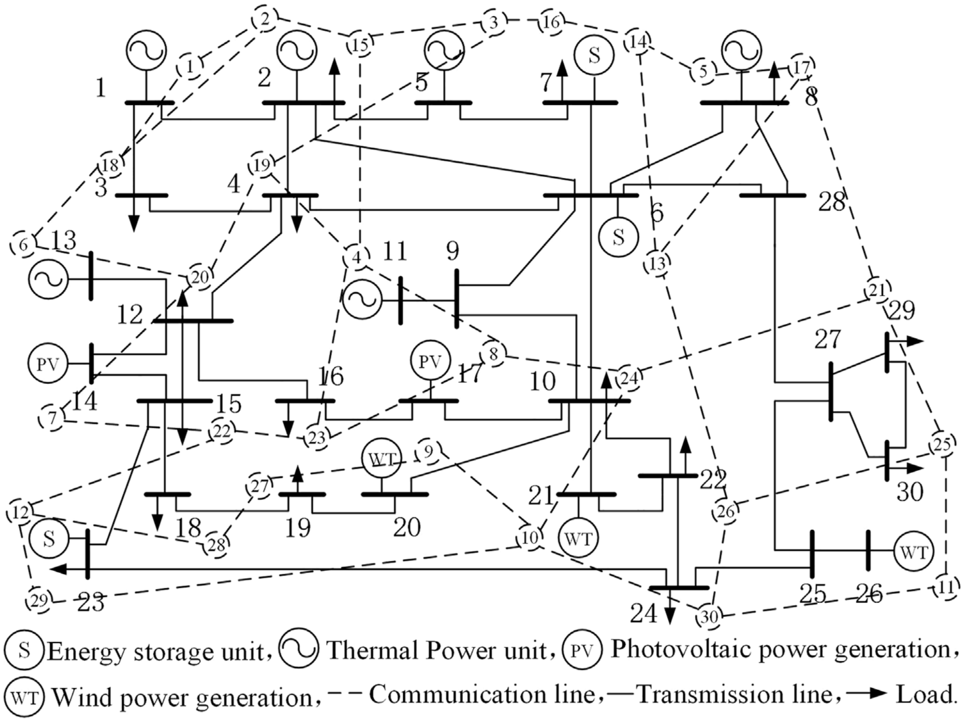

FIGURE 2 | The structure of the improved IEEE30 node system.

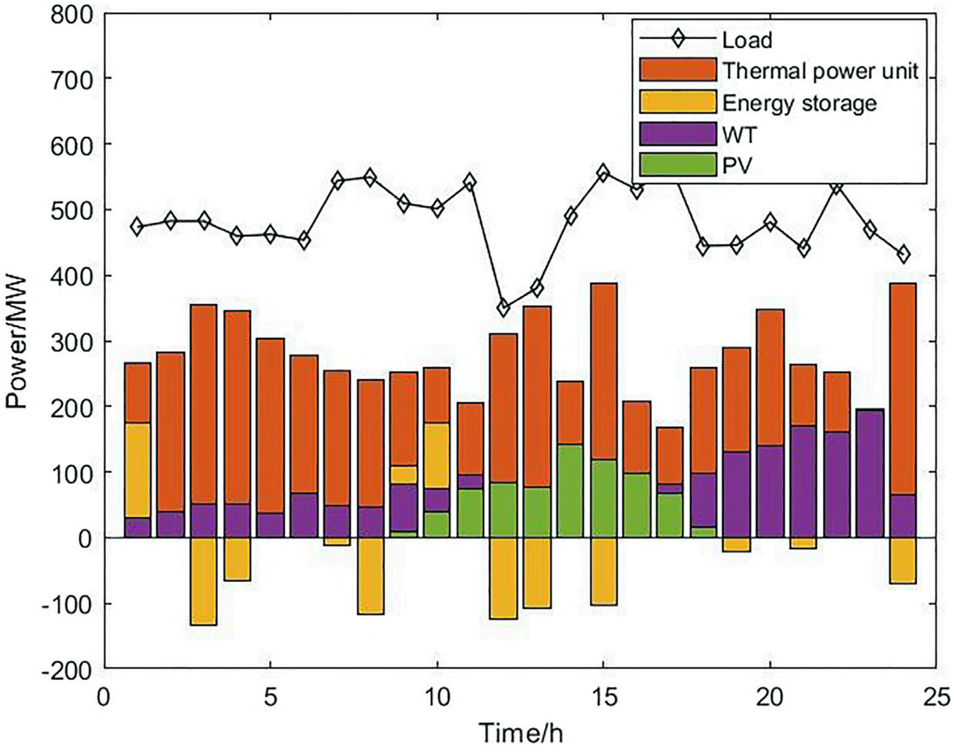

FIGURE 3 | Simulation results of the output of each unit.

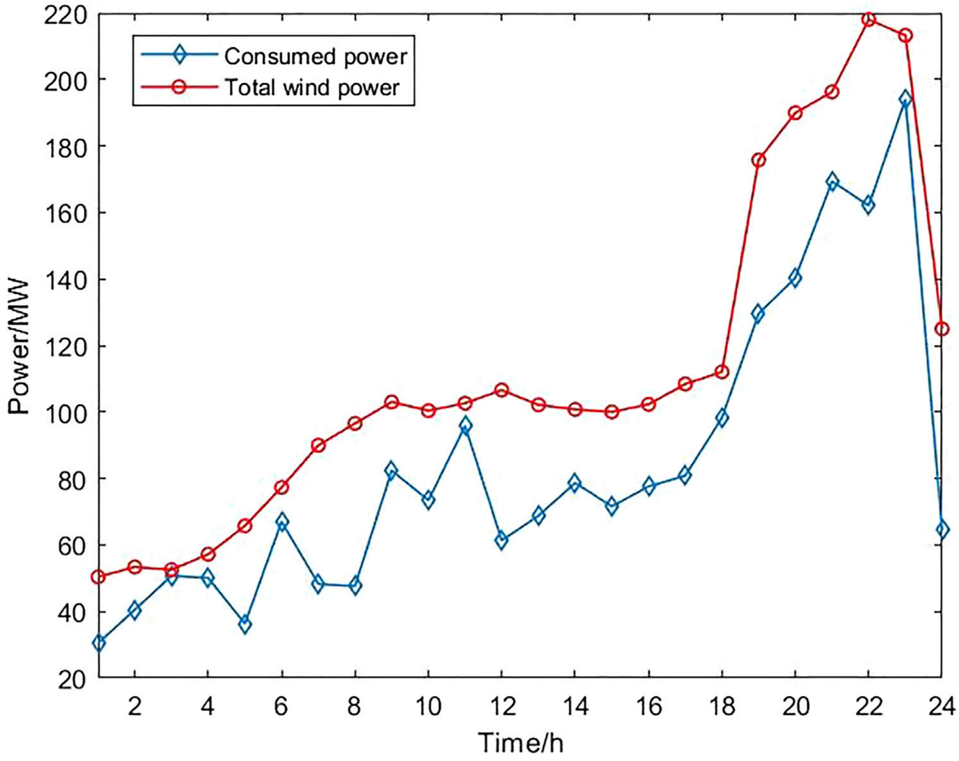

FIGURE 4 | Simulation results of wind power consumption.

center node uses the individual dispatching information of the sub-area as unit information for the lower layer dispatching. When the dispatching strategy is formulated by the cloud center layer, it is issued to the edge node through the information interaction between the cloud center layer and the edge node. The edge node optimizes control of each unit through MAS. The MEC-MAS model realizes the distributed coordination and optimization of each unit. The dispatching results are shown in **Figures 3–5**.

As shown in the experimental results, in order to meet the goal of maximizing the proportion of new energy consumption in the upper layer dispatch, the central cloud layer reduces the output of thermal power units and increases the power storage of energy storage device when the new energy output power is enormous. Meanwhile, in order to meet the financial requirements of system operation in the lower layer dispatching, the cloud center node processes the adjustable consumption part of the new energy unit. For instance, during 9:00–17:00, the actual output of the new energy is large, and the duration is long. At this time, if some thermal power units are shut down, the thermal power units will restart as a cold start (Mahmoodi et al., 2015). In the cold start state, the start-up cost of thermal power units is relatively high. The cloud center node needs to consider the proportion of new energy consumption and the start-up cost of thermal power units when formulating a dispatching strategy, so the proportion of new energy consumption is relatively low during this period. During the period from 21:00 to 23:00, the actual new energy output power reaches the peak stage, and the peak stage lasts for a short time. At this time, the load demand of the system is relatively enormous. To increase the proportion of new energy consumption at the edge nodes, the cloud center node reduces the output of thermal power units (the restart after the system shuts down thermal power units is the hot start, and the start-up cost is low). The proportion of new energy consumption is relatively increased.

In MEC-MAS, there are many types of units in the sub-region, and units depend on the integration of MAS. Therefore, given the distributed dispatching problem in the sub-area of the edge node, we construct the consensus variables of each unit to perform multi-agent distributed optimization control and verify the stability of the model in the distributed system.

4.2 Consensus Analysis of Distributed Unit Optimal Dispatching

In addition to considering a large amount of communication information and the complex types of units in the system, we introduce the interruption of communication between devices.

We select the 20:00 time period for experimental analysis. The experiment assumes that the No. Four thermal power unit is

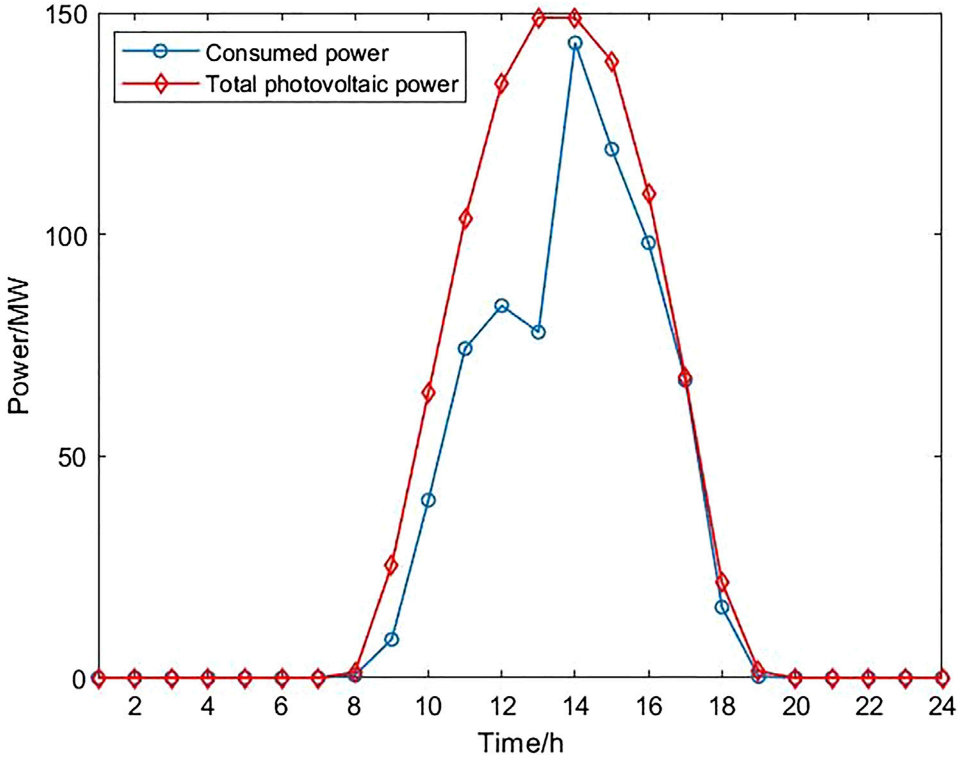

FIGURE 5 | Simulation results of photovoltaic power consumption.

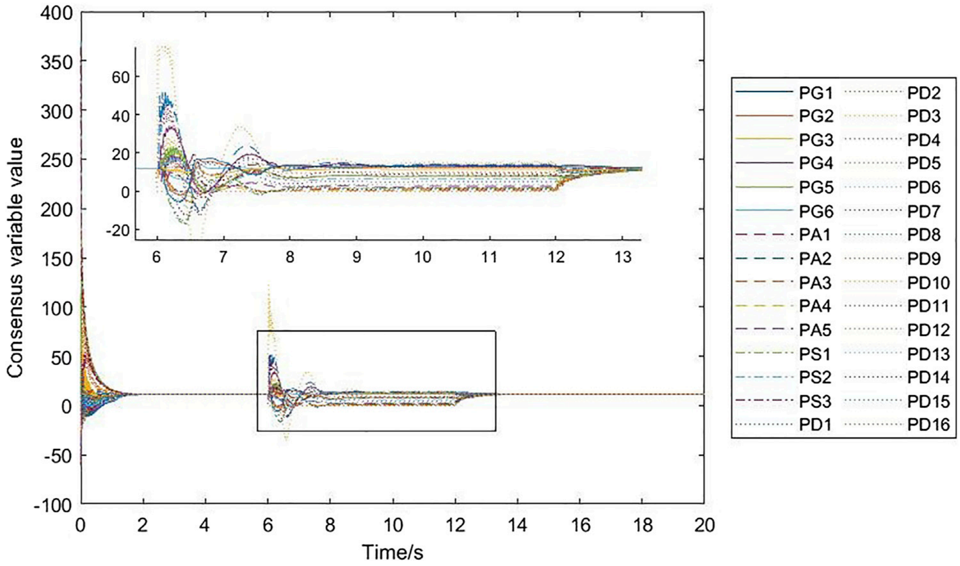

FIGURE 6 | Simulation results of consensus variables.

disconnected from the No. 15 load in the sixth second, the No. 10 new energy unit is disconnected from the No. 24 and No. 29 loads in the sixth second, the No. 12 energy storage device is disconnected from the No. 22 load in the sixth second. The experiment assumes that the system resumes all communications at the 16th second.

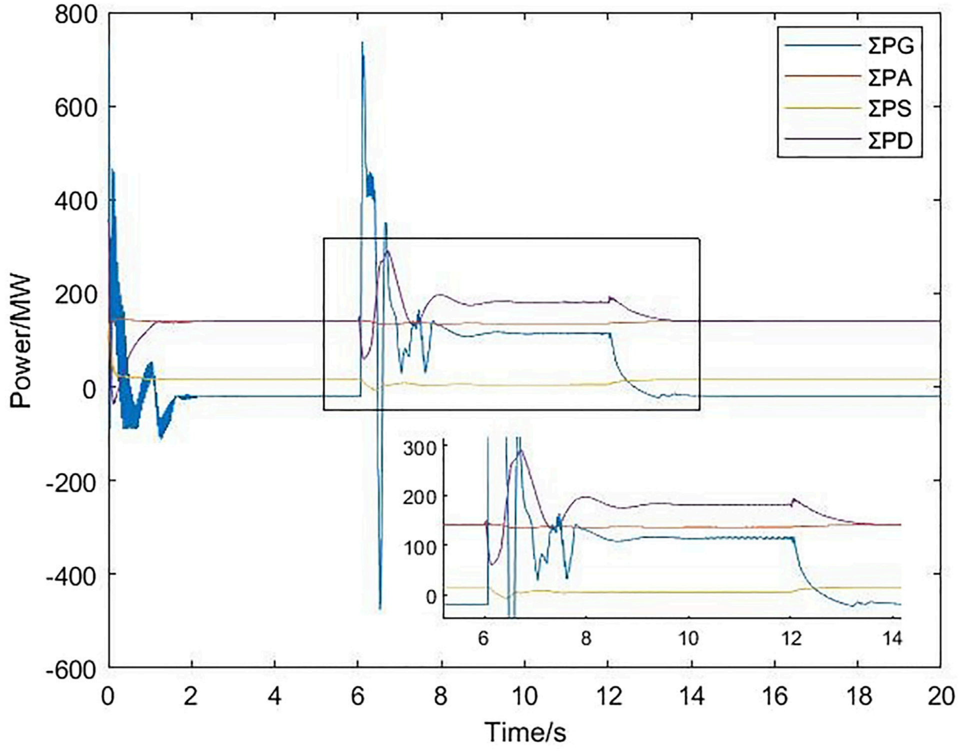

FIGURE 7 | Simulation results of consensus variables.

As shown in **Figure 6**, before the sixth second, the consensus variable of each distributed unit stabilizes at 11.5034. At the sixth second, four communication lines in the MAS system are interrupted, and the system runs to a new steady point. Around the 14th second, all consensus variables in the MAS system reach a new steady point, and the consensus variable at this time is 11.3803. At the 16th second, the faulty communication line resumes regular operation, and the consensus variables of the units are restored to their steady values before the interruption fault occurs (Wang et al., 2019). The consensus variables of each unit in the MAS system all converge to a steady value.

It can be seen from **Figure 7** that the output of each unit in MEC-MAS also corresponds to the optimal unit output in the 20:00 period. The total supply and demand power of the system is balanced. Therefore, through the model and algorithm proposed in this paper for distributed optimal dispatching, the calculation results achieve the effect of centralized optimization dispatching.

5 CONCLUSION

Aiming at the considerable amount of data in the distributed power network and the low efficiency of communication between distributed units, this paper proposes a consensus dispatch model of distributed power network based on MEC-MAS. The following conclusions are obtained through experimental simulation:

1) The distributed power system uses edge computing as the basic framework for hierarchical dispatching. The model decentralizes the processing and storage of data to the edge, which reduces the transmission cost of distributed units and dispatching centers; The model calculates different objective functions at edge nodes and cloud center nodes, which effectively improves the dispatching efficiency of the system.
2) The paper introduces MAS in the edge node of the MEC model. The model integrates the power source, load, and energy storage device in the distributed system through the autonomy and agent collaboration of the MAS, which can effectively realize the hierarchical energy management under the MEC model.
3) Through the hierarchical dispatching model based on MEC-MAS, the unit output is optimized with the goal of new energy consumption ratio and system operating cost. The system achieves the maximum proportion of new energy output power consumption while meeting economic operation.
4) Aiming at problems such as the complexity of generating units in the distributed power system, the lower-level dispatching model regards the autonomous sub-regions composed of distributed generating units as distributed multi-agents and solves the multi-agents through the consensus algorithm. The experimental results prove that the model can quickly restore stability in the case of communication failure. The results also show that the algorithm can ensure that the system is effectively dispatched under the balance of supply and demand.

DATA AVAILABILITY STATEMENT

The original contributions presented in the study are included in the article/Supplementary Material, further inquiries can be directed to the corresponding author.

AUTHOR CONTRIBUTIONS

LW, YL, XW, HW, and GG contributed to the conception of the study; LW, HW, and GG performed the simulation; LW, YL, XW, HW, and GG contributed significantly to analysis and manuscript preparation; LW, YL, HW, and GG performed the data analyses and wrote the manuscript; LW, YL, XW, HW, and GG helped perform the analysis with constructive discussions.

FUNDING

This work was supported by Liaoning Revitalization Talents Program (XLYC1802041) and Liaoning provincial Central Committee guides Local Science and Technology Development Fund Project (2021JH6/10500166).

REFERENCES

D'Andrea, R., and Dullerud, G. E. (2003). Distributed Control Design for Spatially Interconnected Systems. *IEEE Trans. Autom. Contr.* 48, 1478–1495. doi:10.1109/TAC.2003.816954

Feng, X., Butler-Purry, K. L., and Zourntos, T. (2019). A Multi-Agent System Framework for Real-Time Electric Load Management in MVAC All-Electric Ship Power Systems. *IEEE Trans. Power Syst.* 30, 1327–1336. doi:10.1109/TPWRS.2014.2340393

Gong, G. J., Luo, A. Q., Chen, Z. M., Luan, J. Z., An, X. N., Wang, X. P., et al. (2018). Cyber Physical System of Active Distribution Network Based on Container. *Power Syst. Technol.* 42, 3128–3135. doi:10.13335/j.1000-3673.pst.2018.0119

Guan, G. F., Song, Q. W., Liu, H., Xu, Y., Jiang, F., and Li, C. P. (2020). Research on Distribution Network Management and Operation and Maintenance System Based on Edge Computing. *Power Syst. Clean Energy* 36, 90–96. doi:10.3969/j.issn.1674-3814.2020.10.015

He, Y., Chen, Y., Lu, J., Chen, C., and Wu, G. (2019). Scheduling Multiple Agile Earth Observation Satellites with an Edge Computing Framework and a Constructive Heuristic Algorithm. *J. Syst. Archit.* 95, 55–66. doi:10.1016/j.sysarc.2019.03.005

Kumar Nunna, H. S. V. S., and Doolla, S. (2013). Multiagent-based Distributed-Energy-Resource Management for Intelligent Microgrids. *IEEE Trans. Ind. Electron.* 60, 1678–1687. doi:10.1109/TIE.2012.2193857

Li, B., Jia, B. C., Cao, W. Z., Tian, S. M., Qi, B., Sun, Y., et al. (2018). Application Prospect of Edge Computing in Power Demand Response Business. *Power Syst. Technol.* 42, 79–87. doi:10.13335/j.1000-3673.pst.2017.1548

Li, S. H., Miao, W. W., Zeng, Z., Wang, C. J., and Wei, X. S. (2020). Discussion on the Design of Edge Computing Framework Based on Power Internet of Things. *Electr. Power Inf. Commun. Technol.* 18, 51–58. doi:10.16543/j.2095-641x.electric.power.ict.2020.12.008

Li, X., Huang, Q., and Wu, D. (2017). Distributed Large-Scale Co-Simulation for IoT-Aided Smart Grid Control. *IEEE Access* 5, 19951–19960. doi:10.1109/ACCESS.2017.2753463

Mahmoodi, M., Shamsi, P., and Fahimi, B. (2015). Economic Dispatch of a Hybrid Microgrid with Distributed Energy Storage. *IEEE Trans. Smart Grid* 6, 2607–2614. doi:10.1109/TSG.2014.2384031

Olfati-Saber, R., Fax, J. A., and Murray, R. M. (2007). Consensus and Cooperation in Networked Multi-Agent Systems. *Proc. IEEE* 95, 215–233. doi:10.1109/JPROC.2006.887293

Pu, T. J., Chen, N. S., Wang, X. H., Ge, X. J., Li, Z. H., and Yu, J. C. (2016). Application and Architecture of Multi-Source Coordinated Optimal Dispatch for Active Distribution Network. *Automation Electr. Power Syst.* 40, 17–23. doi:10.7500/AEPS20150520010

Sun, H. J., Peng, C. H., and Yi, H. J. (2012). Multi-Objective Stochastic Optimal Dispatch of Power System with Wind Farms. *Electr. Power Autom. Equip.* 32, 123–128. doi:10.3969/j.issn.1006-6047.2012.05.023

Sun, H. Y., Zhang, J. C., Wang, P., Lin, J. Y., Guo, S., and Chen, L. (2019). Edge Computation Technology Based on Distribution Internet of Things. *Power Syst. Technol.* 43, 4314–4321. doi:10.13335/j.1000-3673.pst.2019.1750

Wang, R., Sun, Q., Hu, W., Li, Y., Ma, D., and Wang, P. (2021a). SoC-Based Droop Coefficients Stability Region Analysis of the Battery for Stand-Alone Supply Systems with Constant Power Loads. *IEEE Trans. Power Electron.* 36, 7866–7879. doi:10.1109/TPEL.2021.3049241

Wang, R., Sun, Q., Ma, D., and Liu, Z. (2019). The Small-Signal Stability Analysis of the Droop-Controlled Converter in Electromagnetic Timescale. *IEEE Trans. Sustain. Energy* 10, 1459–1469. doi:10.1109/TSTE.2019.2894633

Wang, R., Sun, Q., Tu, P., Xiao, J., Gui, Y., and Wang, P. (2021b). Reduced-Order Aggregate Model for Large-Scale Converters with Inhomogeneous Initial Conditions in DC Microgrids. *IEEE Trans. Energy Convers.* 36, 2473–2484. doi:10.1109/TEC.2021.3050434

Wang, R., Sun, Q. Y., Zhang, P. J., Gui, Y. H., Qin, D. H., and Wang, P. (2020). Reduced-Order Transfer Function Model of the Droop-Controlled Inverter via Jordan Continued-Fraction Expansion. *IEEE Trans. Energy Convers.* 35, 1585–1595. doi:10.1109/TEC.2020.2980033

Xing, J., Dai, H., and Yu, Z. (2018). A Distributed Multi-Level Model with Dynamic Replacement for the Storage of Smart Edge Computing. *J. Syst. Archit.* 83, 1–11. doi:10.1016/j.sysarc.2017.11.002

Xu, X. L., Song, Y. Q., Yao, L. Z., and Yan, Z. (2019). Source-Load-Storage Distributed Coordinative Optimization of AND (Part I): Consensus Based Distributed Coordination System Modeling. *Proc. CSEE* 38, 2841–2848+3135. doi:10.13334/j.0258-8013.pcsee.171476

Yang, S., Tan, S., and Xu, J.-X. (2013). Consensus Based Approach for Economic Dispatch Problem in a Smart Grid. *IEEE Trans. Power Syst.* 28, 4416–4426. doi:10.1109/TPWRS.2013.2271640

Zhang, T., Wang, C., Wang, L. Y., Zhang, D. F., and Zhang, J. Y. (2019). A Bi-level Optimal Dispatching Model of Electricity Retailers Integrated with VPPs. *Power Syst. Technol.* 43, 952–961. doi:10.13335/j.1000-3673.pst.2018.1439

Zhang, Z., and Chow, M.-Y. (2012). Convergence Analysis of the Incremental Cost Consensus Algorithm under Different Communication Network Topologies in a Smart Grid. *IEEE Trans. Power Syst.* 27, 1761–1768. doi:10.1109/TPWRS.2012.2188912

Zhu, J. Q., Duan, P., and Liu, M. B. (2015). Electric Real-Time Balance Dispatch via Bi-Level Coordination of Source-Grid-Load of Power System with Risk. *Proc. CSEE* 35, 3239–3247. doi:10.13334/j.0258-8013.pcsee.2015.13.006

Conflict of Interest: The authors declare that the research was conducted in the absence of any commercial or financial relationships that could be construed as a potential conflict of interest.

frontiers | Frontiers in Energy Research

ORIGINAL RESEARCH
published: 02 June 2022
doi: 10.3389/fenrg.2022.905454

An Economical Optimization Method for Active Power With Variable Droop Control Considering Frequency Regulation Costs in Integrated Energy Systems

Yuxiu Zang[1,2]*, *Weichun Ge*[1,3], *Shunjiang Wang*[3], *Long Zhao*[2] *and Che Tan*[2]

[1]*School of Electrical Engineering, Shenyang University of Technology, Shenyang, China,* [2]*State Grid Shenyang Electric Power Supply Company, Shenyang, China,* [3]*State Grid Liaoning Electric Power Supply Co., Ltd., Shenyang, China*

As a high proportion of clean energy is connected to the power grid, the occupancy rate of the system synchronous machine decreases, the inertia constant of the system decreases, and the difficulty of frequency adjustment continues to increase. The imbalance of frequency is mainly caused by the imbalance of active power, so the problem of frequency can be transformed into the problem of active power balance. According to the droop control principle, the concept of the equivalent unit regulating power coefficient is proposed, and the equivalent unit regulating power is determined by determining the system parameters and frequency offset. In order to reduce the frequency regulation cost in the integrated energy system, a feasible method considering the frequency regulation cost is the proposed variable droop control active power economic optimization method. First, the integrated energy system in this study consists of carbon capture power plants, a wind turbine generator system (WTGS), a photovoltaic power generation system, and energy storage batteries. All four types of power supply leave spare capacity to participate in frequency regulation through droop control. Second, the concept of the equivalent unit regulating power coefficient (equivalent coefficient) and the mathematical model of the equivalent unit regulating power coefficient of the integrated energy system are put forward. Then, within the allowable range of frequency fluctuations, considering carbon trading and ancillary service markets and aiming at the lowest frequency regulation cost, an economical optimal distribution method is established for active power in an integrated energy system including carbon capture power plants, wind power, photovoltaic, and energy storage. Taking a city in the north as an example, the improved moth flame algorithm is used to solve the problem. The simulation results show that the proposed model can improve the frequency regulation characteristics and reduce the frequency regulation cost.

Keywords: integrated energy system, primary frequency modulation, adaptive droop control, ancillary service market, economic optimization, improved moth flame algorithm

Edited by:
Rui Wang,
Northeastern University, China

Reviewed by:
Qin Jiang,
Sichuan University, China
Jingwei Hu,
Northeastern University, China

***Correspondence:**
Yuxiu Zang
xiudiubiu@163.com

Specialty section:
This article was submitted to
Smart Grids,
a section of the journal
Frontiers in Energy Research

Received: *27 March 2022*
Accepted: *21 April 2022*
Published: *02 June 2022*

Citation:
Zang Y, Ge W, Wang S, Zhao L and Tan C (2022) An Economical Optimization Method for Active Power With Variable Droop Control Considering Frequency Regulation Costs in Integrated Energy Systems. Front. Energy Res. 10:905454. doi: 10.3389/fenrg.2022.905454

1 INTRODUCTION

The frequency regulation task of the traditional power grid is mainly undertaken by thermal power units. With the rapid growth of the proportion of new energy in the power grid, the thermal power units are gradually withdrawn, the traditional frequency regulation units are continuously reduced, and the frequency regulation reserve is continuously reduced. It is even more difficult for traditional generators to meet the power requirements of the system load side as the frequency regulation capability of the grid decreases. Therefore, the renewable energy in the power grid is required to have frequency regulation capability to make up for the reduced frequency regulation unit capacity with the withdrawal of thermal power units (Xie et al., 2019; Xian et al., 2021). Otherwise, there will be serious abandonment of wind and light, which is not conducive to the further development of renewable energy.

For reducing the operating cost of integrated energy in the integrated energy management system, Li et al. (2021a) proposed an IES planning method based on life cycle and energy theory. First, the energy theory is applied to quantify the production efficiency of IES. A complete economic benefit model is established based on the life cycle theory. Compared with the traditional planning scheme considering the average annual cost and energy quality factor, this research method can reduce the planning cost by 23.16% and increase the renewable energy consumption rate by 4.26%. Gao et al. (2022) established a two-tier optimal scheduling model for an integrated energy system with multiple types of energy storage as the core, divided into the day-head scheduling layer and the real-time dispatch layer. This study uses fuzzy control to perform real-time scheduling of electric energy and thermal energy storage, effectively reducing the energy cost of users and improving energy utilization efficiency. Riyaz et al. (2021) discussed the optimum setting point for isolated wind, photovoltaic, diesel, and battery storage electric grid systems. The optimal energy supply for hybrid grid systems means that the load is sufficient for 24 h. This study aims to integrate the battery deprivation costs and the fuel price feature in the optimization model for the hybrid grid. Overall system power generation costs are reduced. Li et al. (2021b) proposed an optimal dispatch framework of PIES, which constructs the operation models under three different time scales, including day-ahead, intraday, and real time. Demand response is also divided into three levels considering its response characteristics and cost composition under different time scales. The example analysis shows that the multi-time scale optimization dispatch model can not only meet the supply and demand balance of PIES, diminish the fluctuation of renewable energy and flatten load curves, but also reduce the operation cost and improve the reliability of energy systems. Researching control and communication methods in the integrated energy system, Wang et al. (2020) proposed a reduced-order small-signal closed-loop transfer function model based on Jordan continued-fraction expansion to assess the dynamic characteristics of the droop-controlled inverter and provide the preprocessing method for the real-time simulation of power systems. Wang et al. (2021a) proposed a reduced-order aggregate model based on a balanced truncation approach to provide the preprocessing approach for the real-time simulation of large-scale converters with inhomogeneous initial conditions in a DC microgrid. This study presents an aggregated approach that involve independent reducing component responses and combine reducing component responses. Based on this, the input-output maps error is reduced. Wang et al. (2021b) proposed a distributed secondary H∞ consensus approach based on the dynamic event-triggered communication method to realize accurate current sharing and efficient operation in the presence of numerous DGs and CPLs.

Regarding the establishment of a comprehensive energy carbon trading mechanism, Sun et al. (2021) minimized the annual total cost of the system by considering the carbon trading cost and studying the operation modes under different carbon trading prices by commercial optimization software. The simulation results show the operation modes in summer are changed with the increase of the carbon trading prices, while the operation modes in winter are not changed with the fluctuation of the carbon trading prices. Wang et al. (2021c) solved the problems of environmental pollution and conflict of interests among multiple stakeholders in the integrated energy system (IES). This study proposes a novel collaborative optimization strategy for a low-carbon economy in IES based on the carbon trading mechanism and Stackelberg game theory. The simulation results verify that in a carbon-constrained environment, all stakeholders can benefit from the proposed transaction mechanism, resulting in an economical and environmentally friendly optimal scheduling of IES. Xiaohui et al. (2019) established an electric–gas-integrated energy system planning model that considers carbon trading. A reward and punishment ladder-type carbon trading cost model is proposed, and its restriction on carbon emission is analyzed. On this basis, a planning model is established to minimize the total costs including the investment cost, operation cost, and carbon trading cost.

For the study of integrated energy frequency adjustment, Pati and Subudhi (2021) illustrated the design and control of load frequency control of a two-area power system. The system is modeled with conventional as well as nonconventional energy sources like wind, solar, and diesel power plants. An effective and efficient controller named tilt integral derivative controller with filter is employed in this study. For tuning controller parameters, a simple yet proficient optimization method called the Jaya algorithm is used. As a high-quality frequency regulation (FR) resource, a community-integrated energy station (CIES) can effectively respond to frequency deviation caused by renewable energy generation, helping to solve the frequency problem of the power system. Li C. et al. (2021) proposed an optimal planning model of CIES considering FR service. An optimal planning model of CIES considering FR service is proposed, with which the revenue of participating in the FR service is obtained under the market mechanism.

Based on the fact that both photovoltaic and wind power use load shedding control, Tian et al. (2016) proposed a

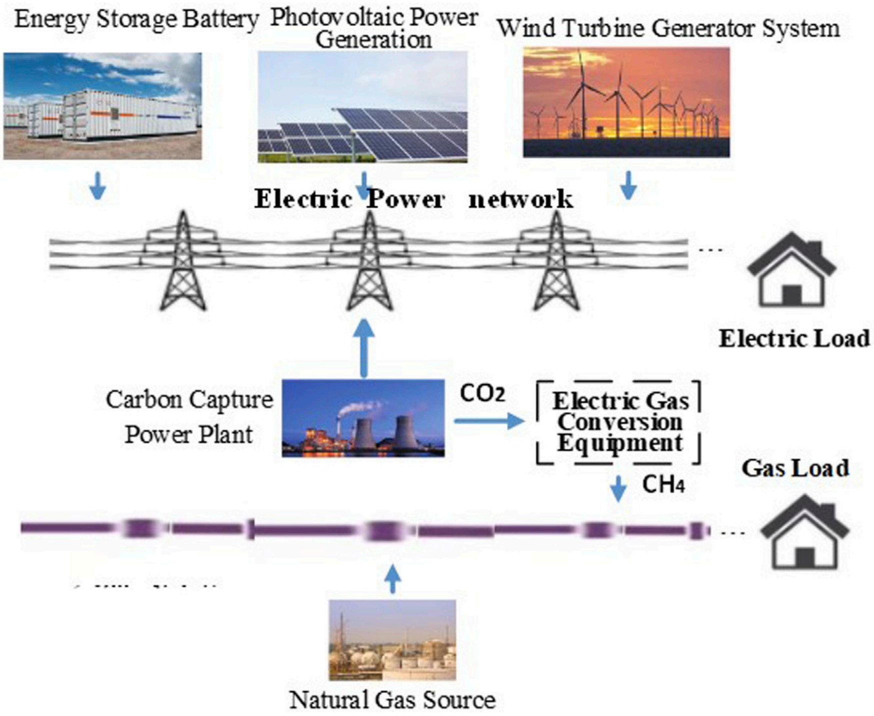

FIGURE 1 | Structure of the integrated energy system.

control scheme for photovoltaic and wind power to participate in grid frequency regulation by segments, and photovoltaics are preferred to participate in grid frequency regulation. Cai et al. (2013) established a wind–solar storage combined power generation system. Both wind power and photovoltaic systems adopt a double-loop control strategy to ensure the maximum power output. The energy storage battery determines the output power of the energy storage battery by controlling the frequency of the grid connection point to stabilize the power fluctuation of the wind and solar output so that the entire wind–solar storage system can output power smoothly, with minimal impact on the frequency of the entire power grid. Ma et al. (2015) determined the dynamic output strategy of wind turbines and photovoltaic power generation and propose an adaptive droop control method, which adaptively adjusts the droop coefficient of each micro-source through the power margin of the networked power supply, giving full play to the micro-source adjustment potential and power support capability. However, the issue of carbon trading costs is not considered. Ma (2019) carried out mathematical modeling for thermal power frequency regulation standby units, hydropower frequency regulation standby units, wind turbines, and energy storage systems, and establish an optimal control strategy and evaluation system for participating in primary frequency regulation of the power grid, but do not consider the participation of photovoltaic units in frequency regulation.

However, previous studies were not thoughtful. Some did not consider the inconsistency between the planned and actual frequency modulation capacity, and some did not consider the frequency regulation capacity of clean energy itself. This research mainly studies the active power optimal allocation of integrated energy systems including thermal-wind-light-storage. This study uses the integrated energy system including carbon capture power plants, energy storage batteries, PV, and WTGS, and puts forward the equivalent unit regulated power model and cost model, taking into account the power market and carbon trading market mechanism, frequency modulation auxiliary service market and network security constraints. An economic optimization method of variable droop control active power aims at minimizing the total frequency modulation cost of carbon capture power plants, energy storage batteries, PV, and WTGS in the integrated energy system. Taking a certain area in the north as an example, the improved moth flame algorithm is used to solve the problem. It verifies the effectiveness of the method proposed in this study in mitigating the frequency shock caused by the current high proportion of clean energy connected to the grid.

2 INTEGRATED ENERGY SYSTEM STRUCTURE

In the modern power grid system, the generation system is no longer just thermal power plants. The integrated energy system studied in this research is shown in **Figure 1**. Its main components include carbon capture power plants (plants), energy storage batteries (batteries), photovoltaic power

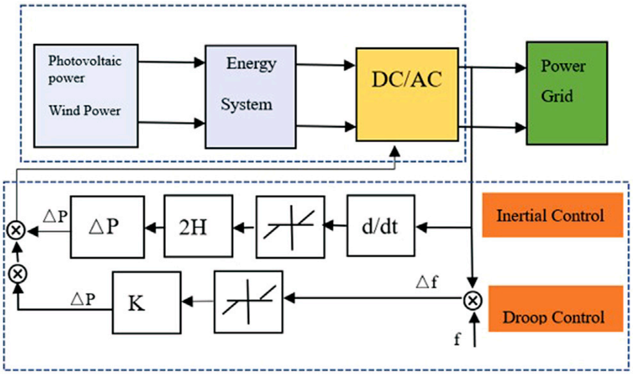

FIGURE 2 | Structure of the integrated energy system.

generation systems (PV), and wind turbine generator system (WTGS). In the comprehensive energy model, it is assumed that all plants are carbon capture power plants. The plants collect, transport, store, and sell part of the carbon dioxide generated by combustion to electricity to gas equipment manufacturers, so as to provide carbon dioxide required for the reaction for electric hydrogen production equipment and obtain income. Whether to participate in frequency regulation the next day is determined by the short-term forecast of clean energy power generation and electricity load, and the enterprise decides to participate in frequency regulation capacity. According to the actual frequency regulation capacity of the enterprise, which determines its participation in frequency regulation income.

The control block diagram is shown in **Figure 2**, in this model, when the system frequency changes less than ±0.2Hz, the system is in a stable state. When the system is in active power balance or frequency dead zone (± 0.3Hz), the batteries operate in the peak regulation mode, and the energy storage battery is charged and discharged according to the peak regulation period. PV and WTGS are generated according to the maximum power tracking (MPPT) (Zhao et al., 2017) mode. Exceeding the grid frequency regulation dead zone, all types of power sources with frequency regulation capability can participate in frequency regulation with their respective frequency regulation characteristics (Zhao et al., 2020) according to the frequency change rate. A certain amount of power is reserved by load shedding operation so that the photovoltaic power generation system has the ability to participate in the system frequency regulation at any time.

The plants regulate the power in the equivalent unit $K_{\pi_1}^G$. As shown in **(2)**, PV and WTGS are adjusted by the adaptive droop coefficient, and the droop coefficient can be regarded as their equivalent unit regulating power coefficient (coefficient). When all the units in the system participate in the unbalanced power regulation, it is assumed that the coefficient of WTGS, PV, and batteries (assuming that the battery is stepless regulation) are $K_{\pi_3}^d$, $K_{\pi_4}^l$, and $K_{\pi_2}^p$. When the frequency fluctuation Δf of is generated by the power grid, the active power variation $\Delta P_{\sum}$ of the system is calculated by **(1)** and distributed in the system. When the system frequency fluctuation is not greater than Δf_1, no action is required in the adjustment dead zone. When the system frequency fluctuation is greater than Δf_1, all power sources participate in frequency regulation to ensure the balance of system active power.

$$\Delta P_{\sum} = \left[K^G \quad K_{\pi_2}^p \quad K_{\pi_3}^d \quad K_{\pi_4}^l \right] \Delta f. \tag{1}$$

There is a linear relationship between the power increment of plants and the frequency change of the state grid (Xiao et al., 2020). The coefficient of the plant is as follows:

$$\Delta P = -K_{\pi_1}^G \Delta f. \tag{2}$$

The reasonable setting of the equivalent coefficient of WTGS will avoid the secondary disturbance to the frequency during the speedy recovery of WTGS. When the frequency change rate is high, the fan has frequency regulation ability, which can meet the frequency regulation, reduce unnecessary wind energy loss, and improve wind energy utilization efficiency. Otherwise, the frequency modulation ability of the fan is weak. The droop control introduces the speed influence factor to limit the fan's participation in frequency modulation, which can avoid the shutdown and off-line accident caused by the fan's excessive use of kinetic energy to participate in frequency modulation (Liao, 2020).

$$K_{\pi_3}^d = \begin{cases} K_{\pi_3}^1 = K_{\min}^d, \left|\frac{\mathrm{d}f}{\mathrm{d}t}\right| < \delta_1 \cup w \le w_1 \\ K_{\pi_3}^2 = \frac{K_{\max}^d \left(|\Delta f| - f_{\min}\right) + K_{\min}^d \left(f_{\max} - |\Delta f|\right)}{|\Delta f|_{\max}}, \delta_1 < \left|\frac{\mathrm{d}f}{\mathrm{d}t}\right| < \delta_2 \cup w_1 < w < w_2. \\ K_{\pi_3}^3 = K_{\max}^d, \left|\frac{\mathrm{d}f}{\mathrm{d}t}\right| > \delta_2 \cup w \ge w_2 \end{cases} \tag{3}$$

By adjusting$K_{\pi_4}^l$, the power distribution error in the process of primary frequency regulation can be reduced, the power oscillation in the process of regulation can be avoided, and the primary frequency regulation performance of PV can be improved (Kayikçi and Milanovic, 2009; Mishra et al., 2013).

$$K_{\pi_4}^l = \begin{cases} K_{\pi_4}^1 = K_{\min}, \left|\frac{\mathrm{d}f}{\mathrm{d}t}\right| < \delta_1 \cap P \neq 0 \\ K_{\pi_4}^2 = \phi \frac{P_0}{P_0 - \Delta f} \Delta f, \delta_1 < \left|\frac{\mathrm{d}f}{\mathrm{d}t}\right| < \delta_2 \cap P \neq 0, \\ K_{\pi_4}^3 = K_{\max}, \left|\frac{\mathrm{d}f}{\mathrm{d}t}\right| > \delta_2 \cap P \neq 0 \end{cases} \tag{4}$$

where $|\Delta f|$ is the absolute value of frequency variation; δ_1 and δ_2 are the range of allowable frequency change rate, respectively. $K_{\min}^d$ is the minimum value of sag coefficient; $K_{\max}^d$ is the maximum sag coefficient. w_1 and w_2 is the minimum and maximum safe wind speed. Where, $\delta_1^l$and δ_2^l are the range of allowable frequency change rate, respectively; P_0 is the rated PV, and $\phi$and $\phi^{'}$ are the adjustment coefficients. At that time $\Delta f > 0.032$Hz, $\phi = -1$, else, $\Delta f < -0.032$Hz, $\phi = 1$.

Energy storage batteries participate in frequency modulation through droop control, and the battery's power status are divided into five types: no power state, minimum power status ($\mathrm{SOC_{min}}$), low power status high power status ($\mathrm{SOC_H}$), and full power status ($\mathrm{SOC_{max}}$).

TABLE 1 | The equivalent unit coefficient of batteries.

		Battery power	
State	$(0, \mathrm{SOC_L})$	$(\mathrm{SOC_L}, \mathrm{SOC_H})$	$(\mathrm{SOC_H}, \mathrm{SOC_{max}})$
Discharge	$K^1_{\mathrm{E},k}$	$K^2_{\mathrm{E},k}$, φ_1	$K^3_{\mathrm{E},k}$
Charge	$K^3_{\mathrm{E},k}$	$K^2_{\mathrm{E},k}$, φ_2	$K^1_{\mathrm{E},k}$

The energy storage batteries system participates in system frequency modulation through virtual droop control. The change curve of virtual unit regulated power of energy storage batteries charge and discharge with energy storage batteries SOC can be regarded as the "s" curve (Zarina et al., 2012; Zadkhast et al., 2017). The curve form is divided into three sections according to the amount of energy storage batteries, and the energy storage batteries system are divided into two types according to charging and discharging states. The change of unit regulated power is shown in **Table 1**.

$$K^p_{\pi_2} = \begin{cases} K^1_{\pi_2} = 0 \\ K^2_{\pi_2} = \dfrac{K_{\max} P_0 e^{\varphi_i}}{K_{\max} + P_0 \left(e^{\varphi_i} - 1\right)} i = 1, 2 \\ K^3_{\pi_2} = K_{\max} \end{cases}, \tag{5}$$

$$\varphi_1 = \frac{n(SOC - 0.1)}{0.2},$$

$$\varphi_2 = \frac{n(0.9 - SOC)}{0.2},$$

where $K^p_{\pi_2}$ is the equivalent coefficient of energy storage batteries. When the stored power of the batteries is greater than SOC_L, it will be discharged at the rated power. At this time, the equivalent coefficient is the maximum. The value decreases with the increase of storage energy batteries; when the batteries have no more power, the storage energy batteries do not participate in frequency modulation. P_0 and n are the two shape parameters of the curve, which determine the shape and value of the curve. n is the curve coefficient. With the change of the coefficient, the curve has different forms.

In summary, PV, WTGS, and storage energy batteries adjust power by changing the equivalent coefficient under different conditions to ensure that their systems are in the best state of frequency regulation, avoiding overregulation that leads to off-grid, resulting in a secondary drop in frequency, jeopardizing grid security. **(1)** can be equivalent to the following matrix:

$$\Delta P = [\sigma_i \varsigma_i \tau_i]\left[K^G_{\pi_1} K^p_{\pi_2} K^d_{\pi_3} K^l_{\pi_4}\right]\Delta f, \tag{6}$$

$$\Delta P = \begin{bmatrix} \sigma_1 & \varsigma_1 & \tau_1 \\ \sigma_2 & \varsigma_2 & \tau_2 \\ \sigma_3 & \varsigma_3 & \tau_3 \\ \sigma_4 & \varsigma_4 & \tau_4 \end{bmatrix} \begin{bmatrix} K^G_{\pi_1} & K^1_{\pi_2} & K^1_{\pi_3} & K^1_{\pi_4} \\ 0 & K^2_{\pi_2} & K^2_{\pi_3} & K^2_{\pi_4} \\ 0 & K^3_{\pi_2} & K^3_{\pi_3} & 0 \end{bmatrix} \Delta f,$$

$$\sum \sigma_i = 1 \sum \varsigma_i = 1 \sum \tau_i = 1,$$

where σ_i, ς_i, and τ_i are binary state variables.

2.1 Integrated Energy System Model

The cost of carbon capture power plants consists of the power generation cost involved in active power regulation and carbon-related costs. Carbon-related costs $C_i(t)$ include carbon tax costs for carbon dioxide emissions from fossil fuel units $C^{\mathrm{CO_2}}(t)$ and carbon transaction costs $C_\mathrm{A}(t)$. At the same time, the carbon capture power plants sell the emitted carbon dioxide to the electricity to hydrogen producers to obtain income (Ros-Mercado and Borraz-Sánchez, 2015; Yang, 2018; Zhou et al., 2018; Tian et al., 2020). After installing carbon capture equipment in the traditional coal-fired power plants, the power plants will be transformed into carbon capture power plants. The carbon capture system can collect and transport the carbon dioxide gas generated by the thermal power plants with η_C and store it with loss of λ_s. The stored carbon dioxide is released on specific occasions and connected with Power to Gas (P2G) for electric hydrogen conversion.

$$\begin{aligned} C^{\mathrm{CO_2}}(t) &= \sum_{m \in \Omega_\mathrm{C}} \left(\delta P_m(t) - M_m^{\mathrm{CO_2}}(t)\right) - \rho_2 \eta_\mathrm{C} \lambda_\mathrm{S} M_m^{\mathrm{CO_2}}(t) + C_\mathrm{A}(t), \\ C_\mathrm{A}(t) &= A_{\mathrm{CO_2}}\left[(\delta - q) P_m(t) - M_m^{\mathrm{CO_2}}(t)\right]. \end{aligned} \tag{7}$$

Referring to **(8)**, we can get the total cost of carbon capture power plants consisting of power generation cost and carbon-related cost:

$$\begin{aligned} C^\mathrm{G}_{\pi_1}(t) &= C'_\mathrm{G}(t) + C^{\mathrm{CO_2}}(t), \\ C'_G(t) &= aP^2(t) + bP(t) + c, \end{aligned} \tag{8}$$

where Ω_C is the set of power plants; $M_m^{\mathrm{CO_2}}(t)$ is the carbon dioxide capture at time t; ρ_2 is the price of carbon dioxide recovery from electricity to gas; $A_{\mathrm{CO_2}}$ is the carbon trading price; δ is the conversion coefficient of carbon dioxide generated by unit power generation; q is the basic share of carbon emission, t/MWh; a, b, c are constants, which are the characteristic coefficient of the unit.

The cost of WTGS and PV is mainly caused by the abandonment. On the premise of ensuring the safe operation and economy of the system, the amount of

TABLE 2 | The cost comparison in three modes.

Mode	Total cost/$	Frequency regulation revenue cost/$	Cost of wind and light abandonment/$
Mode 1	1886026	533	0
Mode 2	1883019	1,065	508
Mode 3	1865732	5602	1,123

abandoned wind and light shall be reasonably reduced. With the increase of the amount of abandoned clean energy, the penalty cost will also increase, so as to restrain the abandonment.

$$C^{dl}(t) = P^{\mathrm{d}}(t)A^{\mathrm{d}} + P^{\mathrm{l}}(t)A^{\mathrm{l}}, \tag{9}$$

where $P^{\mathrm{d}}(t)$ and $P^{\mathrm{l}}(t)$ are the amount of wind and light abandonment at time t, and $A^d$and A^l are the unit cost of wind and light abandonment.

Batteries have a limited number of discharges, and energy storage battery loss is related to deep discharge (Liu et al., 2021). As the depth of discharge of the battery increases, the cycle life of the battery continues to decrease. The cost of a single discharge loss when the battery is discharged is C_E. The depreciation cost of the unit charge and discharge capacity of the energy storage battery is c_E, and the life depreciation cost is as follows:

$$C_{\mathrm{E}}(t) = \sum_{k\in\Omega_E}\sum_{t=1}^{T} f(SOC_k(t))c_E\left|P_{E,k}^{\mathrm{ex}}(t) - P_{E,k}^{\mathrm{c}}(t)\right|, \tag{10}$$

$$f(SOC(t)) = \begin{cases} 1.30 & \leq SOC(t) \leq 0.5 \\ -1.5SOC(t) + 2.05 & 0.5 \leq SOC(t) \leq 1 \end{cases},$$

where $SOC(t)$ is the state of charge in t period.

3 OBJECTIVE FUNCTION AND CONSTRAINTS

This study proposes that all kinds of power sources in the integrated energy system jointly undertake the task of active power balance, On the basis of ensuring frequency stability, a minimum frequency adjustment cost model of the integrated energy system is established as follows:

$$\min C_{\sum} = \min\left(C_{\mathrm{G}}(t) + C^{\mathrm{dl}}(t) + C_{\mathrm{E}}(t) - C^{i}\right), \tag{11}$$

where $C_{\mathrm{G}}(t)$ is the power generation cost of carbon capture power plants; $C_{\mathrm{E}}(t)$ is the energy storage charge and discharge loss cost; $C_{\mathrm{E}}(t)\, C^{\mathrm{dl}}(t)$ is the cost of air and light abandonment; C^i is the income of the frequency regulation.

3.1 Capacity Constraints

$$\begin{aligned} &0 \leq D_{\pi_1}^{\mathrm{G}} \leq D_{\pi_1,\,\max}^{\mathrm{G}}, \\ &0 \leq D_{\pi_3}^{\mathrm{d}} \leq D_{\pi_3\,\max}^{\mathrm{d}}, \\ &0 \leq D_{\pi_4}^{\mathrm{l}} \leq D_{\pi_4,\max}^{\mathrm{l}}, \\ &0 \leq D_{\pi_2}^{\mathrm{p}} \leq D_{\pi_2,\,\max}^{\mathrm{p}}, \end{aligned} \tag{12}$$

where $D_{\pi_1}^{\mathrm{G}}$, $D_{\pi_1}^{\mathrm{G}}$, $K_{\pi_4}^{l}$, and$K_{\pi_2}^{p}$ are the capacity limits of carbon capture power plants, WTGS, PV, and energy storage batteries, respectively.

3.2 System Power Flow Equation Constraint and Transmission Line Power Constraint

$$\begin{cases} P_{\mathrm{G}i} - P_{\mathrm{D}i} = V_i \sum_{j=1}^{n} V_j\left(Gi_j \cos\theta_{ij} + B_{ij}\sin\theta_{ij}\right), \\ Q_{\mathrm{G}i} - Q_{Di} = -V_i \sum_{j=1}^{n} V_j\left(G_{ij}\sin\theta_{ij} - B_{ij}\cos\theta_{ij}\right), \end{cases} \tag{13}$$
$$P_b^{\min}(t) \leq P_b(t) \leq P_b^{\max}(t),$$

where $P_{\mathrm{G}i}$and $Q_{\mathrm{G}i}$ are the active and reactive output of node i generator; $P_{\mathrm{D}i}$and $Q_{\mathrm{D}i}$ are the active and reactive loads of node i; $V_i$and θ_i are the voltage amplitude and phase angle of the node i; $\theta_{ij} = \theta_i - \theta_j$; $G_{ij}$and B_{ij} are the real and imaginary parts of row i and column j of node admittance matrix; $P_{\mathrm{b}}^{\min}(t)$and $P_{\mathrm{b}}^{\max}(\mathrm{t})$ are the lower limit and upper limit of allowable power of transmission line.

Output power constraints and ramp rate constraints of carbon capture power plants:

$$\begin{aligned} &P_{\pi_1,\,\min}^{\mathrm{G}}(t) \leq P_{\pi_1}^{\mathrm{G}}(t) \leq P_{\pi_1,\,\max}^{\mathrm{G}}(t), \\ &R_{\pi_1\,\min}^{\mathrm{G}} \leq P_{\pi_1}^{\mathrm{G}}(t) - P_{\pi_1}^{\mathrm{G}}(t-1) \leq R_{\pi_1\,\max}^{\mathrm{G}}. \end{aligned} \tag{14}$$

Ensure that the output of the carbon capture power plants at t time is within the power constraint range, the plants meet their climbing rate requirements, and the change of carbon collection rate is less than or equal to the maximum value of system capacity.

3.3 Power Constraint of the Energy Storage Batteries System

$$P_{\pi_2,\,\min}^{p}(t) \leq P_{\pi_2}^{\mathrm{p}}(t) \leq P_{\pi_2,\max}^{\mathrm{p}}(t), \tag{15}$$

where $P_{\pi_2,\min}^{\mathrm{p}}(t)$ is the lower limit of batteries release power; $P_{\pi_2,\max}^{\mathrm{p}}(t)$ is the upper limit of batteries absorbed power.

3.4 Dead Zone Constraint

$$0 \leq P_{\pi_1}^{\mathrm{G}} \leq \frac{\Delta f}{f_{\mathrm{N}}} K. \tag{16}$$

In order to avoid unnecessary frequent action of the system, assuming that the frequency modulation dead zone of primary frequency modulation is $\Delta f = 0.03\mathrm{Hz}$, the system shall reserve a certain standby capacity for frequency regulation.

3.5 Energy Balance Constraint

$$P_{\pi_1}^{\mathrm{G}}(t) + P_{\pi_2}^{\mathrm{p}}(t) + P_{\pi_3}^{\mathrm{d}}(t) + P_{\pi_4}^{\mathrm{l}}(t) = P_{\mathrm{D}}. \tag{17}$$

4 IMPROVED MOTH FLAME OPTIMIZATION ALGORITHM

In this study, an improved moth flame optimization (MFO) algorithm is used to solve the nonlinear optimization problem. In MFO, moths are individuals who seek optimization in the search space, save the optimal position that the moth group can find so far, and assign it to the flame. Each moth uses the corresponding flame as the optimization guide, and continuously adjust their flight trajectory to move closer to the global optimal solution. The MFO algorithm is described in detail as follows: The variable of the problem is the position of the moth in the search space. The moth population is represented in the matrix as shown in **(18)**; for all moths, **Eq. 19** is used to store the corresponding fitness values. Another key component in the MFO algorithm is the flame, and the flame position is a variable matrix of the same dimension as the moth position, denoted by **(20)**. The objective function value corresponding to the stored flame is shown in **Formula 21**:

$$M = \begin{bmatrix} m_{1,1} & m_{1,2} & \dots & m_{1,d} \\ m_{2,1} & m_{2,2} & \dots & m_{2,d} \\ \dots & \dots & \dots & m_{n,d} \end{bmatrix}, \tag{18}$$

$$OM = [OM_1, OM_2, \dots, OM_N]^{\mathrm{T}}, \tag{19}$$

$$F = \begin{bmatrix} F_{1,1} & F_{1,2} & \dots & F_{1,d} \\ F_{2,1} & F_{2,2} & \dots & F_{2,d} \\ \dots & \dots & \dots & \dots \\ F_{n,1} & F_{n,2} & \dots & F_{n,d} \end{bmatrix}, \tag{20}$$

$$OF = [OF_1, OF_2, \dots, OF_n]^{\mathrm{T}}, \tag{21}$$

where n is the number of moths and d is the number of variables.

The MFO algorithm assigns each moth a specific flame and uses a logarithmic spiral function to update the moth's position as shown in **the** following equation:

$$M_i = S\left(M_i, F_j\right) = D_i e^{bt} \cos(2\pi t) + F_j, \tag{22}$$

where $D_i = |F_j - M_i|$ is the distance between moth M_i and flame F_j; b is a constant related to the shape of the helix; the random number $t \in [-1, 1]$ $t = -1$ represents the position closest to the flame; $t = 1$ indicates the position furthest from the flame. In the optimization process, in order to further enhance the development ability, it is assumed that t is a random number in $[r, 1]$, and r decreases linearly from −1 to 2. There are n flames at the initial stage of the iteration; the MFO algorithm adaptively reduces the number of flames until the last optimal flame is retained, as shown in **the** following equation:

$$f = round\left(n - l\frac{n-1}{T}\right), \tag{23}$$

where l is the current number of iterations and T is the maximum number of iterations.

In the moth optimization algorithm, due to the characteristics of the spiral motion of the moth, the ability of the algorithm to search for optimization in the local scope is enhanced, but the search in the global scope cannot be better. The moth flame-catching optimization algorithm has the advantages of strong parallel search ability and easy programming. Better coefficients can be found with fewer iterations in multidimensional operation optimization. In this study, a chaotic particle swarm algorithm (CLSPSO) is used to optimize the initial position of the swarm particles to increase the global search ability of the algorithm and avoid falling into local minima, which can effectively make up for the inadequacy of the algorithm for global search.

After the algorithm flow is improved, the improved algorithm is used to solve the active power distribution in the integrated energy system. **Figure 3** shows the flow chart of applying the improved moth flame algorithm to solve the optimal active power.

5 EXAMPLE SIMULATION

WTGS and PV normally use the maximum power point tracking mode for power generation, and energy storage cooperates with clean energy power generation to reduce wind and light abandonment, peak cutting, and valley filling. When the system is within the frequency fluctuation dead band, the system will not adjust. When the frequency fluctuation exceeds the dead band, the power supply in the system will jointly participate in the frequency adjustment. The specific primary frequency modulation characteristics are related to the actual power supply characteristics of the system. The traditional power supply is mainly power plants, and the primary frequency regulation characteristics of power plants can be approximately regarded as a straight line with a slope K.

Due to the continuous development of clean energy, the power structure of the power grid has changed greatly. The primary frequency modulation characteristics of an integrated energy system with a high proportion of clean energy power generation are superimposed by different equivalent coefficients.

Taking a region in the north as an example, there are 100 MW carbon capture power plants, 80 mW WTGS, 80mW PV, and 50 MW energy storage batteries. The capacity parameters are shown in the figure below. This study contains multiple inequality constraints and equality constraints. The MATLAB software is selected and the YALMIP toolkit is used for programming and calculation, respectively. The 24 h before the day is taken as the dispatching cycle, and the duration of each dispatching period is 15 min the clean energy output in the dispatching cycle is shown in **Figure 4**. For the comparison of results, the following three modes are used for comparative analysis:

Mode 1: according to the conventional mode, when the frequency fluctuation exceeds the frequency dead zone due to the change of system active power, only the carbon capture power plants adjust the power output, WTGS and PV continue to maintain the MPPT mode, and the energy storage does not participate in the regulation of active power, and the equivalent unit regulated power $K^{\mathrm{P}}_{\pi_2} = 0$.

Mode 2: when the frequency exceeds the frequency dead band due to the change of active power in the system, the system as a whole participates in the regulation of active power, but the equivalent coefficient does not change with the power change rate and is always a constant value.

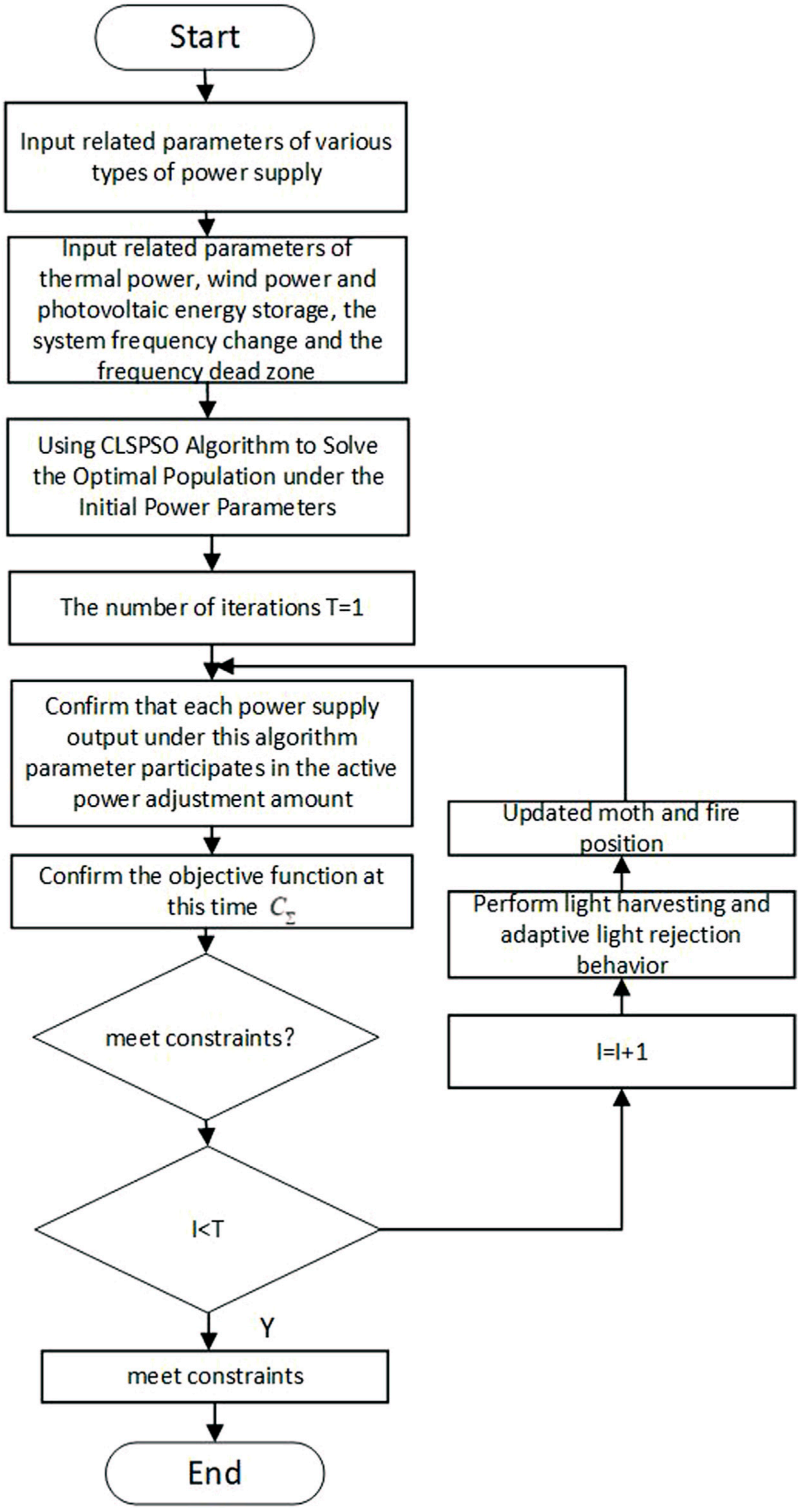

FIGURE 3 | Algorithm flow chart.

Mode 3: when the frequency exceeds the frequency deadband due to the change of active power in the system, the system as a whole participates in the regulation of active power, all power supplies participate in frequency modulation, and the equivalent unit is regulated power changes with the actual situation.

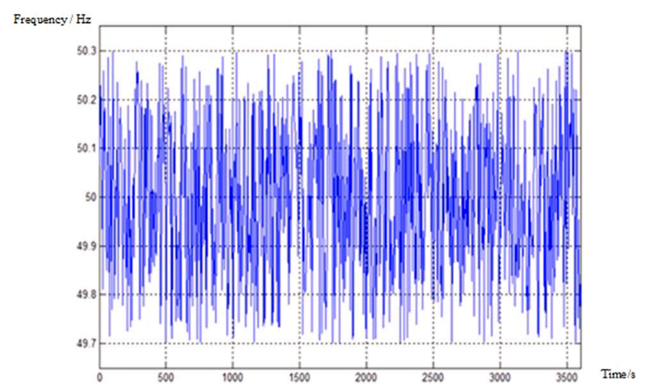

FIGURE 4 | The system frequency variation curve.

Figure 4 shows the system frequency change curve. When the system frequency changes and$\Delta f \leq 0.032$Hz, the system is in the active power balance state without power adjustment. In Mode 1, WTGS and PV all act as MPPT, and the power generation curve is shown in **Figure 5A**. The maximum power generation of WTGS is 3:00–4:00 in the morning and 22:00–24:00 in the evening, and the maximum power generation of PV is 12:00–14:00. At this time, only the carbon capture power plants are adjusted to ensure the stability of the system frequency. **Figure 5B,C** are the comparison curves of WTGS and PV participating in active power adjustment under Mode 2 and Mode 3. **Figure 5B** shows that PV is affected by illumination time and only participates in power adjustment between 6:00 and 18:00.

It can be seen from **Figure 5C** that WTGS has higher power generation at night and can participate in frequency modulation more. When the frequency change rate exceeds the fixed value, in order to ensure the system balance, the participation of WTGS and PV power in power regulation in Mode 3 is significantly greater than that in Mode 2, so as to enhance the ability of the system to regulate active power balance,. The participation of PV and WTGS in active power regulation in Mode 3 is strong, so as to reduce the fluctuation of frequency in the regulation process so that the frequency modulation times of the system are significantly less than that in Mode 2, It shows that the system frequency stability is enhanced in Mode 3 so that the frequency modulation times of the system are significantly less than that in Mode 2. It shows that the system frequency stability is enhanced under Mode 3.

In Mode 3, the regulation mode not only ensures the active power balance of the system but also ensures that the PV does not participate in frequency modulation too frequently. It increases the generation of power and ensures the penetration of clean energy power generation. This mode also alleviates the frequency modulation pressure of

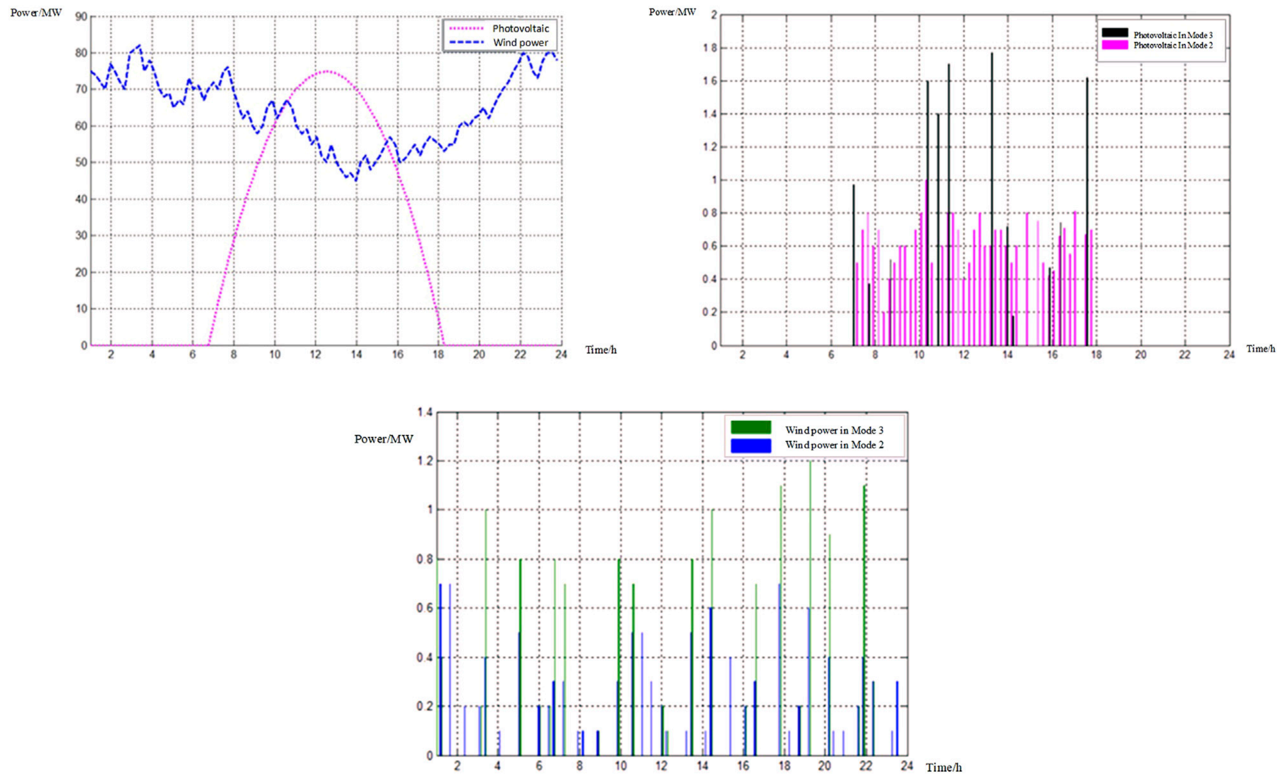

FIGURE 5 | (A) The power of WTGS, PV in Mode 1 to the grid, **(B)** PV participates in active power balance and power regulation in Mode 2 and 3, **(C)** Active power balance regulation power of WTGS in Mode 2 and 3.

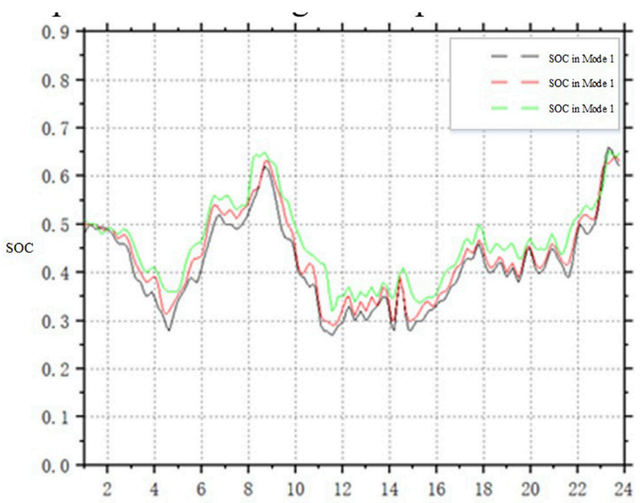

FIGURE 6 | The SOC change diagram in Mode 1, 2, and 3.

synchronous units. It shows that the system frequency stability is enhanced in Mode 3. It ensures the active power balance of the system and PV does not participate in frequency modulation too frequently. In Mode 3, the power generation increases to ensure the penetration of clean energy power generation. This mode also relieves the frequency modulation pressure of the synchronous unit. It shows that the system frequency stability is enhanced in Mode 3. It ensures that the active power of the system is balanced and the frequency is not adjusted too frequently, and the frequency modulation pressure of the synchronous unit is relieved.

As shown in **Figure 6**, due to the contribution of WTGS and PV to the active power balance adjustment, the power fluctuation of the energy storage batteries are significantly reduced compared with the first two scenarios, and the charge and discharge times are reduced by 6.5% compared with Mode 2. In the three Modes, the minimum SOC of the batteries is 0.27, 0.32, and 0.35, and the maximum SOC is 0.65, 0.63, and 0.6. The SOC of the batteries in Mode 3 ranges from SOC_{L} toSOC_{H}, which avoids overcharge and overdischarge. This avoids overcharge, overdischarge, and frequent switching of the batteries, reduces the charging and discharging times of the batteries, and reduces the service life cost of the batteries.

Figure 7A shows the equivalent coefficient of PV, WTGS, and energy storage batteries of the system in Mode 2 and 3. The principle is the same as that of the power plants. The equivalent coefficient of the power supply is less than or equal to zero. PV and WTGS are in the lower half of the coordinate axis. The energy storage batteries can not only charge and store energy but also act as a load. Therefore, both positive and negative values exist. The PV system can only participate in the system regulation during the daytime power generation period. In Mode 2, the frequency change rate is not considered, and the power is adjusted according to the fixed unit regulated power coefficient. When the frequency data is collected in the second window time, it decreases from 50.19 to 49.827 Hz, and the active power imbalance is jointly provided by the three. The regulation capacity of PV and WTGS is limited. When the maximum capacity regulation has been adopted for WTGS and PV, the residual active power gap can only be provided by carbon capture power plants. Excessive frequency change will cause system fluctuation. Although the wind power, WTGS, and PV participate adjust the power actively, it does not solve the actual problem. At this time, if the frequency change rate is large, it is very likely to produce frequency overrun warnings and affect system safety. As can be seen from **Figure 8**, in the same window period, due to WTGS and the energy storage batteries increasing the equivalent unit regulation power, it has greater active power regulation ability, and the frequency rises rapidly to avoid frequency collapse.

As can be seen from **Figure 7B,C**, after monitoring the system frequency for 1,000 consecutive windows, it can be seen that the number of system frequency fluctuations in Mode1, 2, and 3 gradually decreases. The number of dead zones exceeding the system frequency in Mode 3 is less than that in 1 and 2, which means that the system has a fast active power regulation speed and large regulation capacity, and finally enhances the ability of the system to resist frequency fluctuation. In Mode 3, compared with Mode 1, the number of frequency fluctuations exceeding the dead band is reduced by 70%. The active power imbalance of the system caused by frequency fluctuation has improved significantly. According to the scatter diagram of frequency change data in **Figure 7D**, the system frequency change in Mode 3 is reduced by about 40% compared with Mode 1 and 20% compared with Mode 2.

Figure 8 shows the system equivalent unit regulation power coefficient diagram. The variable equivalent coefficient means the variable regulation capacity. In this way, while meeting the regulation of active power, reduce the regulation times and reduce the lost wind energy, improve the utilization rate of clean energy as much as possible on the premise of meeting the system safety.

It can be observed that the droop coefficient is adjusted with the frequency deviation. The larger the frequency deviation, the greater the droop coefficient. The more additional power the fan provides, the frequency deviation decreases, the droop coefficient decreases, and the additional power provided decreases. Although WTGS participates in active power regulation to ensure the system's active power balance at some time, the power to the grid is reduced, but due to the rapid recovery of system frequency the total regulation times are reduced, and the total power used for frequency modulation is reduced.

It can be seen from **Figure 9** that the adjustment speed of active power support is also different for different power generation forms, which is mainly related to the operation characteristics (parameter setting) of the power supply itself. Affected by the climbing rate, the active power of thermal power units changes relatively slowly compared with power electronic components, and the frequency recovery speed is also relatively slow. The response speed of WTGS and PV participating in power regulation is significantly better than that of traditional generator sets. When PV works, due to the

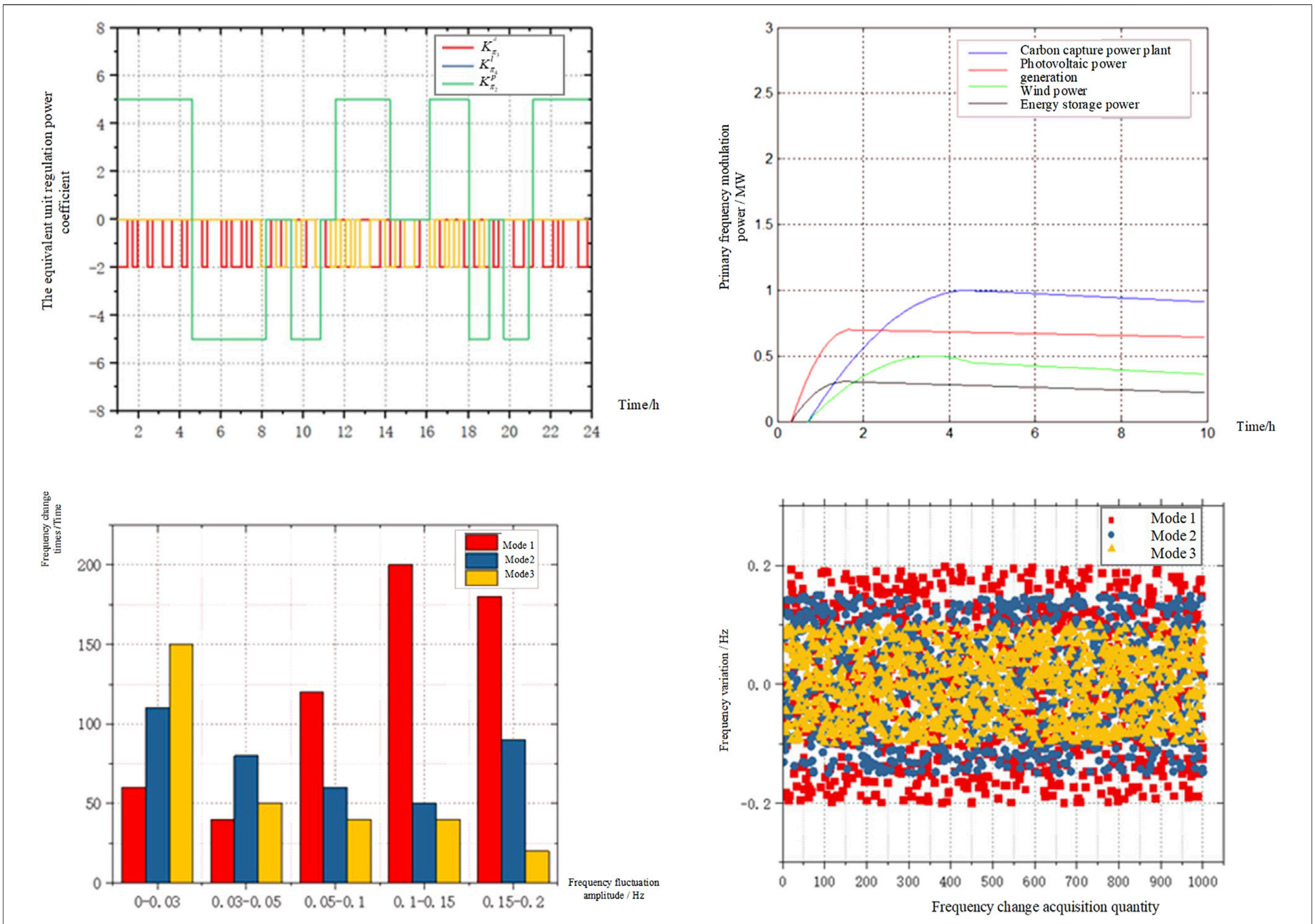

FIGURE 7 | (A) The variation diagram of system equivalent unit regulated power coefficient in Mode 2; **(B)** the active power adjustment curve of each power in the system; **(C)** the frequency variation amplitude in Mode 3; **(D)** the distribution of frequency variation in mode three.

smaller PV inertia time constant compared with WTGS, the regulation speed of active power during the day is faster and the frequency stability is better.

The energy storage battery can stabilize the fluctuation in the process of active power regulation, make the effect of active power regulation smooth, and avoid the decline of power quality in the fluctuating sawtooth floating band. So, although the clean energy power generation in Mode 3 is lower than that in Mode 2, the system frequency is relatively stable due to the system's active power balance, which provides the possibility to improve the grid connection penetration of clean energy. It can be seen from **Figure 9** that when the frequency offset occurs at this time of the system, the carbon capture power plants, WTGS, PV, and energy storage battery all participate in the primary frequency modulation process. In this process, PV and energy storage battery supply improves the response speed of the system to the power imbalance and first responds to the unbalanced power. The non-power plant's supply alleviates the pressure caused by the active power imbalance of the system.

It can be seen that under the control of the three modes, the frequency change of modes 1–3 is from large to small, the frequency response speed of Mode 1 is the slowest and the frequency change is the largest, the maximum frequency fluctuation is 0.2 Hz, and the frequency fluctuation amplitude of Mode 2 is reduced by 0.025 Hz. In Mode 3, the frequency adjustment speed is the fastest and the frequency fluctuation is the smallest of the three Modes, the frequency fluctuation amplitude of Mode 3 is reduced by 20% compared with Mode 1 and 8.5% compared with Mode 2. As can be seen from **Table 2**, compared with mode1 and mode 2, the cost of curtailing wind and light has increased in mode 3, but the overall cost is the lowest.

6 SUMMARY AND OUTLOOK

In this study, from the perspective of ensuring the system frequency stability by controlling the active power of the system, for the integrated energy system including carbon

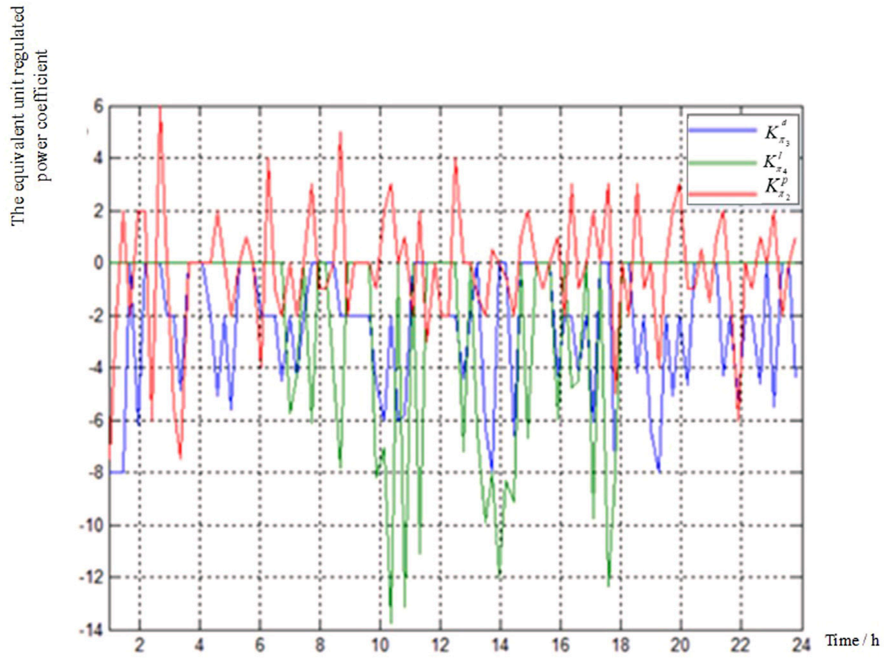

FIGURE 8 | The variation diagram of system equivalent unit regulated power coefficient in Mode 2.

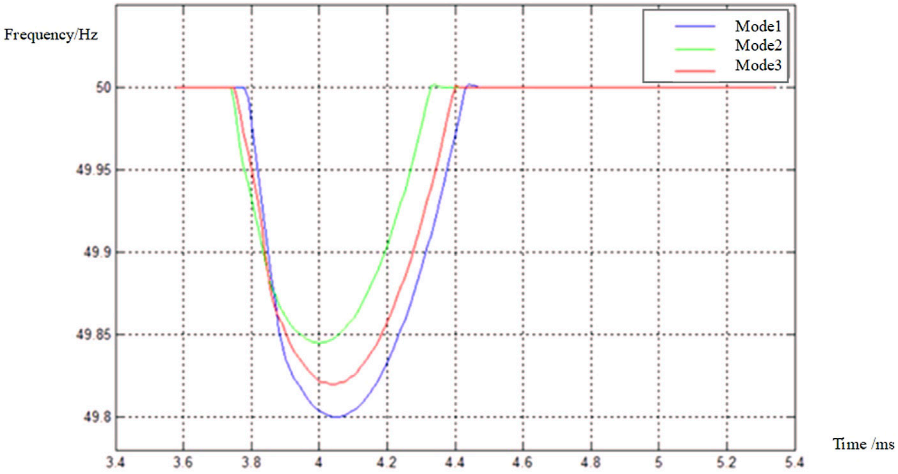

FIGURE 9 | The frequency variation curve in three Modes.

capture power plants, wind turbine generator system, photovoltaic power generation systems, and energy storage batteries, when the system frequency fluctuation exceeds the dead zone, the variable droop control is used to change the system participation. Active power regulation power, an optimal control model of active power cost of an integrated energy system is proposed. The results show:

1) After a high proportion of power electronic components are connected to the power grid, the system inertia is reduced, and the ability of the power grid to resist system frequency fluctuation is reduced. Connecting various energy forms to the power grid and participating in active power regulation can significantly enhance the frequency modulation ability of the power grid.

2) When multiple power sources participate in the system active power regulation, according to the actual system frequency change, the variable equivalent unit regulation power has a better control effect and the lowest cost than the single equivalent unit regulation power.

3) According to the variable equivalent unit regulation power, the number of active power regulations is significantly reduced,

and the fluctuation range of system frequency is significantly reduced. Compared with the traditional method, it is increased by 20%, and compared with the single equivalent unit regulation power, it is increased by 8.5%.4. Reasonable use of clean energy and energy storage to participate in active power regulation, although reducing the power of clean energy on-grid, but reducing the cost of frequency regulation, enhancing the system's ability to resist the imbalance of active power due to the system, reducing the system's lack of regulation ability, and reducing the risk of system security possibility.

4) Rational use of clean energy and energy storage to participate in active power regulation can reduce the online power of clean energy, but reduce the cost of frequency modulation, enhance the ability of the system to resist the imbalance of active power, and reduce the possibility that the insufficient regulation ability of the system may endanger the safety of the system.

5) There are also some limitations in this study. This study assumes that all power supplies participate in frequency modulation at the same time. The sensitivity of clean energy to frequency is different. How to set frequency response or FM priority in the emergency frequency range according to this characteristic is an issue that has not yet been considered in this study.

DATA AVAILABILITY STATEMENT

The original contributions presented in the study are included in the article/Supplementary Material; further inquiries can be directed to the corresponding author.

AUTHOR CONTRIBUTIONS

YZ is responsible for the determination of the research direction of the paper, WG is responsible for the editing of the text, and SW is responsible for the determination of the method. LZ is responsible for the data source. CT is responsible for optimized calculations.

FUNDING

This work was supported by the State Grid Corporation Headquarters Technology Project Research and Application of Industrial Flexible Load Participation in New Energy Consumption Coordinated Decision-Making Technology (Item Code: 5108-202228048A-1-1-ZN).

REFERENCES

Cai, G. W., Kong, L. G., Pan, C., Yang, D. Y., and Sun, Z. L. (2013). Modeling and Grid-Connected Control Strategy of Wind-Solar Storage Combined Power Generation System. *J. Electrotech. Technol.* 28 (9), 196–204. doi:10.3969/j.issn.1000-6753.2013.09.024

Gao, Q., Zhang, X., Yang, M., Chen, X., Zhou, H., and Yang, Q. (2022). Fuzzy Decision-Based Optimal Energy Dispatch for Integrated Energy Systems with Energy Storage. *Front. Energy Res.* 9. doi:10.3389/fenrg.2021.809024

Kayikçi, M., and Milanovic, J. V. (2009). Dynamic Contribution of DFIG-Based Wind Plants to System Frequency Disturbances. *IEEE Trans. Power Syst.* 24 (2), 859–867. doi:10.1109/tpwrs.2009.2016062

Li, C., Li, P., Yu, H., Li, H., Zhao, J., Li, S., et al. (2021). Optimal Planning of Community Integrated Energy Station Considering Frequency Regulation Service. *J. Mod. Power Syst. Clean Energy* 9 (2), 264–273. doi:10.35833/MPCE.2019.000056

Li, P., Wang, Z., Wang, N., Yang, W., Li, M., Zhou, X., et al. (2021a). Stochastic Robust Optimal Operation of Community Integrated Energy System Based on Integrated Demand Response. *Int. J. Electr. Power & Energy Syst.* 128, 106735. doi:10.1016/j.ijepes.2020.106735

Li, P., Zhang, F., Ma, X., Yao, S., Zhong, Z., Yang, P., et al. (2021b). Multi-Time Scale Economic Optimization Dispatch of the Park Integrated Energy System. *Front. Energy Res.* 9, 743619. doi:10.3389/fenrg.2021.743619

Liao, J. L. (2020). *Modeling and Optimization of Primary Frequency Modulation Capability of High-Power Thermal Power Units*. Hangzhou: Zhejiang University.

Liu, T. Q., Zhang, Q., and He, C. (2021). Coordinated and Optimized Operation of Gas-Electricity Integrated Energy Distribution Network System Considering Combined Gas-Electricity Demand Response. *Chin. J. Electr. Eng.* 41 (05), 1664–1677. doi:10.13334/j.0258-8013.pcsee.200385

Ma, C. H., Pan, Z. Y., Liu, C. N., and Li, W. B. (2015). Research on Frequency Modulation of Solar Energy Storage Microgrid Based on Adaptive Droop Control. *Power Syst. Prot. control* 43 (23), 7. doi:10.7667/j.issn.1674-3415.2015.23.004

Ma, Y. B. (2019). *Optimal Control Strategy of Wind-Storage Combined System Participating in Primary Frequency Regulation of Power Grid.* Jilin: Northeast Electric Power University.

Mishra, S., Zarina, P. P., and Sekhar, P. C. (2013). "A Novel Controller for Frequency Regulation in a Hybrid System with High PV Penetration," in IEEE Power & Energy Society General Meeting (Vancouver, BC, Canada: IEEE), 1–5. doi:10.1109/pesmg.2013.6672143

Pati, S. S., and Subudhi, U. (2021). "Frequency Regulation of Solar-Wind Integrated Multi-Area System with SMES and SSSC," in IEEE International Power and Renewable Energy Conference (IPRECON), Kollam, India, 1–4. doi:10.1109/IPRECON52453.2021.9640854

Riyaz, A., Sadhu, P. K., Iqbal, A., Tariq, M., Urooj, S., and Alrowais, F. M. (2021). Power Management of Hybrid Grid System with Battery Deprivation Cost Using Artificial Neural Network. *Front. Energy Res.* 9, 774408. doi:10.3389/fenrg.2021.774408

Ros-Mercado, R. Z., and Borraz-Sánchez, C. (2015). Optimization Problems in Natural Gas Transportation Systems: A State-Of-The-Art Review. *Appl. Energy* 147, 536–555. doi:10.1016/j.apenergy.2015.03.017

Sun, P., Hao, X., Wang, J., Shen, D., and Tian, L. (2021). Low-carbon Economic Operation for Integrated Energy System Considering Carbon Trading Mechanism. *Energy Sci. Eng.* 9 (11), 2064–2078. doi:10.1002/ese3.967

Tian, C., Tian, L., Li, D., Lu, X., and Chang, X. (2016). Control Strategy for Tracking Photovoltaic Output Power Based on Hybrid Energy Storage System. *J. Electrotech. Technol.* 31 (14), 75–83. doi:10.3969/j.issn.1000-6753.2016.14.009

Tian, F., Jia, Y. B., Ren, H. Q., Bai, Y., and Huang, T. (2020). Source-load" Low-Carbon Economic Dispatch of Integrated Energy System Considering Carbon Capture System. *Power Grid Technol.* 44 (09), 3346–3355. doi:10.13335/j.1000-3673.pst.2020.0728

Wang, R., Cheng, S., Zuo, X., and Liu, Y. (2021c). Optimal Management of Multi Stakeholder Integrated Energy System Considering Dual Incentive Demand Response and Carbon Trading Mechanism[J]. *Int. J. Energy Res.* 46, 6246–6263. doi:10.1002/er.7561

Wang, R., Sun, Q., Han, J., Zhou, J., Hu, W., Zhang, H., et al. (2021b). Energy-Management Strategy of Battery Energy Storage Systems in DC Microgrids: A Distributed Dynamic Event-Triggered H_∞ Consensus Control. *IEEE Trans. Syst. Man. Cybern. Syst.*, 1–10. doi:10.1109/TSMC.2021.3129184

Wang, R., Sun, Q., Tu, P., Xiao, J., Gui, Y., and Wang, P. (2021a). Reduced-Order Aggregate Model for Large-Scale Converters with Inhomogeneous Initial Conditions in DC Microgrids. *IEEE Trans. Energy Convers.* 36 (3), 2473–2484. doi:10.1109/tec.2021.3050434

Wang, R., Sun, Q. Y., Zhang, P. J., Gui, Y. H., Qin, D. H., and Wang, P. (2020). Reduced-Order Transfer Function Model of the Droop-Controlled Inverter via

Jordan Continued-Fraction Expansion. *IEEE Trans. Energy Convers.* 35 (3), 1585–1595. doi:10.1109/TEC.2020.2980033

Xian, L., Wen, Y. F., Lu, Y. D., and Lin, X. H. (2021). Research on Frequency Stability Constrained Optimal Scheduling Model of Microgrid with Virtual Synchronous Machine [J/OL]. *Chin. J. Electr. Eng.* 114. doi:10.13334/j.0258-8013.pcsee.210127

Xiao, Y. P., Zhang, L., Zhang, X., and Liu, Q. X. (2020). Coordination Mechanism for Market Clearing of Spot Electric Energy Including Independent Energy Storage and Frequency Regulation Auxiliary Services. *Chin. J. Electr. Eng.* 40 (S1), 167–180. doi:10.13334/j.0258-8013.pcsee.200977

Xiaohui, Z., Xiaoyan, L., Jiaqing, Z., and Wenbo, G. (2019). Electricity–gas-integrated Energy Planning Based on Reward and Penalty Ladder-type Carbon Trading Cost. *IET Generation, Transm. Distribution* 13 (23), 5263–5270. doi:10.1049/iet-gtd.2019.0666

Xie, P., Cai, Z. X., Liu, P., Li, X. H., Zhang, Y., and Sun, Y. (2019). Cooperative Optimization of Energy Storage Capacity of Wind-Solar-Storage Microgrid System Considering the Coupled Effects of Uncertainties on Multiple Time Scales [J]. *Chin. J. Electr. Eng.* 39 (24), 7126–7136+7486. doi:10.13334/j.0258-8013.pcsee.181193

Yang, B. (2018). *Research on the Control Strategy of Energy Storage Participating in Power Grid Frequency Regulation Considering Load Forecasting*. Changsha: Hunan University.

Zadkhast, S., Garcia-Gonzalez, P., Frías, P., and Bauer, P. (2017). Design of Plug-In Electric Vehicle's Frequency-Droop Controller for Primary Frequency Control and Performance Assessment. *IEEE Trans. Power Syst.* 32 (6), 4241–4254. doi:10.1109/tpwrs.2017.2661241

Zarina, P. P., Mishra, S., and Sekhar, P. C. (2012). "Deriving Inertial Response from a Non-inertial PV System for Frequency Regulation," in IEEE International Conference on Power Electronics, Drives and Energy Systems (Bengaluru, India: IEEE), 1–5. doi:10.1109/pedes.2012.6484409

Zhao, J. J., Xu, C. L., Lv, X., and Xu, C. S. (2017). Microgrid Primary Frequency Regulation Reserve Capacity and Energy Storage Optimization Configuration Method. *Chin. J. Electr. Eng.* 37 (15), 4324–4332+4572. doi:10.13334/j.0258-8013.pcsee.161312

Zhao, J. Q., Sun Zhong, H., Yang, Y. H., Wang, Y. H., Hu, G. S., and Chen, G. (2020). Research on the Transaction Mechanism of Distributed Photovoltaics Participating in Frequency Modulation Auxiliary Services. *Glob. Energy Internet* 3 (05), 477–486.

Zhou, R. J., Sun, H., Tang, X. F., Zhang, W., and Yu, H. (2018). Low-carbon Economic Dispatch of Wind Power-Carbon Capture Virtual Power Plants under Double Carbon Constraints. *Chin. J. Electr. Eng.* 38 (06), 1675–1683+1904. doi:10.13334/j.0258-8013.pcsee.170541

Conflict of Interest: YZ, LZ, and CT were employed by State Grid Shenyang Electric Power Supply Company. WG and SW were employed by State Grid Liaoning Electric Power Supply Co., Ltd.

ORIGINAL RESEARCH
published: 09 June 2022
doi: 10.3389/fenrg.2022.907719

Distributed Economic Dispatch Based on Finite-Time Double-Consensus Algorithm of Integrated Energy System

Jun Yang* and Jianhai Du

College of Information Science and Engineering, Northeastern University, Shenyang, China

To reduce the operating cost and enhance the energy utilization efficiency of the integrated energy system (IES), an economic dispatch algorithm is proposed based on finite-time double-consensus. First, an economic dispatch model of IES under two modes of operation, islanded and grid-connected, is constructed considering energy transmission losses. After that, the optimal improved incremental cost and power output allocation of the IES can be found out in finite time. The proposed algorithm contains two finite-time consistency protocols simultaneously that can solve the optimal values of the incremental cost of electricity and heat of integrated energy system, solving the strong coupling problem of multi-energy systems. The proposed algorithm not only has a faster convergence rate but also enables switching freely between the two operation modes. In addition, a distributed method for quickly discovering the total system power mismatch is proposed in the process of algorithm solving. The finite-time convergence of the proposed algorithm is demonstrated. Finally, the IES simulation based on the IEEE 30-node power system and the Bali 32-node thermal system is established. The analysis of the simulation results shows that the algorithm proposed in this paper is effective.

Keywords: distributed economic dispatch, finite time, double-consensus algorithm, double modes of operation, transmission loss, integrated energy system

Edited by:
Wei Hu,
Zhejiang University, China

Reviewed by:
Yushuai Li,
University of Oslo, Norway
Hongxun Hui,
University of Macau, China

****Correspondence:***
Jun Yang
yangjun@mail.neu.edu.cn

Specialty section:
This article was submitted to Smart Grids, a section of the journal Frontiers in Energy Research

Received: *30 March 2022*
Accepted: *09 May 2022*
Published: *09 June 2022*

Citation:
Yang J and Du J (2022) Distributed Economic Dispatch Based on Finite-Time Double-Consensus Algorithm of Integrated Energy System. Front. Energy Res. 10:907719. doi: 10.3389/fenrg.2022.907719

1 INTRODUCTION

At present, the world is facing increasing pressure to save energy and protect the environment, and how to reduce environmental pollution based on ensuring a continuous supply of energy is a problem that countries have to consider (Yang and Su, 2021). Integrated energy system (IES) is a significant way to consume various types of distributed renewable energy, which is important for promoting the consumption of various types of renewable energy and establishing a new type of green and low-carbon power system (Li et al., 2021). IES is a deep integration of multiple energy sources and information technology that can promote the sustainable development of energy. With the increasing demand for IES to replace conventional energy systems in recent years, the research on various key technologies and theories about IES, such as dynamic modeling (Shen et al., 2020), multi-energy flow calculation (Yao et al., 2021), optimal cooperative operation (Qin et al., 2020), energy management (Li et al., 2020) and economic dispatch problem (EDP) (Lu et al., 2021; Liu et al., 2019), is receiving widely concerned.

The EDP has always been a hot issue in power and energy system research, and this is no exception in IES. Economic dispatch (ED) is a dispatching method to achieve the lowest cost through rational utilization of energy and equipment while satisfying safety and energy quality. The EDP can be equated to the planning problem of finding the minimum value of the cost function while satisfying the capacity constraint of each unit and the system power balance constraint. Traditional centralized control algorithms have also been applied to solve EDPs, such as model predictive control (Yu et al., 2019; Huang et al., 2021) and deep reinforcement learning (Lin et al., 2020). The advantage of centralized is reflected in the ease of unified management of resources within the system. Still, there are drawbacks such as high communication requirements, high computational load, and vulnerability to attacks (Xu et al., 2015). To overcome the shortcomings of centralized algorithms, distributed algorithms and multi-agent technology have gradually received widespread attention. Compared with centralized algorithms, distributed algorithms require fewer communication resources and have higher robustness and information security. Several distributed algorithms have been proposed to solve the EDP, such as the alternating direction multiplier method (Chen and Yang, 2018), diffusion algorithm (Chen and Sayed, 2012) and consensus algorithm (Binetti et al., 2014; Yang et al., 2017).

The consensus algorithm is used to achieve the economic optimum of the whole system by iteratively converging the incremental cost of each capacity unit to the consistency. Still, a centralized controller is required in the initially designed algorithm to calculate the total power deviation to ensure the power balance (Pu et al., 2017). Due to the stochastic nature of wind generation, its modeling should be different from conventional units. The uncertainty of the wind turbine output is considered in (Guo et al., 2016), and the power balance is achieved based on projected gradient that gets rid of the centralized control center. Saddle point dynamics is introduced in the iterative process of the consensus algorithm to search for an economically optimal solution in (Bai et al., 2019), which achieves fully distributed. Considering that communication delays always exist in real systems, the time-varying delay is considered in (Huang et al., 2019). The algorithm can still converge under certain communication delay conditions. In modeling the EDP, the cost function of equipment output is usually designed as a convex quadratic function to ensure the speed and convergence of the algorithm. To make the algorithm perform well even when the cost function is a general convex function, a method based on secant approximation is proposed to achieve efficient convergence (Zhong et al., 2021). (Chen et al., 2017; Zaery et al., 2020) use finite-time consensus for solving the EDP so that the algorithm converges in a determined finite time. In addition, issues such as network loss compensation (Sun et al., 2021) and information security encryption (Yan et al., 2021) have been considered.

However, most of the ED algorithms in the above literature are only proposed for power systems. For IESs, there is less literature on solving the EDP by consensus algorithms, and how to deal with the coupling relationship among multiple energy sources is one of the focuses of problem. A double-consensus algorithm is proposed in (Sun et al., 2019) to construct two consistency protocols in parallel to solve the strong coupling between electric and heat and achieve the economic optimum of the whole system. Based on (Sun et al., 2019), a distributed robust algorithm capable of resisting network attacks is proposed (Huang et al., 2022). The event-triggered mechanism is also applied to the economic dispatch problem to reduce the communication between agents (Li et al., 2019).

In summary, finite-time consensus allows the states of the agents to converge quickly to consistency in finite time. Event-triggered consensus (Chen et al., 2022) is to set the trigger function and trigger conditions. The communication between the agents is generated only when trigger conditions are met, which has the advantage of reducing the requirement for communication. The traditional consensus (Hong et al., 2022) haven't the advantages of both. To the authors' knowledge, the finite-time the consensus algorithm to solve the EDP of IES has not been discussed in depth. Based on the results obtained in the previous study, an ED strategy of IES is proposed based on the finite-time double-consensus algorithm in this paper, which can achieve economic optimality in both modes of system operation in islanded and grid-connected. The main contributions are as follows.

1) The ED strategy for IES is proposed based on the finite-time double-consensus algorithm, which solves the strong coupling problem among different energies by simultaneously executing two consistency protocols to achieve economic optimization. The proposed algorithm can achieve fast convergence in a finite time while allowing free and smooth switching between two modes of operation, that is, grid-connected and islanded. A distributed method to discover the total system power mismatch within finite step iterations is proposed to achieve power supply and demand balance during the algorithm execution.
2) The EDP model for IES considering transmission losses of electric and thermal energy is constructed, which has two modes of operation. The electric and thermal output coupling of combined heat and power units (CHPs) is considered in the model. And their operable domains are considered as output constraints.
3) The Lyapunov function for improved incremental cost deviation is constructed and the finite-time convergence of the proposed algorithm is demonstrated by theoretical analysis.

The rest of the paper is organized as follows: ***Preliminaries*** introduces some basic knowledge of graph theory used in this paper. ***Problem Formulation*** introduces the modeling of IES and the optimal solution of the EDP. ***Finite-Time Double-Consensus Algorithm*** proposes the finite-time double-consensus algorithm to solve the EDP. ***Case Studies*** demonstrates the effectiveness of the algorithm through data analysis of the constructed system. ***Conclusion*** summarizes the conclusions and provides an outlook.

2 PRELIMINARIES

2.1 Graph Theory

For any IES containing n agents, its communication network topology graph is generally represented by an undirected graph

$G = (V, E)$, where $V = \{1, 2, \ldots, n\}$ denotes the set of agents and $E \subseteq V \times V$ denotes the set of edges between agents. The elements (i, j) denote that agent i and j are interconnected and can communicate and receive information from each other. If there is a communication line between agent i and j, then agent j is a neighbor of i. The set consisting of all neighbors of agent i is denoted as $\{j \in V | (i, j) \in E\}$. The adjacency matrix $A = [a_{ij}]$ can represent the connectivity of G. For an undirected graph, if there is a communication path between i and j, then $a_{ij} = a_{ji} = 1$; otherwise $a_{ij} = a_{ji} = 0$. The diagonal element $a_{ii} = 0$ is defined. Let $D_i = \sum_{i\in N_i} a_{ij}$, then the diagonal matrix $D = diag(D_i)$ is the degree matrix of G. Define the Laplacian matrix of a graph G as $L = D - A$. An undirected graph G is connected if there exists at least one path between any two agents. For a connected graph G, its Laplacian matrix L has only one zero eigenvalue, and the rest of the eigenvalues are greater than 0. A sequential ordering of all its eigenvalues can be expressed as $0 = \lambda_1(L) < \lambda_2(L) < \ldots < \lambda_n(L)$.

3 PROBLEM FORMULATION

3.1 Integrated Energy System Modeling

Assume an IES with N agents, where the agents include power generating units (PGUs), heat generating units (HGUs) and CHPs. The IES is connected to the distribution network, and the system receives exchange power from the distribution network when operating in grid-connected mode. The operating cost of each unit can be approximated as a convex quadratic function of its output. The cost functions for different types of units can be expressed as follows:

$$C_P = \sum_{i\in N_P} C_{P_i}(P_{G_i}) = \sum_{i\in N_P} \alpha_{P_i} + \beta_{P_i} P_{G_i} + \gamma_{P_i} P_{G_i}^2 \tag{1}$$

$$\begin{aligned} C_C &= \sum_{i\in N_C} C_{C_i}(P_{C_i}, Q_{C_i}) \\ &= \sum_{i\in N_C} \alpha_{C_i} + \beta_{C_i} P_{C_i} + \gamma_{C_i} P_{C_i}^2 + \zeta_{C_i} Q_{C_i} + \eta_{C_i} Q_{C_i}^2 + \theta_{C_i} P_{C_i} Q_{C_i} \end{aligned} \tag{2}$$

$$C_H = \sum_{i\in N_H} C_{H_i}(Q_{H_i}) = \sum_{i\in N_H} \alpha_{H_i} + \beta_{H_i} Q_{H_i} + \gamma_{H_i} Q_{H_i}^2 \tag{3}$$

where C_P, C_C, and C_H denote the total operating costs of PGUs, CHPs, and HGUs, respectively; N_P, N_C, and N_H denote the set of PGUs, CHPs, and HGUs; C_{P_i}, C_{C_i}, and C_{H_i} denote the operating costs of the i th PGU, CHP, and HGU. P_{G_i} and P_{C_i} denote the power output of the i th PGU and CHP. Q_{C_i} and Q_{H_i} denote the heat output of the i th CHP and HGU. $\alpha_{P_i}, \beta_{P_i}, \gamma_{P_i}, \alpha_{C_i}, \beta_{C_i}, \gamma_{C_i}, \zeta_{C_i}, \eta_{C_i}, \theta_{C_i}, \alpha_{H_i}, \beta_{H_i}$, and γ_{H_i} are the operating cost coefficients of the i th PGU, CHP, and HGU, respectively.

At the same time, each unit of the IES has to satisfy some equality constraints and inequality constraints. The equality constraints are electrical and thermal power balance constraints:

$$\sum_{i\in N_P} P_{G_i} + \sum_{i\in N_C} P_{C_i} + P_M - P_L - P_{loss} = 0 \tag{4}$$

$$\sum_{i\in N_H} Q_{H_i} + \sum_{i\in N_C} Q_{C_i} - Q_L - Q_{loss} = 0 \tag{5}$$

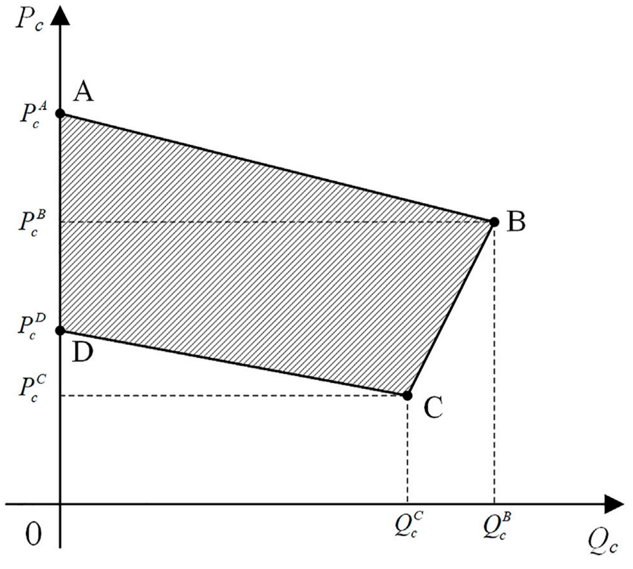

FIGURE 1 | Operable domain of CHP.

where P_L and Q_L denote the total power and thermal load demand, and P_M is the power obtained from the distribution network under the grid-connected mode of system operation. When the system is in islanded mode, $P_M = 0$. P_{loss} and Q_{loss} denote the total transmission loss of electric and thermal power generated by the transmission line and heating pipeline, respectively. They are approximated as functions of the output power, $P_{loss} = \sum_{i\in N_P} B_{P_i} P_{G_i} + \sum_{i\in N_C} B_{C_i} P_{C_i}$, $Q_{loss} = \sum_{i\in N_H} B_{H_i} Q_{H_i} + \sum_{i\in N_C} B_{C_i} Q_{C_i}$, B_{P_i}, B_{C_i}, and B_{H_i} are loss coefficients.

The inequality constraints, that is, the power output limits of PGUs and HGUs and the operable domain constraint of CHPs:

$$\underline{P}_{G_i} \le P_{G_i} \le \bar{P}_{G_i} \tag{6}$$

$$\underline{Q}_{H_i} \le Q_{H_i} \le \bar{Q}_{H_i} \tag{7}$$

The lower and upper limits of the electrical output of the i th PGU are $\underline{P}_{G_i}$ and $\bar{P}_{G_i}$, and the lower and upper limits of the thermal output of the i th HGU are $\underline{Q}_{H_i}$ and $\bar{Q}_{H_i}$, respectively. For CHP, its electric and thermal output is bounded by its operable domain, as shown in **Figure 1**. The boundary of this operable region is specified in the form of a linear inequality (Soroudi, 2017):

$$P_{C_i} - P_{C_i}^A - \left(\frac{P_{C_i}^B - P_{C_i}^A}{Q_{C_i}^B - Q_{C_i}^A} \right) \times Q_{C_i} \le 0 \tag{8}$$

$$P_{C_i} - P_{C_i}^B - \left(\frac{P_{C_i}^C - P_{C_i}^B}{Q_{C_i}^C - Q_{C_i}^B} \right) \times \left(Q_{C_i} - Q_{C_i}^B \right) \ge 0 \tag{9}$$

$$P_{C_i} - P_{C_i}^C - \left(\frac{P_{C_i}^D - P_{C_i}^C}{Q_{C_i}^D - Q_{C_i}^C} \right) \times \left(Q_{C_i} - Q_{C_i}^C \right) \ge 0 \tag{10}$$

$$P_{C_i}^{C} \le P_{C_i} \le P_{C_i}^{A} \tag{11}$$

$$0 \le Q_{C_i} \le Q_{C_i}^{B} \tag{12}$$

where $P_{C_i}^A, P_{C_i}^B, P_{C_i}^C, P_{C_i}^D, Q_{C_i}^A, Q_{C_i}^B, Q_{C_i}^C$, and $Q_{C_i}^D$ are the coordinates of the four vertices A, B, C, and D of the operable domain of the i th CHP on the P_C axis and the Q_C axis as shown in **Figure 1**.

3.2 Economic Dispatch Problem

The EDP of the IES is to distribute the output power of each unit reasonably on the basis of ensuring power balance to minimize the operating cost. The objective function of the EDP is defined as follows:

$$\min\ C = C_P + C_C + C_H + \mu_0 P_M \tag{13}$$

where C is the operating cost of the whole IES and μ_0 is the electricity price of the distribution network.

The equality constraints and inequality constraints are specified in **Eqs. 6–12** also need to be satisfied in solving the objective function. When only the equality constraints are considered, the following Lagrangian function can be constructed:

$$L = C + \mu_P\left(P_L + P_{loss} - \sum_{i\in N_P} P_{G_i} - \sum_{i\in N_C} P_{C_i} - P_M\right) + \mu_H\left(Q_L + Q_{loss} - \sum_{i\in N_H} Q_{H_i} - \sum_{i\in N_C} Q_{C_i}\right) \tag{14}$$

where $\mathcal{L}$ is the Lagrangian function and μ_P, μ_H are the Lagrangian multipliers corresponding to the electrical and thermal power, respectively. The optimal solution of the system can be obtained by finding the partial derivatives from the Karush-Kuhn-Tucker (KKT) condition as

$$\frac{\partial \mathcal{L}}{\partial P_{G_i}} = 2\gamma_{P_i} P_{G_i} + \beta_{P_i} + \mu_P\left(B_{P_i} - 1\right) = 0 \tag{15}$$

$$\frac{\partial \mathcal{L}}{\partial P_{C_i}} = 2\gamma_{C_i} P_{C_i} + \beta_{C_i} + \theta_{C_i} Q_{C_i} + \mu_P\left(B_{CP_i} - 1\right) = 0 \tag{16}$$

$$\frac{\partial \mathcal{L}}{\partial Q_{C_i}} = 2\eta_{C_i} Q_{C_i} + \zeta_{C_i} + \theta_{C_i} P_{C_i} + \mu_H\left(B_{CH_i} - 1\right) = 0 \tag{17}$$

$$\frac{\partial \mathcal{L}}{\partial Q_{H_i}} = 2\gamma_{H_i} Q_{H_i} + \beta_{H_i} + \mu_H\left(B_{H_i} - 1\right) = 0 \tag{18}$$

$$\frac{\partial \mathcal{L}}{\partial P_M} = \mu_0 - \mu_P = 0 \tag{19}$$

$$\frac{\partial \mathcal{L}}{\partial \mu_P} = P_L + P_{loss} - \sum_{i\in N_P} P_{G_i} - \sum_{i\in N_C} P_{C_i} - P_M = 0 \tag{20}$$

$$\frac{\partial \mathcal{L}}{\partial \mu_H} = Q_L + Q_{loss} - \sum_{i\in N_H} Q_{H_i} - \sum_{i\in N_C} Q_{C_i} = 0 \tag{21}$$

The improved incremental cost of each unit is defined as

$$\mu_{P_i}^{P} = \frac{\partial C_{P_i}}{\partial P_{G_i}} \cdot \frac{1}{\left(1 - \dfrac{\partial P_{loss}}{\partial P_{G_i}}\right)} \tag{22}$$

$$\mu_{P_i}^{C} = \frac{\partial C_{C_i}}{\partial P_{C_i}} \cdot \frac{1}{\left(1 - \dfrac{\partial P_{loss}}{\partial P_{C_i}}\right)} \tag{23}$$

$$\mu_{H_i}^{C} = \frac{\partial C_{C_i}}{\partial Q_{C_i}} \cdot \frac{1}{\left(1 - \dfrac{\partial Q_{loss}}{\partial Q_{C_i}}\right)} \tag{24}$$

$$\mu_{H_i}^{H} = \frac{\partial C_{H_i}}{\partial Q_{H_i}} \cdot \frac{1}{\left(1 - \dfrac{\partial Q_{loss}}{\partial Q_{H_i}}\right)} \tag{25}$$

From **Eqs. 15–21**, according to the equal micro-incremental rate criterion, when the cost consumed per unit of active power generated by each unit is the same, that is, when the improved incremental cost μ_P or μ_H of each unit reaches the consistent values μ_P^* and μ_H^*, the overall operating cost of IES takes a minimal value. It achieves the goal of economically optimal dispatch of the system. If the system is operated in grid-connected mode, according to **Eq. 19**, the improved incremental cost μ_P of the system should converge to the electricity price μ_0, then we have

$$\begin{cases} \mu_{P_1}^{P} = \mu_{P_2}^{P} = \ldots = \mu_{P_i}^{P} = \mu_{P_1}^{C} = \ldots = \mu_{P_i}^{C} = \mu_P^*, \textit{islanded mode} \\ \mu_{P_1}^{P} = \mu_{P_2}^{P} = \ldots = \mu_{P_i}^{P} = \mu_{P_1}^{C} = \ldots = \mu_{P_i}^{C} = \mu_0,\ \textit{grid} - \textit{connected mode} \end{cases} \tag{26}$$

$$\mu_{H_1}^{H} = \mu_{H_2}^{H} = \ldots = \mu_{H_i}^{H} = \mu_{H_1}^{C} = \ldots = \mu_{H_i}^{C} = \mu_H^* \tag{27}$$

If the inequality constraint of the objective function is considered, the maximum output power can only reach its upper limit and the minimum can only reach its lower limit. In the case of satisfying this condition, the results of **Eqs. 15–18** can be transformed, and the optimal solution of the improved incremental cost also needs to satisfy the following relation:

$$\begin{cases} \dfrac{2\gamma_{P_i} P_{G_i} + \beta_{P_i}}{1 - B_{P_i}} > \mu_P^*, P_{G_i} = \underline{P}_{G_i} \\[2ex] \dfrac{2\gamma_{P_i} P_{G_i} + \beta_{P_i}}{1 - B_{P_i}} = \mu_P^*, \underline{P}_{G_i} < P_{G_i} < \bar{P}_{G_i} \\[2ex] \dfrac{2\gamma_{P_i} P_{G_i} + \beta_{P_i}}{1 - B_{P_i}} < \mu_P^*, P_{G_i} = \bar{P}_{G_i} \end{cases} \tag{28}$$

$$\begin{cases} \dfrac{2\gamma_{C_i} P_{C_i} + \beta_{C_i} + \theta_{C_i} Q_{C_i}}{1 - B_{CP_i}} > \mu_P^*, P_{C_i} = \underline{P}_{C_i} \\[2ex] \dfrac{2\gamma_{C_i} P_{C_i} + \beta_{C_i} + \theta_{C_i} Q_{C_i}}{1 - B_{CP_i}} = \mu_P^*, \underline{P}_{C_i} < P_{C_i} < \bar{P}_{C_i} \\[2ex] \dfrac{2\gamma_{C_i} P_{C_i} + \beta_{C_i} + \theta_{C_i} Q_{C_i}}{1 - B_{CP_i}} < \mu_P^*, P_{C_i} = \bar{P}_{C_i} \end{cases} \tag{29}$$

$$\begin{cases} \dfrac{2\eta_{C_i}Q_{C_i} + \zeta_{C_i} + \theta_{C_i}P_{C_i}}{1 - B_{CH_i}} > \mu_H^*, Q_{C_i} = \underline{Q}_{C_i} \\ \dfrac{2\eta_{C_i}Q_{C_i} + \zeta_{C_i} + \theta_{C_i}P_{C_i}}{1 - B_{CH_i}} = \mu_H^*, \underline{Q}_{C_i} < Q_{C_i} < \bar{Q}_{C_i} \\ \dfrac{2\eta_{C_i}Q_{C_i} + \zeta_{C_i} + \theta_{C_i}P_{C_i}}{1 - B_{CH_i}} < \mu_H^*, Q_{C_i} = \bar{Q}_{C_i} \end{cases} \tag{30}$$

$$\begin{cases} \dfrac{2\gamma_{H_i}Q_{H_i} + \beta_{H_i}}{1 - B_{H_i}} > \mu_H^*, Q_{H_i} = \underline{Q}_{H_i} \\ \dfrac{2\gamma_{H_i}Q_{H_i} + \beta_{H_i}}{1 - B_{H_i}} = \mu_H^*, \underline{Q}_{H_i} \le Q_{H_i} \le \bar{Q}_{H_i} \\ \dfrac{2\gamma_{H_i}Q_{H_i} + \beta_{H_i}}{1 - B_{H_i}} < \mu_H^*, Q_{H_i} = \bar{Q}_{H_i} \end{cases} \tag{31}$$

Based on the equal micro-incremental rate criterion, the optimal incremental cost of IES can be determined iteratively. A traditional centralized control strategy can achieve this control goal by collecting information from all agents in the system integrated through a control center to calculate the optimal solution to the EDP. However, distributed generators are becoming more and more widely put into use, and centralized control is challenging to meet the demand. How to solve μ_P^* and μ_H^* and achieve the optimal power distribution of IES by distributed methods is what will be discussed in the next section of this paper.

4 FINITE-TIME DOUBLE-CONSENSUS ALGORITHM

To overcome the disadvantages of centralized control, distributed ED algorithms based on incremental cost consistency have been proposed. Each agent only needs to obtain the parameters and states of local and neighbors. There are two main structures of consensus algorithms for solving the EDP. 1) The algorithm proposed by (Pu et al., 2017) requires a central controller to collect the output power information of all agents to obtain the total output power and calculate the total power mismatch to pass to the leader for feedback regulation. It cannot guarantee the power balance if the central controller fails. 2) The algorithm proposed by (Chen and Li, 2021) estimates the power mismatch value of the local agents by each agent in the process of iteration. Finally, the power mismatch estimation value of each agent converges to 0, and the system reaches power balance. This method removes the centralized control center but slows down the algorithm's convergence, which is not conducive to the EDP that requires high convergence speed.

Based on the above algorithms, a distributed ED strategy for IES based on the finite-time double-consensus algorithm is proposed in this paper. The proposed algorithm uses a distributed approach to obtain the total power mismatch and make the improved incremental cost converge to the consistency in finite time, which not only effectively accelerates the convergence speed but also solves the problem of electrical and thermal coupling. At the same time, free switching between two operation modes is also allowed.

4.1 Total Power Mismatch Discovery

Note that the output power information of each unit is available only to the local node and its neighbors. Determining the total power mismatch of the system in a distributed manner is the first problem to be dealt with. Define the net output power of each unit as

$$P_{G_i}^S = P_{G_i} - B_{P_i}P_{G_i} = \left(1 - B_{P_i}\right)P_{G_i} \tag{32}$$

$$P_{C_i}^S = P_{C_i} - B_{CP_i}P_{C_i} = \left(1 - B_{CP_i}\right)P_{C_i} \tag{33}$$

$$Q_{C_i}^S = Q_{C_i} - B_{CH_i}Q_{G_i} = \left(1 - B_{CH_i}\right)Q_{C_i} \tag{34}$$

$$Q_{H_i}^S = Q_{H_i} - B_{H_i}Q_{H_i} = \left(1 - B_{H_i}\right)Q_{H_i} \tag{35}$$

where $P_{G_i}^S$, $P_{C_i}^S$, $Q_{C_i}^S$, and $Q_{H_i}^S$ denote the net output power of the i th PGU, CHP, and HGU, respectively, which can be calculated directly at the local agent and sent to neighbors. The Laplacian matrices defining the communication topologies of the power and thermal networks are $\hat{L}$ and $\tilde{L}$, and the adjacency matrices are $\hat{A} = [\hat{a}_{ij}]$ and $\tilde{A} = [\tilde{a}_{ij}]$, respectively. To ensure that the iterations converge in a finite number of steps, the weight factor update formula for agent i can be chosen as (Kibangou, 2012)

$$w_{ij}(k) = \begin{cases} \dfrac{1}{\lambda_{k+1}(L)}, \ j \epsilon N_i \\ 1 - \dfrac{D_i}{\lambda_{k+1}(L)}, j = i, k = 1, 2, \cdots, m \\ 0, \ otherwise \end{cases} \tag{36}$$

where $\lambda_{k+1}(L)$ represents the eigenvalue of the Laplacian matrix L, which is mentioned at the end of **Section 2.1**. From **Eq. 36**, the weight factor matrices of the power and thermal networks are obtained as $\hat{W}(k) = [\hat{w}_{ij}(k)]$ and $\tilde{W}(k) = [\tilde{w}_{ij}(k)]$, and then the total power output discovery algorithm is designed as follows:

$$P_t^S(k+1) = \hat{W}(k)P_t^S(k) \tag{37}$$

$$Q_t^S(k+1) = \tilde{W}(k)Q_t^S(k) \tag{38}$$

where, $P_t^S = [P_{G_{i,t}}^S, P_{C_{i,t}}^S]^T$ represents the vector of net electric output, and $Q_t^S = [Q_{H_{i,t}}^S, Q_{C_{i,t}}^S]^T$ represents the vector of net thermal output. After iteration, the state of each agent will converge to the average of the initial state of each agent. Assuming that the numbers of agents of both electric and heat network are known as n_P and n_Q, the algorithm converges after $n_P - 1$ and $n_Q - 1$ iterations. The total net electric and thermal output of the system is

$$P_{total}(t) = n_P P_t^S(n_P) \tag{39}$$

$$Q_{total}(t) = n_Q Q_t^S(n_Q) \tag{40}$$

where $P^S(n_P)$ and $Q^S(n_Q)$ are the convergence values of the algorithm after $n_P - 1$ and $n_Q - 1$ iterations. The total power mismatch can be expressed as

$$\Delta P(t) = P_L - P_{total}(t) \tag{41}$$

$$\Delta Q(t) = Q_L - Q_{total}(t) \tag{42}$$

This power mismatch will be used as a feedback quantity when solving for the optimal improved incremental cost μ_P^* and μ_H^* to achieve power balance.

4.2 Optimal Incremental Cost and Output Solution

The agent connected to the distribution network is selected as the leader of the power network to communicate with the distribution network to receive electric price information and connection status information. The finite-time double-consensus algorithm for solving the improved incremental cost is designed as follows:

$$\dot{\mu}_P = \alpha_P \left[\sum_{j \epsilon N_i} \hat{a}_{ij} sig\left(\mu_{P_j}(t) - \mu_{P_i}(t)\right)^m + b\hat{g}_i sig\left(\mu_0 - \mu_{P_i}(t)\right)^m + c \cdot \varepsilon_P \cdot \Delta P(t) \right] \tag{43}$$

$$\dot{\mu}_H = \alpha_H \left[\sum_{j \epsilon N_i} \tilde{a}_{ij} sig\left(\mu_{H_j}(t) - \mu_{H_i}(t)\right)^m + \varepsilon_H \cdot \Delta Q(t) \right] \tag{44}$$

where α_P and α_H are control gains, $sig(x)^m = sgn(x) \cdot |x|^m$, $0 < m < 1$, if agent i is connected to the leader, then $\hat{g}_i = 1$; otherwise $\hat{g}_i = 0$. $b = 1, c = 0$ means the system is in grid-connected mode, when operating in islanded mode then $b = 0, c = 1$. This signal change can be transferred from the distribution network to the leader. ε_P and ε_H are power regulation coefficients.

Lemma 1 (Wang and Xiao, 2010): Let $\vartheta_1, \vartheta_2, \cdots, \vartheta_n \geq 0$ and $0 < d \leq 1$, then we have

$$\sum_{i=1}^{n} \vartheta_i^d \geq \left(\sum_{i=1}^{n} \vartheta_i \right)^d \tag{45}$$

Lemma 2 (Zhang et al., 2012): Let $G = diag(g_i)$, for an undirected connected graph with Laplacian matrix with the following properties:

1)x is a column vector composed of state variables of each agent with $x^T(L+G)x = \frac{1}{2}\sum_{i,j=1}^{n} a_{ij}(x_j - x_i)^2 + \sum_{i=1}^{n} g_i(x_i)^2$.
2)$x^T(L+G)x \geq \lambda_2 x^T x$, where λ_2 is the second smallest eigenvalue of the matrix $(L+G)$ and $\lambda_2 > 0$.

Lemma 3 (Wang and Xiao, 2010): If there exists a continuous positive definite function $V(x)$ of the system, if it satisfies the existence of positive numbers $c > 0$ with $\alpha \in (0, 1)$ and an open neighborhood $V \subseteq \mathcal{D}$ containing the origin, such that

$$\dot{V}(x) + cV(x)^\alpha \leq 0 \tag{46}$$

then the origin is the finite-time stable equilibrium point of the system. $V(x)$ reaches 0 in finite time as follows:

$$T(x) \leq \frac{V(x)^{1-\alpha}}{c(1-\alpha)} \tag{47}$$

Theorem 1: For an undirected connected graph G, the algorithms in **Eqs. 43**, **44** can converge in finite steps.

Proof: Taking **Eq. 43** as an example, define the amount of deviation of the improved incremental cost as $\delta_{Pi}(t) = \mu_{P_i}(t) - \mu_0$ such that the deviation vector $\boldsymbol{\delta_P}(t) = [\delta_{P1}(t), \delta_{P2}(t), \cdots, \delta_{Pn}(t)]$, and since μ_0 is time-invariant, $\dot{\delta}_{Pi}(t) = \dot{\mu}_{Pi}(t)$. The following Lyapunov function is chosen as

$$V(t) = \frac{1}{2}\sum_{i=1}^{n} \delta_{Pi}^2(t) \tag{48}$$

Taking the differential of $V(t)$, then there is

$$\begin{aligned} \dot{V}(t) &= \sum_{i=1}^{n} \delta_{Pi}\dot{\delta}_{Pi} \\ &= \sum_{i=1}^{n} \delta_{Pi} \sum_{j=1}^{n} \hat{a}_{ij} sig\left(\delta_{Pj} - \delta_{Pi}\right)^m - \hat{g}_i sig(\delta_{Pi})^m \\ &= -\frac{1}{2}\left[\sum_{i,j=1}^{n} \hat{a}_{ij}\left(\delta_{Pj} - \delta_{Pi}\right) sig\left(\delta_{Pj} - \delta_{Pi}\right)^m + \sum_{i=1}^{n} 2\hat{g}_i \delta_{Pi} sig(\delta_{Pi})^m \right] \\ &= -\frac{1}{2}\left[\sum_{i,j=1}^{n} \left(\hat{a}_{ij}^{\frac{2}{1+m}} sig\left(\delta_{Pj} - \delta_{Pi}\right)^2 \right)^{\frac{1+m}{2}} + \sum_{i=1}^{n} \left(2\hat{g}_i^{\frac{2}{1+m}} sig(\delta_{Pi})^2 \right)^{\frac{1+m}{2}} \right] \end{aligned} \tag{49}$$

According to Lemma 1, it follows that

$$\dot{V}(t) \leq -\frac{1}{2}\left[\sum_{i,j=1}^{n} \left(\hat{a}_{ij}^{\frac{2}{1+m}} sig\left(\delta_{Pj} - \delta_{Pi}\right)^2 \right) + \sum_{i=1}^{n} \left(2\hat{g}_i^{\frac{2}{1+m}} sig(\delta_{Pi})^2 \right) \right]^{\frac{1+m}{2}} \tag{50}$$

Let $a_{ij} = \hat{a}_{ij}^{\frac{2}{1+m}}$ and $g_i = \hat{g}_i^{\frac{2}{1+m}}$, which is obtained from Lemma 2

$$\begin{aligned} \dot{V}(t) &\leq -\frac{1}{2}\left[2\lambda_2 \boldsymbol{\delta_P^T \delta_P}\right]^{\frac{1+m}{2}} \\ &\leq -\frac{1}{2}\left[4\lambda_2 V(t)\right]^{\frac{1+m}{2}} \end{aligned} \tag{51}$$

Let $c' = \frac{1}{2}(4\lambda_2)^{\frac{1+m}{2}}$, we can get $\dot{V} + c'V^{\frac{1+m}{2}} \leq 0$. Then according to Lemma 3, the error of the improved incremental cost can converge to 0 in finite time $T \leq \frac{2V^{\frac{1-m}{2}}(0)}{c'(1-m)}$.

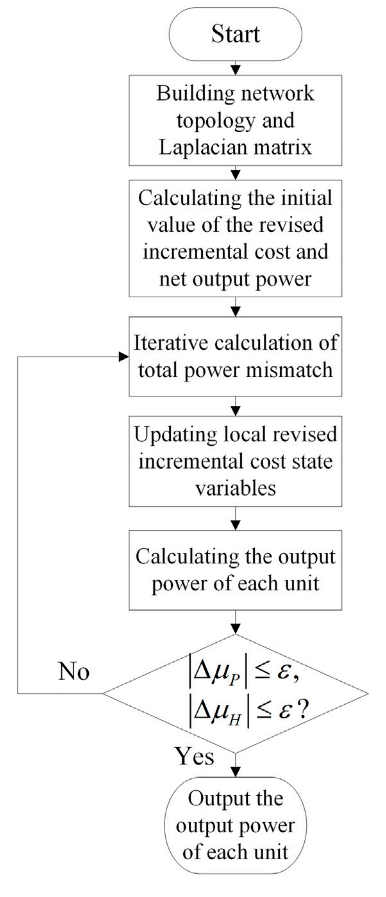

FIGURE 2 | The ED solution process of IES.

Finally, the output power is solved according to the improved incremental cost. When considering the system inequality constraints shown in **Eqs. 6–12**, the output power of each unit can be expressed as

$$P_{G_i}(t) = \begin{cases} \underline{P}_{G_i}, & \dfrac{(1-B_{P_i})\mu_{P_i} - \beta_{P_i}}{2\gamma_{P_i}} < \underline{P}_{G_i} \\ \dfrac{(1-B_{P_i})\mu_{P_i} - \beta_{P_i}}{2\gamma_{P_i}}, & \underline{P}_{G_i} < \dfrac{(1-B_{P_i})\mu_{P_i} - \beta_{P_i}}{2\gamma_{P_i}} < \bar{P}_{G_i} \\ \bar{P}_{G_i}, & \dfrac{(1-B_{P_i})\mu_{P_i} - \beta_{P_i}}{2\gamma_{P_i}} > \bar{P}_{G_i} \end{cases} \tag{52}$$

$$P_{C_i}(t) = \begin{cases} \underline{P}_{C_i}, & \dfrac{(1-B_{CP_i})\mu_{P_i} - \beta_{C_i} - \theta_{C_i}Q_{C_i}}{2\gamma_{C_i}} < \underline{P}_{G_i} \\ \dfrac{(1-B_{CP_i})\mu_{P_i} - \beta_{C_i} - \theta_{C_i}Q_{C_i}}{2\gamma_{C_i}}, & \underline{P}_{G_i} < \dfrac{(1-B_{CP_i})\mu_{P_i} - \beta_{C_i} - \theta_{C_i}Q_{C_i}}{2\gamma_{C_i}} < \bar{P}_{G_i} \\ \bar{P}_{C_i}, & \dfrac{(1-B_{CP_i})\mu_{P_i} - \beta_{C_i} - \theta_{C_i}Q_{C_i}}{2\gamma_{C_i}} > \bar{P}_{G_i} \end{cases} \tag{53}$$

$$Q_{C_i}(t) = \begin{cases} \underline{Q}_{C_i}, & \dfrac{(1-B_{CH_i})\mu_{H_i} - \zeta_{C_i} - \theta_{C_i}P_{C_i}}{2\eta_{C_i}} < \underline{Q}_{C_i} \\ \dfrac{(1-B_{CH_i})\mu_{H_i} - \zeta_{C_i} - \theta_{C_i}P_{C_i}}{2\eta_{C_i}}, & \underline{Q}_{C_i} < \dfrac{(1-B_{CH_i})\mu_{H_i} - \zeta_{C_i} - \theta_{C_i}P_{C_i}}{2\eta_{C_i}} < \bar{Q}_{C_i} \\ \bar{Q}_{C_i}, & \dfrac{(1-B_{CH_i})\mu_{H_i} - \zeta_{C_i} - \theta_{C_i}P_{C_i}}{2\eta_{C_i}} > \bar{Q}_{C_i} \end{cases} \tag{54}$$

$$Q_{H_i}(t) = \begin{cases} \underline{Q}_{H_i}, & \dfrac{(1-B_{H_i})\mu_{H_i} - \beta_{H_i}}{2\gamma_{H_i}} < \underline{Q}_{H_i} \\ \dfrac{(1-B_{H_i})\mu_{H_i} - \beta_{H_i}}{2\gamma_{H_i}}, & \underline{Q}_{H_i} < \dfrac{(1-B_{H_i})\mu_{H_i} - \beta_{H_i}}{2\gamma_{H_i}} < \bar{Q}_{H_i} \\ \bar{Q}_{H_i}, & \dfrac{(1-B_{H_i})\mu_{H_i} - \beta_{H_i}}{2\gamma_{H_i}} > \bar{Q}_{H_i} \end{cases} \tag{55}$$

The output power of each unit can be determined based on the improved incremental cost. If the output power exceeds the limit, it is optimized to the limit of the output power. If the system works in grid-connected mode, $P(t)$ does not need to be involved as a feedback quantity in solving μ_P^*, and the power mismatch is compensated by the exchange power of the distribution network.

According to the above-proposed algorithm, the steps for solving the EDP of the IES are shown in **Figure 2**, and the corresponding steps are described as follows:

Step 1 Each agent updates the information of itself and neighbors through the communication network, constructs the topology of the IES, and sets the Laplacian matrix of the topology diagram of the electric and heat network.
Step 2 Calculating the initial values of the improved incremental cost and net output power according to **Eqs. 22–25**, **Eqs. 32–35**, and determining the initial state variables of each agent.
Step 3 Calculating the total power mismatch value based on the power output of each agent. Updating improved incremental cost state variables according to the power mismatch.
Step 4 Calculating the output power of each unit based on the improved incremental cost. The power exchanged with the distribution network needs to be calculated if operating in grid-connected mode, but not if in islanded mode.
Step 5 Calculating the electric and thermal improved incremental cost errors, and if the errors satisfy the convergence accuracy ε, output the optimal solution for each unit's output; if not, repeat Step 3.

5 CASE STUDIES

5.1 Simulation Setup

To test the effectiveness of the proposed algorithm, a 30–32 nodes IES is built for simulation and analysis. The IES is improved by coupling the IEEE 30-node electric system with the Bali 32-node

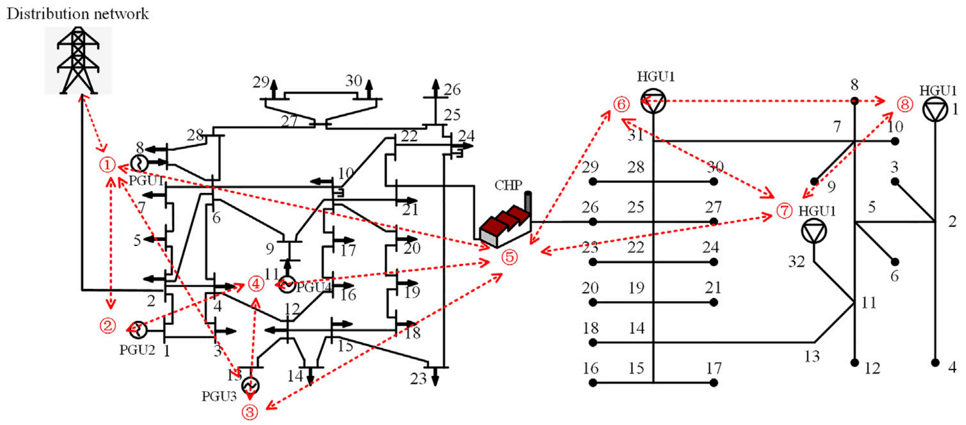

FIGURE 3 | The schematic of 30–32 nodes IES.

TABLE 1 | Cost factor parameters for each unit.

Agent	β_i	γ_i	ζ_i	η_i	θ_i	B_i
1	17.8	0.062	—	—	—	0.042
2	15.4	0.058	—	—	—	0.060
3	18.5	0.063	—	—	—	0.045
4	19.3	0.047	—	—	—	0.055
5	16.5	0.043	8.7	0.035	0.039	0.040
6	12.3	0.037	—	—	—	0.035
7	10.7	0.044	—	—	—	0.036
8	10.6	0.039	—	—	—	0.031

thermal system (Liu et al., 2016), and its communication topology is shown in **Figure 3**.

Agents one to four represent PGUs, agent 5 represents CHP, and agents six to eight represent HGUs. The dashed lines in the figure represent the communication lines among each agent. The communication line exists between agent 1 and the distribution network, which can receive the electricity price sent by the distribution network. The parameters of each distributed unit in the system are set as shown in **Table 1**. The upper and lower output limits of each PGU and HGU are 80 kW and 200 kW. The coordinates of the four vertices of the operational domain of the CHP are (0, 220), (180, 170), (165, 70), and (0, 85). The communication interval among agents is 0.05 s. The model is programmed and solved using the MATLAB 2021a simulation platform.

5.2 Effectiveness Analysis

5.2.1 Analysis of Effectiveness in Islanded Operation Mode

This subsection will verify the effectiveness of the algorithm in islanded operation mode. The system is set in islanded operation mode, and the total electrical power demand P_L and the total thermal power demand Q_L are set to 500kW and 550 kW in the initial state. The initial values of each unit output are $P_{G_1} = 75kW$, $P_{G_2} = 95kW$, $P_{G_3} = 115kW$, $P_{G_4} = 128kW$, $P_{C_i} = 87kW$, $Q_{H_1} = 155kW$, $Q_{H_2} = 170kW$, $Q_{H_3} = 95kW$,

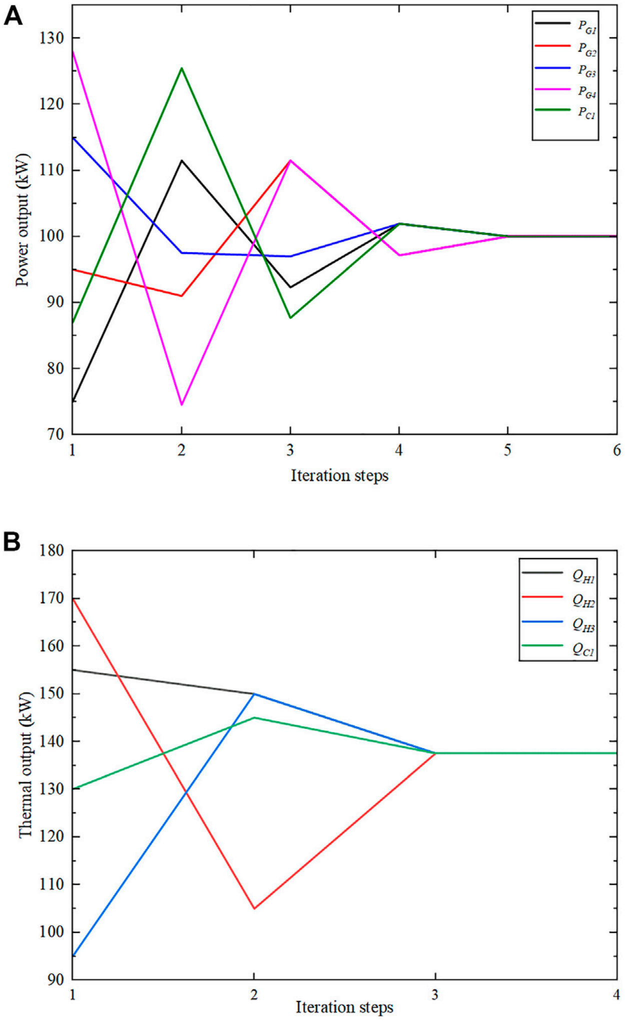

FIGURE 4 | Total output power iterative process. **(A)** Electrical power output. **(B)** Thermal power output.

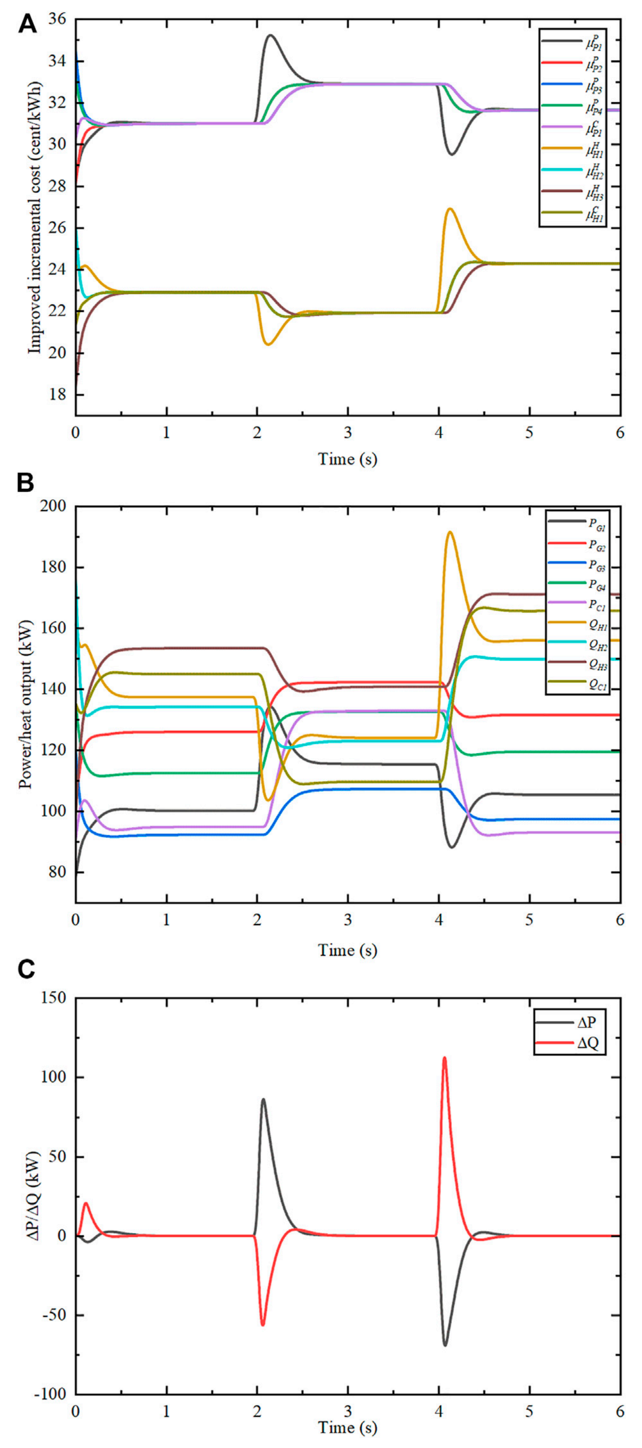

FIGURE 5 | Algorithm results in islanded operation mode. **(A)** Improved incremental cost. **(B)** Power output of each unit. **(C)** Electrical and thermal power mismatch.

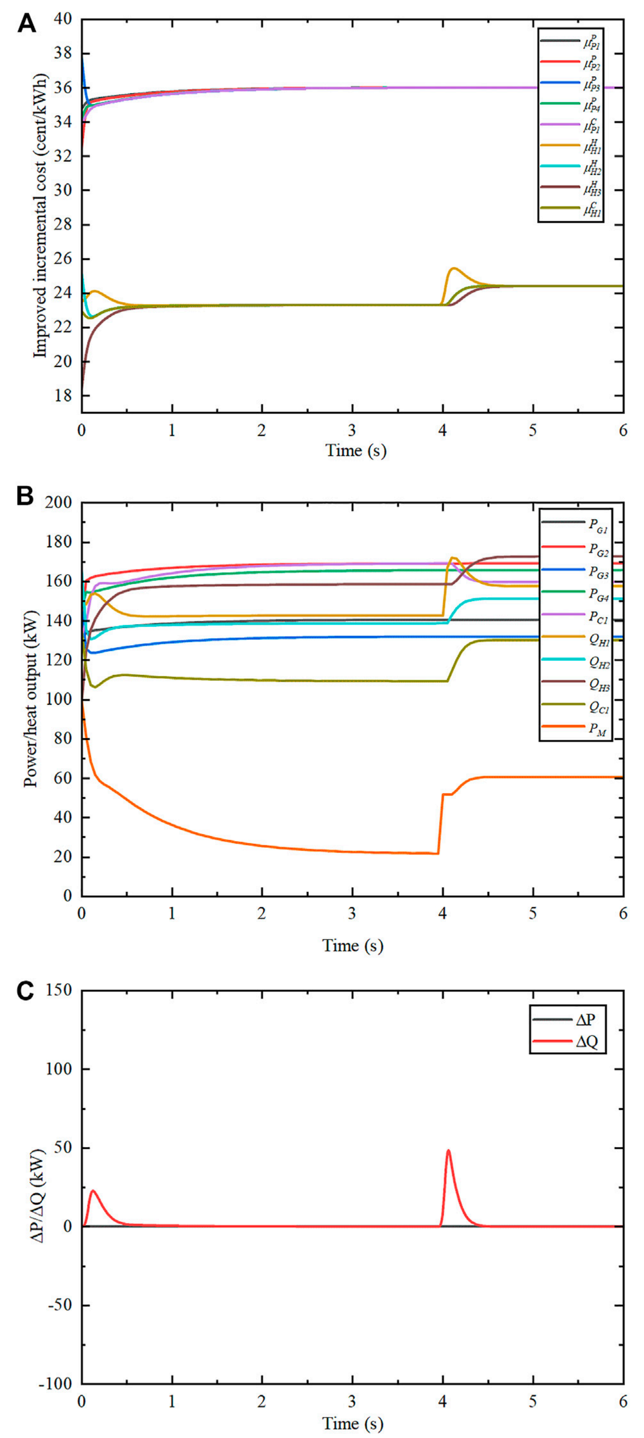

FIGURE 6 | Algorithm results in grid-connected operation mode. **(A)** Improved incremental cost. **(B)** Power output of each unit. **(C)** Electrical and thermal power mismatch.

$Q_{C_1} = 130kW$. First, we verify the effectiveness and convergence speed of algorithms in **Eqs. 43**, **44**. As shown in **Figure 4**, the electric and thermal outputs converge to their initial state averages of $\bar{P} = 100kW$ and $\bar{Q} = 137.5kW$ after several steps of iteration. This demonstrates that the algorithm can accurately estimate the total electric and thermal outputs of the whole system in a distributed manner.

After that, the effectiveness of the proposed finite-time double-consensus algorithm is verified. The operation results are shown in **Figure 5**. **Figure 5A** shows the iterative process of improved incremental cost. **Figure 5B** and **Figure 5C** show the corresponding output and power mismatch of each unit, respectively. As can be obtained from the figures, the power and thermal improved incremental cost converge to the optimal values of 31.0 cent/kWh and 22.91 cent/kWh at $t = 1.2s$, and the output of each unit is $P_{G_1} = 100.19kW$, $P_{G_2} = 126.02kW$, $P_{G_3} = 92.29kW$, $P_{G_4} = 112.53kW$, $P_{C_1} = 94.85kW$, $Q_{H_1} = 137.42kW$, $Q_{H_2} = 134.24kW$, $Q_{H_3} = 153.49kW$, $Q_{C_1} = 145.02kW$. The power mismatch of the system is 0. At $t = 2s$, P_L and Q_L change to 600kW and 480kW. After recalculation, the power and heat improved incremental costs converge to the new optimal values. At $t = 4s$ P_L and Q_L change to 520kW and 620kW, the algorithm can converge to the new optimal value again. When the load demand changes and the algorithm is activated for regulation, the power mismatch of the system fluctuates briefly and finally converges to 0. The system achieves power balance and economic optimum.

5.2.2 Analysis of Effectiveness in Grid-Connected Operation Mode

The system is set in grid-connected operation mode. The distribution network electricity price μ_0 is set to 36 cent/kWh, and the total electric power demand P_L and total thermal power demand Q_L are 760kW and 530kW. The algorithm operation results are shown in **Figure 6**. According to the findings in Section 3.2, when the IES is operated in grid-connected mode, its power improved incremental cost should converge to the distribution network electricity price. The output of each unit is shown in **Figure 6B** as $P_{G_1} = 140.43kW$, $P_{G_2} = 169.05kW$, $P_{G_3} = 131.89kW$, $P_{G_4} = 165.61kW$, $P_{C_1} = 169.08kW$, $Q_{H_1} = 142.72kW$, $Q_{H_2} = 139.71kW$, $Q_{H_3} = 158.55kW$, $Q_{C_1} = 109.28kW$, in addition to the electric power from the distribution network $P_M = 21.78kW$. At $t = 4s$, P_L and Q_L change to 790kW and 590kW, while μ_P remains constant at the convergence value of 36 cent/kWh, and the output of the PGUs remains unchanged. The variation of the electric power obtained from the distribution network is $P_M = 60.53kW$. When the algorithm starts, the thermal power deviation fluctuates and gradually converges to 0, but the electric power mismatch is always 0. This is because the electric power mismatch is always compensated by the distribution network in the grid-connected mode.

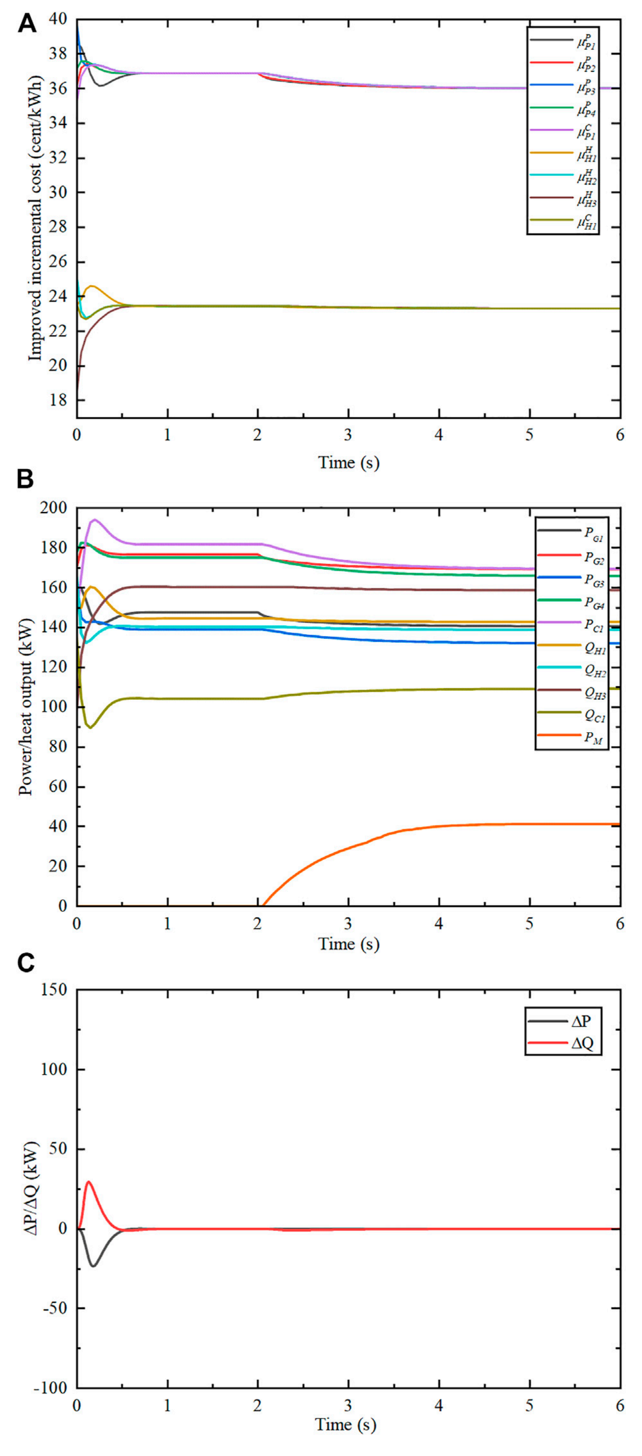

FIGURE 7 | Algorithm results when operation mode switching. **(A)** Improved incremental cost. **(B)** Power output of each unit. **(C)** Electrical and thermal power mismatch.

5.2.3 Operational State Switching Verification

This subsection will focus on testing whether the proposed algorithm can perform free switching between the two operation modes to cope with sudden distribution network faults and reconnection after fault repair. At the initial moment, the system is set in islanded mode with total electrical power demand P_L and total thermal power demand Q_L of 780 and 530 kW. The algorithm results are

TABLE 2 | Comparison of algorithms proposed in related literature.

	This Article	Zaery et al. (2020)	Pu et al. (2017)	Chen and Li, (2021)
Finite-time convergence	√	√	—	—
No centralized control center	√	√	—	√
Satisfy the equality constraint	√	—	√	√
Expanding to IES	√	—	—	—
Consider two modes of operation	√	—	—	√

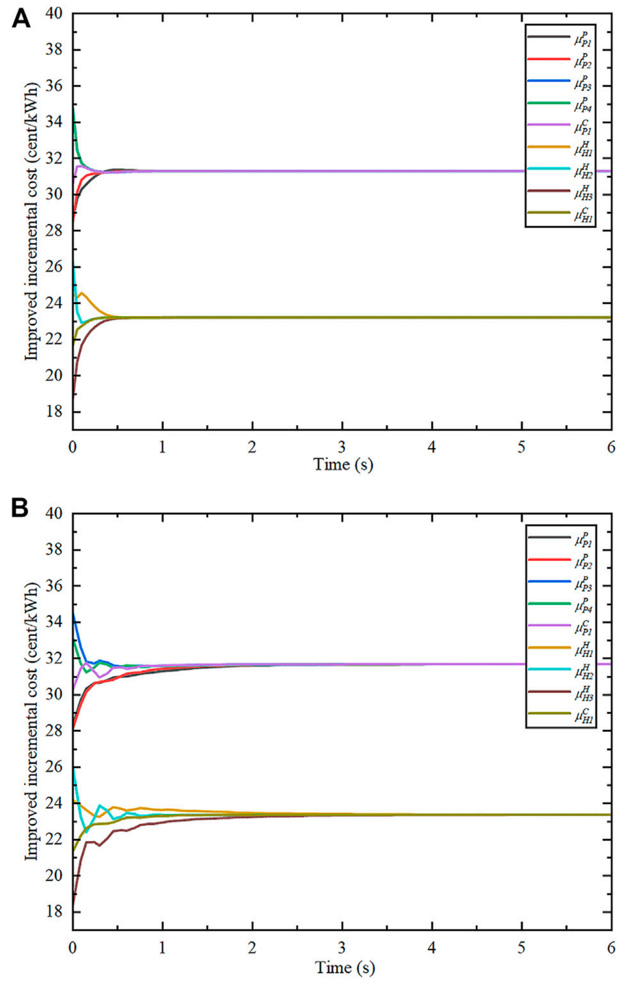

FIGURE 8 | Comparison of the convergence speed of the two algorithms. **(A)** The algorithm proposed in this paper. **(B)** The algorithm proposed in (Chen and Li, 2021).

shown in **Figure 7**. The system operates in islanded mode, so the power exchanged with the distribution network is 0.

At $t = 2s$, the distribution network is reconnected, and the system switches to grid-connected mode to continue operation. μ_P is regulated and finally converges to 36 cent/kWh, and the electrical output is updated to $P_{G_1} = 140.51kW$, $P_{G_2} = 169.15kW$, $P_{G_3} = 132.02kW$, $P_{G_4} = 165.77kW$, and $P_{C_1} = 169.30kW$, while the power to be obtained from the distribution network $P_M = 41.11kW$. Since the total electrical and thermal power demand of the system is the same as before, the value of μ_H and the heat output of each unit remain essentially unchanged. As can be obtained in **Figure 7C**, the deviation of the electric power caused by the change of the improved incremental cost is compensated on the power provided by the distribution network when the operation mode is switched. The deviation of the thermal power only shows small fluctuations and recovers quickly. This proves that the algorithm is still effective when the operation state of the system is switched and does not cause large fluctuations of the power deviation. The proposed algorithm has a "plug-and-play" feature.

5.2.4 Comparison Analysis With Other Algorithms

Finally, the algorithm proposed in this paper is compared with those in other existing papers in the same simulation scenario. **Table 2** shows the comparative analysis with the three algorithms in three existing papers. All three papers also solve the EDP by the incremental cost iterative method. The advantages of the algorithm proposed in this paper is shown in **Table 2**. In addition, **Figure 8** shows the convergence speed of this paper compared with the algorithm proposed in (Chen and Li, 2021) in solving the EDP of the same system. With the same parameters and initial values of each agent, the proposed algorithm converges at about $t = 1s$, while the algorithm in (Chen and Li, 2021) takes about $t = 3s$ to converge. The algorithm proposed in this paper tends to have a faster convergence rate than the algorithm in (Chen and Li, 2021).

6 CONCLUSION

In this article, a distributed algorithm is proposed for solving the EDP of IES, which can obtain the optimal solution in a finite time and can switch smoothly between two operation modes. Firstly, the ED model is developed for IES under two operation modes considering transmission losses. Then, a finite-time double-consensus algorithm is proposed to solve the coupling problem among multiple energies and achieve the economic optimum of the system in finite time. Finally, a simulation study is conducted for the case. Several experiments indicate that the proposed algorithm is effective in two operation modes and has the advantage of fast convergence. The research is essential to enhance economic efficiency and improve the energy utilization of IES.

In the upcoming research work, based on the results obtained from the above studies, the energy types of IES, such as gas and cold, can be further expanded. In addition, communication delay and cyber-attacks need to be considered when designing control strategies to enhance their robustness.

DATA AVAILABILITY STATEMENT

The original contributions presented in the study are included in the article/supplementary material, further inquiries can be directed to the corresponding author.

REFERENCES

Bai, L., Ye, M., Sun, C., and Hu, G. (2019). Distributed Economic Dispatch Control via Saddle Point Dynamics and Consensus Algorithms. *IEEE Trans. Contr. Syst. Technol.* 27 (2), 898–905. doi:10.1109/TCST.2017.2776222

Binetti, G., Davoudi, A., Lewis, F. L., Naso, D., and Turchiano, B. (2014). Distributed Consensus-Based Economic Dispatch with Transmission Losses. *IEEE Trans. Power Syst.* 29 (4), 1711–1720. doi:10.1109/TPWRS.2014.229-943610.1109/tpwrs.2014.2299436

Chen, G., Ren, J., and Feng, E. N. (2017). Distributed Finite-Time Economic Dispatch of a Network of Energy Resources. *IEEE Trans. Smart Grid* 8 (2), 822–832. doi:10.1109/TSG.2016.2516017

Chen, G., and Yang, Q. (2018). An ADMM-Based Distributed Algorithm for Economic Dispatch in Islanded Microgrids. *IEEE Trans. Ind. Inf.* 14 (9), 3892–3903. doi:10.1109/TII.2017.2785366

Chen, J., and Sayed, A. H. (2012). Diffusion Adaptation Strategies for Distributed Optimization and Learning over Networks. *IEEE Trans. Signal Process.* 60 (8), 4289–4305. doi:10.1109/TSP.2012.2198470

Chen, W., and Li, T. (2021). Distributed Economic Dispatch for Energy Internet Based on Multiagent Consensus Control. *IEEE Trans. Autom. Contr.* 66 (1), 137–152. doi:10.1109/TAC.2020.2979749

Chen, Y., Li, C., Qi, D., Li, Z., Wang, Z., and Zhang, J. (2022). Distributed Event-Triggered Secondary Control for Islanded Microgrids with Proper Trigger Condition Checking Period. *IEEE Trans. Smart Grid* 13 (2), 837–848. doi:10.1109/TSG.2021.3115180

Guo, F., Wen, C., Mao, J., and Song, Y.-D. (2016). Distributed Economic Dispatch for Smart Grids with Random Wind Power. *IEEE Trans. Smart Grid* 7 (3), 1572–1583. doi:10.1109/TSG.2015.2434831

Hong, J., Hui, H., Zhang, H., Dai, N., and Song, Y. (2022). Distributed Control of Large-Scale Inverter Air Conditioners for Providing Operating Reserve Based on Consensus with Nonlinear Protocol. *IEEE Internet Things J.*, 1. doi:10.1109/JIOT.2022.3151817

Huang, B., Li, Y., Zhan, F., Sun, Q., and Zhang, H. (2022). A Distributed Robust Economic Dispatch Strategy for Integrated Energy System Considering Cyber-Attacks. *IEEE Trans. Ind. Inf.* 18 (2), 880–890. doi:10.1109/TII.2021.3077509

Huang, B., Liu, L., Zhang, H., Li, Y., and Sun, Q. (2019). Distributed Optimal Economic Dispatch for Microgrids Considering Communication Delays. *IEEE Trans. Syst. Man. Cybern. Syst.* 49 (8), 1634–1642. doi:10.1109/TSMC.2019.2900722

Huang, X., Yang, B., Yu, F., Pan, J., Xu, Q., and Xu, W. (2021). Optimal Dispatch of Multi-Energy Integrated Micro-energy Grid: A Model Predictive Control Method. *Front. Energy Res.* 9, 766012. doi:10.3389/fenrg.2021.766012

Kibangou, A. Y. (2012). "Graph Laplacian Based Matrix Design for Finite-Time Distributed Average Consensus," in Proceedings of the American Control Conference (ACC), Montreal, QC, Canada, 27-29 June 2012, 1901–1906. doi:10.1109/ACC.2012.6315398

Li, P., Zhang, F., Ma, X., Yao, S., Zhong, Z., Yang, P., et al. (2021). Multi-Time Scale Economic Optimization Dispatch of the Park Integrated Energy System. *Front. Energy Res.* 9, 743619. doi:10.3389/fenrg.2021.743619

Li, Y., Gao, D. W., Gao, W., Zhang, H., and Zhou, J. (2020). Double-Mode Energy Management for Multi-Energy System via Distributed Dynamic Event-Triggered Newton-Raphson Algorithm. *IEEE Trans. Smart Grid* 11 (6), 5339–5356. doi:10.1109/TSG.2020.3005179

Li, Y., Zhang, H., Liang, X., and Huang, B. (2019). Event-Triggered-Based Distributed Cooperative Energy Management for Multienergy Systems. *IEEE Trans. Ind. Inf.* 15 (4), 2008–2022. doi:10.1109/TII.2018.2862436

Lin, L., Guan, X., Peng, Y., Wang, N., Maharjan, S., and Ohtsuki, T. (2020). Deep Reinforcement Learning for Economic Dispatch of Virtual Power Plant in Internet of Energy. *IEEE Internet Things J.* 7 (7), 6288–6301. doi:10.1109/JIOT.2020.2966232

Liu, F., Bie, Z., and Wang, X. (2019). Day-Ahead Dispatch of Integrated Electricity and Natural Gas System Considering Reserve Scheduling and Renewable Uncertainties. *IEEE Trans. Sustain. Energy* 10 (2), 646–658. doi:10.1109/TSTE.2018.2843121

Liu, X., Wu, J., Jenkins, N., and Bagdanavicius, A. (2016). Combined Analysis of Electricity and Heat Networks. *Appl. Energy* 162, 1238–1250. doi:10.1016/j.apenergy.2015.01.102

Lu, S., Gu, W., Meng, K., and Dong, Z. (2021). Economic Dispatch of Integrated Energy Systems with Robust Thermal Comfort Management. *IEEE Trans. Sustain. Energy* 12 (1), 222–233. doi:10.1109/TSTE.2020.2989793

Pu, T., Liu, W., Chen, N., Wang, X., and Dong, L. (2017). Distributed Optimal Dispatching of Active Distribution Network Based on Consensus Algorithm. *Proc. CSEE* 37 (6), 1579–1590. doi:10.13334/j.0258-8013.pcsee.160937

Qin, Y., Wu, L., Zheng, J., Li, M., Jing, Z., Wu, Q. H., et al. (2020). Optimal Operation of Integrated Energy Systems Subject to the Coupled Demand Constraints of Electricity and Natural Gas. *Csee Jpes* 6 (2), 444–457. doi:10.17775/CSEEJPES.2018.00640

Shen, F., Ju, P., Shahidehpour, M., Li, Z., Wang, C., and Shi, X. (2020). Singular Perturbation for the Dynamic Modeling of Integrated Energy Systems. *IEEE Trans. Power Syst.* 35 (3), 1718–1728. doi:10.1109/TPWRS.2019.2-95367210.1109/tpwrs.2019.2953672

Soroudi, A. (2017). *Power System Optimization Modeling in GAMS*. Cham: Springer.

Sun, Q., Fan, R., Li, Y., Huang, B., and Ma, D. (2019). A Distributed Double-Consensus Algorithm for Residential We-Energy. *IEEE Trans. Ind. Inf.* 15 (8), 4830–4842. doi:10.1109/TII.2019.2921431

Sun, Y., Wu, X., Wang, J., Hou, D., and Wang, S. (2021). Power Compensation of Network Losses in a Microgrid with BESS by Distributed Consensus Algorithm. *IEEE Trans. Syst. Man. Cybern. Syst.* 51 (4), 2091–2100. doi:10.1109/TSMC.2020.2968605

Wang, L., and Xiao, F. (2010). Finite-Time Consensus Problems for Networks of Dynamic Agents. *IEEE Trans. Autom. Contr.* 55 (4), 950–955. doi:10.1109/TAC.2010.2041610

Xu, Y., Zhang, W., and Liu, W. (2015). Distributed Dynamic Programming-Based Approach for Economic Dispatch in Smart Grids. *IEEE Trans. Ind. Inf.* 11 (1), 166–175. doi:10.1109/TII.2014.2378691

Yan, Y., Chen, Z., Varadharajan, V., Hossain, M. J., and Town, G. E. (2021). Distributed Consensus-Based Economic Dispatch in Power Grids Using the Paillier Cryptosystem. *IEEE Trans. Smart Grid* 12 (4), 3493–3502. doi:10.1109/TSG.2021.3063712

Yang, J., and Su, C. (2021). Robust Optimization of Microgrid Based on Renewable Distributed Power Generation and Load Demand Uncertainty. *Energy* 223, 120043. doi:10.1016/j.energy.2021.120043

AUTHOR CONTRIBUTIONS

Both JY and JD contributed to designing the study, performing the research, analyzing the data, and writing the paper.

FUNDING

This work was supported in part by National Key R&D Program of China under Grant 2018YFA0702200 and in part by National Natural Science Foundation of China under Grant 61773099.

Yang, Z., Xiang, J., and Li, Y. (2017). Distributed Consensus Based Supply-Demand Balance Algorithm for Economic Dispatch Problem in a Smart Grid with Switching Graph. *IEEE Trans. Ind. Electron.* 64 (2), 1600–1610. doi:10.1109/TIE.2016.2615037

Yao, S., Gu, W., Lu, S., Zhou, S., Wu, Z., Pan, G., et al. (2021). Dynamic Optimal Energy Flow in the Heat and Electricity Integrated Energy System. *IEEE Trans. Sustain. Energy* 12 (1), 179–190. doi:10.1109/TSTE.2020.298-868210.1109/tste.2020.2988682

Yu, J., Li, Z., Guo, Y., and Sun, H. (2019). Decentralized Chance-Constrained Economic Dispatch for Integrated Transmission-District Energy Systems. *IEEE Trans. Smart Grid* 10 (6), 6724–6734. doi:10.1109/TSG.2019.2910757

Zaery, M., Wang, P., Huang, R., Wang, W., and Xu, D. (2020). Distributed Economic Dispatch for Islanded DC Microgrids Based on Finite-Time Consensus Protocol. *IEEE Access* 8, 192457–192468. doi:10.1109/access.2020.3032641

Zhang, H., Lewis, F. L., and Qu, Z. (2012). Lyapunov, Adaptive, and Optimal Design Techniques for Cooperative Systems on Directed Communication Graphs. *IEEE Trans. Ind. Electron.* 59 (7), 3026–3041. doi:10.1109/TIE.2011.2160140

Zhong, H., Yan, X., and Tan, Z. (2021). Real-Time Distributed Economic Dispatch Adapted to General Convex Cost Functions: A Secant Approximation-Based Method. *IEEE Trans. Smart Grid* 12 (3), 2089–2101. doi:10.1109/TSG.2020.3049054

Conflict of Interest: The authors declare that the research was conducted in the absence of any commercial or financial relationships that could be construed as a potential conflict of interest.

frontiers | Frontiers in Energy Research

ORIGINAL RESEARCH
published: 13 June 2022
doi: 10.3389/fenrg.2022.913893

Robust Strong Structural Controllability of Complex Power Systems

Yunhe Sun, Dongsheng Yang, Xiaoting Gao and Jia Qin*

College of Information Science and Engineering, Northeastern University, Shenyang, China

Ensuring the control of power systems is crucial for their safe operation. This paper analyses the robust controllability of complex power systems from the structural sighta structural point of view. Stressing the dominant role of generators in the control of power systems, we propose three kinds of controllable networks by generator nodes. Additionally, the satisfied conditions and the relevant proof of zero forcing set in the controllable networks by generator nodes and extra nodes are given. Besides, tThe satisfied conditions and the relevant proofs of the largest set of removable edges that have no -effect on the strong structural controllability in three kinds of controllable networks by generator nodes are also proposed. Finally, the robustness of strong structural controllability of IEEE 39 bus system and IEEE 14 bus system have been analyzed. The zero-forcing set and the largest set of removable edges of IEEE 39 bus system and IEEE 14 bus system are provided.

Keywords: strong structural controllability, robustness, power system, generator control, network modeling

Edited by:
Wei Hu,
Zhejiang University, China

Reviewed by:
Nannan Rong,
Tianjin Polytechnic University, China
Xiao Feng,
University of Southampton, United Kingdom

****Correspondence:***
Dongsheng Yang
yangdongsheng@mail.neu.edu.cn

Specialty section:
This article was submitted to Smart Grids,
a section of the journal Frontiers in Energy Research

Received: *06 April 2022*
Accepted: *20 April 2022*
Published: *13 June 2022*

Citation:
Sun Y, Yang D, Gao X and Qin J (2022) Robust Strong Structural Controllability of Complex Power Systems.
Front. Energy Res. 10:913893.
doi: 10.3389/fenrg.2022.913893

1 INTRODUCTION

With the development of economy and society, the scale of power systems grows rapidlyZhang et al. (2019), ensuring the safe and stable power transmission has thus become a hot research issue Kiaei et al. (2021). There is a growing demand for power systems with high robustness, that is, they can withstand large disturbances, such as transmission line damage, accidental loss of large generators, or heavy load loss Mahmud et al. (2017). Many researches on the control of power systems at the device level have been proposed, such as braking resistor Rubaai et al. (2005), fast valving of turbines Hassan et al. (1999), utilizing reactor and capacitor units Taylor and Leuven (1996), flexible ac transmission system devices Haque (2004), power system stabilizers Chung et al. (2002), and energy storage systems Kiaei et al. (2021). In addition, as the power system as is a special complex network, complex network theory is also an important tool to study its controllability Chu and lu (2017). The controllability analysis of power systems has the question that capturing the time-dependent interactions between the components, which is difficult. Fortunately, the controllability study is based on the complex network theory regardless of the coupling strength between the components.

In complex networks, structural controllability (weak structural controllability) and strong structural controllability are two basic directions of network controllability analysis. The week structural controllability was first proposed by Lin (1974), that means almost all networks of the identical topology have the same controllability. Nevertheless, the dependencies between system parameters in actual networks leads to networks being uncontrollable, although it is weekly structurally controllable. Thus, the notion of strong structural controllability was proposed by Mayeda and Yamada (1979). The network is strong structurally controllable if all admissible numerical realizations of its coupling matrix and control input matrix are controllable. Bowden et al. (2012) extended the strong structural controllability to multiple entry systems. Whereafter, the strong structural controllability were further investigated by constrained matchings Chapman and Mesbahi (2013) and cycle families Jarczyk et al. (2011).

Group (2008) was first proposed the concept of zero-forcing set (ZFS) to investigate the minimum rank problem for symmetric patterned matrices, which is connected with a particular coloring of nodes in a graph. Then, zero forcing set was extended to directed graphs by Barioli et al. (2009). Furthermore, Monshizadeh et al. (2014) has shown the correspondence between zero-forcing sets and the strong structural controllability by the view of a network-centric point. Subsequently, ZFS was widely used in the analysis of strong structural controllability of undirected networks Mousavi and Mesbahi (2018), networks with missing connection information, Jia et al. (2021) and other networks.

When complex network theory is applied to a power system, the accuracy of analysis will be affected by oversimplification of the influence of electrical characteristics Hines et al. (2010), but too much consideration of electrical characteristics will greatly increase the computational complexity. Therefore, the reasonable combination of structural characteristics and electrical characteristics is still an unsolved problem. Li et al. (2015) investigated the weak structural controllability of power systems. The minimum input theorem was used to find the drive node set that makes the network weakly structurally controllable in an unweighted directed model. However, the absent of electrical characteristics makes the research results deviate from the actual situation. Yang et al. (2020) established a directed network model that can reflect the intrinsic direction of the power system for weak structural controllability analysis. The edge weighs were considered in the search method of maximum weak controllable scope. Nevertheless, this work didn't did not consider the different functions of different nodes in control. In particular, the special status of generator nodes is was ignored. In the modern power industry, the control of generators can realize active power control and frequency response, voltage/reactive power control, and ride-through for both voltage and frequency Hatziargyriou et al. (2021). Thus, generator nodes play a dominant role in the control of power systems.

Based on the above research gaps, the main contributions of this paper are as follows:

1. Considering the dominant role of generators in the control of power systems, precisely controllable networks by generator nodes, redundantly controllable networks by generator nodes, and controllable networks by generator nodes, and extra nodes are defined.
2. The satisfied conditions and the relevant proof of zero-forcing set in the controllable networks by generator nodes and extra nodes are given.
3. The satisfied conditions and the relevant proofs of the largest set of removable edges in three kinds of controllable networks by generator nodes are given.

The remains of this paper are organized as follows: **Section 2** introduces the network modeling method of power systems. **Section 3** analyzses the strong structural controllability of power systems. **Section 4** analyzses the robustness of controllable networks by generator nodes. **Section 5** concludes the paper with discussions.

2 NETWORK MODELLING OF POWER SYSTEMS

In this paper, the power system is abstracted as a digraph. Network modeling is the critical prerequisite of structural controllability analysis. The accuracy of structural controllability analysis is closely related to the described natures of power systems in a network model. We assume that the construction structure of power systems and the configuration of generators and loads are known correctly.

2.1 Basic Model Topology Principles

The dynamic characteristics of power systems are so tanglesome entangled that a generic dynamical equation that describes them all is out of the question. Prosperously, the controllability of nonlinear system and its linearized dynamics is are often structurally similar. The power system is described as a digraph $D(V,E)$ with nodes and edges, $V=\{v_1,\ldots,v_N\}$ is the node set, and the $E=\{(v_i,v_j),v_i,v_j\in V\}$ is the edge set, N is the scale of networks. According to Ohm's law, a power system with scale N can be writed written as linear equations, as follows:

$$\begin{bmatrix} U_1 \\ U_2 \\ \vdots \\ U_N \end{bmatrix} = \begin{bmatrix} Z_{11} & Z_{12} & \cdots & Z_{1N} \\ Z_{21} & Z_{22} & \cdots & Z_{2N} \\ \vdots & \vdots & \ddots & \vdots \\ Z_{N1} & Z_{N2} & \cdots & Z_{NN} \end{bmatrix} \begin{bmatrix} I_1 \\ I_2 \\ \vdots \\ I_N \end{bmatrix} \tag{1}$$

where Z_{ij} is the impedance of transmission lines. If there is a transmission line from node v_i to node v_j, then $Z_{ij}=Z_{ji}\neq 0$ or else $Z_{ij}=Z_{ji}=0$. U_i is the voltage of bus, and I_i is the injection current of bus.

The basic topology of the network model is constructed based on the transmission line architecture of power systems. Topology principles in this paper are described as follows.

- The buses of power plants, substations, and loads are abstracted to nodes. The node set is classified into generator node set V_G, transmission node set V_T, and load node set V_L.
- The high voltage transmission lines are abstracted as edges, only the lines whose voltage above 110 KV are considered.
- Parallel transmission lines on the same tower and neglecting shunt capacitor lines are merged to prevent multiple edges in the basic topology model and generate a simple topology model.
- The influences of the relay protection devices and the stability control devices in power systems are not under consideration.

2.2 Definition of Edge Direction

The direction of power flowing was defined as the direction of edges in the network model in some literatures Liu et al. (2018); Dey et al. (2016). However, the direction of power flowing is time-variant, which and only describes the direction of edges in power systems at a certain time. The network model proposed in this paper wants to have an edge direction which can express the intrinsic properties of power systems. Therefore, the author's previous definition of edge direction in a network model of a power system Yang et al. (2020) is used again in this paper, where the direction of an edge is determined by its electrical betweenness.

In graph theory, the betweenness of edges is an important global geometric quantity that reflects the influence of edges in the whole network Freeman (1978). Betweenness of an edge is defined as the portion of the number of shortest paths between all nodes pairs that pass through the edges divided by the number of shortest paths between all node pairs. However, the power is transmitted in complex power systems in accordance with electrical characteristics. The power from node v_i to node v_j flows through every edges in complex power systems. Thus, betweenness in graph theory is unfit for evaluating edges in power systems.

Electrical betweenness of edges is an evaluation index Wang et al. (2011) that, which is related to the network structure and the configuration of generators and loads.

If there is a unit current supplied from the generator node v_i to the load node $v_j (I_i = 1, I_j = -1)$, the voltage of node v_k can be writed as

$$U_k = Z_{ki} - Z_{kj}, \tag{2}$$

The electrical betweenness of edge (v_m, v_n) is the sum of the currents flowing through the edge for all node pairs of generator and load that have unit current transmitted in complex power systems. Then, the electrical betweenness of edge (v_m, v_n) is depicted as follows.

$$B_e(m,n) = \sum_{V_{i \in V_G}, V_{j \in V_L}} \sqrt{W_i W_j} I_{mn}(i,j) \tag{3}$$

W_i is the capacity of generator node v_i, and W_j is the maximal demand of load node v_j. $I_{mn}(i,j)$ is the generated current in the edge (v_m, v_n) when an unit current is supplied from the generator node v_i to the load node v_j. $\sqrt{W_i W_j}$ is the weight coefficient of $I_{mn}(i,j)$.

Assuming that the admittance of edge (v_m, v_n) is y_{mn}, $I_{mn}(i,j)$ can be obtained

$$\begin{aligned} I_{mn}(i,j) &= y_{mn}\left(U_m - U_n\right) \\ &= y_{mn}\left[\left(Z_{mi} - Z_{mj}\right) - \left(Z_{ni} - Z_{nj}\right)\right], \end{aligned} \tag{4}$$

where y_{mn} is admittance.

The electrical betweenness matrix of edges is isomorphic with the impedance matrix, which is an antisymmetric matrix with $B_e(m,n) = -B_e(m,n)^T$. The electrical betweenness matrix is rewrited as:

$$B_e(m,n) = \begin{cases} B_e(m,n) & B_e(m,n) > 0 \\ 0 & B_e(m,n) < 0 \end{cases} \tag{5}$$

The edge direction in the network model: If $B_e(m,n) > 0$, there is an edge from node v_m to node v_n in the network model.

3 STRONG STRUCTURAL CONTROLLABITY OF POWER SYSTEMS

3.1 Weak Structural Controllability and Strong Structural Controllabity

Consider the linear-time-invariant system:

$$\dot{\mathbf{x}}(t) = \mathbf{A}\mathbf{x}(t) + \mathbf{B}\mathbf{u}(t) \tag{6}$$

where $\mathbf{x} = (x_1, \ldots, x_N)^T$ is the node states vector; N is the scale of the system; $\mathbf{A} = \left[a_{ij}\right] \in R^{N\times N}$ is the coupling matrix between nodes; a_{ij} describes the strength of coupling between nodes; $\mathbf{u} = (u_1, u_2, \ldots, u_m)^T$ describes the states of m controllers; and $\mathbf{B} \in R^{N\times m}$ is the control input matrix.

A system is controllable if it can be moves from its initial state x_0 to any desired final state within a limited time. Due to many models of physical and technical systems are being structured, dynamics of nonlinear-time-invariant system is often linear-time-invariant.

Then, let $\overline{\mathbf{A}} = \left[\overline{a_{ij}}\right] \in \{0, *\}_{N\times N}$ denotes the structure pattern of $\mathbf{A}$, and $\overline{\mathbf{B}} \in \{0, *\}^{N\times m}$ represents the structure pattern of $\mathbf{B}$; the element in matrix $\overline{\mathbf{A}}$ or $\overline{\mathbf{B}}$ is equal to zero if the corresponding element in matrix $\mathbf{A}$ or $\mathbf{B}$ is equal to zero, and the other value otherwise.

Based on the network model of power systems in **section 2**, the structure pattern of a power system coupling matrix can be experessed as:

$$\overline{a_{ij}} = \begin{cases} * & B_e(m,n) > 0 \\ 0 & B_e(m,n) = 0 \end{cases} \tag{7}$$

The system $(\overline{A}, \overline{B})$ is *weak structurally controllable*, which means that the admissible numerical realization (A, B) is existed in $A \in \overline{A}$ and $B \in \overline{B}$. The weak structural controllability is such a generic property that almost all systems of the same structure have identical controllability properties. However, the physical dependencies between system parameters in actual systems leads to systems being uncontrollable although it is weekly structurally controllable. Thus, the concept of strong structural controllability was introduced. In this paper, the strong structural controllability of power systems is mainly considered.

The system $(\overline{A}, \overline{B})$ is *strong structurally controllable* if the admissible numerical realization (A, B) is controllable for all $A \in \overline{A}$ and $B \in \overline{B}$.

Theorem 1 Trentelman et al. (2012): A class of systems defined by the structure matrices $\overline{A}$ and $\overline{B}$ is said to be strong structural controllable if $rank(A-\lambda IB)=n$ for all admissible numerical realizations $A \in \overline{A}$, $B \in \overline{B}$, and all eigenvalue $\lambda_i, i=1,\ldots,n$ of A.

Graph theory is also the main direction of analyzing strong structural controllability. Concepts mentioned in this paper are introduced in the following passage, *strong structurally controllable* is reduced to *controllable*.

Out-neighbor: If $(v_m, v_n) \in E$, then node v_n is the out-neighbor of node v_m. In **Figure 1A**, v_4 is the out-neighbor of v_2.

Color change rule: There are white nodes and black nodes in a directed graph $D(V,E)$. If a black node $v_m \in V$ has only out-neighbor $v_n \in V$, it forces v_n to be black. In **Figures 1A,B**, v_1 force v_3 to be black and v_2 force v_4 to be black.

Forcing process: The color change process that repeaterepeats the color change rule until no more color changes is called a forcing process. **Figures 1A–D** is a forcing process. In the first step, v_1 forces v_3 to be black and v_2 forces v_4 to be black. In the second step, v_3 forces v_5 to be black. In the final step, v_5 forces v_6 to be black.

Drive node set: let $V_D \subset V$ is the set of initially black nodes in V, then V_D is drive node set. In **Figure 1A**, drive node set is $V_D = \{v_1, v_2\}$.

Controllable node set: The set of final black nodes after the forcing process is called the controllable node set $V_C(V_D)$ of drive node set V_D. In **Figure 1**, controllable node set of $V_D = \{v_1, v_2\}$ is $V_C(V_D) = \{v_1, v_2, v_3, v_4, v_5, v_6\}$.

Zero forcing set (ZFS): If $V_C(V_D) = V$, then V_D is a zero-forcing set (ZFS). In **Figure 1**, drive node set $V_D = \{v_1, v_2\}$ is a zero-forcing set.

Theorem 2 Monshizadeh et al. (2014): A network system with dynamics 6) is strong structural controllable if and only if $V_D \subset V$ is a zero-forcing set of the structure described digraph $D(V,E)$ of system 6).

3.2 Drive Node set in Power Systems

3.2.1 Controllable Networks by Generator Nodes

The energy flow along the transmission line of a power system changes in real time. The system coupling matrixs of power systems have innumerable numerical implementationswith the same zero-nonzero pattern. Therefore, the power system with the driver nodes' configuration that realizes the weak structure control of the system is possible uncontrollable at a time. Power system is the most important social infrastructure network. It is very important to keep it under control for the safe and stable operation of power systems. Thus, the configuration of drive nodes with strong structural controllability is more in line with the control requirements of a power system.

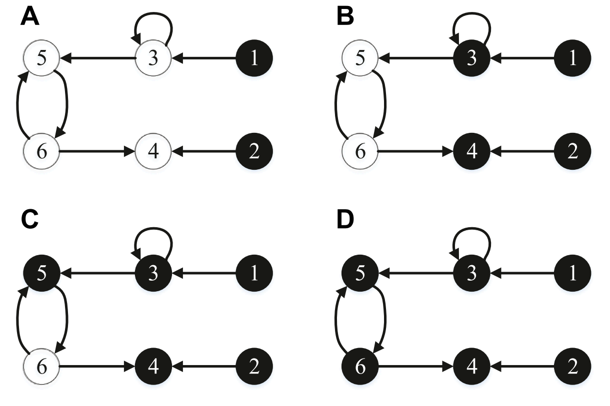

FIGURE 1 | A forcing process based on color change rule in a digraph with six nodes and seven edges. **(A)** A graph with drive node set $V_D = \{v_1, v_2\}$; **(B)** v_1 force v_3 to be black and v_2 force v_4 to be black; **(C)** v_3 force v_5 to be black; **(D)** v_5 force v_6 to be black.

Power systems areis a complex network with special physical characteristics. As shown in the previous network modeling, different nodes have different properties. Therefore, the strong structural controllability analysis of power systems should fully consider the differences between nodes.

In the modern power industry, synchronous generators are widely used in wind power generation, hydroelectric power generation, diesel power generation, and nuclear power generation. Synchronous generators play a dominant role in power systems. Synchronous generators convert part of the mechanical energy into sinusoidal AC electrical energy, while the other part is stored as kinetic energy in the huge rotating mass of the rotor. When the power system is disturbed, the rotor absorbs or releases energy to maintain the internal energy balance of the system. With the development of the power system, it has progressively become more dependent on fast response power electronic devices. The converter interfaces generation technologies can provide numerous services, such as active power control and frequency response, voltage/reactive power control, and ride-through for both voltage and frequency. In a nutshell, the generator node must be a drive node in the digraph of power systems. Then, we have $V_G \subset V_D$ in the strong structural control of power systems.

Due to the special status of generator nodes in power system control, there are three different situations of strong structural controllability of a power network, which are defined as follows.

Definition 1 (*precisely controllable networks by generator nodes*) A structure described digraph of power systems is a precisely controllable network by generator nodes if the following conditions hold:

- The generator node set in the power system happens to be a zero-forcing set ($V_C(V_G) = V$).
- All proper subsets of generator nodes are not zero-forcing sets ($V_C(V_D) \subsetneqq V$ for all $V_D \subsetneqq V_G$).

As despicted in **Figure 2A** digraph of power system with the generator node set $V_G = \{v_4, v_5\}$. Let $V_D = V_G$, then $V_c(V_D) = V$. Furthermore, if $V_D = \{v_4\}$, $V_C(V_D) = \{v_3, v_4\} \subsetneqq V$, and if $V_D = \{v_5\}$, $V_C(V_D) = \{v_2, v_5\} \subsetneqq V$. Thus, the power system in **Figure 2A** is the a precisely controllable networks by generator nodes.

Definition 2 (*redundantly controllable networks by generator nodes*) A structure described digraph of power systems is a redundantly controllable network by generator nodes if there is at least one zero-forcing set is in the proper subset of the generator node set in the power system ($\exists \text{ZFS} \subsetneqq V_G$).

As despicted in **Figures 2A,B** digraph of power system with the generator node set $V_G = \{v_4, v_5\}$. Let $V_D = \{v_5\}$, then $V_C(V_D) = V$. Thus, the power system in **Figure 2B** is the redundantly controllable networks by generator nodes.

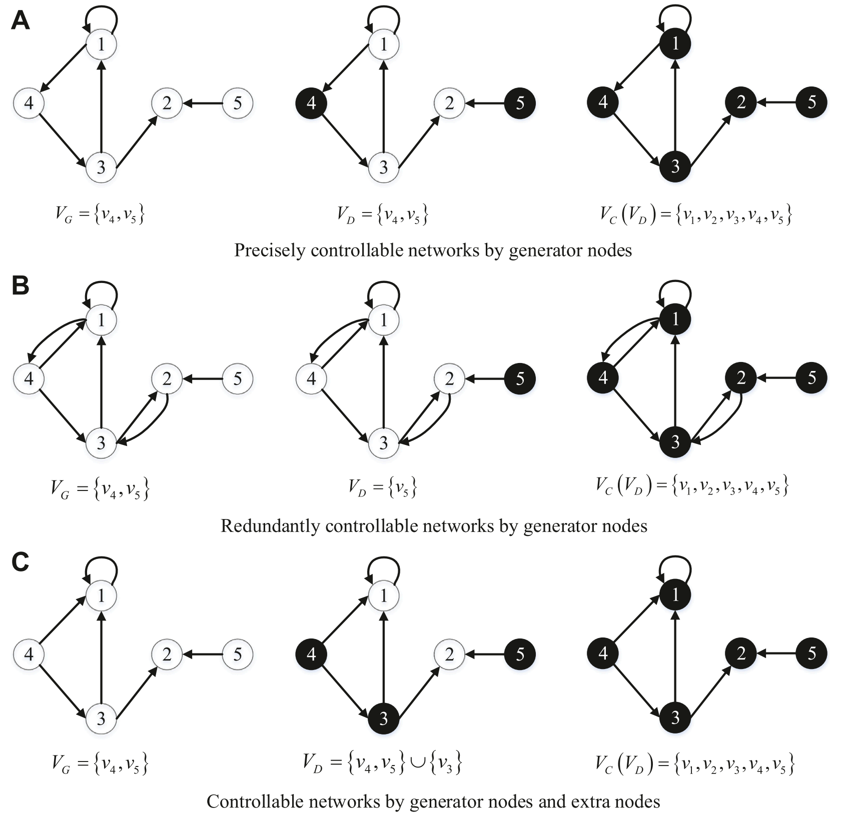

FIGURE 2 | Three kind of controllable networks by generator nodes. **(A)** Precisely controllable networks by generator nodes; **(B)** Redundantly controllable networks by generator nodes; **(C)** Controllable networks by generator nodes and extra nodes.

Definition 3 (*controllable networks by generator nodes and extra nodes*) A structure described digraph of power systems is a controllable networks by generator nodes and extra nodes if the controllable node set of generator node set is the proper subset of node set ($V_C(V_G) \subsetneq V$).

The extra nodes belong to the transmission node set V_T or the load node set V_L. In actual power systems, the substation realizes system control through load station transfer and load cutting strategies. Load nodes achieve system control through demand response.

As despicted in **Figures 2A,C** digraph of power system with the generator node set $V_G = \{v_4, v_5\}$. Let $V_D = V_G$, then $V_C(V_D) = \{v_1, v_2, v_4, v_5\} \subsetneq V$. Furthermore, when $V_D = V_G \cup \{v_4\}$, $V_C(V_D) = \{v_1, v_2, v_3, v_4, v_5\} = V$. Thus, the power system in **Figure 2C** is the controllable networks by generator nodes and extra nodes.

3.2.2 Zero-Forcing Set of Controllable Networks by Generator Nodes and Extra Nodes

In this section, we focus on the zero-forcing set of controllable networks by generator nodes and extra nodes. Because this kind of networks cannot achieve strong structural controllability through generator nodes alone, we will investigate the conditions satisfied to satisfy of extra nodes in their zero-forcing set.

Then, we will introduce some of the concepts used in the follows.

A path is a special kind of graph consists consisting of disjoint edges and nodes.

Distribution of integers on a path: let $p = (V_p, E_p)$ is be a directed path with scale N_p. Let $\alpha \geq N_p$ is be an integer. Let D_p denotes the distribution of integers from 1 to α among N_p nodes of p in a way, and every node is endowed at least one number. Besides, for $i = 1, \ldots, \alpha - 1$, two integers i and $i + 1$ are either assigned to one node, or i is given to a node and $i + 1$ is given to its out-neighbor. Thus, every node $v \in V_p$ is given a set of successive integers, denoted by $d_\alpha(v)$. For every $1 \leq \beta \leq \alpha$, let $v_\alpha(\beta, p)$ is be the node $v \in V_p$ and $\beta \in d_\alpha(v)$. Let $v_\alpha(1, p)$ be the start node of p. Furthermore, let $d_\alpha^{\max}(v) = \max\{\beta : \beta \in d_\alpha(v)\}$ and $d_\alpha^{\min}(v) = \min\{\beta : \beta \in d_\alpha(v)\}$.

For two path p_1 and p_2 with integer distribution D_{p_1} and D_{p_2}. For $v \in p_1$ and $u \in p_2$, we define $d_\alpha(v) = d_\alpha(u)$ if $d_\alpha(v) \cap d_\alpha(u) \neq \varnothing$; $d_\alpha(v) > d_\alpha(u)$ if $d_\alpha^{\min}(v) > d_\alpha^{\max}(u)$; $d_\alpha(v) \geq d_\alpha(u)$ if either $d_\alpha(v) > d_\alpha(u)$ or $d_\alpha(v) = d_\alpha(u)$; $d_\alpha(v) < d_\alpha(u)$ otherwise.

For a distinct directed path set $p = \{p_1, \ldots, p_m\}$, where $p_i = (V_{p_i}, E_{p_i})$ is a path of size N_{p_i}, $i = 1, 2, \ldots, m$. For $\alpha \geq \max(N_{p_i})$, let $D_\alpha^{\Sigma} = \{D_{p_1}, \ldots, D_{p_m}\}$ be the set of distribution of integers from 1 to α in P. Besides, the start nodes of p are the union of start nodes of p_i, $V_\alpha(\beta, P) = \cup_{i=1}^{m} v_\alpha(\beta, p_i)$.

An efficient set of distribution ED_{α}^{Σ} is a set of distribution with $\alpha = 1 - m + \sum_{i=1}^{m} N_{p_i}$, where m is the number of paths. For every $1 \le j < \alpha$, the distributions D_{p_i}, $i = 1, \ldots, m$ have exactly one node in $\cup_{i=1}^{m} V_{p_i}$ such that $d_{\alpha}^{\max}(v) = j$.

The distribution algorithm that gives every node a successive set of integers of a digraph with a zero-forcing set is depicted in **Figure 3**. As shown in **Figure 4**, a digraph $D(V,E)$ is forced by drive nodes $V_D = \{v_4, v_5\}$. After the forcing process, the distribution of integers on two paths $p_1 = \{V_{p_1}, E_{p_1}\}, p_2 = \{V_{p_2}, E_{p_2}\}$ are depicted in **Figure 4**. According to the above definition, the set of distribution $D_{\alpha}^{\Sigma} = \{D_{p_1}, D_{p_2}\}$ is an efficient set of distribution. Furthermore, all edges $(u,v) \in E - E_{p_1} - E_{p_2}$ all have $d_{\alpha}(u) \ge d_{\alpha}(v)$.

Definition 4 (*precisely controllable subnetworks by generator nodes* $D_g(V_g, E_g)$) In controllable networks by generator nodes and extra nodes $D_{V,E}$, let generator nodes be black nodes and other nodes be white. After the forcing process, the final black nodes are denoted in V_g. The edge set E_g is defined, such that $E_g = \{(v_m, v_n)(v_m, v_n) \in E \ and \ v_m, v_n \in V_g\}$. Then, the precisely controllable subnetworks by generator nodes is consist of node set V_g and edge set E_g, and V_G is a ZFS of D_g.

Theorem 3: The precisely controllable subnetworks by generator nodes $D_g(V_g, E_g)$ is consist of a set of paths $P = \{p_1, \ldots, p_{N_G}\}$ $(p_i = \{V_{p_i}, E_{p_i}\})$ with start node set V_G, which has an efficient set of distribution ED_{α}^{Σ}. Besides, the edges $(u,v) \in E_g - \cup_{i=1}^{N_G} E_{p_i}$ all have $d_{\alpha}(u) \ge d_{\alpha}(v)$. Where N_G is the number of generator nodes in V_G.

Proof: V_G with $|V_G| = N_G$ is a zero-forcing set of D_g. $P = \{p_1, \ldots, p_{N_G}\}$ is the set of paths with the maximum forcing chain of V_G with the set of distribution of successive integers $D_{\alpha}^{\Sigma} = \{D_{p_1}, \ldots, D_{p_{N_G}}\}$, which are obtained from the distribution algorithm in **Figure 3**. Furthermore, $\alpha = 1 - N_G + \sum_{i=1}^{N_G} N_{p_i}$, N_{p_i} is the number of nodes in p_i.

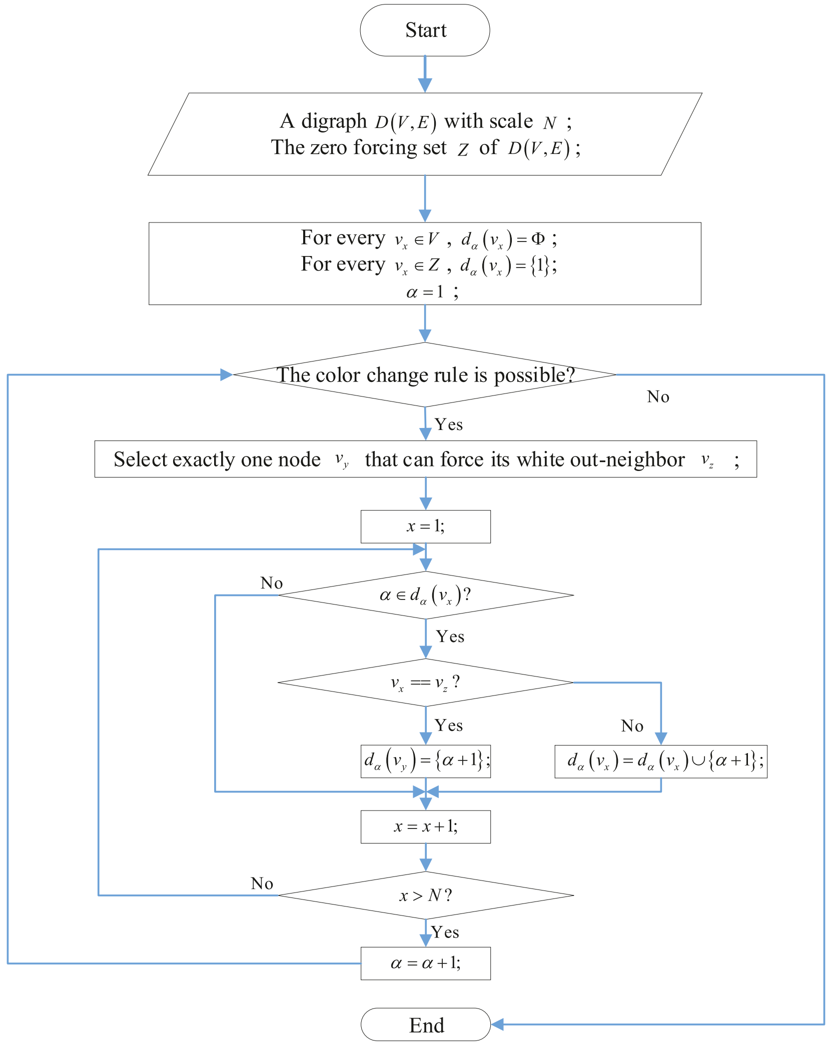

FIGURE 3 | The flowchart of distribution algorithm.

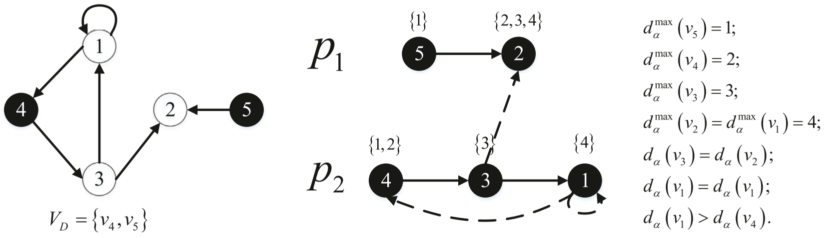

FIGURE 4 | The schematic diagram of successive integers' distribution process.

As described in the distribution algorithm, the nodes in V_G are given {1} in Step 1. Then, exactly one node in D_g is forced to be black in other eachstep. Let v_m be the last black node of p_i in step $j-1$, then $j-1 \in d_\alpha(v_m)$. If in step j, v_m can force v_{m+1} to be black, then $d_\alpha(v_{m+1}) = \{j\}$. Otherwise, $d_\alpha(v_m) = d_\alpha(v_m) \cup \{j\}$, and v_m is still the last black node of p_i. Thus, for $x = 1, \ldots, \alpha - 1$, we have only one node $v \in V_g$ such that $d_\alpha^{\max}(v) = x$. Hence, the set of distribution D_α^Σ is efficient.

Suppose that the edges $(u, v) \in E_g - \cup_{i=1}^{N_G} E_{p_i}$ all have $d_\alpha(u) \geq d_\alpha(v)$ is not true. Then we have $d_\alpha^{\max}(u) < d_\alpha^{\min}(v)$ for $(u, v) \in E_g - \cup_{i=1}^{N_G} E_{p_i}$, v is a out-neighbor of u, and $d_\alpha^{\max}(u) < \alpha$.

If two nodes u and v belong to different path p_i and p_j, respectively. u is not the end node of p_i, because $d_\alpha^{\max}(u) < \alpha$. According to the integer distribution algorithm in **Figure 3**, u is the last black node of p_i in Step $d_\alpha^{\max}(u)$, and it will forces its white out-neighbor in Step $d_\alpha^{\max}(u) + 1$. However, due to $d_\alpha^{\max}(u) < d_\alpha^{\min}(v)$, v is still a white node in Step $d_\alpha^{\max}(u) + 1$. Then, u has two white out-neighbor nodes, and the color change rule cannot be performed. Hence, there is a contradiction.

If two nodes, u and v, belong to a path p_i, as mentioned above, v is a white put-neighbor of u in Step $d_\alpha^{\max}(u) + 1$ in p_i. u will forces v be black in Step $d_\alpha^{\max}(u) + 1$ in p_i. Thus, $(u, v) \in E_{p_i}$. However, $(u, v) \in E_g - \cup_{i=1}^{N_G} E_{p_i}$. There is also a contradiction.

Based on Theorem 3, we can make the inference of the zero-forcing set Z of controllable networks by generator nodes and extra nodes, as shown in Lemma 1.

Lemma 1: The zero-forcing set Z of controllable networks by generator nodes and extra nodes $D(V, E)$ ($|V| = N$) is consists of two parts, $Z = V_G \cup V_{EN}$. We have the precisely controllable subnetworks by generator nodes $D_g(V_g, E_g)$. All nodes in set $V - V_g$ can form a set of paths $P' = \{p_1, \ldots, p_{N_{EN}}\}$ with start node set V_{EN}, where N_{EN} is the number of nodes in V_{EN}. The set of paths $P^\Sigma = P \cup P' = \{p_1, \ldots, p_{N_G}\} \cup \{p_1, \ldots, p_{N_{EN}}\}$ also has an efficient set of distribution $\overline{ED}_\alpha^\Sigma$. The edge $(u, v) \in E_g - \cup_{i=1}^{N_G + N_{EN}} E_{p_i}$ all have $d_\alpha(u) \geq d_\alpha(v)$. Where $\alpha = 1 - (N_G + N_{EN}) + \sum_{i=1}^{N_G + N_{EN}} N_{p_i}$. N_{p_i} is the number of nodes in p_i.

Remark 1: According to Theorem 3, we can infer that for every digraph with a zero-forcing set, all nodes in the digraph can consist of a forcing path set with the start nodes in the zero-forcing set, and the forcing path set has an efficient distribution. Moreover, except for the forcing path set, any edge (u, v) in the digraph satisfies $d_\alpha(u) \geq d_\alpha(v)$. The controllable networks by generator nodes and extra nodes is a digraph with the zero-forcing set $V_G \cup V_{EN}$. Thus, all nodes in the digraph can consist of a forcing path set with the start nodes in $V_G \cup V_{EN}$, and all the other edges (u, v) in the network satisfies $d_\alpha(u) \geq d_\alpha(v)$.

4 ROBUSTNESS OF CONTROLLABLE NETWORKS BY GENERATOR NODES

Transmission lines in a power system can be damaged and disconnected from the system due to factors such as natural disasters or a perceived deliberate attack. Damage to a transmission line causes edges to be removed from its network model. The structural change of a network model also leads to the change of strong structural controllability of networks. Therefore, this paper analyzes the robustness of three kinds of controllable networks by generator nodes.

Definition 5 (*The largest set of removable edges*) The largest set of removable edges E_r is the subset of E in the controllable networks by generator nodes $D(V, E)$ with zero-forcing set Z. Remove If any subsets of E_r are removed, the strong structural controllability of $D(V, E)$ from Z remains. We define $N_R = |E_r|$ as the robustness evaluation parameters of strong structural controllability.

Theorem 4: The largest set of removable edges E_r of precisely controllable networks $D(V, E)$ by generator nodes is $E - \cup_{i=1}^{N_G} E_{p_i}$. Where $p_i(V_{p_i}, E_{p_i}) \in P = \{p_1, \ldots, p_{N_G}\}$. p is the set of paths forced by generator node set V_G, $|V_G| = N_G$.

Proof: According to the color change rule and Theorem 2, the subnetwork $D_s(V_s, E_s) = \cup_{i=1}^{N_G} p_i$ is controllable by V_G. Suppose there exists an edge $(u, v) \in E_s$, such that V_G is still the zero-forcing set of $D_s - \{(u, v)\}$. We know that D_s consists of N_G disjointed paths, and $D_s - \{(u, v)\}$ consists of $N_G + 1$ disjointed paths. It is clear that the size of zero-forcing set Z of $D_s - \{(u, v)\}$ should greater than N_G. Thus, V_G is not a zero-forcing set of $D_s - \{(u, v)\}$. And $D_s - \{(u, v)\}$ can not be controlled by V_G.

Based on Theorem 4, we can get the largest set of removable edges E_r of controllable networks $D(V, E)$ by generator nodes and extra nodes, as shown in Lemma 2.

Lemma 2: The largest set of removable edges E_r of controllable networks $D(V, E)$ by generator nodes and extra nodes is $E - \cup_{i=1}^{N_G + N_{EN}} E_{p_i}$. Where $p_i(V_{p_i}, E_{p_i}) \in P = \{p_1, \ldots, p_{N_G + N_{EN}}\}$. p is the set of

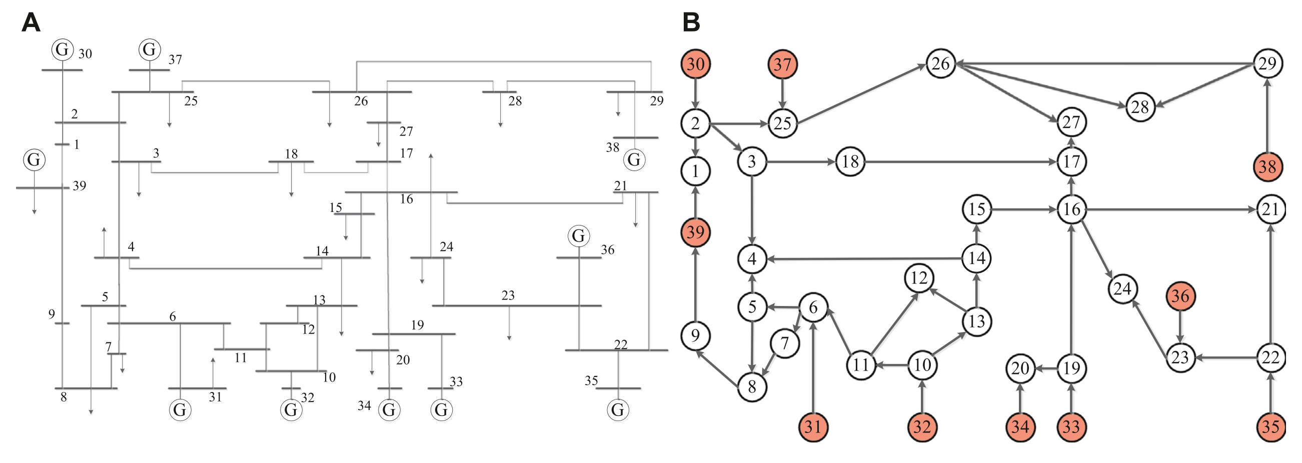

FIGURE 5 | (A) Wiring diagram of IEEE 39 bus system; **(B)** Network model of IEEE 39 bus system. The red nodes are generator nodes.

paths forced by generator node set V_G and extra node set V_{EN}, $|V_G| = N_G$ and $|V_{EN}| = N_{EN}$.

Remark 2: According to Theorem 4, we can infer that for a digraph in which drive node set is a zero-forcing set, the largest set of removable edges contains all edge in the digraph except the edges in the forcing paths that the start nodes belong to its zero-forcing set. The controllable network by generator nodes and extra nodes is a digraph in which the drive node set and the zero-forcing set are both $V_G \cup V_{EN}$. Thus, the largest set of removable edges of the network contains all edges in the digraph except the edges in the forcing paths that the start nodes belong to $V_G \cup V_{EN}$.

Theorem 5: There exists a zero-forcing set $Z \subsetneqq V_G$ of redundantly controllable networks $D(V,E)$ by generator nodes. The largest set of removable edges E_r of redundantly controllable networks $D(V,E)$ by generator nodes is $E - \cup_{i=1}^{|Z|} E_{p_i} + \cup_{j=1}^{N_G-|Z|}(v_x, v_j)$. Where $p_i(V_{p_i}, E_{p_i}) \in P = \{p_1, \ldots, p_{|Z|}\}$, and $v_j \in V_G - Z, (v_x, v_j) \in \cup_{i=1}^{|Z|} E_{p_i}$. p is the set of paths forced by the zero-forcing set $Z \subsetneqq V_G$.

Proof: According to the color change rule and Theorem 2, the subnetwork $D_s'(V_s', E_s') = \cup_{i=1}^{|Z|} p_i$ is controllable by Z. The subnetwork $D_s' - \cup_{j=1}^{N_G-|Z|}(v_x, v_j)$ is a set of paths with the start nodes of V_G $D_s' - \cup_{j=1}^{N_G-|Z|}(v_x, v_j) = \{p_1, \ldots, p_{N_G}\}$. According to Theorem 4, $D_s' - \cup_{j=1}^{N_G-|Z|}(v_x, v_j) = \cup_{i=1}^{|Z|} p_i$ is controllable by V_G, and removing any edge $(u,v) \in D_s' - \cup_{j=1}^{N_G-|Z|}(v_x, v_j)$, $D_s' - \cup_{j=1}^{N_G-|Z|}(v_x, v_j)$ is not controllable by V_G.

5 INSTANCE ANALYSIS

5.1 Instance of Controllable Network by Generator Nodes and Extra Nodes

In this subsection, IEEE 39 bus system is selected to analysis analyze the strong structural controllability and the robustness of strong structural controllability in this paper. There are 39 buses, 10 generator nodes, and 46 edges in the system. The wiring diagram and the network model of IEEE 39 bus system are depicted in **Figures 5A,B**, respectively, where the red nodes are generator nodes.

According to the above definition, the IEEE 39 bus system is the a controllable network s by generator nodes

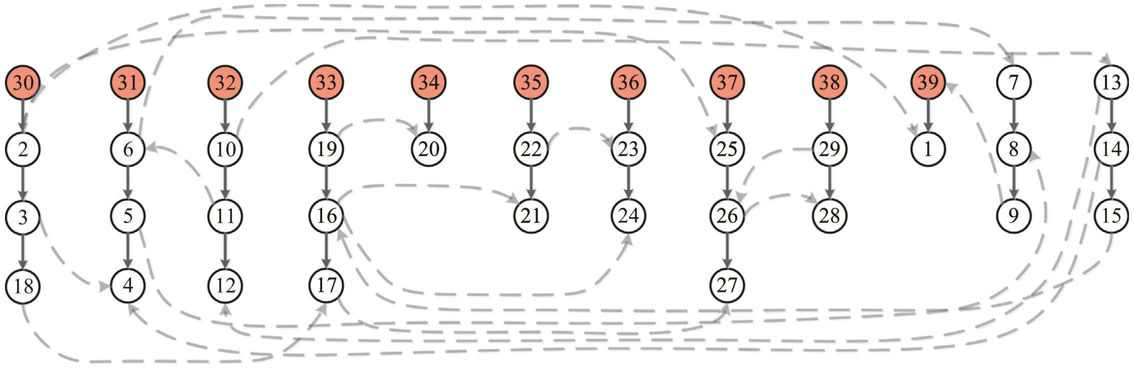

FIGURE 6 | The forcing paths in the IEEE 39 bus system. Solid lines are edges in paths and dotted lines are other edges in the system.

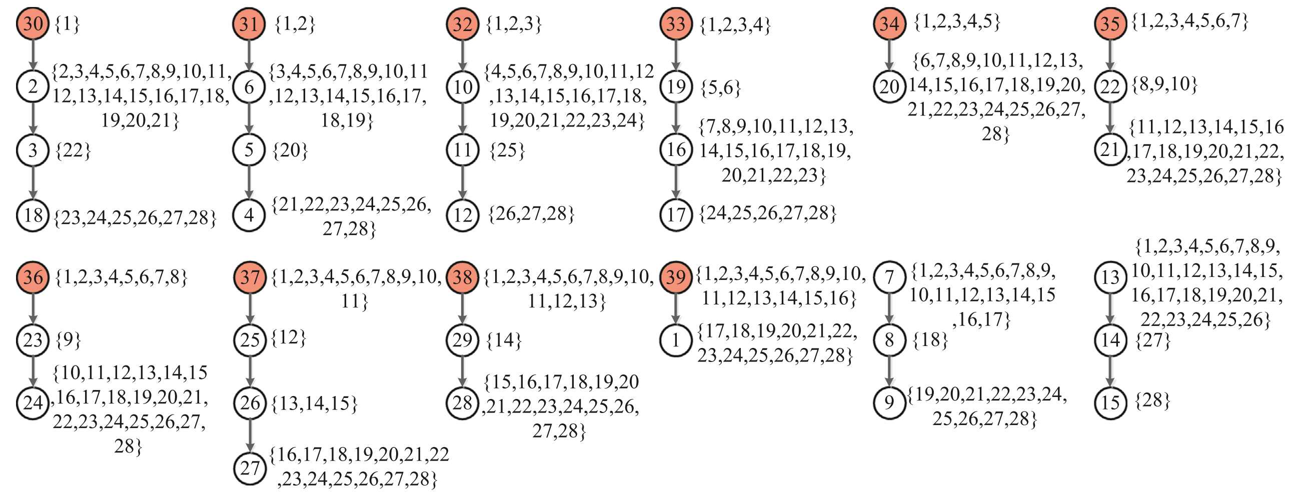

FIGURE 7 | The integer's distribution on the forcing paths of the IEEE 39 bus system.

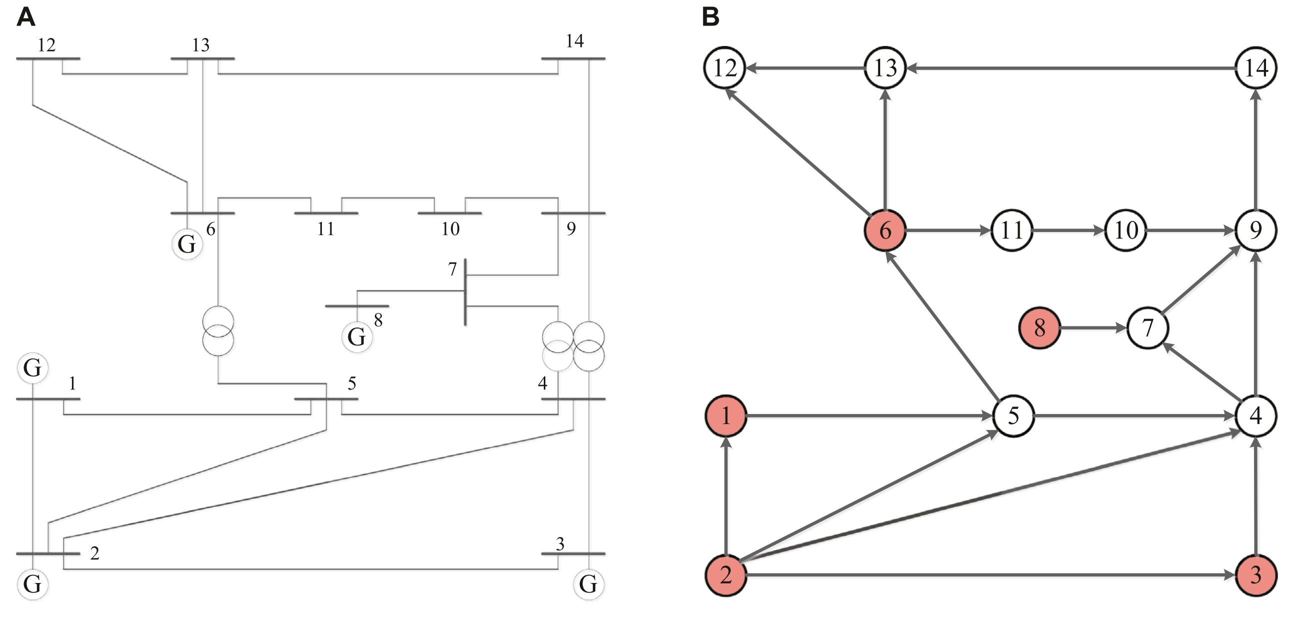

FIGURE 8 | (A) Wiring diagram of IEEE 14 bus system; **(B)** Network model of IEEE 14 bus system. The red nodes are generator nodes.

and extra nodes. A zero-forcing set of the system is $Z = V_G \cup V_{EN} = \{v_{30}, v_{31}, v_{32}, v_{33}, v_{34}, v_{35}, v_{36}, v_{37}, v_{38}, v_{39}\} \cup \{v_7, v_{13}\}$. The forcing paths are depicted in **Figure 6**, where solid lines are edges in path sand dotted lines are other edges in the system. The integer's distribution on these forcing paths are given in **Figure 7**, which is an efficient set of distribution. $\alpha = 1 – 12 + 39 = 28$. For every $1 \le j < 28$, there are is exactly one node in this path set such that $d_\alpha^{\max}(v) = j$. According to the lemma 2, the largest set of removable edges E_r of IEEE 39 bus system is $E - \cup_{i=1}^{10,+,2} E_{p_i}$, which are dotted lines in **Figure 6**. $E_r = \{(v_2, v_1)(v_2, v_{25})(v_3, v_4)(v_5, v_8)(v_6, v_7)(v_9, v_{39})(v_{10}, v_{13})(v_{11}, v_6)(v_{13}, v_{12})(v_{14}, v_4)(v_{15}, v_{16})(v_{16}, v_{21})(v_{16}, v_{24})(v_{17}, v_{27})(v_{18}, v_{17}(v_{19}, v_{20})(v_{22}, v_{23})(v_{26}, v_{28})(v_{29}, v_{26}))\}$.

5.2 Instance of Redundantly Controllable Networks by Generator Nodes

In this subsection, IEEE 14 bus system is selected to analysis analyze the strong structural controllability and the robustness of strong structural controllability in this paper. There are 14 buses, five generator nodes, and 20 edges in the system. The wiring diagram and the network model of IEEE 14 bus system are depicted in **Figures 8A,B**, respectively, where the red nodes are generator nodes.

According to the above definition, the IEEE 14 bus system is the a redundantly controllable networks by generator nodes. A zero-forcing set of the system is $Z \subset V_G = \{v_1, v_2, v_6, v_8\}$. The forcing paths are depicted in **Figure 9A**. The integer's distribution

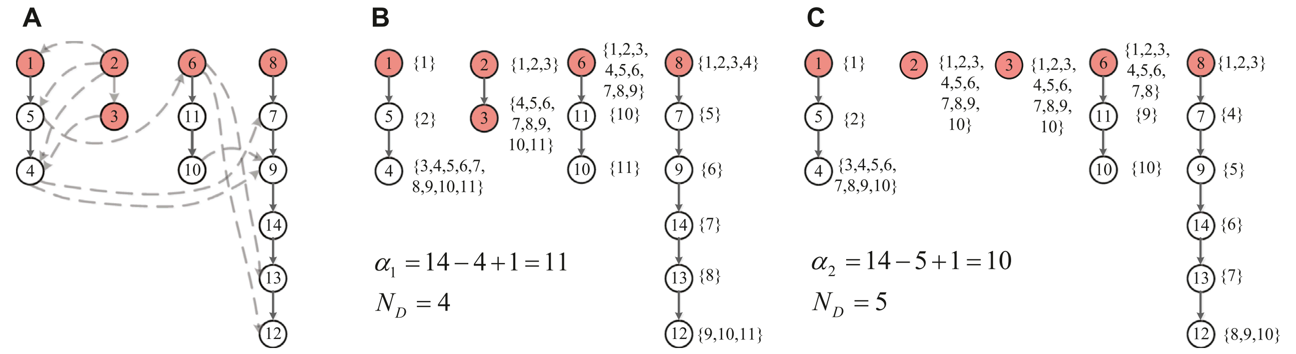

FIGURE 9 | (A) The forcing paths of four drive nodes in the IEEE 14 bus system. **(B)** The integer's distribution on the forcing paths of four drive nodes in the IEEE 14 bus system. **(C)**The integer's distribution on the forcing paths of five drive nodes in the IEEE 14 bus system.

on the forcing paths of four drive nodes are given in **Figure 9B**, which is an efficient set of distribution. $\alpha_1 = 1–4 + 14 = 11$. For every $1 \le j < 11$, there are is exactly one node in this path set such that $d_{\alpha_1}^{\max}(v) = j$.

According to the Theorem 5, the largest set of removable edges E_r of IEEE 14 bus system is $E - \cup_{i=1}^{4} E_{p_i} + \cup_{j=1}^{5-4}(v_x, v_j)$, which are dotted lines in **Figure 9A**. $E_r = \{(v_2,v_1)(v_2,v_3)(v_2,v_4)(v_2,v_5)(v_3,v_4)(v_4,v_7)(v_4,v_9)(v_5,v_6)(v_6,v_{12})(v_6,v_{13})(v_{10},v_9)\}$. Due to v_3 is being a generator node, when all edges in E_r are removed from the IEEE 14 bus system, the system is still strong structuallystructurally controllable. At this point, the zero-forcing set of the system is $Z = V_G = \{v_1, v_2, v_3, v_6, v_8\}$. The integer's distribution on the forcing paths of five drive nodes are given in **Figure 9C**, which is an efficient set of distribution. $\alpha_2 = 1–5 + 14 = 10$. For every $1 \le j < 10$, there are is exactly one node in this path set such that $d_{\alpha_2}^{\max}(v) = j$.

6 CONCLUSION

This paper analyses analyzes the robust strong structural controllability of complex power systems. Considering the dominant role of generators in the control of power systems, we define three kinds of controllable networks by generator nodes, precisely controllable networks by generator nodes, redundantly controllable networks by generator nodes, and controllable networks by generator nodes and extra nodes. Additionally, the satisfied conditions of zero-forcing set in the controllable networks by generator nodes and extra nodes are given in Theorem 3 and Lemma 1, and the relevant proof is also given. Besides, the robustness of strong structural controllability in three kinds of controllable networks by generator nodes are analyzed. We give the satisfied conditions and the relevant proofs of the largest set of removable edges in three kinds of controllable networks by generator nodes. Finally, the robust strong structural controllability of the IEEE 39 bus system is investigated. We have found that the IEEE 39 bus system is the a controllable networks by generator nodes and extra nodes, and the scale of the largest set of removable edges is 19.

DATA AVAILABILITY STATEMENT

The original contributions presented in the study are included in the article/Supplementary Material, further inquiries can be directed to the corresponding author.

AUTHOR CONTRIBUTIONS

YS and DY contributed to the theorem derivation and proof. YS wrote the first draft of the manuscript. XG and JQ contributed to manuscript revision, read, and approved the submitted version.

FUNDING

This work was supported by the National Natural Science Foundation of China (U1908217), the Liaoning Revitalization Talents Program (XLYC1902055), National Key Research and Development Project (2018YFB1700500), and the Fundamental Research Funds for the Central Universities (N180415004).

REFERENCES

Barioli, F., Fallat, S., Hall, H., Hershkowitz, D., Hogben, L., Van der Holst, H., et al. (2009). On the Minimum Rank of Not Necessarily Symmetric Matrices: a Preliminary Study. *Electronic. J. Linear. Algebra.* 18, 126–145. doi:10.13001/1081-3810.1300

Bowden, C., Holderbaum, W., and Becerra, V. M. (2012). Strong Structural Controllability and the Multilink Inverted Pendulum. *IEEE Trans. Autom. Contr.* 57, 2891–2896. doi:10.1109/TAC.2012.2191180

Chapman, A., and Mesbahi, M. (2013). On Strong Structural Controllability of Networked Systems: a Constrained Matching Approach." in Proc. American Control Conf (IEEE), 6126. doi:10.1109/acc.2013.6580798

Ching-Tai Lin, C. T. (1974). Structural Controllability. *IEEE Trans. Autom. Contr.* 19, 201–208. doi:10.1109/tac.1974.1100557

Chu, C.-C., and Iu, H. H.-C. (2017). Complex Networks Theory for Modern Smart Grid Applications: A Survey. *IEEE J. Emerg. Sel. Top. Circuits Syst.* 7, 177–191. doi:10.1109/JETCAS.2017.2692243

Chung, C. Y., Wang, K. W., Tse, C. T., and Niu, R. (2002). Power-system Stabilizer (Pss) Design by Probabilistic Sensitivity Indexes (Psis). *IEEE Trans. Power Syst.* 17, 688–693. doi:10.1109/TPWRS.2002.800914

Dey, P., Mehra, R., Kazi, F., Wagh, S., and Singh, N. M. (2016). Impact of Topology on the Propagation of Cascading Failure in Power Grid. *IEEE Trans. Smart Grid* 7, 1970–1978. doi:10.1109/TSG.2016.2558465

Freeman, L. C. (1978). Centrality in Social Networks Conceptual Clarification. *Soc. Netw.* 1, 215–239. doi:10.1016/0378-8733(78)90021-7

Group, A. M. R. G. W. (2008). Zero Forcing Sets and the Minimum Rank of Graphs. *Linear Algebra its Appl.* 428, 1628–1648. doi:10.1016/j.laa.2007.10.009

Haque, M. H. (2004). Improvement of First Swing Stability Limit by Utilizing Full Benefit of Shunt Facts Devices. *IEEE Trans. Power Syst.* 19, 1894–1902. doi:10.1109/TPWRS.2004.836243

Hassan, F. F., Balasubramanian, R., and Bhatti, T. S. (1999). New Fast Valving Scheme Using Parallel Valves for Transient Stability Improvement. *IEE Proc. Gener. Transm. Distrib.* 146, 330–336. doi:10.1049/ip-gtd:19990176

Hatziargyriou, N., Milanovic, J., Rahmann, C., Ajjarapu, V., Canizares, C., Erlich, I., et al. (2021). Definition and Classification of Power System Stability - Revisited & Extended. *IEEE Trans. Power Syst.* 36, 3271–3281. doi:10.1109/TPWRS.2020.3041774

Hines, P., Cotilla-Sanchez, E., and Blumsack, S. (2010). Do topological Models Provide Good Information about Electricity Infrastructure Vulnerability? *Chaos* 20, 033122. doi:10.1063/1.3489887

Jarczyk, J. C., Svaricek, F., and Alt, B. (2011). "Strong Structural Controllability of Linear Systems Revisited," in Proc. 50th IEEE Conf. on Decision and Control and Eur. Control Conf (IEEE), 1213. doi:10.1109/cdc.2011.6160392

Jia, J., van Waarde, H. J., Trentelman, H. L., and Camlibel, M. K. (2021). A Unifying Framework for Strong Structural Controllability. *IEEE Trans. Autom. Contr.* 66, 391–398. doi:10.1109/TAC.2020.2981425

Kiaei, I., Rostami, M., and Lotfifard, S. (2021). Robust Decentralized Control of Synchronous Generators for Improving Transient Stability of Multimachine Power Grids. *IEEE Syst. J.* 15, 3470–3479. doi:10.1109/JSYST.2020.3025028

Li, Y.-S., Ma, D.-Z., Zhang, H.-G., and Sun, Q.-Y. (2015). Critical Nodes Identification of Power Systems Based on Controllability of Complex Networks. *Appl. Sci.* 5, 622–636. doi:10.3390/app5030622

Liu, B., Li, Z., Chen, X., Huang, Y., and Liu, X. (2018). Recognition and Vulnerability Analysis of Key Nodes in Power Grid Based on Complex Network Centrality. *IEEE Trans. Circuits Syst. II* 65, 346–350. doi:10.1109/TCSII.2017.2705482

Mahmud, M. A., Hossain, M. J., Pota, H. R., and Oo, A. M. T. (2017). Robust Partial Feedback Linearizing Excitation Controller Design for Multimachine Power Systems. *IEEE Trans. Power Syst.* 32, 3–16. doi:10.1109/TPWRS.2016.2555379

Mayeda, H., and Yamada, T. (1979). Strong Structural Controllability. *SIAM J. Control Optim.* 17, 123–138. doi:10.1137/0317010

Monshizadeh, N., Zhang, S., and Camlibel, M. K. (2014). Zero Forcing Sets and Controllability of Dynamical Systems Defined on Graphs. *IEEE Trans. Autom. Contr.* 59, 2562–2567. doi:10.1109/TAC.2014.2308619

Mousavi, S. S., Haeri, M., and Mesbahi, M. (2018). On the Structural and Strong Structural Controllability of Undirected Networks. *IEEE Trans. Autom. Contr.* 63, 2234–2241. doi:10.1109/TAC.2017.2762620

Rubaai, A., Ofoli, A. R., Cobbinah, D., and Kankam, M. D. (2005). Two-layer Supervisory Controller-Based Thyristor-Controlled Braking Resistor for Transient Stability Crisis. *IEEE Trans. Ind. Appl.* 41, 1539–1547. doi:10.1109/TIA.2005.857465

Taylor, C. W., and Van Leuven, A. L. (1996). Caps: Improving Power System Stability Using the Time-Overvoltage Capability of Large Shunt Capacitor Banks. *IEEE Trans. Power Deliv.* 11, 783–792. doi:10.1109/61.489335

Trentelman, H., Stoorvogel, A., and Hautus, M. (2012). *Control Theory for Linear Systems*. Berlin, Germany: Springer.

Wang, K., Zhang, B.-h., Zhang, Z., Yin, X.-g., and Wang, B. (2011). An Electrical Betweenness Approach for Vulnerability Assessment of Power Grids Considering the Capacity of Generators and Load. *Phys. A Stat. Mech. its Appl.* 390, 4692–4701. doi:10.1016/j.physa.2011.07.031

Yang, D.-S., Sun, Y.-H., Zhou, B.-W., Gao, X.-T., and Zhang, H.-G. (2020). Critical Nodes Identification of Complex Power Systems Based on Electric Cactus Structure. *IEEE Syst. J.* 14, 4477–4488. doi:10.1109/JSYST.2020.2967403

Zhang, Z., Qiao, W., and Hui, Q. (2019). Power System Stabilization Using Energy-Dissipating Hybrid Control. *IEEE Trans. Power Syst.* 34, 215–224. doi:10.1109/TPWRS.2018.2866839

Conflict of Interest: The authors declare that the research was conducted in the absence of any commercial or financial relationships that could be construed as a potential conflict of interest.

frontiers | Frontiers in Energy Research

ORIGINAL RESEARCH
published: 16 June 2022
doi: 10.3389/fenrg.2022.911939

Research on Optimal Energy Flow Calculation of an Electro-Thermal Coupled System *via* an Interior-Point Approach

Zhaoying Li[1,2], Yan Zhao[1,2], Jian Xu[1,2] and Qianzhi Shao[3]*

[1]Shenyang Institute of Engineering, Shenyang, China, [2]Key Laboratory of Regional Multi-energy System Integration and Control of Liaoning Province, Shenyang, China, [3]State Grid Liaoning Electric Power Co., Ltd, Shenyang, China

With the contradiction between energy consumption and ecological protection becoming increasingly prominent, it has become a serious issue to study an energy system with high efficiency, low pollution, and strong controllability. The application of the backpressure unit and the peak-shaving electric boiler makes the power grid and the heat grid connected and becomes an electro-thermal coupling system, which can be studied as a representative of the integrated energy system. In this study, to make full use of energy, a power system model considering a large number of distributed energy injections and a multi-source thermal system model are constructed. After the energy flow is solved, the optimization method of the electrothermal coupled system is studied to minimize the fuel consumption and obtain the minimum operating cost. In addition, a more comprehensive algorithm is proposed in this study, and the actual model is used in the fourth section of the article to verify that the algorithm can be practically applied.

Keywords: distributed energy, power system, thermal system, energy flow calculation, optimal energy flow

Edited by:
Rui Wang,
Northeastern University, China

Reviewed by:
Pengning Zhang,
China University of Mining and Technology, China
Jiaqi Shi,
North China Electric Power University, China

****Correspondence:***
Yan Zhao
zhaoyan@sie.edu.cn

Specialty section:
This article was submitted to Smart Grids,
a section of the journal
Frontiers in Energy Research

Received: *03 April 2022*
Accepted: *26 April 2022*
Published: *16 June 2022*

Citation:
Li Z, Zhao Y, Xu J and Shao Q (2022) Research on Optimal Energy Flow Calculation of an Electro-Thermal Coupled System via an Interior-Point Approach.
Front. Energy Res. 10:911939.
doi: 10.3389/fenrg.2022.911939

1 INTRODUCTION

The development of the integrated energy system (IES) can make the allocation of resources more rational and optimal, which is a good way to deal with the huge energy consumption and resource depletion in the current era, and it is also a foundation for the complete transformation of the country's energy structure in the future (Moeini-aghtaie et al., 2014). In the traditional energy systems such as power grids and thermal networks, each energy system has an independent operating system, the coupling between them is not tight, and the energy efficiency is low. The coupling between integrated energy systems is tight, the energy utilization rate is high, and the ability to absorb renewable energy is greatly improved (Liu et al., 2016; Sun et al., 2020; Zhang et al., 2022). When the power grid is actually running to calculate the power flow, the forward-backward method and the Newton–Raphson method are mostly used (Hu et al., 2020). These two methods have a strong theoretical system in the power grid, and their ideas are also relatively mature. However, when it is applied to an electro-thermal combined system, the solution program becomes complicated, the number of iterations is large, and it is difficult to realize the combination between the various systems. At present, many scholars at home and abroad have proposed energy flow solving methods for integrated energy systems (Jia et al., 2014; Xia et al., 2017; Yu et al., 2021). Liu et al. (2021) have refined the heat network and considered the method of solving the energy flow in the case of heat loss. Guo et al. (2019) constructed a unified energy flow solution method based on energy hubs. Li et al. (2015) have considered the effect of adding energy storage elements to the whole system.

The modeling of each part of the network and the energy flow solution of the electro-thermal coupled system are the basis of the optimal energy flow research. As the most important part of this study, the control variables are not given as the general energy flow calculation but need to be determined through optimization, thus forming a nonlinear programming problem with multiple constraints, and the solution methods are also diverse to simplify the nonlinear programming method represented by the gradient method, and the interior point method is used more. The research on the optimal power flow has been very extensive. Zhang et al. (2019) considered the construction of the heat network model more comprehensively and built a refined energy flow solution model on the basis of the heating system. Jiang and Liang. (2015) considered the characteristics of poor performance in traditional AC-DC hybrid power flow calculation and uses the Gaussian method for an iterative solution to improve the applicability of the entire system. To realize the optimal allocation of energy and reduce energy consumption, this study constructs a simplified integrated energy system model and uses a unified solution method to achieve a fast and accurate solution, simple solution process, high calculation accuracy, and simple programming and does not require too many iterations (Krause et al., 2011; Malley and Kroposki, 2013; Chen et al., 2020). When a large number of PV nodes are injected into the system, the PV nodes can be equivalent to improve the traditional forward and backward generation method. In addition, the interior point method chosen in this study in the process of solving the optimal energy flow does not need to find the initial value in the feasible region, and it will adapt quickly when the system scale increases (Wang et al., 2019; Wang et al., 2020; Wang et al., 2021a; Wang et al., 2021b). In the fourth section of the study, an optimal energy flow calculation model including a distributed power grid and a multi-heat source radiant heat grid is established, and two examples are used to analyze the characteristics of the two solutions proposed.

2 RESEARCH ON THE ENERGY FLOW CALCULATION MODEL AND ALGORITHM OF THE COMBINED ELECTRIC-HEAT SYSTEM

2.1 Power System Model

The running state of the power system is not constant, and a power flow equation can be listed in each state. If the column is written as the node voltage, it can be expressed as follows:

$$\dot{U}_i = U_i\angle\theta_i = U_i\left(\cos\theta + j\sin\theta\right). \tag{1}$$

The node power equation of power flow calculation can be expressed as follows:

$$\begin{cases} \Delta P = P_{G,i} - P_{Load,i}, \\ \Delta Q = Q_{G,i} - Q_{Load,i}, \end{cases} \tag{2}$$

where $P_{G,i}$ and $Q_{G,i}$ are the active and reactive power delivered by the generator into the network; $P_{Load,i}$ and $Q_{Load,i}$ are the load active and reactive power corresponding to the node.

2.2 Thermal System Model

The thermodynamic system model is composed of a hydraulic model and a thermodynamic model. According to the hydraulic model of the heat network, the amount of water flowing through the pipeline and the injected water flow at the heat load node can be obtained. The following flow continuity equation is used to express as follows:

$$A_l m = m_c, \tag{3}$$

where A_l is the network correlation matrix of the heat load node relative to each pipeline, and m is the water flow vector through the pipe.

A thermal model can be used to determine the temperature of each node of the thermal network, including the following equations. **Eq. 4** is the equation of node injection heat power, mass flow, and node temperature. **Eq. 5** is the relationship between the temperature of the head and tail of the pipeline. **Eq. 6** is the equation for the outflow of hot water from the heat source through different heat networks and finally mixed at heat loads.

$$\phi = \phi_i - \phi_{Ei} = c_p m\left(T_{il} - T_{ol}\right), \tag{4}$$

$$T_{end} = \left(T_{start} - T_e\right)e^{-\frac{\lambda d}{c_p m}} + T_e + \mu, \tag{5}$$

$$\left(\sum_{a=1}^{n} m_{out,a}\right)T_{out} = \sum_{b=1}^{m} m_{in,b}T_{in,b}, \tag{6}$$

where ϕ is the node injection heat power vector, ϕ_i is the node heat load power vector, ϕ_{Ei} is the node electric boiler injection heat power vector, T_{il} is the temperature of hot water provided by each node, T_{ol} is the temperature of hot water flowing back, T_{end} is the temperature of the hot water as it leaves the pipe, T_{start} is the temperature at which the hot water enters the pipe, T_e is the ambient temperature, λ is the coefficient of heat conduction per unit length of the pipeline, d is the transmission distance of the pipeline, μ is the temperature compensation parameter, $m_{out,a}$ is the branch flow of the branch out of the pipeline for the branch a, and T_{out} is the temperature of hot water flowing back to the pipeline at different locations.

There is often more than one heat source in a thermal system. **Figure 1A** is the schematic diagram of the radiant heat system model with multiple heat sources. In this model, two heat sources are used to heat the heat load at the same time. Then, the two heat sources are transformed into two equivalent heat sources shown in **Figure 1B** to heat the heat load. Therefore, the multi-heat source radiation type heat network is converted into multiple single heat source radiation-type heat networks. The transformation is as follows:

$$m_{k_{ij}} = \frac{m_{H_1}}{m_{H_1} + \ldots + m_{H_i}} m_{k_i}. \tag{7}$$

This is rewritten in the matrix form as

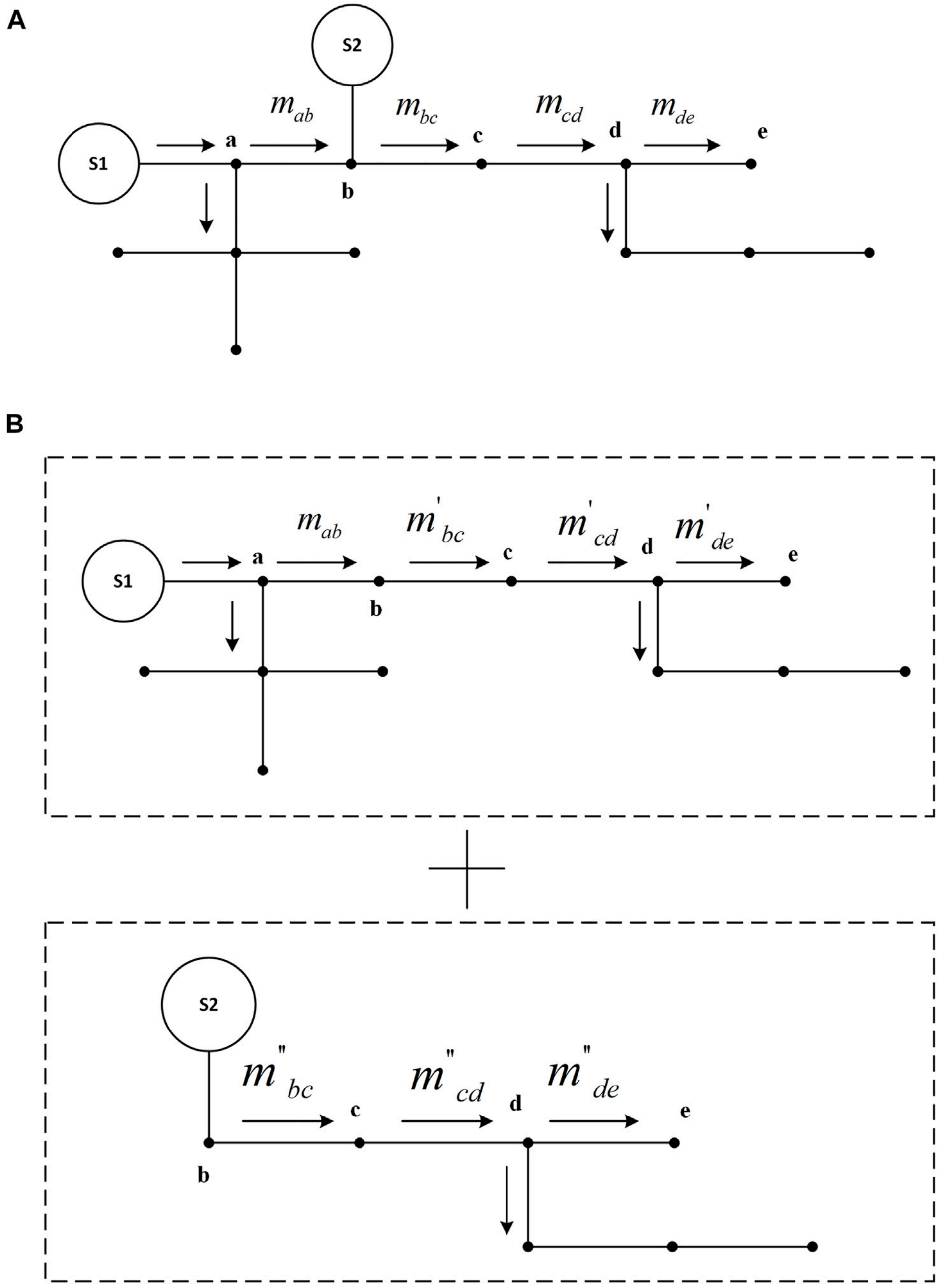

FIGURE 1 | (A) Multi-source radiant thermal system model. **(B)** Single-heat source radiant heat network model.

$$\begin{bmatrix} m_{k_{1\theta}} \\ \cdots \\ m_{k_{N\theta}} \end{bmatrix} = \frac{m_{H_1}}{m_{H_1} + \cdots + m_{H_i}} \begin{bmatrix} m_{k_1} \\ \cdots \\ m_{k_i} \end{bmatrix}, \qquad (8)$$

where, $m_{k_{ij}}$ ($i = 1, \ldots, n$, n represents the number of pipes branching from the node, $j = 1, \ldots, m$, m represents the number of heat sources in the heat network) is the corresponding single heat source radiation heat network after conversion. m_{H_i} ($i = 1, \ldots, n$) is the pipe flow input by the corresponding heat source to the node, and m_{k_i} ($i = 1, \ldots, n$) is the branch flow before conversion, that is, the multi-heat source radiation type heat network corresponds to the pipeline flow.

$$\sum_{i=1}^{m} \phi_{l_i} = \phi_l, \qquad (9)$$

where, ϕ_{l_i} ($i = 1, \ldots, m$, m is the number of heat sources in the heat network) is the equivalent heat load power after the multi-heat source radiation heat network is equivalent to multiple single heat source radiation heat networks, and ϕ_l is the equivalent heat before the node thermal load power.

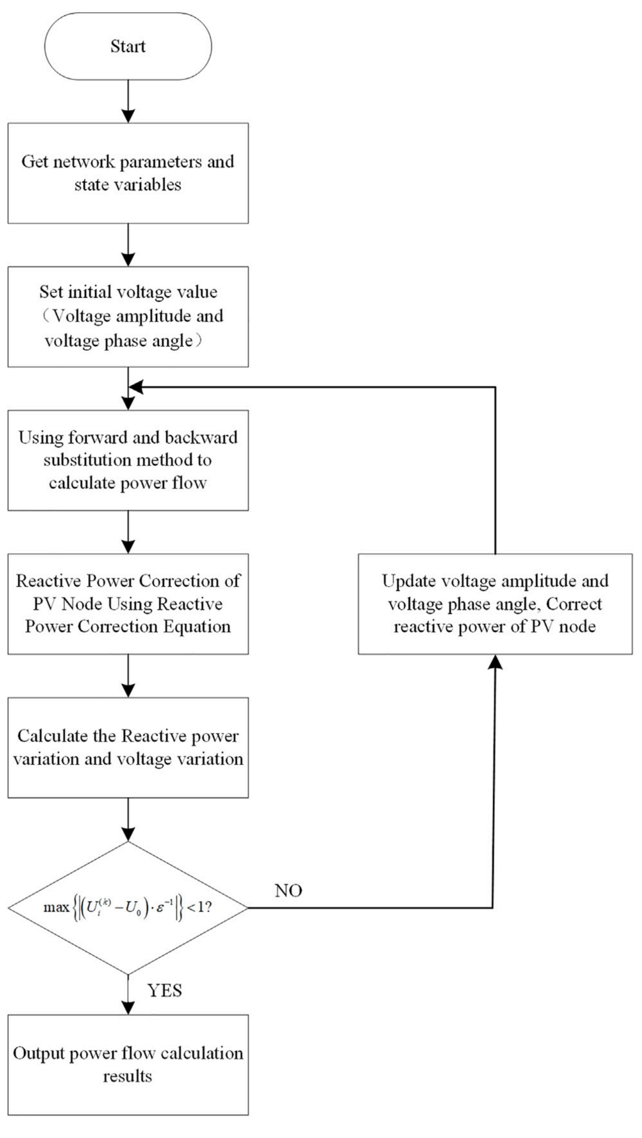

FIGURE 2 | Flow chart of the power flow solution.

2.3 Thermal-Electro Coupled Model

Coupling elements of power systems and thermal systems such as thermoelectric units and heat pumps have the property of generating heat while supplying power. A backpressure unit is a widely used thermoelectric unit, which does not contain a condenser. The exhaust heat in the back pressure unit will be fully utilized, and the thermal efficiency is high. The disadvantage is that the generating capacity of the backpressure unit should be based on heat production, and the regulation sensitivity is not strong. Therefore, the backpressure unit is generally selected as the heat source to play a central role in the thermal system, and the electric boiler is selected to meet the demand for peak shaving.

The thermal power and electrical power emitted by the backpressure unit satisfy the following equation:

$$\zeta^{-1}\cdot\phi_{BY}=P_{BY}, \tag{10}$$

where ζ is the ratio of heat production to electricity production, which is generally a constant value, ϕ_{BY} is the heat power produced by the backpressure unit, and P_{BY} is the electricity generated by the backpressure unit.

The equation of thermal power and electrical power emitted by a peak-shaving electric boiler is as follows:

$$\delta^{-1}\cdot\phi_{EB}=P_{EB}, \tag{11}$$

where δ is the heat-to-electricity ratio, which is generally a constant value, ϕ_{EB} is the thermal power emitted by the peak-shaving electric boiler, and P_{EB} is the electric power generated by the peak-shaving electric boiler.

2.4 Calculation Method of the Energy Flow in the Electro-Thermal Coupled System

At present, Newton–Raphson's energy flow solution method is the most widely used. However, the Newton–Raphson method has the shortcomings of strict requirements on the initial value and more iterations. Therefore, this study proposes an improved forward-backward generation method, which improves the drawbacks that the traditional forward-backward generation method cannot deal with PV nodes, and is extended to the radiant thermal system with multiple heat sources, which reduces the number of iterations and the requirement for initial values. The improvement of the thermal system simplifies the model and improves the calculation speed.

When distributed energy is added to the grid, PV nodes will become more. But the traditional push-back method cannot handle this. Therefore, it can be improved to allow power flow calculations to continue. **Figure 2** shows the flow solution diagram of the improved forward-backward substitution method.

The power loss formula is as follows:

$$\Delta S=\Delta P+j\Delta Q=I^2\left(R_i+jX_i\right)=\frac{P_i^2+Q_i^2}{U_N^2}\left(R_i+jX_i\right) \tag{12}$$

where ΔS is power loss, I is the line current, R_i, X_i are line parameters, and U_N is the rated voltage of the line.

Next, the voltage drop formula of each line is calculated as follows,

$$\Delta U=Z_i\cdot\Delta S^*=\left(R_i+jX_i\right)\left(\Delta P-j\Delta Q\right)=R_i\Delta P+X_i\Delta Q, \tag{13}$$

where ΔU is the longitudinal component of the voltage drop, Z_i, R_i, X_i are line parameters, ΔP is the active loss, and ΔQ is the reactive loss.

For the *PV* nodes, if $\Delta P=0$, the following equation is satisfied:

$$\Delta Q=X_i^{-1}\cdot\Delta U \tag{14}$$

where ΔQ is the reactive power loss, and X_i is the line parameter.

Since the injection of distributed generation into the distribution network will increase the number of *PV* nodes in the power system, a large number of *PV* nodes cannot be calculated by using the forward-backward substitution method. If the initial reactive power value at the power source is set to 0, the *PV* node can be equivalent to a *PQ* node first to facilitate subsequent solutions, and the reactive power at the power source is corrected at each iteration to ensure the real-time data.

The correction equation is as follows:

$$\begin{aligned}\Delta Q &= \gamma\left(Q_i - \sum Q_{ij}\right)\left(1 + e^{-t}\right)\\ &= \gamma\left(\frac{-P_i R - \Delta U_b U_i}{X_a} - Q_{ij}\right)\left(1 + e^{-t}\right),\end{aligned} \tag{15}$$

where $\gamma \in (-1,\ 1)$ is the calculation step length. Generally $\gamma = 0.1$, Q_i is the reactive power calculated by the PV node, Q_{ij} is the reactive power of all branches and nodes connected to the PV node, P_i is the power of the PV node, and X_a are line parameters.

The fact that whether the voltage of each node satisfies the convergence condition of the following equation is judged. If not, the voltage value is updated before the power flow calculation, and the equation is corrected until the voltage satisfies the convergence condition.

The convergence condition is as follows:

$$\max\left\{\left|\Delta U_i^{(k)} \cdot \varepsilon^{-1}\right|\right\} = \max\left\{\left|\left(U_i^{(k)} - U_0\right) \cdot \varepsilon^{-1}\right|\right\} < 1, \tag{16}$$

where ε is the convergence accuracy, $U_i^{(k)}$ is the voltage value obtained by the kth iteration, and U_0 is the initial voltage value.

The aforementioned idea can be extended to the thermal system to be equivalent to the power system. The temperature of the heat network is analogous to the voltage of the power grid, the heat flow is analogous to the current, the heat load node is equivalent to the load, the heat source node is equivalent to the power supply, and the node with known heating temperature is an analogy to the balance node in the power system. Then, according to the coupled part modeling mentioned in 2.3, the sum of thermal power of all equilibrium nodes in the thermal system is transformed into the power of electric load to realize the transformation process of the power flow solution.

3 RESEARCH ON THE OPTIMAL ENERGY FLOW CALCULATION MODEL AND ALGORITHM OF THE ELECTRIC-HEAT COMBINED SYSTEM

3.1 Problem Description

One of the main research problems in this study is the construction of the optimal energy flow model for the entire system and the solution method. The purpose of solving the optimal energy flow is to make the entire system run efficiently and to obtain security guarantees at the same time. Adjustment through certain algorithms of the output of each energy unit can achieve the optimal distribution of energy among various systems. When the model is built, the grid is used as the basis. The thermal grid and the grid are connected together through coupling elements at a certain node, and the thermal power of the thermal grid is converted into electrical power and introduced into the grid. To calculate the optimal energy flow, the objective function must be selected first. In this study, the goal is to minimize the operating cost of the entire system. This is a nonlinear programming problem that considers multiple constraints of independent networks and coupled parts. The following assumptions should be made before modeling:

1) The operating conditions of each power source and a heat source are known (if there is a parallel connection between power sources or heat sources, it will not be considered);
2) The output of each power source and heat source are known;
3) The topologies of the heat grid and the grid are known;
4) The node load size is known;
5) The parameters of the overall network are known.

The mathematical model of the optimal energy flow can be expressed as

$$\begin{cases} \min f(u,x), \\ s.t.\ \begin{array}{l} g(u,x) = 0, \\ h(u,x) \le 0, \end{array} \end{cases} \tag{17}$$

where u is generally an independent variable that can adjust the active and reactive power output of each power supply and the temperature and flow of hot water flowing out of the heat source, and x is generally a variable that follows u, such as the voltage of each node in the power grid and the branch power, the heat network. The temperature of the water flow at each node and the flow of the pipeline at other places are determined; $\min f(u,x)$ is the minimum system operating cost in this study, $g(u,x) = 0$ is the power balance equation of the power grid and the heat network, and $h(u,x) \le 0$ is the inequality constraint.

3.2 Objective Function

If the objective function is to minimize the operating cost, the corresponding coal consumption should be minimized. The heat source selected in this study is a backpressure unit, and a peak-shaving electric boiler is used to assist it, so it can be considered that the objective function established in this study is based on heat production and production. Electricity is a quadratic fitting function of the variable, and the objective function is as follows:

$$\begin{aligned}\min\sum_{i=1}^{N}\Big(&c_{0(i)} + c_{1(i)}P_{BY(i)} + c_{2(i)}P_{BY(i)}^2 + c_{3(i)}D_{BY(i)} + c_{3(i)}D_{BY(i)}^2\\ &+ c_{5(i)}D_{BY(i)}P_{BY(i)}\Big),\end{aligned} \tag{18}$$

where i is the backpressure unit from 1 to n, $c_{0(i)} \sim c_{5(i)}$ is the fitting constant, $P_{BY(i)}$ is the electrical power generated by the backpressure unit, and $D_{BY(i)}$ is the thermal power generated by the backpressure unit.

3.3 Restrictions

3.3.1 Grid Active and Reactive Power Balance Constraints

The equation constraints of the power grid can be considered as the active and reactive power equations of the power flow calculation, and the balance condition is that the inflow power of each node in the power grid is equal to the sum of the outflow and losses:

$$\begin{cases} \sum\limits_{a=1}^{N} P_{BY(a)} - P_a - U_a \sum\limits_{b=1}^{n} U_b\left(G_{ab}\cos\theta_{ab} + B_{ij}\sin\theta_{ab}\right) = 0 \\ \sum\limits_{a=1}^{N} Q_{BY(a)} - Q_a - U_a \sum\limits_{b=1}^{n} U_b\left(B_{ij}\sin\theta_{ab} + G_{ab}\cos\theta_{ab}\right) = 0 \end{cases} \tag{19}$$

where $\sum_{a=1}^{N} P_{BY(a)}$ and $\sum_{a=1}^{N} Q_{BY(a)}$ are the sum of the active power and reactive power of the backpressure units connected to 1 to N unit, and P_a and Q_a are the active and reactive power of the node.

3.3.2 Power Balance Constraints of the Heating Network

The power balance constraints of the heating network include the electric power balance of backpressure unit nodes, the thermal power of heat source nodes, the thermal power used by users and the thermal power supplied by electric boilers, and the temperature balance of hot water flowing into pipes.

$$\phi_i - \phi_{Ei} - c_p m\left(T_{il} - T_{ol}\right) = 0, \tag{20}$$

$$\left(T_{start} - T_e\right)e^{-\frac{\lambda d}{c_p m}} + T_e + \mu - T_{end} = 0, \tag{21}$$

$$\phi_i + c_p m\left(T_{il} - T_{ol}\right) - \phi_{EB} - D_{BY(i)} = 0, \tag{22}$$

where ϕ_i is the node heat load power vector, ϕ_{Ei} is the node electric boiler injection heat power vector, T_{il} is the temperature of hot water provided by each node, T_{ol} is the temperature of hot water flowing back, T_{end} is the temperature of the hot water as it leaves the pipe, T_{start} is the temperature at which the hot water enters the pipe, T_e is the ambient temperature, λ is the coefficient of heat conduction per unit length of the pipeline, d is the transmission distance of the pipeline, and μ is the temperature compensation parameter.

3.3.3 Constraint Conditions of Power Grid Inequality

For all backpressure units, the upper and lower power limits of active and reactive power are met:

$$\begin{cases} P_{BY(i)}^{\min} \le P_{BY(i)} \le P_{BY(i)}^{\max}, \\ Q_{BY(i)}^{\min} \le Q_{BY(i)} \le Q_{BY(i)}^{\max}, \end{cases} \tag{23}$$

where $P_{BY(i)}^{\min}$ and $P_{BY(i)}^{\max}$ are the minimum and maximum active power output of the back pressure unit, and $Q_{BY(i)}^{\min}$ and $Q_{BY(i)}^{\max}$ are the limit values of the reactive power output of the back pressure unit.

Similarly, all peak-shaving electric boilers also meet the upper and lower power limits of active and reactive power:

$$\begin{cases} P_{BE(i)}^{\min} \le P_{BE(i)} \le P_{BE(i)}^{\max}, \\ Q_{BE(i)}^{\min} \le Q_{BE(i)} \le Q_{BE(i)}^{\max}, \end{cases} \tag{24}$$

where $P_{BE(i)}^{\min}$ and $P_{BE(i)}^{\max}$ are the minimum and maximum active power output of the peak-shaving electric boiler, and $Q_{BE(i)}^{\min}$ and $Q_{BE(i)}^{\max}$ are the limit values of the reactive power output of the peak-shaving electric boiler.

To meet the stability of power grid operation, it is necessary to restrict the amplitude of the voltage and the phase angle difference of the voltage:

$$\begin{cases} U_{a(i)}^{\min} \le U_{a(i)} \le U_{a(i)}^{\max} \\ \left|\theta_{a(i)}^{\min} \le U_{a(i)}\right|_{\min} \le \left|\theta_{a(i)} \le \theta_{a(j)}\right| \le \left|\theta_{a(i)} \le \theta_{a(j)_{\max}}\right| \end{cases} \tag{25}$$

where $U_{a(i)}^{\min}$ and $U_{a(i)}^{\max}$ are the upper and lower limits of the voltage amplitude of the i node, and $|\theta_{a(i)} - \theta_{a(j)}|_{\min}$ and $|\theta_{a(i)} - \theta_{a(j)}|_{\max}$ are the limits of the voltage phase angle difference between the two nodes.

3.3.4 Inequality Constraint Conditions of the Heating Network

If the variables m, T_{il} ,T_{ol}, T_{end}, T_{start}, T_e, and $D_{BY(i)}$ of the heating network exceed a certain range, the operation of the whole combined system will become unstable, so the upper and lower limits of these variables should be constrained:

$$\begin{cases} m_{a(i)}^{\min} \le m_{a(i)} \le m_{a(i)}^{\max}, \\ T_{il(i)}^{\min} \le T_{il(i)} \le T_{il(i)}^{\max}, \\ T_{ol(i)}^{\min} \le T_{ol(i)} \le T_{ol(i)}^{\max}, \\ T_{end(i)}^{\min} \le T_{end(i)} \le T_{end(i)}^{\max}, \\ T_{start(i)}^{\min} \le T_{start(i)} \le T_{start(i)}^{\max}. \\ T_{e(i)}^{\min} \le T_{e(i)} \le T_{e(i)}^{\max}, \\ D_{BY(i)}^{\min} \le D_{BY(i)} \le D_{BY(i)}^{\max}, \end{cases} \tag{26}$$

3.3.5 Power Balance Constraint of the Electrothermal Coupling Node

When the backpressure unit is used as the hub of the power grid and the heating network and when the peak-shaving electric boiler assists in regulation, there is the following power balance equation at the junction of the two networks:

$$\begin{cases} \delta^{-1} \cdot \phi_{EB} - P_{EB} = 0, \\ \zeta^{-1} \cdot \phi_{BY} - P_{BY} = 0. \end{cases} \tag{27}$$

The aforementioned formula is the conversion relationship between thermal power and electric power of the backpressure unit and electric boiler.

3.4 Calculation Method of the Optimal Energy Flow in the Electrothermal Coupling System.

Among many methods for solving optimal energy flow, the nonlinear programming method and interior point method are widely used. Compared with the former, the interior point method has the advantages of fast calculation speed and better convergence. When the system is huge, the calculation amount is not as complex as other methods, and the initial value is not particularly strict. Therefore, the interior point method is selected to solve the optimal energy flow of the whole joint system in this study. The traditional interior point method is always in the feasible region in the iterative process. Therefore, it is often difficult to choose the initial value. However, with the emergence of the central trajectory method, it is not necessary to find the initial value in the feasible region of the established model, and the range has changed greatly than the previous one. It only needs to meet the conditions of relaxation variables and disturbance factors, and the requirements for the initial value are no longer so strict.

At first, the interior point method appeared to calculate the optimal power flow in the power grid. When constructing the

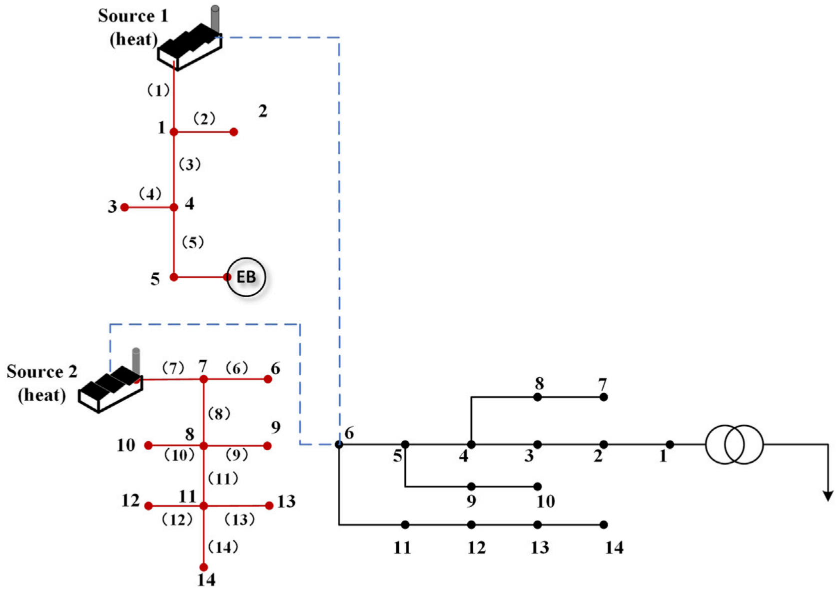

FIGURE 3 | Integrated energy testing system.

TABLE 1 | Heat system pipeline flow.

Heat pipe number	Pipe flow (kg/s)
1	40
2	16.6529
3	21.5897
4	9.3549
5	11.7643
6	4.9764
7	40
8	33.9334
9	4.1648
10	3.9732
11	25.3871
12	6.1745
13	8.8621
14	11.2856

TABLE 2 | Temperature at each node in the heat network.

Node number	Node supply temperature (°C)	Node return temperature (°C)
1	119.8635	35.9729
2	118.6832	35.7832
3	116.9732	34.0842
4	119.3761	35.7906
5	118.8532	35.6818
6	118.7532	35.3986
7	119.6394	35.7867
8	117.5079	34.9103
9	116.0632	34.8903
10	113.9729	34.7865
11	114.2797	34.6984
12	113.9721	33.9721
13	114.1674	34.1957
14	114.3908	34.5772

objective function, it is not necessary to list the state variables and control variables separately like other power flow models. In the interior point method, these two variables are not distinguished, and they are uniformly represented by x. In addition to the active power, reactive power, voltage amplitude, and phase angle of each node, x in this study also includes the thermal power generated by the heat source in the heating network, the temperature and flow rate of water flowing out to the pipeline, the temperature information of the outlet and inlet of each pipeline, and the water flow rate in the pipeline.

After the aforementioned analysis, the optimal power flow model is simplified as the following formula:

$$\begin{cases} \min f(x), \\ s.t. \begin{array}{l} p(x) = 0, \\ q_{\min} \le q(x) \le q_{\max}, \end{array} \end{cases} \tag{28}$$

where $f(x)$ is the minimum operating cost function described in 3.2, $p(x) = 0$ is the equality constraint, $q_{\min} \le q(x) \le q_{\max}$ is the inequality constraint, and x is the set composed of variables P_{BY}, Q_{BY}, P_{BE}, Q_{BE}, U_a, θ_a, D_{BY}, D_{BE}, m, T_{il}, T_{ol}, T_{end}, and T_{start}.

For **Equation 28**, it is difficult to solve the model. Two relaxation variables m and n can be introduced to transform it into the same equality constraint as $p(x) = 0$:

$$\begin{cases} \min f(x), \\ s.t. \begin{array}{l} p(x) = 0, \\ q(x) + m = q_{\max}, \\ q(x) - n = q_{\min}, \\ mn > 0, \end{array} \end{cases} \tag{29}$$

where m and n are relaxation variables, both of which are positive numbers.

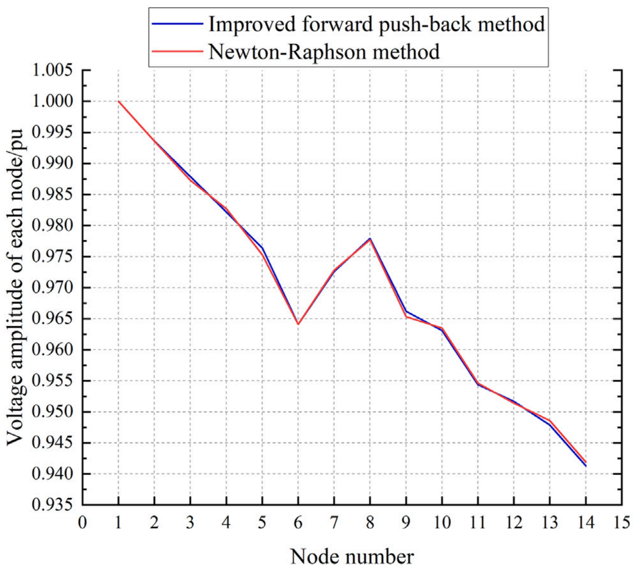

FIGURE 4 | Comparison of power flow calculation results.

If the solution directly according to the aforementioned formula may make the result beyond the feasible range, **Eq. 29** can be combined with the objective function to limit the solution result within the determined range, and once it approaches the boundary, the result increases rapidly and returns to the region again.

TABLE 3 | Setting of optimal power flow operating conditions.

Node number	$T_{il.min}$ (°C)	$T_{il.max}$ (°C)	$T_{ol.min}$ (°C)	$T_{ol.max}$ (°C)
S1	80	120	—	—
S2	80	120	—	—
1	80	120	20	70
2	80	120	20	70
3	80	120	20	70
4	80	120	20	70
5	80	120	20	70
6	80	120	20	70
7	80	120	20	70
8	80	120	20	70
9	80	120	20	70
10	80	120	20	70
11	80	120	20	70
12	80	120	20	70
13	80	120	20	70
14	80	120	20	70

$$\begin{cases} \min f(x) - v\sum_{a=1}^{n}\log\frac{m_a}{n_a}, \\ p(x) = 0, \\ s.t.\, q(x) + m = q_{\max}, \\ q(x) - n = q_{\min}, \end{cases} \tag{30}$$

where v is the perturbation factor; the perturbation factor is used to eliminate inequality constraints and transform them into equality constraints for subsequent solutions.

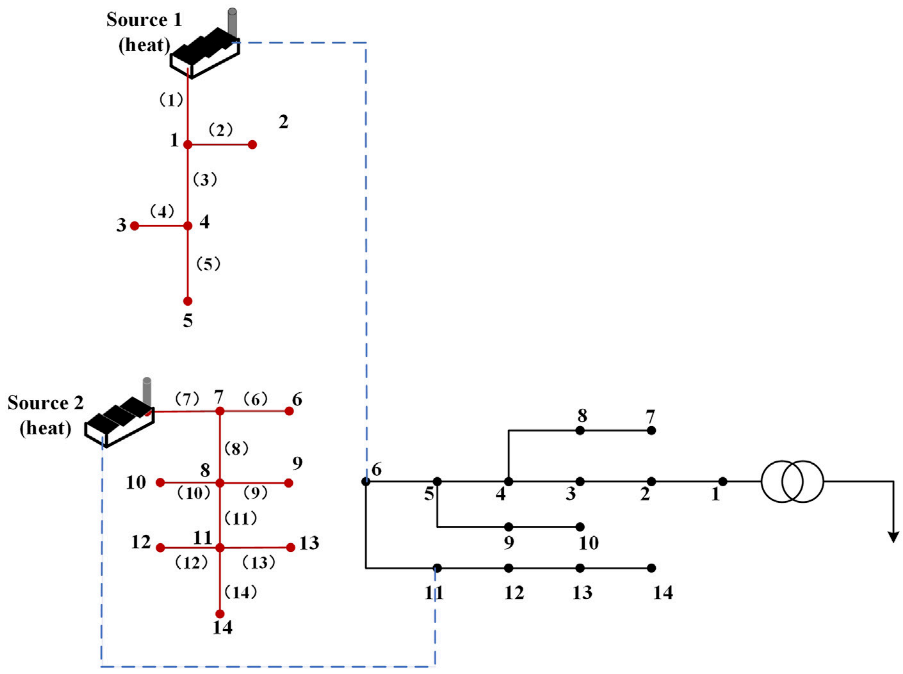

FIGURE 5 | Test model of the electrothermal combined system.

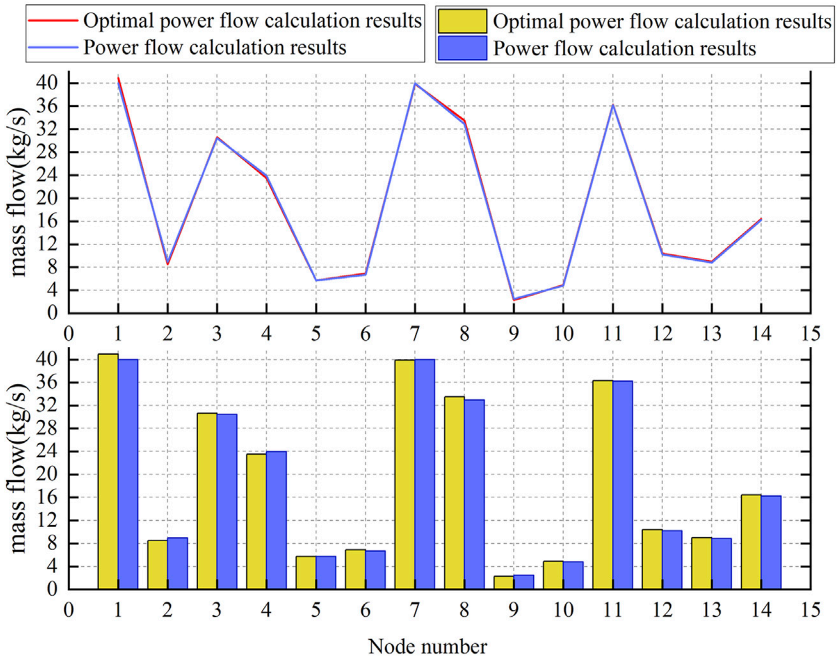

FIGURE 6 | Comparison chart of pipeline flow calculation results.

TABLE 4 | Fitting constant with operating cost as the objective function.

Parameter	c_0	c_1	c_2	c_3	c_4	c_5
S1	1.7532	0.3526	0.0972	0.6752	0.0672	0.0873
S2	1.2656	0.7683	0.0837	0.9773	0.0273	0.0187

TABLE 5 | Water flow of the heat network pipeline (kg/s).

Node number	Optimal power flow calculation results	Power flow calculation results
1	40.9362	40
2	8.4987	8.9305
3	30.5982	30.4281
4	23.5112	23.9387
5	5.7123	5.7243
6	6.8981	6.6928
7	39.8724	40
8	33.4897	32.9073
9	2.2761	2.4917
10	4.8912	4.7982
11	36.2781	36.1920
12	10.3987	10.2139
13	8.9872	8.8193
14	16.4092	16.2384

For equality constraints, Lagrange functions can be constructed to find the extremum of each variable:

$$L = f(x) - \upsilon\sum_{a=1}^{n}\log\frac{m_a}{n_a} - r^T p(x) - s^T\left[q(x) + m - q_{\max}\right] - t^T\left[q(x) - n - q_{\min}\right], \tag{31}$$

where $r^T = [r_1, r_2, \cdots, r_n]^T$, $s^T = [s_1, s_2, \cdots, s_n]^T$, and $t^T = [t_1, t_2, \cdots, t_n]^T$ are multipliers introduced in the constructor.

The partial derivatives of x, m, n, r, s, and t are obtained by using the Lagrange function, and the nonlinear equations are constructed when the derivative value is zero:

$$\begin{cases} \dfrac{\partial L}{\partial x} = \nabla_x f(x) - \nabla_x p(x) r - \nabla_x q(x)(s+t) = 0, \\ \dfrac{\partial L}{\partial r} = p(x) = 0, \\ \dfrac{\partial L}{\partial s} = q(x) + m - q_{\max} = 0, \\ \dfrac{\partial L}{\partial t} = q(x) - n - q_{\min} = 0, \\ \dfrac{\partial L}{\partial n} = NTE - \upsilon E = 0, \\ \dfrac{\partial L}{\partial M} = MSE + \upsilon E = 0, \end{cases} \tag{32}$$

where M, N, S, and T are diagonal matrices with a elements, and E is an identity matrix with a elements.

Newton's method is used to solve the aforementioned differential equation and simplify it, and the simplified modified equation matrix form is as follows:

$$\begin{bmatrix} A & \nabla p(x) \\ \nabla_x^T p(x) & 0 \end{bmatrix}\begin{bmatrix} \Delta x \\ \Delta r \end{bmatrix} = \begin{bmatrix} B \\ C \end{bmatrix}, \tag{33}$$

where the matrices A, B, and C are expressed by the following equations:

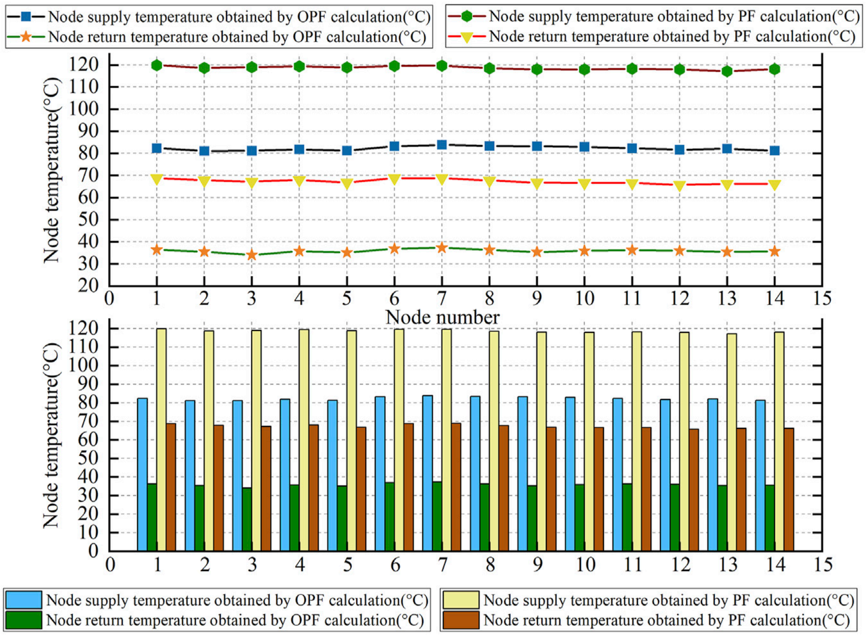

FIGURE 7 | Comparison diagram of the supply and return temperature.

TABLE 6 | Temperature comparison of heating network nodes.

Node number	Optimal power flow calculation results		Power flow calculation results	
	Node supply temperature (°C)	Node return temperature (°C)	Node supply temperature (°C)	Node return temperature (°C)
1	82.3443	36.3529	119.8635	68.7862
2	81.0918	35.4832	118.6832	67.7863
3	81.1273	34.0342	118.9732	67.2435
4	81.8273	35.7346	119.3761	67.9872
5	81.2344	35.1434	118.8532	66.7862
6	83.2321	36.8556	119.5532	68.7863
7	83.8624	37.3234	119.6394	68.8234
8	83.3567	36.3245	118.5079	67.7523
9	83.2449	35.3564	118.0632	66.7852
10	82.8847	35.9075	117.9729	66.6752
11	82.2540	36.2567	118.2797	66.6255
12	81.6624	35.9837	117.9721	65.7852
13	82.0859	35.4557	117.1674	66.2576
14	81.2349	35.6534	118.0938	66.2478

$$A = \nabla_x^2 f(x) + \nabla_x^2 p(x) + \nabla_x^2 h(x)(s+t) + \nabla h(x)\left[M^{-1}S - N^{-1}Z\right]\nabla_x^T h(x), \tag{34}$$

$$B = \nabla_x f(x) - \nabla_x p(x) r - \nabla_x q(x)(s+t) + \nabla_x h(x)\left[N^{-1}Z - U^{-1}W\right]\nabla_x^T h(x), \tag{35}$$

$$C = -p(x). \tag{36}$$

According to **Eq. 33**, a group of solutions closest to the optimal solution can be solved.

4 EXAMPLE VERIFICATION

4.1 Example Verification of the Energy Flow Calculation of the Electrothermal Coupling System

To prove that the aforementioned method can be practically applied, an actual model is used in **Figure 3** as an example to conduct experiments.

In this example, the heat grid and the power grid are coupled through the cogeneration unit. The heat network part includes two heat source nodes source 1 and source 2 using a backpressure unit, a peak-shaving electric boiler located at node 5, and 14 heat load nodes. The peak modulation ratio is 0.45, the thermoelectric ratio is 1.4, and the heat load is 0.5 MW. The length of each pipeline is set to 1.58 km, λ is set to 0.289, and the diameter of the pipeline is set to 100 mm. According to the transformation method of the multi-source radiant heat network in **Section 2.2**, the multi-source radiant heat network is transformed into several single-source radiant heat networks and then the energy flow solution is performed. **Table 1** is the heating system pipeline flow, and **Table 2** is the temperature at each node in the heat network.

The thermal system and power system are coupled through node 6. The thermal power of node 6 is 1.7347 MW, which is converted to 2.2551 MW. The power grid part selects 14 node distribution networks, node 1 is set to 1.00 *pu*, node 2 and node 6 are *PV* nodes, the voltage amplitudes are 0.993 *pu* and 0.964 *pu*, and its node is *PQ* node. According to the flow chart in **Figure 2**, the 1st and 2nd are set to *PQ* nodes for the first iterative, and then, the program is returned to calculate the reactive power correction. The reactive power correction is substituted for the next iterative calculation. After three iterations, the convergence criteria are met, and the result is output. The power flow calculation results obtained by this method are compared with those obtained by the traditional Newton–Raphson method of power flow calculation, as shown in **Figure 4** which verifies the accuracy of this method.

4.2 Example Verification of the Optimal Energy Flow Calculation of the Electrothermal Coupling System

In this chapter, the model of the 14-node grid and 14-node heating network shown in **Figure 5** is selected for example verification. Two heat sources *S*1 and *S*2 in the heating network are connected with 6 and 11 nodes in the grid, respectively. The parameters of the two heat source nodes of the back pressure unit and heat load nodes in the combined system are set as shown in **Table 3**.

When setting the objective function, the minimum operating cost is selected as the objective function, and the fitting constant in the objective function is selected in **Table 4**. After setting the initial values and upper and lower limits of each parameter, the simulation is carried out according to the optimal energy flow calculation method described in **Section 3.4**, and the running cost of the system is minimized by adjusting the thermal power and electric power of the power supply and heat source. The comparison diagram of pipeline flow calculation results of optimal power flow and general power flow is shown in **Figure 6** and **Table 5**. The comparison diagram of the supply and return temperature of each node is shown in **Figure 7** and **Table 6**.

The node temperature obtained from the optimal power flow calculation is determined by optimizing the control variables, while the control variables in the ordinary power flow are initially given. Therefore, it is more economical to introduce the results of the optimal power flow into the actual operation, and the coal consumption will be lower, thus achieving the purpose of the optimal energy flow calculation.

5 CONCLUSION

In this study, an improved forward push-back substitution method is proposed for the combined electric and heat system. First, models of individual systems and coupled parts are built, and the calculation model of the electro-thermal combined system is constructed. The improved forward-backward substitution method is used for energy flow calculation to realize the analysis and calculation of the energy flow of the whole combined system. Finally, through the calculation and analysis of the example of the comprehensive energy test system, it is proved that the idea proposed in this study can be practically used. In the part of the study of the optimal energy flow calculation method, the interior point method is used to find the parameters that meet the optimal operation conditions of the system. By comparing the simulation results of energy flow calculation and optimal energy flow calculation, it can be obtained that the interior point method is feasible and economical to calculate the optimal energy flow of the electrothermal combined system.

DATA AVAILABILITY STATEMENT

The original contributions presented in the study are included in the article/supplementary material, further inquiries can be directed to the corresponding author.

AUTHOR CONTRIBUTIONS

ZL was responsible for the main idea, simulation part, and writing work of this study. YZ and JX were responsible for the mathematical derivation. QS participated in the coordination of the study and reviewed the manuscript.

FUNDING

This work was supported by the Key R&D Program of Liaoning Province (2020JH2/10300101), the Liaoning Revitalization Talents Program (XLYC1907138), the Technology Innovation Talent Fund of Shenyang (RC200252), and the Key R&D Program of Shenyang (GG200252).

ACKNOWLEDGMENTS

The authors acknowledge the funding of the Key R&D Program of Liaoning Province (2020JH2/10300101), the Liaoning Revitalization Talents Program (XLYC1907138), the Technology Innovation Talent Fund of Shenyang (RC200252), and the Key R&D Program of Shenyang (GG200252).

REFERENCES

Chen, B. B., Sun, H. B., Yin, G. X., Wu, W. C., and Guo, Q. L. (2020). Energy Circuit Theory of Integrated Energy System Analysis (II): Hydraulic Circuit and Thermal Circuit. *Proc. CSEE* 40, 2133–2142. doi:10.13334/j.0258-8013.pcsee.200098

Guo, Z. G., Lei, J. Y., Ma, X. Y., Yuan, Z. Y., Dong, B., and Yu, H. (2019). Modeling and Calculation Methods for Multi-Energy Flows in Large-Scale Integrated Energy System Containing Electricity, Gas, and Heat. *Proc. CSU-EPSA.* 31, 97–102. doi:10.19635/j.cnki.csu-epsa.000283

Hu, X., Shang, C., Cheng, H. Z., Wang, L., Chen, D. W., and Li, Y. (2020). Review and Prospect of Calculation Method for Energy Flow in Integrated Energy System. *Automation Electr. Power Syst.* 44, 179–191. doi:10.7500/AEPS20191113001

Jia, H. J., Wang, D., Xu, X. D., and Yu, X. D. (2014). Research on Some Key Problems Related to Integrated Energy Systems. *Automation Electr. Power Syst.* 39, 199–207. doi:10.7500/AEPS20141009011

Jiang, P., and Liang, L. (2015). Reactive Power Optimization of Hybrid AC/HVDC Power System Combining Interior Point Algorithm and Genetic Algorithm. *High. Volt. Eng.* 41, 724–729. doi:10.13336/j.1003-6520.hve.2015.03.004

Krause, T., Andersson, G., Fröhlich, K., and Vaccaro, A. (2011). Multiple-energy Carriers: Modeling of Production, Delivery, and Consumption. *Proc. IEEE* 99, 15–27. doi:10.1109/JPROC.2010.2083610

Li, J. L., Tian, L., and Lai, X. K. (2015). Outlook of Electrical Energy Storage Technologies under Energy Internet Background. *Automation Electr. Power Syst.* 39, 15–25. doi:10.7500/AEPS20150906004

Liu, H., Zhao, C. X., Ge, S. Y., Li, J. F., and Liu, J. Y. (2021). Sequential Power Flow Calculation of Power-Heat Integrated Energy System. *Automation Electr. Power Syst.* 45, 63–72. doi:10.7500/AEPS20200312009

Liu, X., Wu, J., Jenkins, N., and Bagdanavicius, A. (2016). Combined Analysis of Electricity and Heat Networks. *Appl. Energy* 162, 1238–1250. doi:10.1016/j.apenergy.2015.01.102

Moeini-aghtaie, M., Abbaspour, A., Fotuhi-firuzabad, M., and Hajipour, E. (2014). A Decomposed Solution to Multiple-Energy Carriers Optimal Power Flow. *IEEE Trans. Power Syst.* 29, 707–716. doi:10.1109/TPWRS.2013.2283259

OMalley, M., and Kroposki, B. (2013). Energy Comes Together: The Integration of All Systems [Guest Editorial]. *IEEE Power Energy Mag.* 11, 18–23. doi:10.1109/MPE.2013.2266594

Rui, W., Qiuye, S., Pinjia, Z., Yonghao, G., Dehao, Q., and Peng, W. (2020). Reduced-order Transfer Function Model of the Droop-Controlled Inverter via Jordan Continued-Fraction Expansion. *IEEE Trans. Energy Convers.* 35, 1585–1595. doi:10.1109/TEC.2020.2980033

Sun, G. Q., Wang, W. X., Wu, Y., Hu, W., and Jing, J. P. (2020). Fast Power Flow Calculation Method for Radiant Electric-Thermal Interconnected Integrated Energy System. *Proc. CSEE* 40, 4131–4141. doi:10.13334/j.0258-8013.pcsee.190583

Wang, R., Sun, Q., Hu, W., Li, Y., Ma, D., and Wang, P. (2021a). SoC-based Droop Coefficients Stability Region Analysis of the Battery for Stand-Alone Supply Systems with Constant Power Loads. *IEEE Trans. Power Electron.* 36, 7866–7879. doi:10.1109/TPEL.2021.3049241

Wang, R., Sun, Q., Ma, D., and Liu, Z. (2019). The Small-Signal Stability Analysis of the Droop-Controlled Converter in Electromagnetic Timescale. *IEEE Trans. Sustain. Energy* 10, 1459–1469. doi:10.1109/TSTE.2019.2894633

Wang, R., Sun, Q., Tu, P., Xiao, J., Gui, Y., and Wang, P. (2021b). Reduced-order Aggregate Model for Large-Scale Converters with Inhomogeneous Initial Conditions in DC Microgrids. *IEEE Trans. Energy Convers.* 36, 2473–2484. doi:10.1109/TEC.2021.3050434

Xia, T., Chen, Y. W., Guo, Q. L., Sun, H. B., Xiong, W., and Liu, Y. Q. (2017). Power Flow Calculation Based on PSASP for Combined Thermal and Electric Energy System. *Electr. Power Autom. Equip.* 37, 55–61. doi:10.16081/j.issn.1006-6047.2017.06.008

Yu, J., Yang, D., and Chen, Z. (2021). Multi-energy Flow Calculation Based on Energy Cell and Parallel Distributed Computation. *Int. J. Electr. Power & Energy Syst.* 131, 107147. doi:10.1016/j.ijepes.2021.107147

Zhang, T., Li, Z., Wu, Q., Pan, S., and Wu, Q. H. (2022). Dynamic Energy Flow Analysis of Integrated Gas and Electricity Systems Using the Holomorphic Embedding Method. *Appl. Energy* 309, 118345. doi:10.1016/j.apenergy.2021.118345

Zhang, Y. Z., Wang, X. J., He, J. H., and Gao, W. Z. (2019). Optimal Energy Flow Calculation Method of Integrated Energy System Considering Thermal System Modeling. *Trans. China Electrotech. Soc.* 34, 563–570. doi:10.19595/j.cnki.1000-6753.tces.L80501

Conflict of Interest: QS was employed by the State Grid Liaoning Electric Power Co., Ltd.

The remaining authors declare that the research was conducted in the absence of any commercial or financial relationships that could be construed as a potential conflict of interest.

ORIGINAL RESEARCH
published: 21 June 2022
doi: 10.3389/fenrg.2022.915125

Auxiliary Service Market Model Considering the Participation of Pumped-Storage Power Stations in Peak Shaving

Zilong Zhang*, Wenbo Cong, Shizhong Liu, Chenglong Li and Shaolong Qi

Operation and Maintenance Department, Liaoning Pushihe Pumped Storage Co. Ltd., Dandong, China

In the context of insufficient system operation flexibility and increasing peaking pressure caused by the large-scale integration of renewable energy into the grid, a market model for peaking auxiliary services involving pumped storage power stations is proposed in this study. First, taking the minimum peak shaving cost as the optimization goal, the peak shaving value of the participating peak shaving units is quantified, and the mathematical model of the peak shaving auxiliary service market is established. Then, considering that the pumped-storage power station has both source-load characteristics, the peak-shaving value of the pumped-storage power station is deeply excavated to share the peak-shaving pressure of thermal power units, and a compensation mechanism for peak ancillary service fees is established. Finally, the 11-machine, 14-node system topology is proposed to simulate the peak-shaving auxiliary service market model proposed in this study, and the effectiveness of the proposed method is verified.

Keywords: pumped storage power station, peak shaving, ancillary service fee, Shapley value method, expense compensation

Edited by:
Rui Wang,
Northeastern University, China

Reviewed by:
Hongjing Liang,
Bohai University, China
Yushuai Li,
University of Oslo, Norway

****Correspondence:***
Zilong Zhang
zhangzilong187@163.com

Specialty section:
This article was submitted to Smart Grids,
a section of the journal
Frontiers in Energy Research

Received: *07 April 2022*
Accepted: *09 May 2022*
Published: *21 June 2022*

Citation:
Zhang Z, Cong W, Liu S, Li C and Qi S (2022) Auxiliary Service Market Model Considering the Participation of Pumped-Storage Power Stations in Peak Shaving.
Front. Energy Res. 10:915125.
doi: 10.3389/fenrg.2022.915125

INTRODUCTION

In recent years, the installed capacity of renewable energy in China has been increasing. By the end of 2021, China's installed renewable energy capacity reached 3.584 × 108 kW, signifying a year-on-year increase of 23.4% (Lyu et al., 2021). As the proportion of renewable energy connected to the grid continues to increase, the demand for peak shaving capacity of the power grid during the load trough period increases accordingly (Bie et al., 2017; Qi et al., 2019; Li et al., 2019). At the same time, the output of new energy generating units is restricted by primary energy, and they do not have peak shaving capability. The cost of starting and stopping thermal power generating units is high, and they operate in uneconomical areas during deep peak shaving, with insufficient flexibility and poor economy (Shi et al., 2018; Chen et al., 2022; Wang et al., 2020a; Wang et al., 2020b). Pumped-storage power plants have good regulation characteristics and low regulation costs and hence are suitable as the main peak-shaving power sources (Zou et al., 2015; Guo et al., 2018; Wang C. et al., 2020). Therefore, the study of the sharing mechanism of peak shaving auxiliary service cost in the participation of pumped storage power stations is beneficial to improve the flexibility of system operation and the enthusiasm of power generation enterprises to participate in peak shaving.

At present, a large number of research studies have been carried out on the problem of the allocation of peak shaving auxiliary services at home and abroad. Huang, 2020 considered the energy loss and equipment loss factors of thermal power generating units, establishes the peak shaving impact index, and realizes the reasonable allocation of peak shaving costs for thermal power generating units; Ma et al. (2021) studied the allocation and correction mechanism of inter-provincial peak shaving resources to provide theoretical support for cross-provincial scheduling of peak shaving resources; Jian et al. (2018) established an improved peak-shaving auxiliary service fee compensation mechanism model based on Kaldor, which improves the wind power absorption capacity and overall economy of the system; Y. Fu et al. (2019) used the *K*-means clustering algorithm to classify the peak shaving capacity of units and solved the problem of "dimension disaster" in the calculation process when a large number of units participate in peak shaving; Wang et al. (2019) allocated the compensation fee to the user side in the form of additional electricity charges according to the demand for auxiliary services for peak shaving, which effectively improves the equity of fee allocation.

Most of the abovementioned literatures ensure the basic balance of power supply and demand in the system through the market cost allocation mechanism of the peak-shaving auxiliary services participated by thermal power generating units and users and reduce the number of transactions in the real-time balanced power market. However, the grid connection of large-scale photovoltaic and wind power in the system is not considered, and there is lack of pumped storage power stations to participate in peak regulation. In the case of large-scale, grid-connected renewable energy, the anti–peak shaving characteristics of wind power and photovoltaics lead to an increase in the peak-to-valley difference between loads and an increase in the demand for the peak shaving of the power grid. Moreover, the output of wind power and photovoltaic power generation depends on primary energy and cannot participate in peak shaving. The pumped-storage power station has both source and load characteristics, that is, through the reasonable switching between the pumping mode and the power generation mode, the thermal power generating unit can run in a more reasonable output range. Therefore, it is necessary to introduce pumped storage power stations to participate in the auxiliary service market in order to reduce the cost of system peak shaving and increase the enthusiasm of peak shaving power plants to participate in peak shaving. This study first considers the operating state of the units participating in peak shaving, establishes the minimum objective function of the system peak shaving cost, quantifies the peak shaving value of units participating in peak shaving in thermal power plants and pumped storage power stations, studies the peak shaving value of units participating in peak shaving, and establishes a mathematical model for the peak shaving auxiliary service market. Second, considering the good peak-shaving performance of the pumped-storage power station due to its source-load characteristics, it can relieve the pressure of lifting and lowering loads of thermal power plants for multiple periods of time. Therefore, the pumped storage power station is required to participate in peak shaving and bear the baseload to develop its peak shaving performance. Then, according to the idea of a cooperative game in game theory, the Shapley value method is used to allocate the auxiliary service fee for peak shaving and establish a compensation mechanism for the auxiliary service fee for peak shaving. Finally, the validity of the ancillary service market model proposed in this study is verified by an example.

PEAK SHAVING AUXILIARY SERVICE MARKET MODEL

The large-scale integration of wind power into the grid has a great impact on the power system, and it is necessary to rely on auxiliary services to ensure stable operation of the system. In general, the demand for ancillary services is divided into peak-shaving ancillary services, frequency-modulating ancillary services, and spinning reserve ancillary services (Tian et al., 2019). The peak-shaving auxiliary service market guides the participating peak shaving units to make reasonable output adjustments through changes in peak shaving indicators and compensation fees to ensure stable operation of the power grid.

The operating period of the system was set as T and the number of periods is an integer between 1 and 24. The set of thermal power generating units is I, where $I = i_1, i_2, \cdots, i_n$; the set of generating units of pumped storage power stations is H, where $H = h_1, h_2, \cdots, h_n$.

Objective Function

Taking the minimum system peak shaving cost as the optimization goal, the objective function is established as follows:

$$min\, F = C_{\mathrm{PS}} + C_I, \tag{1}$$

$$C_{\mathrm{PS}} = C_{\mathrm{PS}}^{\mathrm{on}} + C_{\mathrm{PS}}^{\mathrm{off}}, \tag{2}$$

$$C_{\mathrm{PS}}^{\mathrm{on}} = \sum_{t=1}^{24} \sum_{h=1}^{H} \begin{bmatrix} m_{h,t}^{\mathrm{ge}}\left(1 - m_{h,t-1}^{\mathrm{ge}}\right) + \\ m_{h,t}^{\mathrm{pw}}\left(1 - m_{h,t-1}^{\mathrm{pw}}\right) \end{bmatrix} C_{\mathrm{on}}^{H}, \tag{3}$$

$$C_{\mathrm{PS}}^{\mathrm{off}} = \sum_{t=1}^{24} \sum_{h=1}^{H} \begin{bmatrix} \left(1 - m_{h,t}^{\mathrm{ge}}\right)\left(m_{h,t-1}^{\mathrm{ge}} - m_{h,t}^{\mathrm{ge}}\right) + \\ \left(1 - m_{h,t}^{\mathrm{pw}}\right)\left(m_{h,t-1}^{\mathrm{pw}} - m_{h,t}^{\mathrm{pw}}\right) \end{bmatrix} C_{\mathrm{off}}^{H}, \tag{4}$$

$$C_I = C_I^D + C_I^{\mathrm{on}} + C_I^{\mathrm{off}}, \tag{5}$$

$$C_I^D = p_i max\{0, P_i - P_{D,i,t}\}, \tag{6}$$

$$C_I^{\mathrm{on}} = \sum_{t=1}^{24} \sum_{i=1}^{I} m_{i,t}\left(1 - m_{i,t-1}\right) C_{\mathrm{on}}^{I}, \tag{7}$$

$$C_I^{\mathrm{off}} = \sum_{t=1}^{24} \sum_{i=1}^{I} \left(1 - m_{i,t}\right)\left(m_{i,t-1} - m_{i,t}\right) C_{\mathrm{on}}^{I}, \tag{8}$$

where F is the peak shaving cost of the system; C_{PS} is the peak shaving cost of the pumped storage unit; C_{I} represents the peak shaving cost of the thermal power generating unit; $C_{\mathrm{PS}}^{\mathrm{on}}$ and $C_{\mathrm{PS}}^{\mathrm{off}}$ represent the start-up and stop-loss costs of the pumped storage unit, respectively; $m_{h,t}^{\mathrm{ge}}$ and $m_{h,t}^{\mathrm{pw}}$ are 0–1 integer variables, that is, $m_{h,t}^{\mathrm{ge}} = 1$ indicates that the pumped-storage unit h is in operation at the pumping condition at time t and $m_{h,t}^{\mathrm{ge}} = 0$ means that the pumped-storage unit h is out of service at the pumping condition at time t; $m_{h,t}^{\mathrm{pw}} = 1$ means that the pumped-storage unit h is in operation at the pumping condition at time t and $m_{h,t}^{\mathrm{pw}} = 0$ means that the pumped-storage unit h is out of operation at the pumping condition at time t; $C_{\mathrm{on}}^{\mathrm{H}}$ and $C_{\mathrm{off}}^{\mathrm{H}}$ are the single start-up and shutdown loss costs of a single pumped-storage unit, respectively; $C_{\mathrm{I}}^{\mathrm{D}}$, $C_{\mathrm{I}}^{\mathrm{on}}$, and $C_{\mathrm{I}}^{\mathrm{off}}$ are the in-depth peak shaving costs, startup peak shaving costs, and shutdown peak shaving costs, respectively; p_i E is the unit price of thermal power generating unit i for peak shaving in excess of deep peak shaving; P_i is the peak-shaving depth threshold of thermal power generating unit i; $P_{D,i,t}$ is the output of thermal power generating unit i at time t; $C_{\mathrm{on}}^{\mathrm{I}}$ and $C_{\mathrm{off}}^{\mathrm{I}}$ are the startup and shutdown costs of the thermal power generating unit, respectively; $m_{i,t} = 1$ indicates that the thermal power generating unit i is in a startup state at time t; $m_{i,t} = 0$ indicates that the thermal power generating unit i is in a shutdown operating state at time t.

The ancillary service market optimization model proposed in this study considering the participation of pumped-storage power stations in peak shaving is a mixed-integer nonlinear model, which is difficult to solve by conventional optimization algorithms. Therefore, the mixed-integer linear model is established as follows:

$$C_{\mathrm{PS},t} \geq C_{\mathrm{on}}^{H}\left[\left(1-m_{h,t-1}^{\mathrm{ge}}\right)+\left(1-m_{h,t-1}^{\mathrm{pw}}\right)\right]+C_{\mathrm{off}}^{H}\left[\left(1-m_{h,t}^{\mathrm{ge}}\right)+\left(1-m_{h,t}^{\mathrm{pw}}\right)\right], \tag{9}$$

$$C_{I,t}^{D} \geq p_i\left(P_i - P_{D,i,t}\right), \tag{10}$$

$$C_{I,t}^{\mathrm{on}} \geq C_{\mathrm{on}}^{I}\left(1-m_{i,t-1}\right), \tag{11}$$

$$C_{I,t}^{\mathrm{off}} \geq C_{\mathrm{on}}^{I}\left(1-m_{i,t}\right), \tag{12}$$

$$C_{\mathrm{PS},t} \geq 0, C_{I,t}^{D} \geq 0, C_{I,t}^{\mathrm{on}} \geq 0, C_{I,t}^{\mathrm{off}} \geq 0. \tag{13}$$

Restrictions

1) Power balance constraints

$$\sum\nolimits_{i\in I} P_i(t) + \sum\nolimits_{h\in H} P_h(t) + \sum\nolimits_{w\in W} P_w(t) = \sum\nolimits_{j\in J} L_j(t), \tag{14}$$

where P_i is the output of the thermal power generating unit i; P_h is the output of the pumped-storage generating unit; P_w is the output of the wind power generating unit w; L_j is the load demand of the node j.

2) Contact line constraints

$$SP_{\mathrm{G,all}} - SP_{\mathrm{L,all}} < P_r, \tag{15}$$

where S is the sensitivity matrix of generator set output and branch power flow; $P_{\mathrm{G,all}}$ is the output vector of the whole generator set; $P_{\mathrm{L,all}}$ is the node load vector; P_r is the branch active power flow constraint vector.

3) Spinning spare constraint

$$\sum\nolimits_{i\in I} P_{i,\max}(t) + \sum\nolimits_{h\in H} P_h(t) + \sum\nolimits_{w\in W} P_w(t) \geq \sum\nolimits_{j\in J} L_j(t) + P_{\mathrm{up}}, \tag{16}$$

$$\sum\nolimits_{i\in I} P_{i,\min}(t) + \sum\nolimits_{h\in H} P_h(t) + \sum\nolimits_{w\in W} P_w(t) \leq \sum\nolimits_{j\in J} L_j(t) + P_{\mathrm{down}}, \tag{17}$$

where $P_{i,\max}$ and $P_{i,\min}$, respectively, represent the upper limit and lower limit of the available output of the thermal power generating unit i; P_{up} and P_{down}, respectively, represent the systems upward and downward reserve requirements.

4) State constraints of thermal power generating sets

$$P_i(t) \in \left(P_{\mathrm{up}}, P_{\mathrm{down}}, P_{i,\max}, P_{i,\min}, V_i\right), \tag{18}$$

where V_i is the maximum ramp rate constraint of the thermal generator set.

5) Wind turbine state constraints

$$P_{w,\min}(t) \leq P_w(t) \leq P_{w,\max}(t), \tag{19}$$

where $P_{w,\max}(t)$ and $P_{w,\min}(t)$ represent the upper limit and lower limit of the available output of wind turbine w, respectively.

6) Pumped-storage power station constraints

$$m_{h,t}^{\mathrm{ge}} P_{\mathrm{PS},min}^{\mathrm{ge}} \leq P_{\mathrm{PS},t}^{\mathrm{ge}} \leq m_{h,t}^{\mathrm{ge}} P_{\mathrm{PS},ax}^{\mathrm{ge}}, \tag{20}$$

$$m_{h,t}^{\mathrm{pw}} P_{\mathrm{PS},min}^{\mathrm{pw}} \leq P_{\mathrm{PS},t}^{\mathrm{pw}} \leq m_{h,t}^{\mathrm{pw}} P_{\mathrm{PS},ax}^{\mathrm{pw}}, \tag{21}$$

$$m_{h,t}^{\mathrm{ge}} + m_{h,t}^{\mathrm{pw}} \leq 1, \tag{22}$$

where $P_{\mathrm{PS,\,max}}^{\mathrm{ge}}$ and $P_{\mathrm{PS,\,min}}^{\mathrm{ge}}$, respectively, represent the upper limit and lower limit of the power generation of the pumped storage power station; $P_{\mathrm{PS,\,max}}^{\mathrm{pw}}$ and $P_{\mathrm{PS,\,min}}^{\mathrm{pw}}$, respectively, represent the upper limit and lower limit of the pumping power of the pumped storage power station; $P_{\mathrm{PS},t}^{\mathrm{ge}}$ and $P_{\mathrm{PS},t}^{\mathrm{pw}}$ represent the output in the power generation mode and the output in the pumping mode of the pumped-storage power station at time t, respectively; the sum of $m_{h,t}^{\mathrm{ge}}$ and $m_{h,t}^{\mathrm{pw}}$ is less than or equal to 1, which means that the pumped storage unit can only be in a single working condition in the pumping mode and the power generation mode at the same time. When the pumped-storage power station participates in peak regulation, the adjustment capacity accounts for a small proportion of the overall installed capacity, so the upper reservoir capacity constraint of the pumped-storage power station is not considered.

Compensation Mechanism for Shapley Value Method Peak -Adjusting Assist Service Costs

According to the optimization result of the peak shaving auxiliary service market model aiming at the minimum peak shaving cost, it is determined as the compensation mechanism for the peak shaving auxiliary service fee. When the pumped storage power station does not participate in peak shaving, the conventional thermal power generating unit undertakes all peak shaving tasks, and the peak shaving cost is F'. When the pumped-storage power station participates in peak shaving and bears the baseload, the peak shaving cost of the whole network is F at this time from the optimization result of the peak shaving auxiliary service market model.

$$F_1' = C_I^{\mathrm{D},\Theta} + C_I^{\mathrm{on},\Theta} + C_I^{\mathrm{off},\Theta}, \tag{23}$$

where $C_{\mathrm{I}}^{\mathrm{D},\Theta}$, $C_{\mathrm{I}}^{\mathrm{on},\Theta}$, and $C_{\mathrm{I}}^{\mathrm{off},\Theta}$ are the in-depth peak shaving cost of thermal power generating units, the peak shaving cost of starting thermal power generating units, and the peak shaving cost of thermal power generating units shutting down, respectively. After the pumped storage power station participates in peak shaving and assumes the baseload, the peak shaving price decreases, that is, $F \geq F'$. The energy storage characteristics and power characteristics of the pumped storage power station can be reasonably switched between the pumping mode and power generation mode so that the thermal power generating unit can operate in a more reasonable output range. During the operation of the peak shaving auxiliary service market, the peak shaving contribution of the units should be quantified and compensated so as to ensure the enthusiasm for participating in the peak shaving power plant. In order to improve the economy of peak shaving of the system, increase the enthusiasm for participating in the market of peak shaving auxiliary services, and develop the peak shaving capabilities of various power plants, it is determined that the amount of compensation for peak shaving costs obtained by participating peak shaving units is not greater than the profit $F - F'$ of the system through this operation mode.

The cost of starting and stopping thermal power generating units is very high, and under low-output operating conditions, it will cause greater wear and tear on the unit, and the loss cost will increase. At the same time, the combustion stability of low-output units is reduced, which may result in combustion-supporting costs such as fuel injection. On the other hand, the pumped storage power station has good regulation ability and low-peak shaving cost because of its combination of source and load characteristics. In order to improve the income and enthusiasm of the power plants participating in peak regulation, this study uses the Shapley value method to allocate compensation fees to deeply explore the peak regulation value of pumped storage power plants.

The traditional peak-shaving auxiliary service market is based on the idea of statistics to allocate compensation fees (Lin et al., 2017). The allocation of compensation fees for power plants participating in the peak-shaving auxiliary service market is a cooperative game problem in game theory (Liu et al., 2018). In order to ensure the equity of the market and the enthusiasm of participating in peak shaving units, considering the synchronism of the unit's peak shaving value and its compensation, the Shapley value method is used to allocate the compensation fee, and the compensation mechanism for the auxiliary service fee for peak shaving with the participation of multiple power plants based on the cooperative game is used (Nan et al., 2021).

It is assumed that all the units participating in peak shaving belong to the set M, and the number of units is m. The peak shaving costs of the joint peak shaving unit $S \subseteq M$ and the joint peak shaving unit S are as follows:

$$F(S) = F - F_p(S), \tag{24}$$

where F is the grid peak shaving cost when the thermal power generating unit bears the baseload.; $F_p(S)$ is the unit in the joint peak shaving unit S participating in the grid peak shaving, and the units in the joint peak shaving unit all bear the power grid peak shaving cost when the baseload is used has $PC(N) = PC_1$.

The revenue function of the joint peak shaving unit is as follows:

$$R(S) = F(S) - \sum_{s \in S} F(S). \tag{25}$$

The peak-shaving ancillary service fee allocated based on the Shapley value method can be expressed as follows:

$$P_{sha,x}(R) = \sum_{s \in S} \frac{(n - |S|)!(|S| - 1)!}{n!} [R(S) - R(S - \{s\})], \tag{26}$$

where x is a certain peak shaving cost apportionment unit, $x = 1, 2, \cdots, n$; $P_{sha,x}(R)$ represents the combined peak shaving unit revenue apportioned to the unit; S represents the joint peak shaving unit including unit x; $|S|$ represents the number of units included in the joint peak shaving unit S; n represents the number of units providing peak shaving auxiliary services; $n!$ represents the participation sequence of all participants in the peak shaving unit N; $S - \{s\}$ represents the removal of the participant x from the joint peak shaving unit S; and $R(S) - R(S - \{s\})$ represents the incremental revenue created by unit S for the combined peak shaving unit.

CASE ANALYSIS

An 11-machine, 14-node system is proposed to simulate and verify the ancillary service market model proposed in this study considering the participation of pumped-storage power stations in peak shaving. The topology of the 11-machine, 14-node system is shown in **Figure 1**. The system has six thermal power generating units, which are located at nodes 2, 3, 7, 10, 12, and 14. The maximum force of the firepower generator is 550 mW, and the minimum output force is 100 MW. There are three pumped storage units located at nodes 4, 8, and 11. There are two wind turbines located at nodes 6 and 13. The system load is distributed in three load nodes, which are located at nodes 1, 5, and 9. The parameters of each branch of the system are shown in **Table 1**. A typical daily wind power generation curve is shown in **Figure 2**. A typical intraday load demand curve is shown in **Figure 3**.

According to the wind power output and load demand on a typical day, it can be seen that wind power has a strong anti–peak shaving characteristic. When the demand peaks in the 9h–13h and 18h–21h load curves, the wind power output is in a trough period. The peak-shaving demand was caused by the power shortage in the system. In the case of the 22–4 h load curve demand trough, wind power generation is in the peak period, causing trough peak regulation demand.

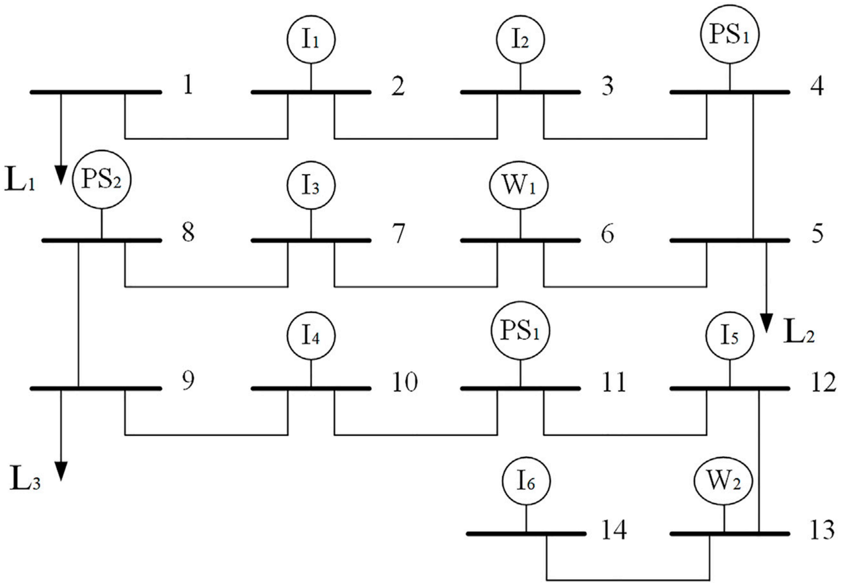

FIGURE 1 | Structure of 11-generator 14-node system topology.

TABLE 1 | 11 generator 14 node system branch parameters.

Branch	First node	Last node	P_r/MW
1	1	2	70
2	2	3	80
3	3	4	80
4	4	5	150
5	5	6	190
6	6	7	200
7	7	8	180
8	8	9	150
9	9	10	100
10	10	11	100
11	11	12	80

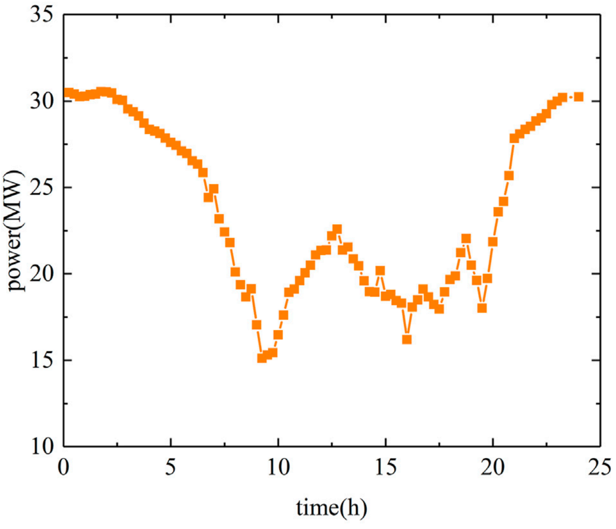

FIGURE 2 | Typical daily wind power generation curve.

The simulation environment uses the mixed-integer linear programming operator programming of the GAMS commercial optimization software to solve the auxiliary service market model proposed in this study considering the participation of pumped storage power stations in peak regulation, and the system optimization process can be solved within 23.3 s. The model and method proposed in this study are time-effective and suitable for scheduling intraday power generation and real-time scheduling.

From the perspective of game theory, all the peak shaving units in the system are nine players. According to the income difference obtained from the optimization results, the cooperative game method is applied to apportion the peak-shaving costs of nine units. The set of all players can be expressed as N = {1, 2, 3, 4, 5, 6, 7, 8, and 9}, and typical 21 non-empty subsets in the set are selected to form a joint peak shaving unit. The method proposed in this study is used to calculate the peak shaving cost of each unit in the combined peak shaving unit. The peak shaving cost of each unit in the joint peak shaving unit is shown in **Table 2**. It can be seen that when only the thermal power generating unit is responsible for peak shaving, the peak shaving cost is the highest. When pumped-storage power stations participate, according to different unit combinations,

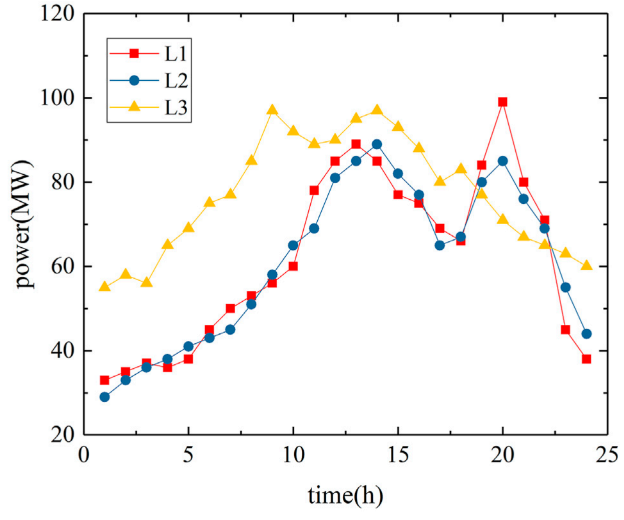

FIGURE 3 | Typical daily load demand curve of each node.

the peak shaving cost can be reduced by up to 50.61%. Considering that the pumped-storage power station participates in peak shaving, the peak-shaving cost is effectively reduced.

Figure 4 is the output curve of the pumped-storage unit, and the peak-shaving operation status of the pumped-storage unit and the thermal power unit at each moment are shown in **Figure 5**. It can be seen that under the auxiliary service market established in this study, considering the participation of pumped-storage power stations in peak shaving from 22 –4 h the next day, the pumped-storage power station works in the pumping mode and is mainly responsible for the task of peak shaving in low valleys. At this time, the thermal power plant can work in a more reasonable output range and does not need to significantly reduce the load. In 9–13 h and 18–21 h, there is a large power shortage in the system. The pumped storage power station works in the power generation mode and is mainly responsible for the task of peak regulation during the peak period. At this time, the thermal power generation unit works in the economic zone. Through the coordination of pumped storage power stations and thermal power plants, the cost of peak regulation is reduced.

TABLE 2 | Peak shaving cost of each unit in the joint peak shaving unit.

Unit	Peak shaving cost/10 × 10^3yuan	Unit combination	Peak shaving cost/10 × 10^3yuan
0	30.46	1, 2, 3	16.11
1	17.52	1, 2, 3, 4	15.66
2	21.63	1, 2, 3, 5	14.72
3	26.44	1, 2, 3, 6	15.13
4	22.78	1, 2, 3, 7	14.24
5	18.45	1, 2, 3, 8	15.87
6	20.16	1, 2, 3, 9	15.96
7	16.53	4, 5, 6, 7, 8, 9	15.76
8	25.62	1, 4, 5, 6, 7, 8, 9	14.88
9	27.88	2, 4, 5, 6, 7, 8, 9	15.17
1, 2, 3, 4, 5, 6, 7, 8, 9	13.77	3, 4, 5, 6, 7, 8, 9	15.48

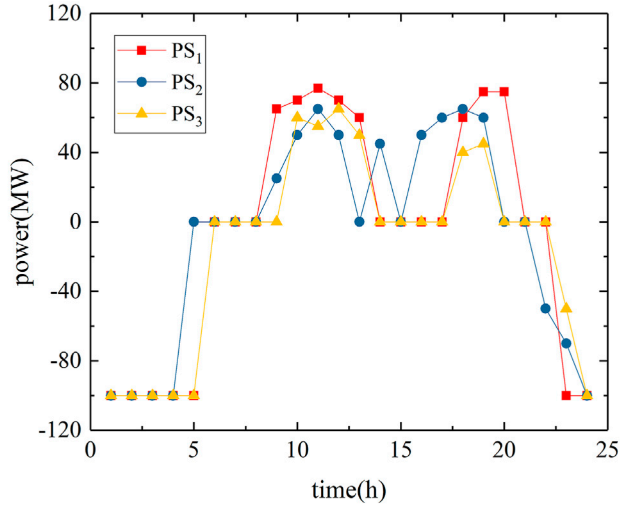

FIGURE 4 | Output curve of the pumped storage unit.

Table 3 shows the unit peak shaving compensation under the two methods of Shapley value and traditional peak shaving auxiliary service fee allocation. It can be seen that the unit with stronger peak shaving capability will receive more compensation for peak shaving costs. At the same time, the amount of peak shaving fee compensation obtained under the Shapley value method is more than that obtained under the traditional peak shaving auxiliary service fee allocation method. The traditional peak-shaving auxiliary service fee allocation method is based on the unit's peak-shaving value index, and the obtained cost-sharing is proportional to its peak-shaving capacity, which leads to low enthusiasm for units with relatively weak peak-shaving capacity and waste of peak-shaving resources. It also increases the peak load of some units. The Shapley value method is based on the marginal contribution of the unit to the alliance revenue, and the cost compensation per unit of peak shaving capacity must be more.

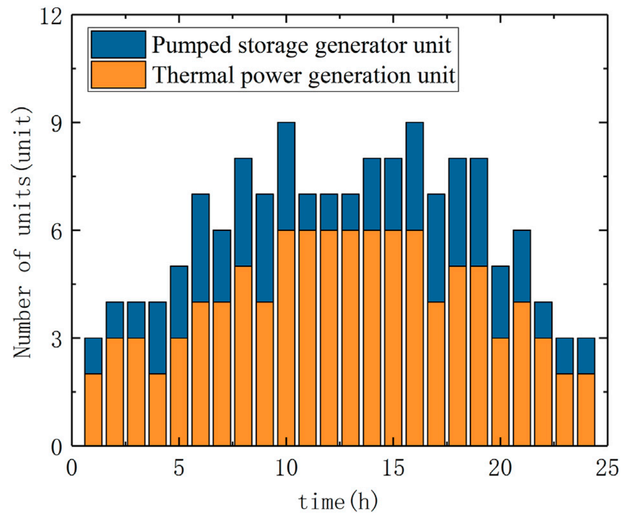

FIGURE 5 | Peak shaving operation status of the pumped storage unit and thermal power unit at each moment.

TABLE 3 | Compensation for unit peak shaving costs under different methods.

Unit	Shapley value method cost compensation/yuan	Traditional method cost compensation/yuan
1	1,411	1,096
2	1,278	952
3	1,213	297
4	1,269	864
5	1,364	1,043
6	1,291	1,022
7	1,475	1,186
8	1,223	375
9	1,201	176

CONCLUSION

In this study, a market model for peak shaving auxiliary services is established based on the background of large-scale grid connection of renewable energy in the power system. First, the pumped storage power station is introduced to participate in peak shaving, the peak shaving value of the units participating in peak shaving is quantified, and the compensation mechanism for peak shaving auxiliary service fees is established. Finally, the model proposed in this study is simulated and verified by an 11-machine, 14-node system. Taking the minimum peak shaving cost as the optimization goal, the peak shaving cost of each unit combination in the combined peak shaving unit is optimized. The results show that the peak shaving cost can be reduced by up to 50.61%. On this basis, the compensation amount of peak shaving costs obtained by the participating peak shaving units is determined according to the difference in peak shaving costs, the Shapley value method is used to allocate peak shaving auxiliary service fees, the enthusiasm of thermal power generating units with weak peak shaving capacity to participate in peak shaving units has been improved, and the peak shaving pressure of thermal power generating units has been eased.

DATA AVAILABILITY STATEMENT

The raw data supporting the conclusion of this article will be made available by the authors, without undue reservation.

AUTHOR CONTRIBUTIONS

ZZ and WC are responsible for the modeling work of the study. SL is responsible for the calculation work of the study. CL and SQ are responsible for the simulation work of the study.

FUNDING

This work is supported by State Grid Xinyuan Holdings Pushihe Company research and application services of key technologies for power station peak regulation assistance and multi-dimensional monitoring based on big data analysis (SGXYPH00YJJS2100149).

REFERENCES

Bie, Z., Wang, X., and Hu, Y. (2017). Review and Prospect of Planning of Energy Internet[J]. *Proc. CSEE* 37 (22), 6445. doi:10.13334/j.0258-8013.pcsee.171188

Chen, X., Huang, L., Liu, J., Song, D., and Yang, S. (2022). Peak Shaving Benefit Assessment Considering the Joint Operation of Nuclear and Battery Energy Storage Power Stations: Hainan Case Study. *Energy* 239, 121897. doi:10.1016/j.energy.2021.121897

Fu, Y., Chen, H., Jiang, X., and Sun, J. (2019). A Bi-layer Peakregulation Compensation Mechanism for Large-Scale Wind Power Integration[J]. *Power Syst. Prot. Control* 47 (4), 51. doi:10.7667/PSPC180261

Guo, Z., Ye, R., Liu, R., and Ye, J. (2018). Optimal Scheduling Strategy for Renewable Energy System with Pumped Storage Station[J]. *Electr. Power Autom. Equip.* 38 (3), 7. doi:10.16081/j.issn.1006-6047.2018.03.002

Huang, Q. (2020). Stochastic Economic Dispatch and Cost Allocation Considering Peak Regulation Influence Coefficient[J]. *Power Syst. Clean Energy* 36 (10), 33. doi:10.3969/j.issn.1674-3814.2020.10.006

Jian, X., Zhang, L., Yang, L., Han, X., and Wang, M. (2018). Deep-peak Regulation Mechanism Based on Kaldor Improvement under Highpenetration Wind Power[J]. *Automation Electr. Power Syst.* 42 (8), 110. doi:10.7500/AEPS20170614027

Li, Y., Zhang, H., Liang, X., and Huang, B. (2019). Event-triggered Based Distributed Cooperative Energy Management for Multienergy Systems[J]. *IEEE Trans. Industrial Inf.* 15 (14), 2008–2022. doi:10.1109/tii.2018.2862436

Lin, L., Zou, L., and Zhou, P. (2017). Multi-angle Economic Analysis on Deep Peak Regulation of Thermal Power Units with Large-Scale Wind Power Integration [J]. *Automation Electr. Power Syst.* 41 (7), 21. doi:10.7500/AEPS20160719005

Liu, W., Li, Y., and Guo, P. (2018). Stackelberg Game Decision for Lord-Source Associated Day-Ahead Peak Load Regulation[J]. *J. Syst. Simul.* 30 (8), 3066. doi:10.16182/j.issn1004731x.joss.201808030

Lyu, J., Zhang, S., Cheng, H., Li, K., and Yuan, K. (2021). Review and Prospect on Coordinated Planning of Energy Flow and Workload Flow in the Integrated Energy System Containing Data Centers[J]. *Proc. CSEE* 41 (16), 5500. doi:10.13334/j.0258-8013.pcsee.210326

Ma, X., Xue, C., Ren, J., Zhang, X., Meng, X., Yang, Y., et al. (2021). Design and Practice of Inter-provincial Peak Regulation Auxiliary Service Market Mechanism for Northwest China Power Grid[J]. *Electr. Power* 54 (6), 2. doi:10.11930/j.issn.1004-9649.202005050

Nan, J., Wang, P., and Li, D. (2021). A Solution Method for Sharply-Based Equilibrium Strategies of Biform Games[J]. *Chin. J. Manag. Sci.* 29 (5), 202. doi:10.16381/j.cnki.issn1003-207x.2018.0642

Qi, W., Li, J., Liu, Y., and Liu, C. (2019). Planning of Distributed Internet Data Center Microgrids. *IEEE Trans. Smart Grid* 10 (1), 762–771. doi:10.1109/tsg.2017.2751756

Shi, Y., Xu, B., Wang, D., and Zhang, B. (2018). Using Battery Storage for Peak Shaving and Frequency Regulation: Joint Optimization for Superlinear Gains. *IEEE Trans. Power Syst.* 33 (3), 2882–2894. doi:10.1109/tpwrs.2017.2749512

Tian, L., Xie, Y., Zhou, G., and Ge, W. (2019). Deep Peak Regulation Ancillary Service Bidding Strategy for CHP Units Based on Two-Stage Stochastic Programming[J]. *Power Syst. Technol.* 43 (8), 2789. doi:10.13335/j.1000-3673.pst.2019.0554

Wang, C., Qiao, Y., Liu, M., Zhao, Y., and Yan, J. (2020c). Enhancing Peak Shaving Capability by Optimizing Reheat-Steam Temperature Control of a Double-Reheat Boiler. *Appl. Energy* 260, 114341. doi:10.1016/j.apenergy.2019.114341

Wang, R., Sun, Q., Ma, D., and Hu, X. (2020b). Line Impedance Cooperative Stability Region Identification Method for Grid-Tied Inverters under Weak Grids[J]. *IEEE Trans. Smart Grid* 11 (4), 2856. doi:10.1109/TSG.2020.2970174

Wang, R., Sun, Q., Zhang, P., Gui, Y., Qin, D., and Wang, P. (2020a). Reduced-Order Transfer Function Model of the Droop-Controlled Inverter via Jordan Continued-Fraction Expansion[J]. *IEEE Trans. Energy Convers.* 35 (3), 1585. doi:10.1109/TEC.2020.2980033

Wang, Y., Liu, L., Li, X., Chen, H., Zhong, J., Shi, K., et al. (2019). Allocation Mechanism of Peak Load Regulation Auxiliary Service Cost[J]. *Guangdong Electr. Power* 32 (2), 1. doi:10.3969/j.issn.1007-290X.2019.002.001

Zou, J., Lai, X., and Wang, N. (2015). Coordinated Operation of Wind Power and Pumped Storage with the Goal of Reducing Wind Abandonment in the Power Grid [J]. *Power Syst. Technol.* 39 (9), 2472. doi:10.13335/j.1000-3673.pst.2015.09.015

Conflict of Interest: Authors ZZ, WC, SL, CL, and SQ were employed by Liaoning Pushihe Pumped Storage Co. Ltd.

frontiers | Frontiers in Energy Research

ORIGINAL RESEARCH
published: 24 June 2022
doi: 10.3389/fenrg.2022.914132

Distributed Secondary Control Strategy Against Bounded FDI Attacks for Microgrid With Layered Communication Network

Fuzhi Wang[1], **Qihe Shan**[1]*, **Fei Teng**[2], **Zhiqiang He**[3], **Yang Xiao**[4] **and Zhiyu Wang**[5]

[1]Navigation College, Dalian Maritime University, Dalian, China, [2]Marine Electrical Engineering College, Dalian Maritime University, Dalian, China, [3]China Railway Rolling Stock Corporation Zhuzhou Institute Co., Ltd., Zhuzhou, China, [4]Department of Computer Science, The University of Alabama, Tuscaloosa, AL, United States, [5]Zhejiang Laboratory, Hangzhou, China

This paper investigates FDI attacks in distributed secondary control strategy for low inertia microgrid with a high proportion of renewable energy and power electronics. Adversaries always aim to tamper information exchange between the neighbor distributed generators (DGs) in microgrids, which results in voltage and frequency deviation leading to power breakdown. To enhance the resilience against FDI attacks of microgrid, a control network layer interconnecting with the original data transmission layer is introduced to form a layered communication network. Due to the higher openness of the layered network, the introduced control network layer also faces to potential FDI attacks. This paper proposed a distributed secondary control strategy against double-layered bounded FDI attacks rather than only attacks in the information transmission layer. The strategy can mitigate FDI attacks launched in the control network layer, and adverse influence on the data transmission layer can also be mitigated caused by FDI attacks launched in the control network layer by designing proper interconnecting matrices. In this paper, the Lyapunov theory is used to demonstrate that the strategy can make the low inertia microgrid still maintain stable against double-layered bounded FDI attacks. The effectiveness of the distributed secondary strategy against bounded FDI attacks is validated in a test microgrid consisting of 4 DGs using the Matlab/Simpower system.

Keywords: layered communication network, distributed secondary control strategy, bounded FDI attacks, inverter-based distributed generator, low inertia microgrids

Edited by:
Wei Hu,
Zhejiang University, China

Reviewed by:
Lefeng Cheng,
Guangzhou University, China
Bingyu Wang,
North China Electric Power University, China
Jianguo Zhou,
Tsinghua University, China
Xuguang Hu,
Northeastern University, China

****Correspondence:***
Qihe Shan
shanqihe@163.com

Specialty section:
This article was submitted to Smart Grids,
a section of the journal Frontiers in Energy Research

Received: *06 April 2022*
Accepted: *11 May 2022*
Published: *24 June 2022*

Citation:
Wang F, Shan Q, Teng F, He Z, Xiao Y and Wang Z (2022) Distributed Secondary Control Strategy Against Bounded FDI Attacks for Microgrid With Layered Communication Network.
Front. Energy Res. 10:914132.
doi: 10.3389/fenrg.2022.914132

1 INTRODUCTION

Grid-connected operation of DGs with a high proportion of renewable energy has become a feature of current microgrids (Liang, 2017; Sockeel et al., 2020), which requires more power electronic equipments to replace part of the synchronous generators in microgrids. This trend can improve the efficiency of energy conversion, but reduce the inertia of microgrids. There exists complex uncertainties in microgrids, ensuring frequency stability is essential for low inertia microgrids.

The operation framework of microgrids is proposed in (Bidram and Davoudi, 2012). When the microgrid is connected to the main grid, its operating frequency and voltage are determined by the main grid (Rui et al., 2020). When the microgrid operates in an islanded mode, the hierarchical control framework regulates its standardized operation. The hierarchical control framework divides the frequency control in the microgrid into three levels. Primary control strategies mean that when loads are suddenly connected or cut off, the output power of microgrids should be increased or decreased accordingly to maintain the balance between the output power and the power required by loads. According to the droop mechanism, when the output power of the microgrid changes, it will lead to a frequency fluctuation. When the rated frequency is 50 Hz, the frequency of the microgrid is allowed to fluctuate between 49.5 and 50.2 Hz. Without human intervention, the microgrid will accommodate the fluctuation in a small range through its frequency capacity. If the fluctuation exceeds the normal range, the microgrid cannot maintain operating frequency stable only by relying on its frequency capacity. At this point, manual secondary control is required. Secondary control strategies refer to design the primary control reference point, which make the reference point change from a fixed value to a dynamic one, and make the operating frequency and voltage of the microgrid fluctuate around the rated value all the time. Finally, tertiary control strategies involve power flow calculation in the microgrid, which aim to optimize the operation of the microgrid economically and efficiently (Wang et al., 2021). It can be seen from three levels of the control framework that secondary control strategies are crucial for the safe operation and high-quality power supply of microgrids, so the reliability of the secondary control strategies level is particularly important. Microgrids mainly focus on security and reliability analysis. Security is to evaluate the ability of the system to maintain continuous power supply in the cases of open and short circuit. Reliability refers to the evaluation of the performance of microgrids for a long time. As long as there is no power breakdown, the reliability evaluation of microgrids will not be affected. It can be seen that security and reliability are defined for general failures. The resilience research aimed at the extreme disturbance or cyberattacks, which is an effective supplement to the security and reliability of microgrids.

In the past microgrid operation, secondary control strategies usually adopted centralized control methods. Due to the wide distribution and strong fluctuation of renewable energy, it is quite necessary to exchange information between neighbor DGs based on distributed energy resources (DERs). However, centralized point-to-point control strategies impose a great burden on communication facilities in this case. At present, centralized secondary control strategies are gradually transitioning to distributed secondary control strategies, which are inspired by the cooperative control based on multi-agent systems (MASs) (Olfati-Saber and Murray, 2004; Bidram et al., 2014; Shafiee et al., 2014). That is, distributed secondary control strategies applied to the microgrid consider each inverter-based DG as an agent, and DGs carry out a lot of information exchange and calculation through the communication network. However, it should be noted that attacks are quite pervasive in the communication network environment. Especially, transmission and distribution network, an obvious target that will generate huge economic losses after being attacked, will attract the attention of potential attackers. For example, Ukraine's power grid was attacked in 2015, resulting in a power outage (Liang et al., 2017). Distributed secondary control strategies seldom consider the adverse influence of attacks in the network environment. If the communication network between the neighbor DGs in the microgrid are attacked, they will gradually deviate from the rated frequency due to the lack of accurate information exchange. In this way, the output frequency of each DG in the microgrid will be out of synchronization and then oscillate. The most pervasive and classic cyber attacks in microgrids include false data injection (FDI) (Liu et al., 2011; Hu et al., 2018; Qu et al., 2021; Sinha et al., 2021) and denial of service (DoS) attacks. FDI attacks show that attackers launch false information into the communication network to tamper with real information. DoS attacks show that attackers send a large number of packets to block communication channels for preventing information exchange. In the operation process of microgrids, the application of firewalls (Salah et al., 2012; Zhang et al., 2019), gates (Condry and Nelson, 2016), and other technologies can effectively defend against DoS attacks. In addition to DoS attacks, FDI attacks also often occur in MASs.

A class of more sophisticated FDI attack can be designed after adversaries have known parameters of system matrices. This class of FDI attacks can evade traditional detection methods, such as χ^2 detection method, while tampering information exchange between neighbor DGs. Therefore, FDI attacks are more destructive and stealthier compared with DoS attacks. Distributed secondary strategies against FDI attacks mainly include detecting and isolating the attacked DG (Manandhar et al., 2014; Beg et al., 2017; Musleh et al., 2020; Xiahou et al., 2022) and designing resilient algorithms to defend against FDI attacks (Jin et al., 2017; Abhinav et al., 2018; Zhou et al., 2020). However, attack detection strategies have large computational burdens, and isolated DG nodes will adversely affect the connectivity of communication networks (Sundaram and Hadjicostis, 2011; Pasqualetti et al., 2012). Attack-resilient strategies have attracted more attention from researchers, which are characterized by improving the resilience of the communication network to effectively mitigate adverse effects caused by stealthy FDI attacks. Through the design of trust-based resilience control protocol in (Abhinav et al., 2018), the adverse influence of FDI attacks on communication links and sensors can be mitigated (Zhou et al., 2020). Adopted aperiodic intermittent control strategy with random switching frequency to improve the resilience of the microgrid against time-varying FDI attacks (Jin et al., 2017). Proposed a communication network structure based on the software-defined network (SDN) of the microgrid, indicating attack-resilient strategies can significantly improve the stability and security of communication networks in the SDN environment. Although (Abhinav et al., 2018) and (Zhou et al., 2020) have improved the resilience of microgrids against FDI attacks, attacked DG nodes still need to be detected and then isolated. However, detection and isolation strategies not only have requirements on the connectivity of communication networks but also have limitations on the number of attacked DGs in the microgrid.

It is worth noting that there exists some work based on a layered communication network against FDI attacks, which is not limited by network connectivity and the number of attacked DGs. The attack-resilient control strategy proposed in

(Gusrialdi et al., 2018) introduces a virtual system with a hidden network, so that the whole system consisting of the original consensus system, virtual system, and attack dynamic is stable without any information about attack position. The strategies discussed above depend on the distributed controller and information exchange between the neighbor DGs, which perhaps are in different network layers. Different vendors produce different types of controller hardware. Accordingly, operating systems in these devices are often designed and developed by different vendors. As a result, strategies designed by researchers are difficult to be applied uniformly in each DG, and it consumes a lot of resources to standardize different operating systems. The SDN is an emerging network structure, it aims to separate the data transmission function from the control function of the communication network (Nunes et al., 2014; Kreutz et al., 2015; Mijumbi et al., 2016). The structure of the microgrid with the layered communication network is shown in **Figure 1**. As can be seen from **Figure 1**, the microgrid is composed of four layers: application layer, control network layer, data transmission layer, and power network layer. The application layer contains energy management, state estimation, data monitoring, and other functions, which are directly controlled by the users. The control network layer and the data transmission layer constitute the layered communication network. Information in the power network layer is transmitted to the layered communication network through sensors, and finally to SCADA in the application layer. After obtaining the power information, SCADA will send the reference information (frequency, voltage, etc.) required for information exchange between neighbor DGs to the data transmission layer. At the same time, the control network layer also can receive the reference information through the design of interconnection matrices.

Based on the introduced control network layer using SDN, (Chen et al., 2021; Zhou et al., 2021) apply the resilient control strategy proposed in (Gusrialdi et al., 2018) to distributed secondary control of the microgrid, and demonstrate that this

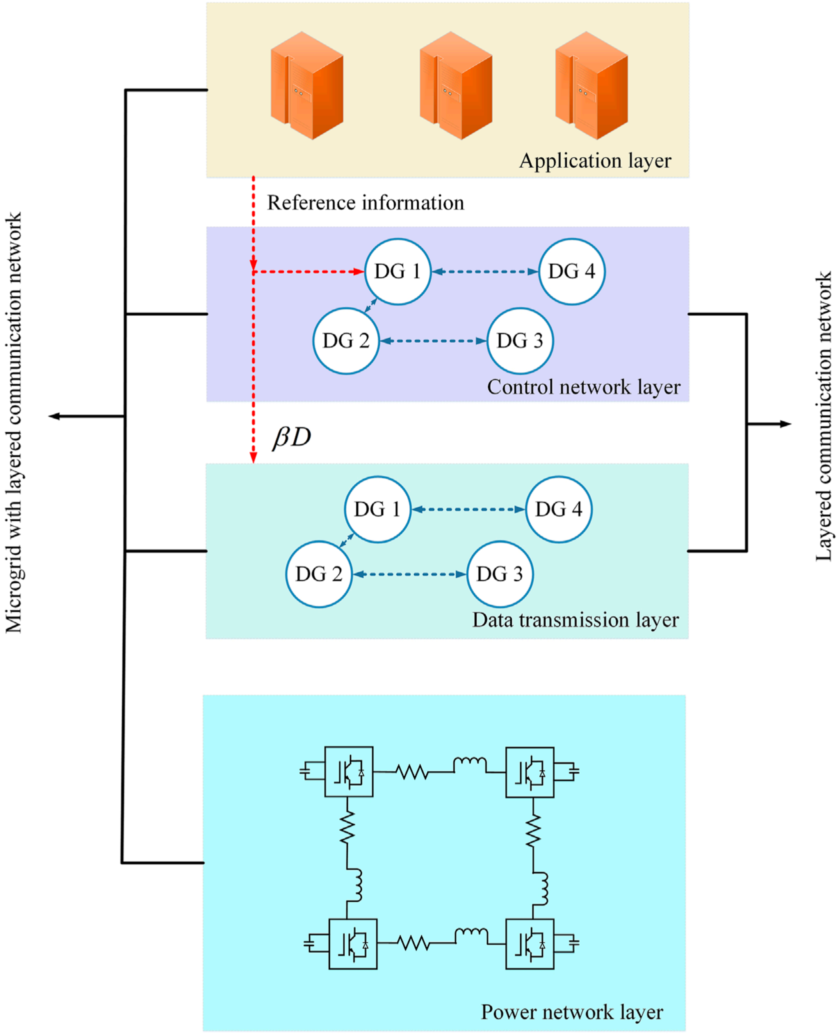

FIGURE 1 | The structure of the microgrid with the layered communication network.

strategy can effectively restrain the adverse influence of FDI attacks on the communication network between DGs (Zuo and Yue, 2022). further proposed a fully distributed control strategy to guarantee the uniformly ultimately bounded containment convergence of multigroup systems to resist unbounded FDI attacks, which have more stronger impact but are more easilier to be detected (Chen et al., 2021; Zhou et al., 2021). believe that the hidden network layer in (Gusrialdi et al., 2018) is less likely to be attacked, but in fact, the control network layer is still possible to be tempered by more stealthier attacks because the openness of the network will become wider after layering the communication network.

To solve this problem, this paper considers the case that bounded FDI attacks are launched in both the data transmission layer and the control network layer, and proposes a distributed secondary control strategy against double-layered bounded FDI attacks in the microgrid. The distributed secondary strategy proposed in this paper can be applied to microgrids with layered communication networks. The data transmission layer is responsible for the transmission of power information, and the control network layer is responsible for the control of information exchange. The layered communication network reduces the requirement on the local controller of each DG, and it is also convenient for managers to replace with advanced control strategies whenever necessary. When both the data transmission layer and control network layer suffered bounded FDI attacks launched by adversaries, angular frequency and active power sharing can maintain stable due to the stronger resilience provided by the layered communication network. And Lyapunov theory is used to demonstrate the strategy can effectively defend against double-layered bounded FDI attacks and maintain the stability of the microgrid.

The rest of this paper is organized as follows. The introduction of the graph theory and the control structure of each DG is presented in **Section 2**. The stability of the proposed strategy under the influence of bounded FDI attacks is demonstrated using Lyapunov theory in **Section 3**. The effectiveness of the proposed distributed secondary control strategy against double-layer bounded FDI attacks is validated in a microgrid test system consisting of 4 DGs using Matlab/Simpower system simulations in **Section 4**, and **Section 5** presents the summary of this paper.

2 PRELIMINARIES

This section introduces the communication network between DGs in the microgrid and the control structure of the inverter-based DG. And a nomenclature containing sets, parameters, and abbreviations is shown in **Table 1**.

TABLE 1 | Nomenclature table.

Symbol	Description
Index and Sets	
i,j	Index of DGs
$(\cdot)^T$	Transpose of the matrix
$\lVert\cdot\rVert$	Euclidean norm of the vector
$diag(\cdot)$	Diagonal matrix
$(\cdot)^e$	System equilibrium point with bounded FDI attacks
Parameters	
m_i	Droop coefficient of DG i
L	Laplacian matrix of the data transmission layer
G_b	The diagonal matrix containing gains between the leader and followers
A	A Hurwitz matrix calculated by L and G_b
H	An Arbitrary Hurwitz matrix
B	The vector of gains between the leader and followers
K,G	Interconnection matrices
Θ_1,Θ_2	The FDI attack vectors
β	The gain of interconnection matrices
Abbreviations	
FDI	False Data injection
DGs	Distributed Generators
MGs	Microgrids
DERs	Distributed Energy Resources
DoS	Denial of Service
SDN	Software-defined Network
SCADA	Supervisory Control and Data Acquisition
VSI	Voltage Source Inverter
DC	Direct Current
AC	Alternating Current
LC	Inductance and Capacitance
PWM	Pulse Width Modulation

2.1 Communication Network Between DGs

The microgrid discussed in this paper is a multi-agent cooperative control system containing N inverter-based DGs. Distributed secondary control strategies can maintain stable operating frequency and voltage only with the support of a communication network. Each DG is treated as an agent node, and the information flow between neighbor DGs is modeled by a direct graph $\varsigma = (v, \varepsilon, A_a)$ consisting of a node set $v = \{v_1, v_2, \ldots, v_N\}$ and an edge set $\varepsilon \subset v \times v$. $A_a = [a_{ij}] \in R^{N\times N}$ represents an adjacency matrix with $a_{ii} = 0$, $(i,j) \in \varepsilon$, $(i,j) \in \varepsilon$. Otherwise, $a_{ij} = 0$. $A_a = [a_{ij}] \in R^{N\times N}$ represents an adjacency matrix with $a_{ii} = 0$. If $(i,j) \in \varepsilon$, $a_{ij} = 1$. Otherwise, $a_{ij} = 0$, (i,j) means information flowing from DG j to DG i. DG j is called DG i's neighborhood if $(i,j) \in \varepsilon$, this is the definition of neighbor in this paper. The set of neighbors of DGi called $N_i = \{j|(i,j) \in \varepsilon\}$. The in-degree matrix D_{in} is a diagonal matrix representing as $D_{in} = diag\{d_1, d_2, \ldots, d_N\}$, where $d_i = \sum_{j=1}^{N} a_{ij} (i = 1, \ldots, N)$ is the number of neighbors of DG i. d_i is also the number of elements in N_i. The corresponding Laplace matrix can be defined as:

$$L_{ij} = \begin{cases} \sum_{j=1}^{n} a_{ij}, i = j \\ -a_{ij}, i \neq j \end{cases} \tag{1}$$

Generally, at least one DG can receive the reference information such as the rated angular frequency ω_{ref} given by SCADA in the application layer as shown in **Figure 1**. Such DG is called the leader in this paper, and the rest of DGs will exchange information through the communication network to track the leader's state. $b_i (i = 1, 2, \ldots, N)$ represents which DG is the leader. If $b_i = 1$, DG i is the leader, otherwise, DG i is not. The dynamic angular frequency expression in the islanded microgrid can be

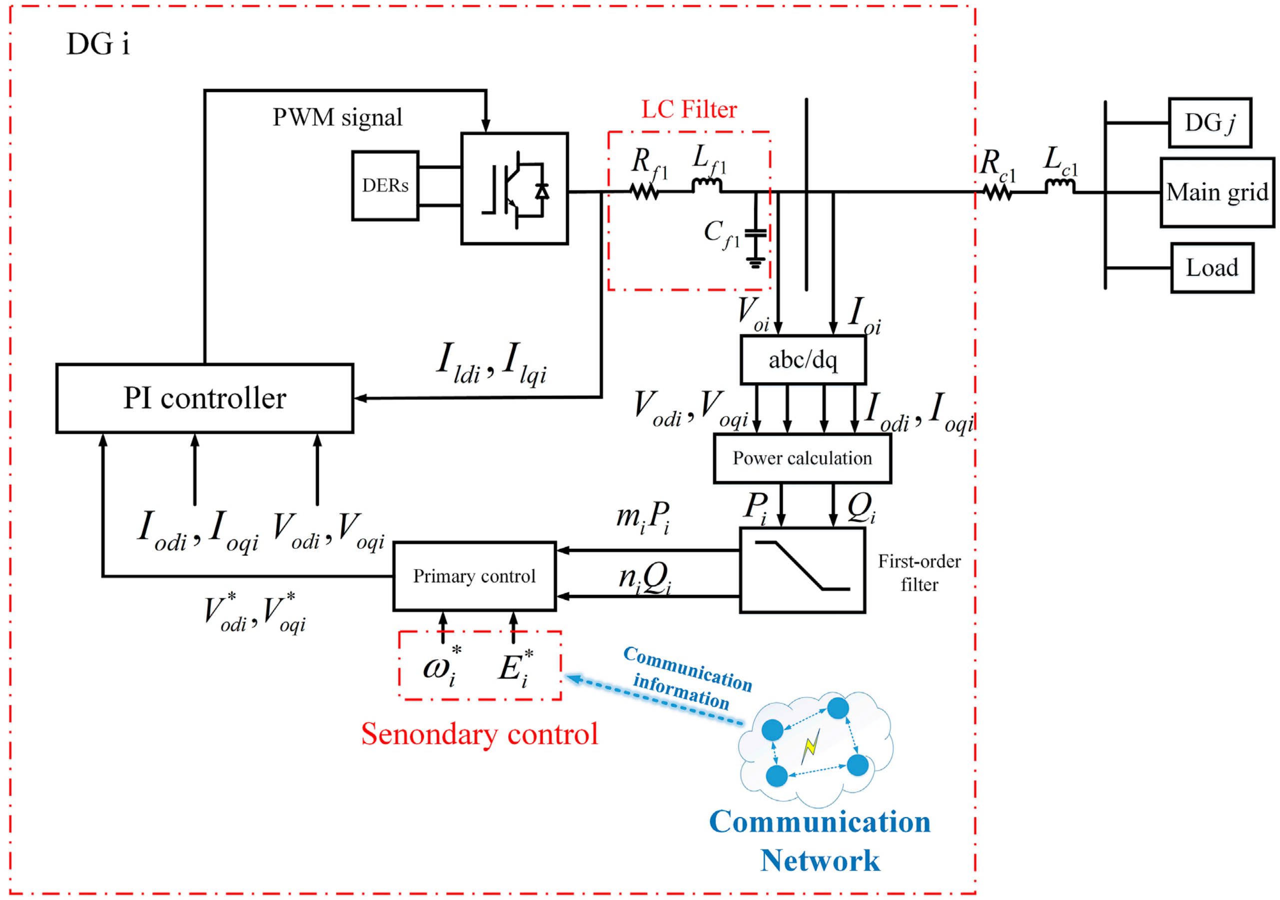

FIGURE 2 | The block diagram of the power electronics model and control structure of each inverter-based DG applied distributed secondary control strategy.

obtained as:

$$\dot{\omega} = -\left(L + G_b\right)\omega + B\omega_{ref} \tag{2}$$

where $B = (b_1, b_2, \ldots, b_N)^T$ and $G_b = diag(b_1, b_2, \ldots, b_N)$ here. (2) is a typical distributed secondary control strategy, but it is obvious that the expression does not consider how to restore the microgrid to the rated operation state when the communication network is attacked. The renewable energy facilities in microgrids are very expensive, and the damage of frequency oscillation to devices is permanent. Therefore, it is very important to design a distributed secondary control strategy against FDI attacks to maintain the stable operation of the microgrid.

2.2 Power Electronics Model and Control Structure of Each Inverter-Based DG

It can be seen from **Figure 1** that the design of the communication network layer is inseparable from the design of the power network layer (Pogaku et al., 2007; Wang et al., 2019; Ge et al., 2021). In this paper, the power network layer refers to an islanded microgrid consisting of multiple DGs. The control structure of each DG is shown in **Figure 2**.

As shown in **Figure 2**, the renewable energy storage device completes the conversion from dc to ac by connecting the port of the voltage source inverter (VSI). The inverter-based DG adopts current voltage double closed loop as control structure. V_{oi} and I_{oi} are output voltage and current of the DG, respectively. In order to more conveniently calculate the output power of each DG, V_{oi} and I_{oi} need to be transformed from abc axes to dq axes. The droop expression of the primary control strategy in **Figure 2** is shown as **(3)**:

$$\begin{cases} \omega_i = \omega_i^* - m_i P_i \\ V_{odi}^* = E^* - n_i Q_i \end{cases} \tag{3}$$

Combining active power P and ω_i^* according **(3)** yields V_{odi}^*, V_{oqi}^* which represents the reference input signal of the voltage loop controller. And how to design ω_i^* is the target of the secondary control strategy. Combining $V_{odi}^*, V_{oqi}^*, I_{odi}, I_{oqi}, V_{odi}$ and V_{oqi} yields the reference input signal of the current loop controller, where I_{odi}, I_{oqi} are output current of the DG. Voltage and current loop controller form PI controller together. Combining the reference input signal of the current loop controller and output current I_{ldi}, I_{lqi} of the inverter yields PWM signals which controls the sequence of switch actions of the inverter. The control circuit of each DG also has several series filters to mitigate the effect of harmonics. The whole DG connects the main grid and other DGs by R and L.

3 DISTRIBUTED SECONDARY CONTROL STRATEGIES AGAINST BOUNDED FDI ATTACKS

Primary control strategies of low inertia islanded microgrids mostly adopt the droop control method. The droop control method means that the microgrid balances the load variation by adjusting the output power of DGs. However, the primary control strategy is differential, that is, although the power balance of the microgrid is maintained, the angular frequency cannot be maintained at the rated value. To solve this shortcoming, secondary control strategies are designed to eliminate the difference value. Distributed secondary control strategies perform as cooperative control methods by sharing local power information between neighbor DGs. Generally, the communication network connectivity of microgrids is often high enough to exchange information, which also lays a potential risk for the spread of attacks rapidly in the communication network. Therefore, the potential attacks in the communication network should be considered when designing distributed secondary control strategies.

3.1 The Distributed Secondary Control Strategy Without FDI Attacks

The work in (Bidram et al., 2013, 2014) adopted the MAS-based distributed cooperative control method using input-output feedback linearization to design secondary control strategy of the microgrid. Once the multi-agent system is linearized by input-output feedback, the secondary control strategy of microgrids will lead to a first-order synchronization problem. The distributed secondary control protocol of each DG is shown in **(4)**, whose purpose is to synchronize the angular frequency of each DG to the rated value. The rated frequency in this paper is set to 50Hz, and accordingly, the rated angular frequency w_{ref} is set to 314 rad/s. The relationship between control protocol and primary control set point is shown in **(5)**:

$$u_i = -c\left[\sum_{j\in N_i} a_{ij}\left(w_i - w_j\right) + g_i\left(w_i - w_{ref}\right) + \sum_{j\in N_i} a_{ij}\left(m_iP_i - m_jP_j\right)\right] \tag{4}$$

$$w_i^* = \int u_i dt \tag{5}$$

Combine **(3)** and **(5)**, the expression $\dot{P}_i$ is shown in **(6)**, where w_{ci} represents the cut-off frequency of each DG. In this way, the angular frequency of microgrids can be obtained after primary control and secondary control adjustment, as shown in **(7)**:

$$\dot{P}_i = -w_{ci}P_i + w_{ci}\left(v_{odi}i_{odi} + v_{oqi}i_{oqi}\right) \tag{6}$$

$$w_i = \int u_i dt - m_iP_i \tag{7}$$

Distributed secondary control strategies without FDI attacks proposed in (Bidram et al., 2013, 2014) keep the angular frequency running within the rated range effectively under the condition of load disturbance. However, these strategies do not consider the case of external attack injection (Abhinav et al., 2018). Indicates that when the control protocol in (Bidram et al., 2014) suffers external FDI attacks, the frequency of each DG cannot be synchronized to the rated value. The severe frequency oscillation of each DG in the attacked microgrid will cause permanent damage to renewable energy facilities in the station, resulting in unnecessary economic losses. The distributed secondary control strategy exchanges information between neighbor DGs through a communication network to design ω_i^* and E^* compensating angular frequency and voltage changes. Obviously, the distributed secondary control strategy without attacks does not consider the adverse influence of cyber attacks when exchanging information between neighbor DGs. The most outstanding innovation of the distributed secondary proposed in this paper compared with the strategy without FDI attacks is that a layered communication network has been considered to enhance the resilience of microgrids against FDI attacks. Therefore, it is necessary to design a distributed secondary control strategy against FDI attacks.

3.2 Distributed Secondary Control Strategy Against FDI Attacks

Researches on cyber attacks in microgrids mainly focus on bounded FDI attacks, because stealthy bounded attacks are easier to disguise and often difficult to be detected by detection algorithms (Liu et al., 2011; Hu et al., 2018). Therefore, a distributed secondary control strategy against double-layered bounded FDI attacks in microgrids with the layered communication network is proposed in this paper, which can be described by

$$\begin{cases} \dot{w} = Aw + \beta Kz + Bw_{ref} + \Theta_1 \\ \dot{z} = Hz - \beta Gw + \beta Dw_{ref} + \Theta_2 \end{cases} \tag{8}$$

where $w = [w_1, w_2, \ldots, w_N]^T$ denotes the angular frequency of each DG in the data transmission layer of the microgrid. $z = [z_1, z_2, \ldots, z_N]^T$ denotes that each DG node in the data transmission layer corresponds to a control node in the control network layer. A can be calculated by $-(L + G_b)$, and H can be chosen as any sparse Hurwitz matrix. P_s, P_h are diagonal matrices, and the design of P_s, P_h, K, G, D is detailed in (Zhang et al., 2015; Gusrialdi et al., 2018). And **(8)** can be rewrited as

$$\begin{cases} \dot{w} = Aw + \beta Kz + Bw_{\mathrm{ref}} + \Theta_1 \\ \dot{z} = Hz - \beta P_h^{-1}K^TP_sw + \beta\left(P_h^{-1}K^TP_s1\right)w_{ref} + \Theta_2 \end{cases} \tag{9}$$

Assumption 1: The FDI attacks Θ_1, Θ_2 in this paper are bounded. It's worth noting that Θ_1, Θ_2 denote external bounded FDI attacks in the data transmission layer and control network layer, respectively. In other words, $\|\Theta_1\| \leq k_1$, $\|\Theta_2\| \leq k_2$, and k_1, k_2 are both constants. Define $\tilde{w} = w - w_{ref}1$ as the difference between w and w_{ref}, **(10)** can be obtained combining **(9)** and $\tilde{w}$, and the equilibrium state of **(10)** satisfies **(11)**:

$$\begin{cases} \dot{\tilde{w}} = A\tilde{w} + \beta Kz + \Theta_1 \\ \dot{z} = Hz - \beta P_h^{-1}K^TP_s\tilde{w} + \Theta_2 \end{cases} \tag{10}$$

$$\begin{cases} 0 = A\tilde{w}^e + \beta Kz^e + \Theta_1^e \\ 0 = Hz^e - \beta P_h^{-1}K^TP_s\tilde{w}^e + \Theta_2^e \end{cases} \tag{11}$$

Define error vectors $\overline{w} = w - w^e$, $\overline{z} = z - z^e$, the error dynamic can be shown as

$$\begin{cases} \dot{\overline{w}} = A\overline{w} + \beta K\overline{z} + \left(\Theta_1 - \Theta_1^e\right) \\ \dot{\overline{z}} = H\overline{z} - \beta P_h^{-1}K^TP_s\overline{w} + \left(\Theta_2 - \Theta_2^e\right) \end{cases} \tag{12}$$

where Θ_1 satisfies $\dot{\Theta}_1 = f(\Theta_1, w)$, Θ_2 satisfies $\dot{\Theta}_2 = f(\Theta_2, z)$. Θ_1^e, Θ_2^e from $0 = f(\Theta_1^e, w^e)$, $0 = f(\Theta_2^e, z^e)$ can be obtained respectively. To solve $\Theta_2 - \Theta_2^e$ in **(12)**, a Lyapunov function need to be determined. By the Lyapunov converse theorem, it is known that there exists a $V_{\Theta_1}(\Theta_1 - \Theta_1^e)$ satisfies **(13)**. Moreover, by the Lipschitz continuity, **(14)** can be obtained as

$$\begin{cases} \gamma_1\|\Theta_1 - \Theta_1^e\|^2 \leq V_{\Theta_1}\left(\Theta_1 - \Theta_1^e\right) \leq \gamma_2\|\Theta_1 - \Theta_1^e\|^2 \\ \dfrac{\partial V_{\Theta_1}}{\partial \Theta_1}f\left(\Theta_1, w^e\right) \leq -\gamma_3\|\Theta_1 - \Theta_1^e\|^2 \\ \left\|\dfrac{\partial V_{\Theta_1}}{\partial \Theta_1}\right\| \leq \gamma_4\|\Theta_1 - \Theta_1^e\| \end{cases} \tag{13}$$

$$\begin{cases} \|f\left(\Theta_1, w\right) - f\left(\Theta_1, w^e\right)\| \leq \gamma_5\|w - w^e\| \\ \|f\left(\Theta_1, w^e\right) - f\left(\Theta_1^e, w^e\right)\| \leq \gamma_6\|\Theta_1 - \Theta_1^e\| \end{cases} \tag{14}$$

Similarly, we have $V_{\Theta_2}(\Theta_2 - \Theta_2^e)$ satisfies **(15)** and **(16)**:

$$\begin{cases} \gamma_7\|\Theta_2 - \Theta_2^e\|^2 \leq V_{\Theta_2}\left(\Theta_2 - \Theta_2^e\right) \leq \gamma_8\|\Theta_2 - \Theta_2^e\|^2 \\ \dfrac{\partial V_{\Theta_2}}{\partial \Theta_2}f\left(\Theta_2, w^e\right) \leq -\gamma_9\|\Theta_2 - \Theta_2^e\|^2 \\ \left\|\dfrac{\partial V_{\Theta_2}}{\partial \Theta_2}\right\| \leq \gamma_{10}\|\Theta_2 - \Theta_2^e\| \end{cases} \tag{15}$$

$$\begin{cases} \|f\left(\Theta_2, z\right) - f\left(\Theta_2, z^e\right)\| \leq \gamma_{11}\|z - z^e\| \\ \|f\left(\Theta_2, z^e\right) - f\left(\Theta_2^e, z^e\right)\| \leq \gamma_{12}\|\Theta_2 - \Theta_2^e\| \end{cases} \tag{16}$$

where $\gamma_i (i = 1, 2, \ldots, 12)$ are all positive constants. Computing the time derivation of $V_{\Theta_1}(\Theta_1 - \Theta_1^e)$ yields $\frac{\partial V_{\Theta_1}}{\partial \Theta_1}f(\Theta_1, w)$. Combining **(13)** and **(14)** yields **(17)** as

$$\begin{aligned} &\frac{\partial V_{\Theta_1}}{\partial \Theta_1}f\left(\Theta_1, w\right) \\ &\quad = \frac{\partial V_{\Theta_1}}{\partial \Theta_1}\left[f\left(\Theta_1, w^e\right) + f\left(\Theta_1, w\right) - f\left(\Theta_1, w^e\right)\right] \\ &\quad = \frac{\partial V_{\Theta_1}}{\partial \Theta_1}f\left(\Theta_1, w^e\right) + \frac{\partial V_{\Theta_1}}{\partial \Theta_1}\left[f\left(\Theta_1, w\right) - f\left(\Theta_1, w^e\right)\right] \\ &\quad \leq -\gamma_3\|\Theta_1 - \Theta_1^e\| + \gamma_4\gamma_5\|\Theta_1 - \Theta_1^e\|\|w - w^e\| \end{aligned} \tag{17}$$

Similarly, combining **(15)** and **(16)** yields **(18)** as

$$\begin{aligned} &\frac{\partial V_{\Theta_2}}{\partial \Theta_2}f\left(\Theta_2, z\right) \\ &\quad = \frac{\partial V_{\Theta_2}}{\partial \Theta_2}\left[f\left(\Theta_2, z^e\right) + f\left(\Theta_2, z\right) - f\left(\Theta_2, z^e\right)\right] \\ &\quad = \frac{\partial V_{\Theta_2}}{\partial \Theta_2}f\left(\Theta_2, z^e\right) + \frac{\partial V_{\Theta_2}}{\partial \Theta_2}\left[f\left(\Theta_2, z\right) - f\left(\Theta_2, z^e\right)\right] \\ &\quad \leq -\gamma_7\|\Theta_2 - \Theta_2^e\| + \gamma_8\gamma_9\|\Theta_2 - \Theta_2^e\|\|z - z^e\| \end{aligned} \tag{18}$$

To demonstrate that the layered communication network is stable against double-layered bounded FDI attacks, we choose a Lyapunov function as

$$\begin{aligned} V = {} & \beta\overline{w}^TP_s\overline{w} + \beta\overline{z}^TP_h\overline{z} + V_{\Theta_1}\left(\Theta_1 - \Theta_1^e\right) + V_{\Theta_2}\left(\Theta_2 - \Theta_2^e\right) \\ & - 2\overline{z}^TP_hK^{-1}\left(\Theta_1 - \Theta_1^e\right) - 2\overline{w}^T\left(K^T\right)^{-1}P_h\left(\Theta_2 - \Theta_2^e\right) \end{aligned} \tag{19}$$

Next, the time derivation of V need to be computed. And $\dot{V}_{\Theta_1}(\Theta_1 - \Theta_1^e)$ and $\dot{V}_{\Theta_2}(\Theta_2 - \Theta_2^e)$ have been known from **(17)**, **(18)**. Define $2\overline{z}^TP_hK^{-1}(\Theta_1 - \Theta_1^e)$ and $2\overline{w}^T(K^T)^{-1}P_h(\Theta_2 - \Theta_2^e)$ as V_1, V_2. Then compute the time derivation of V_1, V_2, **(20)** and **(21)** can be obtained as

$$\begin{aligned} \dot{V}_1 = {} & 2\overline{z}^TP_hK^{-1}\left[f\left(\Theta_1, w\right) - f\left(\Theta_1^e, w^e\right)\right] \\ & + 2\overline{z}^TH^TP_hK^{-1}\left(\Theta_1 - \Theta_1^e\right) + 2\left(\Theta_2 - \Theta_2^e\right)^TP_hK^{-1} \\ & \times\left(\Theta_1 - \Theta_1^e\right) \end{aligned} \tag{20}$$

$$\begin{aligned} \dot{V}_2 = {} & 2\overline{w}^T\left(K^T\right)^{-1}P_h\left[f\left(\Theta_2, z\right) - f\left(\Theta_2^e, z^e\right)\right] \\ & + 2\overline{w}^TA^T\left(K^T\right)^{-1}P_h\left(\Theta_2 - \Theta_2^e\right) + 2\left(\Theta_1 - \Theta_1^e\right)^T\left(K^T\right)^{-1} \\ & \times P_h\left(\Theta_2 - \Theta_2^e\right) \end{aligned} \tag{21}$$

$$\begin{aligned} \dot{V}_1 - \dot{V}_2 = {} & 2\overline{z}^TP_hK^{-1}\left[f\left(\Theta_1, w\right) - f\left(\Theta_1, w^e\right)\right] \\ & + 2\overline{z}^TP_hK^{-1}\left[f\left(\Theta_1, w^e\right) - f\left(\Theta_1^e, w^e\right)\right] \\ & + 2\overline{z}^TH^TP_hK^{-1}\left(\Theta_1 - \Theta_1^e\right) - 2\overline{w}^T\left(K^T\right)^{-1}P_h \\ & \times\left[f\left(\Theta_2^e, z\right) - f\left(\Theta_2^e, z^e\right)\right] - 2\overline{x}^T\left(K^T\right)^{-1}P_h \\ & \times\left[f\left(\Theta_2, z^e\right) - f\left(\Theta_2^e, z^e\right)\right] - 2\overline{w}^TA^T\left(K^T\right)^{-1}P_h \\ & \times\left(\Theta_2 - \Theta_2^e\right) \end{aligned} \tag{22}$$

Since A is a Hurwitz matrix, there exists a matrix $P_s > 0$ such that $A^TP_s + P_sA < 0$. Similarly, we choose a Hurwitz and sparse matrix H, and there exists a matrix $P_h > 0$ such that $H^TP_h + P_hH < 0$. Define $Q_s = A^TP_s + P_sA$ and $Q_h = H^TP_h + P_hH$. The time derivation of V can be obtained as $\dot{V} = \beta\overline{w}^TQ_s\overline{w} + \beta\overline{z}^TQ_h\overline{z} + \frac{\partial V_{\Theta_1}}{\partial \Theta_1}f(\Theta_1, w) + \frac{\partial V_{\Theta_2}}{\partial \Theta_2}f(\Theta_2, z)$. Combining **(17)** and **(18)**, **(23)** can be obtained as

$$\begin{aligned} \dot{V} \leq {} & \beta\overline{w}^TQ_s\overline{w} + \beta\overline{z}^TQ_h\overline{z} - \gamma_3\|\Theta_1 - \Theta_1^e\| \\ & + \gamma_4\gamma_5\|\Theta_1 - \Theta_1^e\|\|w - w^e\| - \gamma_7\|\Theta_2 - \Theta_2^e\| \\ & + \gamma_8\gamma_9\|\Theta_2 - \Theta_2^e\|\|z - z^e\| + \dot{V}_1 - \dot{V}_2 \end{aligned} \tag{23}$$

where Q_s, Q_h, P_h, P_s, A, H, and K are all known matrices, and $\beta > 0$, $\beta\overline{w}^TQ_s\overline{w} < 0$, and $\beta\overline{z}^TQ_h\overline{z} < 0$. It can be observed that $\dot{V} < 0$ for all large values of β, hence the equilibrium state of the layered communication network exists as w^e, z^e satisfing **(11)**, in other words, **(12)** is stable. $z^e = H^{-1}(\beta P_h^{-1} K^T P_s \tilde{w}^e - \Theta_2^e)$ can be obtained from **(11)**, and then $\tilde{w}^e = (A + \beta^2 K H^{-1} P_h^{-1} K^T P_s)^{-1}(\beta^2 K H^{-1}\Theta_2^e - \Theta_1^e)$. And compute the time derivation of $\tilde{w}^e$, **(24)** can be obtained as

$$\begin{aligned}\lim_{t\to\infty} w(t) = w_{ref} + \left(A + \beta^2 K H^{-1} P_h^{-1} K^T P_s\right)^{-1} \\ \times \left(\beta^2 K H^{-1}\Theta_2^e - \Theta_1^e\right)\end{aligned} \qquad (24)$$

Obviously, the larger β is, the closer the angular frequency of the microgrid with layered communication network is to the rated operating value w_{ref} when influenced by bounded FDI attacks. How to select the most appropriate β is an optimization problem, which is also the future work of this paper. In conclusion, in the case that both the data transmission layer and the control network layer are influenced by bounded FDI attacks, the angular frequency can be restored to the rated operating value w_{ref}. In this section, the stability of the proposed strategy against bounded FDI attack is demonstrated using Lyapunov theory.

4 SIMULATION ANALYSIS

The effectiveness of the proposed distributed secondary control strategy against double-layer bounded FDI attacks is validated in a microgrid test system consisting of 4 DGs using Matlab/Simpower system simulations in this section.

Before initiating the simulation test on the microgrid composed of DGs, this section will verify the influence of bounded FDI attacks on DGs with different inertia shown as **Figure 3**. Set a set of DG i (i = 1, 2, 3, 4), droop coefficients of them are 3e-4, 4e-4, 5e-4, 6e-4, respectively. As shown in the figure below, with the increase of the active power output of each DG, the operating angular frequency also gradually decreases correspondingly, which is caused by the differential droop control mechanism. When the active power output reaches 2500 W, the same bounded FDI attacks are injected into the controllers of all DGs. Moreover, to ensure the effect of comparison, the location of external attacks are set within the controller of each DG. In this way, the size and position of attacks are guaranteed to be identical for each DG, and then the influence of attacks on DGs with different inertia can be observed distinctly. It can be seen that the operating angular frequency of DG1 is the least affected by attacks, while that of DG4 is the most affected. This shows that the frequency oscillation of the low inertia microgrid composed of DGs is more severe after being attacked. The distributed secondary control strategy designed in this paper can not only eliminate the difference phenomenon caused by droop control mechanism, but also effectively alleviate the influence caused by bounded FDI attacks in the low-inertia microgrid composed of DGs, so that the microgrid can operate at the rated angular frequency.

The circuit and communication topology of the microgrid test system are shown in **Figure 4**. The specifications of the microgrid test system are shown in **Table 2**, and the time step of the test microgrid test system is set to be 5e-6s.

Set DG1 in **Figure 4** as the leader, that is, only DG1 can receive the reference information of sent by SCADA. Matrixs of the distributed secondary control strategy proposed in this paper is selected as follows

$$A_a = \begin{bmatrix} 0 & 1 & 0 & 1 \\ 1 & 0 & 1 & 0 \\ 0 & 1 & 0 & 0 \\ 1 & 0 & 0 & 0 \end{bmatrix}, D_{in} = \begin{bmatrix} 2 & 0 & 0 & 0 \\ 0 & 2 & 0 & 0 \\ 0 & 0 & 1 & 0 \\ 0 & 0 & 0 & 1 \end{bmatrix}, B = \begin{bmatrix} 1 \\ 0 \\ 0 \\ 0 \end{bmatrix} \qquad (25)$$

$$H = \begin{bmatrix} -4 & 0 & 0 & 1 \\ 2 & -5 & 0 & 0 \\ 0 & 1 & -3 & 0 \\ 0 & 0 & 2 & -4 \end{bmatrix}, K = \begin{bmatrix} -2 & 1 & 0 & 0 \\ 1 & -2 & 0 & 1 \\ 0 & 0 & -2 & 0 \\ 0 & 1 & 0 & -2 \end{bmatrix},$$

$$A = \begin{bmatrix} -3 & 1 & 0 & 1 \\ 1 & -2 & 1 & 0 \\ 0 & 1 & -1 & 0 \\ 1 & 0 & 0 & -1 \end{bmatrix} \qquad (26)$$

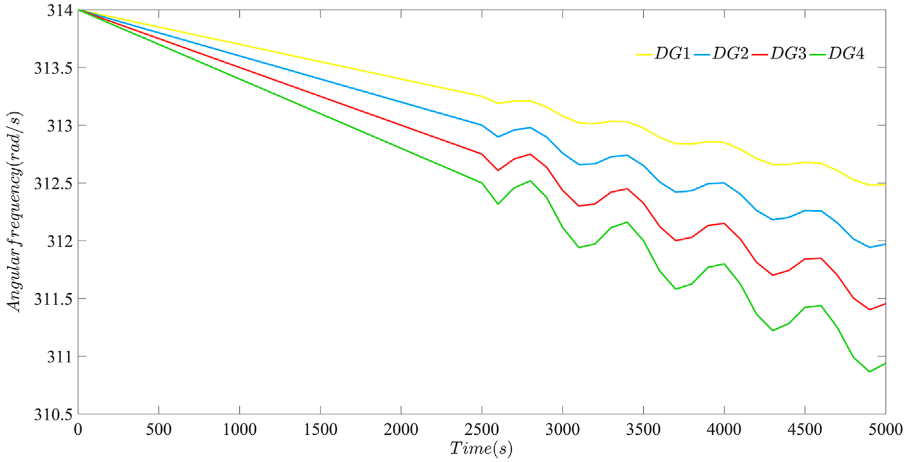

FIGURE 3 | Effect of bounded FDI attacks on angular frequency of DG i (i = 1, 2, 3, 4) with different inertia.

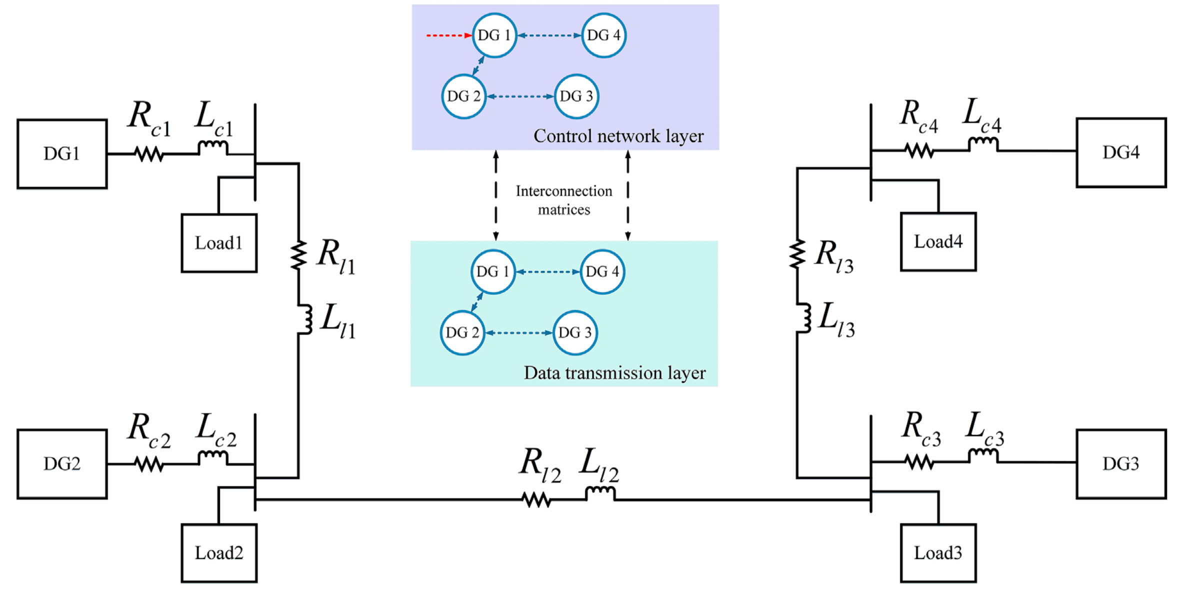

FIGURE 4 | The circuit model of the microgrid with the layered communication network.

TABLE 2 | Specifications of the microgrid test system with the layered communication network.

<table>
<tr><th colspan="4">Specifications setting of DGs, Lines, and Loads</th></tr>
<tr><td colspan="2">DG 1 and DG 2</td><td colspan="2">DG 3 and DG 4</td></tr>
<tr><td colspan="2">$m_P 3 \times 10^{-4}$</td><td colspan="2">$m_P 5 \times 10^{-4}$</td></tr>
<tr><td colspan="2">$n_Q 1 \times 10^{-2}$</td><td colspan="2">$n_Q 2 \times 10^{-2}$</td></tr>
<tr><td colspan="2">$L_c 0.35\ mH$</td><td colspan="2">$L_c 0.35\ mH$</td></tr>
<tr><td colspan="2">$R_c 0.03$</td><td colspan="2">$R_c 0.03$</td></tr>
<tr><td colspan="2">$R_f 0.1$</td><td colspan="2">$R_f 0.1$</td></tr>
<tr><td colspan="2">$C_f 50\mu F$</td><td colspan="2">$C_f 50\mu F$</td></tr>
<tr><td>Line12</td><td colspan="2">Line23</td><td>Line34</td></tr>
<tr><td>$R_{l1} 0.23\Omega$</td><td colspan="2">$R_{l2} 0.35\Omega$</td><td>$R_{l3} 0.23\Omega$</td></tr>
<tr><td>$L_{l1} 1 \times 10^{-6} mH$</td><td colspan="2">$L_{l2} 1 \times 10^{-6} mH$</td><td>$L_{l3} 1 \times 10^{-6} mH$</td></tr>
<tr><td>Load1</td><td>Load2</td><td>Load3</td><td>Load4</td></tr>
<tr><td>$R_{L1} 3\Omega$</td><td>$R_{L2} 3\Omega$</td><td>$R_{L3} 2\Omega$</td><td>$R_{L4} 2\Omega$</td></tr>
<tr><td>$L_{L1} 0.0064\ mH$</td><td>$L_{L2} 0.0064\ mH$</td><td>$L_{L3} 0.0032\ mH$</td><td>$L_{L4} 0.0032\ mH$</td></tr>
</table>

where A_a is the adjacency matrix, D_{in} is the in-degree matrix. B is the pinned matrix, and $b_1 = 1$ means the DG1 acting as the leader. A can be calculated by $-(D_{in} + G_b - A_a)$, where $G_b = diag(B)$. K can be chosen to be any invertible sparse matrix. P_s, P_h can be calculated by methods **Section 3** introduced. To verify the effectiveness of the distributed secondary control strategy against attacks proposed in this paper, bounded FDI attacks that are not easily detected are defined as

$$\Theta = k \sin(mt + \varphi) + n \tag{27}$$

where k, m, and n are constants, and $\varphi \in [0, 2\pi]$ represents the phase angle. The bounded FDI attacks in the layered communication network studied in this paper are selected as follows:

$$\Theta_1 = \begin{bmatrix} 4\sin(t) \\ 4\sin(2t) \\ -4\cos(t) \\ -4\cos(2t) \end{bmatrix}, \Theta_2 = \begin{bmatrix} 4 \\ -4\sin(t) \\ -4 \\ 4\sin(t) \end{bmatrix} \tag{28}$$

It is obvious that $\|\Theta_1\| \leq 4$, $\|\Theta_2\| \leq 4$ are both bounded. This section compares the resilience against bounded FDI attacks for existing distributed secondary strategies through simulation including: 1) the distributed secondary control strategy without FDI attacks; 2) the distributed secondary control strategy with the layered communication network which only considers FDI attacks in the data transmission layer. 3) This paper the distributed secondary control strategy proposes in this paper which considers FDI attacks in both the data transmission layer and the control network layer. The effectiveness of the distributed secondary control strategy designed in 4) is validated in the microgrid test system when the bounded FDI attack is launched at t = 8 s.

4.1 Performance of the Distributed Secondary Control Strategy Without FDI Attacks

The angular frequency of the microgrid when bounded FDI attacks are launched in the communication network is shown in **Figure 5**. It is obvious that angular frequency of the distributed secondary control strategy with FDI attacks can maintain stable when there exists no attacks before t = 8 s. However, once FDI attacks launched at t = 8 s, angular frequency of the microgrid oscillates violently after t = 8 s in **Figure 5A**, which deviates from the normal frequency fluctuation range of the microgrid and are unable to maintain stable. Performances of **Figure 5A**

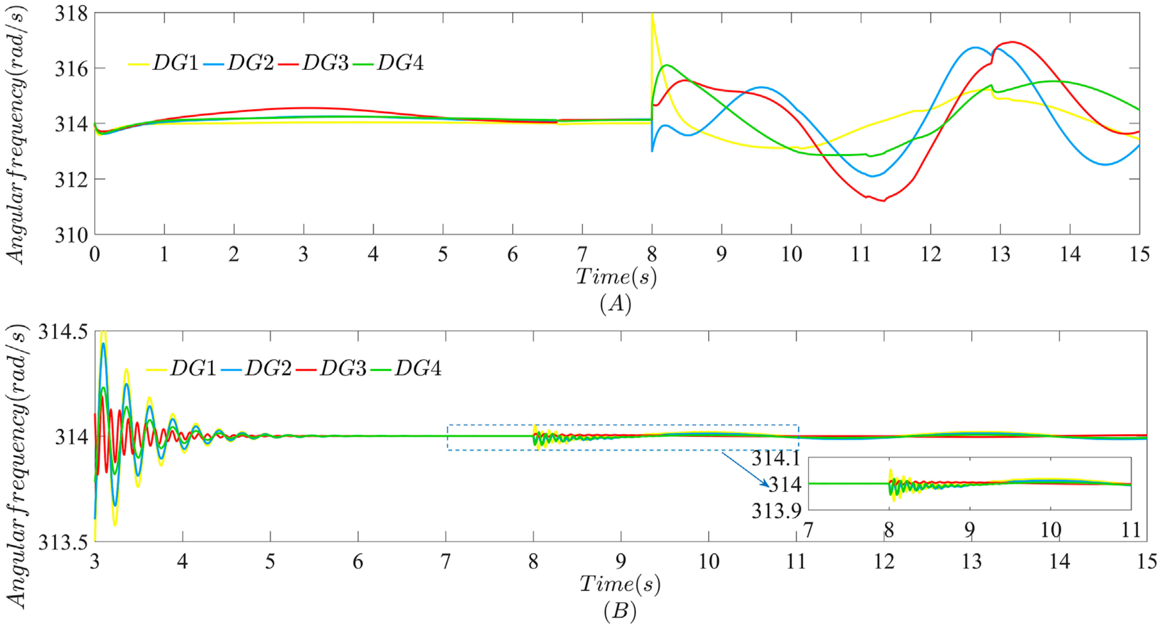

FIGURE 5 | Performance of the angular frequency against the bounded FDI attack launched only in the data transmission layer at t = 8 s: **(A)** Using the distributed secondary strategy without FDI attacks; **(B)** Using the strategy proposed in this paper.

indicates that traditonal distributed secondary strategy lacks the ability against FDI attacks. Therefore, it is necessary to design a distributed secondary control strategy with stronger resilience against bounded FDI attacks to maintain stable of the microgrid.

4.2 The Distributed Secondary Control Strategy With the Layered Communication Network Which Only Considers FDI Attacks in the Data Transmission Layer

The layered communication network separates the data transmission function and the control function from the communication network. The data transmission layer is only responsible for information exchange between neighbor the DGs, such as angular frequency and voltage. The control network layer is responsible for implementing the designed strategy, and the local controller of each DG corresponds to a virtual node control in the control network layer. The privacy of power information is directly related to the security of the microgrid operation. The existing strategies in (Chen et al., 2021; Zhou et al., 2021) consider the attacks only launched in the data transmission layer, but do not discuss how to defend against attacks in the control network layer. The distributed secondary control strategy based on the layered communication network against bounded FDI attacks proposed in this paper has considered cases that FDI attacks launched in the control network layer. At the same time, the distributed secondary strategy proposed in this paper does not affect the case when bounded FDI attacks are launched in the data transmission layer but the control network layer are not. **Figure 5B** shows it is obvious that the distributed secondary control strategy proposed in this paper can still keep the angular frequency of each DG around the rated value when the bounded FDI attack only launched in the data transmission layer.

4.3 The Distributed Secondary Control Strategy Proposes in This Paper Which Considers FDI Attacks in Both the Data Transmission Layer and the Control Network Layer

Compared with the distributed secondary control strategy without FDI attacks in **(4)**, distributed secondary control strategies with the layered communication network undoubtedly enhances the resilience of the microgrid against external bounded FDI attacks. As can be seen from **Figures 6**, **7**, the consensus angular frequency value of each DG is 314 rad/s, that is, 50 Hz of the corresponding frequency value. The consensus value of the active power sharing is 1.5, which ensures that each DG provides active power for microgrid loads in proportion to droop coefficients. And the consensus value of the control network layer is zero. The control network layer has no practical physical meaning causing a high security level, but it is not completely free of risks. Bounded FDI attacks $\|\Theta_1\| \leq 4, \|\Theta_2\| \leq 4$ are launched in the data transmission layer and the control network layer respectively. Performances of the microgrid are shown in **Figures 6**, **7**.

As can be seen from **Figures 6**, **7**, the strategy proposed in this paper can achieve the purpose of the existing work, such as the stability of angular frequency and active power sharing. Moreover, the case that FDI attacks launched in the control network layer also can be solved. In other words, the distributed secondary strategy extends the function of layered

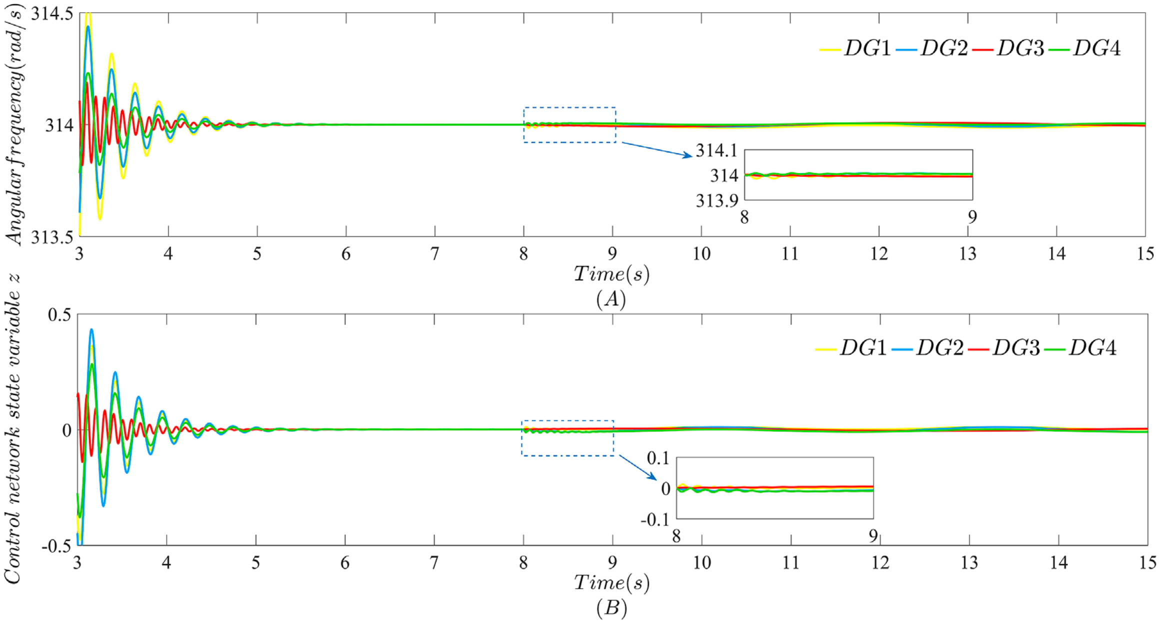

FIGURE 6 | Performance of each DG in the microgrid after bounded FDI attacks are launched at t = 8 s in both the data transmission layer and the control network layer with $\beta = 40$: **(A)** Angular frequency; **(B)** Control network state variable *z*.

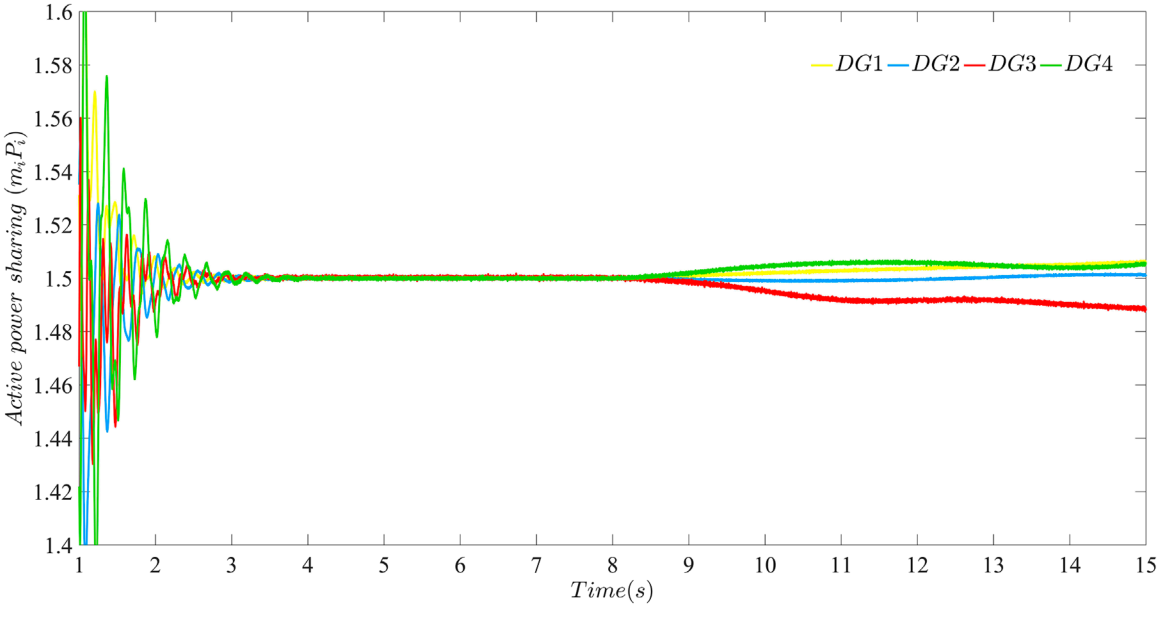

FIGURE 7 | The active power sharing of each DG in the microgrid after bounded FDI attacks are launched at t = 8 s in both the data transmission layer and the control network layer with $\beta = 40$.

communication networks used by existing work. Compared with the existing work, this paper will also consider the influence of FDI attacks in data transmission layer and control network layer on each other. It is worth mentioning that **Figures 6**, **7** show the case with $\beta = 40$ in the distributed secondary strategy proposed in this paper.

According to **(24)** in **Section 3**, when $\beta > 0$ is a large enough constant value, the larger its value is, the closer the angular frequency of each DG in the microgrid will be to the rated value w_{ref}. For this purpose, performances of the microgrid using the distributed secondary control strategy proposed in this paper with $\beta = 100$ are shown in **Figures 8**, **9**.

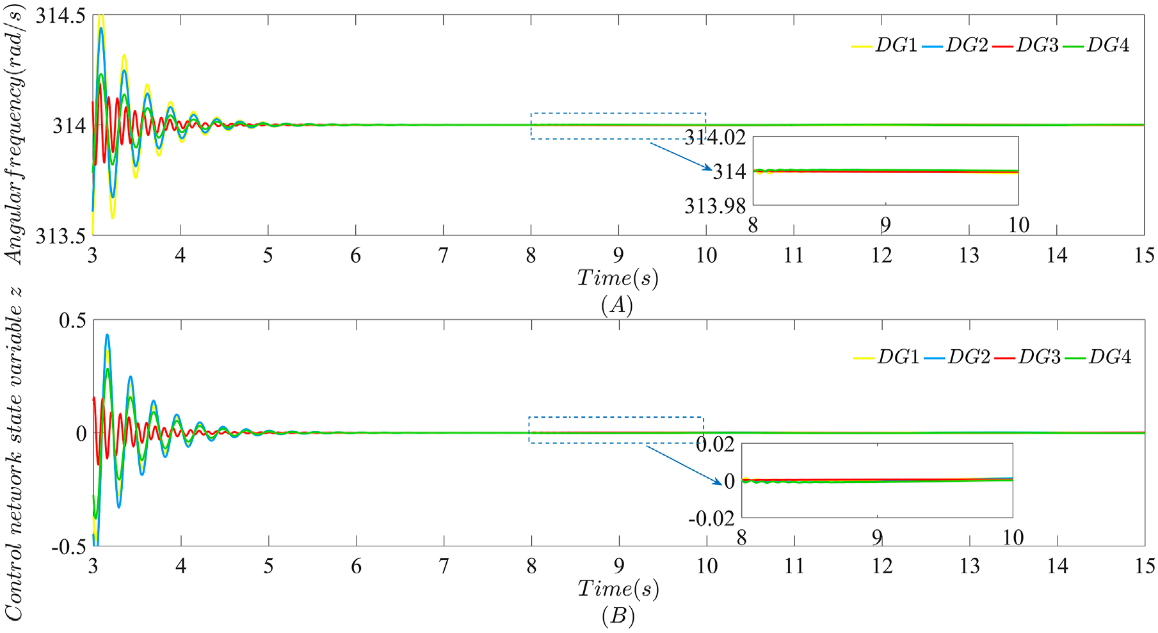

FIGURE 8 | Performance of each DG in the microgrid after bounded FDI attacks are launched at t = 8 s in both the data transmission layer and the control network layer with $\beta = 100$: **(A)** Angular frequency; **(B)** Control network state variable *z*.

As can be seen from **Figures 8**, **9**, the layered communication network of the microgrid becomes more resilient against bounded FDI attacks launched at t = 8 s using the distributed secondary control strategy proposed in this paper with $\beta = 100$. Compare **Figures 6**, **8** and **Figures 7**, **9**, respectively. It can be seen the oscillations of angular frequency and active power sharing caused by bounded FDI attacks launched at t = 8 s in the data transmission layer using the strategy with $\beta = 100$ are mitigated faster than performances in the microgrid using the distributed secondary control strategy proposed in this paper with $\beta = 40$. In a word, cases shown in **Figures 6–9** are to perform the resilience of the microgrid using the distributed secondary strategy proposed in this paper against bounded FDI attacks only launched at t = 8 s.

However, attacks once launched, can only be sustained and random in the actual network environment. Sustained attacks means that the attacker will not stop the action after launch attacks at one moment, but continue to launch attacks at the next moment so that the accumulated attacks will cause greater impact on the communication network of the microgrid. Information exchange also exists between the data transmission layer and the control network layer. Each DG node in the data transmission layer has a corresponding virtual node in the control network layer. The DG node in the data transmission layer uploads power information such as angular frequency to the virtual node in the control network layer for real-time control. Accordingly, the randomness of attacks means that external attacks will not be launched in the data transmission layer and the control network layer at the same time. That is, attacks in double-layer can be launched separately. And since the information exchange is bidirectional, external attacks launched in the data transmission layer or the control network layer actually affect the other layer, even if the other layer is not attacked.

To validate the resilience of the strategy proposed in this paper to sustained and random attacks in the actual network environment, the simulation process is as follows: The secondary control strategy starts at t = 0 s. The bounded FDI attack Θ_1 is launched in the data transmission layer at t = 7 s. The bounded FDI attack Θ_2 is launched in the network control layer at t = 8 s. The bounded FDI attack $2\Theta_1$ is launched in the data transmission layer at t = 9 s. The bounded FDI attack $2\Theta_2$ is launched in the network control layer at t = 10 s. The total simulation time is set to be 15 s.

It is obvious that external sustained and random bounded FDI attacks are launched in the data transmission layer at t = 7 s and t = 9 s from **Figure 10** and in the control network layer at t = 8 s and t = 10 s from **Figure 11**. When, the data transmission layer is attacked but the control network layer is not. The same condition happens at t = 8 s and t = 10 s. Attacks are launched at t = 7 s and t = 9 s in the data transmission layer is attacked but the control network layer is not. And attacks are launched at t = 8 s and t = 10 s in the control network layer is attacked but the data transmission layer is not. As can be seen from **Figure 10** and **Figure 11**, although attacks are not launched in the control network layer, the data transmission layer still are effected by attacks due to the information exchange between the two layers. In this paper, by designing interconnection matrix reasonably, the data transmission layer itself can mitigate the impact of attacks, and the control network layer can also quickly mitigate the influence due to information exchange. After the layered communication network mitigates the impact of direct

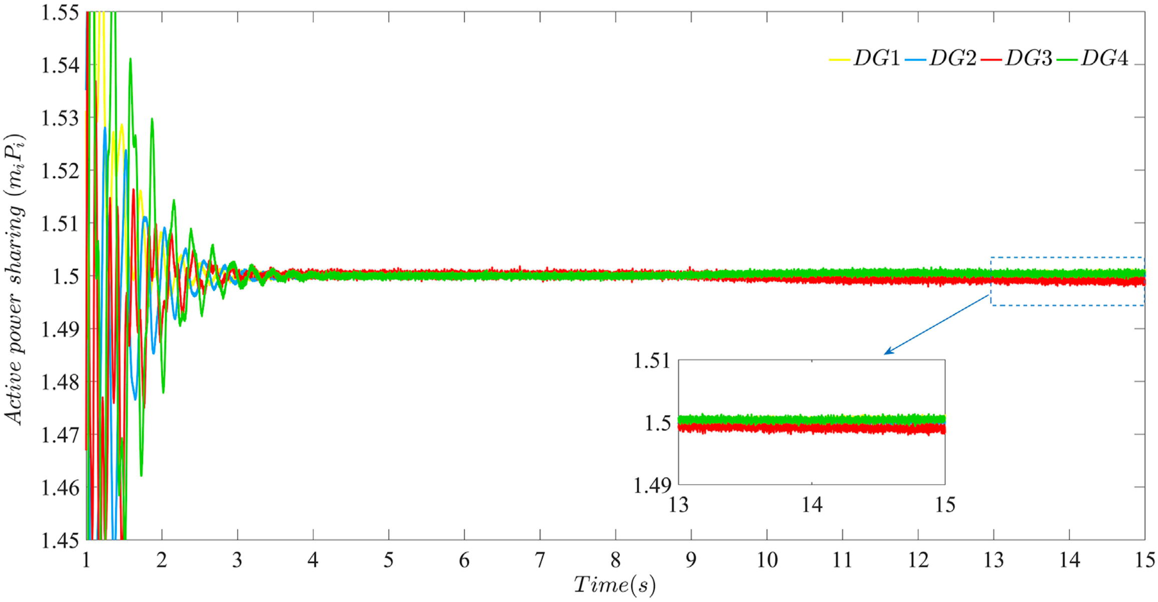

FIGURE 9 | The active power sharing of each DG in the microgrid after bounded FDI attacks are launched at t = 8 s in both the data transmission layer and the control network layer with β = 100.

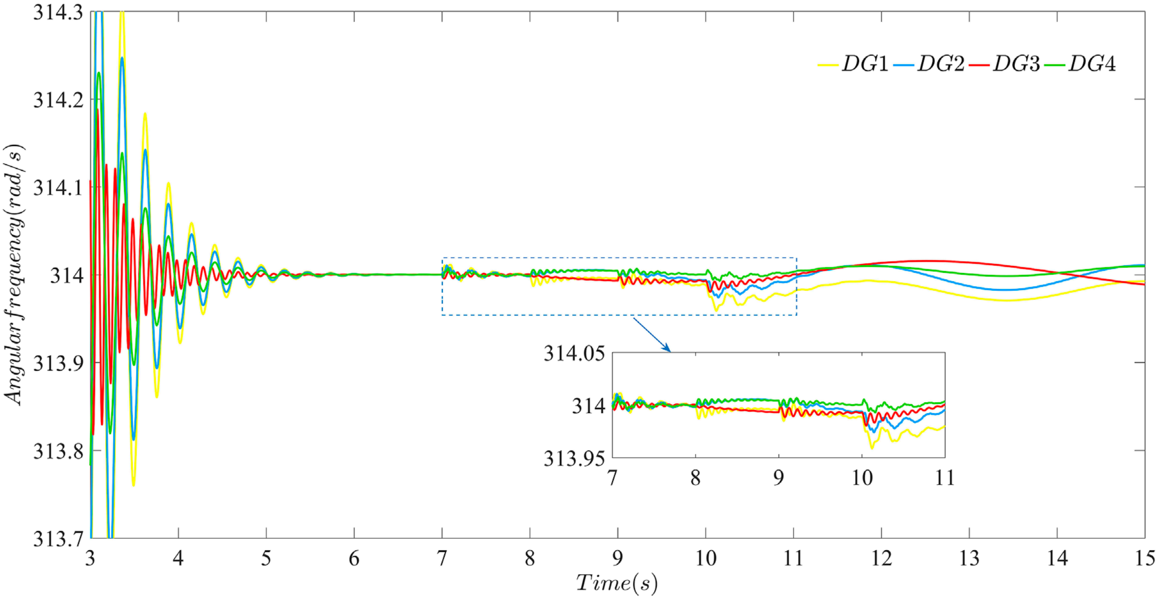

FIGURE 10 | The effectiveness of the layered communication network against sustained and random bounded FDI attacks using the distributed secondary strategy proposed in this paper: performance of the data transmission layer against attacks with β = 40.

attacks and the influence of cross-layer information exchange, the angular frequency still converges to 314 rad/s and the state variable z converges to 0. Similarly, the layered communication network using the distributed secondary strategy proposed in this paper can also mitigate the impact of direct attacks and the influence of cross-layer information exchange at t = 8 s and t = 10 s, respectively. The above cases have shown that the distributed secondary strategy proposed in this paper can effectively deal with the randomness of attack in real network environment.

Moreover, It can be seen from **Figure 10** that the data transmission layer is directly affected by attacks launched at t = 7 s and t = 9 s, and is influenced by attacks from the

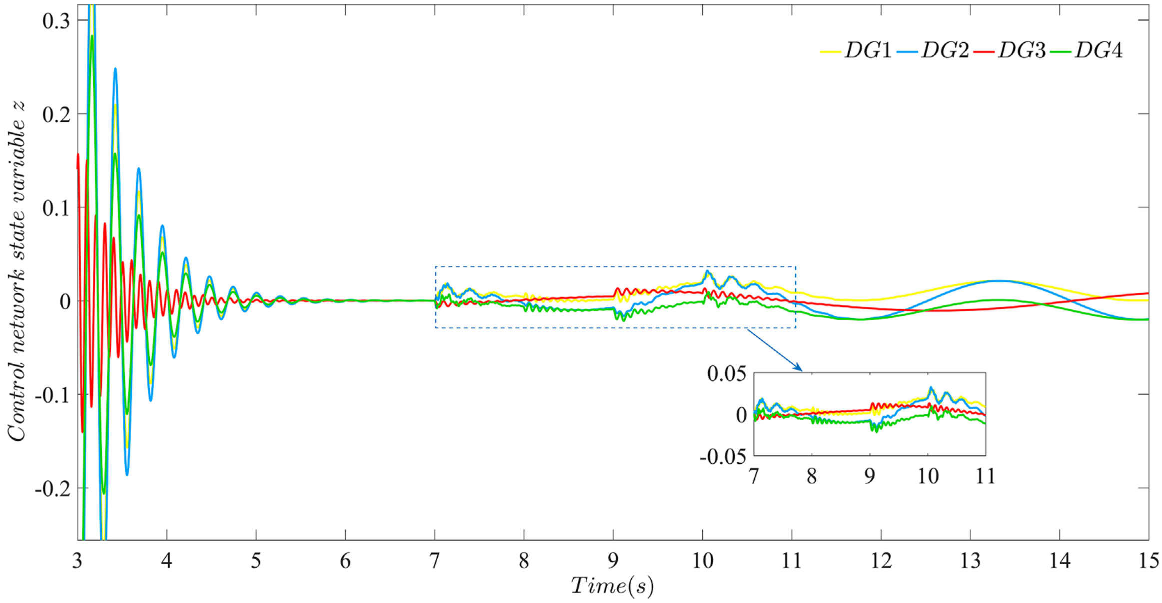

FIGURE 11 | The effectiveness of the layered communication network against sustained and random bounded FDI attacks using the distributed secondary strategy proposed in this paper: performance of the control network layer against attacks with $\beta = 40$.

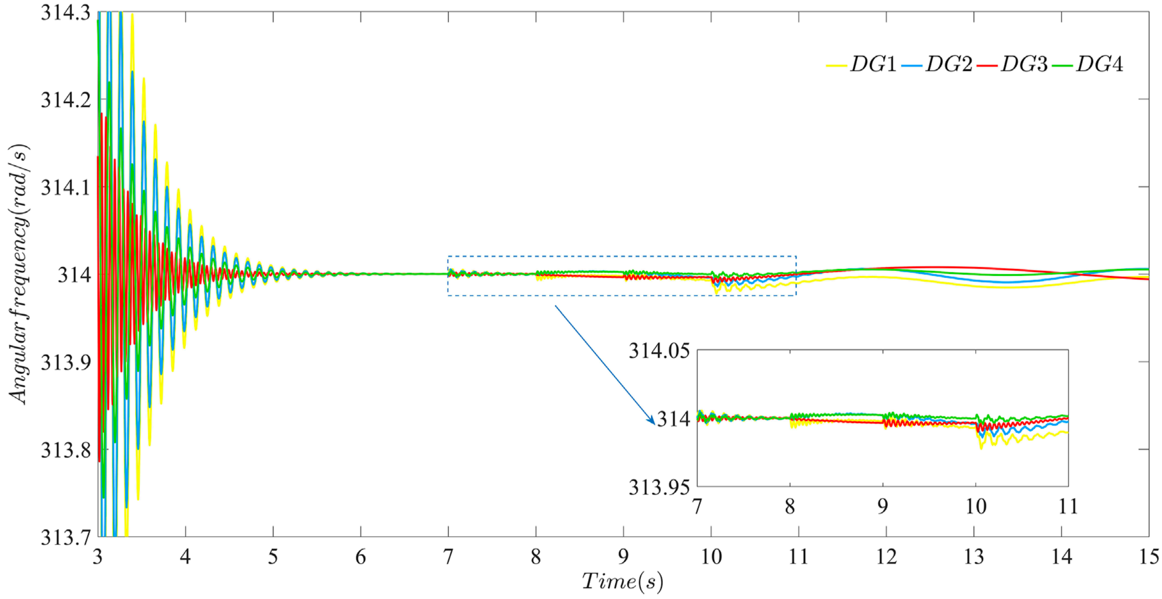

FIGURE 12 | The effectiveness of the layered communication network against sustained and random bounded FDI attacks using the distributed secondary strategy proposed in this paper: performance of the data transmission layer against attacks with $\beta = 100$.

control network layer due to information exchange at t = 8 s and t = 10 s. Attacks always exist and gradually accumulate in the layered communication network, which can be mitigated using the distributed secondary strategy proposed in this paper. Cases in **Figures 12**, **13** show that after β increased to 100, the distributed secondary control strategy proposed in this paper becomes more resilient to the sustained and random bounded FDI attack launched in the double-layer communication network from t = 7 s to t = 10 s. Compare **Figures 10**, **12** and **Figures 11**, **13**, respectively. It can be seen the strategy with $\beta = 100$ can strengthen the resilience of the microgrid against sustained and random attacks compared with the condition with $\beta = 40$.

All the above cases show that the distributed secondary control strategy in the microgrid with layered communication

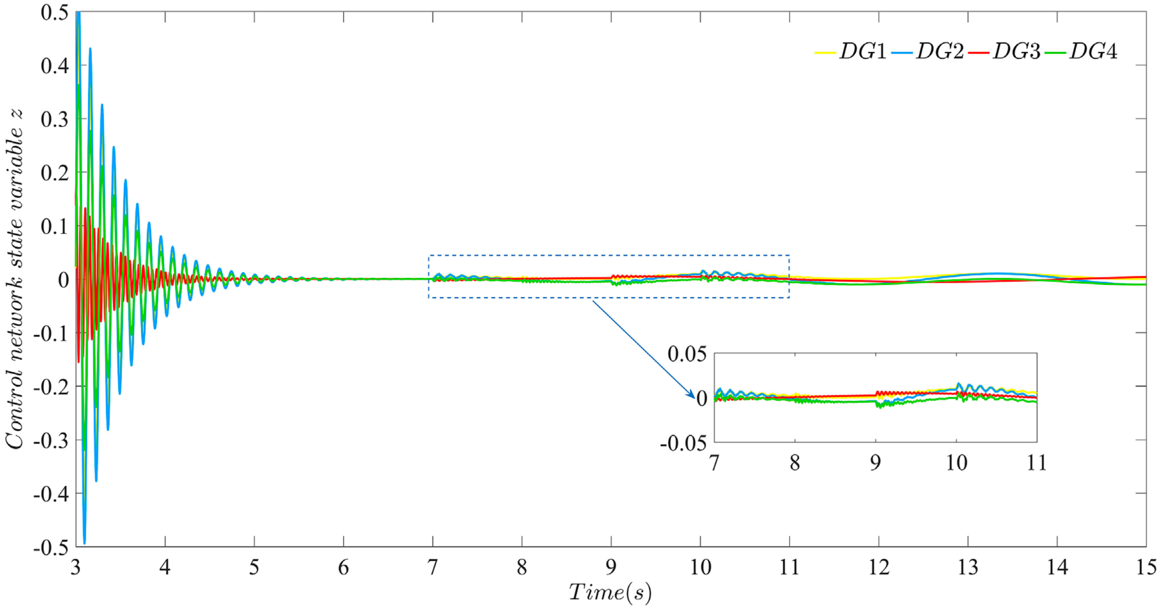

FIGURE 13 | The effectiveness of the layered communication network against sustained and random bounded FDI attacks using the distributed secondary strategy proposed in this paper: performance of the control network layer against attacks with $\beta = 100$.

network proposed in this paper can effectively mitigate external bounded FDI attacks, and the resilience of the strategy against attacks can be enhanced by increasing β. Compared with the simulation results of the distributed secondary control strategy without FDI attacks and the distributed secondary control strategy against FDI attacks in the data transmission layer, the distributed secondary control strategy proposed in this paper is more practical in the case that bounded FDI attacks are launched in both the data transmission layer and the control network layer.

5 CONCLUSION

In this paper, a distributed secondary control strategy against bounded FDI attacks has been proposed for low inertia microgrids with the layered communication network to enhance the resilience to bounded FDI attacks. For the problem that stealthy bounded FDI attacks have been launched in the layer communication network extensively, the strategy proposed in this paper can keep angular frequency stable against attacks. Moreover, Lyapunov theory has been used to demonstrate that the microgrid consisting of DGs remains stable even when bounded FDI attacks are launched in both the data transmission layer and the control network layer, and the angular frequency can be closer to the rated value by increasing β. Finally, a microgrid test system consisting of four inverter-based DGs has been set up using Matlab/Simpower system. Firstly, simulation results have validated that the distributed secondary control strategy without FDI attacks cannot defend against external bounded FDI attacks. Secondly, simulation results have validated that the distributed secondary control strategy proposed in this paper can maintain the angular frequency stable even when external bounded FDI attacks are launched only in the data transmission layer. Finally, simulation results have shown when sustained and random bounded FDI attacks are launched in both the data transmission layer and the control network layer, the angular frequency also runs within the allowed fluctuation range around the rating value, which validate the effectiveness of the distributed secondary strategy proposed in this paper. In future work, the authors will combine the practical application, such as seaport microgrid, to specify the layered network theory used in this paper to solve more complex attack types.

DATA AVAILABILITY STATEMENT

The datasets presented in this article are not readily available because the original contributions presented in the study are included in the article/Supplementary Material, further inquiries can be directed to the corresponding author. Requests to access the datasets should be directed to QS shanqihe@163.com.

AUTHOR CONTRIBUTIONS

FW and QS designed the experiments, research methods. QS performed the format analysis. The tools analysis, data processing, and writing the original draft were carried out by FT. ZH solved the application problem of research methods. ZW performed the writing-review on references. YX contributed to proof reading and project/organization management. All authors have read and agreed to the published version of the manuscript.

FUNDING

This work is supported in part by the National Natural Science Foundation of China (under grant nos. 51939001, 61803064, 61751202, 61903092, 61976033, and U1813203); the Science and Technology Innovation Funds of Dalian (under grant no. 2018J11CY022); the Liaoning Revitalization Talents Program (under grant nos. XLYC1908018 and XLYC1807046); the Natural Science Foundation of Liaoning (2019-ZD-0151,20170540098); the Fundamental Research Funds for the Central Universities (under grant nos. 3132019345, 3132020103, and 3132020125).

REFERENCES

Abhinav, S., Modares, H., Lewis, F. L., Ferrese, F., and Davoudi, A. (2018). Synchrony in Networked Microgrids Under Attacks. *IEEE Trans. Smart Grid* 9, 6731–6741. doi:10.1109/TSG.2017.2721382

Beg, O. A., Johnson, T. T., and Davoudi, A. (2017). Detection of False-Data Injection Attacks in Cyber-Physical Dc Microgrids. *IEEE Trans. Ind. Inf.* 13, 2693–2703. doi:10.1109/TII.2017.2656905

Bidram, A., and Davoudi, A. (2012). Hierarchical Structure of Microgrids Control System. *IEEE Trans. Smart Grid* 3, 1963–1976. doi:10.1109/TSG.2012.2197425

Bidram, A., Davoudi, A., Lewis, F. L., and Guerrero, J. M. (2013). Distributed Cooperative Secondary Control of Microgrids Using Feedback Linearization. *IEEE Trans. Power Syst.* 28, 3462–3470. doi:10.1109/tpwrs.2013.2247071

Bidram, A., Lewis, F. L., and Davoudi, A. (2014). Distributed Control Systems for Small-Scale Power Networks: Using Multiagent Cooperative Control Theory. *IEEE Control Syst. Mag.* 34, 56–77. doi:10.1109/MCS.2014.2350571

Chen, Y., Qi, D., Dong, H., Li, C., Li, Z., and Zhang, J. (2021). A Fdi Attack-Resilient Distributed Secondary Control Strategy for Islanded Microgrids. *IEEE Trans. Smart Grid* 12, 1929–1938. doi:10.1109/TSG.2020.3047949

Condry, M. W., and Nelson, C. B. (2016). Using Smart Edge Iot Devices for Safer, Rapid Response with Industry Iot Control Operations. *Proc. IEEE* 104, 938–946. doi:10.1109/JPROC.2015.2513672

Ge, P., Zhu, Y., Green, T. C., and Teng, F. (2021). Resilient Secondary Voltage Control of Islanded Microgrids: An Eskbf-Based Distributed Fast Terminal Sliding Mode Control Approach. *IEEE Trans. Power Syst.* 36, 1059–1070. doi:10.1109/TPWRS.2020.3012026

Gusrialdi, A., Qu, Z., and Simaan, M. A. (2018). Competitive Interaction Design of Cooperative Systems Against Attacks. *IEEE Trans. Autom. Contr.* 63, 3159–3166. doi:10.1109/TAC.2018.2793164

Hu, L., Wang, Z., Han, Q.-L., and Liu, X. (2018). State Estimation Under False Data Injection Attacks: Security Analysis and System Protection. *Automatica* 87, 176–183. doi:10.1016/j.automatica.2017.09.028

Jin, D., Li, Z., Hannon, C., Chen, C., Wang, J., Shahidehpour, M., et al. (2017). Toward a Cyber Resilient and Secure Microgrid Using Software-Defined Networking. *IEEE Trans. Smart Grid* 8, 2494–2504. doi:10.1109/tsg.2017.2703911

Kreutz, D., Ramos, F. M. V., Esteves Verissimo, P., Esteve Rothenberg, C., Azodolmolky, S., and Uhlig, S. (2015). Software-Defined Networking: A Comprehensive Survey. *Proc. IEEE* 103, 14–76. doi:10.1109/jproc.2014.2371999

Liang, G., Weller, S. R., Zhao, J., Luo, F., and Dong, Z. Y. (2017). The 2015 Ukraine Blackout: Implications for False Data Injection Attacks. *IEEE Trans. Power Syst.* 32, 3317–3318. doi:10.1109/TPWRS.2016.2631891

Liang, X. (2017). Emerging Power Quality Challenges Due to Integration of Renewable Energy Sources. *IEEE Trans. Ind. Appl.* 53, 855–866. doi:10.1109/tia.2016.2626253

Liu, Y., Ning, P., and Reiter, M. K. (2011). False Data Injection Attacks Against State Estimation in Electric Power Grids. *ACM Trans. Inf. Syst. Secur.* 14, 21–32. doi:10.1145/1952982.1952995

Manandhar, K., Cao, X., Hu, F., and Liu, Y. (2014). Detection of Faults and Attacks Including False Data Injection Attack in Smart Grid Using Kalman Filter. *IEEE Trans. Control Netw. Syst.* 1, 370–379. doi:10.1109/tcns.2014.2357531

Mijumbi, R., Serrat, J., Gorricho, J.-L., Bouten, N., De Turck, F., and Boutaba, R. (2016). Network Function Virtualization: State-Of-The-Art and Research Challenges. *IEEE Commun. Surv. Tutorials* 18, 236–262. doi:10.1109/comst.2015.2477041

Musleh, A. S., Chen, G., and Dong, Z. Y. (2020). A Survey on the Detection Algorithms for False Data Injection Attacks in Smart Grids. *IEEE Trans. Smart Grid* 11, 2218–2234. doi:10.1109/TSG.2019.2949998

Nunes, B. A. A., Mendonca, M., Nguyen, X.-N., Obraczka, K., and Turletti, T. (2014). A Survey of Software-Defined Networking: Past, Present, and Future of Programmable Networks. *IEEE Commun. Surv. Tutorials* 16, 1617–1634. doi:10.1109/SURV.2014.012214.00180

Olfati-Saber, R., and Murray, R. M. (2004). Consensus Problems in Networks of Agents with Switching Topology and Time-Delays. *IEEE Trans. Autom. Contr.* 49, 1520–1533. doi:10.1109/TAC.2004.834113

Pasqualetti, F., Bicchi, A., and Bullo, F. (2012). Consensus Computation in Unreliable Networks: A System Theoretic Approach. *IEEE Trans. Autom. Contr.* 57, 90–104. doi:10.1109/TAC.2011.2158130

Pogaku, N., Prodanovic, M., and Green, T. C. (2007). Modeling, Analysis and Testing of Autonomous Operation of an Inverter-Based Microgrid. *IEEE Trans. Power Electron.* 22, 613–625. doi:10.1109/TPEL.2006.890003

Qu, Z., Dong, Y., Qu, N., Li, H., Cui, M., Bo, X., et al. (2021). False Data Injection Attack Detection in Power Systems Based on Cyber-Physical Attack Genes. *Front. Energy Res.* 9. doi:10.3389/fenrg.2021.644489

Rui, W., Qiuye, S., Dazhong, M., and Xuguang, H. (2020). Line Impedance Cooperative Stability Region Identification Method for Grid-Tied Inverters under Weak Grids. *IEEE Trans. Smart Grid* 11, 2856–2866. doi:10.1109/tsg.2020.2970174

Salah, K., Elbadawi, K., and Boutaba, R. (2012). Performance Modeling and Analysis of Network Firewalls. *IEEE Trans. Netw. Serv. Manage.* 9, 12–21. doi:10.1109/TNSM.2011.122011.110151

Shafiee, Q., Guerrero, J. M., and Vasquez, J. C. (2014). Distributed Secondary Control for Islanded Microgrids-A Novel Approach. *IEEE Trans. Power Electron.* 29, 1018–1031. doi:10.1109/TPEL.2013.2259506

Sinha, A., Mohandas, M., Pandey, P., and Vyas, O. P. (2021). Cyber Physical Defense Framework for Distributed Smart Grid Applications. *Front. Energy Res.* 8. doi:10.3389/fenrg.2020.621650

Sockeel, N., Gafford, J., Papari, B., and Mazzola, M. (2020). Virtual Inertia Emulator-Based Model Predictive Control for Grid Frequency Regulation Considering High Penetration of Inverter-Based Energy Storage System. *IEEE Trans. Sustain. Energy* 11, 2932–2939. doi:10.1109/tste.2020.2982348

Sundaram, S., and Hadjicostis, C. N. (2011). Distributed Function Calculation via Linear Iterative Strategies in the Presence of Malicious Agents. *IEEE Trans. Autom. Contr.* 56, 1495–1508. doi:10.1109/tac.2010.2088690

Wang, R., Sun, Q., Hu, W., Li, Y., Ma, D., and Wang, P. (2021). Soc-Based Droop Coefficients Stability Region Analysis of the Battery for Stand-Alone Supply Systems with Constant Power Loads. *IEEE Trans. Power Electron.* 36, 7866–7879. doi:10.1109/TPEL.2021.3049241

Wang, R., Sun, Q., Ma, D., and Liu, Z. (2019). The Small-Signal Stability Analysis of the Droop-Controlled Converter in Electromagnetic Timescale. *IEEE Trans. Sustain. Energy* 10, 1459–1469. doi:10.1109/tste.2019.2894633

Xiahou, K., Liu, Y., and Wu, Q. H. (2022). Decentralized Detection and Mitigation of Multiple False Data Injection Attacks in Multiarea Power Systems. *IEEE J. Emerg. Sel. Top. Ind. Electron.* 3, 101–112. doi:10.1109/JESTIE.2021.3112919

Zhang, F., Kodituwakku, H. A. D. E., Hines, J. W., and Coble, J. (2019). Multilayer Data-Driven Cyber-Attack Detection System for Industrial Control Systems Based on Network, System, and Process Data. *IEEE Trans. Ind. Inf.* 15, 4362–4369. doi:10.1109/tii.2019.2891261

Zhang, H., Li, Z., Qu, Z., and Lewis, F. L. (2015). On Constructing Lyapunov Functions for Multi-Agent Systems. *Automatica* 58, 39–42. doi:10.1016/j.automatica.2015.05.006

Zhou, Q., Shahidehpour, M., Alabdulwahab, A., and Abusorrah, A. (2020). A Cyber-Attack Resilient Distributed Control Strategy in Islanded Microgrids. *IEEE Trans. Smart Grid* 11, 3690–3701. doi:10.1109/TSG.2020.2979160

Zhou, Q., Shahidehpour, M., Alabdulwahab, A., Abusorrah, A., Che, L., and Liu, X. (2021). Cross-Layer Distributed Control Strategy for Cyber Resilient Microgrids. *IEEE Trans. Smart Grid* 12, 3705–3717. doi:10.1109/tsg.2021.3069331

Zuo, S., and Yue, D. (2022). Resilient Containment of Multigroup Systems Against Unknown Unbounded Fdi Attacks. *IEEE Trans. Ind. Electron.* 69, 2864–2873. doi:10.1109/TIE.2021.3066941

Conflict of Interest: Author ZH is employed by China Railway Rolling Stock Corporation Zhuzhou Institute Co., Ltd.

The remaining authors declare that the research was conducted in the absence of any commercial or financial relationships that could be construed as a potential conflict of interest.

frontiers | Frontiers in Energy Research

ORIGINAL RESEARCH
published: 04 August 2022
doi: 10.3389/fenrg.2022.945231

Security Region of Integrated Heat and Electricity System Considering Thermal Dynamics

Zhuhua Wang, Wencheng Huang and Xiaowei Cai*

College of Physics and Electromechanics, Longyan University, Longyan, China

The broad development of integrated heat and electricity systems (IHES) improved the energy utilization efficiency, but it also increased the risk of cascaded accidents and the difficulty of operation. The security region that defines the permitted operation range is efficient for the planning and control of IHESs, while the accurate formulation of security region boundary renders its applications. To address this problem, this article first proposes a novel equivalent thermal model (ETM) to build the direct connection between the operations states and the control variables in the heating system. The ETM directly characterizes the network response to the inputs and accurately describes the dynamic process in the heat system. On this basis, the method to construct the security region for IHES is presented considering the thermal dynamics, where the critical boundary is formulated with a set of accurate hyperplanes. To describe the thermal dynamics, numerical simulations from different aspects verify the effectiveness of the ETM. The results of security region indicate that the thermal dynamics influence the operation security and renewable penetration in the power system significantly.

Keywords: integrated heat and electricity system, security region, thermal dynamics, equivalent thermal model, security region boundary (SRB)

Edited by:
Wei Hu,
Zhejiang University, China

Reviewed by:
Solomon Giwa,
Olabisi Onabanjo University, Nigeria
Angel Barragan Cervera,
University of Jaume I, Spain

Correspondence:
Zhuhua Wang
81988003@lyun.edu.cn

Specialty section:
This article was submitted to
Smart Grids,
a section of the journal
Frontiers in Energy Research

Received: *16 May 2022*
Accepted: *20 June 2022*
Published: *04 August 2022*

Citation:
Wang Z, Huang W and Cai X (2022)
Security Region of Integrated Heat and
Electricity System Considering
Thermal Dynamics.
Front. Energy Res. 10:945231.
doi: 10.3389/fenrg.2022.945231

1 INTRODUCTION

Sustaining development of society and further innovation of energy utilization technology promoted the cross-cutting and integrated evolution of multienergy fields (Mancarella, 2014; Zhang et al., 2021a). As an important component of energy system, the integrated heat and electricity system (IHES) owns the characteristics of low carbon and high efficiency through the energy cascade utilization and multienergy optimization (Bitar et al., 2011; Ma et al., 2018). Its technical exploration has become the current research hotspot.

Security and economy are the fundamental requirements for the operation of IHES, which is also the basis of optimal scheduling and simultaneous control. However, the wide applications of coupling equipment, such as combined heat and power units (CHPs) and heat pumps, caused deeper interdependency between the power system (PS) and the heating system (HS), and it increased the concerns about coordinate operation. On the one hand, the dynamics at HS side (Sanjari et al., 2016; Cruz et al., 2018), which is also named thermal inertia, provides extra flexibility for the operation of the PS and promotes the penetration of renewables like photovoltaics (PVs). On the other hand, the inaccurate quantization of thermal dynamics is more likely to misguide the normal operation of IHES, thereby threatening the security of PS. Different from the PS, the thermal loads are largely influenced by the environmental factors, and this further increased the possibility of operational accidents (Li et al., 2016). A well-known electric and thermal power failure in China during 2012 is the consequence of thermal load upsurge and electric line damage, which is caused by the arctic weather, and influenced several hundred thousand inhabitants (Sina, 2009). Thus, accurately describing the response characteristic of the system state to the external inputs and analyzing the operational security under different conditions is essential for the future development of IHES.

Some methods have been proposed to study the feasibility and security of IHESs containing the operation assessment, prevention and simultaneous control, and robust planning. In terms of operation assessment, reference (Wei et al., 2018) proposed a cascading fault transfer model for PS based on graph theory and constructed the structure to evaluate the system vulnerability region. Reference (Yan et al., 2014) further optimized the evaluation structure combined with the graph theory with the physical features. In (Jiang et al., 2014; Nan et al., 2020), the concept of operation security was extended into integrated gas and electricity system, and the bidirectional coupling influence was analyzed. In terms of prevention and control, a steady-state security control strategy was proposed in (Chen et al., 2020) based on sensitivity analysis. Next, to formulate the thermal dynamics, reference (Zhang et al., 2021b) proposed an equivalent model based on the partial differential equations. Then, the global sensitivity matrix was built to describe the coupling between electric and thermal states. Also, a rolling dynamic security control was developed to ensure the normal operation under uncertainties. As for robust optimization, a coordinate optimization method was proposed in (He et al., 2018) for IHES considering the N-1 constraints and critical equipment accidents, and the multiple uncertainties were further included in (Li and Xu, 2019).

The literatures above studied the operation of IHES from different aspects. However, the analysis is conducted through traverse or optimization with various constraints. The deficiencies are summarized as follows: 1) The methods above focus on the specific operation states and are unable to obtain the operational margin visually. 2) The states proposed by optimization probably locate at the operation boundary, and the security cannot be ensured with unexpected deviations. In contrast, the security region (SR) model formulates the control strategy by delineating the operation boundary and provides the feasible operation range visually. Thus, it is an efficient method to handle the mentioned deficiencies.

Derived from the SR of PS, the SR in IHES is defined as a set of energy flow injections that satisfies the energy flow equations and operational security constraints (Liu, 1986). During the analysis of SR, the SR boundary is critically significant since it restricts the feasible points and presents the security margin visually. In this regard, reference (Xiao et al., 2012) adopted the hyperplanes to approximate the SR boundary and then constructed SR for IHES. In (Xiao et al., 2017), the convex hull method was used to build the robust SR for integrated energy system. The SR problem was formulated into a robust nonlinear programming model and solved by IPOPT. Despite the normal operation constraints, to study the SR under different accidents, the N-1 constraints were considered in (Chen et al., 2017) and (Liu et al., 2020). In (Jahromi and Bouffard, 2017), the SR in demand spaces with multiregion transmission constraints was formulated. The research indicated that the uncertain renewables like wind power and PV significantly influence the size of SR. On this basis, (Chiang and Jiang, 2018) characterized the SR of IHES with optimal energy flow and explored its potential to promote the renewable consumption. Then, the model was extended into (Wei et al., 2015), considering the PV uncertainty, and was used for robust dispatching.

The existing research studies mainly focus on the PS and integrated electricity and gas system, while the study on IHES is relatively few. In addition, the regions constructed by the current literatures are probably different from the real conditions because the dynamic transmission process is omitted. Also, this may result in an inaccurate assessment of the operation state. Moreover, according to the topology analysis, the operation states in HS are alternately solved through the pipes and nodes. It is challenging to build a direct connection between state variables and disturbance in HS, which increase the difficulty to formulate the SR boundary. To address the mentioned problems, this article proposes an equivalent thermal model (ETM) to quantitatively describe the intuitive relationships between the operation states and external disturbance in HS. Then, to formulate the accurate SR boundary, the methods to construct the SR for IHES based on ETM considering the thermal dynamics are presented. The main contributions of this article are summarized as the following:

1) An equivalent thermal model is formulated. The model constructs the intuitive connection between state and control variables instead of the recursive process in operation analysis.
2) The approach to constructing the SR of IHES considering thermal dynamics is proposed. Based on the hyperplane method, the formulation of security region boundary (SRB) is presented. The simulation results indicate that the thermal dynamics influence the SR and PV consumption of IHES significantly.

The remainder of this article is organized as follows. **Section 2** describes the modeling of IHES. **Section 3** proposes the ETM. **Section 4** constructs the SR for IHES and the corresponding hyperplane for SRB. Case study and conclusion are given in **Sections 5**, **6**.

2 ENERGY FLOW IN INTEGRATED HEAT AND ELECTRICITY SYSTEM

The structure of IHES contains three parts: the PS, the HS, and the coupling units. Both the energy systems consist of sources, networks, and loads. The energy flow distribution in PS, HS, and coupling units are given in the following part.

2.1 Energy Flow in Power System

The power flow balance at buses is expressed as the following: the energy flow in PS usually describes the active and reactive power flow distribution. Since that, the PS and HS mainly interacts through the active power flow, and this article adopts the direct

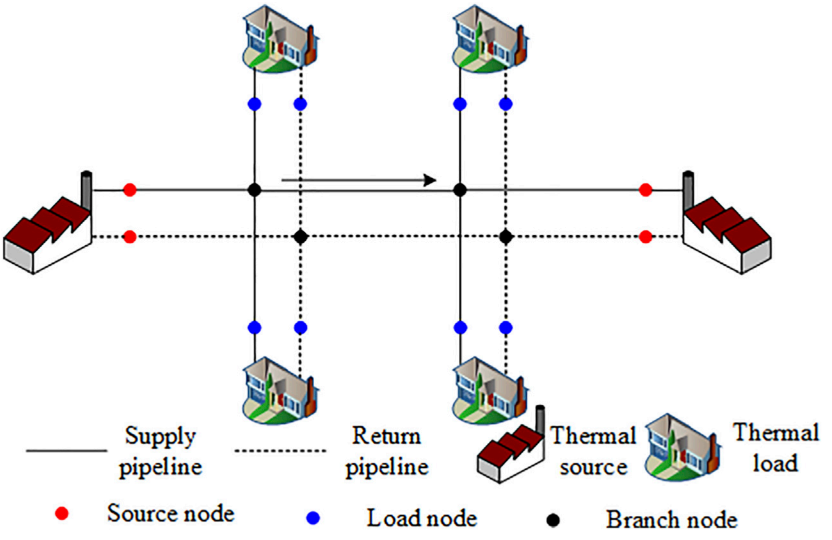

FIGURE 1 | Structure of heating system.

current (DC) power flow model to describe the state distribution. The model is expressed as (Li et al., 2016):

$$P_{L,i} - P_{V,i} - P_{G,i} = \sum_{j\varpi i} B_{ij}\left(\theta_i - \theta_j\right) \tag{1}$$

$$P_{ij} = B_{ij}\left(\theta_i - \theta_j\right) \tag{2}$$

$$\theta_{sl} = 0 \tag{3}$$

where $P_{L,i}$, $P_{V,i}$, and $P_{G,i}$ denote the active power of load, active power output of PV, and generators at bus i in PS, respectively; θ_i denotes the voltage phase angle at bus I; B_{ij} denotes the susceptance between bus i and bus j; P_{ij} denotes the active power flow between bus i and bus j; subscript sl denotes the variables of the slack bus. **Eq. 1** denotes the active power balance at each bus; **Eq. 2** denotes the active power flow balance at each branch; **Eq. 3** indicates that the voltage phase angle at the slack bus equals to zero. The above equations restrict the output active power of the generators with the given load distribution.

2.2 Energy Flow in Heating System

The thermal sources and loads in HS are connected through the supply and return network, and each of the networks demonstrates a similar structure. As illustrated in **Figure 1**, the thermal power produced by the thermal sources are first transferred with supply water flow by circulation pumps. After arriving the load side, the consumers exchange the thermal power, and the water flow reflows into the return network. Next, finally, the return water starts at the load nodes, transfers to the source nodes, and forms a cycle. Thus, the energy flow model in HS usually contains the thermal parts and the hydraulic parts. In this study, to formulate the HS model, the widespread constant-mass-flow control strategy is adopted. In the condition, the time-varying requirements of thermal consumers are satisfied by adjusting the source supply temperature with the fixed mass flow distribution (Li et al., 2016; Zhang et al., 2021a). Due to the superior stability, the strategy is mostly adopted in North China and North Europe.

For simplification, the temperature mentioned in this article is defined as the temperature mismatch between the absolute temperature and the ambient temperature, which is expressed as the following:

$$T = T' - T^{amb} \tag{4}$$

where T' denotes the absolute temperature, and T^{amb} denotes the ambient temperature. The thermal model describes the distribution of temperature and thermal power. First, the node in the HS is modeled as the heat exchanger.

$$\phi = Cm^{nd}\left(T^{s,nd} - T^{r,nd}\right) \tag{5}$$

In **Eq. 5**, ϕ denotes the thermal power consumption, which is positive at load nodes and negative at sources nodes; the superscripts nd denotes the variables at nodes, and C denotes the specific heat capacity of water; the superscripts s and r denote the variables in supply and return networks, respectively. Second, the node temperature after flow mixing is expressed as the following:

$$T_j^{nd} \sum_{i\in Lv^j} m_i^{br} = \sum_{i\in In^j} T_i^{e,br} m_i^{br} \tag{6}$$

Eq. 6 is an equivalent representation of energy conservation at nodes, where the superscripts br denote the variables at pipeline; superscript e denotes the variables at the end of the pipeline, In^j denotes the set of pipelines that end at node j; Lv^j denotes the set of pipelines leaves from node j. Third, the temperature at the beginning of pipeline equals to the temperature at the corresponding node, which is expressed as the following:

$$T_i^{b,br} = T_j \ i \in Lv^j \tag{7}$$

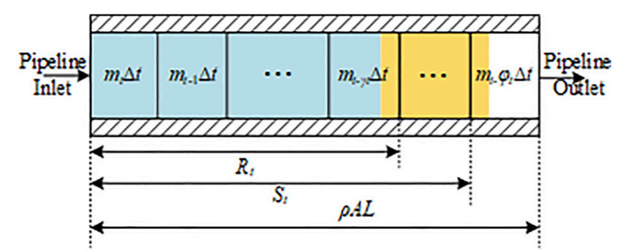

FIGURE 2 | Flow schematic diagram of pipeline in heating system.

Next, finally, the pipe temperature conductivity equation describes the temperature distribution along the pipe. Here, we adopted the widely used node method to formulate the corresponding equation, and its procedure contains two steps: 1) model the time delay and 2) model the transfer loss.

Since the thermal power is transferred through water flow with a slow velocity, the adjustment at the pipeline inlet temperature takes a certain time delay to influence the pipeline outlet temperature. Thus, the node method discretizes the mass flow inside the pipeline into different micro elements, and each of the micro elements takes a different time delay to arrive the pipeline outlet, as shown in **Figure 2** (Li et al., 2016).

The elements in yellow denote the mass flow injecting into the pipeline at t. The element in blue denotes the mass flow injecting into the pipeline during a continuous time interval. The figure indicates that the mass flow injecting into pipeline at t leaves at t-γ_t. Next, correspondingly, the mass flow injecting into pipeline at t-1 leaves at t-φ_t. For arbitrary pipeline i, its time labels $\gamma_{i,t}$ and $\varphi_{i,t}$ can be obtained from (Li et al., 2016):

$$\gamma_{i,t} = \min\left(i\text{: } s.t. \sum_{k=t-j}^{t} m^{br}_{i,k}\Delta t \geq \rho A_i L_i \right) \tag{8}$$

$$\varphi_{i,t} = \min\left(j\text{: } s.t. \sum_{k=t-j}^{t} m^{br}_{i,k}\Delta t \geq \rho A_i L_i + m_{i,t}\Delta t \right) \tag{9}$$

where A is the cross-section area of the pipeline, ρ is the water density, Δt is the time length, and L is the pipeline length. On this basis, the pipeline outlet temperature is formulated as the linear weighted sum of the temperature series at the pipeline inlet. Considering the time delay, the pipeline outlet temperature without transfer loss is formulated as the following:

$$\begin{aligned}\left(m^{br}_{i,t}\Delta t\right)T^{e,s,br,wl}_{i,t} &= \left(m^{br}_{i,t}\Delta t + \rho A_i L_i - S_{i,t}\right)T^{b,s,br,wl}_{i,t-\varphi_{i,t}} \\ &+ \sum_{k=t-\varphi_{i,t}+1}^{t-\gamma_{i,t}-1} \left(m^{br}_{i,t}\Delta t\right)T^{b,s,br}_{i,t} + \left(R_{i,t} - \rho A_i L_i\right)T^{b,s,br}_{i,t-\gamma_{i,t}}\end{aligned} \tag{10}$$

$$\begin{aligned}\left(m^{br}_{i,t}\Delta t\right)T^{e,r,br,wl}_{i,t} &= \left(m^{br}_{i,t}\Delta t + \rho A_i L_i - S_{i,t}\right)T^{b,r,br}_{i,t-\varphi_{i,t}} \\ &+ \sum_{k=t-\varphi_{i,t}+1}^{t-\gamma_{i,t}-1} \left(m^{br}_{i,t}\Delta t\right)T^{b,r,br}_{i,t} + \left(R_{i,t} - \rho A_i L_i\right)T^{b,r,br}_{i,t-\gamma_{i,t}}\end{aligned} \tag{11}$$

where $R_{i,t}$ denotes the mass flow injecting into the pipeline i between t-γ_t and t; $S_{i,t}$ denotes the mass flow injecting into the pipeline i between t-φ_t+1 and t; $T^{e,s,br,wl}_{i,t}$ and $T^{e,r,br,wl}_{i,t}$ denote the pipeline outlet temperature in the supply and return network, respectively, at t without transfer loss. The expressions of $S_{i,t}$ and $R_{i,t}$ are the following:

$$R_{i,t} = \sum_{k=t-\gamma_{i,t}}^{t} m_{i,k}\Delta t \tag{12}$$

$$S_{i,t} = \begin{cases} R_{i,t} & \varphi_{i,t} \leq \gamma_{i,t} + 1 \\ \sum\limits_{k=t-\delta_{i,t}+1}^{t} m_{i,k}\Delta t & \varphi_{i,t} > \gamma_{i,t} + 1 \end{cases} \tag{13}$$

On this basis, the pipeline outlet temperature is further modified considering the transfer loss, which is expressed as the following:

$$T^{e,s,br}_{i,t} = K_{i,t}T^{e,s,br,wl}_{i,t} \tag{14}$$

$$T^{e,r,br}_{i,t} = K_{i,t}T^{e,r,br,wl}_{i,t} \tag{15}$$

$$K_{i,t} = \exp\left(-\frac{\lambda_i \Delta t}{A_i C \rho}\left(\gamma_{i,t} + \frac{1}{2} + \frac{S_{i,t} - R_{i,t}}{m^{br}_{i,t-\gamma_{i,t}}\Delta t} \right)\right) \tag{16}$$

where $T^{e,s,br}_{i,t}$ and $T^{e,r,br}_{i,t}$ denote pipeline outlet temperature in the supply and return network, respectively; λ denotes the thermal transfer coefficient.

2.3 Energy Flow in Coupling Units

The PS and HS are usually coupled with the energy cogeneration and conversion equipment. In this article, the extraction CHP units and heat pumps are adopted for analysis. Next, the feasible region is used to describe the relationship between thermal power and electric power in CHP units and heat pumps. The feasible region of CHP units is constructed with several extreme points, whose mathematical formulation is expressed as (Zhang et al., 2021b):

$$\begin{cases} 0 \leq P_{\text{CHP}} \leq P^{\max}_{\text{CHP}} \\ 0 \leq \phi_{\text{CHP}} \leq \phi^{\max}_{\text{CHP}} \\ \eta_{CHP,1}\phi_{\text{CHP}} \leq P_{\text{CHP}} \leq P^{\max}_{\text{CHP}} - \eta_{CHP,2}\phi_{CHP} \end{cases} \tag{17}$$

where P_{CHP} and ϕ_{CHP} are the generated electric and thermal power of CHP units, $P^{\max}_{CHP}$ and $\phi^{\max}_{CHP}$ are the maximum electric and thermal power output of CHP units, and $\eta_{CHP,1}$ and $\eta_{CHP,2}$ are the coefficients in CHP units. The feasible region of heat pump is expressed as the following:

$$\phi_{HP} = \eta_{HP}P_{HP} \tag{18}$$

where P_{HP} and ϕ_{HP} are the consumed electric power and generated thermal power of heat pump; η_{HP} is the conversion coefficient of heat pump.

3 EQUIVALENT THERMAL MODEL

As shown in **Section 2**, the electric load and sources are directly connected through the energy flow in **Eq. 1**. Therefore, adjusting the source output according to the load distribution is comparatively easier. However, the thermal source and loads are connected through pipelines. The states at loads are obtained using the recursive computation based on **Eqs. 6**, **7**, causing an implicit relationship between the thermal sources and loads. In this section, to formulate the direct expression between the temperatures at thermal sources and nodes, an ETM based on the node method is proposed, so that the model of HS can be aggregated like that of PS for further analysis.

Since the HS studied in this article operates at the constant-mass-flow control strategy, the m^{br} and m^{nd} in **Eqs. 5–16** are fixed. In this condition, **Eqs. 8**, **9** can be rewritten as the following:

$$\gamma_{i,t} = \gamma_i,\ \varphi_{i,t} = \varphi_i = \gamma_i + 1 \tag{19}$$

Substituting **Eq. 19** into **Eqs. 12**, **13**, we can get the following:

$$S_{i,t} = S_i,\ R_{i,t} = R_i,\ S_i = R_i \tag{20}$$

Based on **Eq. 12**, **Eqs. 10**, **11** can be simplified as the following:

$$T^{e,s,br}_{i,t} = \beta_{1,i} T^{b,s,br}_{i,t-\varphi_i} + \beta_{2,i} T^{b,s,br}_{i,t-\gamma_i} \tag{21}$$

$$T^{e,r,br}_{i,t} = \beta_{1,i} T^{b,r,br}_{i,t-\varphi_i} + \beta_{2,i} T^{b,r,br}_{i,t-\gamma_i} \tag{22}$$

$$\beta_{1,i} = K_i \frac{m_i \Delta t + A_i L_i \rho - S_i}{m_i \Delta t},\ \beta_{2,i} = K_i \frac{R_i - A_i L_i \rho}{m_i \Delta t} \tag{23}$$

With **Eqs. 21**, **22**, the dynamic thermal conductivity equations are transformed into the linear equations that directly relates the pipe inlet temperature series and pipe outlet temperature. Then, we introduce the following incidence matrixes for simplification.

(1) The incidence matrix that relates the nodes and the corresponding pipelines leaving from the nodes is defined as $\boldsymbol{A}^{+}$. The dimension of $\boldsymbol{A}^{+}$ is $N_d \times N_p$, where N_d and N_p denote the number of nodes and pipelines in HS. The element in $\boldsymbol{A}^{+}$ is expressed as the following:

$$a^{+}_{ij} = \begin{cases} 1 & \text{the mass flow leaving from node } i \\ & \text{and injecting into pipeline } j \\ 0 & \text{node } i \text{ is not releted with} \\ & \text{pipeline } j \text{ topologically} \end{cases} \tag{24}$$

(2) The incidence matrix that relates the nodes and the corresponding pipelines leaving from the nodes is defined as $\boldsymbol{A}^{-}$. The dimension of $\boldsymbol{A}^{-}$ is $N_d \times N_p$. The element in $\boldsymbol{A}^{-}$ is expressed as the following:

$$a^{-}_{ij} = \begin{cases} 1 & \text{the mass flow leaving from pipeline } j \\ & \text{and injecting into node } i \\ 0 & \text{node } i \text{ is not releted with} \\ & \text{pipeline } j \text{ topologically} \end{cases} \tag{25}$$

(3) The incidence matrix that relates the nodes temperature and the pipeline inlet temperature is defined as $\boldsymbol{A}^{tp}$. The dimension of $\boldsymbol{A}^{tp}$ is $N_p \times N_d$. The element in $\boldsymbol{A}^{tp}$ is expressed as the following:

$$a^{tp}_{ij} = \begin{cases} 1 & \text{node } j \text{ is the inlet of pipeline } i \\ 0 & \text{node } j \text{ is not releted} \\ & \text{with pipeline } i \text{ topologically} \end{cases} \tag{26}$$

It should be noted that the mentioned incidence matrixes $\boldsymbol{A}^{+}$, $\boldsymbol{A}^{-}$, and $\boldsymbol{A}^{\mathrm{tp}}$ are constant in HS with constant-mass-flow strategy. However, all these matrixes demonstrate different values in supply and return network. Thus, in this study, $\boldsymbol{A}^{s,+}$ and $\boldsymbol{A}^{r,+}$, $\boldsymbol{A}^{s,-}$ and $\boldsymbol{A}^{r,-}$, and $\boldsymbol{A}^{s,tp}$ and $\boldsymbol{A}^{r,tp}$ are different constant matrixes.

With the incidence matrixes $\boldsymbol{A}^{s,+}$ and $\boldsymbol{A}^{r,+}$, the mass flow leaving from the nodes can be reformulated as **Eq. 27** in matrix form.

$$\boldsymbol{D}^{s,+} = \boldsymbol{A}^{s,+} \boldsymbol{m}^{br} + \boldsymbol{m}^{nd},\ \boldsymbol{D}^{r,+} = \boldsymbol{A}^{r,+} \boldsymbol{m}^{br} - \boldsymbol{m}^{nd} \tag{27}$$

The mass flow injecting into the nodes can be reformulated as **Eq. 28** in matrix form.

$$\boldsymbol{D}^{s,-} = \boldsymbol{A}^{s,-} \mathrm{diag}\left(\boldsymbol{m}^{br}\right),\ \boldsymbol{D}^{r,-} = \boldsymbol{A}^{r,-} \mathrm{diag}\left(\boldsymbol{m}^{br}\right) \tag{28}$$

where diag in the above equations refers to the operation that transforms a vector into a diagonal matrix. Reformulating the temperature equation with **Eqs. 27**, **28**, we can get the following:

$$\boldsymbol{D}^{s,+} \boldsymbol{T}^{s,nd}_{t} = \boldsymbol{D}^{s,-} \boldsymbol{T}^{e,s,br}_{t},\ \boldsymbol{D}^{r,+} \boldsymbol{T}^{r,nd}_{t} = \boldsymbol{D}^{r,-} \boldsymbol{T}^{e,r,br}_{t} \tag{29}$$

Besides, **Eqs. 21**, **22** can be rewritten as the following:

$$\boldsymbol{T}^{e,s,br}_{t} = \boldsymbol{\beta}_1 \boldsymbol{T}^{b,s,br}_{t-\varphi} + \boldsymbol{\beta}_2 \boldsymbol{T}^{b,s,br}_{t-\gamma},\ \boldsymbol{T}^{e,r,br}_{t} = \boldsymbol{\beta}_1 \boldsymbol{T}^{b,r,br}_{t-\varphi} + \boldsymbol{\beta}_2 \boldsymbol{T}^{b,r,br}_{t-\gamma} \tag{30}$$

$$\boldsymbol{\beta}_1 = \mathrm{diag}\left(\beta_{1,i}\right),\ \boldsymbol{\beta}_2 = \mathrm{diag}\left(\beta_{2,i}\right) \tag{31}$$

Substituting **Eqs. 30**, **32** into **Eq. 29**, we can get the following:

$$\begin{aligned} \boldsymbol{D}^{s,+} \boldsymbol{T}^{s,nd}_{t} &= \boldsymbol{D}^{s,-} \left(\boldsymbol{\beta}_1 \boldsymbol{T}^{b,s,br}_{t-\varphi} + \boldsymbol{\beta}_2 \boldsymbol{T}^{b,s,br}_{t-\gamma}\right) \\ &= \boldsymbol{D}^{s,-} \boldsymbol{\beta}_1 \boldsymbol{A}^{s,tp} \boldsymbol{T}^{s,nd}_{t-\varphi} + \boldsymbol{D}^{s,-} \boldsymbol{\beta}_2 \boldsymbol{A}^{s,tp} \boldsymbol{T}^{s,nd}_{t-\gamma} \end{aligned} \tag{32}$$

$$\begin{aligned} \boldsymbol{D}^{r,+} \boldsymbol{T}^{r,nd}_{t} &= \boldsymbol{D}^{r,-} \left(\boldsymbol{\beta}_1 \boldsymbol{T}^{b,r,br}_{t-\varphi} + \boldsymbol{\beta}_2 \boldsymbol{T}^{b,r,br}_{t-\gamma}\right) \\ &= \boldsymbol{D}^{r,-} \boldsymbol{\beta}_1 \boldsymbol{A}^{r,tp} \boldsymbol{T}^{r,nd}_{t-\varphi} + \boldsymbol{D}^{r,-} \boldsymbol{\beta}_2 \boldsymbol{A}^{r,tp} \boldsymbol{T}^{r,nd}_{t-\gamma} \end{aligned} \tag{33}$$

Defining $\boldsymbol{H}^{s1}=\boldsymbol{D}^{s,-}\boldsymbol{\beta}_1\boldsymbol{A}^{s,tp}$, $\boldsymbol{H}^{s2}=\boldsymbol{D}^{s,-}\boldsymbol{\beta}_2\boldsymbol{A}^{s,tp}$, $\boldsymbol{H}^{r1}=\boldsymbol{D}^{r,-}\boldsymbol{\beta}_1\boldsymbol{A}^{r,tp}$, $\boldsymbol{H}^{r2}=\boldsymbol{D}^{r,-}\boldsymbol{\beta}_2\boldsymbol{A}^{r,tp}$, **Eqs. 33**, **35** can be expanded as the following:

$$\begin{aligned} \begin{bmatrix} \boldsymbol{D}^{s,+}_{g} & \boldsymbol{0} & \boldsymbol{0} \\ \boldsymbol{0} & \boldsymbol{D}^{s,+}_{d} & \boldsymbol{0} \\ \boldsymbol{0} & \boldsymbol{0} & \boldsymbol{D}^{s,+}_{l} \end{bmatrix} \begin{bmatrix} \boldsymbol{T}^{s,nd}_{t,g} \\ \boldsymbol{T}^{s,nd}_{t,d} \\ \boldsymbol{T}^{s,nd}_{t,l} \end{bmatrix} &= \begin{bmatrix} \boldsymbol{H}^{s1}_{11} & \boldsymbol{H}^{s1}_{12} & \boldsymbol{H}^{s1}_{13} \\ \boldsymbol{H}^{s1}_{21} & \boldsymbol{H}^{s1}_{22} & \boldsymbol{H}^{s1}_{23} \\ \boldsymbol{H}^{s1}_{31} & \boldsymbol{H}^{s1}_{32} & \boldsymbol{H}^{s1}_{33} \end{bmatrix} \begin{bmatrix} \boldsymbol{T}^{s,nd}_{t-\varphi_g,g} \\ \boldsymbol{T}^{s,nd}_{t-\varphi_d,d} \\ \boldsymbol{T}^{s,nd}_{t-\varphi_l,l} \end{bmatrix} \\ &+ \begin{bmatrix} \boldsymbol{H}^{s2}_{11} & \boldsymbol{H}^{s2}_{12} & \boldsymbol{H}^{s2}_{13} \\ \boldsymbol{H}^{s2}_{21} & \boldsymbol{H}^{s2}_{22} & \boldsymbol{H}^{s2}_{23} \\ \boldsymbol{H}^{s2}_{31} & \boldsymbol{H}^{s2}_{32} & \boldsymbol{H}^{s2}_{33} \end{bmatrix} \begin{bmatrix} \boldsymbol{T}^{s,nd}_{t-\gamma_g,g} \\ \boldsymbol{T}^{s,nd}_{t-\gamma_d,d} \\ \boldsymbol{T}^{s,nd}_{t-\gamma_l,l} \end{bmatrix} \end{aligned} \tag{34}$$

$$\begin{aligned} \begin{bmatrix} \boldsymbol{D}^{r,+}_{g} & \boldsymbol{0} & \boldsymbol{0} \\ \boldsymbol{0} & \boldsymbol{D}^{r,+}_{d} & \boldsymbol{0} \\ \boldsymbol{0} & \boldsymbol{0} & \boldsymbol{D}^{r,+}_{l} \end{bmatrix} \begin{bmatrix} \boldsymbol{T}^{r,nd}_{t,g} \\ \boldsymbol{T}^{r,nd}_{t,d} \\ \boldsymbol{T}^{r,nd}_{t,l} \end{bmatrix} &= \begin{bmatrix} \boldsymbol{H}^{r1}_{11} & \boldsymbol{H}^{r1}_{12} & \boldsymbol{H}^{r1}_{13} \\ \boldsymbol{H}^{r1}_{21} & \boldsymbol{H}^{r1}_{22} & \boldsymbol{H}^{r1}_{23} \\ \boldsymbol{H}^{r1}_{31} & \boldsymbol{H}^{r1}_{32} & \boldsymbol{H}^{r1}_{33} \end{bmatrix} \begin{bmatrix} \boldsymbol{T}^{r,nd}_{t-\varphi_g,g} \\ \boldsymbol{T}^{r,nd}_{t-\varphi_d,d} \\ \boldsymbol{T}^{r,nd}_{t-\varphi_l,l} \end{bmatrix} \\ &+ \begin{bmatrix} \boldsymbol{H}^{r2}_{11} & \boldsymbol{H}^{r2}_{12} & \boldsymbol{H}^{r2}_{13} \\ \boldsymbol{H}^{r2}_{21} & \boldsymbol{H}^{r2}_{22} & \boldsymbol{H}^{r2}_{23} \\ \boldsymbol{H}^{r2}_{31} & \boldsymbol{H}^{r2}_{32} & \boldsymbol{H}^{r2}_{33} \end{bmatrix} \begin{bmatrix} \boldsymbol{T}^{r,nd}_{t-\gamma_g,g} \\ \boldsymbol{T}^{r,nd}_{t-\gamma_d,d} \\ \boldsymbol{T}^{r,nd}_{t-\gamma_l,l} \end{bmatrix} \end{aligned} \tag{35}$$

where the subscripts g, d, and l denote the source nodes, branch nodes, and load nodes in HS, respectively; T^{nd}_{g}, T^{nd}_{b}, and T^{nd}_{l} are the node temperature vectors at source, branch, and load nodes, respectively.

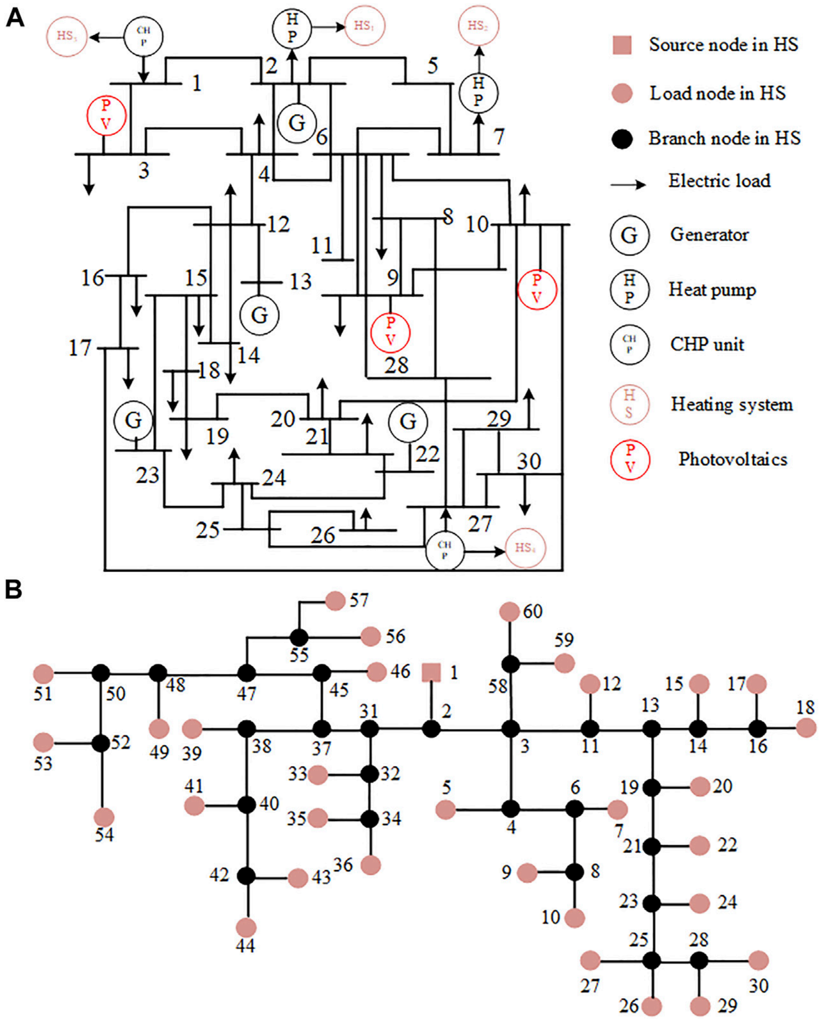

FIGURE 3 | Structure of integrated heat and electricity systems in case study. **(A)** Structure of power system. **(B)** Structure of heating system.

According to the topology of HS shown in **Figure 1**, the mass flow leaving from sources must equal to its injecting mass flow. Thus, $D_g^{s,+}$ in **Eq. 35** must be **0**. Besides, the mass flow cannot leave from the branch nodes and inject into the source nodes nor leave from the load nodes and inject into branch nodes through the pipelines. Therefore, H_{23}^{s1} and H_{33}^{s1} must be **0**. Since the source nodes are equivalent loads and the load nodes are equivalent sources in the return network, $D_l^{r,+}$, H_{21}^{r1}, and H_{31}^{r1} are also **0**. On this basis, the latter two rows in **Eq. 35** can be rewritten as the following:

$$\boldsymbol{T}_{t,d}^{s,nd} = \left(\boldsymbol{D}_d^{s,+}\right)^{-1}\left(\boldsymbol{H}_{21}^{s1}\left(\boldsymbol{T}_{t-\varphi_g,g}^{s,nd} + \boldsymbol{T}_{t-\gamma_g,g}^{s,nd}\right) + \boldsymbol{H}_{22}^{s1}\left(\boldsymbol{T}_{t-\varphi_d,d}^{s,nd} + \boldsymbol{T}_{t-\gamma_d,d}^{s,nd}\right)\right) \tag{36}$$

$$\boldsymbol{T}_{t,l}^{s,nd} = \left(\boldsymbol{D}_l^{s,+}\right)^{-1}\left(\boldsymbol{H}_{31}^{s1}\left(\boldsymbol{T}_{t-\varphi_g,g}^{s,nd} + \boldsymbol{T}_{t-\gamma_g,g}^{s,nd}\right) + \boldsymbol{H}_{32}^{s1}\left(\boldsymbol{T}_{t-\varphi_d,d}^{s,nd} + \boldsymbol{T}_{t-\gamma_d,d}^{s,nd}\right)\right) \tag{37}$$

Also, similarly, the former two rows in **Eq. 36** can be rewritten as the following:

$$\boldsymbol{T}_{t,d}^{r,nd} = \left(\boldsymbol{D}_d^{r,+}\right)^{-1}\left(\boldsymbol{H}_{22}^{r1}\left(\boldsymbol{T}_{t-\varphi_g,d}^{r,nd} + \boldsymbol{T}_{t-\gamma_g,d}^{r,nd}\right) + \boldsymbol{H}_{23}^{r1}\left(\boldsymbol{T}_{t-\varphi_d,l}^{r,nd} + \boldsymbol{T}_{t-\gamma_d,l}^{r,nd}\right)\right) \tag{38}$$

$$\boldsymbol{T}_{t,g}^{r,nd} = \left(\boldsymbol{D}_g^{r,+}\right)^{-1}\left(\boldsymbol{H}_{12}^{r1}\left(\boldsymbol{T}_{t-\varphi_d,d}^{r,nd} + \boldsymbol{T}_{t-\gamma_d,d}^{r,nd}\right) + \boldsymbol{H}_{13}^{r1}\left(\boldsymbol{T}_{t-\varphi_l,l}^{r,nd} + \boldsymbol{T}_{t-\gamma_l,l}^{r,nd}\right)\right) \tag{39}$$

Eqs. 37–40 are the equivalent aggregation of the thermal model in HS, which combine the states at source nodes and the other nodes. As a result, the influence of adjustments at the sources on the other nodes can be directly reflected.

4 SECURITY REGION OF INTEGRATED HEAT AND ELECTRICITY SYSTEM

In the IHES, the electric and thermal states are determined by the output of generators and coupling units. To ensure the operational security, the operators need to adjust the controllable states to restrict the controlled states within a

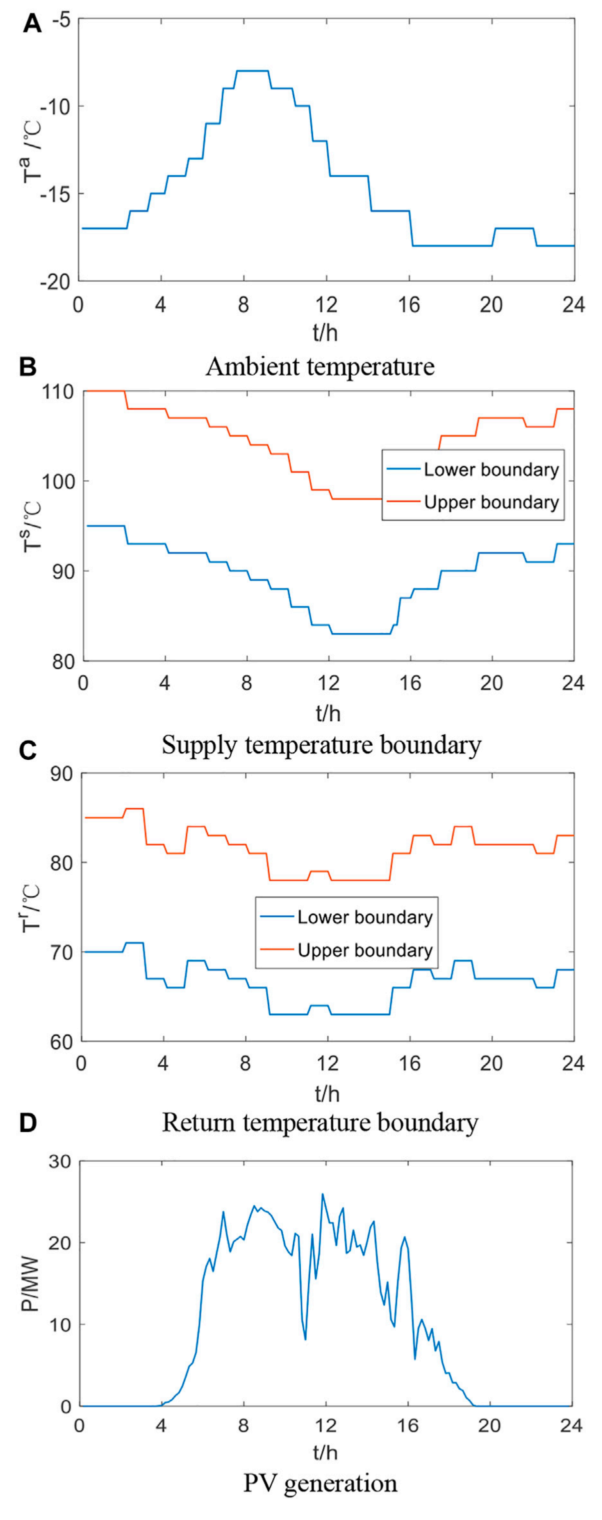

FIGURE 4 | Parameters in heating system.

feasible range. Defining x as the controllable states, y as the controlled states, f as the equality equations that determines the SRB, g as the inequality equations that determines the SRB, the SR of IHES is constructed below.

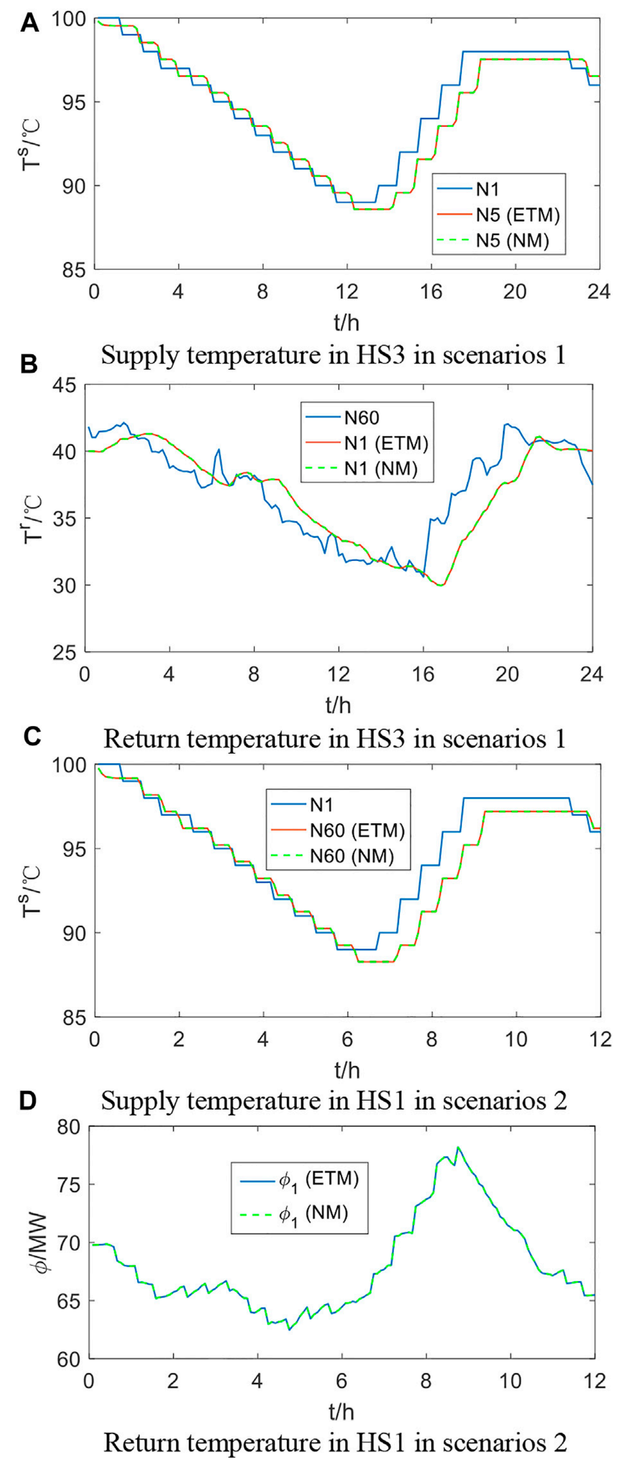

FIGURE 5 | Simulation results in heating system.

4.1 Model of Security Region

In the PS, the controllable states refer to the active power output of the generators, while the controlled states refer to the active power consumption of electric loads, the active power output of PVs, the active branch power flow, and the bus voltage phase

TABLE 1 | Computation time comparison.

Scenario	HS1-ETM (s)	HS1-NM (s)	HS3-ETM (s)	HS3-NM (s)
1	0.0047	0.012	0.0049	0.010
2	0.0056	0.010	0.0054	0.0098

angle (Chen et al., 2017). The SR in PS with DC power flow model is expressed as the following:

$$\begin{cases} \boldsymbol{x}_e = (\boldsymbol{P}_G),\ \boldsymbol{y}_e = \left(\boldsymbol{P}_V, \boldsymbol{P}_L, \boldsymbol{P}_{ij}, \boldsymbol{\theta}\right) \\ SR_e = \{\boldsymbol{y}_e\colon \boldsymbol{f}_e(\boldsymbol{x}_e, \boldsymbol{y}_e) = 0,\ \boldsymbol{g}_e(\boldsymbol{x}_e, \boldsymbol{y}_e) = 0\} \end{cases} \tag{40}$$

The equality equation $\boldsymbol{f}_e$ contains **Eqs. 1–3**. The inequality equation $\boldsymbol{g}_e$ contains the constraints on the active power output of generators and PVs, the active power flow on the branches, and the phase angles, as shown below.

$$\begin{aligned} &P_G^{\min} \le P_G \le P_G^{\max},\ 0 \le P_V \le P_V^{\max}, \\ &P_{ij}^{\min} \le P_{ij} \le P_{ij}^{\max},\ -\pi \le \theta \le \pi \end{aligned} \tag{41}$$

In the HS, the controllable states refer to the thermal power output of the heat pumps and CHPs, while the controlled states refer to the node supply and return temperature. The SR in HS with ETM is expressed as the following:

$$\begin{cases} \boldsymbol{x}_h = (\boldsymbol{\phi}_{CHP}, \boldsymbol{\phi}_{HP}),\ \boldsymbol{y}_e = \left(\boldsymbol{T}^{s.nd}, \boldsymbol{T}^{r.nd}\right) \\ SR_h = \{\boldsymbol{y}_h\colon \boldsymbol{f}_h(\boldsymbol{x}_h, \boldsymbol{y}_h) = 0,\ \boldsymbol{g}_h(\boldsymbol{x}_h, \boldsymbol{y}_h) = 0\} \end{cases} \tag{42}$$

The equality equation $\boldsymbol{f}_h$ contains **Eqs. 5**, **37–40**. The inequality equation $\boldsymbol{g}_h$ contains three parts: 1) thermal comfort constraints of load supply temperature; 2) thermal security constraints of return temperature and source supply temperature; 3) thermal power constraints of source output; the ramping rate constraints of CHP units, which are shown in **Eqs. 44–47**, respectively.

$$T_l^{s,nd,\min} \le T_l^{s,nd} \le T_l^{s,nd,\max},\ T_d^{s,nd,\min} \le T_d^{s,nd} \le T_d^{s,nd,\max} \tag{43}$$

$$T^{r,nd,\min} \le T^{r,nd} \le T^{r,nd,\max},\ T_g^{s,nd,\min} \le T_g^{s,nd} \le T_g^{s,nd,\max} \tag{44}$$

$$\phi_g^{\min} \le \phi_g \le \phi_g^{\max} \tag{45}$$

$$-\delta\phi_{\mathrm{CHP}}^{\max} \le \phi_{\mathrm{CHP},t} - \phi_{\mathrm{CHP},t-1} \le \delta\phi_{\mathrm{CHP}}^{\max} \tag{46}$$

where ϕ_g^{min} and ϕ_g^{max} denote the minimum and maximum output of thermal source; $T_{l/d/g}^{s,nd,min}$ and $T_{l/d/g}^{s,nd,max}$ denote the minimum and maximum supply temperature at the load/branch/source nodes; $T^{r,nd,min}$ and $T^{r,nd,max}$ denote the minimum and maximum return temperature; δ denote the ramping rate of CHP units, which is 0.05 in this article. The SR for IHES is the intersection of the SRs of PS and HS with the constraints on the coupling units considered. The model of SR for IHES is expressed as the following:

$$SR_{IHES} = \left\{ \begin{array}{l} (\boldsymbol{y}_h, \boldsymbol{y}_e)\colon \\ \boldsymbol{f}_e(\boldsymbol{x}_e, \boldsymbol{y}_e) = 0, \boldsymbol{f}_h(\boldsymbol{x}_h, \boldsymbol{y}_h) = 0, \boldsymbol{f}_{cp}(\boldsymbol{x}_h, \boldsymbol{y}_h, \boldsymbol{x}_e, \boldsymbol{y}_e) = 0 \\ \boldsymbol{g}_e(\boldsymbol{x}_e, \boldsymbol{y}_e) \le 0, \boldsymbol{g}_h(\boldsymbol{x}_h, \boldsymbol{y}_h) \le 0, \boldsymbol{g}_{cp}(\boldsymbol{x}_h, \boldsymbol{y}_h, \boldsymbol{x}_e, \boldsymbol{y}_e) \le 0 \end{array} \right\} \tag{47}$$

where $\boldsymbol{f}_{cp}$ contains the equality constraints in **Eq. 18**, and $\boldsymbol{g}_{cp}$ contains inequality constraints in **Eq. 17**.

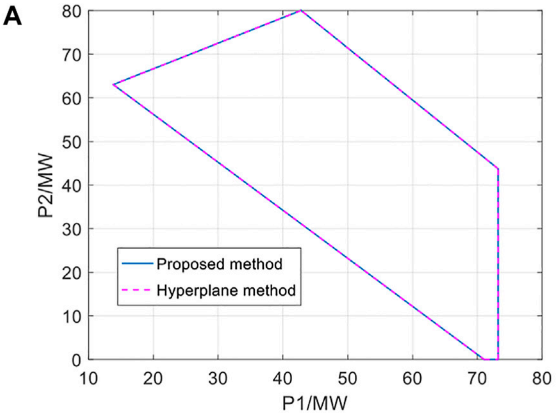

SR of IHES for generator 1 and 2 with PV

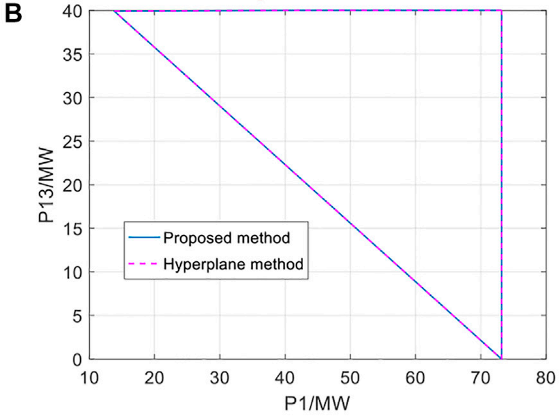

SR of IHES for generator 1 and 13 with PV

FIGURE 6 | Security region comparison between the proposed method and hyperplane method.

4.2 Formulation of Security Region Boundary

The SRB corresponds to a set of critical operation points where one of the inequality constraints becomes equality constraints, while the other inequality constraints are satisfied. Since the constraints in **(47)** are linear, the SRB can be obtained by solving the upper and lower boundaries with linear programming. In this article, Matlab 2018b is used for programming, and Cplex 12.9 is used for problem solving.

5 CASE STUDIES

To verify the effectiveness of the proposed method, a modified system is studied to investigate the SR of IHES. The IHES contains a modified IEEE 30-bus system and four independent HSs. Three PVs are integrated into the PS at buses 3, 9, and 10. The four HSs and PSs are coupled with 2 CHP units and 2 heat pumps. The four HSs demonstrate the same structure but different parameters. The diagram of the IHES is shown in **Figure 3** and all the parameters are given in (Baidu, 1234).

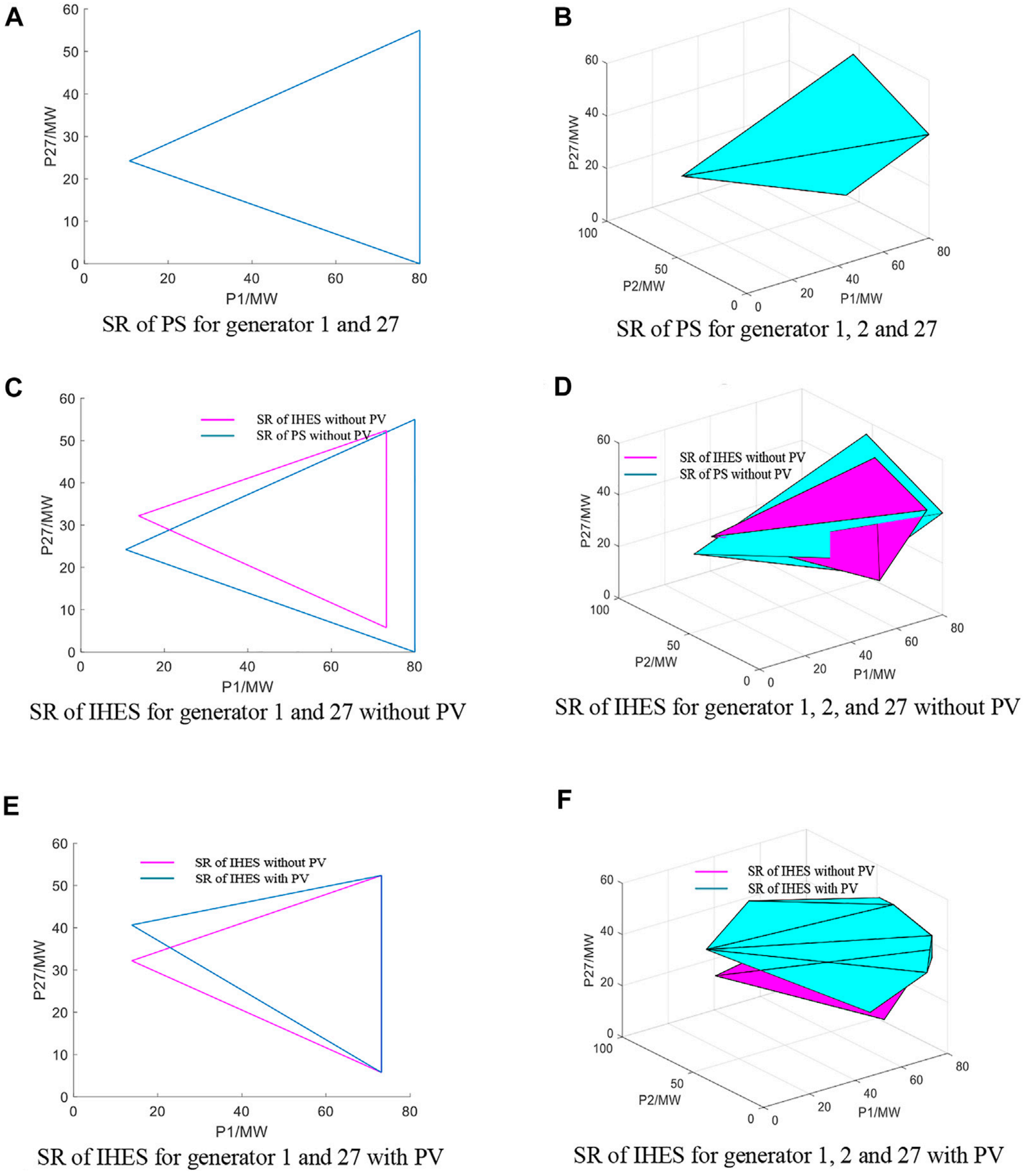

FIGURE 7 | Security region in power system and integrated heat and electricity systems.

The curves of ambient temperature, PV output, the upper and lower boundaries of node temperature in HS are shown in **Figure 4**. The simulation contains two aspects: 1) verify the accuracy of the proposed ETM and 2) analyze the influence of thermal dynamics on SR of HS. Next, to verify the accuracy of ETM, the recursion-based node method (NM) in (Li et al., 2016) is used as reference in **Section 5.1**.

5.1 Accuracy of the Equivalent Thermal Model

In this section, the proposed ETM is compared with the recursion-based NM to verify the effectiveness. Two systems (HS1 and HS2) are simulated in two scenarios, including the following: scenario 1) $\Delta t = 10$ min; scenarios and 2) $\Delta t = 5$ min. The results are shown in **Figure 5**. As shown the figures, with the given boundary conditions, the results by ETM and NM are the same regardless of different simulation steps. This is understandable because the ETM is derived from NM without any simplification. However, to obtain the explicit expression of the load temperature, the ETM directly relates all the node temperature. As a consequence, the recursion is no longer needed during computation. The comparison regarding the computation time is given in **Table 1**, which further indicates the superiority of the ETM in efficiency.

5.2 Influence of Thermal Dynamics on Security Region of Power System

This section aims to verify the accuracy of the proposed SR model and analyze the influence of thermal dynamics on SR of PS. First, we compare the calculated SR with the hyperplane method proposed in (Li et al., 2020). The results are shown in **Figure 6**. As shown in the figures, the results by the proposed method and hyperplane method are almost the same. The area of SR for generator 1 and 2 and generator 1 and 13 by two methods is 2,149 MW^2 and 1,189 MW^2, respectively. This is understandable because the proposed method is completely linear. With the proposed method, no approximation or simplification occurs during the SR construction. Thus, the SR boundary governed by **Eq. 47** is essentially a set of multivariate linear equations, which is the same with the traditional hyperplane method.

Then, we performed the analysis to investigate the SR in IHES. The analysis contains two aspects: 1) analyze the influence of thermal dynamics, as shown in the comparison of **Figures 7A–D**; 2) analyze the influence of PV integration, as shown in the comparison of **Figures 7C–F**. From the figures, it is obvious that the combined operation shrinks the size of the SR in PS, since additional constraints from HS are added into the SR formulation. To ensure that the node temperature in HS satisfies the thermal comfort, the PS is required to increase the minimum active power generation and decrease the maximum active power generation. The size of SR in PS shrinks up to 15.6% in average. From **Figures 7C–F**, the observation exists that significant changes occur on the SR of IHES when the system is integrated with PV. The uncertain generation of PV is usually considered as an equivalent PQ bus with negative active power consumption. Next, the PV integration decreases the active power consumption in the whole system so that the generators can provide the active power in a wider range. As a consequence, the SR of IHES expands in both 2-dimensional and 3-dimensional space.

6 CONCLUSION

In order to explore the combined analysis of PS and HS integration, this study studies the operational security of the IHES based on SR. First, an ETM is proposed to build the direct relationship between the source states and load states in HS, with which the response to load fluctuation can be constructed at generators. On this basis, the SR of IHES, considering the thermal dynamics, is constructed, including the recognition of controlled/controllable variables and the formulation of the SRB. Next, finally, the influence of PV uncertainty on the SR of IHES is further analyzed. Case studies indicate that the proposed ETM is efficient for heating system analysis, and the combined operation of PS and HS will shrink the size of SR due to the additional constraints from HS side. Besides, the PV uncertainty demonstrates significant influence of the SR of IHES and is likely to increase the size of SR by providing extra generation capacity. The integration of large-scale heating systems and the dynamics from coupling equipment side will be the future research focus to explore the influence of the thermal dynamics on the PS.

DATA AVAILABILITY STATEMENT

The original contributions presented in the study are included in the article/Supplementary Material, and further inquiries can be directed to the corresponding author.

AUTHOR CONTRIBUTIONS

Zhuhua Wang: Conceptualization, methodology and writing; Wencheng Huang: Paper revision; Xiaowei Cai: Response and proofreading.

FUNDING

This work was supported by Regional Development Project of Fujian Provincial Department of Science and Technology (Grant. 2021H4025).

REFERENCES

Baidu Case Data Online. Available at: https://pan.baidu.com/s/1BZJ-VoWz931gWRECKP9l3w (The secret is 1234.

Bitar, E., Khargonekar, P. P., and Poolla, K. (2011). Systems and Control Opportunities in the Integration of Renewable Energy into the Smart Grid. *IFAC Proc. Vol.* 44, 4927–4932. doi:10.3182/20110828-6-it-1002.01244

Chen, H., Shao, J., Jiang, T., Zhang, R., Li, X., and Li, G. (2020). Security Control Measures for Integrated Energy System Based on Sensitivity Analysis. *Proc. CSEE* 15.

Chen, S., Wei, Z., Sun, G., Wei, W., and Wang, D. (2017). Convex Hull Based Robust Security Region for Electricity-Gas Integrated Energy Systems. *IEEE Trans. Power Syst.* 34 (3), 1740–1748. doi:10.1109/TPWRS.2018.2888605

Chiang, H.-D., and Jiang, C.-Y. (2018). Feasible Region of Optimal Power Flow: Characterization and Applications. *IEEE Trans. Power Syst.* 33 (1), 236–244. doi:10.1109/tpwrs.2017.2692268

Cruz, M. R. M., Fitiwi, D. Z., Santos, S. F., and Catalão, J. P. S. (2018). A Comprehensive Survey of Flexibility Options for Supporting the Low-Carbon Energy Future. *Renew. Sustain. Energy Rev.* 97, 338–353. doi:10.1016/j.rser.2018.08.028

He, C, Wu, L., Liu, T., and Bie, Z. (2018). Robust Co-Optimization Planning of Interdependent Electricity and Natural Gas Systems with a Joint N-1 and Probabilistic Reliability Criterion. *IEEE Trans. Power Syst.* 33 (2), 2140–2154. doi:10.1109/TPWRS.2017.2727859

Jahromi, A. A., and Bouffard, F. (2017). On the Loadability Sets of Power Systems-Part I: Characterization. *IEEE Trans. Power Syst.* 32 (1), 137–145. doi:10.1109/tpwrs.2016.2547945

Jiang, X. S., Jing, Z. X., Li, Y. Z., Wu, Q. H., and Tang, W. H. (2014). Modelling and Operation Optimization of an Integrated Energy Based Direct District Water-Heating System. *Energy* 64, 375–388. doi:10.1016/j.energy.2013.10.067

Li, X., Tian, G., Shi, Q., Jiang, T., Li, F., and Jia, H. (2020). Security Region of Natural Gas Network in Electricity-Gas Integrated Energy System. *Int. J. Electr. Power & Energy Syst.* 117, 105601. doi:10.1016/j.ijepes.2019.105601

Li, Z., Wu, W., Shahidehpour, M., Wang, J., and Zhang, B. (2016). Combined Heat and Power Dispatch Considering Pipeline Energy Storage of District Heating Network. *IEEE Trans. Sustain. Energy* 7 (1), 12–22. doi:10.1109/tste.2015.2467383

Li, Z., and Xu, Y. (2019). Temporally-coordinated Optimal Operation of a Multi-Energy Microgrid Under Diverse Uncertainties. *Appl. Energy* 240, 719–729. doi:10.1016/j.apenergy.2019.02.085

Liu, C.-C. (1986). A New Method for the Construction of Maximal Steady-State Security Regions of Power Systems. *IEEE Trans. Power Syst.* 1 (4), 19–26. doi:10.1109/tpwrs.1986.4335009

Liu, L., Wang, D., Hou, K., Jia, H., and Li, S. (2020). Region Model and Application of Regional Integrated Energy System Security Analysis. *Appl. Energy* 280, 115072. doi:10.1016/j.apenergy.2019.114268

Ma, H., Wang, B., Gao, W., Liu, D., Sun, Y., and Liu, Z. (2018). Optimal Scheduling of a Regional Integrated Energy System with Energy Storage Systems for Service Regulation. *Energies* 11, 195. doi:10.3390/en11010195

Mancarella, P. (2014). MES (Multi-energy Systems): An Overview of Concepts and Evaluation Models. *Energy* 65, 1–17. doi:10.1016/j.energy.2013.10.041

Nan, L., Wu, L., Liu, T., Liu, Y., and He, C. (2020). Vulnerability Identification and Evaluation of Interdependent Natural Gas-Electricity Systems. *IEEE Trans. Smart Grid* 11 (4), 3558–3569. doi:10.1109/tsg.2020.2968178

Sanjari, M. J., Karami, H., and Gooi, H. B. (2016). Micro-generation Dispatch in a Smart Residential Multi-Carrier Energy System Considering Demand Forecast Error. *Energy Convers. Manag.* 120, 90–99. doi:10.1016/j.enconman.2016.04.092

Sina (2009). Electric and Thermal Power Failure in Harbin. Available at: http://news.sina.com.cn/o/2009-11-15/060816609684s.shtml

Wei, W., Liu, F., and Mei, S. (2015). Dispatchable Region of the Variable Wind Generation. *IEEE Trans. Power Syst.* 30 (5), 2755–2765. doi:10.1109/tpwrs.2014.2365555

Wei, X., Zhao, J., Huang, T., and Bompard, E. (2018). A Novel Cascading Faults Graph Based Transmission Network Vulnerability Assessment Method. *IEEE Trans. Power Syst.* 33 (3), 2995–3000. doi:10.1109/tpwrs.2017.2759782

Xiao, J., Guo, W., Wang, C., and Li, F. (2012). Distribution System Security Region: Definition, Model and Security Assessment. *IET Gene. Trans. Dis.* 6 (12), 1029–1035. doi:10.1049/iet-gtd.2011.0767

Xiao, J., Zu, G., Gong, X., and Li, F. (2017). Observation of Security Region Boundary for Smart Distribution Grid. *IEEE Trans. Smart Grid* 8 (4), 1731–1738. doi:10.1109/tsg.2015.2505325

Yan, J., He, H., and Sun, Y. (2014). Integrated Security Analysis on Cascading Failure in Complex Networks. *IEEE Trans.Inform.Forensic Secur.* 9 (3), 451–463. doi:10.1109/tifs.2014.2299404

Zhang, S., Gu, W., Lu, S., Yao, S., Zhou, S., and Chen, X. (2021). Dynamic Security Control in Heat and Electricity Integrated Energy System with an Equivalent Heating Network Model. *IEEE Trans. Smart Grid* 12 (6), 4788–4798. doi:10.1109/TSG.2021.3102057

Zhang, S., Gu, W., Yao, S., Lu, S., Zhou, S., and Wu, Z. (2021). Partitional Decoupling Method for Fast Calculation of Energy Flow in a Large-Scale Heat and Electricity Integrated Energy System. *IEEE Trans. Sustain. Energy* 12 (1), 501–513. doi:10.1109/tste.2020.3008189

Conflict of Interest: The authors declare that the research was conducted in the absence of any commercial or financial relationships that could be construed as a potential conflict of interest.

NOMENCLATURE

Abbreviations

IHES Integrated heating and electricity system

PS Power system

HS Heating system

ETM Equivalent thermal model

CHP Combined heat and power

PV Photovoltaic

SR Security region

DC Direct current

NM Node method

Indices

$\boldsymbol{L/V/G}$ Subscript of load/photovoltaic/generator in PS

$\boldsymbol{nd/br}$ Superscript of node/pipeline in HS

$\boldsymbol{s/r}$ Superscript of supply/return network

$\boldsymbol{b/e}$ Superscript of beginning/end of the pipeline

$\boldsymbol{Lv/In}$ Set of leaving/injecting pipelines

$\boldsymbol{e/h/cp}$ Subscript of variables in PS/HS/coupling units

$\boldsymbol{g/d/l}$ Subscript of source/branch/load node in HS

Parameters and Variables

$\boldsymbol{P}$ Active power

$\boldsymbol{\theta}$ Voltage phase angle

$\boldsymbol{P_{ij}}$ Active/reactive power at electric branch

$\boldsymbol{T'/T}$ Absolute/relative temperature

$\boldsymbol{T^{amb}}$ Ambient temperature

$\boldsymbol{m}$ Mass flow rate

$\boldsymbol{\phi}$ Thermal power

$\boldsymbol{A/L/\lambda}$ Cross-section area/length of pipeline

$\boldsymbol{C/\rho}$ Specific heat capacity/density of water

$\boldsymbol{\varphi/\gamma}$ Time labels in node method

$\boldsymbol{R_t}$ Injected mass flow between t and t-γ_t

$\boldsymbol{S_t}$ Injected mass flow between t and t-φ_t+1

$\boldsymbol{\Delta t}$ Time interval

$\boldsymbol{K}$ Transfer coefficient in node method

$\boldsymbol{\eta}$ Coefficients in CHP and heat pump model

$\boldsymbol{\beta}$ Coefficients in ETM

$\boldsymbol{A^{+/-/\mathrm{tp}}}$ Topological incidence matrix in ETM

$\boldsymbol{D^{+/-}}$ Mass flow matrix leaving from/injecting into nodes in ETM

$\boldsymbol{H^{+/-}}$ Mass flow matrix leaving from/injecting into nodes in ETM

$\boldsymbol{H_{ij}^{1/2}}$ Coefficient matrixes in ETM

$\boldsymbol{x/y}$ Controllable/controlled state

$\boldsymbol{f/g}$ Equality/inequality equations in IEHS

$\boldsymbol{\delta}$ Rampling rate of CHP unit

Frontiers in
Energy Research

Advances and innovation in sustainable, reliable and affordable energy

Explores sustainable and environmental developments in energy. It focuses on technological advances supporting Sustainable Development Goal 7: access to affordable, reliable, sustainable and modern energy for all.

Discover the latest Research Topics

See more →

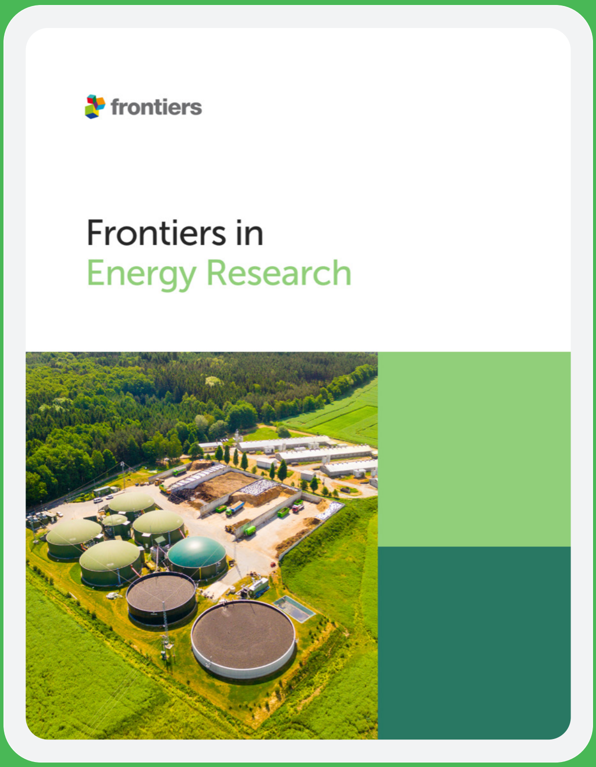

frontiers

Frontiers in
Energy Research

Frontiers

Avenue du Tribunal-Fédéral 34
1005 Lausanne, Switzerland
frontiersin.org

Contact us

+41 (0)21 510 17 00
frontiersin.org/about/contact